UNDERSTANDING THE ROLE OF MATERIALS IN THE DURABILITY OF PRESTRESSED CONCRETE IN MARINE ENVIRONMENTS

A Dissertation
Presented to
The Academic Faculty

By

Alvaro Paul

In Partial Fulfillment
of the Requirements for the Degree
Doctor of Philosophy in the
School of Civil and Environmental Engineering

Georgia Institute of Technology
December 2015

UNDERSTANDING THE ROLE OF MATERIALS IN THE DURABILITY OF PRESTRESSED CONCRETE IN MARINE ENVIRONMENTS

Approved by:

Dr. Lawrence F. Kahn, Co-advisor
School of Civil and Environmental Engineering
Georgia Institute of Technology

Dr. Kimberly E. Kurtis, Co-advisor
School of Civil and Environmental Engineering
Georgia Institute of Technology

Dr. Preet M. Singh
School of Materials Science and Engineering
Georgia Institute of Technology

Dr. Mauricio Lopez
Department of Construction Engineering and Management
Pontificia Universidad Católica de Chile

Dr. T. Russell Gentry
School of Architecture
Georgia Institute of Technology

Date Approved: November 02, 2015

ACKNOWLEDGEMENTS

The completion of this PhD has been a hard and demanding process that I would not be able to overcome without the help of many people.

First and most importantly, I would like to express my deepest gratitude to my family for their endless encouragement throughout these years and the unconditional support even at the most difficult times. They provided the main motivation to successfully complete my PhD at Georgia Tech.

I would also like to thank my advisors, Dr. Kimberly Kurtis and Dr. Lawrence Kahn, for their patience, advice, and guidance during my research. They provided insightful comments and challenging discussion to my work that helped me improve as a researcher and engineer. Dr. Preet Singh was an active member of the two research projects that comprise this thesis and offered kind support and extremely valuable help in the corrosion testing. I also appreciate the time and suggestions of my committee members Dr. Mauricio Lopez and Dr. Russell Gentry.

I am very grateful of my coworker and friend Captain Lorintz Gleich, who played a key role in the construction, testing, and analysis of prestressed concrete piles reinforced with stainless steel. I also extend my gratitude to Nan Gao, who provided remarkable collaboration during testing of the flexure and shear capacity of the piles.

During these years, I have been very lucky to find the company and support of an invaluable group of people. Help given by Dr. Amal Jayapalan, Dr. Boyeon Lee, Dr. Passarin Jongvisuttisun, Dr. Chris Shearer, Dr. Nathan Mayercsik, Dr. Lisa Burris, Dr. Giovanni Loreto, Daniel Schuetz, Mitchell McKay, Bradley Dolphyn, Marc Knapp,

Elizabeth Nadelman, Mehdi Rashidi, Behnaz Zaribaf, Ahmad Shalan, Michel Badetti, Natalia Cardelino, La Sasha Walker, Prasanth Alapati, and Gun Kim included smart technical contributions, but also generous personal advice, friendship, and outstanding support. I also want to thank Seo-Hun Lee, Oghuzan Togay, Chris Wilson, Humberto Orellana, and Alissa Hooker for their friendship and company during the early stages of my life in Atlanta.

I would like to acknowledge the valuable assistance provided by undergraduate research assistants Simon Reiter, Daniela Remolina, Jaime Ghitelman, John Jung, and Tyler Young.

I would like to express my gratitude to the staff of the School of Civil and Environmental Engineering, especially Daniela Estrada, who was another member of our group and a friend during all these years, and Jeremy Mitchell, the manager of the Structures and Materials Lab, who was always available to provide guidance and technical assistance.

The financial support for the development of this research was provided by the Georgia Department of Transportation through Research Project Numbers 11-34 and 13-15. Also GDOT members Mr. Paul Liles, Assistant Division Director of Engineering; Mr. Ben Rabun, Bridge and Structures Engineer; Mr. Scott Harris, Aggregate Geologist; Ms. Georgene Geary, State Research Engineer; Mr. Peter Wu, Bureau Chief; and Ms. Supriya Kamatkar, Research Engineer, provided many valuable suggestions and help throughout the research. Mr. Richard Potts, Mr. Doug Pankey, Mr. Jesus Marin and Mr. Joe Shepherd of Standard Concrete Products along with Mr. Bill Johnston of TIC Marine and Heavy Civil Corp. were very helpful with all pile construction operations.

TABLE OF CONTENTS

LIST OF TABLES

LIST OF FIGURES

LIST OF SYMBOLS

95% AMS	95% of the average maximum strain for transfer length determination
A	Al_2O_3 in cement chemistry notation
C	CaO in cement chemistry notation
$\overline{C}$	CO_2 in cement chemistry notation
C_2S	Belite, dicalcium silicate ($2CaO \cdot SiO_2$ or Ca_2SiO_4)
C_3A	Aluminate, tricalcium aluminate ($3CaO \cdot Al_2O_3$ or $Ca_3Al_2O_6$)
C_3S	Alite, tricalcium silicate ($3CaO \cdot SiO_2$ or Ca_3SiO_5)
C_4AF	Ferrite, tetracalcium aluminoferrite ($4CaO \cdot Al_2O_3 \cdot Fe_2O_3$ or Ca_2AlFeO_5)
CH	Calcium hydroxide
C-S-H	Calcium silicate hydrate phase
d_b	Nominal diameter of strand
E_c (E)	Concrete modulus of elasticity
E_{ci}	Concrete modulus of elasticity at release
F	Fe_2O_3 in cement chemistry notation
f_{cgp}	Concrete stress at the center of gravity of prestressing strands
$f_{c,28}'$	Concrete compressive strength at 28 days
f'_c	Design compressive strength of concrete
f_{ci}'	Concrete compressive strength at release
f_{pe} (f_{se})	Effective stress in the prestressing steel after losses
f_{ps}	Stress in the prestressing strand at nominal strength of member

f_{pu} (f_{su})	Tensile strength of prestressing strand
f_{pt}	Stress in the prestressing strand prior to transfer
f_{py}	Yield strength of prestressing strand
f_{si} (f_{si})	Stress in prestressing strand after strand release
f_{sp}	Splitting tensile strength of concrete
H	H_2O in cement chemistry notation
K	K_2O in cement chemistry notation
l_d	Development length
l_e	Embedment length for development length testing
l_t	Transfer length
M	MgO in cement chemistry notation
M_{cr}	Cracking moment
M_n	Nominal flexural resistance
N	Na_2O in cement chemistry notation
S	SiO_2 in cement chemistry notation
$\overline{S}$	SO_3 in cement chemistry notation
V_{cw}	Nominal shear resistance provided by tensile stresses in concrete
V_u	Factored shear force
w/c	Water to cement mass ratio
w/cm	Water to cementitious material mass ratio
ε_u	Strain in prestressing strand at ultimate state
κ	AASHTO multiplier for development length estimation

LIST OF ABBREVIATIONS

AASHTO	American Association of State Highway and Transportation Officials
ACI	American Concrete Institute
AISI	American Iron and Steel Institute
APE	American Pile Driving Equipment, Inc.
ASR	Alkali-silica reaction
ASTM	American Society for Testing and Materials
BSE	Backscattered electron
CSS	Concrete surface strain method for transfer length determination
CTL	Chloride threshold level
DEF	Delayed ettringite formation
DEMEC	Detachable Mechanical Strain Gauge
EAC	Environmentally assisted cracking
EDS	Energy-Dispersive X-Ray Spectroscopy
FHWA	Federal Highway Administration
GDOT	Georgia Department of Transportation
HE	Hydrogen embrittlement
HPC	High-performance concrete
HSC	High-strength concrete
HSSS	High-strength stainless steel
ISA	Internal sulfate attack

ITZ	Interfacial transition zone
LRFD	Load and Resistance Factor Design
LVDT	Linear Variable Displacement Transformer
MSA	Maximum size (diameter) of aggregate
PREN	Pitting resistance equivalency number
RCPT	Rapid Chloride Permeability Test
RH	Relative humidity
SCC	Stress corrosion cracking
SCM	Supplementary cementitious material
SS	Stainless steel
UNS	Unified Numbering System
USGS	United States Geological Survey
UTS	Ultimate tensile strength
UV-VIS	Ultraviolet-Visible Spectrophotometry
VP-SEM	Variable Pressure Scanning Electron Microscopy
VWSG	Vibrating wire strain gauge
XRD	X-Ray Diffraction
μXRF	X-Ray Fluorescence Spectroscopy

SUMMARY

The durability of prestressed concrete structures in marine environments is of increasing concern. Traditionally, emphasis of research on this topic has been placed on the chloride diffusivity and permeability of the cement paste in order to increase the service life of prestressed concrete structures, while the characteristics and properties of the aggregate and steel reinforcement has received limited attention. This thesis encompasses two relatively unexplored topics regarding prestressed concrete durability in coastal regions.

Recently, stainless steel alloys have been proposed to replace conventional prestressing reinforcement for concrete bridge piles in coastal regions in order to provide a 100+ year service life. Investigation of the performance of precast, prestressed concrete piles using duplex high-strength stainless steel (HSSS) 2205 prestressing strands and austenitic stainless steel (SS) 304 transverse, spiral reinforcement shows that these piles can be built following conventional construction procedures and driven to refusal without visible damage. Flexural and shear capacities of the piles are greater than predicted by AASHTO LRFD and ACI 318 specifications, while experimental prestress losses and development and transfer lengths are lower than values predicted by AASHTO LRFD. These results, in addition to the superior corrosion resistance providing a 100+ year service life, demonstrate that duplex HSSS 2205 can be used for prestressing strands in combination with austenitic SS 304 for the transverse confinement and shear reinforcement for prestressed concrete piles, using the same design requirements and

construction procedures used for conventional prestressing strand and wire reinforcement.

Additionally, this research evaluates the suitability of a sulfide- and sulfate-bearing aggregate obtained from a previously unexploited deposit in a coastal lowland region in Georgia. These sands produce low-pH condition in contact with moisture. Their impact on the early-age behavior, mechanical properties, and durability of cement-based materials is examined on mortar and concrete specimens. Results show a high variability of the composition of the sands and their performance when used in concrete and mortar, delays of the early-age hydration kinetics and setting time of mortar mixtures, earlier onset of reinforcement corrosion in structural concrete, and varied mechanical properties when acidic sands mined from the same source are used in concrete. The presence of sulfate and alkali feldspar minerals in the acidic sands was also shown to increase the potential of mortar mixtures to develop delayed ettringite formation (DEF) when exposed to high-temperature curing, such as during production in precast facilities.

This thesis demonstrates that prestressed concrete bridge piles, reinforced with the proposed stainless steel alloys, can be effectively implemented in coastal regions but that aggregates from lowland coastal deposits may negatively impact the performance of cement-based materials. Overall, these findings demonstrate that the selection of reinforcement materials and aggregate should be examined as rigorously as the design elements (e.g., cementitious materials composition, concrete mixture proportions) more routinely assessed for marine structures.

CHAPTER 1

INTRODUCTION

Reinforced concrete structures in marine environments are exposed to demanding conditions that may compromise their specified design service life or lead to premature failure. The effect of the exposure of concrete and reinforced concrete to seawater has been extensively studied for more than a century (Mehta, 1991). As a result, chloride-induced corrosion of steel reinforcement, carbonation, sulfate and biological attack of concrete, alkali-aggregate reactions, freezing and thawing damage, and surface deterioration by abrasion have been identified as durability problems typically affecting marine structures (Moser et al., 2011a; ACI 357, 2014; Gjørv, 2014); deterioration evidenced in bridge piles by the action of some of these mechanisms is shown in Figures 1.1 and 1.2 (Moser et al., 2011a).

Among these deterioration mechanisms, chloride-induced corrosion is traditionally considered the primary cause of service life decrease of marine and coastal structures (Koch et al., 2002; Jones et al., 2015) and consequently, in order to increase long-term durability, much emphasis has been placed on assessments and modeling of the permeability and chloride diffusivity of concrete (Mehta, 1980; Bentz et al., 2014). Even when concrete deterioration is usually a result of the combined action of several mechanisms, the service life of concrete marine structures is commonly estimated based upon chloride-induced corrosion alone.

(a)

(b)

Figure 1.1 Corrosion-induced longitudinal cracking of prestressed concrete bridge piles (Moser et al., 2011a).

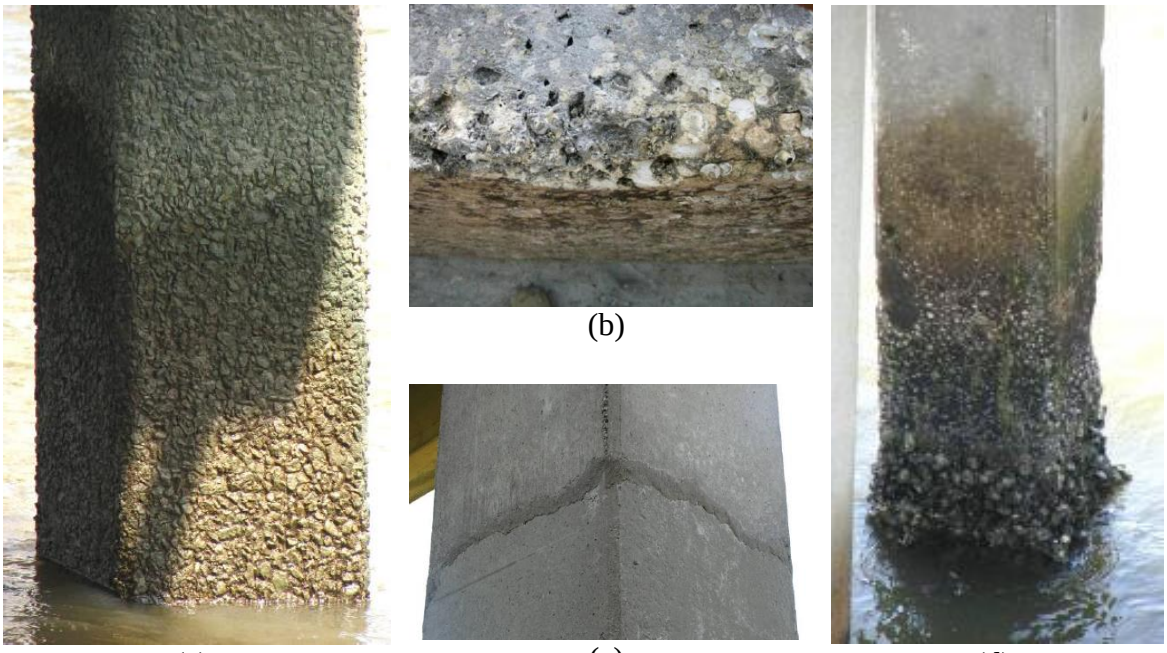

Figure 1.2 Deterioration evidenced by prestressed concrete bridge piles due to (a) abrasion, (b) biological attack by boring sponge, (c) overdriving, and (d) a combination of several mechanisms (Moser et al., 2011a).

A 'Tuuti' plot is a common means for conceptualizing service life, for example, as the sum of the initiation period, time needed for chloride ions to reach reinforcement depth and initiate corrosion by depassivation of steel, and the propagation period, time period between corrosion initiation and a limit state where further deterioration of the structure is no longer tolerable, as shown in Figure 1.3 (Bertolini et al., 2013). Other deterioration modes, which can occur in conjunction with chloride ingress and corrosion and which may exacerbate those effects, such as sulfate attack and alkali-silica reaction (ASR), have not been properly included in service life models (Azizinamini et al., 2013).

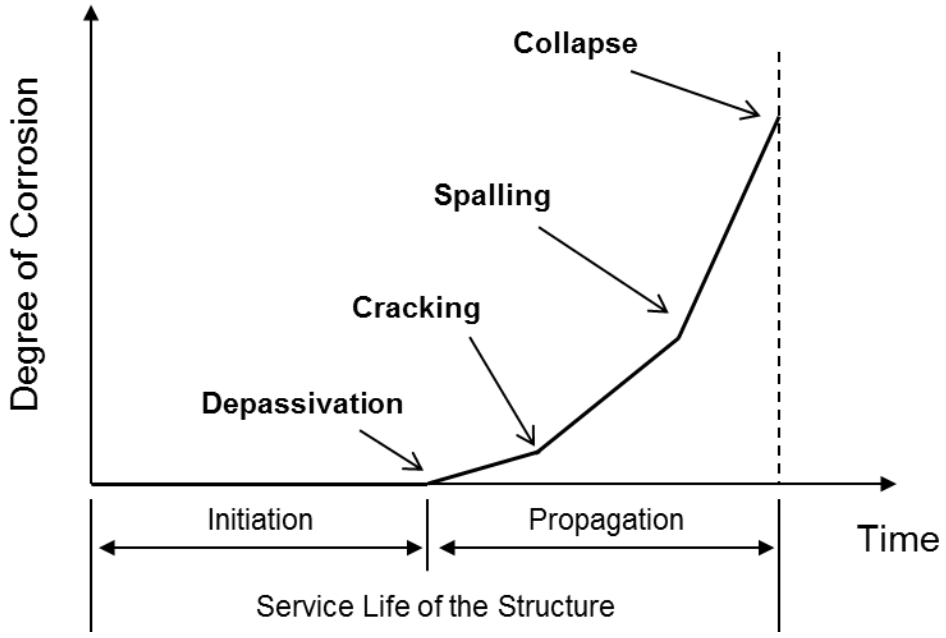

Figure 1.3 Deterioration rates at different periods of the service life of concrete structures (Bertolini et al., 2013; Tuuti, 1982).

Some argue that this conventional approach of service life estimation has not shown good correlation with in field performance of concrete marine structures (Gjørv, 2014). As a result, interest in examining the combined influence of multiple deterioration mechanisms on the durability of marine structures is growing (Holland, 2012; Holland et al., 2014), and some more sophisticated service life models are considering multiple deterioration mechanisms (FIB, 2006; Nguyen et al., 2008; Baroghel-Bouny et al., 2011; Bentz et al., 2014; Demis et al., 2014). Yet, while a substantial body of knowledge exists surrounding the physicochemical interactions of the cement-based binding fraction and the marine environment, considerably less attention has been given to specific durability issues associated with the aggregate fraction, resulting in a critical gap in our knowledge which limits our ability to accurately predict service life in cases where marginal or newly exploited aggregate sources may be used.

Additionally, recent circumstances have increased the awareness about the durability of marine structures. As noted by Mehta (1991), increasing world population and specifically a migration of the population to coastal regions has intensified the magnitude of coastal and offshore construction. During the 20th century, the population of the world coasts increased dramatically leading to a disproportionate population density in coastal regions (Figure 1.4), trend which is expected to continue through the 21st century (Nicholls et al., 2007). Small and Nicholls (2003) estimated that a 23% of the world population lives within 100 km from coastline and that the population density in coastal regions is about three times higher than the global average.

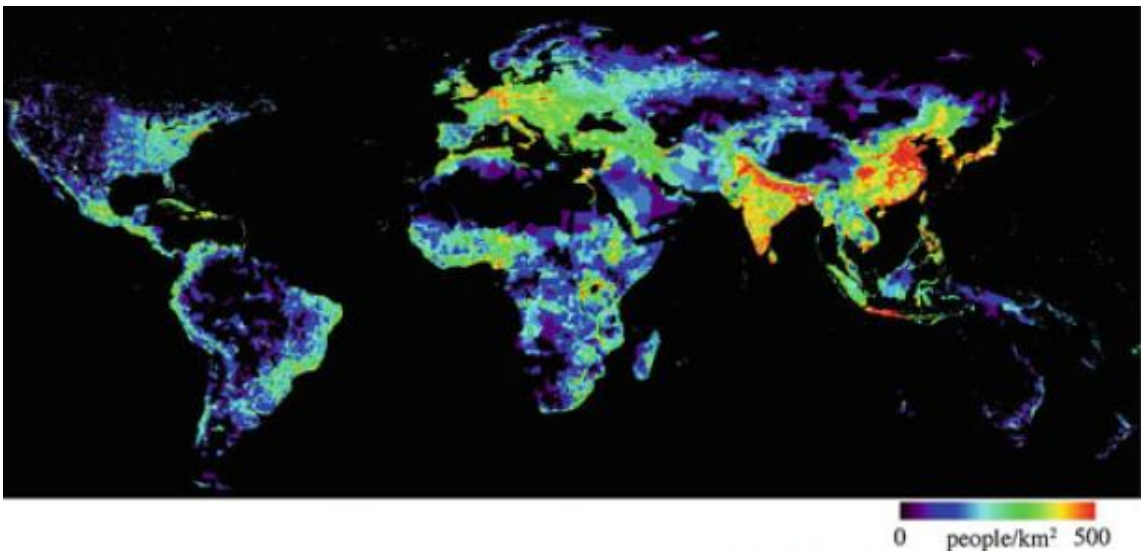

Figure 1.4 Global distribution of population (Small, 2011).

A similar behavior is observed in the US, where the population growth during the second half of the 20th century was higher in coastal regions (Figure 1.5). Using data from the US Census Bureau, the National Oceanic and Atmospheric Administration (NOAA, 2013) estimated that 39% of the country's population lives in coastal shoreline

counties that represent a 10% of the total land area, if Alaska is excluded. As a result of this demographic trend, an average population density of 446 hab./mi^2 (172.2 hab./km^2) was calculated in coastal counties in 2010, 4.2 times higher than the country global average. By 2020, an increase of 37 hab./mi^2 (14.3 hab./km^2) is expected in coastal counties, compared to 11 hab./mi^2 (4.3 hab./km^2) for the entire country.

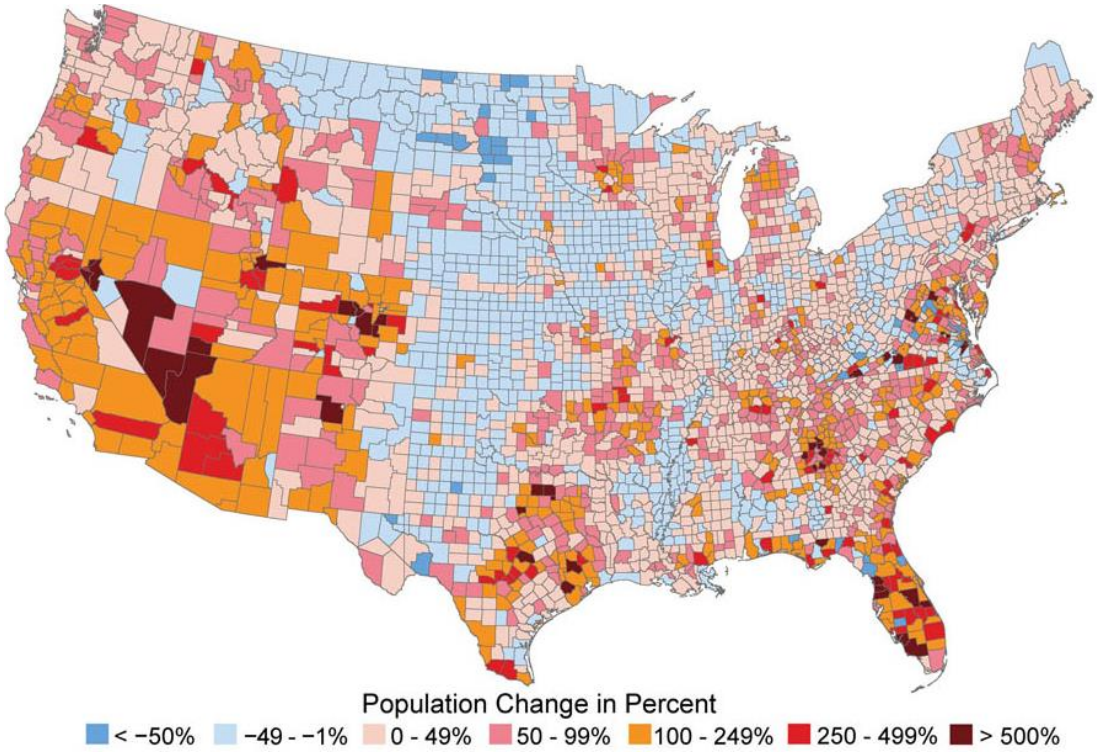

Figure 1.5 Population change in US counties in the 1970-2008 period (Karl et al., 2009).

Consequences of the rapid urbanization of the coasts include the enlargement of natural coastal inlets and saltwater intrusion into surface and ground waters (Nicholls et al., 2007). Also, the influence of human activity exacerbates the impact of climate change in coastal regions, where increasing risk of coastal erosion, more frequent extreme weather events (hurricanes, cyclones, storms, flooding), acidification of the oceans, and

the rise of the global mean sea level up to 2 ft. (0.6 m) or more by 2100 are expected (Nicholls et al., 2007; IPCC, 2014). Then, a higher vulnerability of marine and coastal structures can be anticipated due to the potential increase of the interaction between infrastructure and the marine environment.

One of the consequences of the increasing coastal construction is the higher demand of local materials for production of concrete, which has pushed the exploitation of new sources of aggregates of questionable, or at the very least unknown, suitability. Also, the need for an improved design for service life has led regulatory agencies, such as Federal Highway Administration (FWHA) and state DOTs, to stimulate the development of initiatives to address the durability and service life of new and existent infrastructure (Azizinamini et al., 2013). An example of this effort is the FHWA goal of 75 to 100 years for bridge service life which, in the case of prestressed concrete structures in marine environments, cannot be provided by conventional construction and design practices (Moser et al., 2011a). In response, investigation of the use of more corrosion resistant steel reinforcement has begun (Moser et al., 2012). In particular, the knowledge base surrounding the practical use and field performance of corrosion resistant prestressing strand in precast concrete is needed.

The research included in this thesis studies the performance, and especially the durability, of portland cement-based materials in the context of coastal or marine construction and provides new understanding regarding the influence of coastal aggregate sources and corrosion resistant steel on durability of marine structures. First, the effect of a coastal, low-lying sand deposit, recently exploited for use in construction but which is sulfide or sulfate-containing (also referred as “acidic sands” throughout the document),

on factors affecting constructability and service life are examined. Next, prestressed concrete bridge piles produced with stainless steel prestressing strands and transverse confinement and shear reinforcement are studied as a more durable alternative for construction in coastal regions.

1.1 Purpose of Research

1.1.1 Use of Acidic Sands in Cement-Based Materials

In 2012, 131 million metric tons of construction sand and gravel were sold or produced in the US to be used as concrete aggregates, of which 12.4% corresponds to the South Atlantic geographic division (Bolen, 2014). The high volumes of mined sand and gravel have environmental, health, permitting, safety, and zoning implications that have driven these operations away from urban regions, increasing the costs associated to transportation (USGS, 2015). The difficulties of finding new aggregates mining sources, in addition to the high rates of construction and aggregate demands in coastal regions, have created concern for supply deficiencies in the next years; the San Francisco Bay and San Diego areas in California are examples of coastal regions where depletion of existent aggregate reserves are projected in the next 20 years (Clinkenbeard, 2012).

In Georgia, preliminary analysis performed by the Georgia Department of Transportation (GDOT) identified the presence of iron sulfide and noted unusually low pH in sand samples from a previously unexploited, unique geological source located in the Georgia Lower Coastal Plain. Tertiary and quaternary uppermost sediments from this area are composed mostly of pale to dark-green, phosphatic, very sandy micaceous clays which are interbedded with fine to coarse phosphatic sand (Herrick and Vorhis, 1963).

The sand deposit, located in the Pamlico geological formation, corresponds to a lowland habitat, flanked by natural barrier systems, in Hinesville, GA (Hails and Hoyt, 1969). The sand has been extracted from depths of 70 to 80 ft. (21.3 to 24.4 m) and corresponds to the Pliocene geological age (2.6 to 5.3 million years before present).

It is known that presence of sulfate- or sulfide-bearing minerals in aggregates used in concrete can be problematic. While calcium sulfate dihydrate (or gypsum) is commonly added to portland cement to control the reaction of the tricalcium aluminate phase, for any cementitious clinker and source of sulfate an optimal content or ratio of these components can be identified which produces appropriate setting characteristics and early strength development in concrete (Taylor, 1997). As a result, additional sources of sulfate (SO_3, commonly denoted $\overline{S}$) can affect time to set and strength development, particularly at early ages. At later ages, if sulfur-containing species derived from aggregates interact chemically with the surrounding hydrated cement paste, expansion and cracking and other forms of damage may result; this is "internal sulfate attack" (ISA) as the source of the aggressive ion is within the concrete, rather than external (as in "sulfate attack"). Internal sulfate attack is most commonly observed in the Middle East (see for example Al-Abidien [1987]). In cases of mass concrete construction or some hot weather construction where internal temperature of the concrete exceeds 65-70 °C (150-158 °F), damage by delayed ettringite formation (DEF) may also be problematic due to the potential increased availability of sulfates (Atahan and Dikme, 2010).

Further, oxidation of some such sulfide-bearing minerals can result in the production of sulfuric acid. Acids can substantially interfere with and potentially prevent setting of plastic concrete and can lead to significant degradation of hardened properties,

largely because products of cement hydration are unstable at pH lower than 9-11. In reinforced concrete, if the pore solution pH is sufficiently lowered to depassivate the steel or if the sulfate ion concentration is sufficiently high to locally compromise the passive layer, corrosion can occur prematurely. Thus, the presence of sulfates in sufficient amounts within the mineral phases comprising an aggregate source, as well as the associated production of acids, have the potential to negatively affect both the early age properties and long-term durability of concrete, but these potential effects have not been the subject of extensive prior published research.

1.1.2 Stainless Steel as an Alternative Reinforcement

Two previous research projects, funded by GDOT, have studied the deterioration process of prestressed concrete bridge piles in Georgia coastal regions and the proper selection of concrete mixtures and prestressing steel in order to increase the service life of prestressed concrete piles in marine environments to 100 or more years.

The first project studied the environmental conditions at which bridges are exposed in marine environments of Georgia. The deterioration evidenced by precast prestressed concrete piles of eleven inspected bridges had service lives between 24 and 58 years at the time of the inspection, and corrosion damage of conventional steel prestressing strands and wires was evident (Moser et al., 2011a). Based on the degradation mechanisms of prestressed concrete piles in marine environments found in the first project, the second project recommended two stainless steel alloys (duplex grades 2205 and 2304) and two high-performance concrete mixtures intended to improve the durability of prestressed concrete piles (Holland et al., 2012; Moser et al., 2012).

The main findings obtained in these two previous reports were:

- Precast prestressed concrete piles in Georgia coastal regions evidence accelerated chloride intrusion and significant cracking and damage due to corrosion of reinforcement, sulfate attack, surface abrasion, biological attack from boring sponges, and pile over-driving.

- Conventional steel AISI 1080 used in prestressing strands does not provide the necessary corrosion resistance to reach the required service life goal for bridges in marine environments.

- The presence of crevices and surface imperfections in prestressing strands generates additional sites for corrosion initiation that reduces the chloride threshold limit (CTL) compared to individual wires.

- Duplex high strength stainless steel grade 2205 (HSSS 2205, also known as UNS S31803 per ASTM A 276) exhibited the best corrosion resistance among the analyzed, strain-hardened high strength stainless steels.

- Duplex high strength stainless steel grade 2205 and 2304 prestressing strands are able to be produced using the existing facilities and procedures used for conventional grade AISI 1080 prestressing strand production.

The implementation of this new developed high strength stainless steel (HSSS) on real scale precast prestressed concrete piles can provide a better understanding of its performance, in order to be adopted for use in marine environments. Additionally, for the development the piles, a shear and confinement spiral wire should be implemented. Such wire should provide the required strength and stiffness, and be compatible with the HSSS strand in order to avoid the development of galvanic corrosion.

1.2 Objectives

The global objective of this research is to contribute to the understanding of the durability of concrete infrastructure in marine environments through the assessment of two relatively unexplored topics. One topic is the impact of the use of acidic or sulfate/sulfide-bearing coastal sands in cement-based materials, and the other is the performance of prestressed concrete bridge piles reinforced with stainless steel prestressing strands. Both topics involve durability assessment of concrete in marine environments and emphasize emerging trends in materials utilization. This research encompasses both the exploration of marginal materials in regions which are developing rapidly and resources have grown depleted and the use of high performance materials in applications where increased service life are prioritized.

For the investigation on acidic sands, the performance of sand sources from coastal regions, including those containing sulfide or sulfate minerals, are evaluated for their suitability as fine aggregate in concrete. The effect of sulfide or sulfate-containing sand on 1) early age properties (i.e., setting time, early age strength), 2) strength development, and 3) durability will be compared to those of other accepted coastal sand sources.

Toward the development of corrosion-free precast prestressed concrete piles for use in Georgia's coastal, marine environment, the evaluation of precast concrete piles constructed with high-strength stainless steel prestressing strand and spiral wire reinforcement and with high-durability concrete is assessed. Ease of fabrication, driving without failure or cracking, and sufficient flexural and shear strength capacities meeting standard AASHTO LRFD provisions is evaluated. In addition, this research determines if

the transfer and development lengths of stainless steel strand satisfy standard AASHTO LRFD provisions, examines the long-term durability of the strand and concrete under marine conditions, and provides specifications and design recommendations for corrosion-free piles which may be implemented by GDOT. The scope of this second research objective is limited to testing duplex high strength stainless steel grade 2205 (HSSS 2205, UNS grade S31803) and conventional AISI 1080 steel for prestressing strand and using stainless steel grade 304 (SS 304, UNS grade S30400) and conventional plain wire (ASTM A1064, 2015) for shear and confinement reinforcement, based upon prior research by Moser et al. (2012).

1.3 Organization of Dissertation

This dissertation is composed of seven chapters.

Chapter 2 reviews common mechanisms for deterioration of prestressed concrete structures in marine environments. The literature review included in this chapter addresses the potential impact of the use of sulfide- and sulfate-bearing sands on the properties of cement-based materials, the characteristics of prestressing reinforcement, the corrosion mechanisms associated with prestressing steel, a description of stainless steel properties, and the use of stainless steel as an alternative to conventional reinforcement and prestressing steel.

Chapter 3 describes the characteristics of the analyzed acidic sands, the mixture design of mortar and concrete mixtures, and the tests performed to study the effect of the acidic sands in portland cement systems. The early-age behavior of mortar using acidic sands is analyzed by Vicat setting time and isothermal calorimetry; mechanical properties

are analyzed by the study of the compressive strength and dynamic elastic modulus on time; and the durability is examined through accelerated corrosion test, chloride permeability, and surface resistivity.

Chapter 4 presents the study of the susceptibility of mortar mixtures using acidic sands to develop ISA and DEF. The monitoring of expansion for at least 15 months, compressive strength of mortar cubes, and the study of the condition of specimens by Variable Pressure SEM are included in the analysis.

Chapter 5 summarizes the design, construction, and instrumentation of the pile specimens, including the properties of the concrete and steel used in the construction of the piles. Results from the study of the driving capacity, prestress losses, and flexural and shear capacity are presented. Analysis of the durability of the piles is performed by the assessment of the condition of steel and concrete of smaller specimens placed in the Savannah River.

Chapter 6 includes the study of the bond performance of the stainless steel prestressing strands in the piles. The transfer and development length of piles are measured and the experimental results are compared to AASHTO and ACI requirements and proposed expression developed by previous studies.

Chapter 7 includes the main conclusions and recommendations for practice and further research of this study.

Appendices include the discussion of some topics mentioned but not fully explained in the body of the dissertation, the calculation of prestress losses and structural performance of the piles, and they show the detailed results of some of the tests.

Measurements are expressed in two unit systems, US Customary and International System of Units (SI).

CHAPTER 2

LITERATURE REVIEW

2.1 Deterioration of Reinforced Concrete Structures in Marine Environments

According to Aïtcin (2003), the durability of reinforced concrete structures in marine regions can be compromised by the combined action of four types of harmful environmental factors:

a) chemical factors, as a result of the presence of ions dissolved in seawater.

b) physical factors, including freezing and thawing, and wetting and drying cycles.

c) mechanical factors, including the kinetic action of waves and erosion due to the presence of sand and gravel particles, floating debris, and floating ice in the seawater.

d) factors associated with the fluctuations of the sea level, such as tides and storms.

Additionally, damaged concrete structures in marine environment have shown deterioration that can be attributed to construction and materials variables, including improper mix design, poor concrete placement, and crack formation due to excessive deflection due to load application, overdriving of precast piles, thermal stresses in mass concrete, and expansive reactions involving the formation of ettringite or alkali-silica reaction gel (Mehta, 1980).

The deterioration of concrete elements also depends on the exposure zone. ACI 357.3R-14: Guide for Design and Construction of Waterfront and Coastal Concrete Marine Structures (2014) defines four exposure zones, listed as follows:

a) Submerged zone: region below the mean lower low water (MLLW) where concrete is continuously covered by seawater. MLLW refers to the mean lower sea level during low tide.

b) Tidal zone: region between the MLLW and mean higher high water (MHHW) where concrete is wetted by tides. MHHW is the mean higher sea level during high tide.

c) Splash zone: region above the MHHW where concrete is mostly in dry condition but occasionally wetted by the action of waves or wind-driven spray.

d) Atmospheric zone: region where concrete is not directly exposed to seawater, but it is exposed to ocean air and winds carrying sea salts.

Figure 2.1 summarizes the deterioration processes by exposure zone, where the previously defined tidal and splash zones are shown combined (Mehta, 1991).

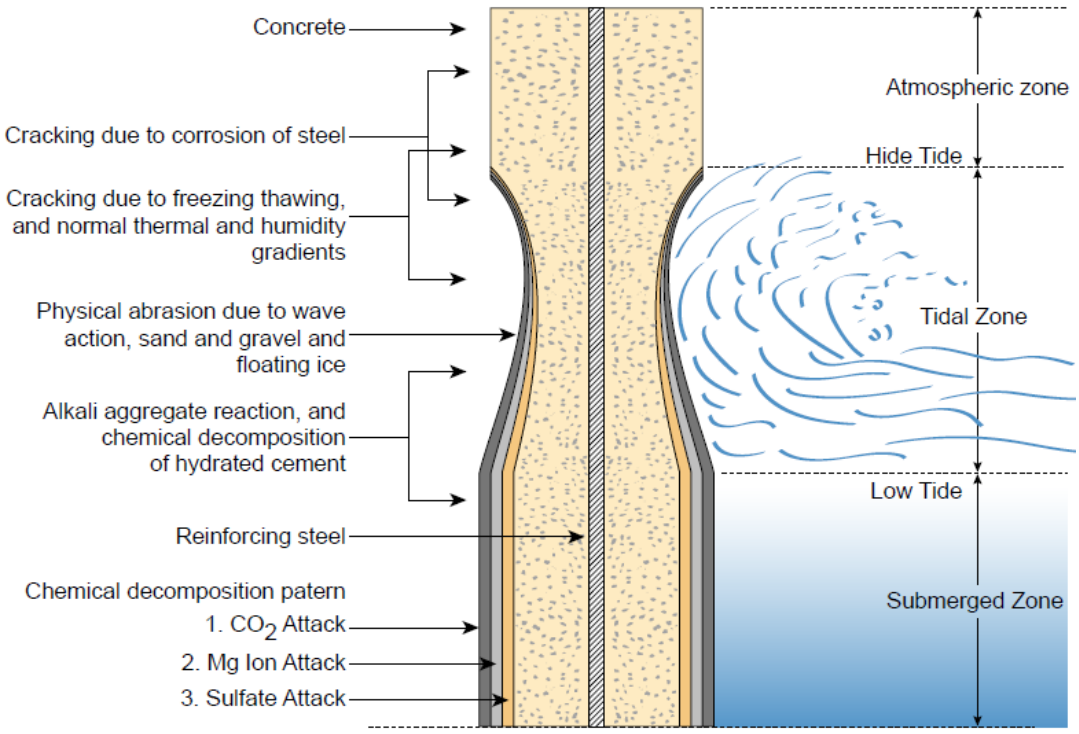

Figure 2.1 Deterioration of reinforced concrete exposed to seawater (Mehta and Monteiro, 2006).

Commonly, concrete is most vulnerable in the splash and tidal zones, where it is possible to observe cracking and spalling due to reinforcement corrosion, wetting and drying, and frost action, chemical decomposition of hydration products of cement, and loss of material due to impact of waves (Mehta, 1980). Abundance of chlorides, water, and oxygen makes tidal and splash zones especially susceptible to chloride-induced corrosion, which is the most prominent and reported durability problem in coastal concrete structures (ACI 357, 2014).

The accelerated deterioration of concrete structures in marine environments leads to a significant decrease of the predicted service life. Kurtis et al. (2013) estimated the predicted service life of reinforced concrete exposed to urban and marine environments. The diffusion coefficient of concrete was estimated from rapid chloride permeability tests (RCPT) performed on concrete mixtures with different water-to-cementitious material ratios (*w/cm*) and varying additions of supplementary cementitious materials (SCMs) and limestone filler addition, and then used as input for service life modeling. Regardless of the concrete mixture used, life cycle analysis using ACI's Life-365 software (Ehlen et al., 2009) showed that the exposure of reinforced concrete elements to severe marine environments reduces service life by 68% to 78% in comparison with the service life of the same elements exposed to a mild urban environment (Figure 2.2).

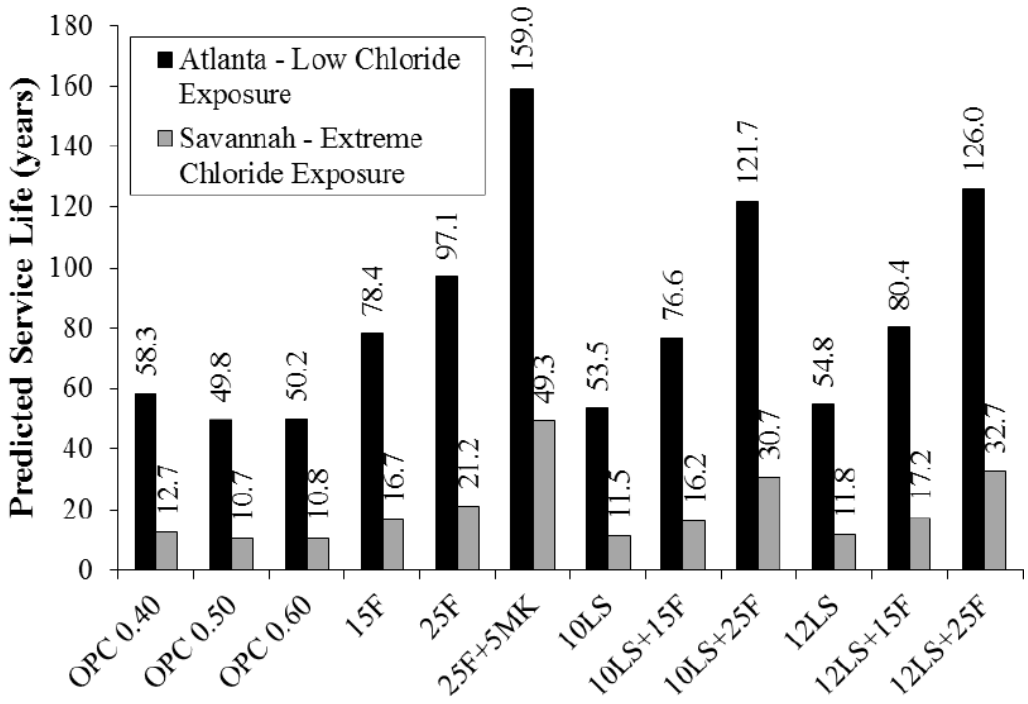

Figure 2.2 Impact of chloride exposure level on the predicted service life. OPC: portland cement, F: Class F fly ash, MK: metakaolin, LS: interground fine limestone powder (Kurtis et al., 2013).

In prestressed concrete, the failure mechanism due to corrosion of steel may differ significantly from conventional reinforced concrete. The nominal strength of prestressed concrete is dependent on the prestressing force. Thus, the corrosion of the prestressing steel and the subsequent reduction of the strand will have a higher impact compared to reinforced concrete structures. In extreme cases, corrosion of prestressing reinforcement can lead to catastrophic failure of prestressed concrete elements, which may occur without outward evidence (Nawy, 2009).

In the case of prestressed concrete piles exposed to marine environments, there are several mechanisms that contribute to the deterioration of these elements; the corrosion of the steel reinforcement is the most prevalent damage evidenced (Cannon et al., 2006). A survey of the condition of concrete bridges in the Georgia coastal region

performed by Moser et al. (2011a) showed extensive damage of the substructure and superstructure. Most significant damage to piles was found in the submerged and tidal zones of bridges in contact with brackish water, where the most common deterioration features were abrasion of concrete, cracking and spalling of concrete, and corrosion staining. Analysis of water samples showed a pH between 5.88 and 7.47, and water salinity and sulfate concentration consistent with brackish water (0.1-2.5% NaCl concentration and 1,000-2,700 mg/L SO_4^{2-}, respectively). Further examination of the piles identified chloride-induced corrosion and high chloride concentration in the tidal and splash zones, and evidence of concrete deterioration due to sulfate attack, carbonation, and the action of boring sponges.

These observations are consistent with the evaluation of prestressed concrete piles in the coast of Florida performed by Cannon et al. (2006). Half-cell potentials suggesting high probability of active corrosion of the reinforcement (≤ -350 mV) were reported in the splash zone of piles, and higher chloride concentration was measured in submerged, splash, and tidal zones. Additionally, severe corrosion of the prestressing strands was observed at the pick-up points suggesting that accelerated chloride intrusion occurred at these regions.

The highest concentration of chloride in concrete piles partially submerged in seawater has been measured between 0 and 1 ft. (0 and 30.5 cm) above the waterline (Hartt and Rosemberg, 1980). Capillary flow of seawater and transverse evaporation of water from the sides of the piles explain the high concentration of residual salts in these regions (Chaix et al., 1995). Availability of moisture, chlorides, and oxygen at the splash and tidal regions can explain the higher corrosion rates and damage.

As a result of this severe environment, an important impact on service life of concrete marine structures has been reported. Along the coastline of Norway, half of the concrete bridges built after 1970 exhibited steel corrosion within the 25 years after construction (Østmoen et al., 1993). In the Persian Gulf region, Normand (1986) found poor performance of reinforced concrete marine structures, with considerable damage due to reinforcement corrosion after 3 to 10 years in some cases. In the US, some bridge sub-structures in the coastal area of Georgia are replaced after less than 40 years of service, according to GDOT. The reduced service life of bridge structures generates higher maintenance and repair costs. Yunovich et al. (2002) estimated repair and replacement annual cost of $8.3 billion for bridges in USA, and increasing costs are estimated for future years (Darwin, 2007; Gjørv, 2014). Additionally, the Federal Highway Administration (FHWA) has instructed the increase of the service life of new bridges to 100 years or more (Moser et al., 2011a). This objective cannot be reached in marine environments using conventional construction practices for prestressed concrete.

2.2 Effects of Acidic Sands on Performance of Structural Concrete

Sulfur represents a 0.07% of the constituents of Earth's crust (Brimblecombe, 2003), where it is found in gypsum and metal sulfides. Sulfur in the atmosphere is mostly contained in sulfur dioxide (SO_2) and hydrogen sulfide (H_2S) derived from volcanic activity, while in seawater, sulfur is found mainly as dissolved sulfate (Böttcher, 2011). Microbial sulfate reduction is the most important process for the presence of iron sulfides in soils, and evaporitic sulfate materials like gypsum and dihydrate can be precipitated from seawater (Rickard and Luther, 2007; Böttcher, 2011).

Soils containing sulfidic materials, also known as acid sulfate soils, are present in marine environments, after formation of wetlands, lakes and disposal ponds by human activity, or due to saline groundwater discharge produced by vegetation clearing. Undisturbed sulfide minerals do not present acidification, which is triggered by exposure to oxygen in the air and occurs when the amount of acid produced overcomes the buffer capacity of the soil (Fitzpatrick et al., 2009).

The presence of sulfide and sulfate in aggregate sources, and their potential for low pH, could affect the properties of cement-based materials containing them. A review of the effects of the oxidation of iron sulfides, the occurrence of internal sulfate attack and delayed ettringite formation, and the effects of low pH conditions in concrete are presented below.

2.2.1 Sulfide Mineral Oxidation in Concrete

Sulfide minerals are metal sulfide compounds that include chalcopyrite ($CuFeS_2$), sphalerite (ZnS), molybdenite (MoS_2), galena (PbS), cinnabar (HgS), and pyrite (FeS_2).

Pyrite is the most commonly found sulfide in geological environments. When sulfides are exposed to the air, they react with oxygen and water to release protons (H^+) and sulfate ions (SO_4^{2-}). Overall, this reaction results in a decrease in pH. Equations 2.1 to 2.4 summarize the oxidation reaction for pyrite (Nordstrom, 2011; Menendez et al., 2013).

$$FeS_{2\,(s)} + 7/2\ O_{2\,(g)} + H_2O_{\,(l)} \rightarrow Fe^{2+}{}_{(aq)} + 2\ SO_4^{2-}{}_{(aq)} + 2\ H^+{}_{(aq)} \quad (2.1)$$

$$Fe^{2+}{}_{(aq)} + 1/4\ O_{2\,(g)} + H^+{}_{(aq)} \rightarrow Fe^{3+}{}_{(aq)} + 1/2\ H_2O_{\,(l)} \quad (2.2)$$

$$Fe^{3+}{}_{(aq)} + 3\ H_2O_{\,(l)} \rightarrow Fe(OH)_{3\,(s)} \downarrow + 3\ H^+{}_{(aq)} \quad (2.3)$$

$$FeS_{2\,(s)} + 14\ Fe^{3+}{}_{(aq)} + 8\ H_2O_{\,(l)} \rightarrow 15\ Fe^{2+}{}_{(aq)} + 2\ SO_4^{2-}{}_{(aq)} + 16\ H^+{}_{(aq)} \quad (2.4)$$

The oxidation of sulfide minerals depends on the mineral type (monosulfide or disulfide), solubility, defects, and surface area, as well as temperature and the presence of bacteria. Monosulfide (e.g., FeS and ZnS) reactivity increases with increasing solubility due to the reaction with acid to form H_2S, which oxidizes to form sulfur and sulfate. Disulfides (e.g., FeS_2 and FeAsS) will not form H_2S, but elemental sulfur and thiosulfate ($S_2O_3^{2-}$). Also, some sulfides, such as molybdenite, are fairly insoluble and undergo very slow oxidation. Finer particles will react and dissolve faster (Nordstrom and Southam, 1997; Nordstrom, 2011). Additionally, several types of bacteria catalyze the oxidation reaction, reducing elemental sulfur into sulfuric acid (Hawkins, 2014).

In concrete, the presence of mineral sulfides even as a minor constituent of aggregates can produce deleterious reactions. Two common mineral sulfides found in aggregate are pyrite (FeS_2) and pyrrhotite ($Fe_{1-x}S$, where x = 0 to 0.125), a less ordered and consequently more reactive form of iron sulfide (Hawkins, 2014). Pyrite and

pyrrhotite can be present in igneous, metamorphic or sedimentary rocks, and usually develop in marine environments, inland wet regions, or close to faults. The formation of pyrite in sedimentary deposits is associated with the reaction of iron minerals with H_2S, generated by sulfate reduction under bacterial action, to produce metastable iron monosulfides, which transform into pyrite (Berner, 1984). The availability of organic matter and dissolved sulfate control the rate of the reaction and the amount of pyrite formed. Marine conditions commonly provide suitable conditions for this reaction. In particular, in oxygen-depleted regions under the surface of marine sediments, higher concentrations of pyrite have been reported due to conditions which are favorable for the degradation of less reactive iron minerals by H_2S (Berner, 1984).

Pyrite and pyrrhotite oxidize in presence of water and oxygen in a chemical, electrochemical, or bacterially catalyzed process which starts in the first minutes of exposure (Chandra and Gerson, 2010) and over time develops acidic by-products rich in iron and sulfate (Rodrigues et al, 2012). The oxidation of iron sulfides may be accelerated in conditions of higher alkalinity, such as the high pH environment provided by cement paste in mortar and concrete mixtures. These reactions can be summarized by Equations 2.5 and 2.6 (Schmidt et al, 2011).

$$2\ FeS + 2\ H_2O + 4.5\ O_2 \rightarrow Fe_2O_3 + 2\ H_2SO_4 \quad (2.5)$$

$$2\ FeS_2 + 4\ H_2O + 7.5\ O_2 \rightarrow Fe_2O_3 + 4\ H_2SO_4 \quad (2.6)$$

Two evident effects of the oxidation reaction could be noted. One is the volume increase resulting from the oxidization of iron sulfides, with the volume of the products

around 1.3 to 1.7 times those of the reactants. Depending of the degree of degradation, the expansion will generate stresses over the aggregates or cement paste. If the expansion overcomes the strain limit of the aggregates or surrounding cementitious material, it will lead to cracking (Schmidt et al, 2011). A second effect is the generation of sulfuric acid that produces an accelerated drop of pH at the moment when iron sulfides take contact with water, followed by a more gradual decrease until a stable value is reached, generally after several days (Chinchón-Payá et al., 2012). The pH reduction of pyrite is greater than pyrrhotite, producing a final value of 3 compared to 4.5, while pyrrhotite's supply of sulfate and ferrous ions is higher than the case of pyrite. The implications of a pH reduction on the local or global properties of concrete containing such aggregate are not clear, but it is well known that products of portland cement hydration are unstable at pH below 9-11, depending upon the phase (Glasser, 2004).

In addition, also in portland cement-based materials, an indirect effect of the oxidation of iron sulfides and the consequent release of sulfate ions is the potential formation of late ettringite and also gypsum. Durability could be compromised due to internal sulfate attack and/or delayed ettringite formation (DEF) in such cases.

2.2.2 Internal Sulfate Attack

Internal sulfate attack (ISA) is a particular case of sulfate attack where the sources of sulfate come from one or more constituent materials, commonly from cementitious materials or contaminated aggregates. ISA could occur due to the presence of sulfate-bearing aggregates or over-sulfation of the cement. In these cases, a SO_3 content greater

than 5 or 6% by weight of cement is generally believed to be necessary to generate expansion (Scrivener and Skalny, 2005).

Products of internal sulfate attack include gypsum (calcium sulfate dihydrate) and ettringite. In the presence of magnesium, the formation of brucite, among other products, is possible (Neville, 2004). The late formation of ettringite, in particular, is sometimes associated with deleterious expansion, which can compromise mechanical properties and increase permeability. The formation of gypsum is also associated with a decrease in strength, loss of adhesion, and potential decrease in pore solution pH. Overall, ISA can compromise the strength and integrity of the affected concrete, leading to a decrease in service life.

2.2.3 Delayed Ettringite Formation

DEF can lead to expansion, cracking, and loss of mechanical properties and durability of concrete. This damage is commonly attributed to the formation of ettringite after concrete hardens (Taylor et al., 2001), and it has been associated with concrete which has experienced exposure to temperatures exceeding 150-158 °F (65-70 °C). DEF has been noted to produce damage in precast concrete, where steam and higher temperature curing are used, and in mass concrete elements, where the heat evolution from cement hydration can lead to high internal temperatures (Thomas et al., 2008; Thomas and Ramlochan, 2004).

Ettringite ($C_6A\overline{S}_3H_{32}$) is a product of ordinary portland cement (OPC) hydration. It is first formed during the hydration of tricalcium aluminate (C_3A), when C_3A reacts with gypsum ($C\overline{S}\cdot H_2$) and water. As the sulfate availability decreases during early

hydration (which is the common case in most cements), ettringite is considered as a metastable phase, decomposing into calcium monosulfoaluminate hydrate or "monosulfate" ($3C_4A\bar{S}H_{12}$), a phase that contains less sulfate and binds less water than ettringite (Mindess et al., 2003). Ettringite can precipitate from solutions containing Ca^{2+}, $Al(OH)_4^-$, SO_4^{2-}, and OH^-, although the presence of KOH in concentrations above 0.5M may prevent its precipitation (Brown and Bothe, 1993; Skalny et al, 2002). Solubility product of ettringite at 25 °C (77 °F), K_{sp}, is 2.8×10^{-45} (Damidot and Glasser, 1992).

While the mechanisms for damage by DEF remain the subject of continued study, it is believed that in OPC systems when internal temperatures exceed 150-158 °F (65-70 °C), subsequently, in presence of moisture, the release of sulfate and aluminate ions from C-S-H are understood combine with monosulfate to form late ettringite in confined spaces, which can produce expansion (Taylor et al., 2001; Ekolu et al, 2006; Flatt and Scherer, 2008). With high temperatures during initial curing, ettringite is not a stable phase and decomposes, even at early ages. As a result, the aluminate and sulfate ions released are bound to the complex structure of the primary product of portland cement hydration, the calcium silicate hydrate or "C-S-H". Here, aluminum can be substituted for silicon or can occupy interlayer spaces in C-S-H, where sulfates can also be loosely bound (Taylor et al., 2001). After cooling, ettringite can form by dissolution and precipitation, a reaction that consumes the sulfate present in monosulfate, pore solution and C-S-H, alumina from monosulfate, calcium from monosulfate and C-S-H, and water. In addition, a later decrease in the pore solution pH (such during consumption of hydroxyls and alkalis during the formation of alkali silica reaction gel), can also spur the release of aluminates and sulfates from C-S-H, leading to secondary ettringite formation.

Ettringite stability also depends on the pH of the pore solution and the availability of reactants. At pH levels lower than 11.5–12, ettringite can decompose to form hydrates of aluminum and/or gypsum (Santhanam et al., 2001), while when the pH is high (> 13) the formation of monosulfate is favored (Taylor et al., 2001). Similarly, Taylor et al. (2001) shows that cements with SO_3 content above 3% and Al_2O_3 content above 4% could generate ettringite after cooling, suggesting the existence of one or more "pessimum" SO_3/Al_2O_3 ratios.

The way this late formed ettringite produces expansion remains a subject of ongoing examination, but it is mostly accepted that 1) an initial curing at a temperature above 150 °F (65 °C) is needed for DEF to occur, 2) the cement or binder chemistry determines the amount of ettringite, and 3) the stresses developed as a result of DEF reaction depend on the microstructure of mortar or concrete (Taylor et al., 2001).

Currently, no standard test has been adopted in USA by ASTM or AASHTO to assess materials, material combinations, or curing practices for the occurrence of DEF in portland cement concrete. Nevertheless, common methods are used in practice, mostly involving mortar bars specimens exposed to an initial hot curing cycle, followed by immersion in limewater at standard room temperature. The length of the mortar bars is monitored over time, and their expansion over time is calculated.

Commonly used curing regimes for examining the potential for DEF are the Kelham and Fu methods, and the Duggan test (Grabowski et al., 1992; Kelham, 1997; Folliard et al., 2006). While the Kelham method generally produces higher expansions, earlier expansions are obtained by the Fu method (Folliard et al., 2006). It should be noted that no expansion limit has been defined for a deleterious expansion due to DEF,

but regularly 0.1% is considered an acceptable reference for mortars (Petrov and Tagnit-Hamou, 2004; Pavoine et al., 2012; Tovar-Rodríguez et al., 2013).

For the analysis of acidic sands included in this document, the Kelham method was used to assess the potential for DEF when the various sands were combined with cements of varying composition. The Kelham method was selected because it involves a hot curing cycle and not an additional drying cycle as the Fu method and Duggan test. Details of the temperature-time variation in the Kelham curing cycle are shown in Figure 2.3. The Kelham method (Kelham, 1997), increasingly used in recent research, resembles the heating regime of a precast concrete operation (see Figure 2.3) and also addresses initial heat generation and accumulation during mass concrete placements.

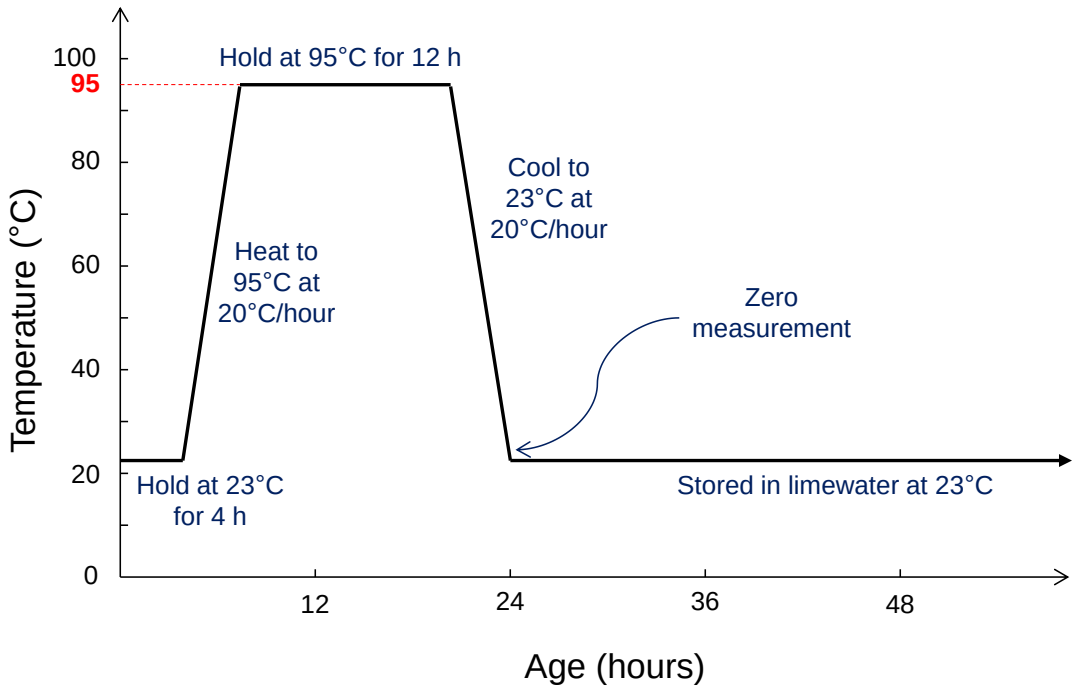

Figure 2.3 Kelham early-age curing cycle (modified from Bauer et al. [2006]).

2.2.4 Influence of Low pH Conditions

The exposure of concrete to acidic conditions can adversely affect its performance, including loss of strength and adhesion in the paste and as a result in the concrete and by earlier initiation of and accelerated rate of corrosion of steel reinforcement.

In good quality concrete, steel embedded in concrete is exposed to an alkaline environment (pH > 12.5), developing a thin (5-10 nm), highly protective and insoluble passive film, which provides considerable corrosion resistance to the steel. The composition of the passive layer in carbon steels is variable throughout its thickness, with a protective FeO (Fe(II) oxides) layer adjacent to the steel substrate and a less protective layer, mostly composed of Fe(III) oxides, such as Fe_3O_4 and α–Fe_2O_3, in contact with concrete (Ghods et al., 2012; Gunay et al., 2013). A reduction of the pH makes this passive layer thermodynamically unstable and a faster dissolution of steel can be induced (Hansson, 1984). In the case of prestressed concrete, the acidification of the crevice region, space left by the prestressing wires with oxygen deficiency, leads to an earlier corrosion initiation compared to reinforced concrete and to a reduced chloride threshold limit (CTL) compared to an isolated prestressing wire (Moser et al., 2011b). More details of the processes that lead to corrosion of steel reinforcement are given in Section 2.3.2.

Release of sulfate ions into the pore solution can also impact the corrosion of embedded steel. While presence of even a high concentration of sulfate ions in the cement paste does not affect the time to corrosion initiation or the corrosion rate of steel (Al-Amoudi and Maslehuddin, 1993), the combined presence of chloride and sulfate ions may produce a synergistic effect on the corrosion rate. Using the linear polarization

resistance method, Dehwah et al. (2002) measured higher corrosion current of steel in chloride environments when the concentration of sulfate increased. The lower corrosion resistance has been attributed to a higher concentration of free chloride ions produced by the reaction of sulfate ions with C_3A, which reduces the proportion of bound chloride in the cement paste, and to a decrease of the electrical resistivity of concrete when the moisture content is lower than 4–5% (Saleem et al., 1996; Dehwah et al., 2002).

Additionally, exposure to acid – or any pH lower than the high pH common in portland cement-based systems – can compromise the stability the hydrated phases, which act to bind the aggregate together, providing strength and impermeability. When concrete is exposed to an acid environment (e.g., in sewer pipes, wastewater treatment plants, or cooling towers), the reduction of the pH of the pore solution will induce the selective decomposition of hydration products: calcium hydroxide at pH below 12.6, ettringite at pH below 10.7, and C-S-H at pH below ~10.5 (Beddoe and Dorner, 2005). The loss of these cement hydrates will decrease adhesion, compromising mechanical properties and increasing permeability.

In the case of sulfuric acid attack, the effects of acid attack can be combined with those of sulfate attack. That is, calcium hydroxide will react with sulfate to form gypsum (Monteny et al., 2000). The formation of other sulfate-bearing phases may also be possible, depending upon the pH.

2.3 Use of Stainless Steel for Prestressing Strands

2.3.1 Characteristics of Prestressing Reinforcement

Conventional prestressing steel is a pearlitic (α-ferrite + Fe_3C [cementite]) eutectoid steel with approximate elemental composition 0.75-0.88% C, 0.6-0.9% Mn, 0.05% S (max), 0.04% P (max), and traces of other elements, such as Si, Mo, Cr, and Ni (Moser et al., 2011a), conforming specification AISI 1080. Microstructure of the longitudinal and transverse orientations of the prestressing steel is shown in Figure 2.4, where white plates correspond to ferrite phase and black plates correspond to cementite phase. The anisotropic microstructure is oriented on the direction of cold drawing.

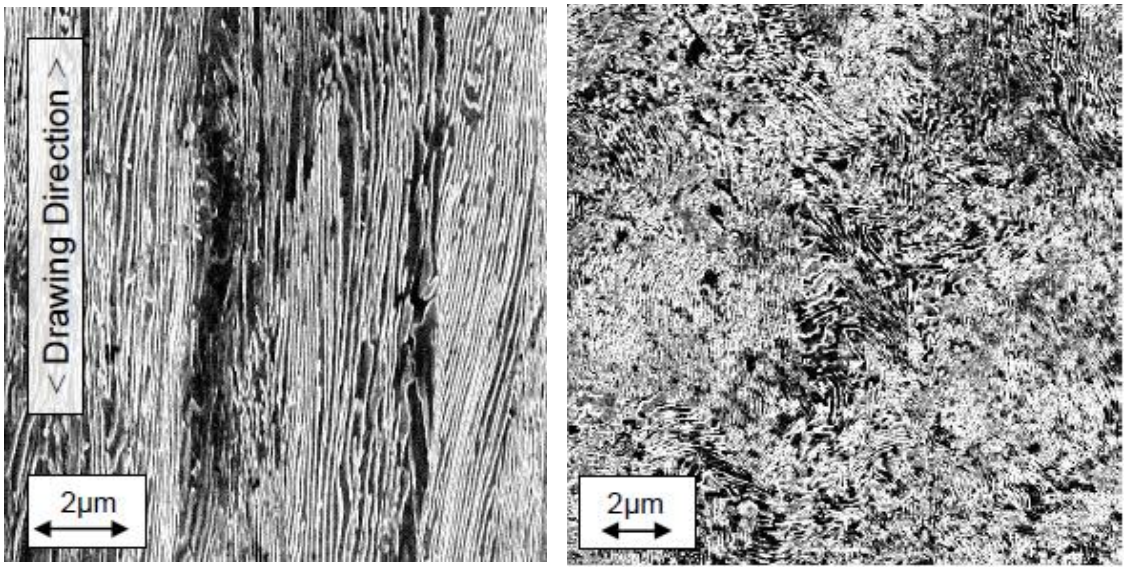

(a) (b)

Figure 2.4 Microstructure of the (a) longitudinal and (b) transverse direction of prestressing steel (Moser et al., 2011a).

Prestressing steel reinforcement has higher yield and ultimate tensile strength than typical reinforced concrete reinforcement (Figure 2.5), in order to provide effective prestressing even after prestress losses reduce the magnitude of the prestressing force.

Most common specified ultimate tensile strengths (UTS) are 250 and 270 ksi (1,724 and 1,862 MPa), and they are typically stressed to a 60% to 80% of the UTS; ultimate strain is about 7% and a modulus of elasticity of 29,000 ksi (200 GPa) is recommended by AASHTO (2013) and ACI 318 (2011) provisions.

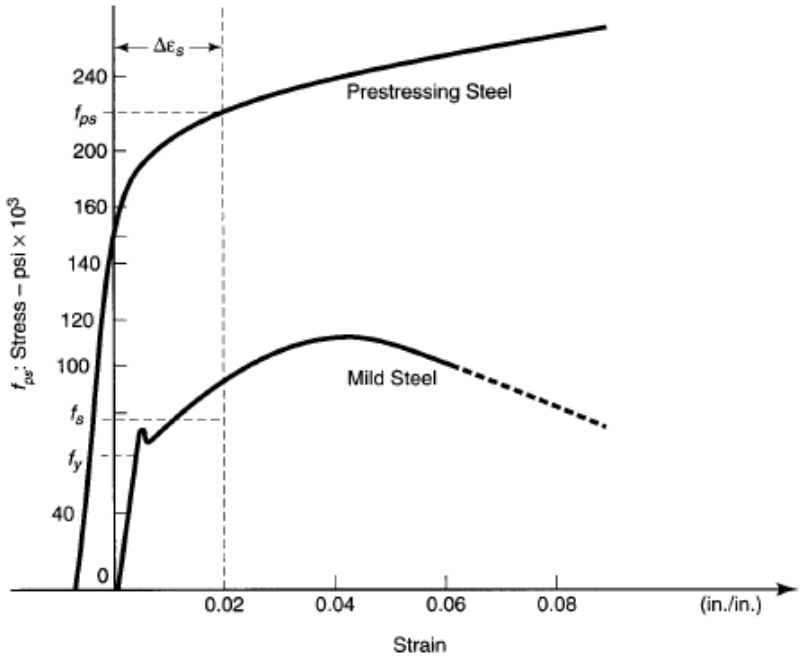

Figure 2.5 Stress-strain diagram of prestressing steel compared to mild steel (Nawy, 2009).

Prestressing steel is available in three forms: 1) uncoated wires (stress-relieved or low relaxation), 2) uncoated strands (stress-relieved or low relaxation), and 3) uncoated high-strength steel bars. Prestressing wires are cold-drawn to increase their tensile strength, followed by a stress relieving process in which wires are exposed to temperatures about 700 °F (371 °C) to remove residual stresses in steel. Low-relaxation wires and strands are subjected to the combined action of high temperature of stress relieving and stress approximately 40% of the UTS. Low-relaxation steel has a relaxation

stress loss less than 2% to 3%, which is 25% of that of typical stress-relieved steel (Nawy, 2009; Moser et al., 2011a).

Standard strands are composed of seven wires; six of them twisted around one slightly larger central wire (Figure 2.6a). A compacted strand can also be formed to maximize the steel area of the 7–wire strand for a given nominal diameter (Figure 2.6b). The nominal diameter of the strand, d_b, ranges from 3/8 to 0.6-in. (9.5 to 15.2 mm).

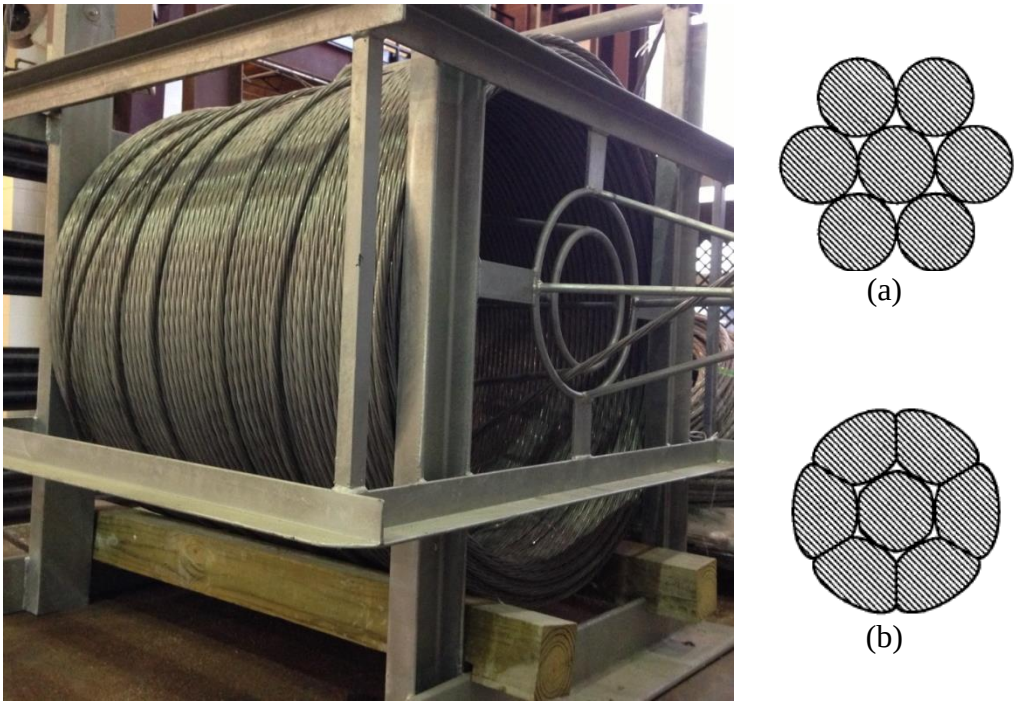

Figure 2.6 (a) Standard strand section and (b) compacted strand section (Nawy, 2009).

Prestressing wires are coated in $ZnPO_4$ to ease the cold working process and to provide a protective layer from the atmosphere before being placed in concrete. It has been shown that imperfections of this coating can be expected due to scratching, stranding, or cold-working. As a result, corrosion may initiate at these imperfection sites well before the breakdown of the $ZnPO_4$ layer (Moser et al., 2011b).

2.3.1.1 Prestress losses

Prestressed concrete elements undergo losses of the initial prestressing force over time. The estimation of prestress losses allows the determination of the effective prestress acting on a prestressed concrete section, and to evaluate actual concrete stresses and deformation during the service life of a structure (Tadros et al., 2003).

Prestress losses in pretensioned members can be classified in two categories depending on the time when they occur (Nawy, 2009): immediate elastic shortening of concrete and time-dependent losses, which include creep and shrinkage of concrete and stress relaxation of steel. Elastic prestress gains can also be produced when live and superimposed loads are applied to the prestressed element, but usually they are not included explicitly in the estimation by codes (Figure 2.7).

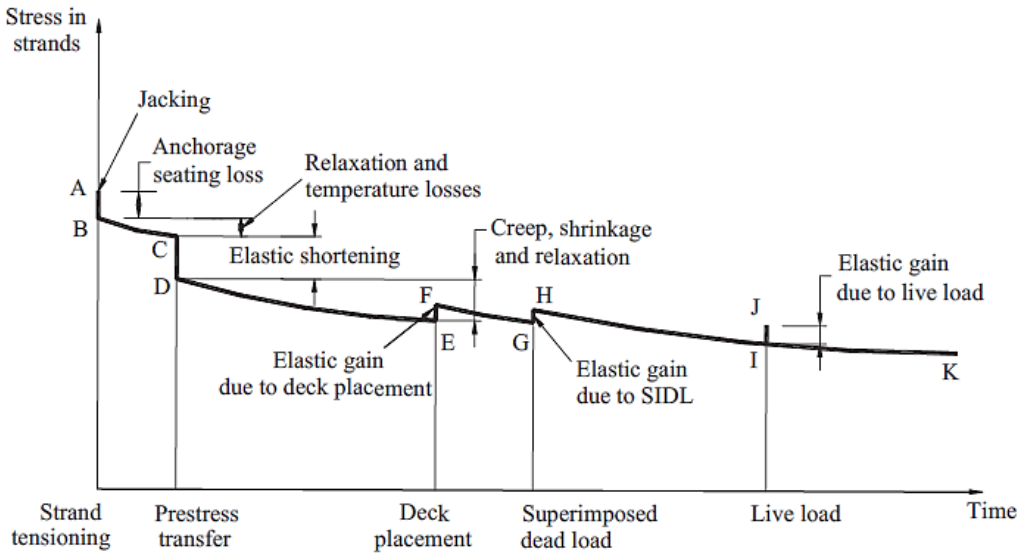

Figure 2.7 Change of stress on strands due to prestress losses (Tadros et al., 2003).

Due to the application of the prestressing force, concrete experiences elastic shortening that simultaneously induces shortening of bonded strands. As the strands

shorten, a fraction of the prestressing force is lost. When additional forces are applied to the element, the elongation of the strands produces elastic gains (Tadros et al., 2003).

Steel stresses are reduced over time due to the stress relaxation under a sustained strain. Relaxation losses depend on the time that such strain is imposed to the strand and the magnitude of the prestressing force that produces the elongation. ASTM A416 limits relaxation losses in low-relaxation strands, after 1,000 hours of testing, to 2.5% of the initial stress when axially loaded at 70% of the UTS, and to 3.5% when the load is 80% of the UTS.

Prestress losses due to creep and shrinkage of concrete are commonly the principal source of losses in prestressed concrete elements (Bandyopadhyay and Sengupta, 1986; Tadros et al., 2003). Deformation of concrete due to creep and shrinkage produces the shortening of the prestressing strands and reduces the prestressing force applied to the member. Generally, the estimation of creep and shrinkage losses has a higher uncertainty compared with the other losses, given the number of factors that affect their magnitude. Creep losses depend on the environmental conditions, dimension and geometry of the element, the magnitude and duration of load application, mixture proportion and mechanical properties of concrete, time and method of curing, and age of concrete at transfer. Shrinkage losses are determined by environmental conditions, dimension and geometry of the element, mixture proportion of concrete, time and method of curing, and age of concrete at transfer.

AASHTO LRFD (2013) estimates the losses of pretensioned elements using Equation 2.7.

$$\Delta f_{pT} = \Delta f_{pES} + \Delta f_{pLT} \tag{2.7}$$

where total losses, Δf_{pT}, are the sum of losses due to elastic shortening, Δf_{pES}, and long-term losses, Δf_{pLT}.

Δf_{pES} combines elastic losses and gains and is calculated using Equation 2.8.

$$\Delta f_{pES} = \frac{E_{ps}}{E_{ct}} f_{cgp} \tag{2.8}$$

where E_{ps} is the elastic modulus of steel, E_{ct} is the elastic modulus of concrete at transfer, and f_{cgp} is the stress in concrete at the center of gravity of prestressing strands after transfer.

AASHTO estimates Δf_{pLT} by two different techniques: the approximate or lump-sum method, and the refined method. The lump-sum method calculates long-term losses using a single equation that combines creep, shrinkage and relaxation losses. The refined method estimates the contribution of every source of losses individually.

Examples of the use of both AASHTO methods for the estimation of prestress losses are given in Appendix Q.

2.3.1.2 Transfer and development lengths: Code provisions and research estimations

The transfer length of prestressing strand in pretensioned concrete elements is the distance, from the start of the bonded section, over which the strand transfers the initial tensile stress to compressive stress in concrete through bond stresses (Reutlinger, 1999). The flexural bond length is defined as the additional length of prestressing strand beyond the transfer length over which bond is developed to allow the strand to reach the stress at the nominal flexural strength of the member (Meyer, 2002). The development length is

the sum of transfer and flexural bond length. Transfer of stress from strand to concrete along the development length can be represented by diagram in Figure 2.8.

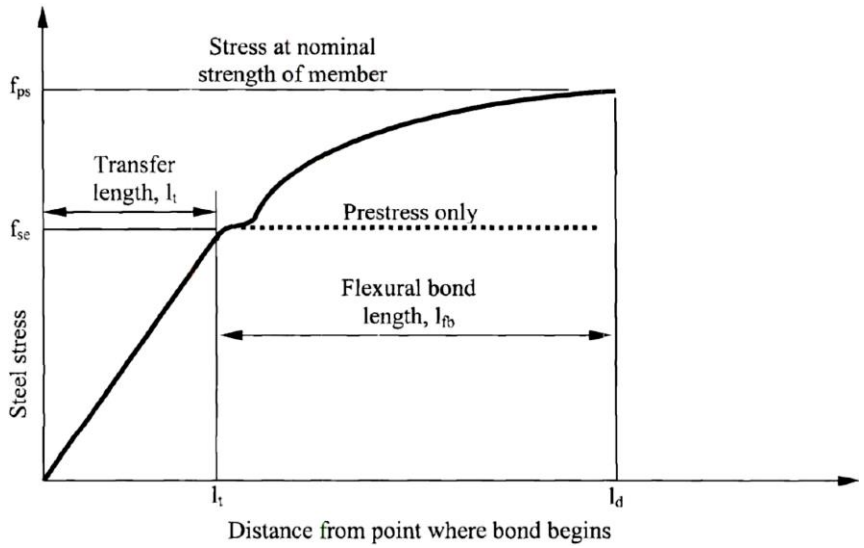

Figure 2.8 Strand stress along development length (Meyer, 2002).

The bond between the prestressing strand and concrete depends on three mechanisms: 1) adhesion, 2) Hoyer's Effect, and 3) mechanical interlocking (Russell and Burns, 1993).

Adhesion is the chemical bond between steel and concrete that prevents strand slip as bond stresses increase to a critical stress level. After the critical stress is reached, adhesion causes brittle failure, and resistance provided by the chemical bond is reduced to zero. Adhesion has a small contribution to transfer bond and bond development under applied loads (Russell and Burns, 1993; Reutlinger, 1999).

Hoyer's Effect was first described by Hoyer and Friedrich (1939) as a consequence of the mechanical properties of steel and construction procedures of pretensioned concrete elements. After the pretensioned load is applied, the diameter of

the strand is reduced by the Poisson's effect. Then, when the strand is released in hardened concrete, the strand expands laterally creating a normal force in concrete in order to counteract the expansion. However, prestress along the strand in the transfer region is not uniform, and the variation of the strand diameter will create a wedge action, which is greater closer to the end of the element. As a result, the normal force in concrete induces friction that anchors the strand and restrains its relative movement with respect to concrete. Hoyer's effect has a higher effect on bond in the transfer region and a negligible impact when additional loads are applied. Diagram in Figure 2.9 describes the wedge action produced by Hoyer's effect.

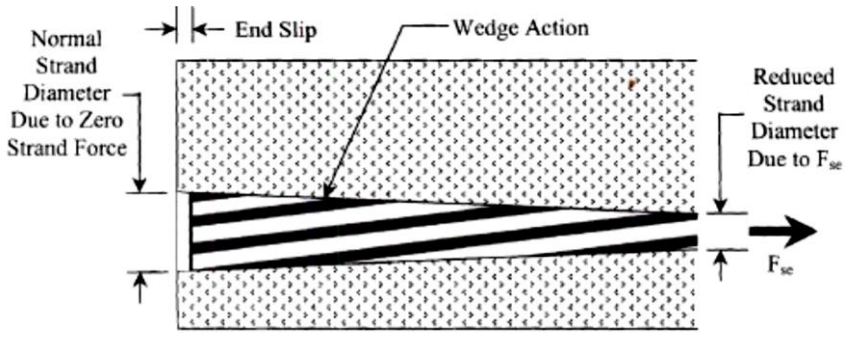

Figure 2.9 Hoyer's Effect in prestressing strand (Meyer, 2002).

Mechanical interlocking is a consequence of the physical characteristics of the pretensioned strand. Standard strand is composed of six wires wound around a central wire. The helical pattern of the strand creates deformities that are surrounded by concrete, creating an envelope. If the strand is pulled from concrete, ridges at the external wires restrict movement by mechanical interlock (Russell and Burns, 1993; Meyer, 2002). Mechanical interlocking is the dominant mechanism that enhances bond in the flexural bond region.

The expressions for development and transfer length calculation according to ACI 318 and AASHTO LRFD, and the proposed equations from previous studies are given below. Variables and units used in this section are detailed as follows:

l_t: transfer length, in inches.
l_d: development length, in inches.
d_b: nominal diameter of the prestressing strand, in inches.
f_{ps}: stress in prestressing steel at nominal flexural strength, in ksi.
f_{pt}: stress in prestressing strand, in ksi.
f_{si}: stress in prestressing strand after transfer, in ksi.
f_{se}: effective stress in prestressing strand after losses, in ksi.
f_{su}: ultimate strength of prestressing strand, in ksi.
E_{ci}: elastic modulus of concrete at release, in ksi.
f_c': design compressive strength of concrete, in ksi.
f_{ci}': compressive strength of concrete at release, in ksi.
M_{cr}: cracking moment, in kip-in.
M_n: nominal flexural resistance, in kip-in.
V_u: factored shear force, in kips.
V_{cw}: nominal shear resistance provided by tensile stresses in concrete in the web, in kips.

a) AASHTO LRFD (2013).

The determination of transfer and development lengths of prestressing strands is covered in Section 5.11.4 of the 6th Edition of AASHTO LRFD Bridge Design Specifications (2013). Equations 2.9 and 2.10 are proposed for l_t and l_d, respectively.

$$l_t = 60 \cdot d_b \tag{2.9}$$

$$l_d \geq \kappa \cdot \left(f_{ps} - \frac{2}{3} f_{pe} \right) \cdot d_b \tag{2.10}$$

where κ is 1.6 for pretensioned members with a depth greater than 24.0-in. (61.0 cm), and 1.0 otherwise. Units from expression in parenthesis in Equation 2.10 should be disregarded.

Expression for l_d was adopted mainly as a result of the experimental study of Hanson and Kaar (1959), while the addition of factor κ was adopted after a FHWA memorandum in 1988, based on poor transfer and development length test results at the North Carolina State University (Cousins et al., 1986; Reutlinger, 1999).

b) ACI 318 (2011).

Equations 2.11 and 2.12 are proposed for l_t and l_d, respectively, in Section 12.9 of the Building Code Requirements for Structural Concrete (ACI 318-11).

$$l_t \geq \frac{f_{se} \cdot d_b}{3{,}000} \tag{2.11}$$

$$l_d \geq \left(\frac{f_{se}}{3{,}000}\right) \cdot d_b + \left(\frac{f_{ps} - f_{se}}{1{,}000}\right) \cdot d_b \tag{2.12}$$

where the stresses f_{se} and f_{ps} are expressed in psi, and the values calculated from expressions in parenthesis should be used as constants without units.

Transfer length expression in Equation 2.11 was established after experimental studies of Hanson and Kaar (1959) and Kaar et al. (1963), and it considered the calculated length in order to provide proper bond performance under an average transfer bond stress of 400 psi (2.76 MPa).

It should be noted that, when factor κ = 1.0 in Equation 2.10, the equations for development length provided by ACI 318 and AASHTO LRFD coincide.

Equations for transfer and development length in AASHTO and ACI are based on limited test results. Expressions were developed from conditioned Grade 250 prestressing strands, with a maximum strand diameter of ½-in. (12.7 mm), and without the use or consideration of the traditional construction procedures in the prestressed concrete industry (Hanson and Kaar, 1959). Extensive research has been developed in order to propose better estimations of l_t and l_d (Reutlinger, 1999). Some of the equations proposed by previous studies for the estimation of transfer and development length of prestressed concrete elements are described below.

c) Martin and Scott (1976).

Martin and Scott (1976) reevaluated the results from Kaar et al. (1963) and proposed a conservative limit for l_t for strand diameters ranging from ¼-in (6.35 mm) to 0.6-in. (15.24 mm), shown in Equation 2.13. Additionally, a bi-linear relationship (Equation 2.14) was developed by fitting the experimental data of Hanson and Kaar (1959), in order to provide the maximum stress in the strand at ultimate condition, given an embedment length l_x. The use of the ultimate tensile strength of prestressing strand in Equation 2.14 can be used to estimate the development length.

$$l_t = 80 \cdot d_b \tag{2.13}$$

$$\begin{aligned} f_{ps} &\le \left(\frac{135}{d_b^{1/6}} + 31 \right) \frac{l_x}{80 \cdot d_b} \qquad for \quad l_x \le 80 \cdot d_b \\ f_{ps} &\le \frac{135}{d_b^{1/6}} + \frac{0.39 \cdot l_x}{d_b} \qquad for \quad l_x > 80 \cdot d_b \end{aligned} \tag{2.14}$$

where l_x is the embedment length, in inches.

d) Zia and Mostafa (1977).

Estimations of l_t and l_d provided by Zia and Mostafa (1977) are empirical relationships based on a literature survey of bond development testing. The parameters considered in this study were: type of steel (strand or wire), prestress level, nominal diameter of strands, surface condition of strands, compressive strength of concrete, type of loading, type of strand release, and type of confining reinforcement.

Analysis of test data determined that transfer length depends on the initial stress in the strand and the compressive strength of concrete at transfer. As a result of the linear regression analysis of reported results, conservative equations for l_t and l_d were proposed for strands up to ½-in. (12.7 mm). It was suggested that the second term of Equation 2.12 from ACI Code, corresponding to the flexural bond length, should be increased by 25% to properly control bond failure of prestressing strands.

Equations 2.15 and 2.16 account for the effect of strand size, initial prestress level, and concrete strength at transfer; they are applicable for concrete strengths ranging from 2,000 to 8,000 psi (13.8 to 55.2 MPa).

$$l_t = 1.5\frac{f_{si}}{f_{ci}^{'}}d_b - 4.6 \tag{2.15}$$

$$l_d = \left(1.5\frac{f_{si}}{f_{ci}^{'}}d_b - 4.6\right) + 1.25\left(f_{su} - f_{se}\right)\cdot d_b \tag{2.16}$$

e) Deatherage, Burdette, and Chew (1989).

An experimental study performed on 20 AASHTO Type I girders at the University of Tennessee by Deatherage et al. in 1989 suggested that the use of ACI

estimation of the transfer length (Equation 2.12) for ½, ½ special, 9/16, and 0.6-in. diameter Grade 270 prestressing strands should consider the stress in prestressing strand after transfer, f_{si}, instead of the stress in prestressing strand after losses, f_{se} (Equation 2.17). Also, an increase of 50% of the flexural bond length in AASHTO and ACI expression for development length was proposed to avoid bond failure, as shown in Equation 2.18.

$$l_t = \frac{f_{si} \cdot d_b}{3} \tag{2.17}$$

$$l_d = \frac{f_{si} \cdot d_b}{3} + 1.50\left(f_{su} - f_{se}\right) \cdot d_b \tag{2.18}$$

f) Russell and Burns (1992).

A comprehensive study of the influence of the size and shape of prestressed concrete sections, number of strands, nominal diameter of strands, debonding, confining reinforcement, and strand spacing was developed at the University of Texas, Austin, in 1992 (Russell, 1992; Russell and Burns, 1993). They concluded that bond failure is a result of shear cracking through the transfer region. Thus, the prevention of these cracks will allow the strand to develop its prestressing force and the additional tension required by external loads. Proposed expressions for l_t and l_d consider a criterion to prevent cracking in the transfer region. However, variables analyzed by Russell and Burns did not include the strength of concrete.

Equations 2.19 and 2.20 were suggested for strands fully bonded to the ends of the members, where the following guidelines are met: $M_{cr} > l_t \cdot V_u$ and web shear cracks are prevented to occur in the transfer zone if $V_u > V_{cw}$.

$$l_t = \frac{f_{se} \cdot d_b}{2} \tag{2.19}$$

$$l_d = \frac{M_n}{M_{cr}} l_t \tag{2.20}$$

g) Mitchell, Cook, Khan, and Tham (1993).

Study developed by Mitchell et al. (1993) was focused on the impact of compressive strength of high-strength concrete on the bond performance of prestressing strand. Rectangular prestressed concrete beams were eccentrically prestressed with 3/8, ½, and 0.62-in. (9.5, 12.7, and 15.7 mm) diameter strands (Reutlinger, 1999). Compressive strength of concrete varied from 3,000 to 7,310 psi (20.7 to 50.4 MPa) at transfer, and from 4,500 to 12,900 psi (31.0 to 88.9 MPa) at 28 days. Beams were tested under three and four-point bending and two types of failures were identified: flexural failure defined by crushing of concrete in the compressive zone, and bond failure, where a significant strand slip was measured, followed by premature shear or flexural failure. They concluded that the increase of concrete strength at release decreases the transfer length, while the increase of concrete strength at 28 days decreases the flexural bond length. In order to prevent bond failure, Equations 2.21 and 2.22 were proposed for the estimation of l_t and l_d, respectively.

$$l_t = 0.33 f_{si}\, d_b \sqrt{\frac{3}{f'_{ci}}} \tag{2.21}$$

$$l_d = 0.33 f_{si}\, d_b \sqrt{\frac{3}{f'_{ci}}} + \left(f_{ps} - f_{se}\right) \cdot d_b \sqrt{\frac{4.5}{f'_c}} \tag{2.22}$$

h) Buckner (1995).

In order to consider a broad range of recommendations found in the research, an extensive literature review was conducted by Buckner (1995). The analysis of test results determined that the use of Equation 2.23 was a reasonable estimation of the transfer length for seven-wire, low-relaxation, Grade 250 and 270 strands in normalweight concrete with design compressive strength higher than 3,500 psi (24.1 MPa).

$$l_t = \frac{f_{si}\, d_b}{3} \tag{2.23}$$

In the case of development length test results, a great discrepancy of test methods and determination of poor bond performance was found. Buckner (1995) suggested that, instead of considering the strand stress at ultimate for development length estimation, the ultimate strain affects more directly the flexural bond strength between strand and concrete. Thus, Equation 2.24 was proposed.

$$l_d = \frac{f_{si}\, d_b}{3} + \lambda \cdot \left(f_{su} - f_{se}\right) \cdot d_b \tag{2.24}$$

where the multiplying factor applied to flexural bond length, λ, is calculated using the strain in prestressing strand at nominal strength: $1.0 \le \left[\lambda = 0.6 + 40 \cdot \varepsilon_{ps}\right] \le 2.0$. ε_{ps} is the strain corresponding to f_{su}.

Additionally, Buckner developed Equation 2.25 for the best fit of transfer length results considering an apparent elastic modulus, calculated from previous studies based upon the midspan strains reported right after release.

$$l_t = \frac{1{,}250 \cdot f_{si}\, d_b}{E_{ci}} \tag{2.25}$$

i) Lane (1998).

A FHWA study was performed on rectangular prestressed concrete elements, AASHTO Type II beams, and prestressed concrete sub-deck panels in order to evaluate the AASHTO equation for development length (Lane, 1998). Two primary types of failures were identified. A flexural failure due to crushing of concrete in the compression zone, and bond failure, where strand slip exceeded 0.01-in. (0.254 mm) and shear cracking was observed at the ends of the elements.

Analysis of results showed that the most influential parameters were the stress in the prestressing strand prior to transfer, f_{pt}, the nominal diameter of the strand, and the strength of concrete at 28 days.

Suggested expressions, given in Equations 2.26 and 2.27, provided a 95% confidence level for the experimental data.

$$l_t = \frac{4 \cdot f_{pt} \cdot d_b}{f'_{c,28}} - 5 \tag{2.26}$$

$$l_d = \left(\frac{4 \cdot f_{pt} \cdot d_b}{f'_{c,28}} - 5 \right) + \left(\frac{6.4 \cdot \left(f_{ps} - f_{se} \right) \cdot d_b}{f'_{c,28}} + 15 \right) \tag{2.27}$$

j) Meyer (2002).

Meyer (2002) studied the transfer and development length of 0.6-in. (15.24 mm), low-relaxation strands in high-strength lightweight concrete, with concrete strengths of 8,000 and 10,000 psi (55.2 and 68.9 MPa). This study was performed on pretensioned AASHTO Type II girders, and Equations 2.28 and 2.29 were proposed for estimation of l_t and l_d, respectively.

$$l_t = 50 \cdot d_b \sqrt{\frac{6{,}000}{f'_{ci}}} \tag{2.28}$$

$$l_d = \left(50 \sqrt{\frac{5{,}000}{f'_{ci}}} + f_{ps} - f_{se} \right) \cdot d_b \tag{2.29}$$

Additionally, the best fit of experimental results was determined by Equations 2.30 and 2.31.

$$l_t = 50 \cdot d_b \sqrt{\frac{4{,}000}{f'_{ci}}} \tag{2.30}$$

$$l_d = \left(50 \sqrt{\frac{2{,}500}{f'_{ci}}} + f_{ps} - f_{se} \right) \cdot d_b \tag{2.31}$$

k) Ramirez and Russell – NCHRP Report 603 (2008).

The specifications provided by Section 5: "Concrete Structures" of AASHTO LRFD Bridge Design Specifications are mostly developed for concrete compressive strengths between 4.0 and 10.0 ksi (27.6 to 68.9 MPa). In order to broaden the applicability of AASHTO LRFD, Ramirez and Russell (2008) developed expressions for transfer and development length for high-strength, normal weight concretes, with compressive strength up to 15 ksi (103.4 MPa).

Transfer and development lengths were measured on rectangular and I-shaped pretensioned concrete beams. Similar to previous research results, it was observed that the increase of concrete strength decreases the transfer and development length in high-strength concrete.

Equations 2.32 and 2.33 were proposed as modifications of current ACI and AASHTO equations, extending the applicability of the codes to design concrete strength of 14 ksi (96.5 MPa).

$$l_t = \min\left(\frac{120}{\sqrt{f'_{ci}}} \cdot d_b,\ 40 \cdot d_b\right) \tag{2.32}$$

$$l_d = \min\left(\left[\frac{120}{\sqrt{f'_{ci}}} + \frac{225}{\sqrt{f'_c}}\right] \cdot d_b,\ 100 \cdot d_b\right) \tag{2.33}$$

2.3.2 Corrosion Mechanisms of Prestressing Strands

The corrosion of prestressed concrete may be triggered by the action of different mechanisms. The two most common mechanisms are carbonation and chloride-induced corrosion; both of these involve the diffusion of deleterious elements through concrete, which eventually reach the depth of the prestressing strand and can initiate active corrosion. Additionally, environmentally-induced cracking can be produced in prestressing strands by two mechanisms: 1) stress corrosion cracking (SCC) and 2) hydrogen-assisted cracking (HAC) by hydrogen embrittlement (HE). These mechanisms of corrosion of prestressing steel strands are described below.

2.3.2.1 Carbonation-induced corrosion

Carbonation of concrete is initiated by the diffusion of airborne carbon dioxide (CO_2), or solubilized carbonates in saturated or partially saturated concrete, through concrete porosity. Reaction between CO_2 and components of cement paste (calcium hydroxide ($Ca(OH)_2$, sodium hydroxide (NaOH), potassium hydroxide (KOH), and calcium silicate hydrate (C-S-H)) may affect the service life of concrete structures (Bohni, 2005). The two main consequences of carbonation are: 1) decrease in pH due to the reduction in hydroxide concentration in the pore solution which is a process that compromises the passive layer of steel, and 2) the change of concrete permeability due to volume changes and microcracking caused by chemical reactions (Johanneson and Utgenannt, 2001) and also due to pore blocking and crack filling as a result of the formation of carbonation products. The consumption of $Ca(OH)_2$ and alkali hydroxides (NaOH and KOH) due to the reaction with carbon dioxide and water is shown in

Equations 2.34 to 2.36. This consumption of hydroxyl ions lowers the pH of the pore solution from the original value (above 12.5) to values between 6 and 9, due to the formation of less soluble carbonates (Bohni, 2005).

$$Ca(OH)_2 + CO_2 + H_2O \rightarrow CaCO_3 + 2\ H_2O \quad (2.34)$$

$$2\ NaOH + CO_2 + H_2O \rightarrow Na_2CO_3 + 2\ H_2O \quad (2.35)$$

$$2\ KOH + CO_2 + H_2O \rightarrow K_2CO_3 + 2\ H_2O \quad (2.36)$$

In concrete where $Ca(OH)_2$ becomes depleted, carbonation of C-S-H can also occur and lead to a further increase of porosity and permeability (Papadakis, et al, 1991; Neville, 1995; Johanneson and Utgenannt, 2001). Also, selective decomposition of C-S-H can occur at pH lower to 10.5 (Beddoe and Dorner, 2005). Carbonation of C-S-H can be represented by Equation 2.37 (Papadakis, et al, 1991).

$$3CaO{\cdot}2SiO_2{\cdot}3H_2O + 3\ CO_2 + H_2O \rightarrow 3CaCO_3{\cdot}2SiO_2{\cdot}4H_2O \quad (2.37)$$

Carbonation of concrete begins at the exterior surface of concrete and infiltrates inward producing a low pH front (Bertolini et al., 2013). According to Mehta and Monteiro (2006), when no chloride ions are present in solution, the passive layer of reinforcing steel is stable for pH values above 11.5. Once the carbonation front reaches the depth of the steel strand and the pH is reduced below 9.5, the protective oxide film is destroyed and active corrosion of the strand will initiate (Berkeley and Pathmanaban, 1990; Papadakis et al., 1991). Except for fully saturated concrete, a sufficient supply of

oxygen can reach the steel surface. The availability of oxygen is important for the passive film development, but it also affects the corrosion rate and corrosion potential. In the absence of chlorides, the passive film will break down slowly according to Equation 2.38, where FeOOH represent the passive film (Jones, 1996).

$$FeOOH + H_2O \rightarrow Fe^{3+} + 3\ OH^- \quad (2.38)$$

The rate of carbonation is at a maximum in the 50%–90% humidity range. Consequently, the most aggressive environments for carbonation-induced corrosion occur with alternating semi-dry and wet cycles. During the semi-dry periods, the carbonation rate increases and during the wet periods the steel corrosion rate increases (Rosenberg et al., 1989). High ambient CO_2 concentration, shallow cover, high permeability of concrete, and the presence of cracks are also factors that increase the rate of carbonation.

2.3.2.2 Chloride-induced corrosion

Chloride-induced corrosion occurs when ingress of chlorides causes a breakdown of the protective, passive oxide film of steel, leading to active corrosion. While chlorides can come from internal or external sources, the corrosion of prestressing steel strands in non-carbonated concrete can only occur once the chloride content at the steel surface has reached a critical limit to initiate corrosion, called the chloride threshold level (CTL). Below the CTL, the passive film is thermodynamically stable and inhibits corrosion of the steel.

The CTL depends on several interdependent factors, including pH of concrete, concrete composition, temperature, $[Cl^-]/[OH^-]$ molar ratio, electrochemical potential of the steel, and local condition of the concrete-steel interface and, therefore, it is not possible to determine a unique CTL for corrosion of embedded steel in concrete (Bertolini et al., 2013; Gjørv, 2014). Once corrosion is initiated, the corrosion rate depends on the source of chlorides, the transport mechanism involved, and several environmental factors (e.g., temperature and RH). Possibly, the type of reinforcing steel would also affect the propagation period rate. Electrochemical testing performed by Hurley and Scully (2006, 2013) on carbon steel, austenitic stainless steel grades 316L and 316LN, duplex stainless steel grade 2102, and a Fe-9% Cr alloy showed longer initiation (CTL) and propagation times in the case of stainless steels.

Chloride ions exist in concrete in two forms, bound or free. Only the free chloride ions which are dissolved in the pore solution are able to participate in the corrosion process. As a result, free chloride concentration, and not the total chloride concentration in concrete, is critical for the CTL. Bound chlorides are those ions which react with other chemicals inside concrete and are no longer able to cause corrosion. For example, chloride ions can react with calcium aluminate (C_3A) present in cement paste to form Friedel's salt ($C_3A \cdot CaCl_2 \cdot 15H_2O$). Studies have demonstrated that increasing the C_3A content of concrete from 2.43% to 14% increased the CTL by a factor of 2.85 (Kurtis and Mehta, 1997). However, sulfate present in Na_2SO_4 and $MgSO_4$ can affect the stability of bound chlorides, replacing Cl^- by SO_4^{2-} in Friedel's salt structure. This reaction releases Cl^- and may increase the content of ettringite in concrete (Geng et al., 2015). Also, the presence of sulfate ions in the pore solution has evidenced negative effects on the

protective properties of passive oxide layers (Ghods et al., 2009), although Moser (2011) showed negligible effects of sulfate ions in the passivation behavior of carbon steel.

Currently, most design codes set limits on the amount of chloride introduced from raw materials during the manufacturing of concrete. The use of contaminated mixing water, unwashed aggregate or sand, or admixtures can also be sources of internal chlorides. In the past, calcium chloride was used extensively as an accelerating admixture before being forbidden because of its ties to corrosion. With internal chloride levels limited, the major source of chlorides is the ingress from the surrounding environment of the structure. The main sources of environmental chlorides are deicing salts and seawater (Bertolini et al., 2013).

Chloride penetration into concrete is a complex function of position, environment, and concrete properties (Bertolini et al., 2013). Chloride permeation can occur due to a large pressure gradient such as in pressure vessels or piping. Chloride absorption can occur through capillary suction of a moisture gradient where cyclic wetting and drying occur, but absorption has been shown to be unable to penetrate to the depth of the steel when adequate cover is provided (Holland et al., 2012). Thus, the primary transport mechanism for chlorides to penetrate concrete is diffusion.

Mathematical models are able to predict a chloride profile based on depth, time, apparent diffusion coefficient, and the surface chloride content. The apparent diffusion coefficient depends on the pore structure of the concrete and can vary based on *w/cm*, compaction, curing, age, addition of SCMs, or type of cement. Often, the apparent diffusion coefficient is used as a parameter to describe the resistance of concrete to chloride penetration; the lower the coefficient value, the higher the resistance to chloride

penetration. This coefficient is also used to estimate the time a particular chloride threshold will be reached at the depth of steel and corrosion will initiate (Bertolini et al., 2013). However, if cracks are present, they allow a shorter path for deleterious material to reach the steel.

When the passive layer of steel is exposed to Cl^- concentrations below the CTL, the protective Fe(II) inner layer transforms to Fe(III) oxides, increasing the Fe(III)/Fe(II) ratio and decreasing the protective nature of the passive layer (Gunay et al., 2013). Chloride-induced transformation of the passive layer is the result of the combined action of reactions given in Equations 2.39 to 2.41 (Ghods, 2010).

$$Fe_xO + (2x)Cl^- + H_2O \rightarrow xFe(OH)Cl_2 + (2-x)OH^- + (3x-2)e^- \quad (2.39)$$

$$Fe_xO + (x)Cl^- + H_2O \rightarrow xFe(OH)_2Cl + (2-2x)OH^- + (3x-2)e^- \quad (2.40)$$

$$Fe_xO + (3x)Cl^- + H_2O \rightarrow xFeCl_3 + 2OH^- + (3x-2)e^- \quad (2.41)$$

Chemical products of these reactions ($Fe(OH)Cl_2$, $Fe(OH)_2Cl$, and $FeCl_3$) are unstable and they will decompose into Fe(III) oxides and free chlorides (Gunay et al., 2013), which will contribute to further corrosion of the steel. This autocatalytic process explains the accelerated corrosion of steel in chloride-induced corrosion (Jones, 1996).

Moser et al. (2011b) conducted a chloride-induced corrosion test on conventional AISI 1080 7–wire prestressing strand and a wire. They found that the CTL for the prestressing wire was similar to normal rebar. However, the CTL for prestressing strand was significantly lower. In fact, the strand would initiate corrosion at one-third the level of chlorides (Figure 2.10).

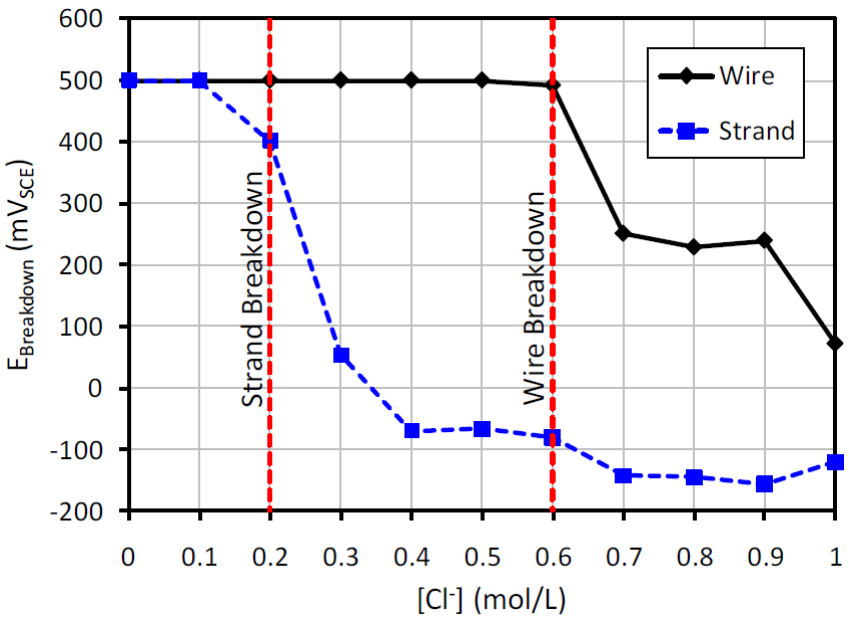

Figure 2.10 Breakdown potential versus chloride concentration for prestressing strand and wire (Moser et al., 2011b).

In carbonated concrete, the decrease in pH value and the presence of chloride ions act simultaneously. A lower pH will weaken or completely remove the passive protective layer of the steel. Therefore, chlorides can induce a more accelerated corrosion of steel. Moser et al. (2012) observed this effect in prestressing strands exposed to simulated carbonated concrete solution, where only a small addition of chlorides was necessary to initiate corrosion.

Corrosion will preferentially initiate on defect sites in the passive film. Film defects can be originated from grain boundaries, slip steps due to dislocations, or metal surface defects (Frankel, 1998). Moser et al. (2011b) showed that surface defects can also be originated during strand fabrication and stressing. Breakdown of the passive film is typically a localized phenomenon which results in the creation of a macro-galvanic cell (Rosenberg et al., 1989). Once the CTL is reached, localized pitting corrosion will likely occur.

a) Pitting corrosion

The mechanism of pitting corrosion on prestressing steel strands is similar to conventional steel reinforcement. Once the passive layer has been breached, the exposed areas undergo active corrosion. The local active area will act as an anode where the iron will readily dissolve, and the surrounding passive areas will act as a cathode (Rosenberg et al., 1989; Frankel, 1998). Meanwhile, the positively charged metal surface attracts the aggressive anions which will migrate to the site. The general corrosion reaction is given in Equation 2.42 (Jones, 1996; Frankel, 1998).

$$Fe^{2+} + 2\,H_2O + 2\,Cl^- \rightarrow Fe(OH)_2 + 2\,H^+ + 2\,Cl^- \qquad (2.42)$$

Analogous to Equations 2.39 to 2.41, Equation 2.42 shows that chloride ions are not consumed in the reaction. Instead, the chlorides dissolve the iron and then recycle to further react with more iron ions. Simultaneously, the pH inside the pit will drop because hydrogen ions are produced. As a result, pitting becomes an autocatalytic process, as shown in Figure 2.11 (Jones, 1996; Bertolini, et al, 2013; Frankel, 1998; Schmuki, 2002).

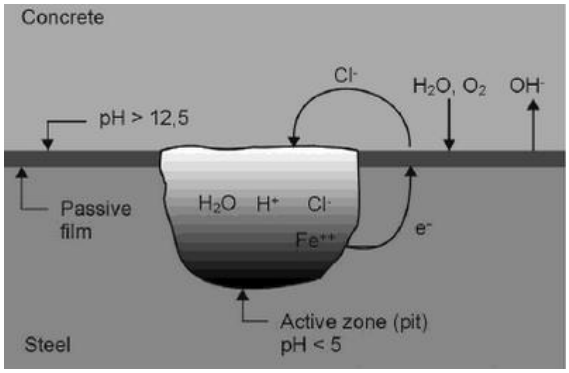

Figure 2.11 Schematic representation of pitting corrosion of steel in concrete (Bertolini et al., 2013).

b) Crevice corrosion

Although crevice corrosion of prestressing steel usually has not been considered a critical issue due to the closing of gaps between wires when strands are stressed, Moser et al. (2011a) showed that this type of corrosion can occur when imperfections on the protective coating provide preferential sites for corrosion initiation. A forensic analysis of a prestressed concrete bridge pile in the Georgia coastal region confirmed that crevice corrosion occurs, as seen in Figure 2.12 (Holland et al., 2012).

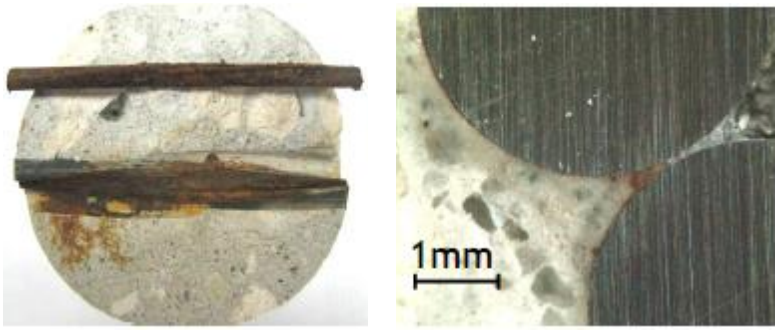

Figure 2.12 Core sample from corroded prestressed bridge pile evidencing crevice corrosion (Holland et al., 2012).

Moser et al. (2011a) also suggested that strand is more prone to initiate crevice corrosion because the alkaline cement paste is in contact with the outer surface of the strand wires. Once corrosion initiates in the crevices and acidifies the local area, a local concentration cell between the inner and outer portions of the strand develops and makes the environment more aggressive. After the initiation, the proposed mechanism of crevice corrosion propagation in chlorinated environments is very similar to the autocatalytic pitting mechanism.

At later ages, corrosion can spread to the strand surface due to a limited mass transport of reactants to the crevice regions. The model of initiation and propagation can be observed in Figure 2.13.

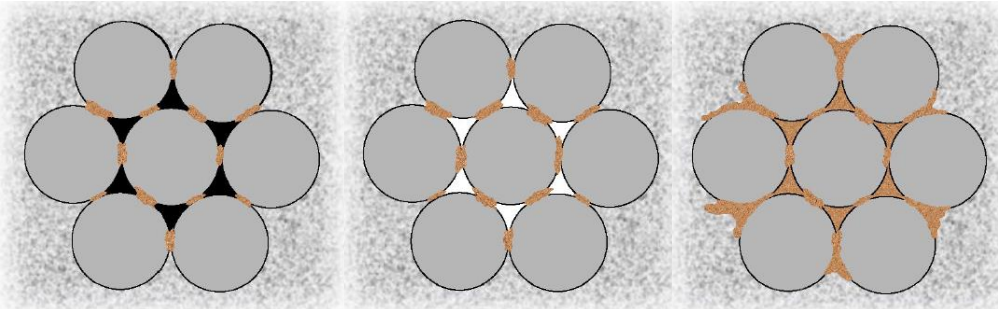

Figure 2.13 Crevice corrosion: initiation, propagation into the crevice regions, and spread of the attack to strand surface (Moser et al., 2011a).

2.3.2.3 Environment-induced cracking (EIC)

While carbonation- and chloride-induced corrosion are observed on reinforced concrete and on prestressed concrete structures, high-strength prestressing steel also shows an increased susceptibility to environmentally-induced cracking (EIC). EIC results from the combination of susceptible material and a corrosive environment. Two common mechanisms of EIC are a) stress corrosion cracking (SCC) and b) hydrogen embrittlement (HE), which can occur independently or simultaneously, and cause hydrogen-assisted cracking (HAC).

These three mechanisms may significantly reduce mechanical properties of prestressing steel. While prestressing steel is typically loaded to 60-80% of the UTS, the reduction of tensile stresses due to EIC can cause a catastrophic and brittle failure without even considering service loads. Because of their resulting brittle mode of failure, stress

corrosion cracking, hydrogen embrittlement and hydrogen-assisted cracking are of great concern and are described below.

a) Stress corrosion cracking (SCC)

Stress corrosion cracking is the phenomena where a metal under tensile stresses forms sharp, defined cracks due to exposure to a certain environment. Commonly, cracking due to SCC takes the form of intergranular or transgranular cracking; that is, cracks form along the grain boundaries or through the grains. Cracks generally start at surface discontinuities like corrosion pits, grain boundaries, microstructure defects, or fabrication defects.

The two most common theories to explain the crack propagation phenomenon are electrochemical dissolution and stress sorption. The electrochemical dissolution theory proposes that galvanic cells are formed on the grain boundaries, and localized metal dissolution initiates a crack. Then, the stress disturbs the brittle oxide film over new anodic material, which is corroded. This process continues and the crack propagates within the material. The stress-sorption theory suggests that adsorbed deleterious elements reduce the cohesion between metal ions creating a weakened boundary, and the applied stress causes crack growth along this boundary (ACI 222.2R, 2001; Jones, 1996). In the case of prestressing strands, hydrogen is generally the element that causes the brittle fracture of steel and thus, hydrogen assisted cracking (HAC) is the prevailing EIC mechanism.

Independent from the mechanism of initiation and propagation, SCC occurrence will depend on the type of metal or alloy used and the conditions of the environment. A

stress field ahead of the crack tip can be characterized by a stress intensity factor, K_I. This parameter is related to both the stress level and crack size. When K_I reaches a critical threshold level, failure occurs. SCC will occur when K_I = 43 MPa·$m^{0.5}$ and a brittle fracture will occur when K_I = 86 MPa·$m^{0.5}$ (Darmawan and Stewart, 2007). Several tests have shown that present day prestressing strand has K_I values well above the SCC critical threshold in atmospheric and chloride environments. Thus, conventional steel strands are resistant to SCC in these environments (Nurnberger, 2002; Toribio and Ovejero, 2005; Darmawan and Stewart, 2007).

b) Hydrogen embrittlement (HE) and hydrogen-assisted cracking (HAC)

Hydrogen embrittlement (HE) is the reduction of ductility of metals and alloys due to the absorption of hydrogen atoms into the metal lattice (Fontana, 1986). HE does not require stress to occur, and hydrogen can be introduced during manufacturing of strand and strand storage, and during precast concrete pile construction and life of the pile. Some sources of hydrogen are welding, electroplating, hydrogen gas, cathodic polarization, and corrosion products. Hydrogen atoms present on the metal surface penetrate the metal lattice occupying different positions in the microstructure.

Hydrogen atoms trapped in the metal lattice are mainly responsible for the occurrence of HE on prestressing steel, because they deform the steel lattice. This deformation affects the mechanical properties of the steel, and straining the lattice limits the ductile slip mechanism and reduces toughness. The level of embrittlement increases with the amount of hydrogen trapped inside the steel (Recio et al., 2013), and some chemicals have been shown to accelerate HE, including hydrogen sulfide (H_2S), carbon dioxide (CO_2), chloride (Cl^-), cyanide (CN^-), and ammonium ions (NH_4^+).

Novokshchenov (1994) found that the susceptibility of steel to HE increases with increased carbon content, increased cold working, increased stress relieving, increased chloride concentration, and increased temperature. Additionally, forensics performed on structures affected by HE have revealed that embrittled steel presents the following characteristics: lower tensile strength reflects a loss of ductility due to hydrogen absorption, failure occurs over a broad range of applied stress, time to failure depends on the applied stress, and below a critical stress, failure does not occur (ACI 222.2R, 2001). However, hydrogen uptake is a function of environmental pH and HE is only observed with pH lower than 7. Thus, hydrogen absorption is not feasible when steel is in a passive state (Griess and Naus, 1980).

HE can act concurrently with SCC to form hydrogen-assisted cracking (HAC). Cracks are initiated by pitting corrosion which causes a local concentration of hydrogen ions and a lower pH. Simultaneously, hydrogen also has a tendency to concentrate where tensile stresses are the highest within the metal lattice, near the crack tip. The crack will propagate once the lattice is sufficiently embrittled, combined with an adequate tensile force (Figure 2.14). This process will continue to repeat itself and lead to steel failure as long as hydrogen and stress remain present (Bertolini et al., 2013). Conventional AISI 1080 prestressing steel, tested using the Federation Internationale de la Precontrainte test (FIP-test), has showed high resistance, but not complete immunity to HAC susceptibility (Nurnberger, 2002; Toribio and Ovejero, 2005; Wu and Nurnberger, 2009).

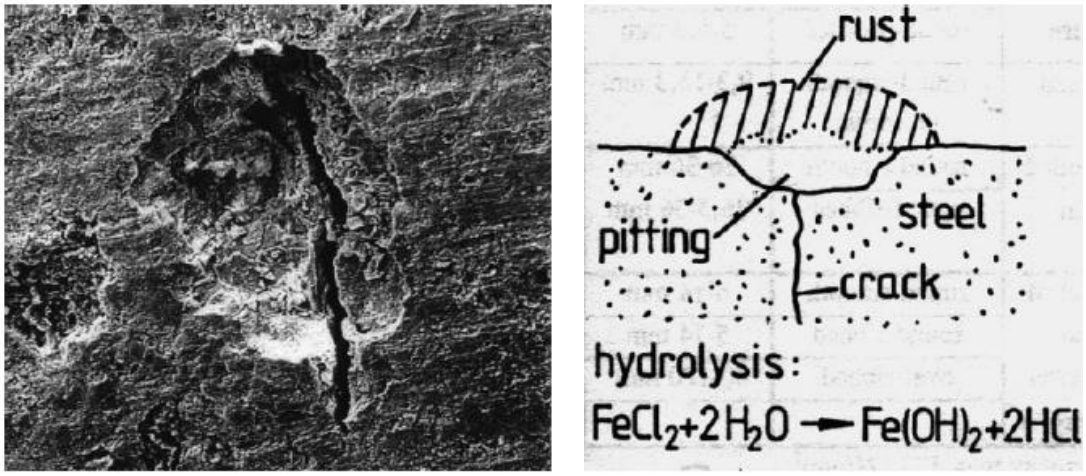

Figure 2.14 HAC of steel in concrete at a pit site (Nurnberger, 2002).

2.3.2.4 Alternative reinforcement for corrosion prevention

To prevent the high cost associated with maintenance, corrosion-resistant reinforcement has been proposed to reduce chloride-induced corrosion. These alternative reinforcement systems include galvanized reinforcement, epoxy-coated reinforcement, and stainless steel reinforcement.

Galvanized steel has a coating of zinc that protects steel, acting as an anode and increasing the time to corrosion initiation. Galvanized steel forms a passive layer in the alkaline environment of concrete, similar to the case of conventional steel. However, even when the corrosion initiation is delayed by the presence of a zinc coating, the durability of galvanized steel in marine environments is insufficient. It has been estimated that galvanized steel can corrode in about 5 years when exposed to aggressive environments (Bautista and Gonzalez, 1996). Also, uncertainty of structural response of this material is introduced by the effect of galvanizing on the brittleness of bars with different composition and degrees of work hardening (Azizinamini et al., 2013).

Epoxy-coated bars reduce considerably the diffusion of oxygen and chloride through a barrier organic coating that protects reinforcing steel from corrosion. Some disadvantages include the degradation of the epoxy coating in alkaline moist conditions in concrete, the permeability of the coating to water (Weyers et al., 2006; Azizinamini et al., 2013), and the weaker adhesion of the reinforcement and concrete (Rasheeduzzafar et al., 1992). As a result, field and experimental studies predict that the use of epoxy-coated bars extends the service life of carbon steel in chloride-bearing concrete no more than 5 years (Weyers et al., 2006).

Stainless steels are iron-chromium alloys that have a high corrosion resistance. Austenitic and austenitic-ferritic (duplex) stainless steel have shown more favorable potential to be used as reinforcement in concrete structures due to their excellent corrosion resistance when exposed to chloride-containing concrete (Wu and Nurnberger, 2009), and they have been effectively used in coastal bridges. However, the main concern in adopting this steel is the higher material cost. Moser et al. (2012) estimated in 2011 that austenitic grades 304 and 316 had a cost 6.9 and 9.6 times higher than conventional steel, respectively, while duplex grade 2205 had a cost 8.8 times higher than conventional carbon steel. Life cycle cost analysis has shown that the use of stainless steel reinforcement is cost-effective in marine environments, considering the extended service life and the minimal maintenance costs for structures made with stainless steel reinforcement (Azizinamini et al., 2013).

2.3.3 Properties of Stainless Steels

Stainless steel (SS) is a general denomination for ferrous alloys with a minimum chromium content of 10.5–11.0 wt. %. Presence of chromium allows the formation of a thin, self-healing chromium oxide layer that gives stainless steel a higher corrosion resistance than conventional steel, even in severe marine environments (Figure 2.15).

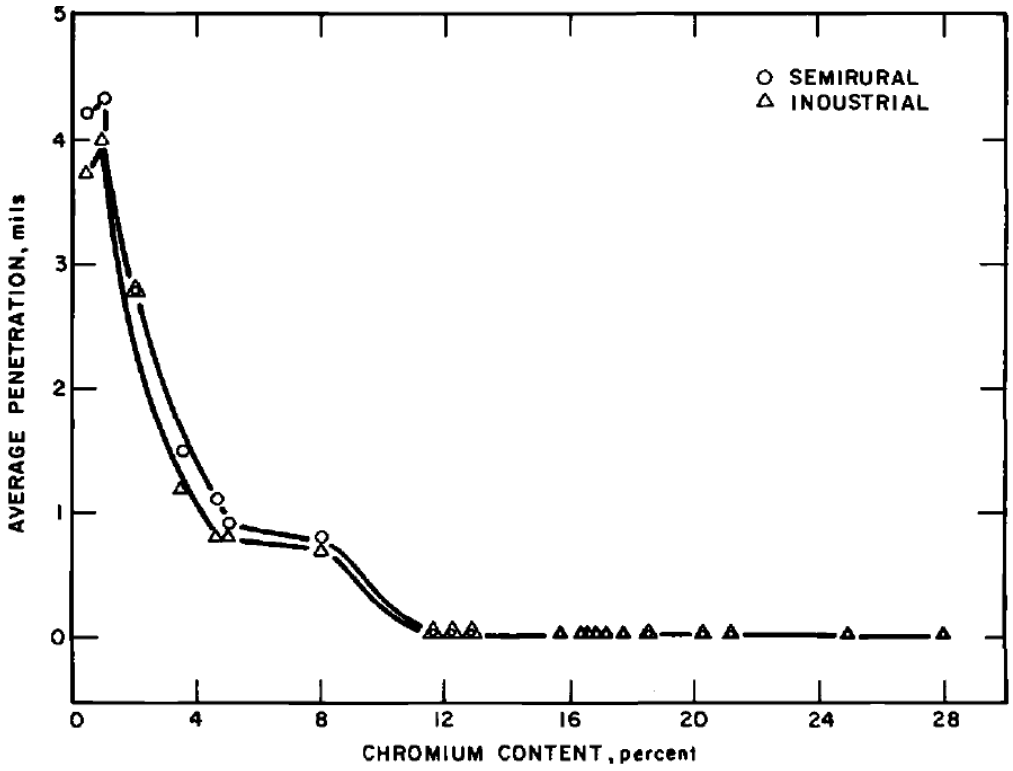

(a)

Figure 2.15 Effect of chromium content on corrosion depth of stainless steel on (a) urban and semi-rural, and (b) marine environments (Schmitt and Mullen, 1969).

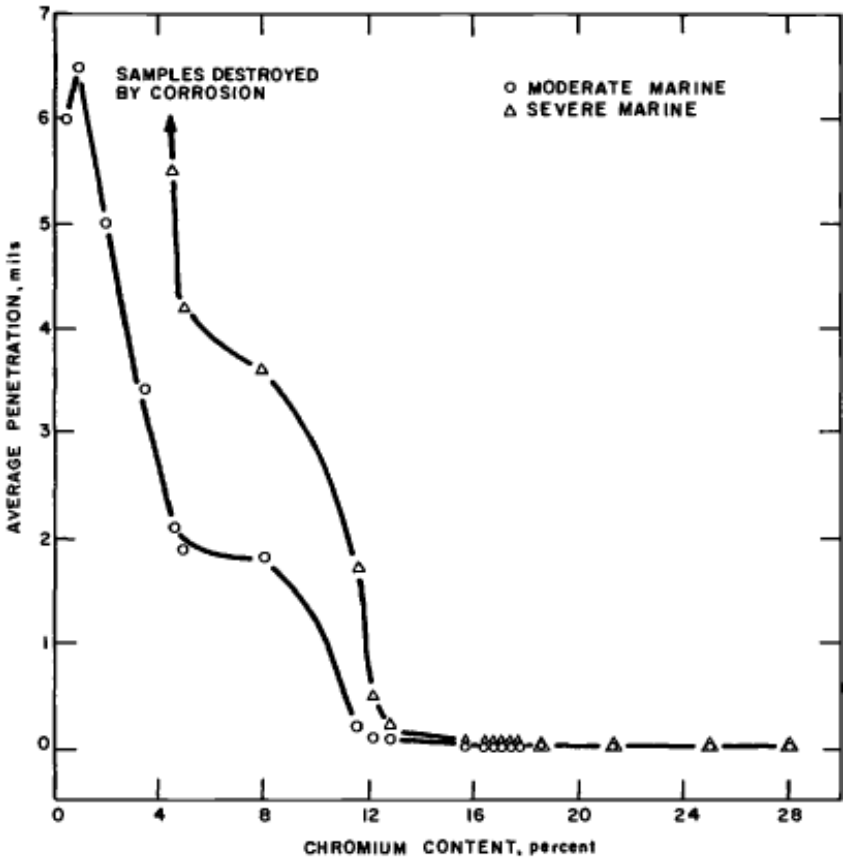

(b)

Figure 2.15 (cont.) Effect of chromium content on corrosion depth of stainless steel on (a) urban and semi-rural, and (b) marine environments (Schmitt and Mullen, 1969).

The composition of stainless steels used in civil and mechanical engineering applications is highly variable, but commonly elements such as Mn, P, S, Si, Ni, Mo, and N are present (ASTM A276, 2015). Consequently, a broad range of mechanical properties and corrosion resistance can be obtained. For instance, the addition of Mo enhances the resistance to pitting formation, while Ni addition increases the stability of austenite (Lo et al., 2009).

2.3.3.1 Classification of stainless steels

Stainless steels are commonly classified as austenitic, ferritic, duplex (austenitic-ferritic), martensitic, and precipitation hardening.

Austenitic stainless steels are iron-chromium alloys that form face-centered cubic (FCC) austenite phase, with typical composition of Cr and Ni greater than 18% and 8%, respectively. They usually are non-magnetic and have high ductility, toughness, and work hardening during cold drawing. Also, nickel acting synergistically with chromium provides improved corrosion resistance compared with other stainless steels (Jones, 1996; Moser et al, 2012). Austenitic stainless steels are the most widely used stainless steels. Most common austenitic grades, AISI 304 and AISI 316, have been used in construction elements exposed to marine and urban environments, and also as reinforcement in concrete structures (Wallinder et al., 2002; Hartt et al., 2006). When austenitic SS is exposed to cold drawing higher to 40%, its microstructure can partially or fully transform to martensite, process that affect the mechanical properties and reduce the corrosion resistance of steel (Wu and Nurnberger, 2009).

Ferritic stainless steels have a body-centered cubic (BCC) structure and they are alloyed mostly with 12–16% of chromium that acts as ferrite stabilizer. Little amounts of Mo and Ni can also be incorporated. Ferritic SS grades have higher ultimate and yield strengths, and lower ductility, toughness, and corrosion resistance compared to austenitic grades (Moser et al., 2012).

Martensitic and precipitation hardening stainless steels usually have high strengths but, due to their lower corrosion resistance, they are more commonly used in mild environments (Jones, 1996).

Duplex stainless steels are composed of a ferrite-austenite dual microstructure, in roughly equal proportions. Duplex SS grades generally have a chromium content between 21% and 27%, and additions of Ni (1.5-24.5%), Mo (0.3-6.1%), and N (0.05-0.27%). Some duplex SS grades include minor contents of W and Cu (Alvarez-Armas, 2008). The dual-phase structure combines the superior mechanical properties of the ferrite phase with the high corrosion resistance of the austenite phase.

Duplex SS grades can be categorized by their pitting resistance equivalency number (PREN), calculated using the weight fraction of Cr, Mo, and N (Equation 2.43).

$$PREN = \%Cr + 3.3 \cdot \%Mo + \beta \cdot \%N \tag{2.43}$$

where β is 30 for duplex grades, and 16 otherwise. This number provides a relative comparison of the expected resistance to pitting corrosion in marine environments, but it does not give a good measure of the corrosion resistance of stainless steel.

Generally, duplex SS with PREN lower than 30 are categorized as lean duplex grades, PREN between 30 and 40 defines standard duplex grades, and SS with higher PREN are considered superduplex alloys (Alvarez-Armas, 2008). Most common duplex grade is standard duplex 2205 (ASTM A276 grade UNS S32205). SS 2205 and lean duplex grades 2101 and 2304 (UNS S32101 and S32304, respectively) have been tested as reinforcement in concrete structures due to the higher corrosion resistance compared to austenitic grades (Moser et al., 2011; Hartt et al., 2006).

Characteristics of the most common stainless steel grades are given in Table 2.1.

Table 2.1 Composition and PREN of the most common stainless steels (Moser et al., 2012).

Grade	Type	**Composition (wt. %)** – Fe Balance						PREN
		C	N	Cr	Ni	Mo	Other	
304	Austenitic	0.04	0.06	18.2	8.1	------	------	19.2
316	Austenitic	0.04	0.06	17	11	2.8	------	27.2
430	Ferritic	0.04	------	16.5	------	------	------	16.5
2101	Duplex	0.03	0.22	21.5	1.5	0.3	5 Mn	29.1
2205	Duplex	0.02	0.17	22	5.5	3	------	37.0
2304	Duplex	0.02	0.10	23	4.8	0.3	------	27.0

2.3.3.2 Mechanical properties of stainless steels

Compared to conventional carbon steel used in structural applications, stainless steel exhibits a different stress-strain behavior. No clear yield point is appreciable and post-yield behavior cannot be modeled as a flat plateau (Gardner, 2005). Ramberg-Osgood expression (Equation 2.44) is often used to represent the stress-strain relation of SS before yield (Ramberg and Osgood, 1941).

$$\varepsilon = \frac{\sigma}{E_0} + 0.002\left(\frac{\sigma}{\sigma_{0.2}}\right)^n \qquad \text{for } \sigma \le \sigma_{0.2} \tag{2.44}$$

where E_0 is the initial elastic modulus, $\sigma_{0.2}$ is the stress obtained by the 0.2% offset method, σ is the tensile strength, ε is the tensile strain, and n is a parameter calculated using Equation 2.45.

$$n = \frac{\ln(20)}{\ln\left(\frac{\sigma_{0.2}}{\sigma_{0.01}}\right)} \tag{2.45}$$

where $\sigma_{0.01}$ is the stress obtained by the 0.01% offset method.

Rasmussen (2003) proposed an expression for the stress-strain behavior after yield (Equation 2.46).

$$\varepsilon = \frac{\sigma - \sigma_{0.2}}{E_{0.2}} + \varepsilon_u \left(\frac{\sigma - \sigma_{0.2}}{\sigma_u - \sigma_{0.2}}\right)^m \qquad \text{for } \sigma > \sigma_{0.2} \tag{2.46}$$

where $E_{0.2}$ is the tangent elastic modulus at yield point, σ_u is the ultimate tensile strength, ε_u is the ultimate tensile strain, and m is a parameter calculated using Equation 2.47.

$$m = 1 + 3.5\frac{\sigma_{0.2}}{\sigma_u} \tag{2.47}$$

Equations 2.44 and 2.46 showed good agreement with tensile test results performed on austenitic grades AISI 304, AISI 304L, and AISI 316L, duplex grade 2205, and ferritic grades AISI 430 (UNS 43000) and 3Cr12 (UNS 41050) (Rasmussen, 2003).

Additionally, stainless steels exhibit higher retention of strength and stiffness at elevated temperatures compared to conventional steel (Gardner, 2005).

2.3.3.3 Use of stainless steel in prestressed concrete elements

Studies of the use stainless steel to improve the corrosion resistance of prestressing strands have been focused on austenitic grades, given their good corrosion

resistance. Cold-drawn strands and wires of grades 304, 316, and 316LN (low carbon, nitrogen enhanced steel) have been produced with ultimate tensile strengths between 203 and 268 ksi (1,400 to 1,850 MPa) and stress relaxation of 7% (Moser et al., 2012). Good resistance to chloride-induced corrosion has been reported, with no corrosion initiation at Cl^- concentrations as high as 1.5 M, higher concentration than expected in seawater (Hurley and Scully, 2006). Phase transformation to martensite higher to 50% has been observed in production of grade 304 specimens (Milad et al., 2008), which can explain a lower resistance to pitting corrosion and chloride-assisted SCC compared to grades 316 and 316 LN (Wu and Nurnberger, 2009). Application of austenitic stainless steel prestressing strands in full scale structures has not been reported.

Duplex high-strength stainless steel (HSSS), similar in composition to grade 2205, was analyzed as a replacement of carbon prestressing steel by Shirahama et al. (1999). Duplex HSSS was cold-drawn and stranded, the UTS was 237 ksi (1,636 MPa), the ultimate strain was 4.0%, and stress relaxation was 0.5% at an accelerated 10-hour test. Experimental analysis showed low susceptibility to chloride-induced corrosion, pitting corrosion, HE, and SCC.

Use of Nitronic 33 stainless steel (conforming requirements for austenitic ASTM A580 grade XM-29), 3/16-in. (4.76 mm) diameter 7-wire prestressing strands in marine structures was reported by Jenkins (1987). Nitronic 33 strands had 17.7% Cr, 12.2% Mn, and 3.5% Ni. UTS and ultimate strain of wires were 136 ksi (937.7 MPa) and 33.3%, respectively. The study included full scale piles and the measurement of the corrosion potential over time, which showed enhanced corrosion protection compared to piles using carbon steel.

Moser et al. (2012) analyzed different HSSS grades to select the most promising to be used as a replacement of conventional AISI 1080 steel in prestressing strands. Low-relaxation wires of austenitic grades 304 and 316, martensitic grade 17-7, and duplex grades 2101, 2304, and 2205 were prepared using conventional practice. UTS of stainless steel wires varied from 181 to 225 ksi (1,250 to 1,550 MPa), and a lack of strain hardening after yielding was observed (Figure 2.16).

Analysis of the fracture surface showed a non-ductile failure in duplex HSSS 2205 samples. Corrosion testing of wires showed lower chloride-induced corrosion susceptibility of duplex grades 2205 and 2304 in alkaline and carbonated simulated environments.

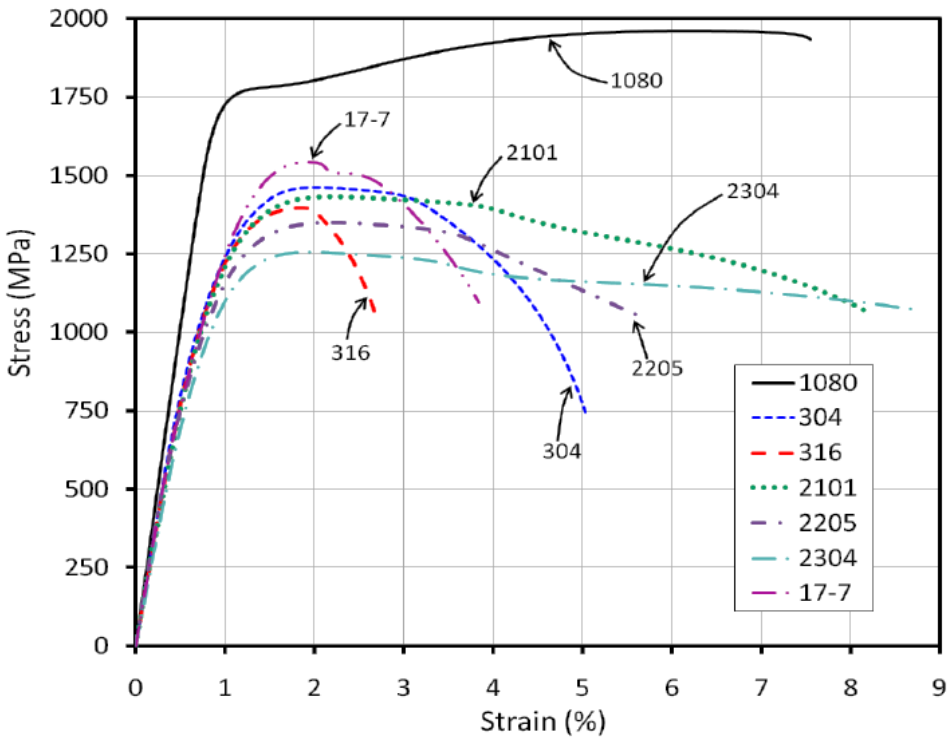

Figure 2.16 Stress-strain curves for conventional AISI 1080, austenitic 304 and 316, martensitic 17-7 and duplex 2101, 2205 and 2304 wires (Moser et al., 2012). (1 MPa = 145 psi)

Using traditional procedure of stranding and conditioning, 7–wire prestressing strands were confectioned using duplex HSSS 2205 and 2304. Under the same testing conditions used for the corrosion resistance of wires, duplex HSSS 2304 strands showed pitting corrosion initiation for alkaline and carbonated formation with Cl^- concentration of 0.5M, concentration level expected in seawater. Duplex HSSS 2205 strands showed no corrosion evidence at Cl^- concentration of 1.00 M in alkaline and carbonated solutions (Moser et al., 2012).

Schuetz (2013) tested the mechanical properties of duplex grades 2205 and 2304 prestressing strands. Duplex HSSS strands showed less ductility, elastic modulus, ultimate strain, and UTS than AISI 1080 steel strands (Figure 2.17).

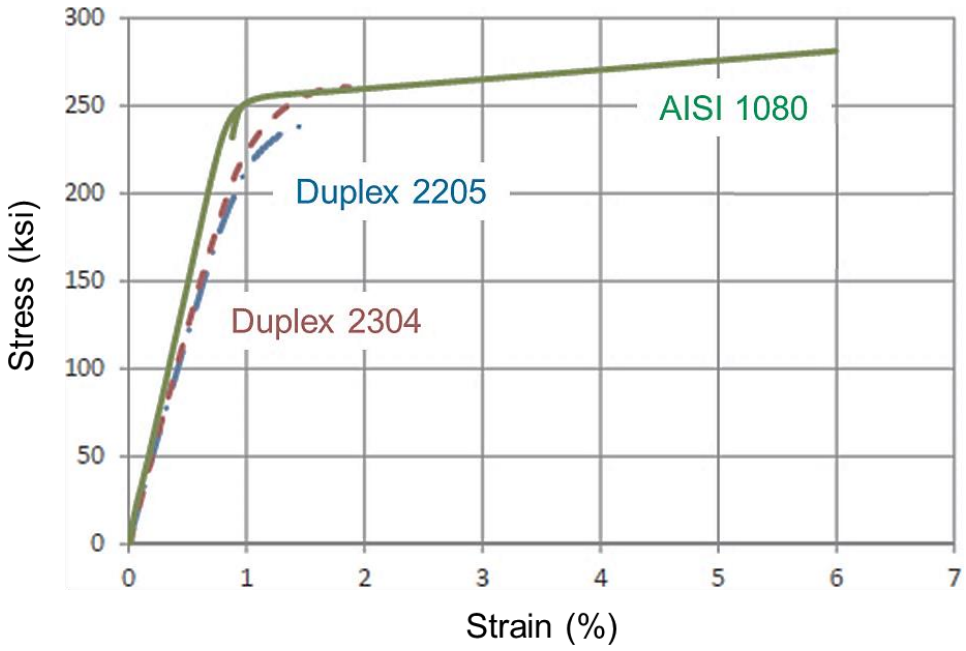

Figure 2.17 Stress-strain curves for conventional AISI 1080 steel, and duplex grades 2205 and 2304 prestressing strands (modified from Schuetz [2013]). (1 ksi = 6.9 MPa)

CHAPTER 3

EFFECT OF ACIDIC SANDS IN CEMENT-BASED MATERIALS

Following the characterization of the acidic sands, the analysis of the effects of acidic sands in cement-based materials was divided in 1) early-age behavior of mortar samples, 2) mechanical properties of concrete, and 3) durability of mortar and concrete using acidic sands, as shown in Figure 3.1, in order to address the specific objectives presented in Section 1.2.

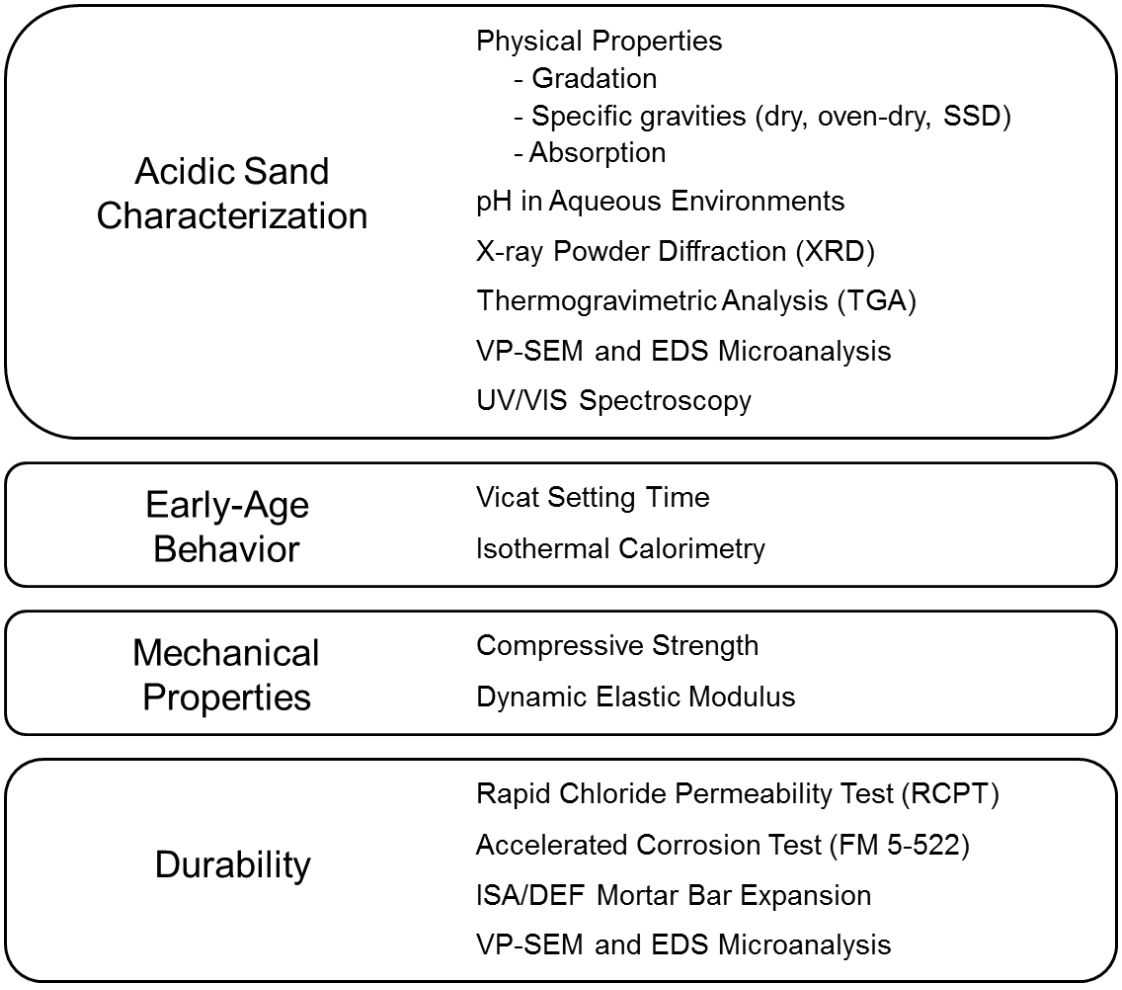

Figure 3.1 Acidic sands evaluation tests.

While sand characterization, early-age behavior assessment, and mechanical properties are included in Chapter 3, the study of the durability of portland cement systems using acidic sands is divided in two parts and the potential for ISA and DEF reaction is analyzed separately in Chapter 4.

3.1 Introduction

Sulfate is traditionally included in portland cement as natural gypsum in order to regulate the setting time of concrete. The amount of gypsum in portland cements is limited by standards, but additional sulfate present in aggregates can lead to undesirable effects on the early-age behavior strength development, volume stability (Taylor, 1997), and corrosion resistance of concrete.

Additionally, the oxidation of reactive forms of iron sulfide present in aggregates can release sulfate ions and decrease the pH of cement-based materials, depending on the relative amount and reactivity of sulfide. This can lead to early-age cracking of concrete, formation of additional ettringite, formation of voluminous corrosion products of iron (Tagnit-Hamou et al., 2005).

In this chapter, the effect of Site H and Site D sands on the early-age behavior of cement-based materials is studied using isothermal calorimetry and Vicat setting time test. The development of mechanical properties is analyzed by the measurement of compressive strength and dynamic elastic modulus of concrete specimens during the first 90 days of hydration, and the durability is assessed through the measurement of the chloride permeability, surface resistivity measurement, and corrosion resistance of concrete.

3.2 Properties of Materials

3.2.1 Characterization of Acidic Sands

Three different sands were considered in this study (Figure 3.2). These include samples from two different stockpiles, denoted as Sites H and D, of a quarry production facility in Hinesville, Georgia. Sands obtained from different stockpiles correspond to different extraction times, being Site H sand more recent that Site D sand. These sands were compared with natural siliceous sand, approved by the Georgia Department of Transportation (GDOT) and obtained from an alluvial/marine deposit in Roberta, Georgia. Throughout this document the sands will be referred using these denominations: Control, Site H, and Site D sands. The term "acidic sands" is also used for Site H and Site D sands.

According to the producer, Site H sand has a water soluble sulfate (SO_4^{2-}) content of 0.037% and a pyritic sulfur content of 0.020%, while Site D sand has a negligible amount of pyrite and 0.029% of water soluble sulfate content. The control sand has insignificant amounts of sulfate and pyritic sulfur.

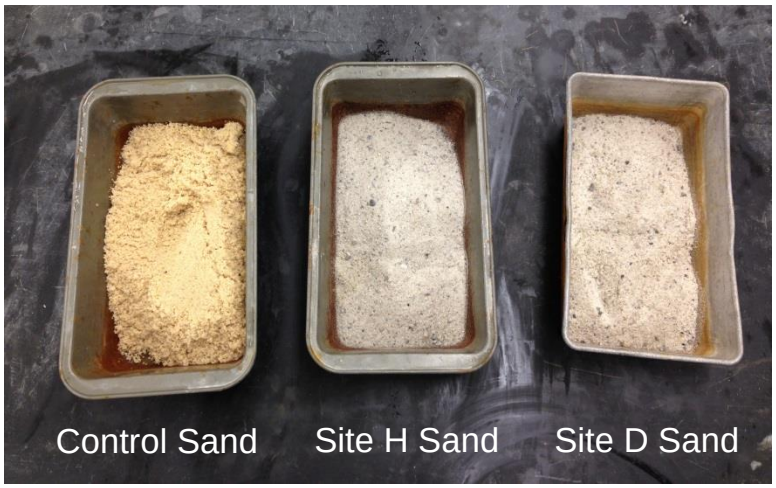

Figure 3.2 Appearance of analyzed sands.

3.2.1.1 Physical properties of sands

The aggregate gradation (see Figure 3.3) was measured using sieve analysis following ASTM C136, while the specific gravities (SG) and absorption were obtained according to ASTM C128 (Table 3.1).

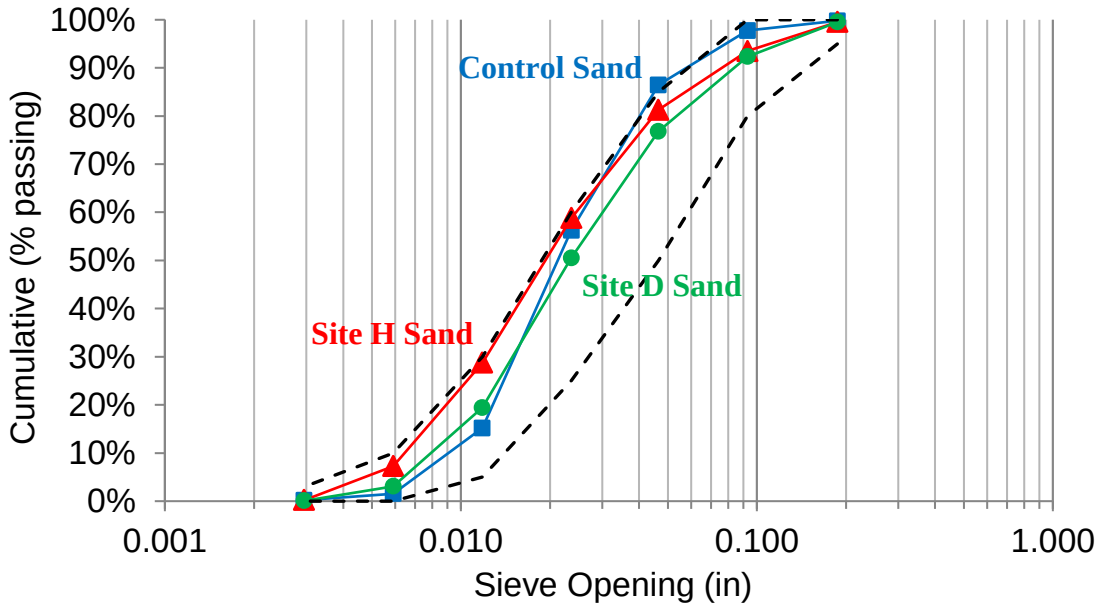

Figure 3.3 Gradation curves of sands. Dashed lines show limits for fine aggregate according to ASTM C33. (1-in. = 25.4 mm)

Table 3.1 Physical properties of sands.

	Apparent SG (Dry)	SG Oven Dry	SG Saturated Surface Dry	Absorption	Fineness Modulus
Control Sand	2.66	2.63	2.64	0.32%	2.43
Site H Sand	2.61	2.59	2.60	0.27%	2.31
Site D Sand	2.62	2.60	2.61	0.19%	2.58

Site H sand is relatively finer than Site D and Control sands, but all the sands have a percentage of particles finer than 75 μm (2.95×10^{-3}-in.) lower than 0.25%, below

the ASTM C33 maximum for fine aggregate (3.0%). The physical properties served as input for mortars and concrete mixture designs.

3.2.1.2 pH of sands in aqueous environments

To assess variations in pH among the sands, 250 g (0.55 lbs.) oven-dried samples of each of the sands were immersed in 300 ml (10.1 oz.) tap water (pH = 6.95) in sealed containers, at 23 °C (73 °F), during 790 days (Figure 3.4). To cool the sands to room temperature, samples were kept in the containers for 30 minutes, after which water was added. The first pH measurement was taken 30 minutes after water addition using a Thermo Scientific Orion 3-Star Plus pH Portable Meter. Measurements were taken every 1 or 2 days during the first month and at a lower frequency afterwards.

Figure 3.4 Specimens for pH measurements.

Variation of pH during the first month is shown in Figure 3.5a. Control sand exhibits a near-neutral pH of just under 7, while the pH for Site D and Site H is acidic, exhibiting values of ~3 or less. A drop of pH to acidic levels in Site H and Site D samples occurred in the first 30 minutes, and pH of Site D sample remained lower to Site H

sample during the first month. The evolution of pH during 790 days is given in Figure 3.5b, where it is observed a slower pH stabilization of Site H sand compared to Site D sand. Final pH of acidic sands and Control sand was 2.70 and 6.91, respectively.

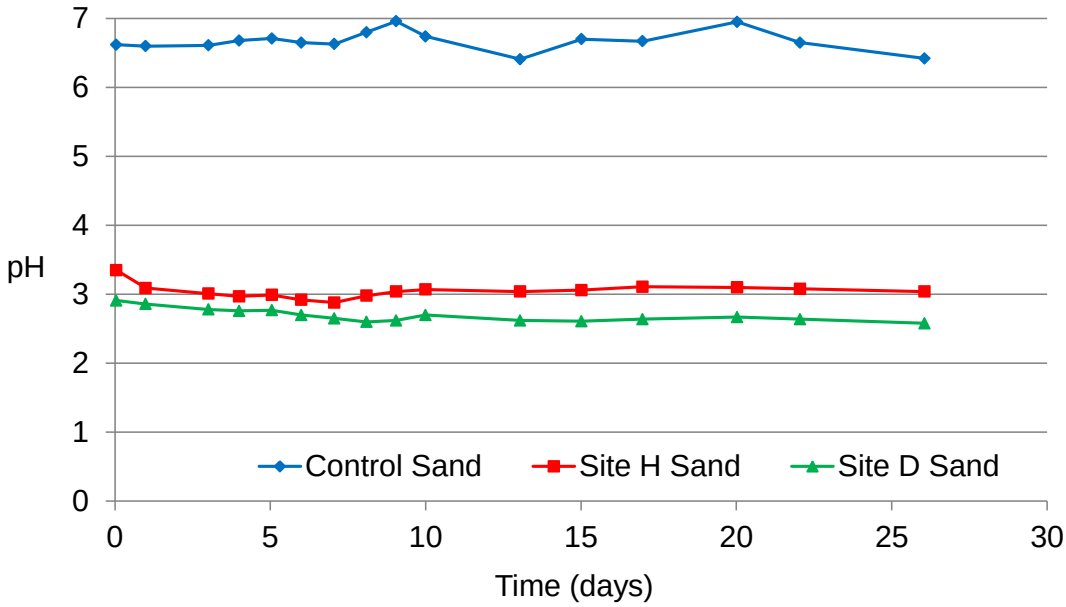

(a)

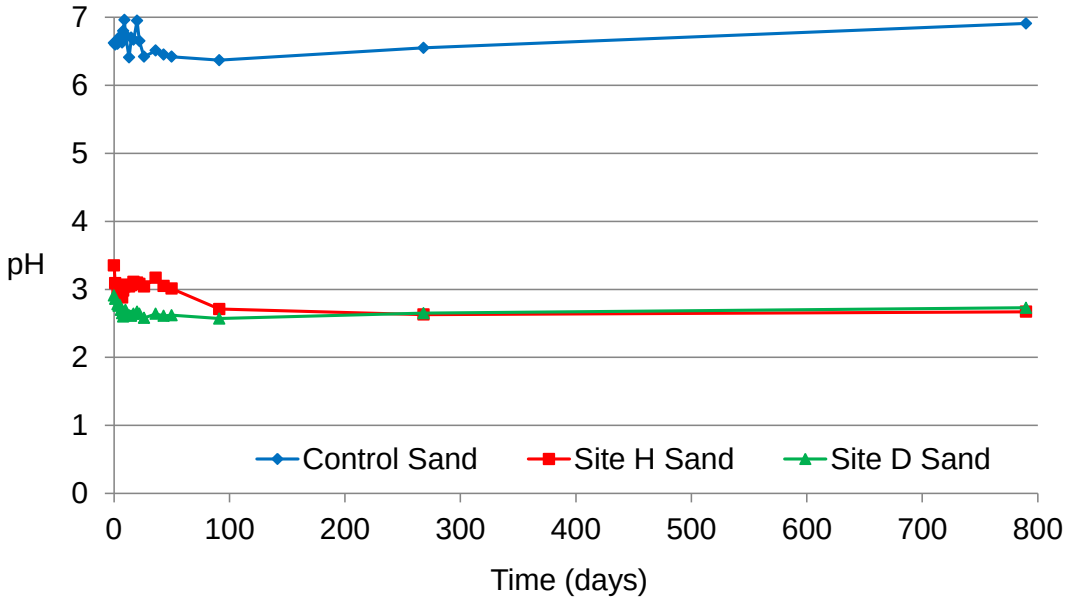

(b)

Figure 3.5 pH variation of sands over time during (a) the first 26 days and (b) during 790 days. Initial pH of water was 6.95 for all the samples.

The variation in pH over time is consistent with pH values associated with the oxidation of pyrite observed by Chinchón-Payá et al. (2012) using a similar test set up. Presence of a yellow-brown precipitate in Site D container (Figure 3.6) and higher turbidity of Site H sample (Figure 3.4) can be attributed to the presence of iron oxide formed during oxidation. Also, the curves in Figure 3.5 indicate an ongoing reaction that could be explained by the autocatalytic nature of pyrite oxidation in presence of acidophilic bacteria. However, pyrite was identified by the producer only for the Site H sand, not in Site D, while both sands showed similarly low pH values in water.

Figure 3.6 Precipitate in container with Site H sand.

Measurement of pH was also performed in diluted mortar samples, following a similar procedure to the one used for sands immersed in water. After the sands had cooled to room temperature, a cement paste composed of 300 ml (10.1 oz.) deionized (DI) water and 5 g (0.011 lbs.) Type I/II cement was mixed with the sands. Cement

pastes were mixed separately and their pH was measured right before mixing the paste with the sands, while pH of diluted mortar was first measured 1 minute after mixing.

Figure 3.7 shows the evolution of pH during 45 hours, where a small difference in the pH of mortars is observed. In the Control sand sample, the same pH value was measured in cement paste and diluted mortar at 1 minute from mixing, followed by an asymptotic pH increase. Mortar using Site H and Site D sand evidenced a decrease of pH of 0.15 and 0.05 with respect to cement paste after 1 minute, respectively. However, after 45 hours, pH of every sample converged to 12.73.

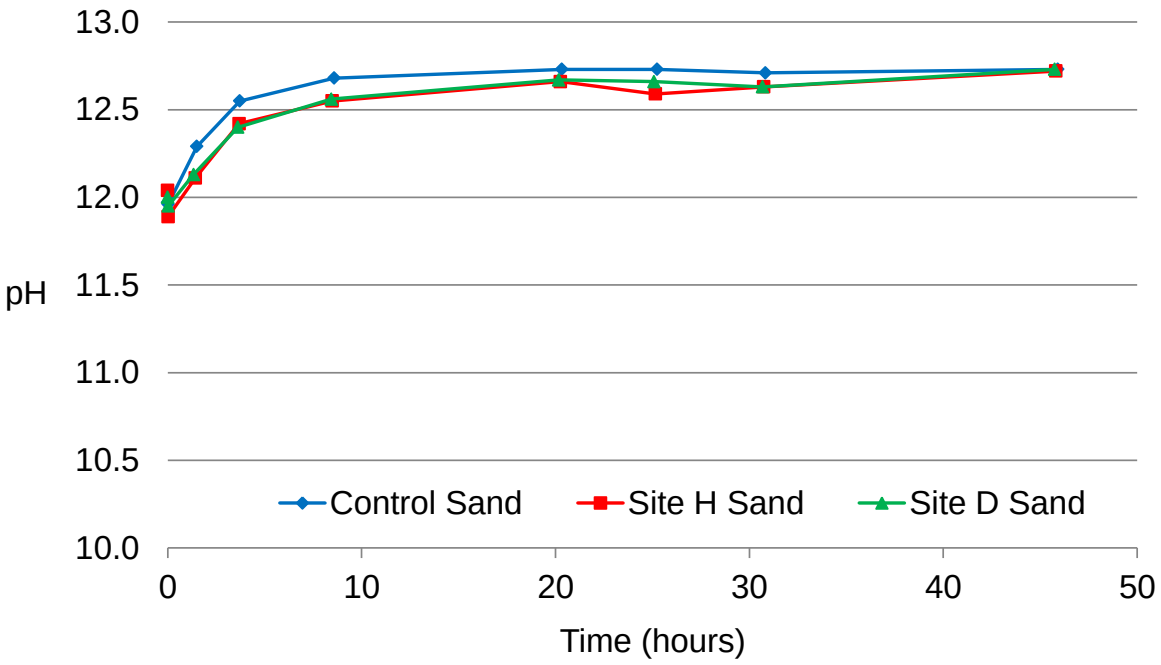

Figure 3.7 pH variation of mortar samples.

3.2.1.3 XRD and TGA analysis of sands

To identify crystalline phases in each sand source, powder X-ray Diffraction (XRD) was performed on a PANalytical X'Pert Materials Research Diffractometer,

equipped with a Cu-Kα X-ray source and a fast linear detector. Phase identification of the XRD patterns was performed using commercial software MDI Jade 9.

Oven-dried samples of sand were manually crushed in a porcelain mortar and passed through a No. 100 sieve (150 μm [5.9×10^{-3}-in.]). Then, powdered sand was ground on a Retsch PM 100 planetary ball for 3 minutes and only the material passing a No. 200 sieve (75 μm [2.95×10^{-3}-in.]) was used for XRD analysis. Samples were scanned in the 5-70° range, with a scan step size of 0.0167°, and at 40 mA and 45 kV.

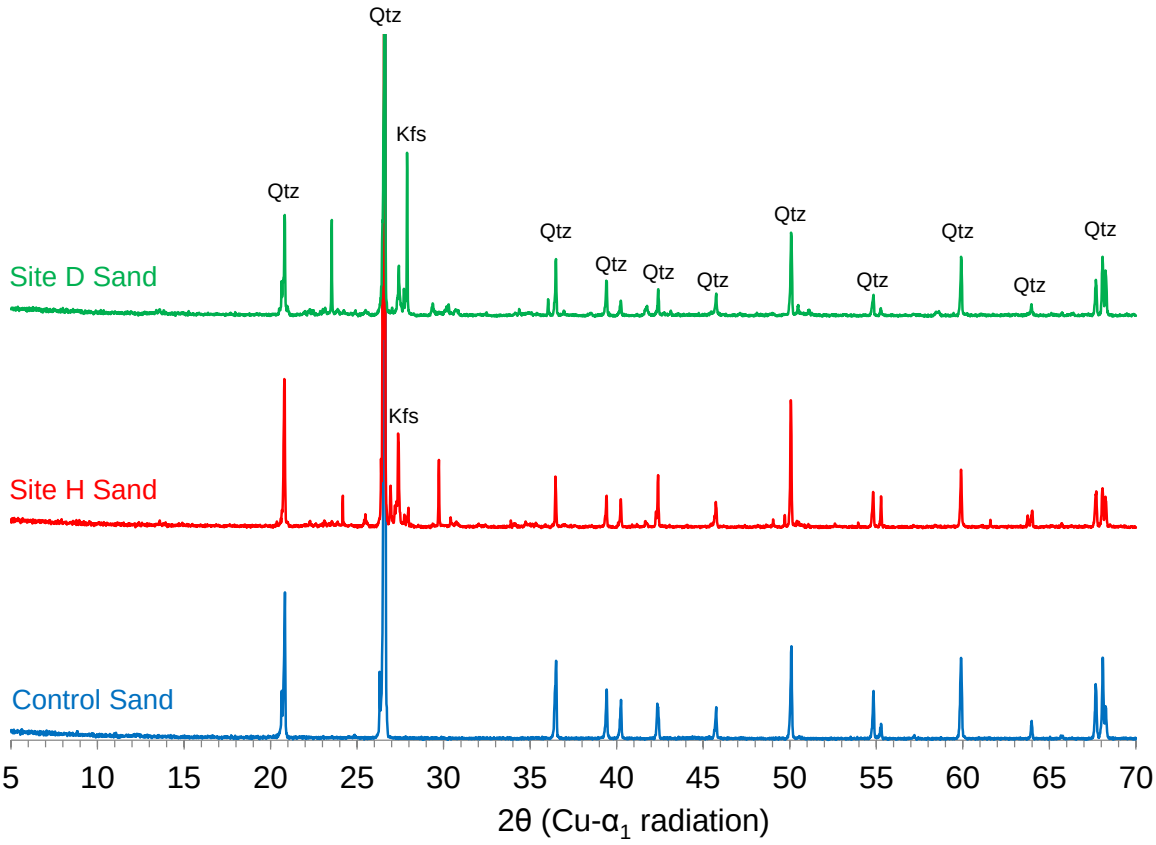

Figure 3.8 XRD pattern of the sands (Qtz = quartz, Kfs = potassium feldspar). Main peak at 2θ = 26.67° was truncated to highlight the differences between the sands.

XRD pattern of Control sand (Figure 3.8) shows a 99% agreement with pure α-quartz (SiO_2), while Site H and Site D sands present additional peaks that can be

attributed to alkali and plagioclase feldspar. Peaks in the XRD patterns of acidic sands between 2θ = 27° and 29° are consistent with the presence of microcline (alkali feldspar, $KAlSi_3O_8$); in the case of Site D sand, the presence of labradorite (plagioclase feldspar, $Na_{0.5\text{-}0.6}Ca_{0.4\text{-}0.5}Al_{1.3\text{-}1.6}Si_{2.4\text{-}2.6}O_8$) is also probable.

The rest of the peaks present on the XRD patterns of acidic sands do not show a clear agreement with other mineral phases. However, in Site H sand, the potential presence of picromerite ($K_2SO_4 \cdot MgSO_4 \cdot 6H_2O$), langbeinite ($K_2Ca_2(SO_4)_3$), and hedenbergite ($Ca(Fe^{2+},Mg)Si_2O_6$) was identified, while peaks in Site D sand show agreement with mercallite ($KHSO_4$) and arcanite (K_2SO_4).

Additionally, different ranges of sizes were also analyzed for sieved fractions of Site H sand. XRD patterns shown in Figure 3.9 indicate that the differences in composition are present mainly on the smallest particle sizes (finer than 75 µm).

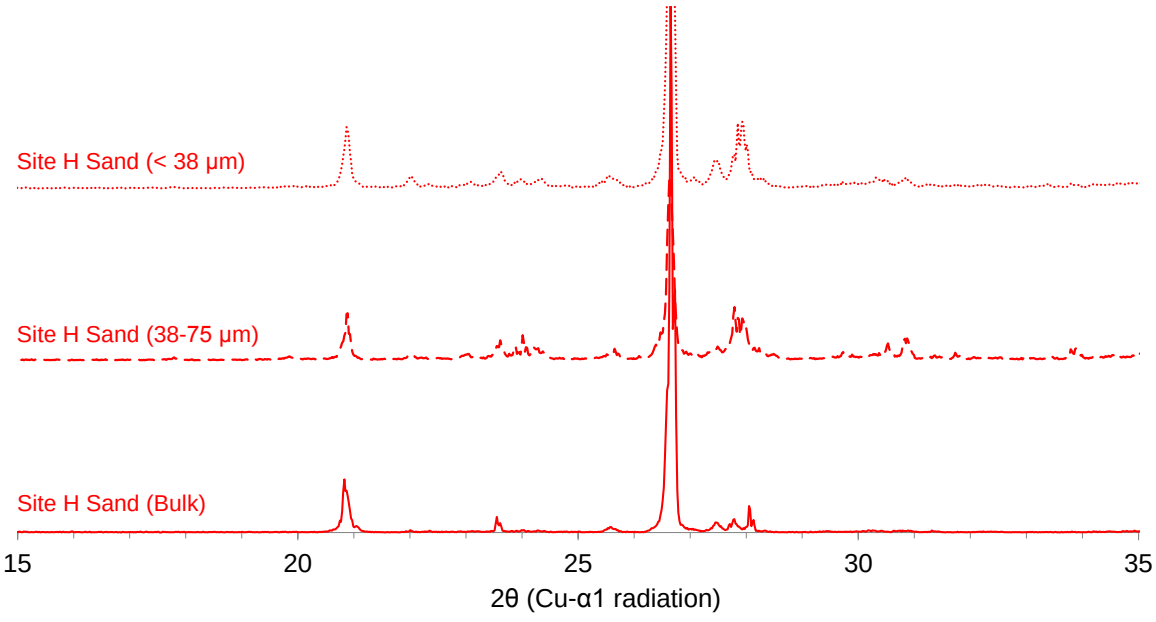

Figure 3.9 XRD pattern of different sizes of Site H sand. Main peak at 2θ = 26.67° was truncated to highlight the differences between the samples.

The characterization of the sands was complemented by thermogravimetric analysis (TGA) combined with differential thermal analysis (DTA). DTA curves (Figure 3.10), normalized by ignited mass at every temperature, show the familiar phase transition of quartz, around 573 °C (1,063 °F), from α-quartz to β-quartz (Tsuneyuki et al., 1990).

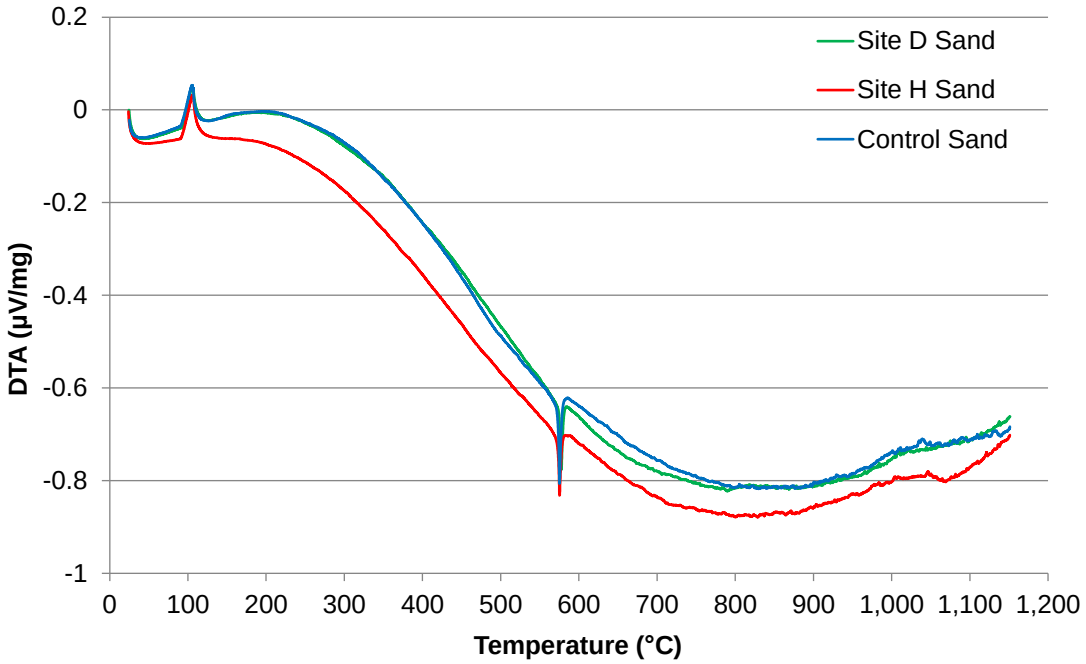

Figure 3.10 Differential thermal analysis curves for control, site H, and site D sands. (°F = °C×1.8+32)

DTA curves are similar for all the sands, but TG curves (Figure 3.11) show a more pronounced mass loss around phase transition temperature for control sand, and further mass decrease after this point for acidic sands. This mass decrease at higher temperatures is more pronounced in the case of the smaller particle sizes of Site D and Site H sand (Figure 3.12).

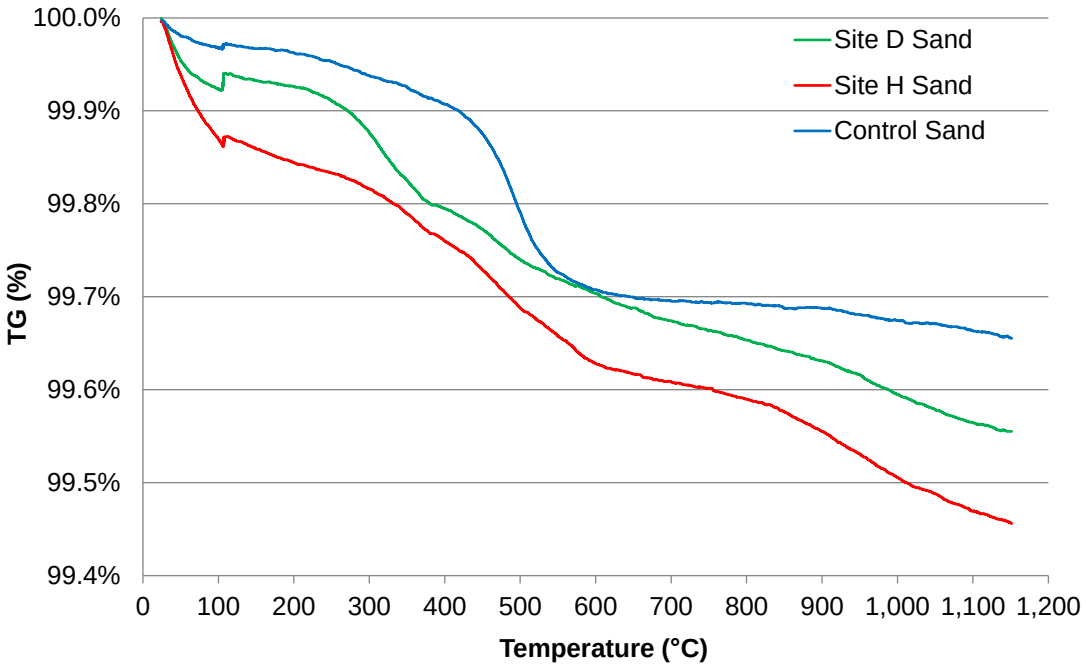

Figure 3.11 Thermogravimetric curves for control, site H, and site D sands. (°F = °C×1.8+32)

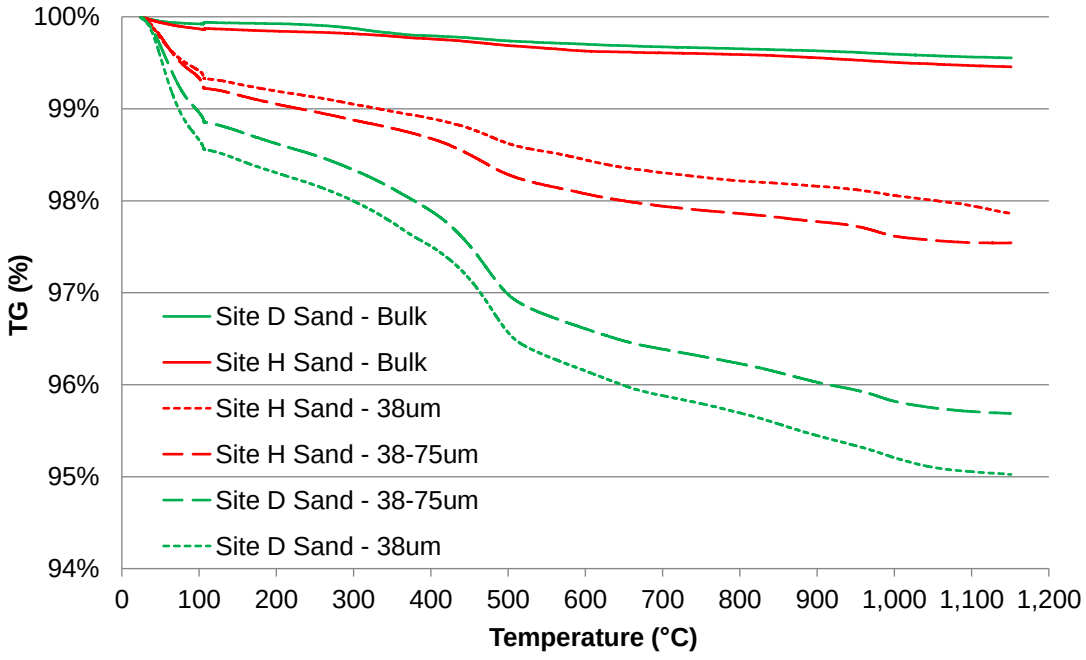

Figure 3.12 TG curves for different particle sizes of site H and site D sands. (°F = °C×1.8+32)

3.2.1.4 SEM images and EDS analysis of sands

Oven-dried, untreated aggregate particles of the three sands were analyzed using a Hitachi S-3700N Variable Pressure SEM (VP-SEM). Phase identification of minerals was performed using EDS microanalysis. Micrographs were produced at 20 kV, with backscattered signal, and chamber pressure of 25 Pa.

Micrographs of Control sand evidence a homogeneous particle composition, where quartz (SiO_2) is the only mineral phase identified, which confirms the results of the XRD analysis. Acidic sands, on the other hand, have a more variable morphology and composition, as shown in Figures 3.13 and 3.14 for Site D and Site H sand, respectively. Results of EDS microanalysis of VP-SEM micrographs are given in Appendix A.

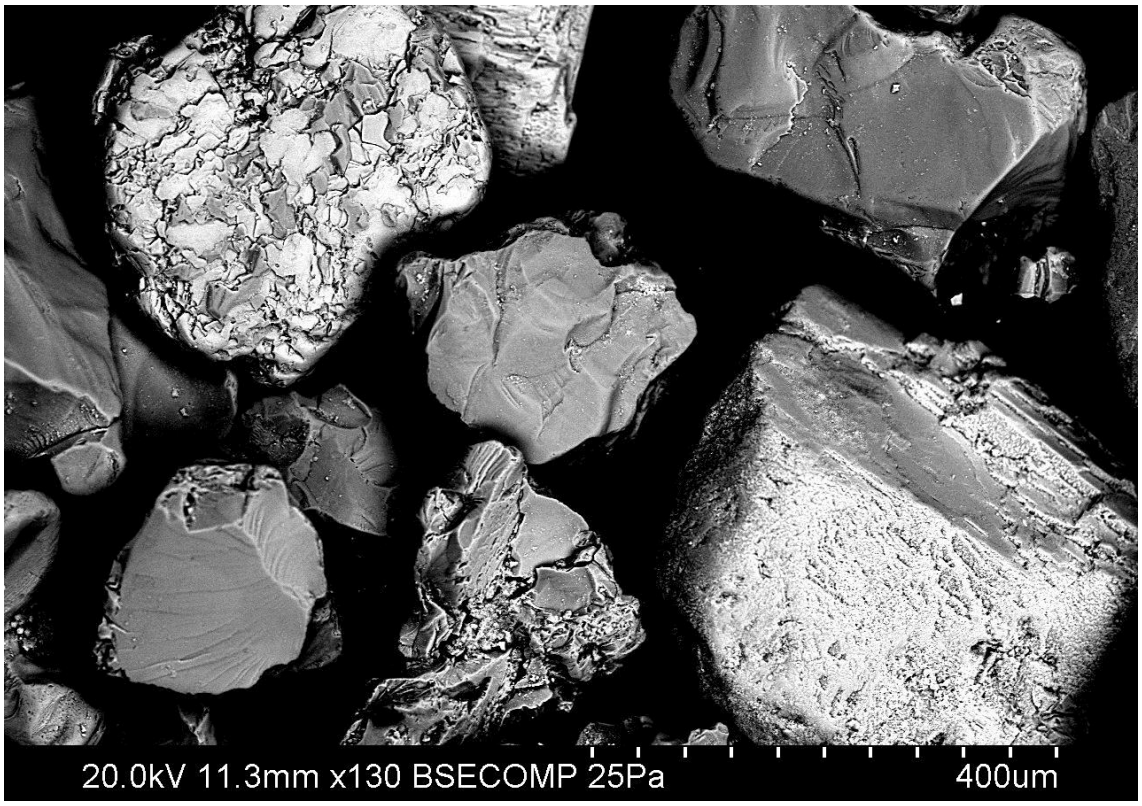

Figure 3.13 VP-SEM micrograph of Site D sand.

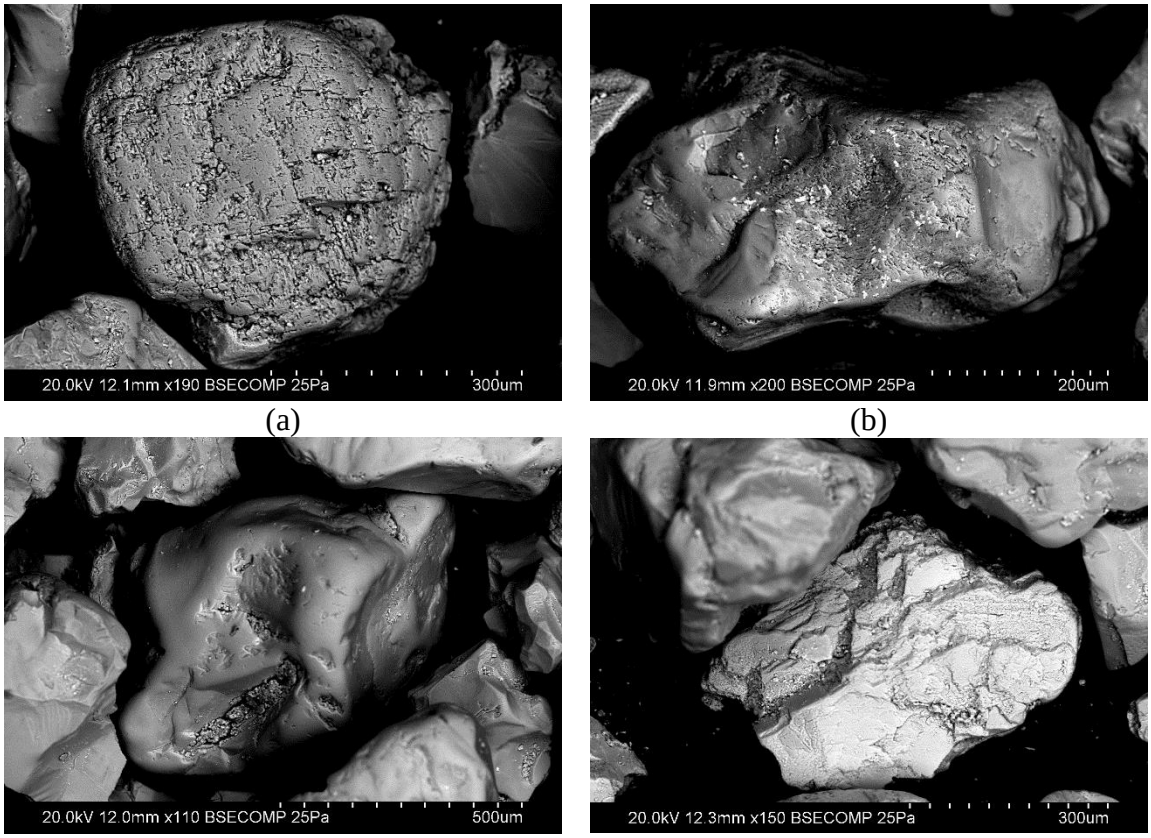

Figure 3.14 VP-SEM micrographs of Site H sand.

Site H and Site D sand show a broad range of surface roughness and particle shape. Particles of both acidic sands are composed primarily of quartz, although in most of the cases this is not the only mineral phase present. A fraction of alkali-aluminosilicate particles is present in the acidic sands, while potassium feldspar and, in lower proportion, sodium feldspar are also observed as mineral inclusions in several silica-based particles. Some particles are only composed of various phases of alkali feldspar.

Additionally, zircon (zirconium silicate, $ZrSiO_4$) inclusions not larger to 50 μm are present in acidic sand particles mainly composed of silica and alkali feldspar. Minor presence (< 1% of the molar fraction) of iron, titanium, calcium, magnesium, phosphorus, and sulfur is also observed in EDS spectra of Site H and Site D sand.

3.2.1.5 Water-soluble sulfate content of sands

Water-soluble sulfate (SO_4^{2-}) content of sands was measured following standard ASTM D4130 and using a UV-VIS Spectrophotometer. Oven-dried samples of the acidic sands were ground in a porcelain mortar and passed through a No. 30 sieve (600 μm [2.4×10^{-2}-in.]). Extraction of water-soluble sulfate was performed following Appendix A of the ACI 201.2R: Guide to Durable Concrete (2008). Ten grams of sieved material were mixed with 200 ml of DI water and the solution was stirred in a mechanical plate during 1 hour. Then, the solution was filtered through a Whatman No. 40 filter paper using a Nalgene vacuum filter holder.

A series of 5 standard sodium sulfate solutions and a blank sample were prepared in order to build a calibration curve for the measurements. A volume of 20 ml of the filtered solutions was mixed with 5 ml of a glycerin-acid stabilizing solution. Then, a mass of 0.3 grams of barium chloride ($BaCl_2\cdot2H_2O$) was added to all the solutions to form a suspension of barium sulfate ($BaSO_4$).

UV-absorbance of the samples was measured between wavelengths 350 to 600 nm, at a scan speed of 978 nm/min, and with a scan step of 0.5 nm. Following recommendation of ASTM D4130, absorbance values at 425 nm were used for the calculation of the water-soluble sulfate content of the sands.

Water-soluble sulfate content of Site D and Site H sands were 0.036 wt. % and 0.031 wt. %, respectively.

3.2.2 Cement Composition

In total, five cements (labeled A through E) have been included in this investigation (Table 3.2). A range in cement composition was selected in order to understand interactions between cement and sand sources which may influence performance, including the occurrence and characteristics of a DEF reaction. According to previous research (Kelham, 1996; Taylor et al., 2001; Zhang et al., 2002a; Ramlochan et al., 2003; Pavoine et al., 2012), ASTM C150 cement type, cement fineness, C_3A content, alkali content, SO_3 content, and sulfate-to-alumina ratio (SO_3/Al_2O_3) each may influence the potential for DEF, although no definite relationship between DEF reaction and cement composition has been established yet.

Cement B (Type V) and D (Type III) represent extreme cases of low and high susceptibility to DEF, respectively, while Cements A, C, and E correspond to different compositions of the more commonly used Type I/II and Type I cement. Because alkali contents in cements are usually limited to control alkali-silica reaction (ASR) in concrete, high-alkali cement was not considered, with all the cements examined having a $(Na_2O)_{eq}$ lower than 0.6%.

Table 3.2 Oxide analysis and Bogue potential composition of cements.

	Cement A	**Cement B**	**Cement C**	**Cement D**	**Cement E**
ASTM C150 Type	I/II	V	I/II	III	I
Blaine Fineness, m^2/kg	393	376	413	498	401
SiO_2	19.78%	21.10%	19.58%	19.81%	19.40%
Al_2O_3	4.61%	3.95%	4.79%	5.52%	5.48%
Fe_2O_3	3.37%	4.42%	3.38%	3.31%	3.33%
CaO	62.75%	62.49%	64.20%	63.99%	63.83%
MgO	3.07%	3.05%	1.06%	0.79%	0.79%
Na_2O	0.13%	0.08%	0.19%	0.11%	0.12%
K_2O	0.53%	0.55%	0.45%	0.55%	0.63%
$(Na_2O)_{eq}$	0.49%	0.44%	0.49%	0.47%	0.53%
TiO_2	0.25%	0.24%	0.25%	0.33%	0.33%
Mn_2O_3	0.18%	0.22%	0.02%	0.04%	0.04%
P_2O_5	0.07%	0.10%	0.12%	0.23%	0.23%
SrO	0.08%	0.06%	0.05%	0.20%	0.20%
BaO	0.06%	0.06%	0.06%	0.06%	0.06%
SO_3	2.55%	2.35%	3.26%	4.14%	3.18%
LOI	2.57%	1.33%	2.61%	1.67%	1.64%
C_3S	62.08%	54.50%	66.26%	56.34%	61.76%
C_3A	6.50%	2.97%	6.97%	9.03%	8.88%
C_2S	9.89%	19.38%	6.15%	14.29%	9.03%
C_4AF	10.26%	13.45%	10.28%	10.06%	10.14%
SO_3/Al_2O_3 (mass ratio)	0.55	0.59	0.68	0.75	0.58
SO_3/Al_2O_3 (molar ratio)	0.70	0.76	0.87	0.96	0.74

3.2.3 Mixture Designs for Mortar and Concrete

3.2.3.1 Mortar Mixtures

Mortar mixtures were prepared following mixing procedure indicated in ASTM C305. Cements A to E and DI water were used to prepare mortar specimens for the analysis of early-age behavior and the assessment of ISA/DEF potential.

To examine early-age properties, isothermal calorimetry and Vicat setting time tests were performed from mortars produced with the mixture shown in Table 3.3. The amount of cement and water were selected from standard ASTM C807 (Vicat setting time), while the amount of sand was calculated to complete 1 liter of mortar. The *w/c* and sand-to-cement ratio were 0.50 and 1.37, respectively, for all the mixtures.

Table 3.3 Mortar mixture design for isothermal calorimetry test and setting time determination.

Constituent	**Mixture Design,** lbs./yd^3	**Mixture Design,** kg/m^3
Cement	1,264	750
Water	632	375
Fine Aggregate	1,734	1,029

Mortar mixture design for early-age properties (Table 3.3) was not suitable for the preparation of mortar bars and cubes. A high flowability was obtained for this mixture, increasing the risks of having segregation or excessive bleeding. For this reason, the sand-to-cement ratio was increased to 2.75, according to ASTM C109 requirement for 2-in. (50 mm) mortar cubes. The *w/c* was kept at 0.50. The occurrence of DEF or ISA was assessed using this mixture design, shown in Table 3.4.

Table 3.4 Mortar mixture design for evaluation of potential for DEF and ISA.

Constituent	**Mixture Design,** lbs./yd^3	**Mixture Design**, kg/m^3
Cement	910	540
Water	459	272
Fine Aggregate (SSD)	2,500	1,483

3.2.3.2 Concrete Mixture

The concrete mixture composition conforms to class AA1 of the GDOT Specification 500: Concrete Structures. The *w/c* was 0.43 and air entrainment admixture was included in order to achieve 3-4% of air (Table 3.5). This mixture design, using Cement A, was used to prepare cylindrical specimens for compressive strength, dynamic elastic modulus, rapid chloride permeability, and accelerated corrosion tests.

Table 3.5 Concrete mixture design conforming GDOT Class AA1.

Constituent	**Mixture Design,** lbs./yd^3	**Mixture Design,** kg/m^3
Cement	675	400
Water	291	173
Coarse Aggregate (SSD)	1,838	1,090
Fine Aggregate (SSD)	1,127	668
AE admixture (MB AE90)	0.7 oz./cwt	10.35 ml

Additionally, the slump was determined using standard ASTM C143 and the air content of fresh concrete was obtained using the air meter Type B and the procedure described in standard ASTM C231. The results for these properties can be observed in

Table 3.6. The difference observed for concrete using Site H sand is attributable to its higher fineness (see Figure 3.3 and Table 3.1).

Concrete cylinders for mechanical properties determination were cast in 4×8-in. (10.2×20.3 cm) molds, covered with a plastic lid and demolded after 24 hours. Then, they were labeled and stored under fogroom curing (23.0±2.0 °C [73.5±3.5 °F], RH > 98%) until the age of testing.

Table 3.6. Slump and air content of fresh concrete.

	Slump (in.)	**Slump** (cm)	**Air content** (%)
Control Sand	1.5	3.8	3.5
Site H Sand	0.5	1.3	2.5
Site D Sand	2.0	5.1	3.5

3.3 Description of Tests for Acidic Sands Evaluation

3.3.1 Isothermal Calorimetry of Mortar Mixtures

To evaluate the effect of the acidic sands on the hydration kinetics of cements with variable cement composition (see Table 3.2), isothermal calorimetry was performed at 25 °C (77 °F) in an 8-channel TAM AIR microcalorimeter, with a precision of ±2 µW and accuracy greater than 95%, following standard ASTM C1679. The preparation was performed with a hand-held mixer and it followed the procedure given for mortar preparation in ASTM C305. Deionized water was used to avoid the interaction of additional elements in the reaction.

Eight samples were prepared for every cement, three per each acidic sand and two for control. The reason for the use of an additional sample for the acidic sands is the concern for their variability. In every case, the ampules were filled with 15 ± 1 g (33.1×10^{-3} ± 2.2×10^{-3} lbs.) of mortar, recording the weight with a precision of 0.01 g (2.20×10^{-5} lbs.). All the replicates of the same mixture were introduced into the calorimeter within a minute, to control interactions with the rest of the samples. Also, the time of initial contact between cement and water, and the time where the ampules were loaded into the calorimeter were recorded to ease the post-analysis.

The power of every ampule was recorded in mW every 60 seconds and later normalized by mass of cement. Data was collected for at least three days for every cement (i.e., Cements A-E in Table 3.2).

3.3.2 Setting Time by Vicat Needle Method

Setting time was measured using standard ASTM C807. The same mixture composition used for isothermal calorimetry was considered for this test (see Table 3.3). This method considers the use of the Vicat apparatus, a metallic base were the tested specimen is placed under a needle that is release from a fixed position. The depth of penetration of the specimen is monitored in time in order to obtain the setting time.

The specimen consisted of a mortar sample casted in a plastic conical ring with the height of 40 mm (1.585-in.). Two specimens were prepared per mixture. Between measurements, the specimens were kept on close containers at high RH to avoid drying. The penetration of the needle is monitored until a value of 10 mm (0.394-in.) or less is obtained. The time between the initial contact of cement and water and time when 10 mm (0.394-in.) of penetration is observed is considered the setting time of mortar.

3.3.3 Determination of Dynamic Elastic Modulus

Along with the compressive strength test, the dynamic elastic modulus was measured at 28 and 90 days, on 4×8-in. (10.2×20.3 cm) cylinders, according to ASTM C215. Three cylinders per mixture were measured at each age of testing. Using the impact resonance method, the fundamental resonant frequency was obtained. In this non-destructive test, the cylinder is placed on a steel support that allows the cylinder to vibrate freely after a strike is applied by an impactor at the center of the end surface. An accelerometer triggers data acquisition and a waveform analyzer record the resonant longitudinal frequency (see Figure 3.15). This value was used to calculate the dynamic elastic modulus using Equation 3.1.

$$Dynamic\ E = DM(n')^2 \quad (3.1)$$

where M is the mass of the concrete specimen, in kg, n' is the fundamental longitudinal frequency, in Hz, and D is calculated from $5.093(L/d^2)$, with L, the length of the cylinder, in meters, and d, the diameter of the cylinder, in meters.

Figure 3.15 Dynamic elastic modulus set up.

Three replicate cylinders were tested for each mixture and age of testing. It should be noted that the dynamic E obtained by ASTM C215 is higher than the static E obtained by the conventionally used ASTM C469. Depending on the equation used to relate both mechanical properties, the difference ranges between 20 to 30% (Popovics et al., 2008).

3.3.4 Rapid Chloride Permeability Test (RCPT)

The RCP test (Figure 3.16) was performed on 2-in. (5.1 cm) sections of 4×8-in. (10.2×20.3 cm) cylinders obtained after 56 days of fogroom curing. Concrete was prepared using the mixture design shown in Table 3.5. Two replicate specimens were

tested per analyzed sand, following the procedure included in standard ASTM C1202. These sections were saturated at vacuum pressure in water for three hours, and soaked under water for 18 hours. Then, cells at the ends of the specimen were mounted. One cell contains a 3% NaCl solution and the other contains a 0.3N NaOH solution, both solutions accessible to the concrete specimens. The test was initiated when electrical connections were attached to impose a voltage of 60 V during 6 hours, and the charge that pass along the specimen was recorded. According to ASTM C1202, chloride penetrability can be assessed according to the total charge at the end of the test.

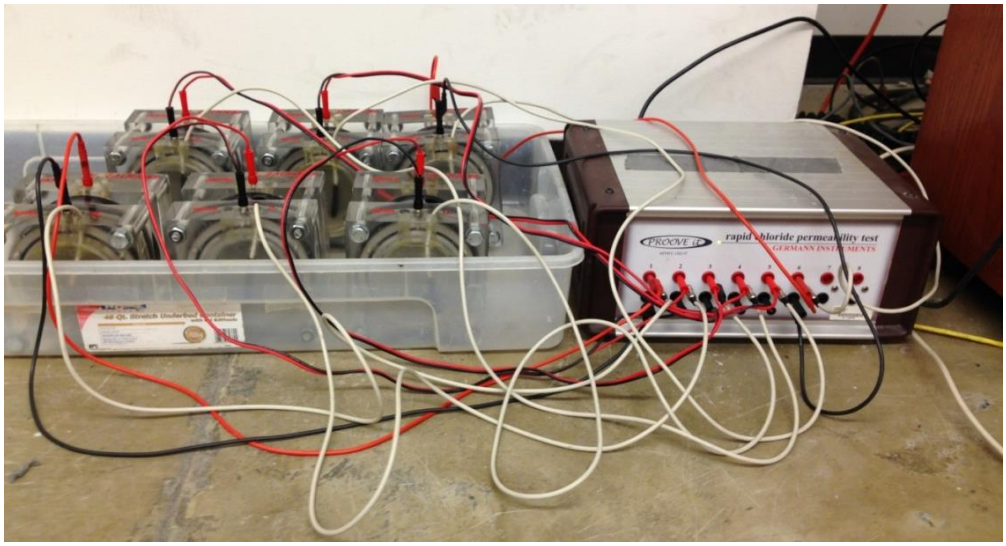

Figure 3.16 RCPT set up. Two specimens per mixture were tested at 56 days from casting.

3.3.5 Accelerated Laboratory Method for Corrosion Testing of Reinforced Concrete Using Impressed Current (FM 5-522)

The accelerated corrosion test Florida Method (FM) 5-522 (Florida DOT, 2000) was performed to evaluate the effect of the analyzed sands on the corrosion behavior of reinforced concrete. This test can be used to compare the time to corrosion among

different concrete mixtures. This test was selected in consultation with GDOT and the sand producer as a means to assess the influence of the sand source on the potential for corrosion in concrete. The test provides relatively rapid results compared to other standardized test methods for corrosion.

The concrete specimens for this test were prepared using the same mix design exposed above (see Table 3.5), using Cement A (Type I/II cement), with the addition of superplasticizer (Glenium 3030NS) at 3 oz./cwt. (1.956 ml/kg. of cement). The specimens had dimensions 4-in. (10.2 cm) diameter by 5.75-in. (14.6 cm) height and a #4 rebar (½-in. [12.7 mm] nominal diameter) embedded through the mid-length of each cylinder (Figure 3.17). The steel bars were preconditioned through a bath of sulfuric acid solution and mechanical brushing that removed the iron oxide of the surface, per standard specifications.

Figure 3.17 Corrosion test samples with dimensions 4-in. (10.2 cm) diameter by 5.75-in. (14.6 cm) height. The exposed rebar was embedded to the mid-height of the cylinder.

After demolding, the specimens were cured 28 days in a fogroom and were subsequently immersed in a 5% NaCl solution for additional 28 days, as described in the test procedure. The bars were not protected during the curing process or during immersion, but the condition of the steel surface was evaluated and no evidence of corrosion was observed. After this period, the specimens were stored in open polyethylene containers, submerged partially in a 5% NaCl solution, with the solution waterline at 3 to 4-in. (7.6 to 10.2 cm) from the bottom of the tank (Figure 3.14), depth that was controlled during the execution of the test. 5% NaCl solution was circulated in the test container using an external pump. Also, the top section of the rebar was sandblasted to assure the electrical connection. An additional rebar was also immersed in the solution (Figure 3.15) as a counter electrode for the impressed current to maintain the applied voltage. Then, a voltage of 6 V was applied between the concrete-embedded bars and the counter electrode, step that represent the time zero measurement. To measure the current flow of the circuits, 0.1 Ω electrical shunts were included in every circuit. Potential drop across this shunt was recorded and used to measure the current throughout these tests. Additionally, the applied voltage was measured at different points to control the applied potential value required by FM 5-522. Three specimens for each type of sand were tested and the formation of surface cracks in concrete and corrosion products was constantly monitored.

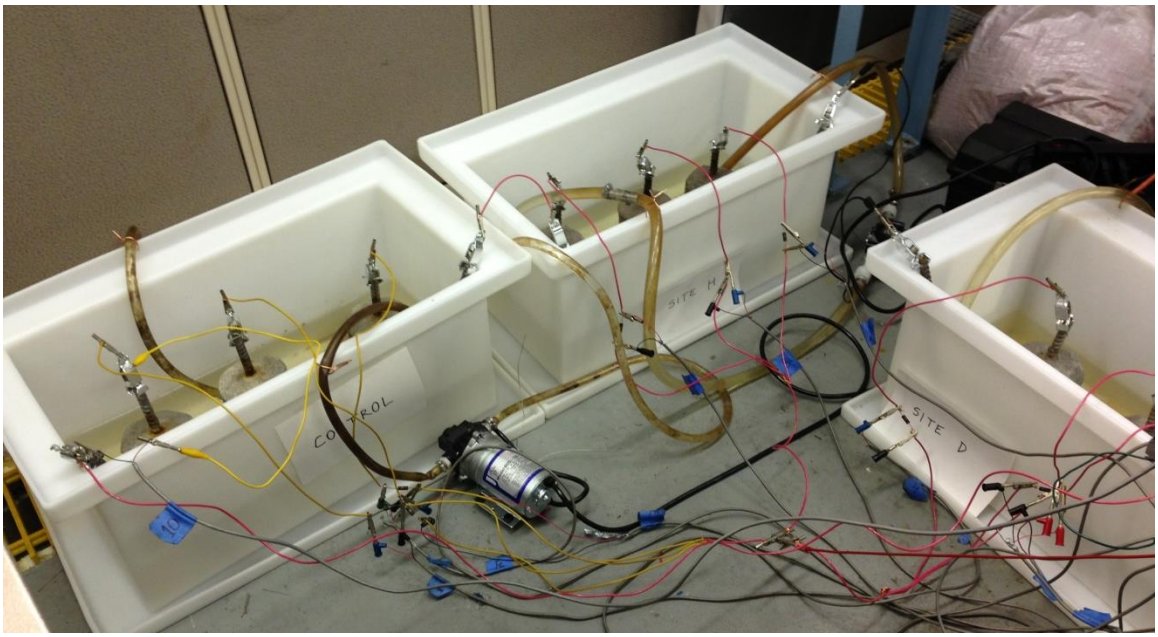

Figure 3.18 HDPE tanks for the corrosion test. A pump was used to keep a uniform concentration of the NaCl solution.

Figure 3.19 Specimens corresponding to each sand type were kept separately to avoid interaction during the test.

3.4 Effect of Acidic Sands on Early-Age Properties

The effect of sulfate in concrete at early ages is commonly associated with the addition of natural gypsum, compositionally a mixture of calcium sulfate dihydrate and anhydrite, to clinker to control the occurrence of flash set, a result of the very fast hydration of C_3A (Lawrence, 2004).

In portland cement systems, the hydration of C_3S and C_3A phases controls the early-age hydration kinetics. A 50% to 70% of the mass fraction of cement corresponds to C_3S; thus, the hydration of this phase dominates the development of properties of cement-based materials. The hydration of both phases follows similar reaction patterns, in which an initial rapid reaction quickly reduces its rate and it is followed by a period of slow reaction (Scrivener and Nonat, 2011).

The addition of gypsum increases the duration of the slow reaction period in C_3S and produces higher peaks of hydration rate (Quennoz and Scrivener, 2013). Also, gypsum affects the morphology of the hydration products formed from C_3S. Sulfate adsorption in C-S-H surfaces charges them negatively and produces the formation of divergent C-S-H needles as a result of electrical repulsion (Mota et al., 2015). In the case of C_3A, it is believed that the otherwise excessively fast C_3A hydration is delayed by the adsorption of sulfate ions on the C_3A surface, process which is reverted when the sulfate ions in solution are depleted. After the consumption of the available calcium sulfate in solution, sulfate ions desorb from C_3A surface and a rapid increase of the dissolution rate occur (Bullard et al., 2011).

The slow reaction period is followed by an acceleration of the reaction rate. Calorimetry curves of properly sulfated cements usually show a main C_3S hydration peak

at around 10 hours of hydration, followed by a peak corresponding to the hydration of C_3A. This second peak of C_3A hydration produces ettringite formation, where the sulfate ions are believed to be released from C-S-H phases (Bullard et al., 2011). Experimental evidence from Bensted (1983) suggests that setting of cement is commonly produced during the acceleration period due to the rapid growth of C-S-H and CH.

Kinetics during the acceleration period is believed to be controlled by the growth of C-S-H needle-like structure on the surface of grains. At the end of the accelerated reaction period, when calorimetry curves show maximum peaks of heat release, it has been proposed that the growth of C-S-H needles is no longer possible and the formation of denser inner starts at a slower rate (Scrivener et al., 2015). Sometimes an additional peak is observed in calorimetry curves at 20 to 30 hours of hydration, corresponding to the formation of AF_m phases (Bullard et al., 2011).

In order to evaluate the effect of the additional sulfate provided by Site H and Site D sands, setting times are evaluated by the Vicat needle test and the heat evolution during the first 4 days of hydration is measured using isothermal calorimetry.

3.4.1 Setting Time by Vicat Needle Test

Two specimens were tested per mixture of mortar using Cements A to E, sand-to-cement ratio of 1.37, and *w/c* of 0.5. Setting time represents the point when the solidification process is finished, and the cement paste starts to develop stiffness (Mehta and Monteiro, 2006).

Results of the test are given in Figure 3.20, where error bars show the range of results for every mortar mixture.

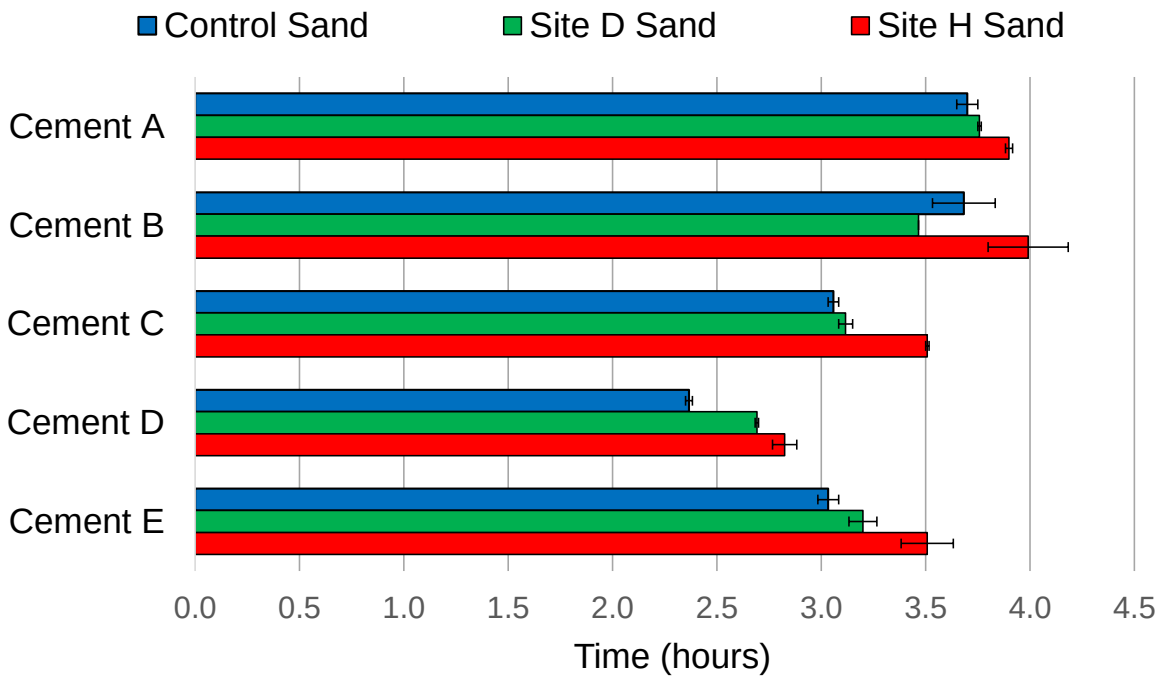

Figure 3.20 Setting times of mortars. Error bars show the range of results for each mixture.

Vicat setting time results show that the type of sand used clearly affects the setting time. For every cement tested, mortar using Site H sand (red bars in Figure 3.20) exhibits the longest setting time. This increase of setting time ranges from 5.4% (or 12 minutes) for Cement A (Type I/II) to 19.4% (28 minutes) for Cement D (Type III) compared to control specimens, as shown in Table 3.7. Particularly, it can be observed that in mortar mixtures with earlier setting times measured in control specimens, higher delays were measured when Site H sand was used.

In mortar mixtures using Site D sand, a different situation is observed. Samples with Cement A and C (Type I/II) show a slight increase of the average setting time compared to control, while mortar using Cement B (Type V) show a decrease of the setting time. Similar to Site H sand samples, the higher delay of setting time is observed in specimens using portland cements with high C_3A content (Cement D and E).

Table 3.7 Delay of setting time for mortar mixtures using acidic sands, compared to control samples.

Mortar Mixture		Difference with respect to control (%)	Difference with respect to control (min)
Cement A (Type I/II)	Site H Sand	5.4%	12
	Site D Sand	1.6%	4
Cement B (Type V)	Site H Sand	8.4%	19
	Site D Sand	– 5.9%	– 13
Cement C (Type I/II)	Site H Sand	14.7%	27
	Site D Sand	1.9%	4
Cement D (Type III)	Site H Sand	19.4%	28
	Site D Sand	13.7%	20
Cement E (Type I)	Site H Sand	15.7%	29
	Site D Sand	5.5%	10

The delays observed in Site H and D sand samples suggest that the composition of the sands influences the cement setting behavior. One possibility is that the presence of sulfate or sulfide delays the hydration. Additional sulfates from the sands, then, could lead to additional retardation in hydration reactions.

3.4.2 Isothermal Calorimetry

Isothermal calorimetry at 25 °C (77 °F) was performed on mortar mixtures using Cements A to E. Cement-to-sand ratio and *w/c* were kept constant at 1.37 and 0.5, respectively, three replicates were used per mixture containing an acidic sand, and two replicates were used for control specimens.

3.4.2.1 Rate of heat evolution

Calorimetric curves are a measure of the heat evolved by exothermic reactions, provided mostly by the hydration of C_3S and C_3A. Figures 3.21 to 3.25 show heat evolution curves for the first 40 hours of hydration for each of five cements as mortars with each of the three sand sources. Calorimetry results suggest that setting of cement paste occurred during the initial stage of the acceleration period. However, it should be noted that mortars were exposed to different temperatures (25 °C [77 °F] for calorimetry test vs. 23 °C [73.4 °F] for Vicat setting test) and humidity (closed containers vs. containers at RH close to 100%) during the tests.

It can be observed that hydration of all five cements is delayed most in the presence of Site H sand. Site D sand shows an intermediate behavior between Control and Site H sand.

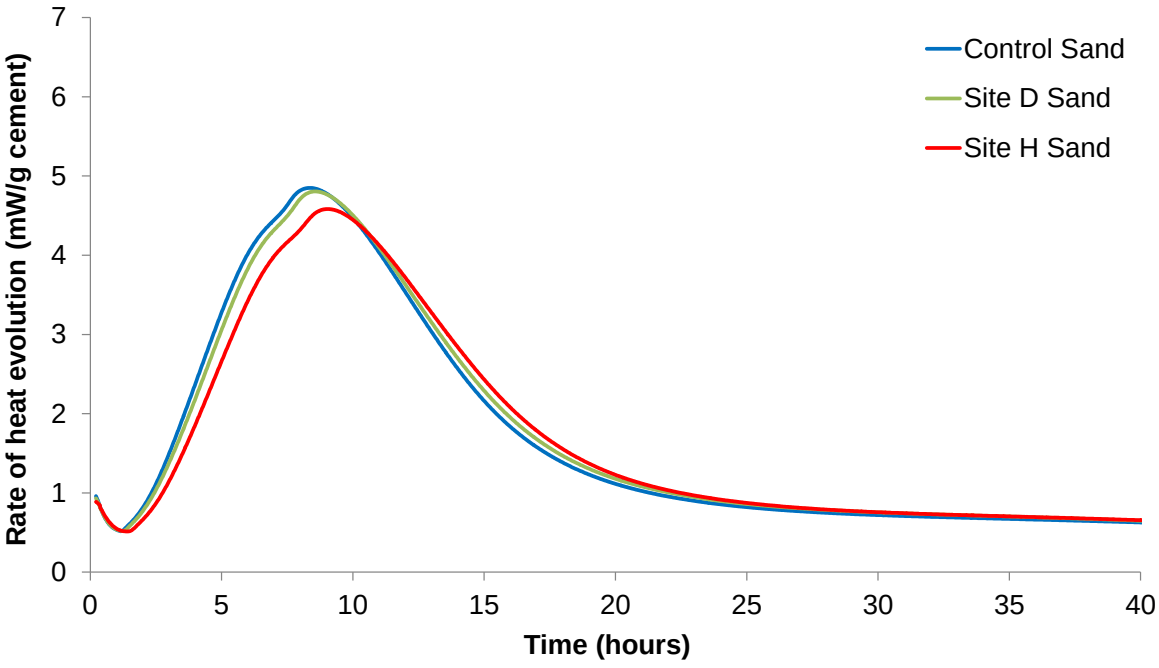

Figure 3.21 Calorimetry results for mortar mixtures prepared with Cement A (Type I/II).

For Cement A (Figure 3.21), use of Site H sand results in a delay in the maximum peak of hydration, which occurs at 9.1 hours instead of 8.4 hours (as observed in the control). Additionally, a lower peak of heat of hydration and a lower slope during the acceleration period are observed in Site H sand samples. With the Site D sand, the maximum peak occurs at 8.6 hours, which is a more moderate retardation but is also appreciable in this test. This is consistent with the results of setting time for the same cement (Figure 3.20).

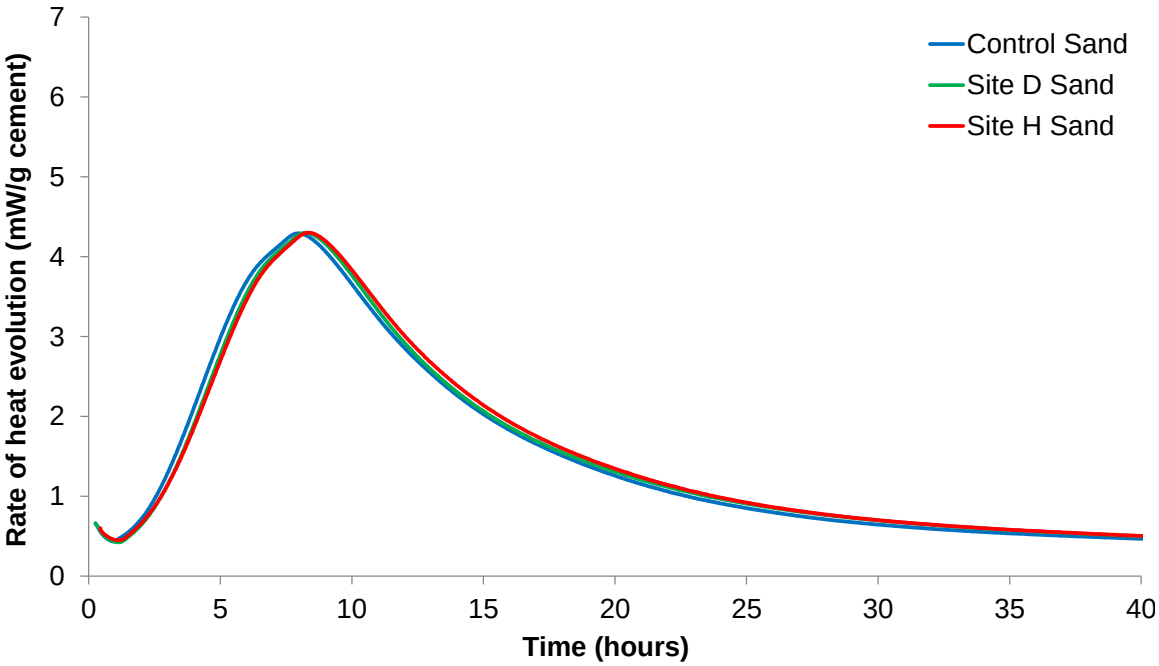

Figure 3.22 Calorimetry results for mortar mixtures prepared with Cement B (Type V).

For Cement B (Figure 3.22), a Type V cement with lower C_3A (2.97% compared to 6.50%) and C_3S (54.50% compared to 62.08%) contents than Cement A (Type I/II), the delay is less pronounced when acidic sands are used. Site H sand delays the peak of

hydration from 8.0 hours to 8.3 hours, while Site D sand exhibits the maximum peak at 8.3 hours.

Calorimetry curves for mortars using Cement A and B show a smaller peak occurring earlier than the maximum peak. This smaller peak can be attributed to the hydration of the aluminate phases and the formation of ettringite.

Cement C (Figure 3.23) is a Type I/II cement with a higher amount of sulfate than Cement A, but also a higher amount of C_3A, being the SO_3/C_3A mass ratio equal to 0.47. The maximum peaks were at 5.5 hours for Control sand, 5.8 hours for Site D sand, and 6.0 hours for Site H sand.

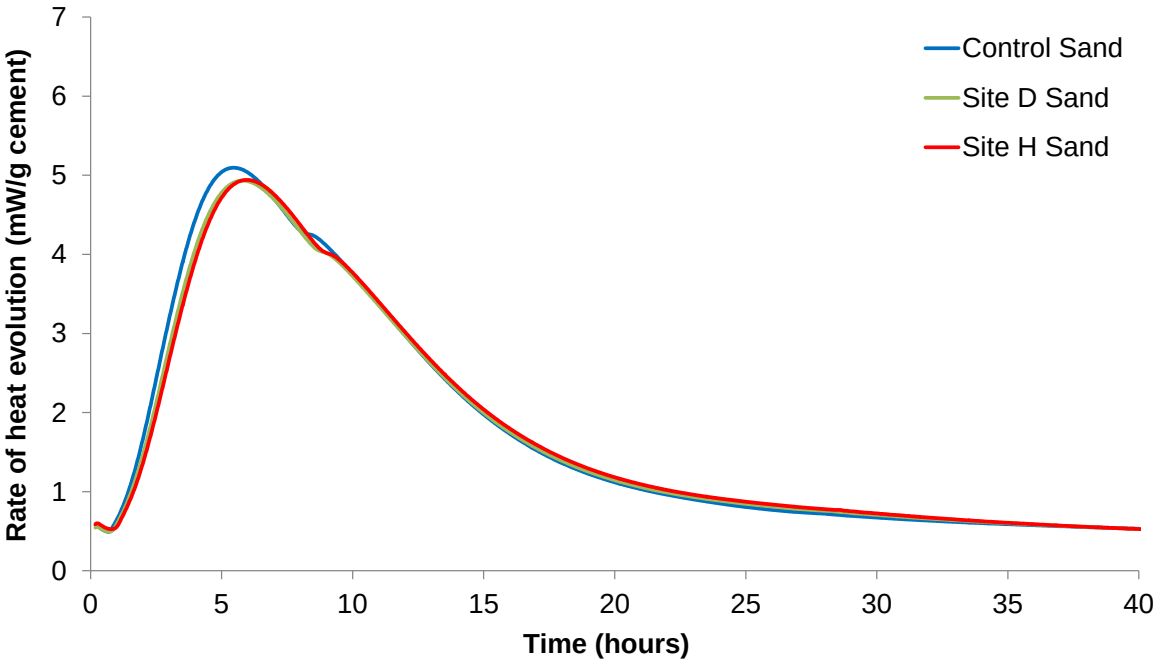

Figure 3.23 Calorimetry results for mortar mixtures prepared with Cement C (Type I/II).

In the case of Cement D (Type III cement, C_3A content of 9.03%, C_3S content of 56.34%, and sulfate content of 4.14%) maximum peaks were at 5.7 hours for Control sand, 6.0 hours for Site D sand, and 6.1 hours for Site H sand.

The calorimetry curves for Cements C and D show different patterns compared to Cements A and B curves. In Figures 3.23 and 3.24, a smaller peak, possibly formed due to the hydration of the aluminate phases, can be observed 2 to 3 hours after the main peak of C_3S hydration.

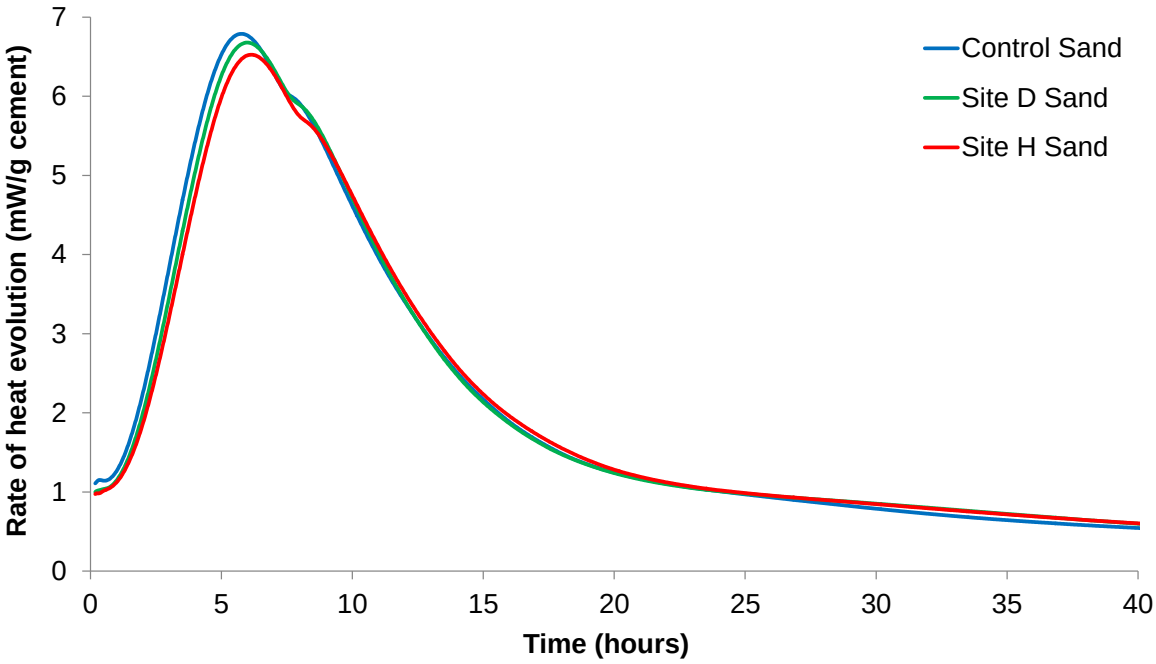

Figure 3.24 Calorimetry results for mortar mixtures prepared with Cement D (Type III).

Mortars using Cement E (Figure 3.25) show the presence of two similar peaks corresponding to hydration of C_3A and C_3S. Maximum rates for the first peak occurred at 5.5 hours for Control sand, 5.5 hours for Site D sand, and 5.9 hours for Site H sand, while for the second peak they occurred at 6.6 hours for Control sand, 6.7 hours for Site D sand, and 7.1 hours for Site H sand.

Cement E samples were the only case where the calorimetry curve of an acidic sand, particularly Site D sand, exhibited higher maximum rates of hydration and where

the slope of the curve during the acceleration period coincide compared to results of control specimens.

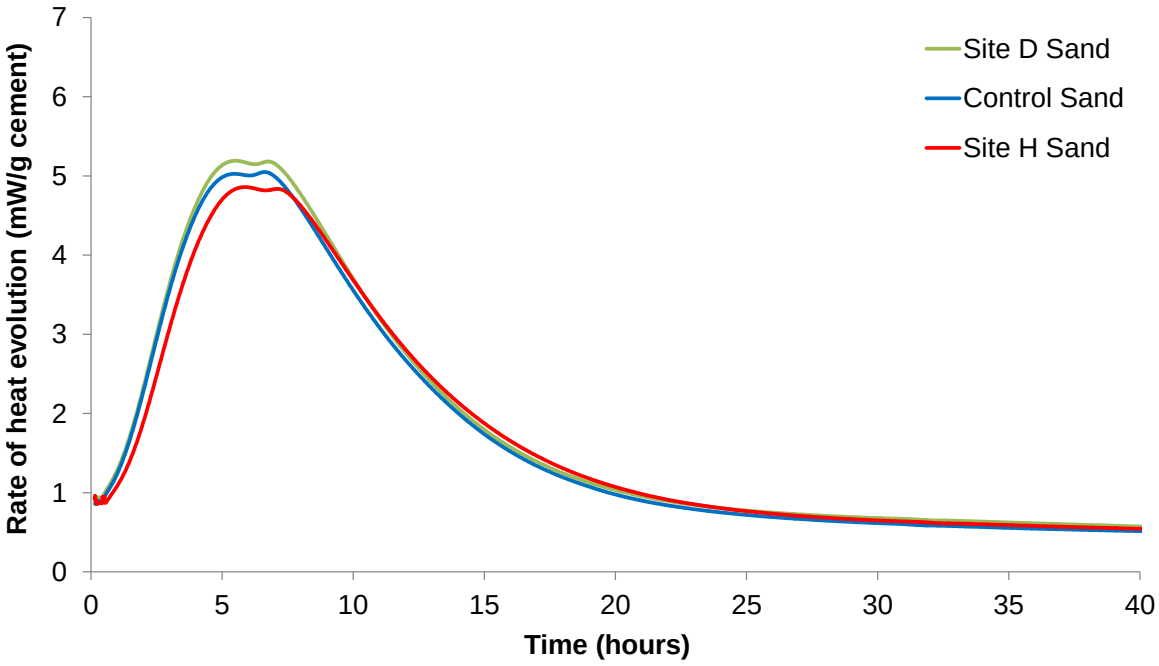

Figure 3.25 Calorimetry results for mortar mixtures prepared with Cement E (Type I).

3.4.2.2 Cumulative heat of hydration

Figure 3.26 shows the curves for the cumulative heat evolved during the first 96 hours of hydration. As expected from their respective cement compositions (Table 3.2), highest heat of hydration was measured in samples containing Cement D, Type III cement with the highest fineness and C_3A content, while lowest heat of hydration was measured in Cement B (Type V) samples. For mortars prepared using Cements A, C, and D, negligible variations are observed at 96-100 hours for every type of sand. For mortars using Cement B (Type V), cumulative heat evolved after 96 hours was 3.1% and 1.5% higher than control for Site H sand and Site D sand samples, respectively. For mortars

using Cement E (Type I), cumulative heat at 99 hours was 2.6% and 4.1% higher than control for Site H sand and Site D sand samples, respectively.

This suggests that beyond 4 days, any delays in hydration due to minor constituents in the sand are likely to be less apparent.

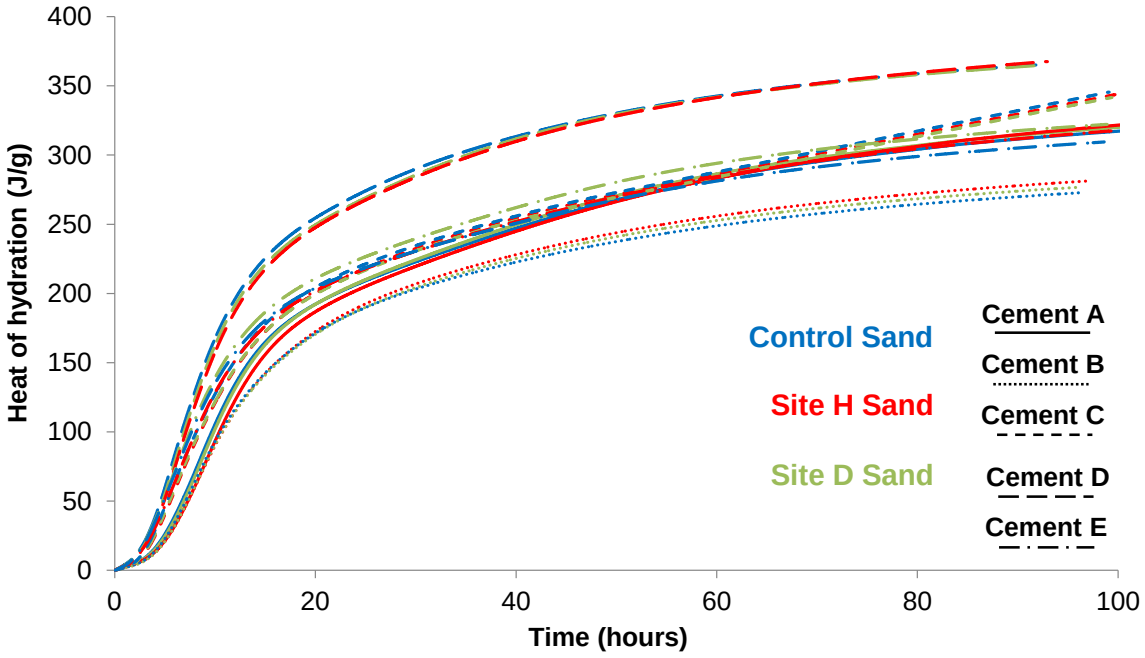

Figure 3.26 Cumulative heat of hydration curves for the first 4 days.

Using the Bogue composition of cement (Table 3.2), the total heat of hydration, in Joules per gram of cement, can be estimated from the relative mass fraction of cement compounds as shown in Equation 3.2 (Bogue, 1947).

$$H_{Total} = 500 \cdot C_3S + 260 \cdot C_2S + 866 \cdot C_3A + 420 \cdot C_4AF + 624 \cdot SO_3 + 1186 \cdot CaO_{free} + 850 \cdot MgO \quad (3.2)$$

Equation 3.2 assumes that cement particles will hydrate completely and, therefore, represent a maximum theoretical value. If the amount of sulfate measured in the acidic sands by UV/VIS spectrophotometry is included in Equation 3.2, negligible increases of the maximum heat of hydration are calculated, which is consistent with the experimental results.

3.4.2.3 Degree of hydration modeling

The degree of hydration can be calculated as the experimental cumulative heat of hydration at time *t* divided by the total heat of hydration estimated by Equation 3.2. In order to model mathematically the degree of hydration, the experimental data can be characterized by the parametric exponential model shown in Equation 3.3 (Schindler and Folliard, 2005).

$$\alpha(t) = \alpha_u e^{-(\tau/t)^{\beta}} \quad (3.3)$$

where $\alpha(t)$ is the degree of hydration at time *t*, α_u is the maximum degree of hydration, τ is the hydration time parameter, and β is the hydration shape parameter.

Using the results of the calorimetry test, a least-square fit of the model was used to calculate α_u, τ, and β for every tested mortar mixture. The modeled degree of hydration on time was compared with the calculated values from calorimetry results for each cement, as shown in Appendix B. Good agreement is observed, except for Cement C, where the total heat evolution at 100 hours was increasing at a faster rate compared to the rest of the cements. This aspect can affect the quality of the curve fitting, since the model

assumes the stabilization of the heat of hydration. Thus, parameters calculated for Cement C specimens could be poor estimations of their degree of hydration.

The calculated parameters of every mortar mixture are shown in Table 3.8.

Table 3.8 Least-square fit parameters for the exponential model of hydration.

Mortar Mixture		α_u	β	τ (hours)
Cement A (Type I/II)	Control Sand	0.802	0.821	13.69
	Site H Sand	0.831	0.813	15.35
	Site D Sand	0.804	0.846	13.88
Cement B (Type V)	Control Sand	0.690	0.981	12.04
	Site H Sand	0.714	0.991	12.65
	Site D Sand	0.704	0.987	12.53
Cement C (Type I/II)	Control Sand	0.939	0.623	15.16
	Site H Sand	0.924	0.648	15.40
	Site D Sand	0.927	0.635	15.53
Cement D (Type III)	Control Sand	0.858	0.951	9.08
	Site H Sand	0.877	0.923	9.96
	Site D Sand	0.866	0.937	9.54
Cement E (Type I)	Control Sand	0.769	0.763	10.55
	Site H Sand	0.806	0.767	11.83
	Site D Sand	0.803	0.744	10.71

The parameter α_u represents the maximum degree of hydration. Thus, a higher α_u indicates a potential greater maximum degree of hydration in a particular mix (Jayapalan et al., 2014). Similar values of α_u are observed for each sand (Table 3.8). Site H sand results show the highest potential α in every case except using Cement C.

The hydration shape parameter β represents the slope of the degree of hydration curve. A higher β is an indication of a lower degree of hydration at early ages and a greater degree of hydration at later ages (Jayapalan et al., 2014).

The hydration time parameter τ represents the time to reach the peak reaction rate and possibly setting time. A higher τ shows a deceleration of the reaction at early ages (Jayapalan et al., 2014).

The modeled parameters in Table 3.8 show that Site H sand exhibits a greater deceleration than Site D sand, observation consistent with the analysis of the curves of rate of hydration exposed above (Figures 3.21 to 3.25). These results suggest higher sulfate content in Site H sand than Site D sand. However, UV/VIS spectrophotometry results show a similar sulfate content in both acidic sands, while the producer reported higher sulfate content in Site H sand. Given the variability of the properties of the analyzed acidic sands, the measurement of the sulfate content of acidic sands should be performed on a larger number of samples.

Overall, these data demonstrate that the sands do influence the cement hydration reaction kinetics, with Site H sand generally producing greater delays in early hydration than Site D sand. Both sands, however, do result in some retardation of early hydration reactions, and these delays appear to be linked to the sulfate content in the sand. Further, the interaction between the sand and the cement is also dependent upon the cement composition. This suggests that some variability in early age behavior can be expected when combining these sands with different cements or cementitious systems.

3.5 Effect of Acidic Sands on Mechanical Properties

3.5.1 Compressive Strength Results

Figure 3.27 shows the average compressive strength measured at ages 1, 3, 7, 28, 56, and 91 days for concrete mixtures using each type of sand. All concretes were prepared at *w/c* 0.43 using Cement A (Type I/II cement), following GDOT AA–1 mix designs (Table 3.5). Individual results of the test for each cylinder can be observed in Appendix C, along with the average and standard deviation for each sand and age.

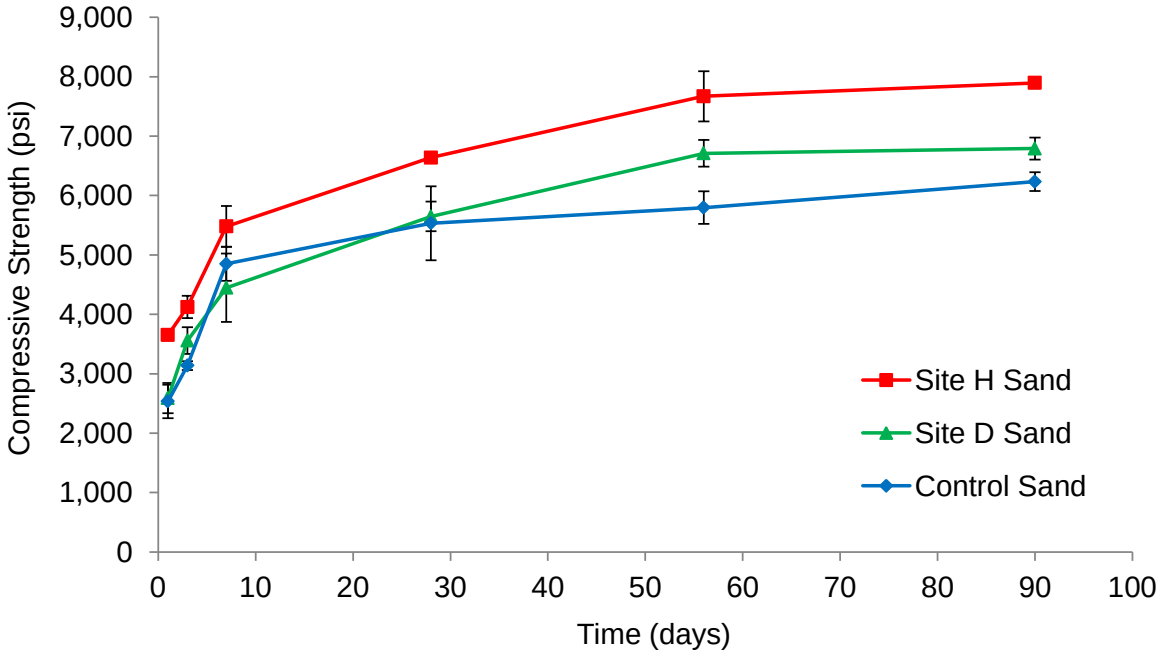

Figure 3.27 Average compressive strength of concrete at 1, 3, 7, 28, 56, and 90 days after casting. Each point corresponds to the average of three cylinders and the error bars show the standard deviation. (1,000 psi = 6.9 MPa)

Table 3.9 shows the results of the statistical analysis on the statistical similarity of the results for the acidic sand (μ_h and μ_d) with respect to Control sand (μ_c), where μ_i is the mean of the normal distribution of compressive strength of sand *i*, at a particular age. For each hypothesis testing, the table shows the decision of the test for α = 5% and the p-

value. The p-value is the conditional probability of rejecting H_0 given that H_0 is true. Thus, a low p-value indicates that the occurrence of H_0 is very unlikely, and this assumption is consequently rejected.

Table 3.9 Statistical analysis of compressive strength results. Similarity of the results observed using acidic sands compared to control is tested.

Age of Testing	**Test H_0: $\mu_c = \mu_h$** ($\alpha = 5\%$)	**p-value**	**Test H_0: $\mu_c = \mu_d$** ($\alpha = 5\%$)	**p-value**
1 day	Reject H_0	0.67%	Fail to Reject H_0	96.37%
3 days	Reject H_0	0.07%	Fail to Reject H_0	9.13%
7 days	Fail to Reject H_0	6.28%	Fail to Reject H_0	59.86%
28 days	Reject H_0	3.09%	Fail to Reject H_0	95.79%
56 days	Reject H_0	0.21%	Reject H_0	2.78%
90 days	Reject H_0	0.01%	Fail to Reject H_0	40.13%

Samples using Site H sand show a higher strength compared to control samples, except at 7 days, while samples using Site D sand show a different behavior. At early ages (i.e., up to 28 days), concretes containing control and Site D sand exhibit statistically similar compressive strength. At later ages, the results show a higher value for Site D sand at 56 days, but similar at 90 days.

Repeating the statistical analysis performed above in the comparison with control samples, Table 3.10 indicate that the compressive strength of Site H samples is higher compared to Site D samples, at every age of testing. Because Site D and H sand were obtained from the same sand deposit, the variability in the concrete compressive strength is a potential concern in terms of consistency. Additionally, GDOT Specification 500 indicates that GDOT AA1 mix designs should have a 28-days compressive strength higher than $f'_c+2 \cdot s$, where f'_c and s are obtained from tables and correspond, in the case

of AA1 mixtures, to 4,500 psi and 540 psi (31.0 and 3.7 MPa), respectively. Therefore, the minimum required strength is 5,580 psi (38.5 MPa). The averages of samples prepared using Site H and Site D sands are higher than this value, while the average for Control sand samples at the same age is slightly lower (see Appendix C). At 28 days, Control sand samples show a standard deviation of 621 psi (4.3 MPa), higher than the recommended by GDOT.

Table 3.10 Variability between Site H and Site D sand samples.

Age of Testing	**Test H_0: $\mu_d = \mu_h$** ($\alpha = 5\%$)	**p-value**
1 day	Reject H_0	0.584%
3 days	Reject H_0	2.177%
7 days	Reject H_0	4.799%
28 days	Reject H_0	0.177%
56 days	Reject H_0	2.020%
90 days	Reject H_0	0.262%

A reduction of the compressive strength is a consequence of any type of sulfate attack (Neville, 2004). In this case, a higher strength is obtained in concrete using Site H sand, and a similar strength is obtained when Site D sand is used. These results indicate that there is no evidence of occurrence of ISA in the use of these acidic sands.

3.5.2 Dynamic Elastic Modulus Results

The dynamic elastic modulus of concrete was tested at 28 and 90 days of age and results are shown in Table 3.11. Similar to the compressive strength results at these ages,

the Site H sand concretes show highest values of dynamic modulus at both ages examined, while results for Site D and Control sand samples are similar (see Table 3.12).

Table 3.11 Dynamic elastic modulus at 28 and 90 days. (1 ksi = 6.9 MPa)

	Dynamic E @ 28 days, ksi	**Std Dev,** ksi	**Dynamic E @ 90 days,** ksi	**Std Dev,** ksi
Control Sand	**5,200**	80	**5,331**	224
Site H Sand	**5,505**	90	**5,764**	160
Site D Sand	**5,386**	37	**5,671**	108

Table 3.12 Statistical analysis of dynamic elastic modulus results.

Age of Testing	**Test H_0: $\mu_c = \mu_h$** ($\alpha = 5\%$)	**p-value**	**Test H_0: $\mu_c = \mu_d$** ($\alpha = 5\%$)	**p-value**
28 days	Reject H_0	0.879%	Fail to Reject H_0	5.346%
90 days	Reject H_0	4.519%	Fail to Reject H_0	17.423%

The dynamic elastic modulus is an estimation of the static elastic modulus by non-destructive methods (NDT). The static elastic modulus is consistently lower than the dynamic elastic modulus, but a linear correlation has been observed in experimental values obtained for both mechanical properties. However, the selection of the equation to relate both values will depend on parameter such as the test used to determine the dynamic modulus, the geometry of the specimens, or the vibration mode (Popovics et al., 2008). This difference between the static and dynamic elastic moduli is a consequence of the composite nature of concrete, being the results obtained for each property consistent with different composite phase models. According to Popovics et al. (2008), the best agreement between the dynamic elastic modulus obtained by ASTM C215, using

longitudinal vibration of cylinders, with the static elastic modulus obtained by ASTM C469 is the British Standard equation (BS8110, Part 2) shown in Equation 3.4.

$$E_s = 1.25 \cdot E_d - 19 \quad (3.4)$$

where E_s and E_d correspond to the static and dynamic moduli, in GPa.

The value for the static modulus of elasticity can also be calculated from ACI 318-11: Building Code Requirements for Structural Concrete and Commentary, using the compressive strength of concrete. A comparison between these calculations is shown in Table 3.13.

Table 3.13 Estimations of the static modulus of elasticity from ACI 318 and BS 8110 equations. (1 ksi = 6.9 MPa)

	Age	**Control Sand**	**Site H Sand**	**Site D Sand**
Static E ACI 318 (ksi)	28 d	4,240	4,644	4,283
	90 d	4,499	5,065	4,627
Static E BS 8110 (ksi)	28 d	3,744	4,126	3,977
	90 d	3,908	4,450	4,333

Sulfate content influences the physical microstructure of portland cement systems. It has been suggested that a sulfate (SO_3) content between 2 to 3.5% may optimize compressive strength at different testing times (Soroka and Abayneh, 1986; Sersale et al., 1991). The higher mechanical properties of Site H sand samples suggest that the additional sulfate content provided by this acidic sand increased the total sulfate content closer to the optimum.

3.6 Effect of Acidic Sands on Durability

An important aspect of the study of acidic sands is the assessment of the effect of sulfide- and sulfate-bearing sands on the long-term performance of mortar and concrete. Particularly, the reduction of the pH on an aqueous environment could lead to mixtures more prone to corrosion, or the presence of sulfate in the aggregate could lead to internal sulfate attack, or in the case of elevated temperature curing, to DEF. The potential for these deleterious interactions is examined, as well as results from standard testing of concrete mixtures, including rapid chloride permeability and surface resistivity. While results of surface resistivity, RCPT and accelerated corrosion tests are analyzed in Section 3.6, the evaluation of ISA and DEF reactions in mortar mixtures including acidic sands is discussed in Chapter 4.

3.6.1 RCPT Results

RCPT provides an indication of the quality of the concrete, as measured by the charge passed (measured in Coulombs, C) across a saturated concrete specimen, as performed by ASTM C1202. Here, two concrete samples prepared with *w/c* of 0.43, were tested per each type of sand, at 56 days from casting. For all three concrete mixtures, the RCPT results correspond to moderate permeability. Results show a similar trend than the observed on the results of the mechanical properties. That is, Site D and Site H sands having lower charge passed, compared to the control sample (Table 3.14). Filling of pores by secondary products, such as ettringite, could contribute to a lower charge passed during this test.

Table 3.14 Total charge passed during RCPT.

Sample	**Charge Passed,** Coulombs		**Chloride Ion Penetrability**
	Average	Std Dev	
Control Sand	**3,975**	345	Moderate
Site D – Sand	**3,064**	577	Moderate
Site H – Sand	**3,354**	634	Moderate

In addition to RCPT, surface resistivity of concrete was measured after more than two years from mixing, using a four-electrode Wenner probe, following standard AASHTO TP 95 (2011). This test provides an indication of the ability of concrete to resist chloride ion penetration, and it has evidenced good correlation with chloride diffusivity, RCPT results, and concrete strength (Sengul and Gjorv, 2008; Kessler et al., 2008; Tanesi and Ardani, 2012).

Surface resistivity of concrete was measured on saturated 4×8-in. (10.2×20.3 cm) cylinders, at 780 days from casting. Concrete samples were stored under fogroom curing until testing and water from the surface of the cylinders was removed using a damp cloth before the measurements. Results of the test are given in Table 3.15.

Table 3.15 Surface resistivity of concrete.

Sample	**Surface Resistivity,** kΩ·cm		**Chloride Ion Penetrability**
	Average	Std Dev	
Control Sand	**19.3**	1.2	Moderate
Site D – Sand	**18.1**	1.1	Moderate
Site H – Sand	**18.3**	0.9	Moderate

According to the AASHTO standard, measured resistivities correspond to moderate chloride permeability for all the mixtures.

3.6.2 Accelerated Corrosion Test

Corrosion activity of each concrete-embedded steel bar was measured in terms of the current flowing between the counter electrode and the embedded bar. The measured current is a function of the corrosion rate of the embedded steel. Also, the voltage applied during the test was measured and controlled. An average value of 5.998 V was recorded during the 60 days of the test at the start and at the end of the circuit. The maximum and minimum measured voltages were 6.059 and 5.918 V, respectively.

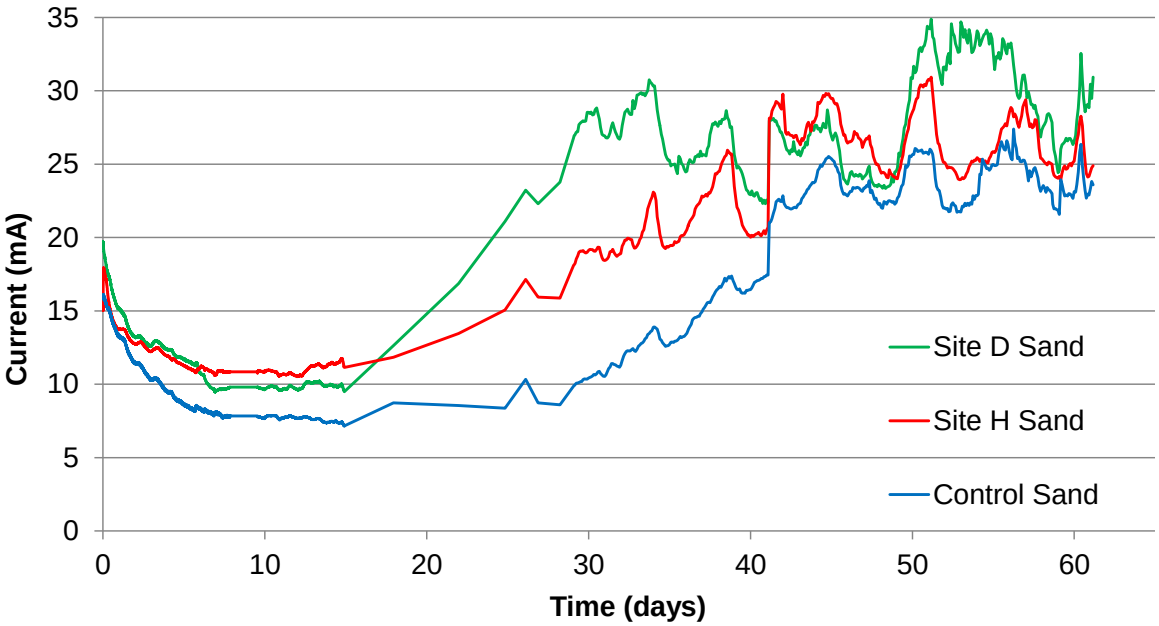

Figure 3.28 Current over time for concrete samples exposed to a NaCl solution. Every line represents the average of three specimens.

The results of the corrosion test can be observed in Figure 3.28, which shows the average current during the test. Three specimens were tested each time and tests were repeated two times under the same conditions. The results coincided in terms of the time to corrosion initiation, magnitude of current, and evolution of current over time (see

Appendix D, Figure D.1). The variability of the current evolution among different specimens of the same type of sand is shown in Appendix D, Figures D.2 to D.4.

As observed in Figure 3.28, an initial reduction in the current occurred in the first 6 to 8 days due to the stabilization of the passive layer of the embedded steel in all tested concrete samples, followed by a plateau. This approximately constant value corresponds to the average daily current, I_{avg}. Using Ohm's law and I_{avg}, the average daily resistance of concrete, R_{avg}, can be calculated following the standard.

After ~15 days, an increment of the current flow for Site D and Site H samples indicates an increase in the corrosion activity for these embedded steel bar surfaces due to the destabilization of the passive layer, exposing active steel that corrodes at a faster rate. After ~28 days, the control samples also show this increment (abrupt change of slope).

Site H and D specimens exhibited higher current throughout the test compared to control. Tests were stopped at day 61, when no significant changes of current were observed, and R_{avg} and time-to-failure (time of corrosion initiation) were calculated for every concrete mixture, as shown in Table 3.16.

Table 3.16 Average resistance and time to failure of concrete samples for the corrosion test.

	Average daily resistance, R_{avg} (Ohm)	**Time-to-failure** (days)
Control Sand	776.6	28.23
Site D Sand	607.3	14.84
Site H Sand	550.4	14.86

These results indicate that the use of Site H and Site D sands accelerates the corrosion initiation of the reinforcement and decreases the protection of concrete against

corrosion of the embedded reinforcement. This statement was qualitatively corroborated with the visual evaluation of the deterioration of the samples over time. Samples including Site D and Site H sands evidenced a more extensive formation of corrosion products, surface discoloration, and earlier cracking compared to control samples. At day 30 from the start of the current monitoring, the extent of cracking and corrosion products was considerable higher for the samples with Site H and D sands. Figures 3.29 to 3.31 show the evolution of damage for the samples during the test.

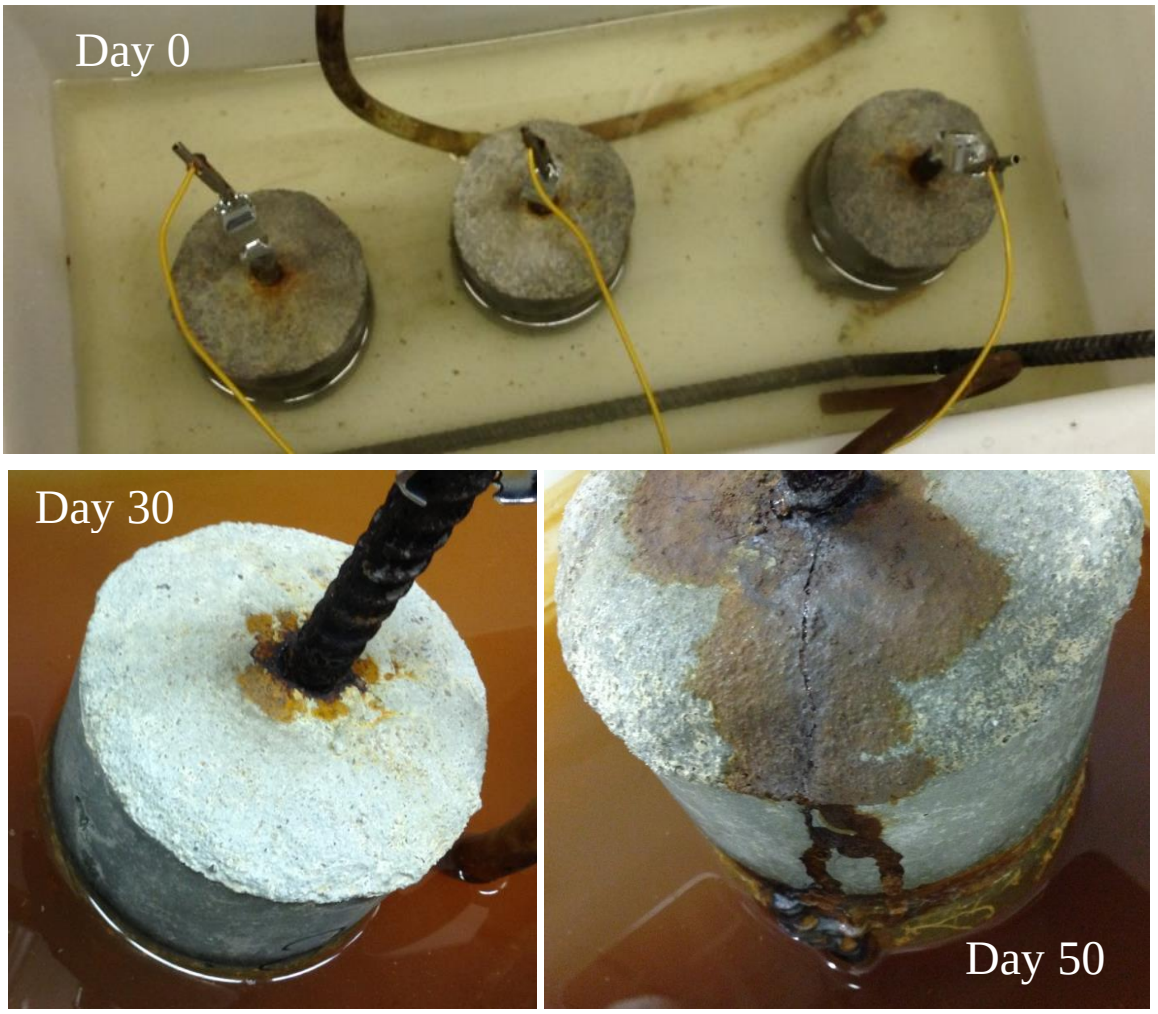

Figure 3.29 Specimens for Control Sand at 0, 30, and 50 days from the start of the test.

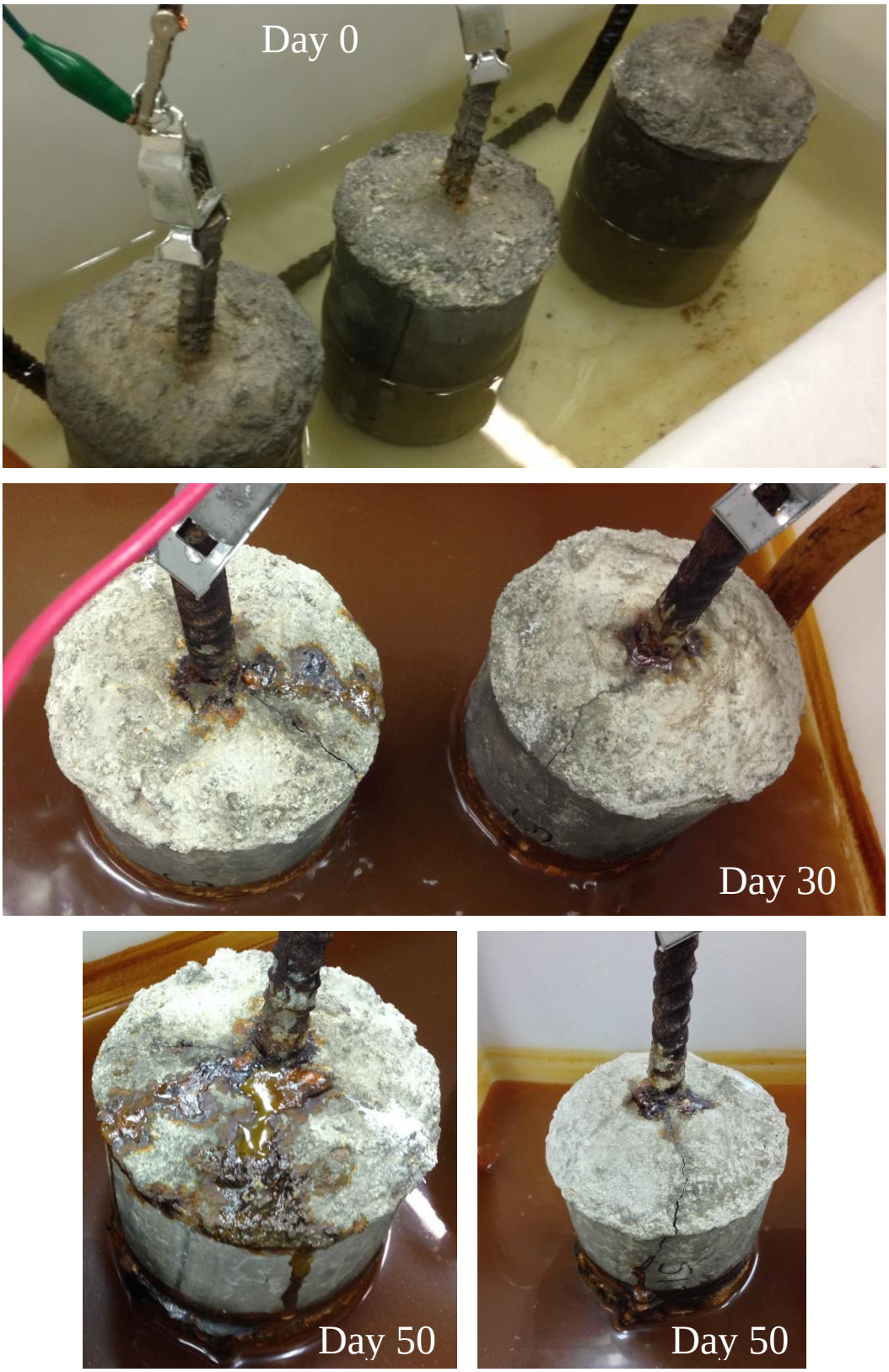

Figure 3.30 Specimens for Site D Sand at 0, 30, and 50 days from the start of the test.

Figure 3.31 Specimens for Site H Sand at 0, 30, and 50 days from the start of the test.

Concrete specimens developed radial cracks after corrosion initiation, which can be attributable to the generation of tensile stresses due to the higher volume of corrosion products, regularly 3 to 4 times the volume of iron (Rosenberg et al., 1989). At high levels of cracking, corrosion products formed on the embedded rebar leaked to the surface of the specimens.

At the end of the test, the condition of concrete and embedded steel bar was monitored. Similar damage pattern was observed in all the specimens, as shown in Figure 3.32, where discoloration of concrete evidences the transport of corrosion product through the cracks.

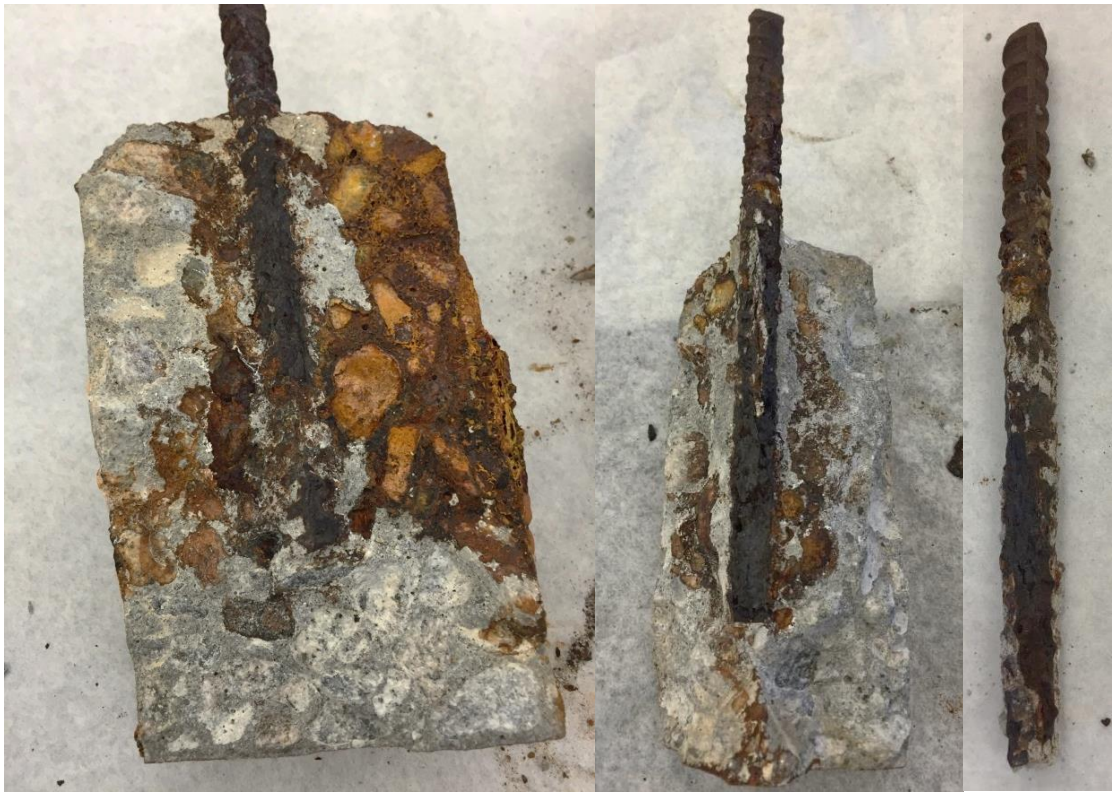

(a) (b) (c)

Figure 3.32 Final condition of steel reinforcement and concrete in corrosion test specimens using (a) Control sand and (b) Site H sand. (c) Typical condition of steel rebar at the end of the test.

Steel reinforcement exhibited a considerable higher deterioration in the segment embedded in concrete and exposed to a high concentration of chlorides, where only a small fraction of steel remained intact at the end of the test (Figure 3.32c). Usually chloride-induced corrosion is initiated by a localized breakdown of the passive layer, followed by an accelerated dissolution of the anodic portion of steel (see Section 2.3.2.2); however, no corrosions pits were observed at the rebar surface of tested specimens. This absence of visible pits can be attributed to the advanced degree of deterioration of the embedded steel bar, but the final condition of rebar suggests that corrosion occurred in a more uniform way along the steel in contact with concrete. Corrosion of larger regions of the reinforcement may occur at high concentrations of chlorides or when presence of chlorides is accompanied by a decrease of concrete pH (Bertolini et al., 2013).

Prior to the corrosion test, samples were submerged for 28 days in a 0.5M NaCl solution, similar chloride concentration than observed in seawater. Therefore, a homogeneous presence of chloride ions in the proximity of rebar is expected at the beginning of the test. Then, ingress of additional chloride ions during the test can increase the chloride concentration to critical levels uniformly along the rebar.

As shown in Section 3.2.1.2, the alkaline nature of concrete overcomes the drop of pH produced by the use of acidic sands. However, when Site H and Site D sands are used, the additional content of sulfate can affect the corrosion resistance of concrete. Al-Amoudi and Maslehuddin (1993) showed that although an increase of sulfate concentration does not affect the time to corrosion initiation of the steel reinforcement, the combined exposure to sodium chloride and sodium sulfate can increase significantly the reinforcement corrosion rate. The effect of sulfate in corrosion is commonly

attributed to the increase of free chlorides in the pore solution and a decrease of the electrical resistivity of concrete (Dehwah et al., 2002).

Sulfate ions can replace chloride ions in the microstructure of Friedel's salt, increasing the concentration of free chlorides and, as a result, accelerating the active corrosion of steel. Chloride ions can accelerate the dissolution of the passive film by the adsorption and ingress of Cl^- ions through the outer layers of the passive film (Gunay et al., 2015), forming soluble chlorocomplexes of iron that releases Fe^{3+} and can generate corrosion products more voluminous than iron (Mehta, 1991). This effect is believed to be influenced by the source of sulfates. Sulfate ions diffusion in concrete is between 10 to 100 times lower than chloride ions (Obserholster, 1986), therefore, presence of sulfate ions from internal sources would have a higher impact on corrosion initiation.

Additionally, a decrease of the electrical resistivity of concrete has been measured at low moisture contents, when the sulfate concentration is increased in chloride-containing concrete (Saleem et al., 1996; Dehwah et al., 2002).

Also, a higher presence of sulfate in the pore solution has been associated with a less protective passive layer of embedded steel (Ghods et al., 2009).

CHAPTER 4

INFLUENCE OF THE USE OF ACIDIC SANDS ON INTERNAL SULFATE ATTACK (ISA) AND DELAYED ETTRINGITE FORMATION (DEF)

4.1 Introduction

The use of sulfide- and sulfate-bearing sand (acidic sands) in cement-based materials can increase the potential of internal sulfate attack (ISA) and delayed ettringite formation (DEF) occurrence.

The action of sulfate from internal sources, most commonly contaminated aggregates or over-sulfated cement, can produce deleterious expansion and deterioration of concrete, process referred as internal sulfate attack (ISA) (Skalny et al., 2002). ISA is traditionally controlled by standards limits on the sulfate content in cement. For example, ASTM C150 limit for SO_3 content in portland cements is between 2.3% and 4.5%, which are the maximum values for Type V and Type III cement, respectively. Sulfate amount needed to induce ISA-expansion is above 5-6% by weight of cement, in which case fast expansions may occur within 6 months (Scrivener and Skalny, 2005). In the case of contaminated aggregates, ASTM C1038 or a similar test have been employed for assessments of deleterious sulfate content and reference values from sulfate resistance tests have been commonly adopted for experimental evaluation of ISA (Atahan and Dikme, 2010; Kheder and Assi, 2010; Atahan and Dikme, 2011). ASTM C1157 defines expansion limits of 0.02% at 14 days for ASTM C1038, 0.1% at 6 months for ASTM C1012 when moderate sulfate resistance is needed, and 0.05% at 6 months and 0.1% at 1 year for ASTM C1012 when high sulfate resistance is needed. ACI 318-14 also

establishes a maximum ASTM C1012 expansion limit of 0.1% at 18 months when concrete structures are exposed to high concentrations of water-soluble sulfate. For evaluation of contaminated aggregates, ISA-expansion higher than 0.1% has been traditionally considered deleterious (Crammond, 1984; Ouyang et al., 1988; Atahan and Dikme, 2011).

DEF can occur in heat-cured concrete, when curing temperatures exceed 65-70 °C (150-158 °F). After hardening, the formation of ettringite in small pores (<100 nm [3.94×10^{-6}-in.]) may lead to damaging expansion and cracking (Taylor et al., 2001), according to the mechanism explained in Section 2.2.3. DEF-associated damage has been reported in prestressed, precast and mass concrete elements (Thomas et al., 2008; Thomas and Ramlochan, 2004), where temperature of concrete can rise above safe limits. In prestressed concrete girders, concrete temperatures as high as 97 °C (207 °F) has been measured in traditional and high-performance concrete (Myers and Carrasquillo, 1998; Kehl and Carrasquillo, 1998). Higher and earlier DEF-expansion is usually observed at higher curing temperatures (Folliard et al., 2006; Pavoine et al., 2012).

Although there is no clear understanding of the relationship between cement composition and DEF damage, generally higher content of sulfate, tricalcium aluminate (C_3A), and alkalis, and higher Blaine specific area have shown strong correlation with higher expansion and cracking (Zhang et al., 2002b; Pavoine et al., 2012). The former characteristics are usually desired in cements used in precast and prestressed concrete operations in order to improve the early-age strength of concrete.

Along with sulfate content, the type and solubility of sulfate phases also has an impact on the development of ISA and DEF. Alkali and calcium sulfate are highly

soluble phases and can be considered to have a similar impact on ISA/DEF reaction in portland cement systems (Scrivener and Skalny, 2005). On the other hand, barium sulfate ($BaSO_4$, baryte) is not soluble enough to be considered a concern.

Although no expansion limit has been defined for a deleterious DEF-expansion, regularly 0.1% is considered an acceptable reference for mortar bars (Ramlochan et al., 2004; Petrov and Tagnit-Hamou, 2004; Tovar-Rodríguez et al., 2013).

As summarized by Skalny et al. (2002), previous studies that have reported SEM images of concrete damaged by the action of DEF, in backscattered electron (BSE) signal mode, regularly show partial or complete rims (gaps, cracks, or bands) around aggregates, formation of a two-tone C-S-H structure, presence of secondary ettringite in those gaps, nests of secondary ettringite within paste, and microcracking of the paste. Tosun and Baradan (2010) also observed non-expansive rounded clusters of ettringite in air voids and large pores, with diameters between 15 and 20 μm and formed from Al-rich species.

4.2 ISA and DEF Evaluation

The potential for the acidic sands to initiate deleterious expansion associated to ISA and DEF was assessed by tests performed on mortar bars and cubes using Control and Site H sand. For ISA, tests were performed according to ASTM C1038 limewater exposure conditions while, to assess the potential for DEF, replicate mortar samples were initially cured at high temperature according to the Kelham curing cycle (Figure 2.3) and were subsequently soaked in separate limewater baths. All samples were prepared at a

common water-to-cement ratio of 0.5 and sand-to-cement ratio of 2.75; expansion of mortar bars was measured periodically.

4.2.1 Preparation of Mortar Specimens

Ten bars and twelve cubes were prepared using the mixture design in Table 3.4 and the mixing procedure given by ASTM C305, for Cements A to E (Table 3.2). For each batch of mortar, half were cured in moist containers at room temperature for 24 hours after casting to evaluate the occurrence of ISA, and half of the specimens were exposed to the Kelham high-temperature curing cycle, explained in Section 2.2.3, to assess the potential for DEF.

During the high-temperature curing cycle the RH is kept at 100%. To reach this value, Kelham (1997) sealed the molds in polyethylene bags together with water soaking cloths, but this procedure was replaced by metallic trays containing water. To avoid evaporation of water during the high-temperature regime, the containers were sealed. Also, a metallic grid was used to separate the water and the mortar samples. After these trays were removed from the oven, the presence of water inside the containers was confirmed to avoid the exposure of the samples to undesired effects, such as drying or plastic shrinkage. Figures 4.1 to 4.3 show the preparation of the specimens.

At the end of the curing cycles, mortars bars and cubes were stored in separate limewater containers to avoid leaching and cross interaction between different specimens. Storage of the mortar specimens in limewater at room temperature would be analogous to exposure of concrete to moisture during storage or service.

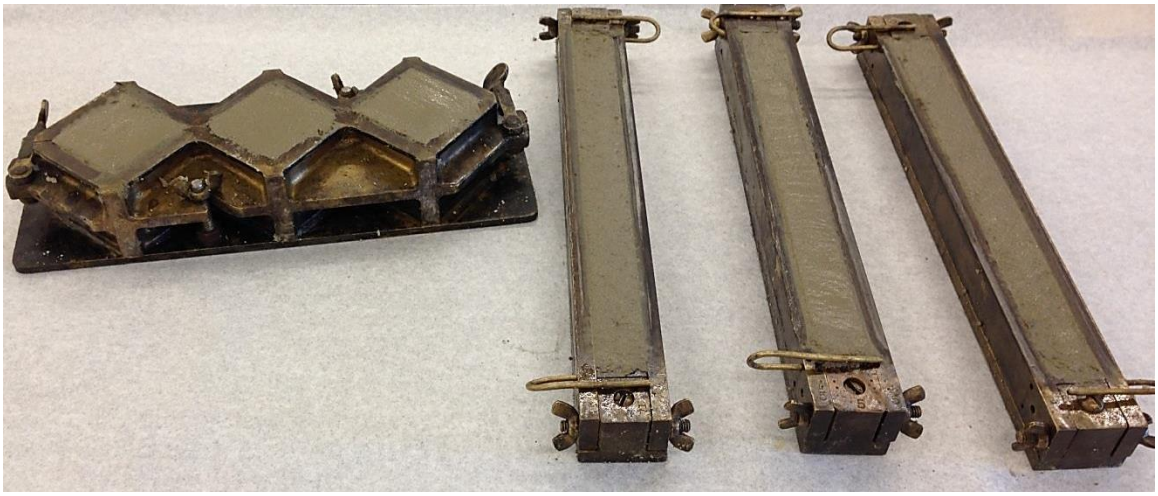

Figure 4.1 Mortar bars for length change testing and mortar cubes for compressive strength evaluation over time.

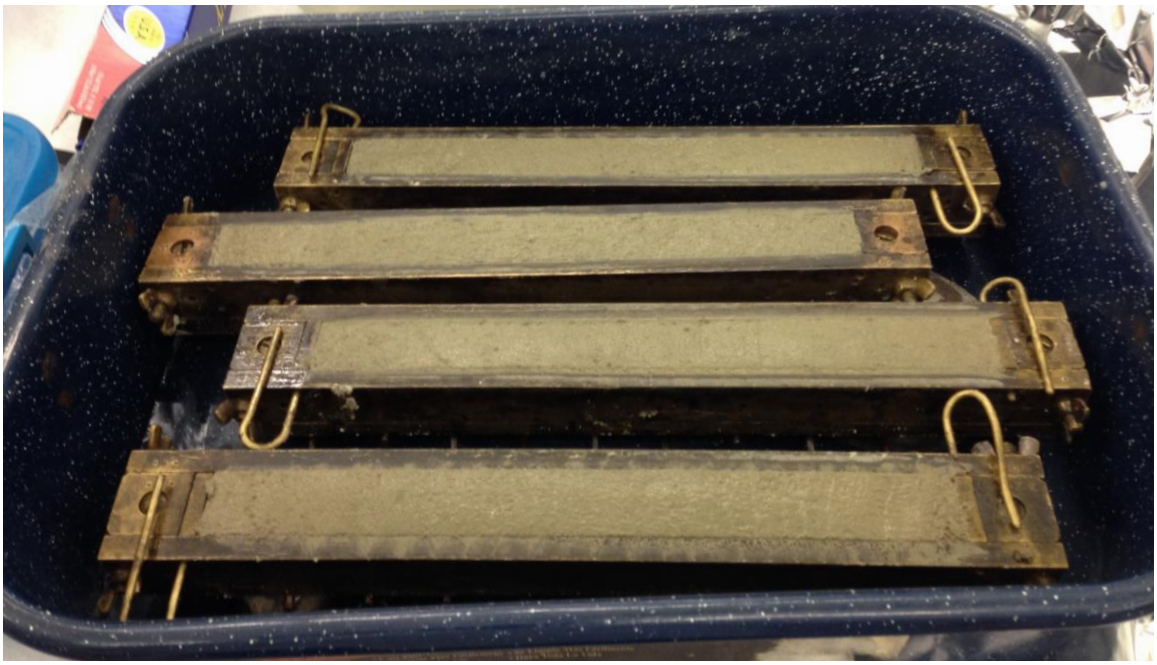

Figure 4.2 Metallic tray used to provide a moist condition during Kelham curing cycle.

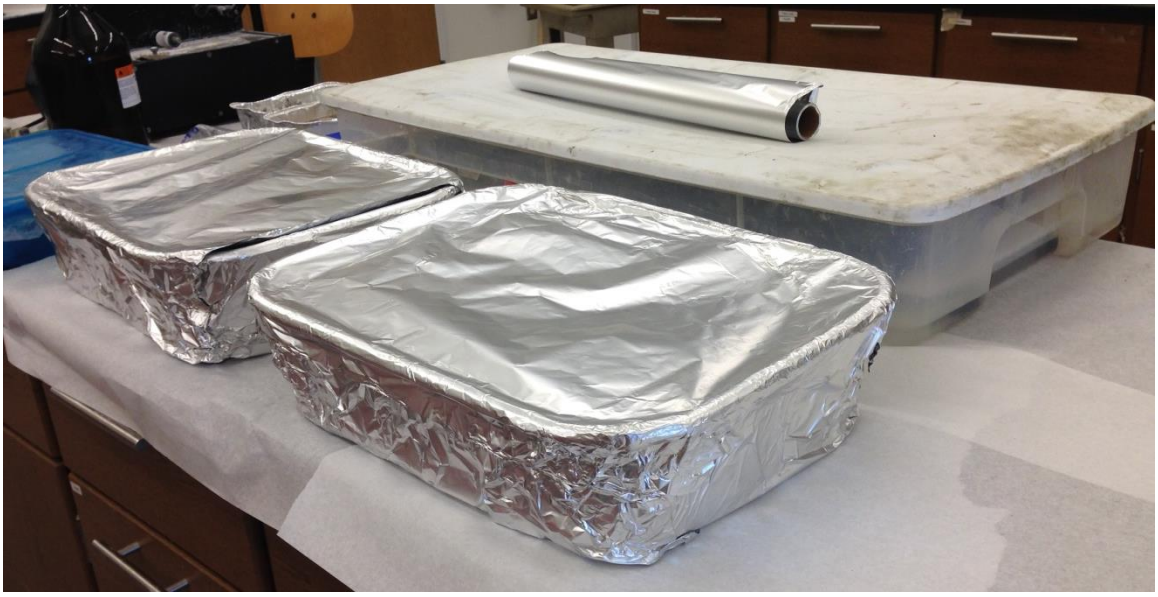

Figure 4.3 Mortar samples were kept on moist environments for the first 24 hours after casting. Aluminum foil was used to avoid water evaporation during Kelham curing cycle.

4.2.2 Testing Procedure

Twenty-four hours after casting, the initial length of the mortar bars was measured using an apparatus conforming to ASTM C490, including a digital dial gauge with a precision of 0.002 mm (7.87×10^{-5}-in.). Periodic measurements of the length of the bars were recorded on time using the same apparatus, under laboratory temperature (23±2 °C [73.5±3.5 °F]) and humidity (50±5%). Before every measurement, the specimens were rotated gently until the reading from the dial stabilized. Every measurement was performed in the same position and orientation of the bar, to minimize the noise in the determination of the length change of the samples. ISA- and DEF-expansion measurements were performed for at least 15 months to better evaluate the reaction kinetics in mortars using acidic sand and because standard ASTM C1038 is designed to assess sulfate contents in cement, rather than sand.

Compressive strength of companion cubes was tested at 28 and 100 days from casting, following standard ASTM C109. Three cubes were tested for every sand and curing temperature (Figure 4.4).

Variable Pressure Scanning Electron Microscopy (VP-SEM) images and EDS microanalysis were performed on mortar bar sections using a VP-SEM Hitachi S-3700N (Figure 4.5), at 25 and 30 kV, with a working distance of 5 and 10 mm, BSE signal, and chamber pressure of 25 Pa, in order to monitor the extent of expansive reactions and damage development. Micrographs of mortar sections were produced at late stages of expansion. For heat-cured mortars, one sample of every cement type was analyzed for each sand (considering Type I/II a cement of similar composition to Type I cement).

Figure 4.4 Compression frame used for compressive strength testing of mortar cubes.

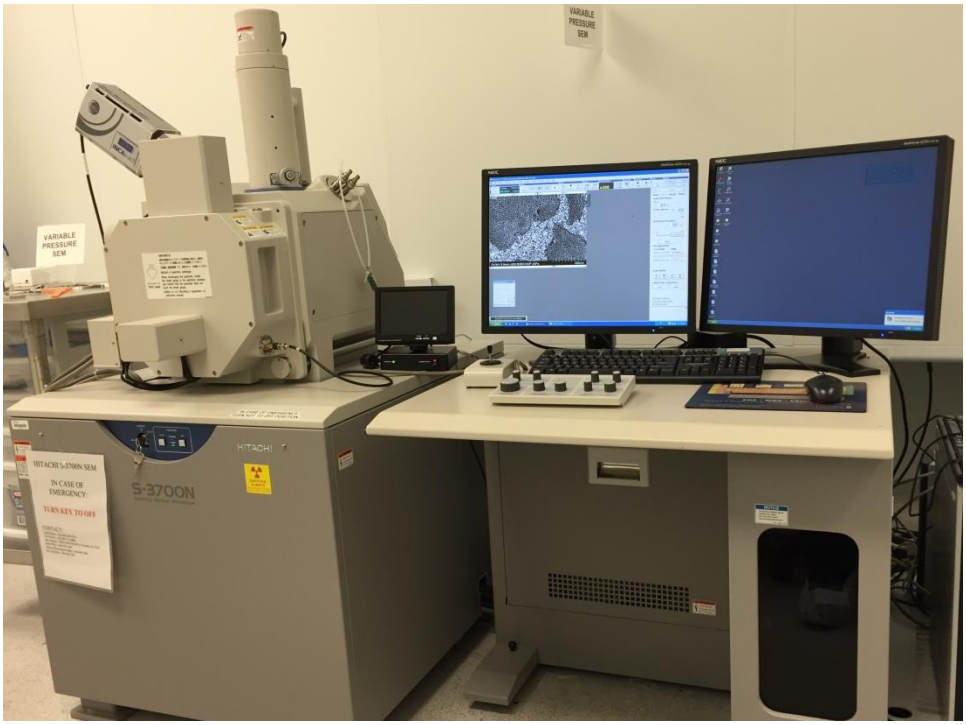

Figure 4.5 VP-SEM Hitachi S-3700N used for mortar bar evaluation.

The preparation of mortar bar sections for VP-SEM analysis was designed to obtain an accurate understanding of the condition of the samples, minimize the formation of additional microcracks, avoid the removal of ettringite crystals, and to prevent the crystallization of additional products as a result of drying. In order to preserve the original condition of the mortar bar sections, they were cut using an ethanol cooled diamond saw at 30 rpm and pulverized material on the surface was carefully removed using a lint-free wipe and ethanol. To avoid loss of moisture, mortar sections were kept in hermetic plastic bags. Then, sections were analyzed after less than three hours from cutting, in moist condition.

4.3 Evaluation of Internal Sulfate Attack

4.3.1 Expansion of Mortar Bars Cured at Room Temperature

Figures 4.6 to 4.10 show the length change measurement of mortar bars cured at room temperature (23 °C [73 °F]). Cement D and E were included later to this research; therefore, 15 months of results are shown for these cements instead of more than 21 months for Cement A to C. In order to compare the magnitude of the expansions, the graphs have the same vertical scale with a maximum value of 0.10%.

Samples containing Control and Site H sand and exposed to a room temperature curing regime showed a 24-hour expansion of around 0.006% due to water absorption after 1 day of limewater storage. After that, an almost negligible expansion is observed in the samples. At 14 days from casting, expansion values ranged between 0.002% and 0.009%, while at 1 year expansion results ranged between 0.008% and 0.021%.

Mortar prepared with Cement A (Type I/II) and Site H sand exhibits the highest expansion, 0.026% at 672 days, which is likely a consequence of water uptake over time (Folliard et al., 2006; Al Shamaa et al., 2015).

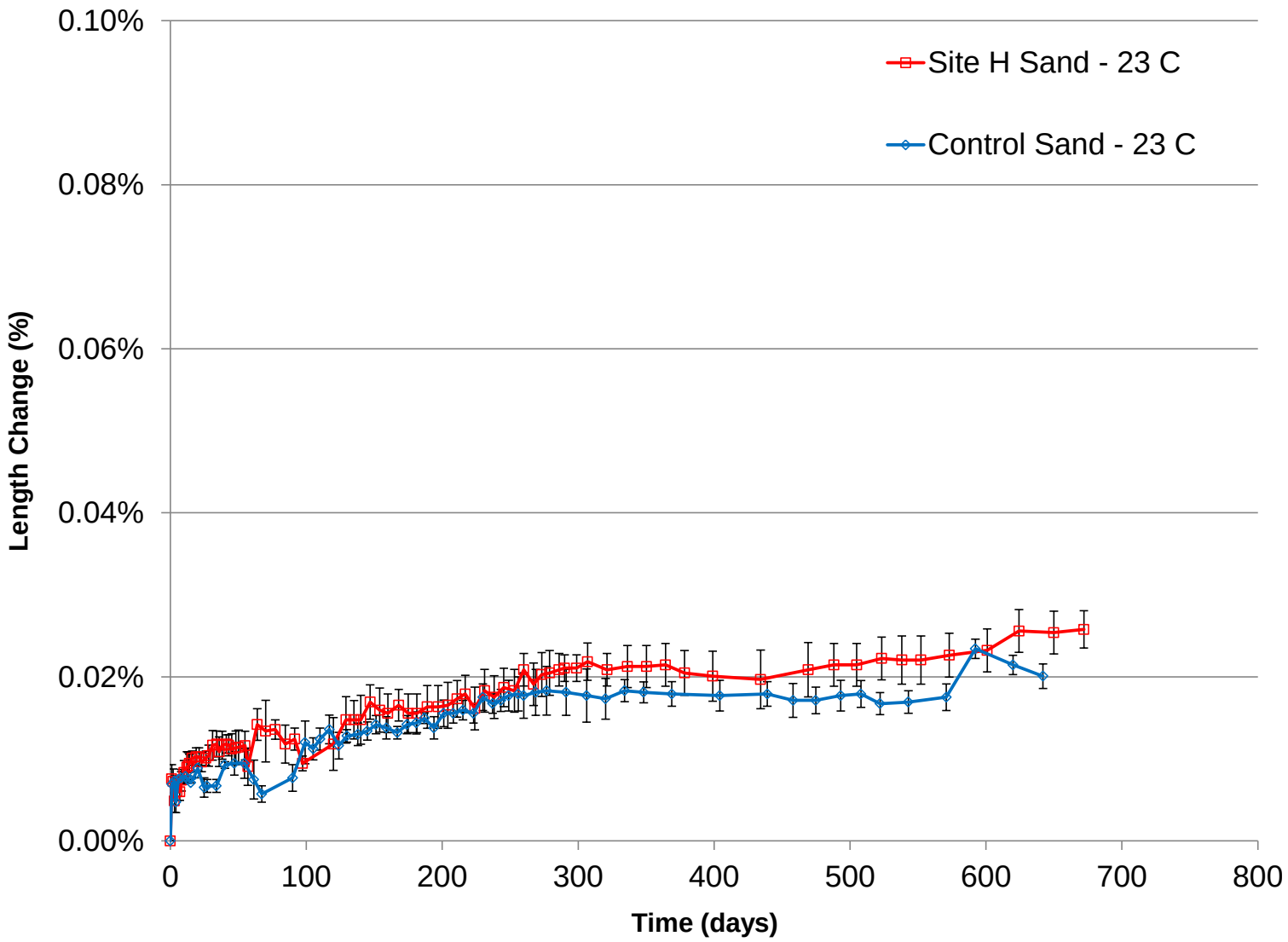

Figure 4.6 Expansion of mortar bars due to ISA (Cement A). Error bars represent standard deviation.

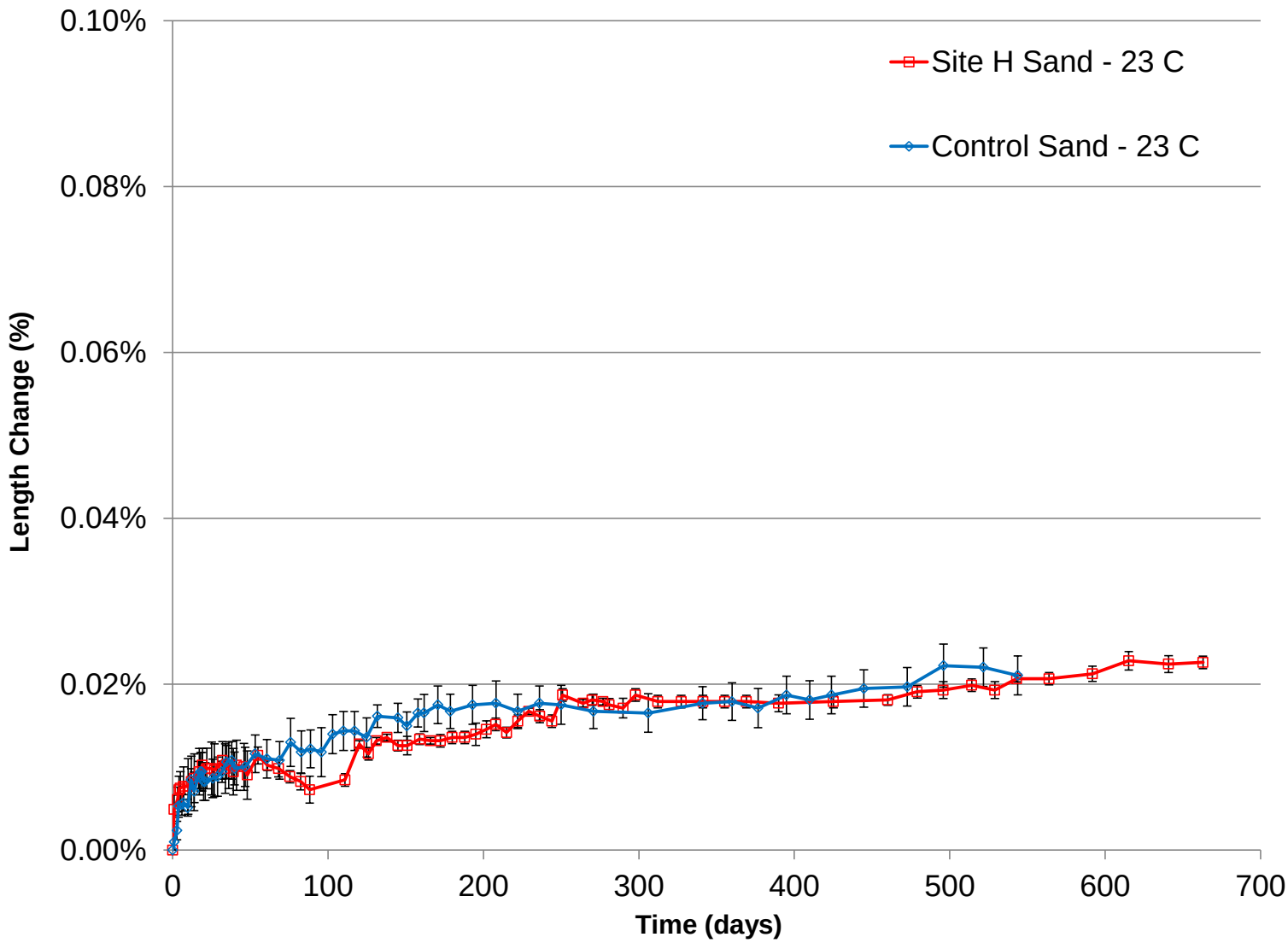

Figure 4.7 Expansion of mortar bars due to ISA (Cement B). Error bars represent standard deviation.

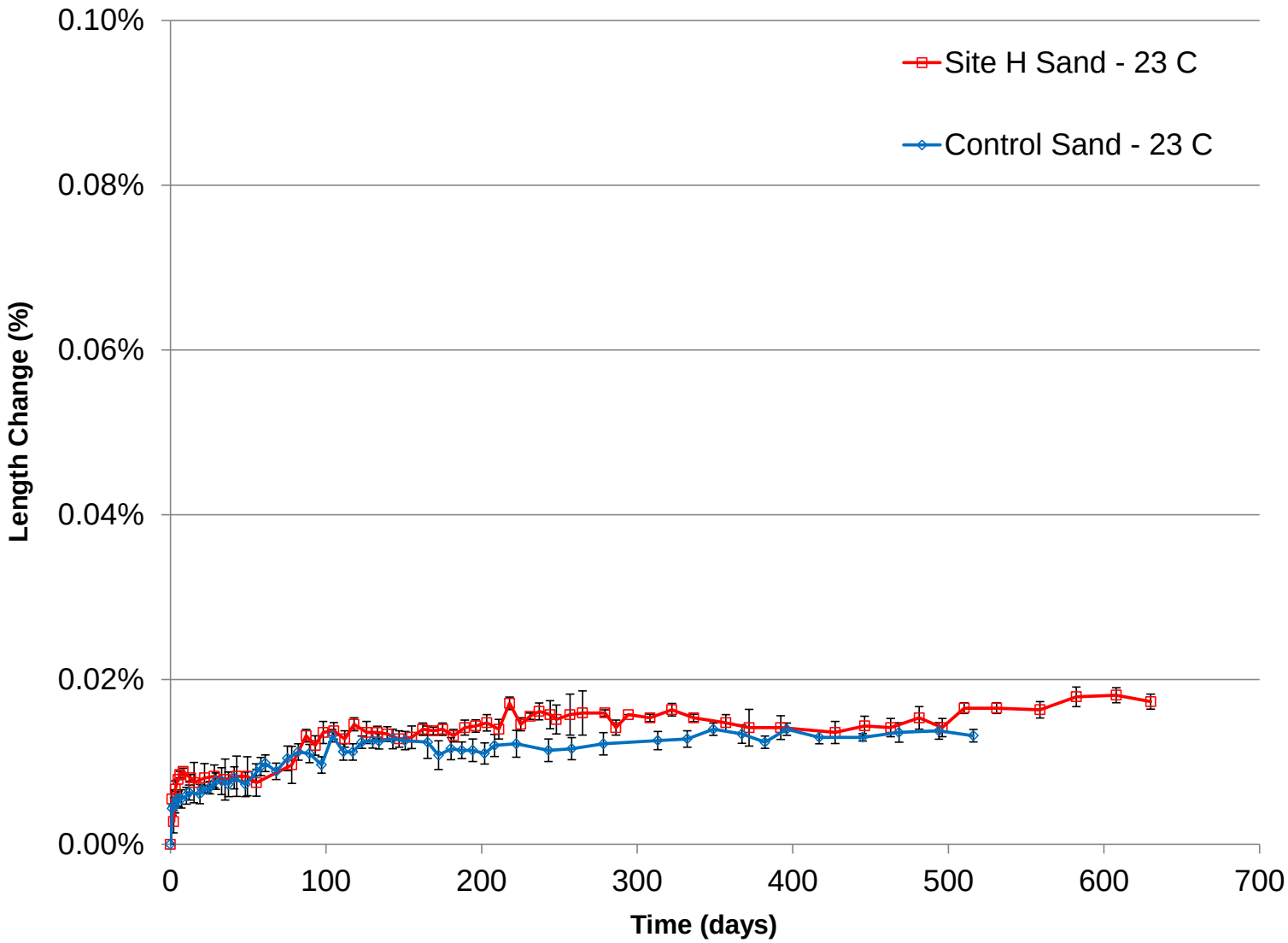

Figure 4.8 Expansion of mortar bars due to ISA (Cement C). Error bars represent standard deviation.

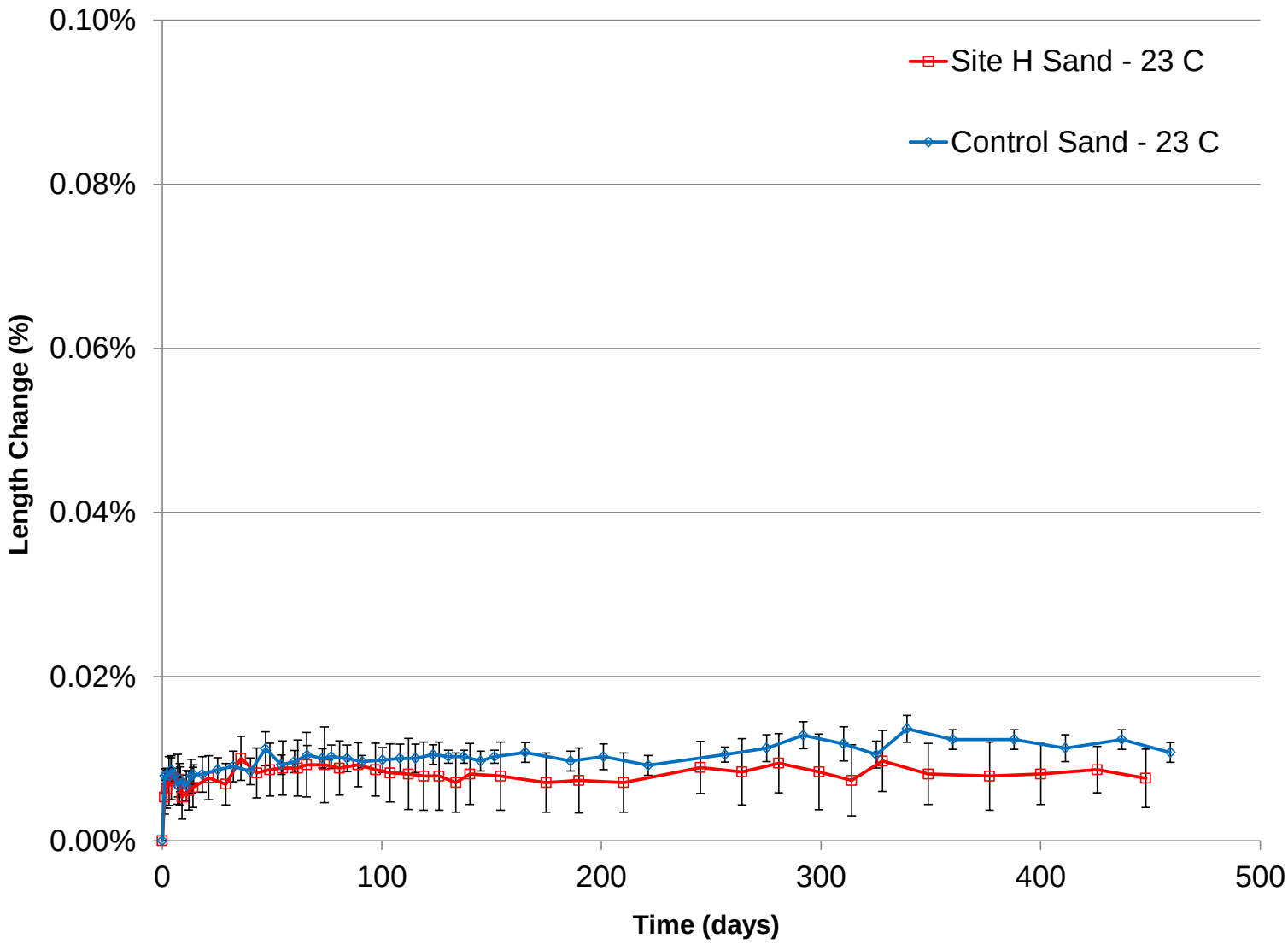

Figure 4.9 Expansion of mortar bars due to ISA (Cement D). Error bars represent standard deviation.

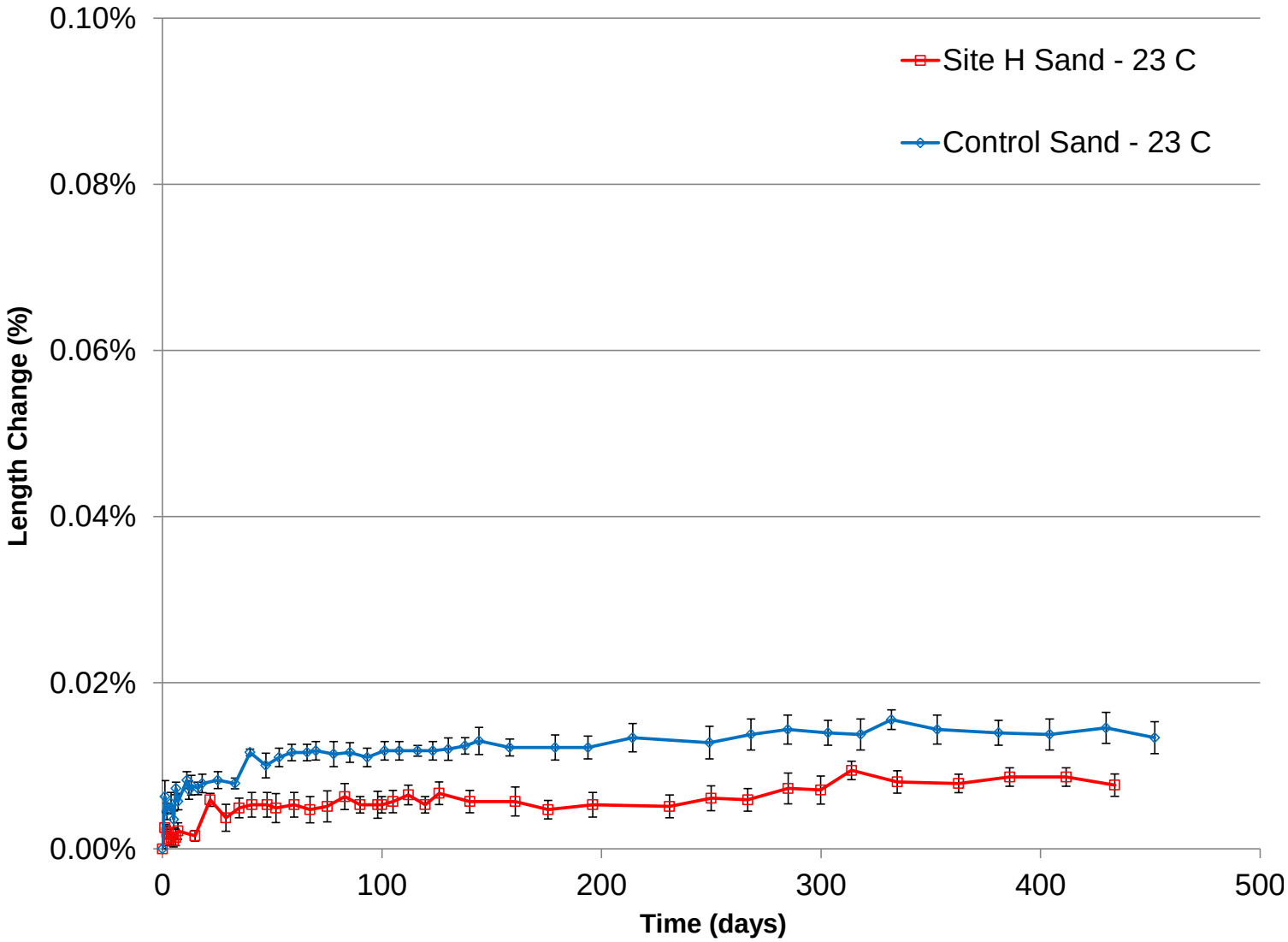

Figure 4.10 Expansion of mortar bars due to ISA (Cement E). Error bars represent standard deviation.

4.3.2 Microstructure Evaluation of Mortar Bars

Section samples were taken from mortar using Cement D (Type III) and Control sand (sample D-C-23), at day 298, when average expansion was 0.013% and from mortar using Cement B (Type V) and Site H sand (sample B-H-23), at day 663, when average expansion was 0.023%.

VP-SEM images of these samples, shown in Figures 4.11 to 4.13, exhibit a good general condition of mortar. Formation of secondary ettringite was only observed in some air voids of sample D-C-23, in smaller amount compared to calcium hydroxide, which can be attributed to the higher amount of alumina and sulfate of Cement D compared to the Cement B used in sample B-H-23. No deleterious effect of the use of acidic sand in mortar was observed.

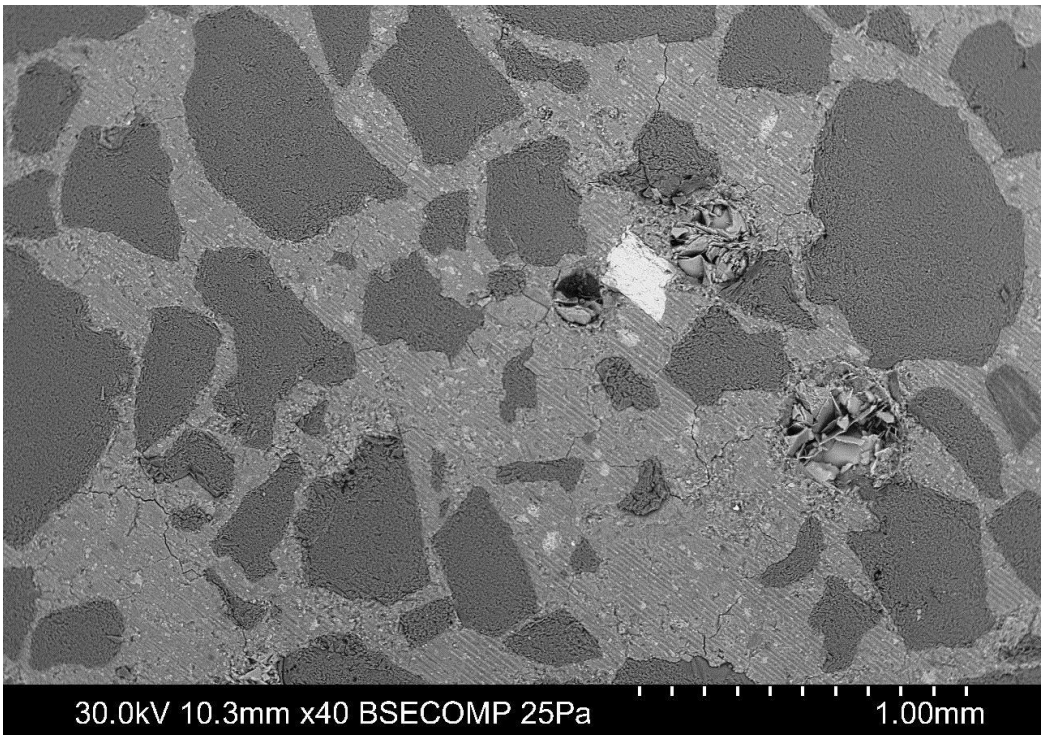

Figure 4.11 VP-SEM micrographs of mortar using Cement D (Type III) and Control sand.

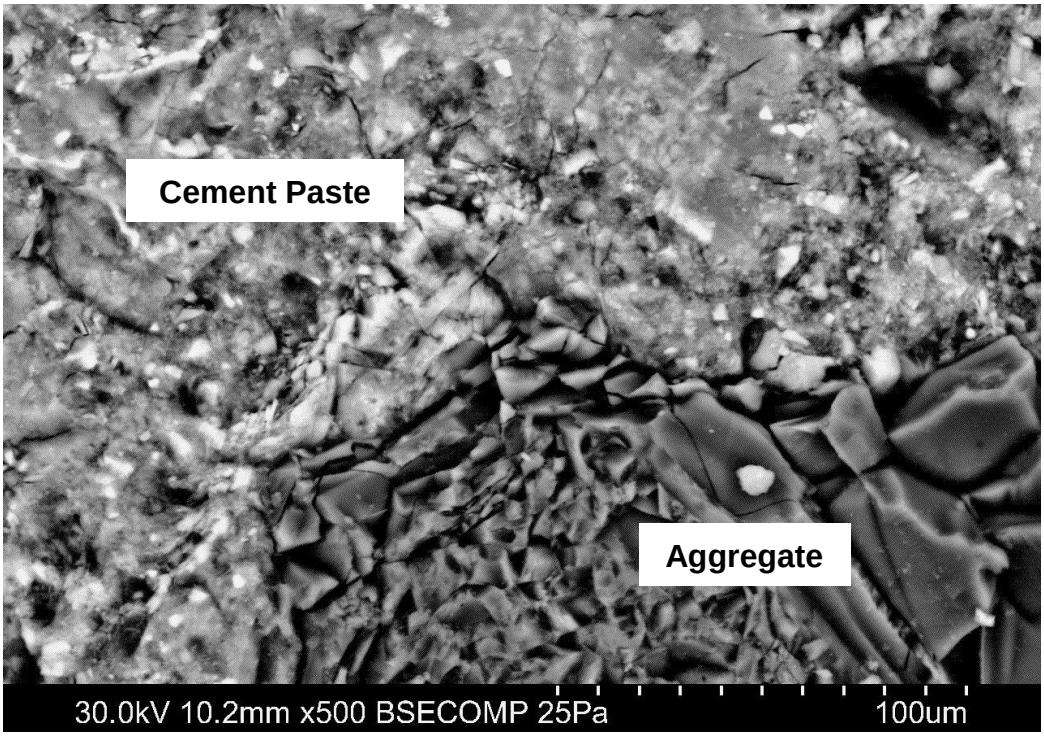

Figure 4.12 VP-SEM micrographs of mortar using Cement D (Type III) and Control sand.

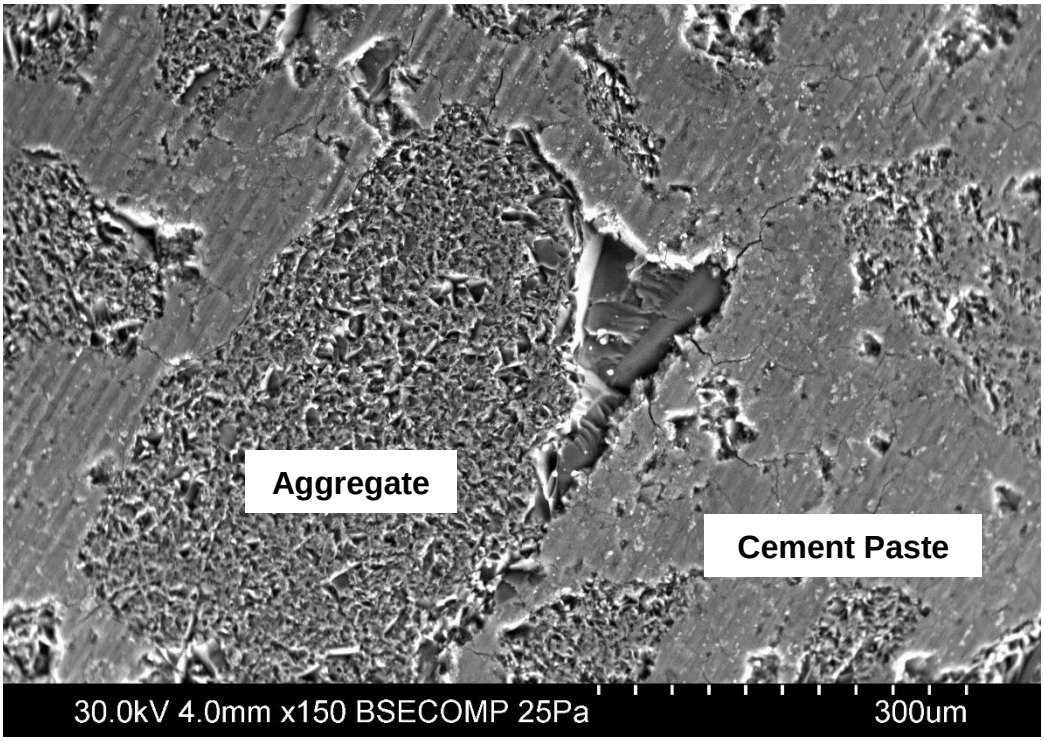

Figure 4.13 VP-SEM micrographs of mortar using Cement B (Type V) and Site H sand.

4.3.3 Compressive Strength of Mortar Cubes

Figure 4.14 shows the compressive strength of mortar cubes at 28 and 100 days. It is observed an increase of the average compressive strength at 100 days compared to the 28 days measurement, except for mortar using Cement D (Type III) and Site H sand, where the difference is not statistically significant. Deterioration of concrete and mortar associated with deleterious formation of ettringite usually lead to a significant decrease of compressive strength (Neville, 2004).

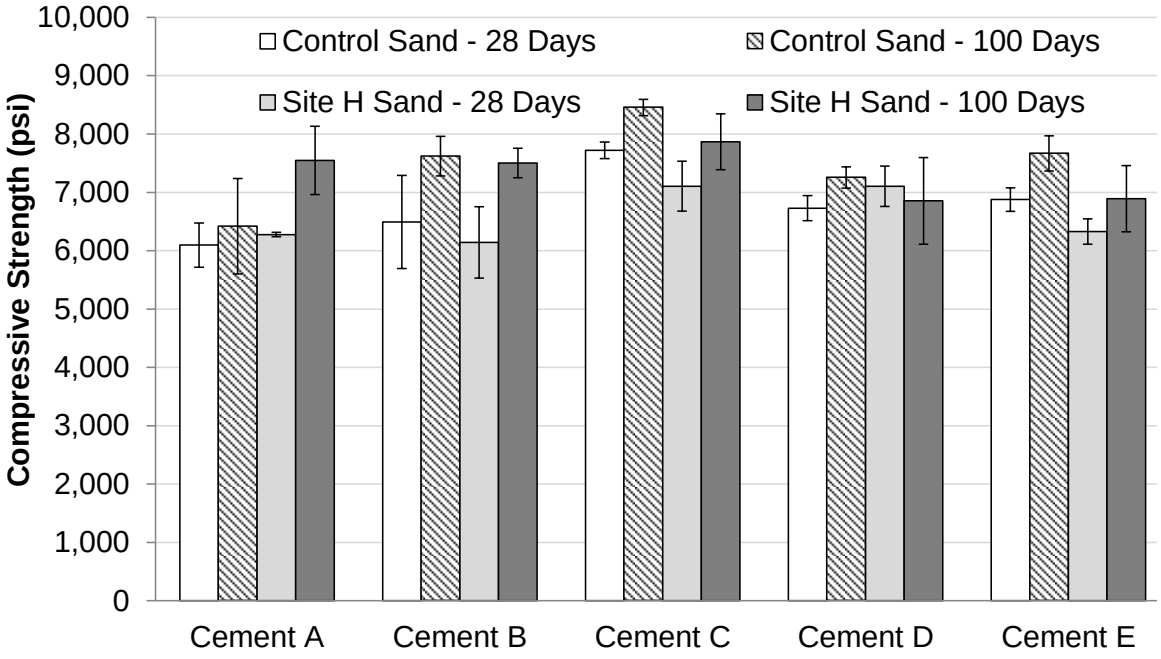

Figure 4.14 Compressive strength at 28 and 100 days of mortar cubes exposed to laboratory temperature curing. Error bars show standard deviation of results. (1,000 psi = 6.9 MPa)

The absence of damaging expansion and the increase of strength on time indicate that ISA did not affect mortar mixtures prepared with acidic sands. Thus, these results can be used to evaluate the effect of DEF on the compressive strength heat-cured mortar.

4.4 Evaluation of Delayed Ettringite Formation

4.4.1 Expansion of Heat-Cured Mortar Bars

Expansion results corresponding to heat-cured mortars using Cement A to E are shown in Figures 4.15 to 4.19. All the graphs have the same vertical scale, except for Cement D (Type III), which exhibited the highest expansions. Graphs show results for Site H sand samples in red and Control sand samples in blue. It should be noted that samples prepared using Cement D and E were cast more recently, and hence about 450 days of data are available currently compared to more than 650 days for Cements A, B, and C. Length change monitoring was stopped when no variation was observed among consecutive measurements.

Error bars included in the expansion curves show the standard deviation calculated from the length measurements on three mortar bars. However, two mortar bars containing Site H sand and Cement D broke after day 113. Thus, following expansion values of this mixture correspond to measurements performed on the remaining bar.

Error bars in expansion curves of mortar using Type I or Type I/II cement and Site H sand show a considerably larger dispersion of results, which could be attributed to the higher variability in composition of the acidic sand compared to Control sand.

Expansion of heat-cured mortars exhibited the familiar S-shaped curve commonly observed in DEF-affected specimens under similar testing procedure (Ramlochan et al., 2003). An initial latency period of almost negligible expansion is followed by a period of high expansion rate and a final stage of slower, asymptotic expansion.

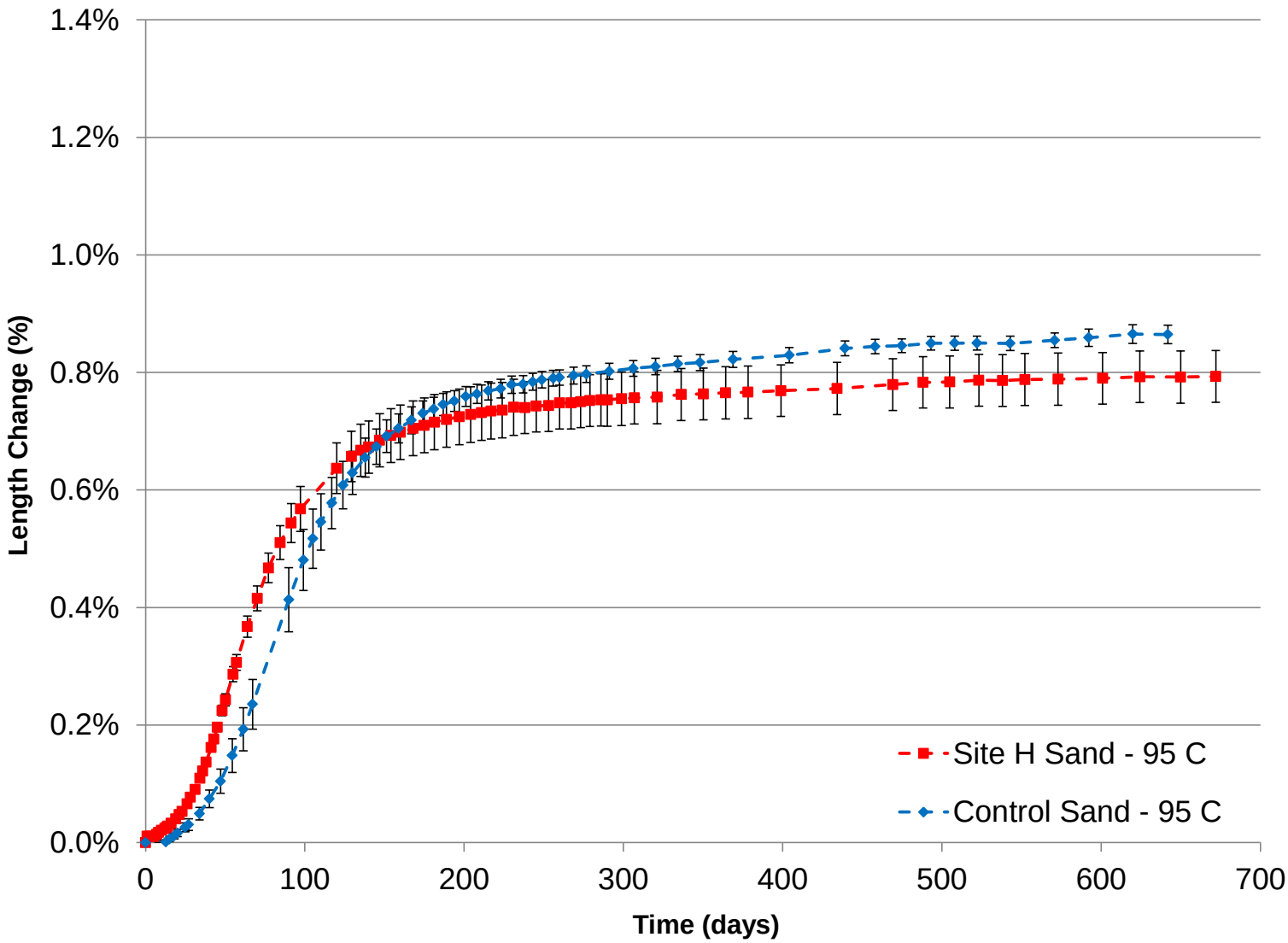

Figure 4.15 Expansion of mortar bars due to DEF (Cement A). Error bars represent standard deviation.

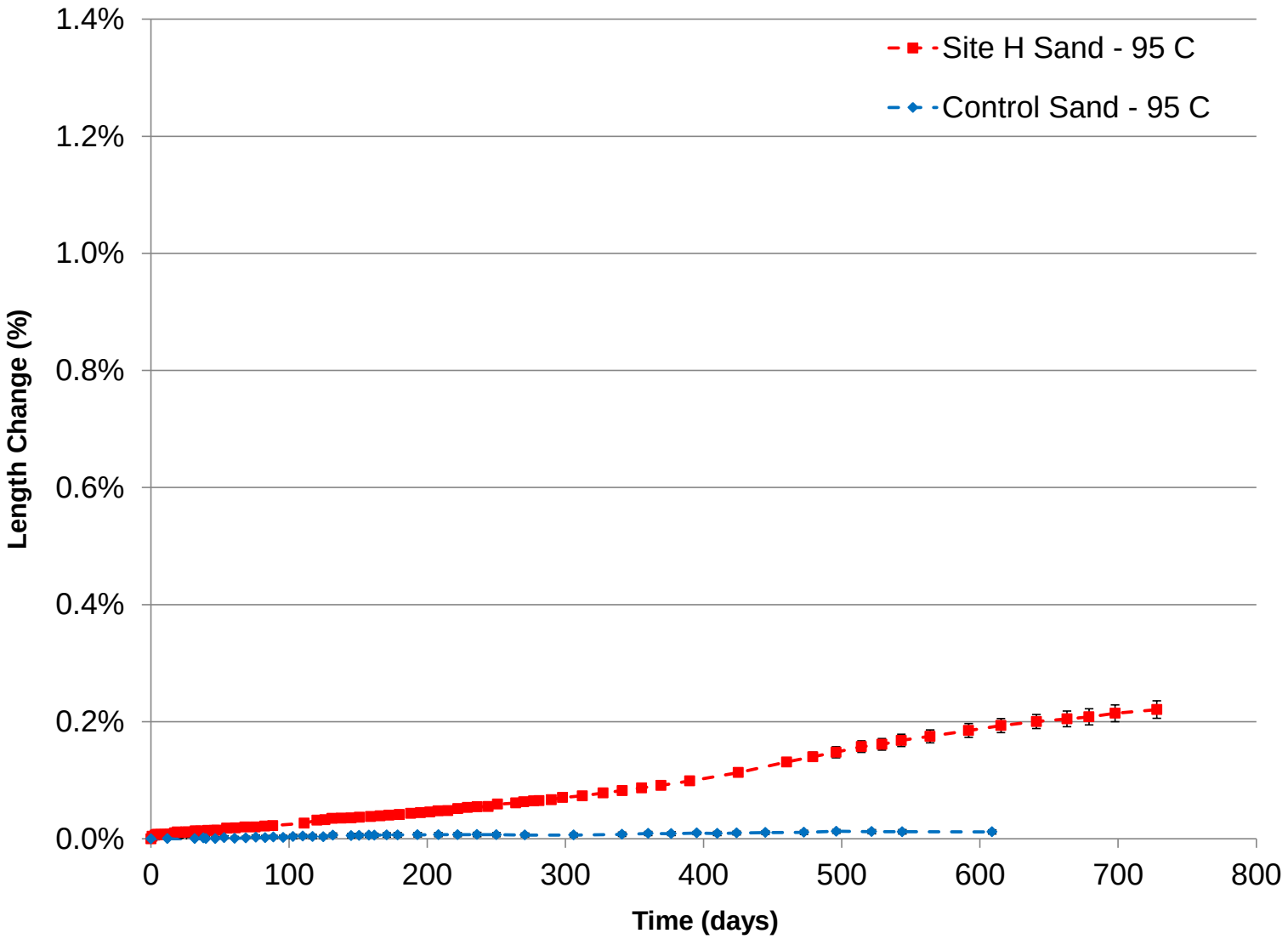

Figure 4.16 Expansion of mortar bars due to DEF (Cement B). Error bars represent standard deviation.

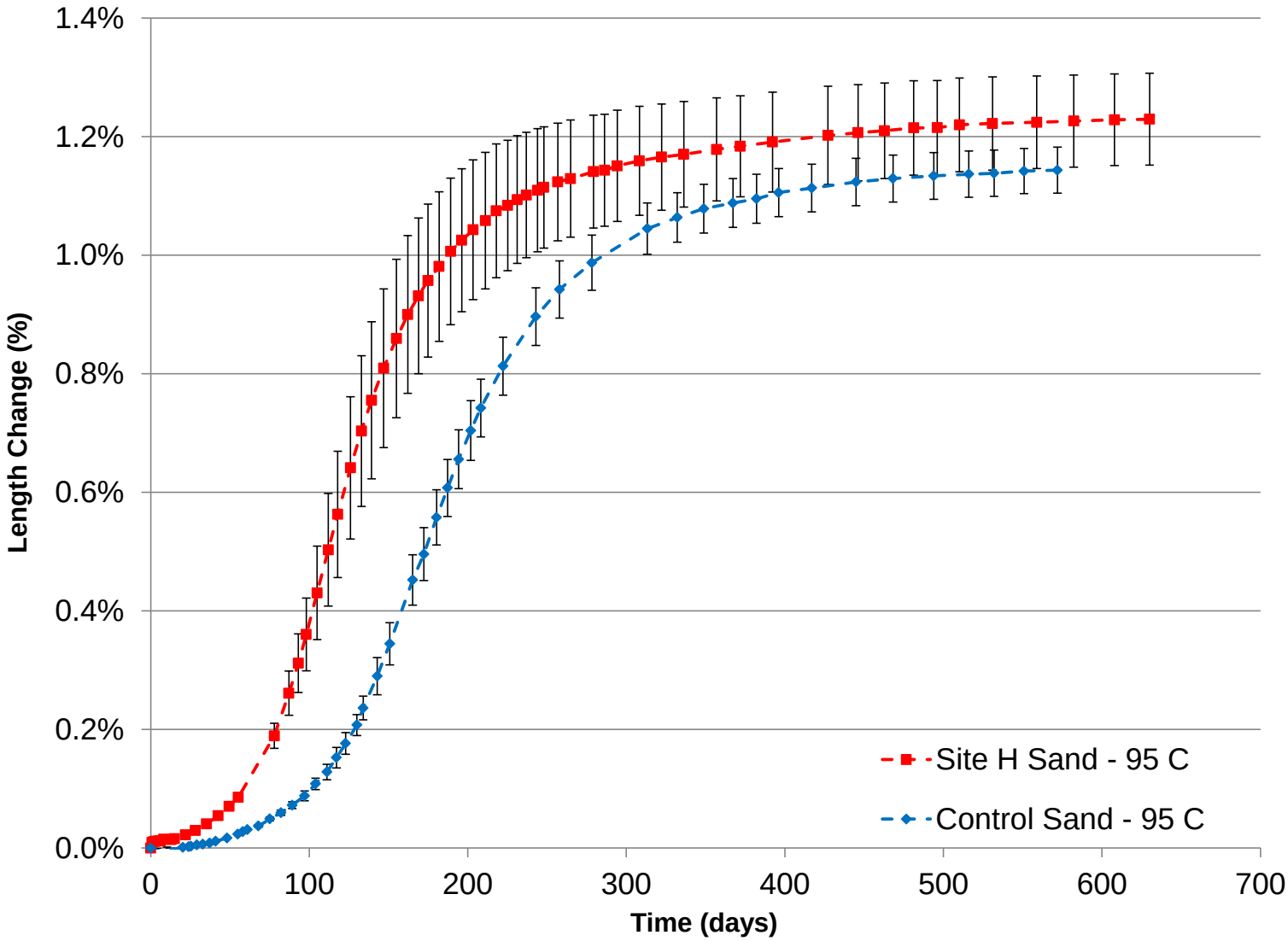

Figure 4.17 Expansion of mortar bars due to DEF (Cement C). Error bars represent standard deviation.

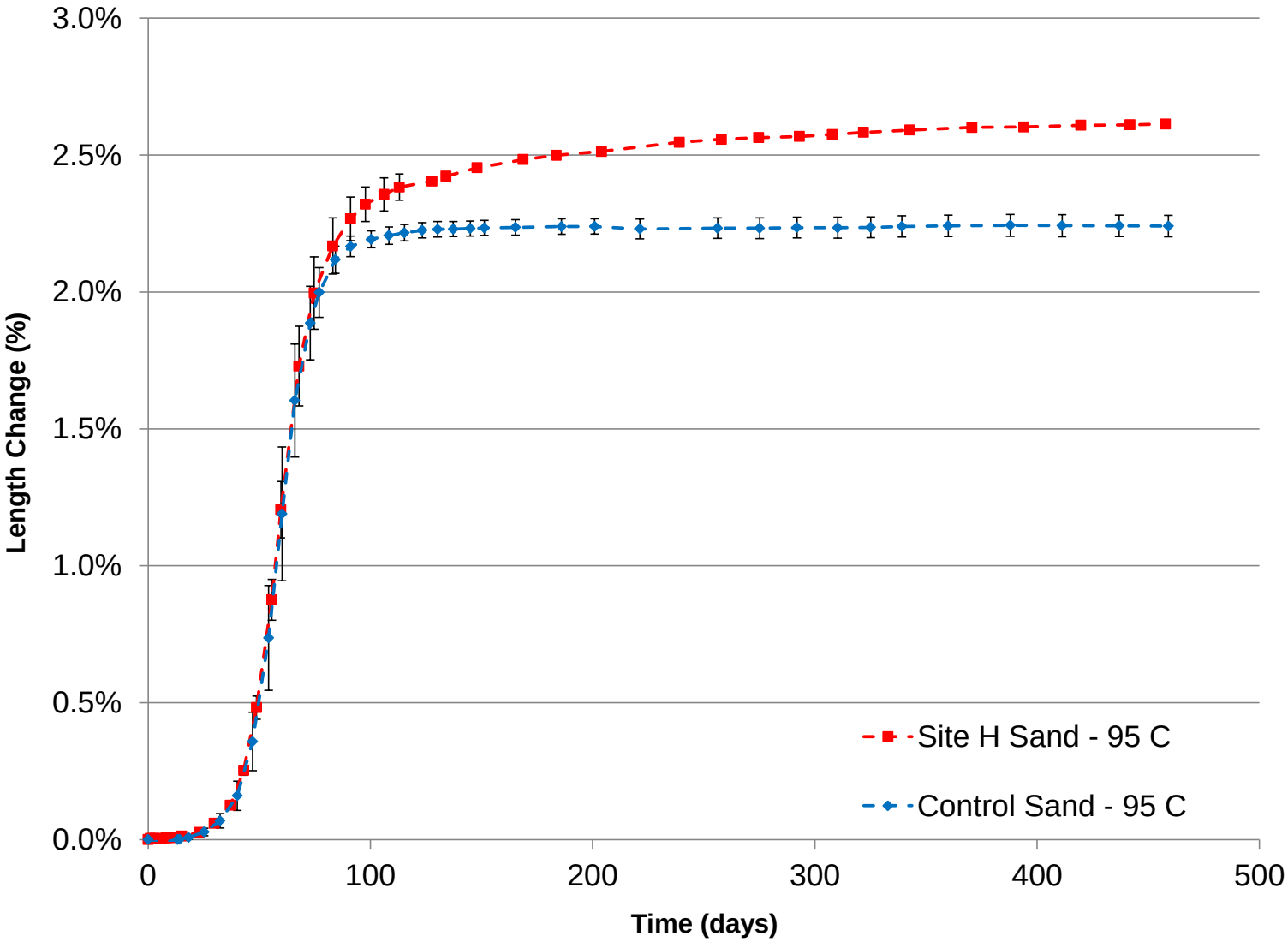

Figure 4.18 Expansion of mortar bars due to DEF (Cement D). Error bars represent standard deviation.

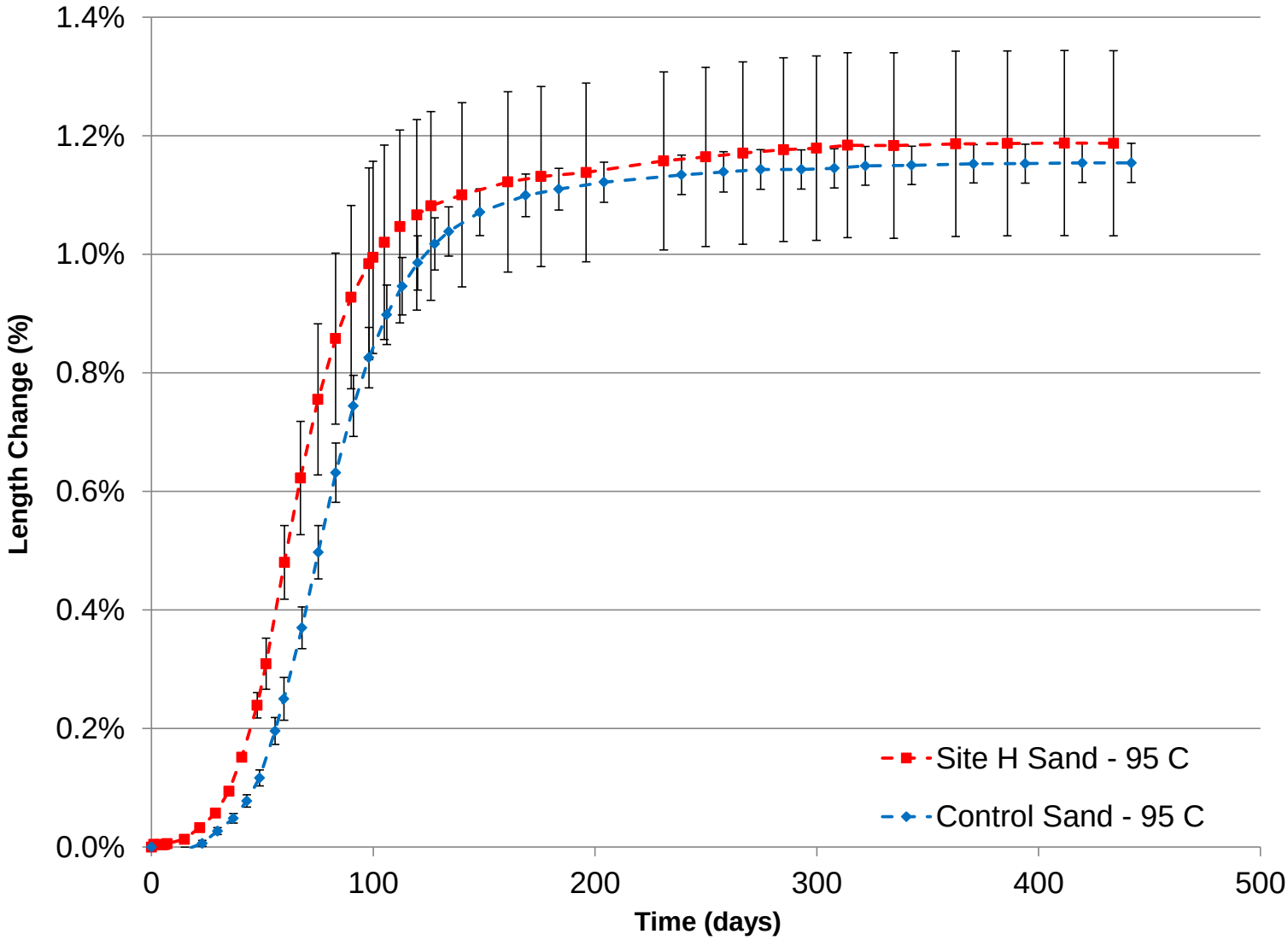

Figure 4.19 Expansion of mortar bars due to DEF (Cement E). Error bars represent standard deviation.

Twenty-four hours after demolding, Control sand samples exposed to the Kelham curing method showed thermal shrinkage strains of 0.004% to 0.010%. In contrast, expansion of 0.004 to 0.011% at 24 hours from demolding was observed for heat-cured mortar bars prepared with Site H sand.

Heat-cured mortar using Cement D (Type III) exhibited the highest expansions; for reference, the value for expansion when mixed with Site H sand reached 26 times higher than the expansion limit of 0.1% used for alkali silica reaction in ASTM C1260 and for sulfate attack in ASTM C1012 experimental evaluation on the same type of bars. In fact, this expansion limit (0.1%) was reached as early as 33 days for mortar using Cement A and Site H sand (Table 4.1).

Table 4.1 Expansion onset ($\varepsilon \geq 0.03\%$) and time of expansion $\geq 0.1\%$ of heat-cured mortar bars.

Cement	Sand	Expansion onset (days)	Expansion at 14 days (%)	Time at $\varepsilon = 0.1\%$ (days)
Cement A (Type I/II)	Control	27	0.004%	46
	Site H	16	0.028%	33
Cement B (Type V)	Control	--------	0.000%	--------
	Site H	120	0.008%	390
Cement C (Type I/II)	Control	61	-0.001%	101
	Site H	28	0.015%	58
Cement D (Type III)	Control	25	0.001%	35
	Site H	23	0.013%	34
Cement E (Type I)	Control	30	-0.005%	46
	Site H	20	0.013%	36

The start of the period of fast expansion does not occur at a clearly defined time. Thus, to avoid an arbitrary definition of this value, expansion onset was considered at the time when expansion results were higher than the maximum expansion observed in mortar cured at room temperature. A strain of 0.03% was selected to identify the initiation of DEF-expansion and linear interpolation was used to estimate the day when this expansion occurred. Values of expansion onset for every mortar mixture are included in Table 4.1 and discussed in Section 4.4.1.1.

As shown in Table 4.1, expansions at 14 days were lower than the expansion limit for ASTM C1038 of 0.02%, except for mortar using Cement A (Type I/II) and Site H sand. Regardless of the cement used, mortar mixtures using Site H sand showed a higher expansion at 14 days compared to the use of Control sand. However, based upon the expansion results shown in Figures 4.15 to 4.19, expansion at 14 days is not a good parameter to identify potentially expansive mixtures or to predict the maximum DEF-expansion.

4.4.1.1 Effect of acidic sand and cement composition on mortar expansion

The impact of Site H sand on DEF-expansion results varied depending on the cement composition. In every case, the use of the acidic sand showed a quantifiable effect.

In the case of Cement D (Type III), expansion started at similar times for mortar using Site H and Control sands (Table 4.1 and Figure 4.18), but the accelerated expansion period ended first for Control sand samples. As a result, maximum expansion in mortar using Site H sand was 16.5% higher than the average maximum expansion of Control

sand samples. The deceleration of the expansion has been commonly attributed to the consumption of sulfate and alumina sources (Tosun and Baradan, 2010), which suggests that the higher availability of sulfate in samples containing Site H sand can maintain the development of the DEF reaction for a longer period.

Mortar containing Cement B (Type V) and Control sand show expansion levels similar to the observed in mortar bars cured at room temperature. At 545 days, average expansion was 0.012%, below maximum limits required for ASTM C1012 and C1038. Type V cement, due its lower content of C_3A, is considered a sulfate-resisting cement. Also, the lower SO_3 content of this cement type favors monosulfate formation over ettringite formation (Taylor et al., 2001). Folliard et al. (2006) performed similar DEF testing using three types of fine aggregate (siliceous and limestone sand, manufacture limestone sand, and mixed quartz/chert sand), Type V cement, and an initial high-temperature curing following the Kelham procedure. After 1,200 days of limewater storage, they measured negligible expansion and very little difference between the samples.

The use of acidic sand in mortar prepared with Cement B produced DEF-expansion. Average expansions of 0.1% and 0.2% were measured at 390 and 641 days, respectively. Mortar bars using Cement B (Type V) and Site H sand exhibited a much slower expansion compared to Cement D samples. The slow expansion of these samples would not be considered deleterious according to reference limits, but expansion onset occurred at 120 days, followed by an increase of the expansion rate. Between days 120 and 485, i.e., a period of 1 year, mortar bars expanded 0.12%. Mortar and concrete

samples cannot undergo this level of tensile strain without cracking (Scherer, 2004a), therefore, some damage is expected as a result of this DEF-expansion.

When Type I or Type I/II cement was used in heat-cured mortar bars (Cements A, C, and E), an earlier expansion onset was observed on Site H sand specimens (Table 4.1). Also, at earlier stages of expansion, higher expansions were measured when the acidic sand was used. This effect of acceleration of the DEF-reaction is more clearly observed when the rate of expansion, derivative of the expansion curves, is plotted on time.

In Figures 4.20 to 4.22, it is observed that the maximum expansion rate is higher and is reached earlier in Site H sand samples compared to Control sand samples. In every case, expansion initiation is followed by higher expansion rates in Site H sand samples.

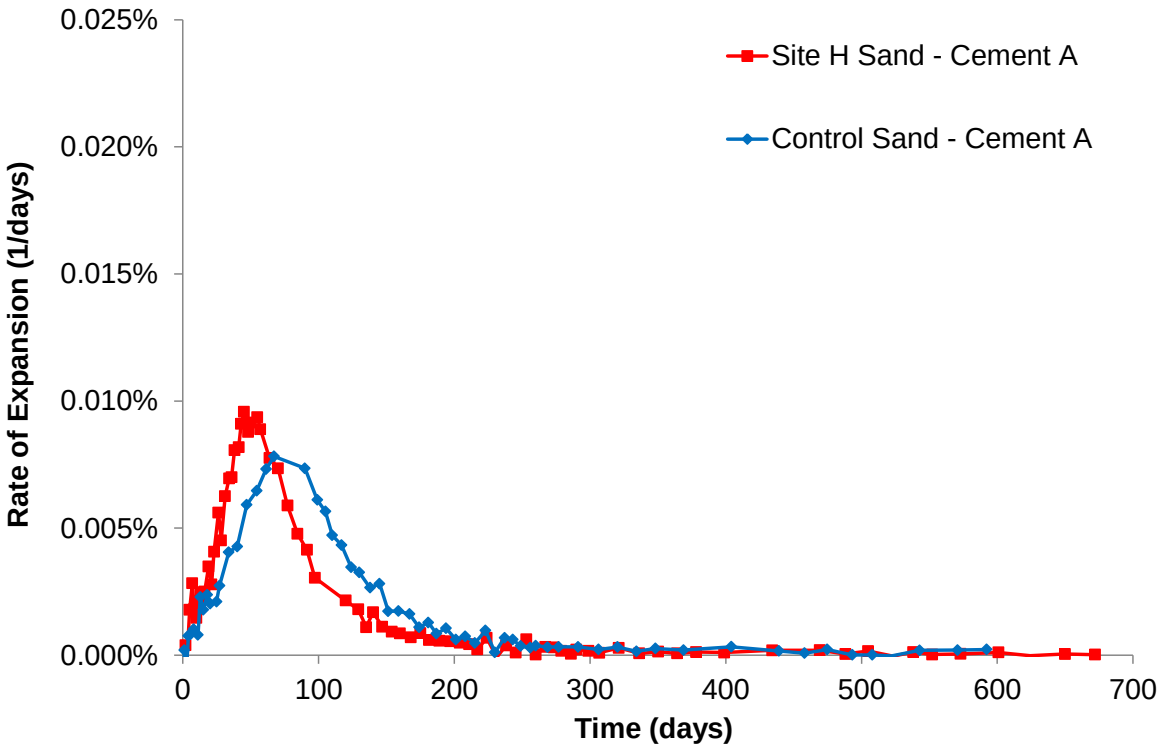

Figure 4.20 Rate of expansion of mortar bars using Cement A (Type I/II).

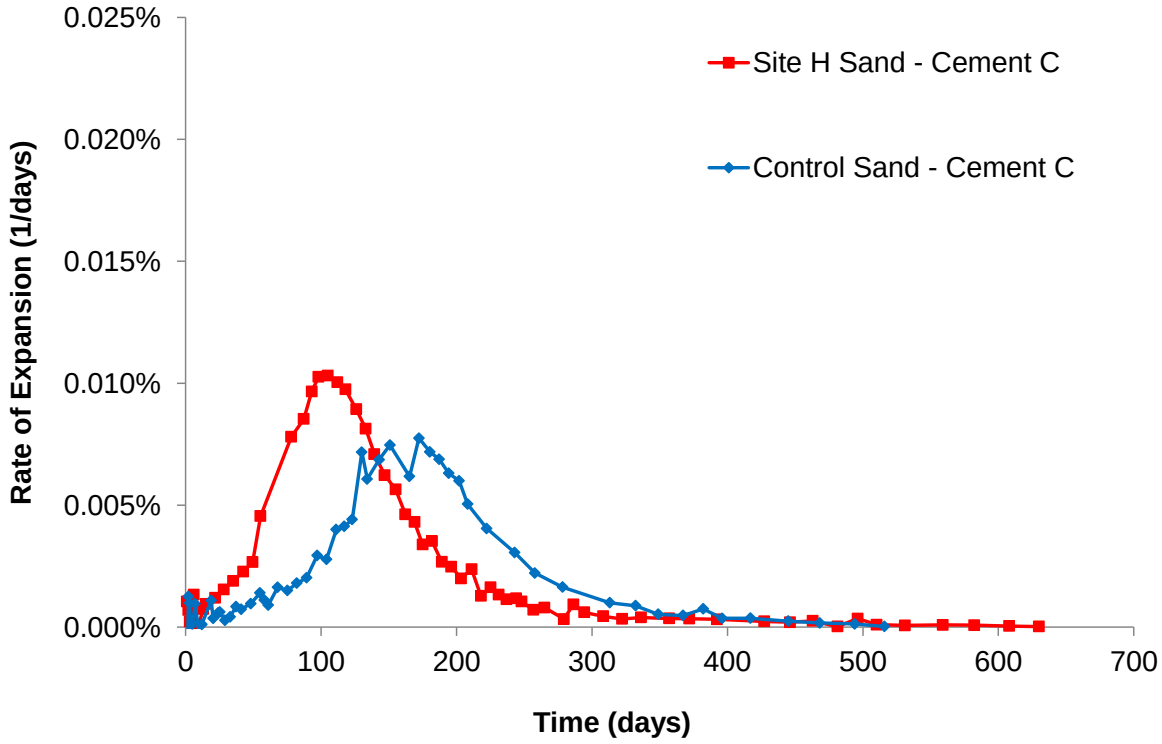

Figure 4.21 Rate of expansion of mortar bars using Cement C (Type I/II).

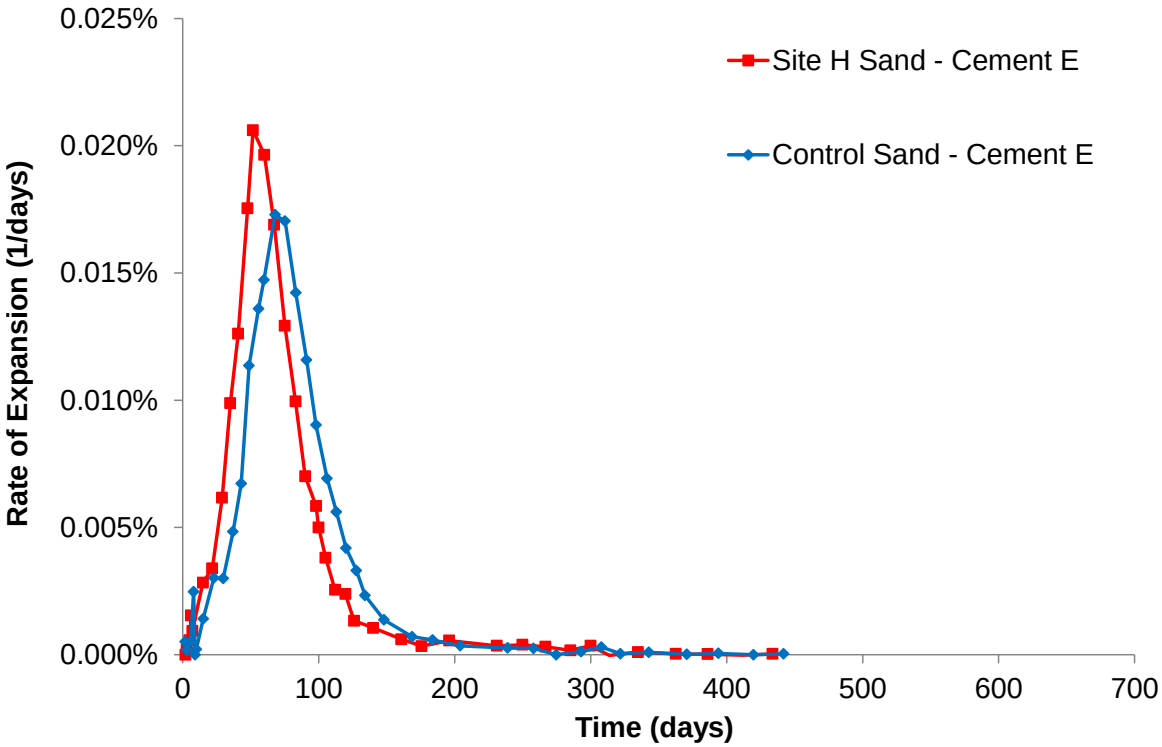

Figure 4.22 Rate of expansion of mortar bars using Cement E (Type I).

During moist storage, sulfate ions desorbed from C-S-H migrates by diffusion and, when in contact to alumina sources, form small ettringite crystals in nanometric pores that can potentially produce expansion. Scherer (2004b) estimated a diffusion coefficient in the order of 10^{-13} m^3/s for sulfate ions migrating from inner C-S-H, which determines a migration rate of about 400 μm in 20 days. The presence of Site H sand provides an additional and more distributed source of sulfate, which can increase the feasibility of ettringite formation and the amount of expansive ettringite formed.

4.4.1.2 Parametric function of DEF-expansion

Expansion curves of heat-treated mortar bars resemble a sigmoid function ('S'-shaped curve). Larive (1997) developed a kinetics parametric function for an isothermal stress-free expansion test, shown in Equation 4.1. Even though this function was developed for an alkali aggregate reaction, Equation 4.1 can be used to model DEF-expansion curves shown in Figures 4.20 to 4.22.

$$\varepsilon(t) = \varepsilon(\infty)\frac{1-\exp\left(-t/\tau_c\right)}{1+\exp\left(-t/\tau_c + \tau_L/\tau_c\right)} \tag{4.1}$$

where $\varepsilon(\infty)$ is the maximum expansion, $\varepsilon(t)$ is the expansion at time t, τ_c is the characteristic time parameter, in days, and τ_L is the latency time parameter, in days.

Latency time, τ_L, represents the time to the inflection point of the curve and, therefore, a lower τ_L indicates an earlier development of the reaction. Characteristic time, τ_c, is related to the time from the inflection point of the curve to the period of maximum expansion and a lower τ_c indicates a faster reaction after the point of maximum expansion

rate. Parameters τ_L and τ_c depend on the temperature at which the test is carried out but, since heat-cured mortars were exposed to the same temperature history, time parameters are assumed constant for each mortar mixture and they can be compared in mortars using different cements. If a different curing temperature is used, τ_L and τ_c are expected to change.

Parameters τ_L and τ_c were calculated for heat-cured mortars using Type I or Type I/II cement using a least-square fit of the parametric function in Equation 4.1. $\varepsilon(\infty)$ was assumed to be the highest experimental expansion, while parameters τ_L and τ_c were the ones that minimized the sum of squares of the difference between calculated and experimental $\varepsilon(t)$. Calculated values of τ_L and τ_c are given in Table 4.2.

Table 4.2 Values for τ_L and τ_c for mortar mixtures using Type I or Type I/II cements.

Cement	Sand	τ_L (days)	τ_c (days)
Cement A (Type I/II)	Control	90.0	34.9
	Site H	64.9	30.6
Cement C (Type I/II)	Control	181.3	38.3
	Site H	122.4	36.6
Cement E (Type I)	Control	81.9	18.7
	Site H	67.6	18.9

While τ_c values are similar for mortars using Control and Site H sand, τ_L indicates an earlier development of the DEF reaction when Site H sand is used in mortar using Type I/II or Type I cement.

4.4.2 Microstructure Evaluation of Heat-Cured Mortar Bars

4.4.2.1 Powder XRD

XRD microanalysis was performed to identify differences on the crystalline phases after DEF-expansion. Samples of heat-cured mortar at late stages of expansion were crushed in a porcelain mortar and passed through a No. 100 sieve (150 µm [5.9×10^{-3}-in.]). Then, powdered material was ground on a Retsch PM 100 planetary ball for two series of 3 minutes. Material passing a No. 200 sieve (75 µm [2.95×10^{-3}-in.]) was used for XRD analysis, in order to minimize the intensity of peaks corresponding to quartz. Samples were scanned in the 5-70° range, with a scan step size of 0.0167°, and at 40 mA and 45 kV. XRD patterns of the analyzed mortars are shown in Figure 4.23.

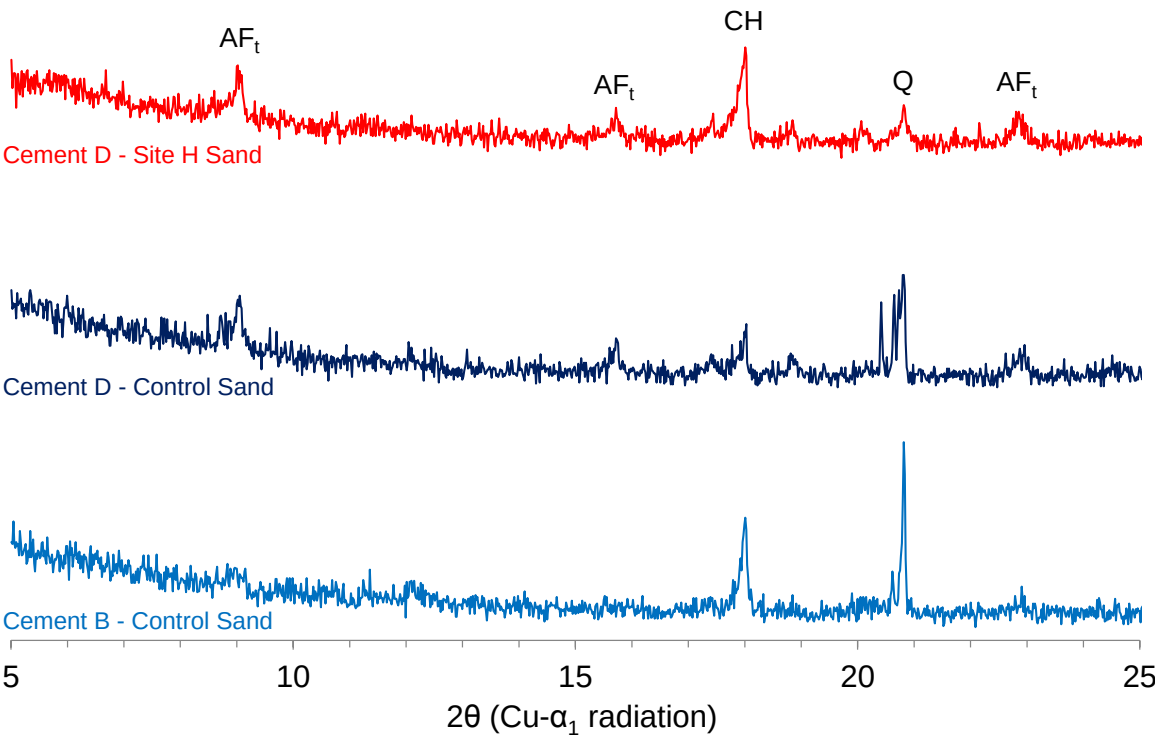

Figure 4.23 XRD patterns of heat-cured mortar bars. Q: quartz, CH: calcium hydroxide, AF_t: ettringite.

XRD patterns of mortar samples using Cement D and Control sand (obtained at 452 days from casting), Cement D and Site H sand (434 days), and Cement B and Control sand (536 days) are shown only in the range 5-25° to highlight the peaks corresponding to hydration products of cement. Of particular interest is the relative amount of ettringite among the samples.

In Figure 4.23, it is observed that mortar samples including Cement D (Type III) show a higher amount of crystalline ettringite detected compared to mortar using Cement B (Type V), however no appreciable differences are observed between intensity peaks of Site H and Control sand samples. As mentioned by Flatt and Scherer (2008), ettringite forming in small pores and likely responsible of DEF-expansion is virtually undetected by XRD and SEM-EDS analyses. Thus, ettringite peaks in the XRD patterns in Figure 4.23 probably correspond to secondary ettringite. The higher amount of secondary ettringite in mortar using Type III cement is not a surprising finding, given the higher amount of alumina and sulfate in this cement compared to Type V cement.

4.4.2.2 VP-SEM and EDS microanalysis

In order to identify the condition of mortar undergoing high expansion, VP-SEM was performed on samples from mortar bars cured at high temperature and prepared using Cement A (Type I/II), B (Type V), and D (Type III), and Control and Site H sand. Figures 4.24 to 4.28 summarize the features found in DEF-affected mortar and a selection of micrographs for every mortar mixture is given in Appendix E. EDS microanalysis was used for phase identification.

Micrographs of heat-cured mortar bars at later ages of expansion showed damage commonly attributed to DEF, except for samples of mortar bars containing Cement B (Type V) and Control sand that did not exhibited significant cracking. Only common features found on every DEF-affected samples were presence of gaps between some aggregates and cement paste, partial filling of these gaps with ettringite, and formation of secondary ettringite on air voids. Higher damage was observed on samples with higher expansion; particularly, mortar bars using Cement A (Type I/II) and D (Type III) exhibited more extensive microcracking and damage.

Figure 4.24 shows the typical crack pattern caused by DEF reaction, where some aggregates are partially surrounded by ettringite rims, approximately 5 to 15 μm (1.97×10^{-4} to 5.91×10^{-4}-in.) thick. Some cracks, probably originated from aggregate gaps, extend through the paste and connect with cracks formed in similarly damaged aggregate particles. Aggregate gaps formation and ettringite filling apparently is a non-uniform process, given their preferential occurrence only on some directions and aggregate surface regions.

Figure 4.25 shows an air void completely filled with secondary ettringite, in mortar containing Cement D (Type III) and Site H sand. Ettringite forming in voids was also observed in mortar using Cement A (Type I/II) and B (Type V), but in lower amounts, which suggests that the amount of secondary ettringite formed depends on the amount of reactants (i.e., calcium, alumina, and sulfate) present in mortar.

Other feature associated with DEF, but present only in most damaged samples, was the formation of nests of ettringite within the paste or at short distance from a ITZ, as shown in Appendix E.

Mortar samples including Site H sand evidenced a higher compositional variation of the aggregate compared to Control sand, as shown in Section 3.2.1.4, where an important presence of alkali feldspar minerals, mainly potassium feldspar, were found forming aggregate particles or combined with silica-based aggregates (Figure 4.26). Additionally, several impurities were observed within Site H sand particles, including zirconium, iron, sulfur, phosphorous, and titanium. Some small particles, with diameters 50 to 150 μm (1.97×10^{-3} to 5.91×10^{-3}-in.) and likely corresponding to zircon ($ZrSiO_4$) and ilmenite ($FeTiO_3$), were also found within the cement paste or inside aggregate particles, as shown in Figure 4.27b. Ettringite rims also formed around some these particles when they were surrounded by cement paste.

Ilmenite aggregate has been used in heavyweight concrete for radiation shielding (Makarious et al., 1996; Sakr and El-Hakim, 2005), given its high specific gravity (~4.2). Also, the use of zircon powder has been explored for the production of ultra-high-performance concrete (Wille and Naaman, 2013). No adverse chemical reaction has been reported on the use of these aggregates in concrete.

In some cases, aggregates fell out during the cutting process, probably due to the weak interface as a consequence of the formation of an ettringite rim. The exposed layer of ettringite exhibited a denser arrangement of ettringite crystals compared to crystals precipitating in air voids, as shown in Figure 4.28.

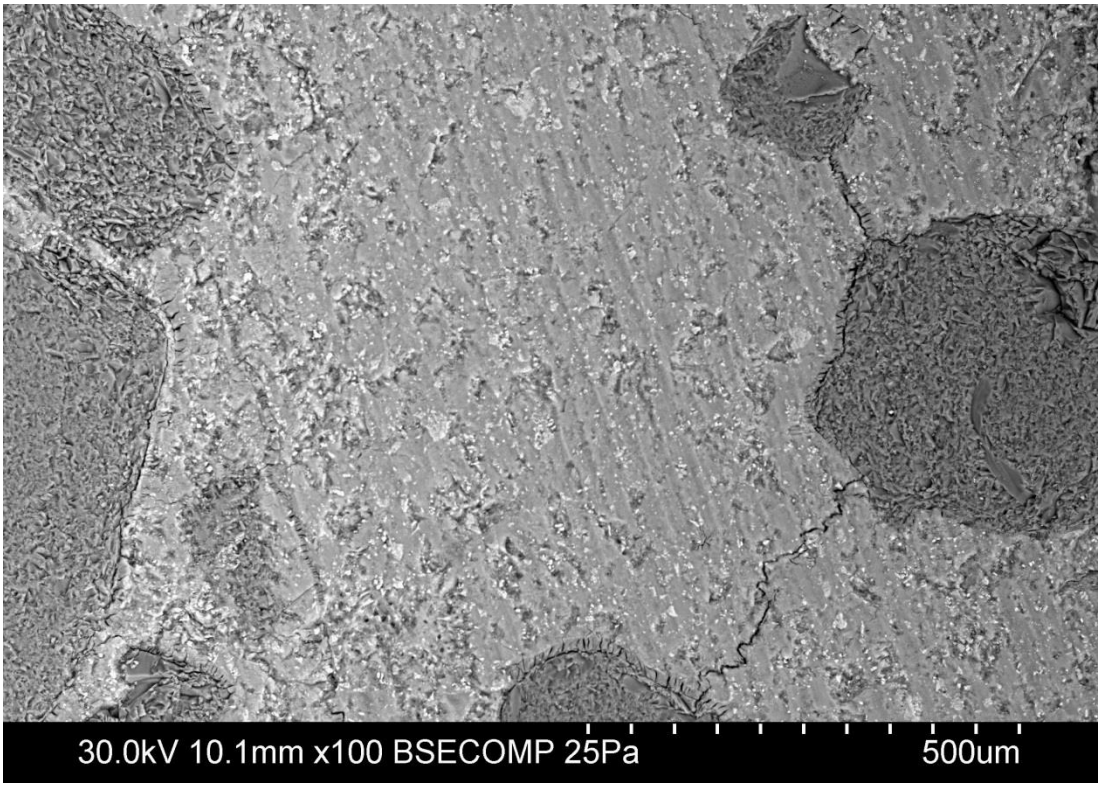

(a)

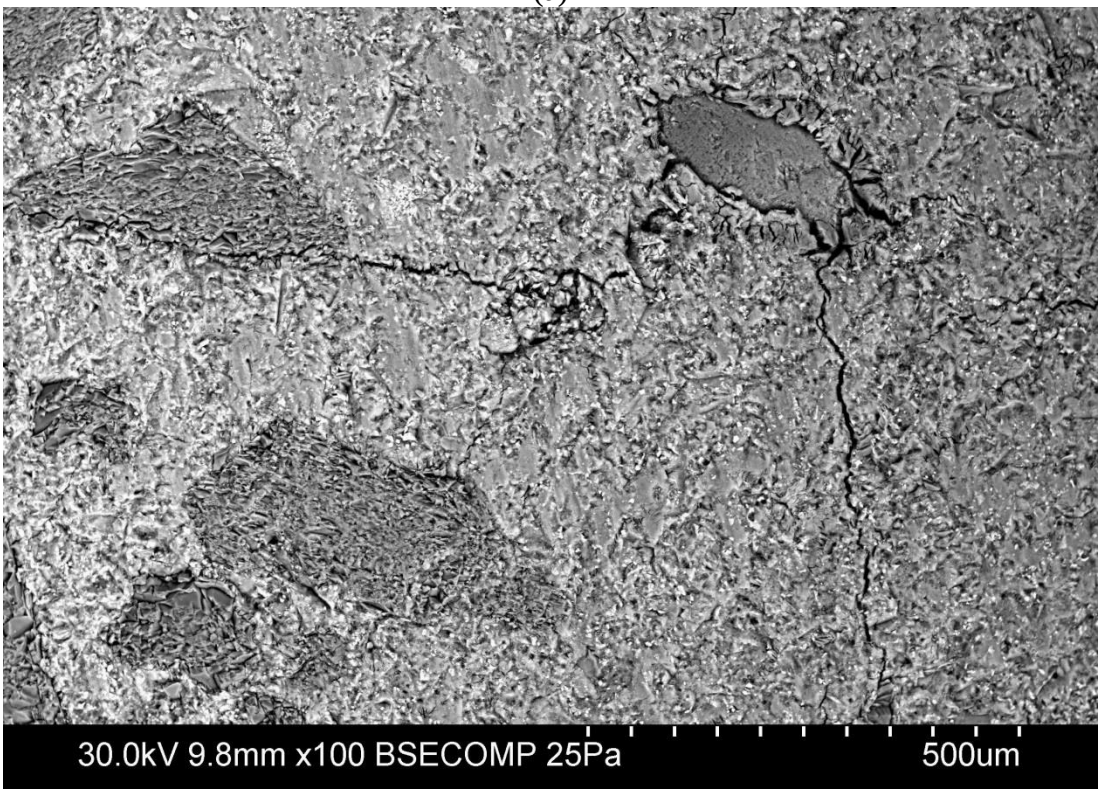

(b)

Figure 4.24 Cracking and ettringite formation associated to DEF in mortar using Site H sand and Cement D.

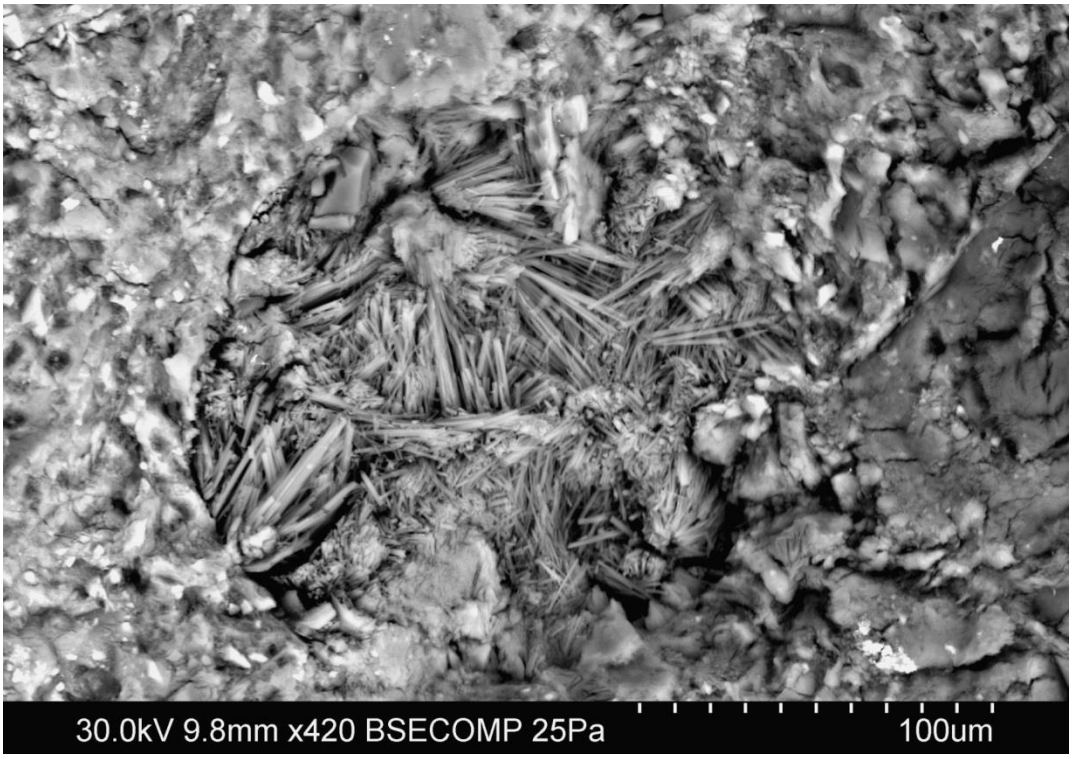

Figure 4.25 Ettringite filling a void of mortar using Site H sand and Cement D.

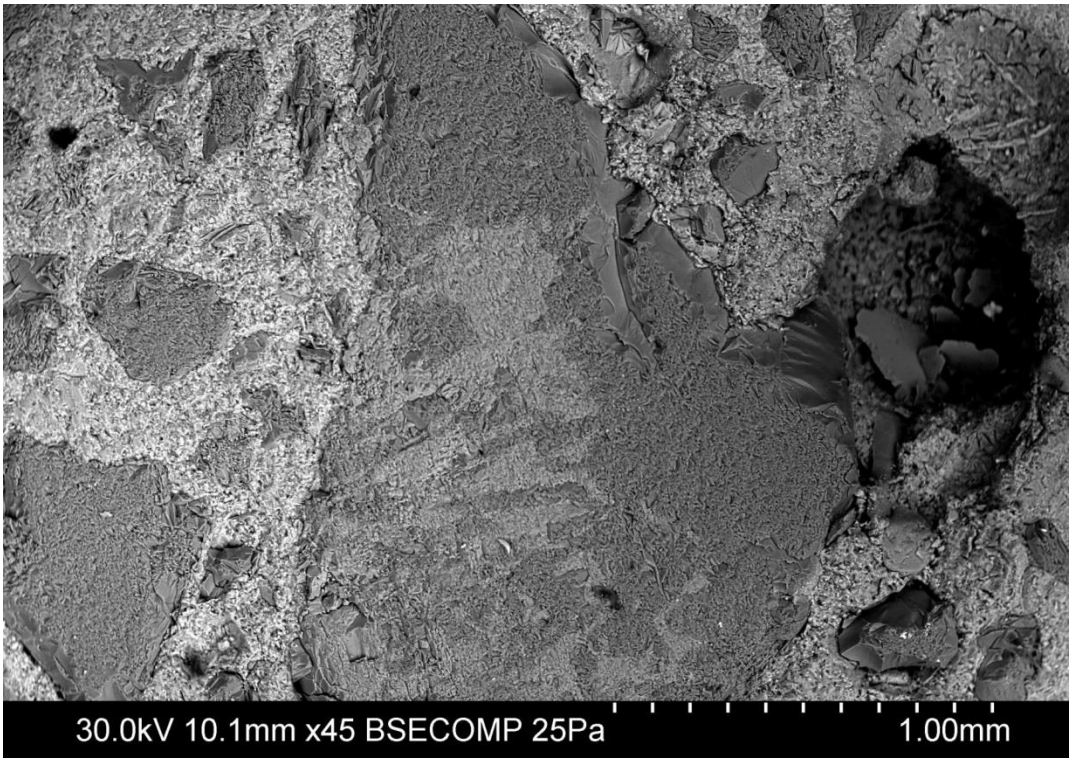

Figure 4.26 Aggregate with variable composition. Darker regions: quartz, brighter regions: potassium feldspar.

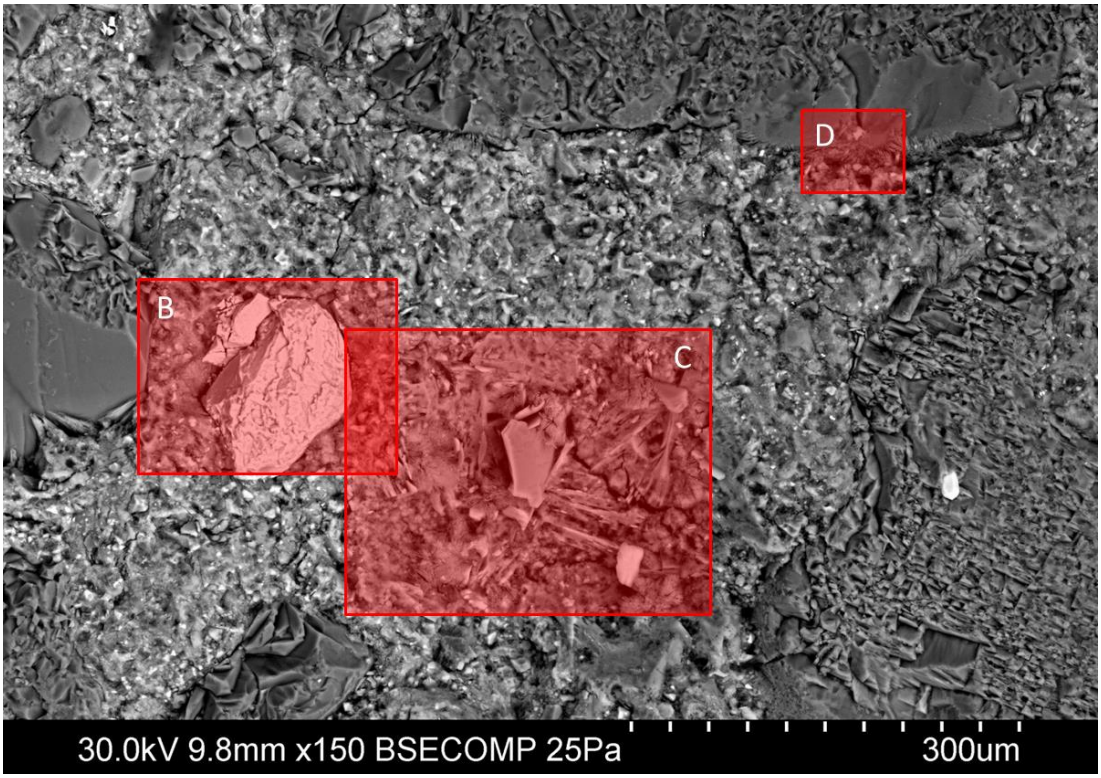

(a)

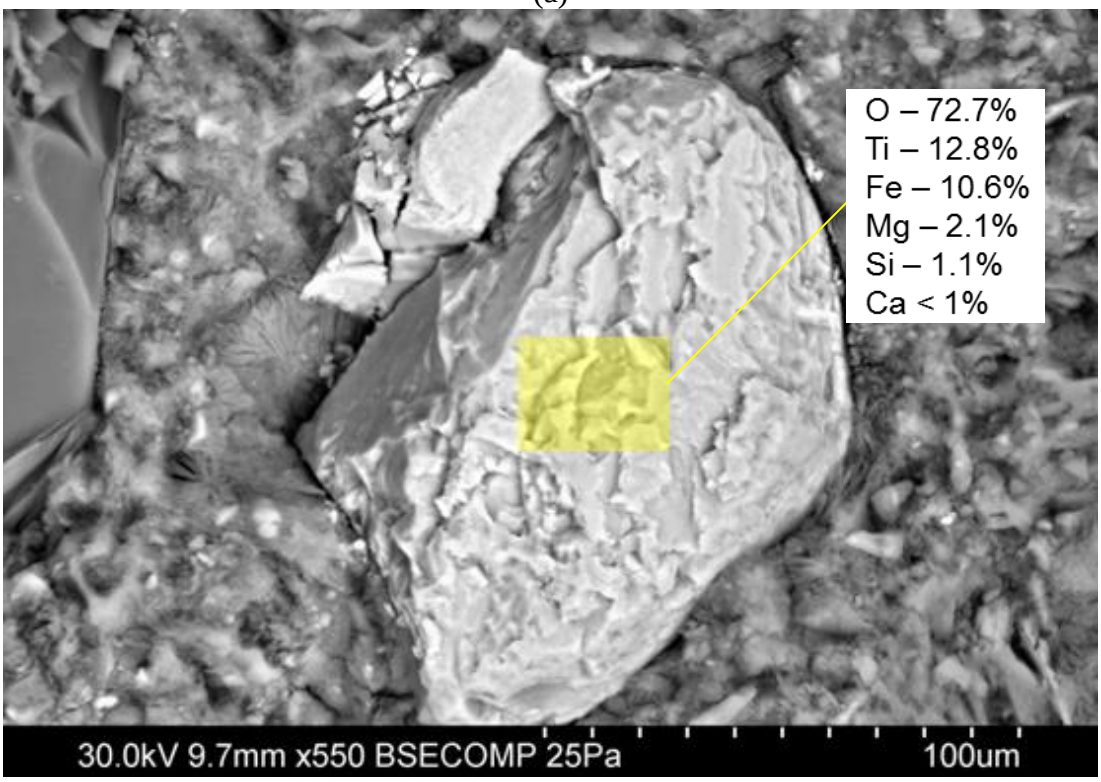

(b)

Figure 4.27 (a) VP-SEM micrograph of mortar using Site H sand and Cement D, (b) ilmenite-bearing aggregate, (c) presence of ettringite and calcium hydroxide within cement paste, and (d) ettringite rim around aggregate.

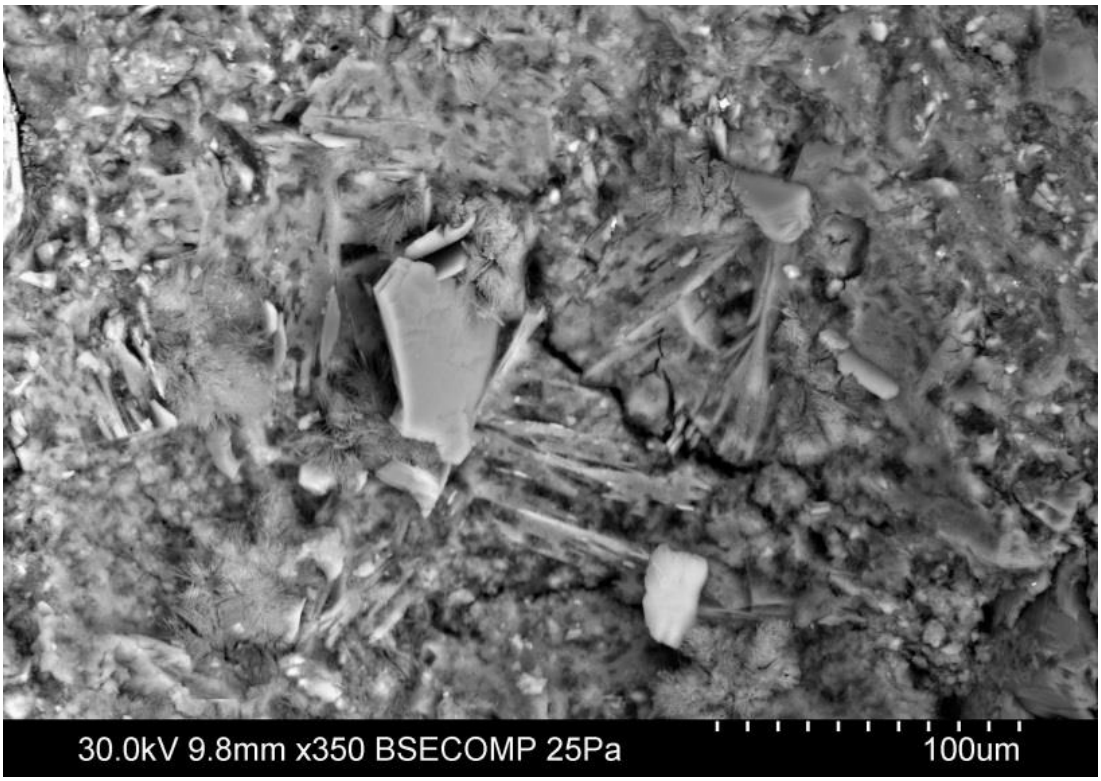

(c)

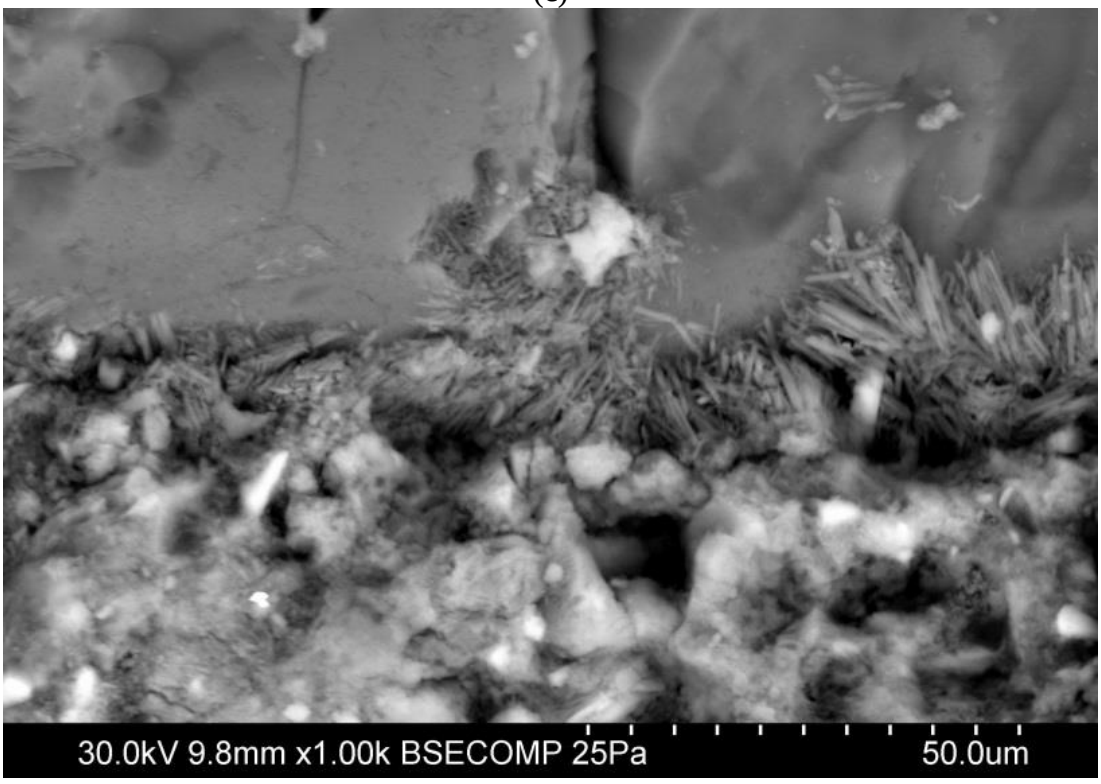

(d)

Figure 4.27 (cont.) (a) VP-SEM micrograph of mortar using Site H sand and Cement D, (b) ilmenite-bearing aggregate, (c) presence of ettringite and calcium hydroxide within cement paste, and (d) ettringite rim around aggregate.

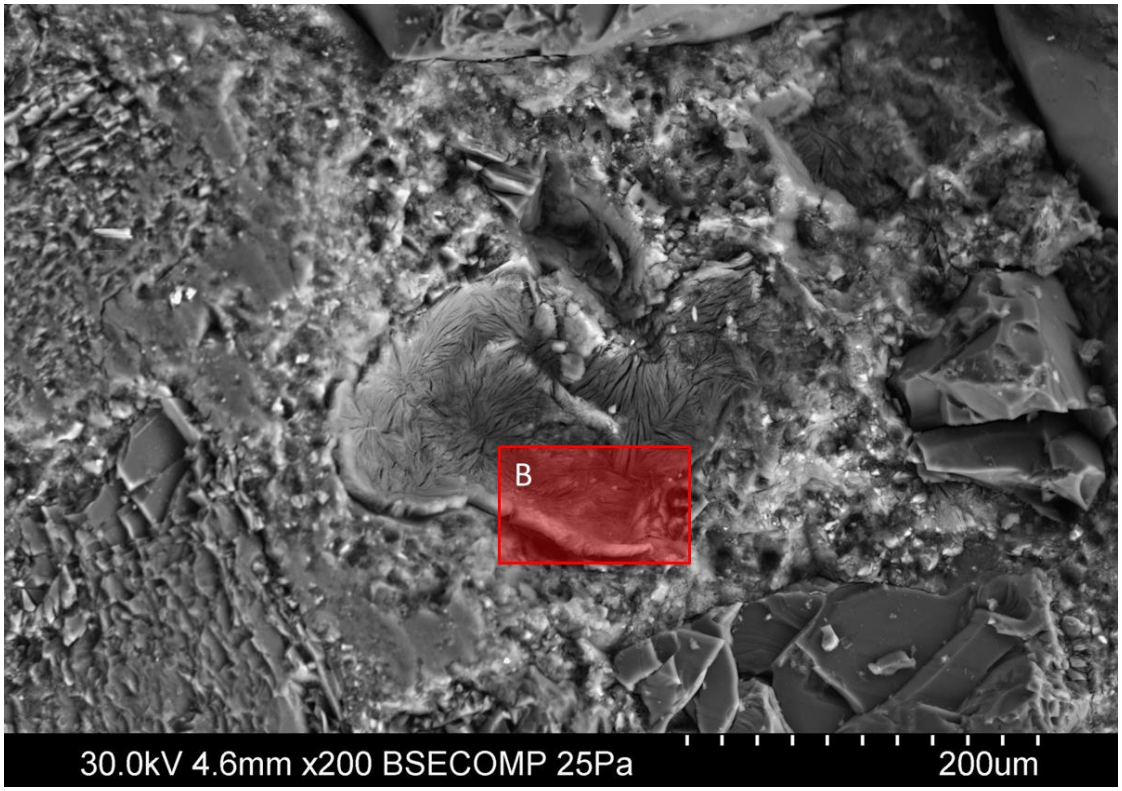

(a)

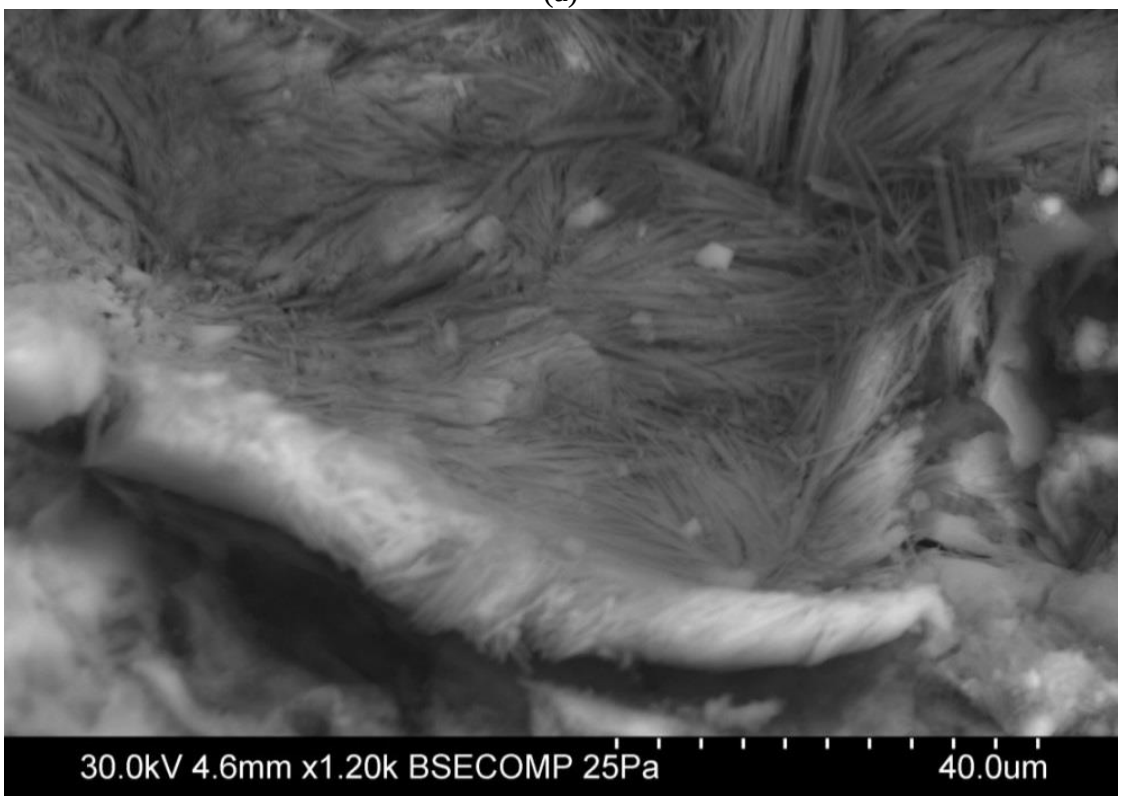

(b)

Figure 4.28 (a) VP-SEM micrograph of ettringite rim and (b) dense ettringite.

4.4.2.3 Alkali release from acidic sands

As shown in Section 3.2.1.4, acidic sands investigated in this research present a high fraction of particles completely or partially formed by alkali feldspar, mainly potassium feldspar. The presence of alkali feldspar in the acidic sands can also impact the development of the DEF-reaction.

Figure 4.29 shows a colored image following a μXRF-scanning elemental analysis performed by Dr. Tyler Ley at Oklahoma State University. A 2.54×2.54 cm (1×1-in.) polished, transverse section of a heat-cured mortar bar containing Site H sand and Cement B (Type V) was scanned using an Orbis μXRF (40 kV, 1mA, and scan acquisition time of 300 ms). It is observed in Figure 4.29 that Site H sand is composed by particles rich in Al and K and siliceous particles, in similar proportion, and that potassium feldspar is preferentially present in small aggregate particles (< ~1 mm [3.94×10^{-2}-in.]).

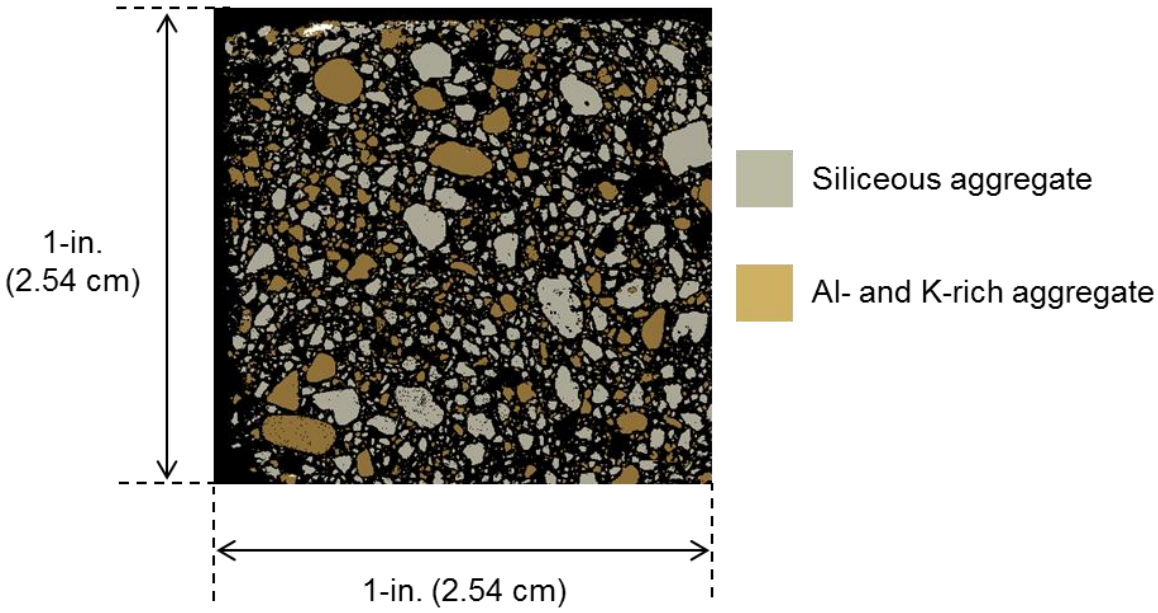

Figure 4.29 XRF elemental image of bar section from heat-cured mortar using Site H sand and Cement B (Type V). Sample preparation and scanning was performed by Dr. Tyler Ley's research group at Oklahoma State University.

Feldspar-bearing rocks can react with calcium hydroxide in saturated solutions, releasing alkalies as a result, reaction which is significantly accelerated at high temperatures (van Aardt and Visser, 1977a; 1977b). Measurements of leached alkalies from basalt aggregates to the pore solution of hardened concrete performed by Goguel (1995) ranged from 0.1% to 1.0% Na_2O_e, depending on the composition of the aggregate. In the case of aggregates more commonly used in concrete (e.g., granite), Bérubé et al. (2002) measured alkali release between 0.1 to 12.7 kg/m^3 Na_2O_e, with an average of 2.2 kg/m^3 Na_2O_e, after 1.5 years of storage in a 0.7M alkaline solution, at 38 °C (100 °F).

Additionally, significant alkali release has been measured from feldspar minerals in mortar stored at 38 °C (100 °F). In this case, sodium and potassium are released indistinctly into the pore solution in a process that extends for months at an approximately constant release rate. Alkali release in field concrete would be slower, but decomposition of feldspar minerals in aggregates would extend for longer periods (Constantiner and Diamond, 2003). Based on the kinetics of the reaction and the change of composition of feldspar-rich aggregates in mortar, the mechanism of alkali release would correspond to ion exchange between alkali ions in the aggregates and Ca^{2+} ions in the pore solution (Yujiang et al., 2008). Potassium feldspar and sodium plagioclase appear to be the most susceptible minerals for alkali release, due to the weak bonding of Na^+ and K^+ in an oxide or silicate matrix that allows ion removal by dissolution in aqueous solution or cation exchange (Broekmans, 2012).

Even though alkali release in cement-based materials have been studied as a phenomenon that can trigger ASR in otherwise innocuous mixtures, the higher concentration of alkali in pore solution can also influence DEF.

Analysis of the pore solution composition by Ramlochan et al. (2004) showed that the source of sulfate for the formation of expansive ettringite is not the pore fluid, but the adsorbed sulfate by C-S-H during the heat curing period. At early ages, the sulfate concentration in the pore fluid depends on the alkali concentration and temperature. A higher temperature and alkalinity of the pore solution will keep a higher concentration of sulfate during the heat cure and, therefore, will increase the amount of adsorbed sulfate by C-S-H. Later, during the storage period, alkali leaching will be equilibrated by desorption of sulfate from C-S-H. Even the release of only a fraction of the alkali present in feldspar minerals, before or during the high-temperature curing, can increase or accelerate the expansion from DEF.

Additionally, high sulfate and alkali content increase the rate of C_3S hydration at early-ages, which may decrease the porosity and connectivity of the cement paste at the end of the heat curing period. As mentioned by Taylor et al. (2001), a given amount of ettringite will produce higher expansion in small and poorly connected pores.

Figure 4.30b shows the EDS element map of a region of heat-cured mortar using Cement A (Type I/II) and Site H sand, at 674 days from casting. Along with a higher concentration of sulfate at the interfacial transition zone (ITZ) due to the formation of ettringite rims around the aggregates, it can be observed that the portion of the aggregate containing alkali feldspar (Al-rich region) exhibits a higher concentration of potassium close to the edge of the aggregate. This higher concentration suggests that alkali release may have occurred in mortar.

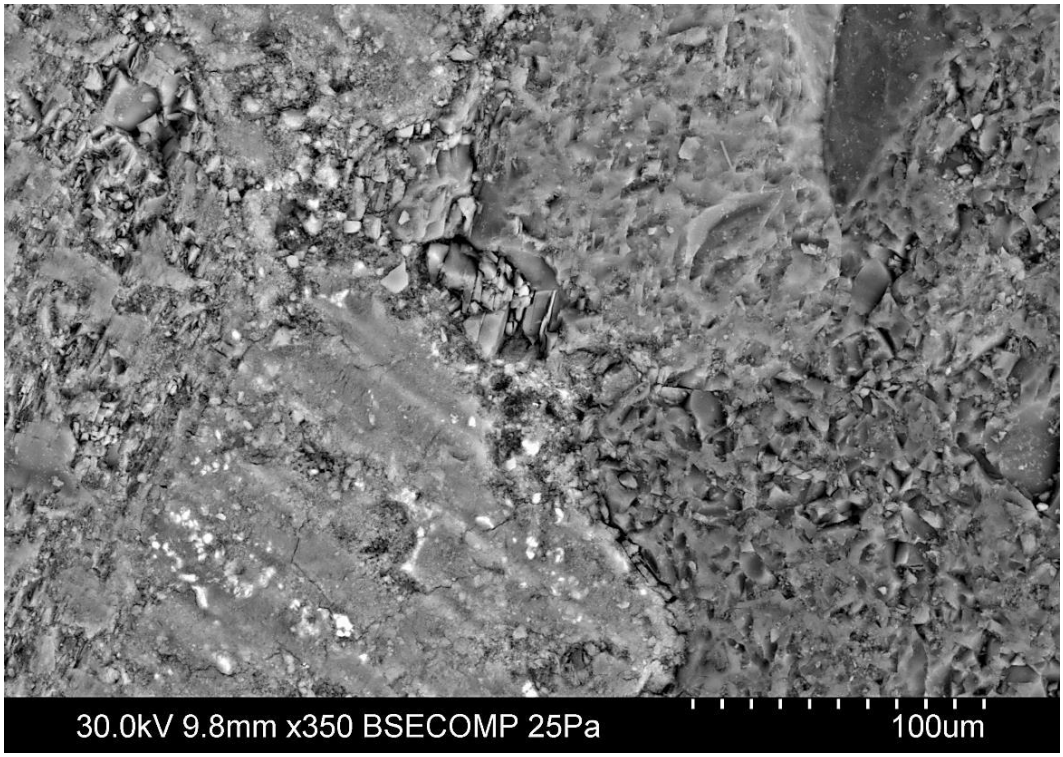

(a)

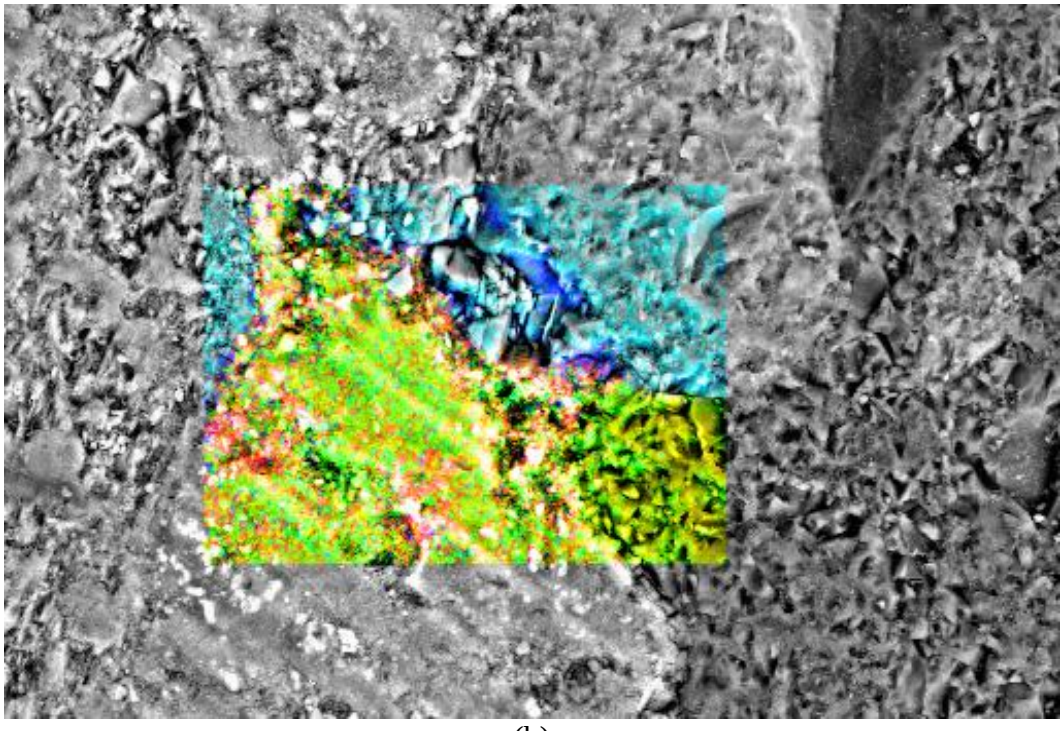

(b)

Figure 4.30 (a) Original VP-SEM micrograph and (b) X-ray element map of mortar using Cement A and Site H sand. Green: Si (16.1%), yellow: Ca (9.9%), light blue: Al (2.3%), blue: K (1.8%), and orange: S (0.4%).

4.4.3 Compressive Strength of Heat-Cured Mortar Cubes

In addition to DEF-expansion measured in mortar bars, 2-in. (5.1 cm) mortar cubes prepared from the same batches were exposed to the same conditions and kept in separate limewater containers. DEF-expansion produces increase of microcracking and sometimes gaps in the paste-aggregate interphase. Consequently, samples affected by significant expansion can show deterioration of the compressive strength.

4.4.3.1 Compressive strength of heat-cured mortar cubes

The compressive strength was evaluated at 28 and 100 days from mixing in order to evaluate the effect of the initial curing temperature, the type of sand used in mortar, and the DEF reaction. Compressive strength results of heat-cured mortars are given in Figure 4.31, where error bars show the standard deviation of results.

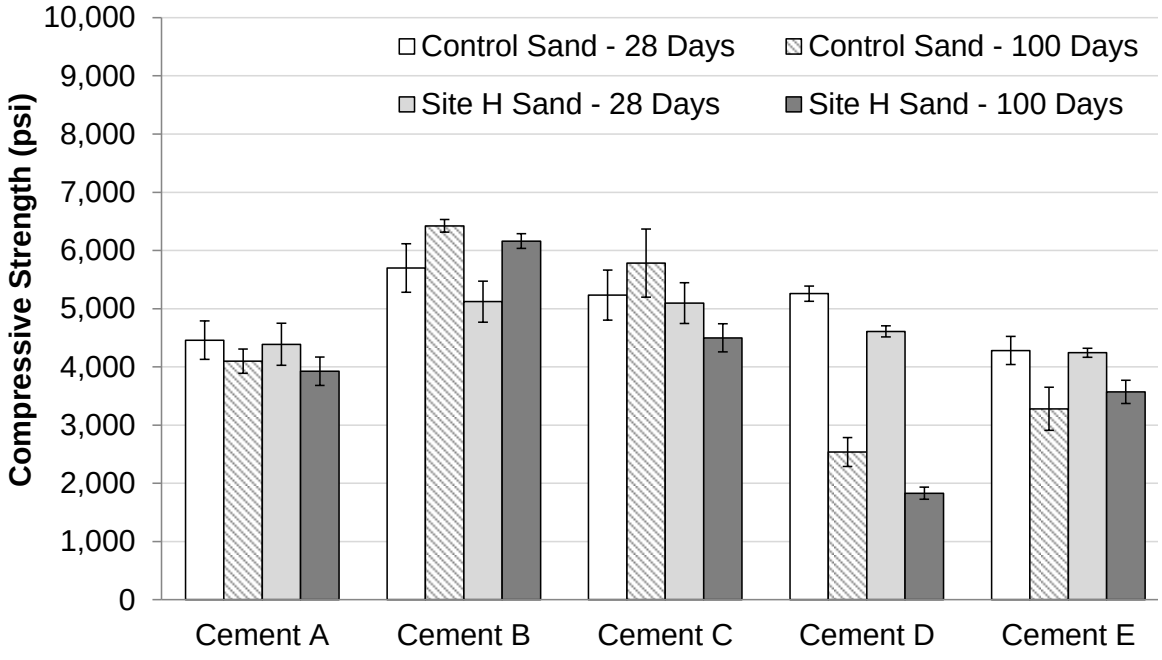

Figure 4.31 Compressive strength of heat-cured mortar cubes, at 28 and 100 days. (1,000 psi = 6.9 MPa)

Compressive strength results of heat-cured mortar show that mixtures undergoing DEF-expansion exhibit lower strengths at 100 days compared to 28 days. This effect is more evident in mortar using Cement D (Type III), where DEF-expansion was negligible at 28 days and higher than 2.0% at 100 days for both types of sand. While mortars using Cement D and cured at room temperature showed small variations between strengths at 28 and 100 days, the same mixtures cured at high-temperature exhibited a decrease of 52% and 60% of the compressive strength at 100 days compared to 28 days strength, for Control and Site H sand samples, respectively.

Mortars using Type I or Type I/II cement show a decrease of compressive strength at 100 days that can be associated to the magnitude of DEF-expansion at testing. For Cement E (Type I), a decrease of strength of 23% and 16% was measured at 100 days for Control and Site H sand samples, respectively, when expansions were 77% and 86% of the maximum expansion for the same type of sand. In the case of Cement A (Type I/II) mortars, which expansions at 100 days were 55% and 72% of the maximum for Control and Site H sand, respectively, lower differences were observed between strength at 28 and 100 days (11% and 8% for Control and Site H sand, respectively).

The impact of DEF-expansion on strength was even clearer in the case of Cement C (Type I/II) mortars, where an increase of the compressive strength at 100 days was measured on Control sand specimens. This mortar mixture exhibited a expansion of 0.088% at 100 days, which apparently did not produce considerable damage in mortar specimens and that support the use of a 0.1% expansion limit. In Site H sand samples using the same cement, DEF-expansion at 100 days of 0.40%, 33% of the maximum, and a decrease of the average compressive strength of 12% were measured.

In heat-cured mortars using Cement B (Type V), minor expansions were measured at 28 and 100 days. Consequently, average compressive strength at 100 days was higher than strength at 28 days, similar trend that the observed in results for mortar cured at room temperature, which suggests strength gain due to an ongoing hydration of cement. However, average strengths were still lower for heat-cured mortar regardless of the sand or testing time.

The effect of the use of acidic sands on the compressive strength of heat-cured mortars was significant only in mortar containing Cement D (Type III), where lower strengths were measured at 28 and 100 days compared to control specimens. For mortars using Type I, I/II, and V cements, similar strengths were observed in both types of sand.

DEF-expansion produced a detrimental effect on the compressive strength of mortar specimens. Higher decrease of the strength at 100 days compared with strength at 28 days was observed at higher DEF-expansion. The damaging effect of DEF on strength apparently starts at the first half of the accelerated expansion period.

4.4.3.2 Effect of curing temperature on compressive strength

In order to assess the impact on strength of the initial high-temperature curing and the development of the DEF reaction, the ratio between the average compressive strength of mortar cubes cured at high-temperature and at room temperature was calculated. Mortar specimens cured at different temperatures were prepared from the same batch and exposed to the same storing conditions.

Calculated ratios for every mortar mixture are shown in Table 4.3 for 28 and 100 days testing.

Table 4.3 Ratio of average compressive strength for different curing temperatures.

Cement	Age of Testing	Type of Sand	$\frac{\overline{f}_{95℃}}{\overline{f}_{23℃}}$ (%)
Cement A (Type I/II)	28 days	Control Sand	73.1%
		Site H Sand	69.9%
	100 days	Control Sand	63.8%
		Site H Sand	52.0%
Cement B (Type V)	28 days	Control Sand	87.8%
		Site H Sand	83.4%
	100 days	Control Sand	84.3%
		Site H Sand	82.1%
Cement C (Type I/II)	28 days	Control Sand	67.8%
		Site H Sand	71.7%
	100 days	Control Sand	68.4%
		Site H Sand	57.2%
Cement D (Type III)	28 days	Control Sand	78.2%
		Site H Sand	63.9%
	100 days	Control Sand	35.0%
		Site H Sand	26.7%
Cement E (Type I)	28 days	Control Sand	62.3%
		Site H Sand	67.1%
	100 days	Control Sand	42.8%
		Site H Sand	51.8%

The effect of the application of the Kelham curing cycle on the strength of mortar specimens can be appreciated in mortar using Cement B and Control sand, which heat-cured bar sample did not exhibit DEF-expansion. Heat-cured cubes prepared with this mortar mixture show an average compressive strength 12% and 16% lower at 28 and 100 days, respectively, than mortar cubes cured at room temperature. High-temperature curing can increase microcracking of the cement paste.

As shown by Klieger (1958), an increase of moist-curing temperature of concrete as low as 10 °C (17 °F) can decrease the compressive strength tested at 28, 90, and 365 days. This shows that curing temperatures higher than the recommended by ASTM C31 (23.0±2.0 °C [73.5±3.5 °F]) will produce lower strengths at later ages. It is believed that concrete cured at higher temperatures will develop non-uniformly distributed hydrated products that will generate weak zones in the material (Mindess et al., 2003)

Myers and Carrasquillo (1998) reported microcracking, distinguishable only by optical microscopy analysis, occurring primarily on the ITZ of concrete used in prestressed precast beams, with higher degree of microcracking for higher concrete temperature during hydration. Maximum measured concrete temperature was 93.3 °C (200 °F), similar to the maximum temperature applied during the Kelham curing cycle. Additionally, higher microcracking was observed on the ITZ of siliceous fine aggregate compared to limestone fine and coarse aggregate. This difference was attributed to the chemical bonding formed between cement paste and limestone and dolomitic minerals present on the aggregates. The weak mechanical interlocking of siliceous aggregate has been also considered the reason for the higher DEF susceptibility of this type of aggregate compared to limestone aggregate (Lawrence, 2004; Tosun and Baradan, 2010). Another factor that can play a role on early-age microcracking is the higher coefficient of thermal expansion of siliceous sand compared to limestone and dolomitic limestone, which can result in higher tensile stresses and microcracking in concrete (Bentz et al., 2011).

When DEF-expansion was measured on the mortar bars, a higher reduction of the strength was appreciable in heat-cured compared to cubes cured at room temperature. For

mortar using Cement D (Type III) and Site H sand, which bar specimens exhibited the highest expansion, the compressive strength at 100 days was 6,854 psi for cubes cured at room temperature and 1,830 psi for heat-cured mortar cubes.

Similar trend was observed on other mortar mixtures that exhibited DEF-expansion, but with smaller differences than the observed in Cement D samples. It should be noted, however, that DEF-expansion was still developing or close to start at 100 days, which indicate that the impact on strength may be higher at later ages.

CHAPTER 5

PERFORMANCE OF PRESTRESSED CONCRETE PILES USING STAINLESS STEEL REINFORCEMENT

Chapters 5 and 6 include the study of the use of duplex HSSS 2205 strands and austenitic SS 304 spiral wire reinforcement on full-scale prestressed concrete piles. The evaluation and testing of the piles was divided into four topics: materials characterization, structural performance of piles, pile driving performance, and durability assessment, as shown in Figure 5.1.

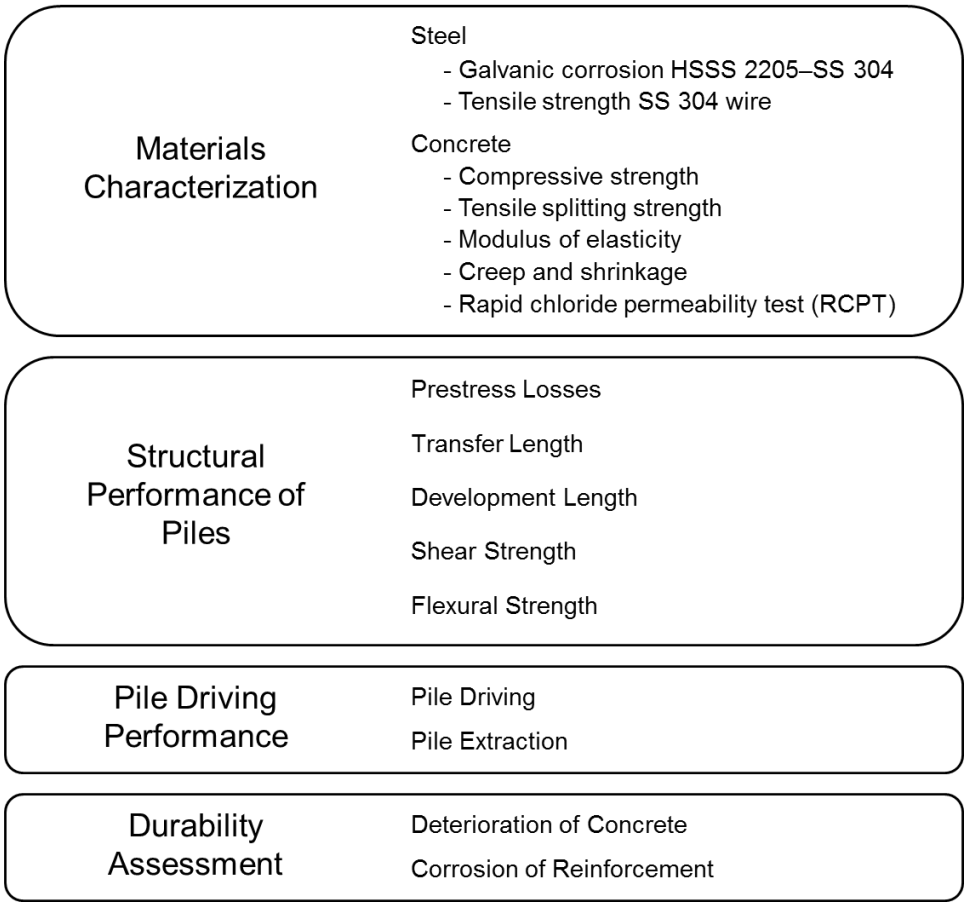

Figure 5.1 Stainless steel strand and shear/confinement reinforcement evaluation tests.

Along with a detailed description of the construction of the pile specimens, Chapter 5 includes three of the topics shown in Figure 5.1: Material Characterization, Pile Driving Performance, and Durability Assessment. From the assessment of the structural performance of piles, the study of prestress losses and shear and flexural strengths are also included in this chapter, while the experimental determination of transfer and development lengths is described in Chapter 6.

5.1 Introduction

Previous studies by Moser et al. (2012) and Schuetz (2013) have shown that the use of duplex high strength stainless steel grade 2205 (HSSS 2205, UNS grade S31803) for prestressing strand and austenitic stainless steel grade 304 (SS 304, UNS grade S30400) for shear and confinement reinforcement can improve the long term performance of bridges in marine environments. Even under conservative assumptions, the estimated life-cycle cost of piles using stainless steel reinforcement represent about 18% of the cost of the conventional design for a project period of 100 years, as detailed in Appendix F: Life Cycle Cost Analysis of the Use of Stainless Steel Reinforcement.

The performance of prestressed concrete piles using duplex HSSS 2205 strands and austenitic SS 304 transverse shear reinforcement is assessed in this chapter. Prestress losses, flexural and shear strengths, driving performance, and long term durability are compared to piles using conventional reinforcement and to AASHTO and ACI requirements, in order to determine if the suggested stainless steel grades can be used in prestressed concrete piles, using the same design requirements and construction procedures used for conventional steel.

5.2 Design and Construction of Prestressed Concrete Piles

Three 70-ft. long (21.3 m), 16-in. (40.6 cm) square piles were built using duplex HSSS 2205 prestressing strands and austenitic SS 304 transverse, spiral reinforcement, while two of the same size piles were built using conventional (AISI 1080) prestressing strands and transverse wire reinforcement as control specimens. These full scale piles were used to determine the driving performance, shear and flexural capacities of piles, transfer length, and prestress losses. The design followed GDOT requirements, and the piles were built in the Savannah plant of Standard Concrete Products (Figure 5.2). Additionally, two 27-ft. (8.2 m) long, 16-in. (40.6 cm) square piles were constructed with each type of strand in order to test the development length, and four 20-in. (50.8 cm) long pile specimens were built using each type of strand for long-term durability assessment. The durability specimens were left underwater in the Savannah River. Periodic evaluations of corrosion of steel and concrete degradation are being performed.

Figure 5.2 Standard Concrete Products plant, located in Savannah, GA.

5.2.1 Design of Prestressed Concrete Piles

The piles were designed according to GDOT requirements detailed on GDOT Specification 3215 for prestressed concrete piles. The dimensions of a 16×16-in. (40.6×40.6 cm) square pile cross section and reinforcement layout are shown in Figure 5.3. The conventional prestressing reinforcement is 7–wire low relaxation strands, with a nominal diameter of $^{7}/_{16}$-in. (11.1 mm), and minimum ultimate tensile strength (UTS) of 270 ksi (1,862 MPa). GDOT also requires the use of concrete conforming class AAA of the GDOT Specification 500 "Concrete Structures" and use of steel wire spirals for shear reinforcement conforming ASTM A1064 or AASHTO M32.

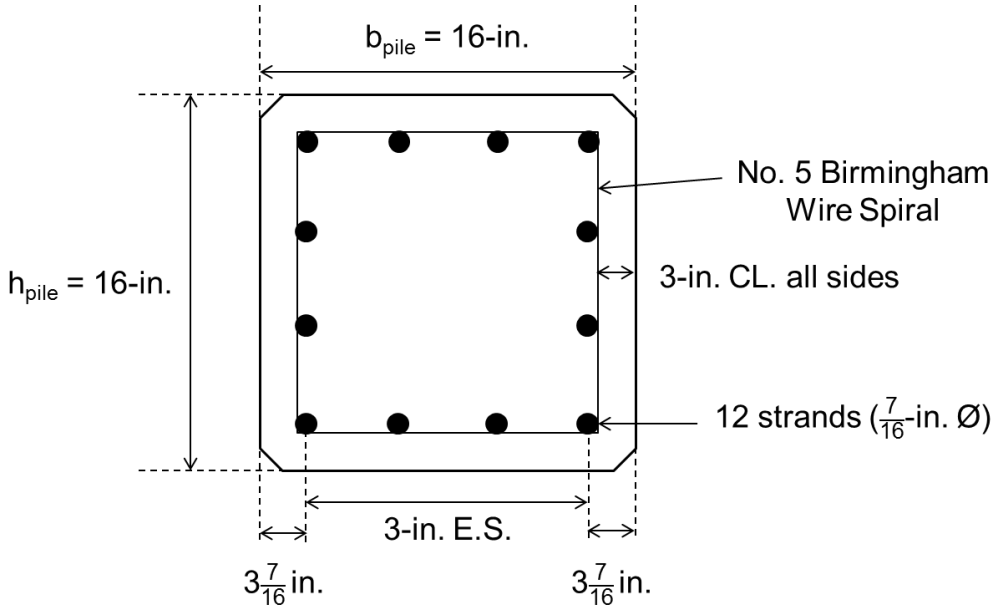

Figure 5.3 Cross section of a Grade 270 strand, 16-in. squared pile (GDOT Spec 3215). (1-in. = 2.54 cm)

In order to calculate the stresses developed at the depth of the strands, the actual dimensions of the transverse cross sections of the piles were measured and are given in Appendix G.

The transverse shear reinforcement is No. 5 Birmingham gauge wire (nominal W3.4 standard gauge) with a minimum yield stress of 70 ksi (482.6 MPa) (Figure 5.3). The wire spiral spacing along the pile is shown in Figure 5.4. At the pile ends, the 8 turns with 1-in. (2.54 cm) spacing prevents bursting due to stressing and due to pile driving; spacing is then increased to 16 turns with 3-in. (7.62 cm) spacing followed by 6-in. (15.24 cm) spacing throughout the middle length of each pile.

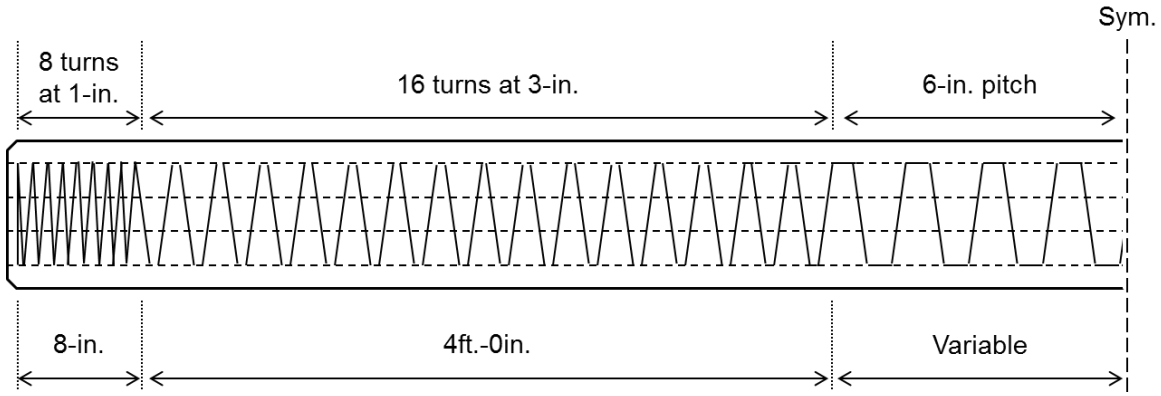

Figure 5.4 Wire spiral layout for prestressed concrete piles. (1-in. = 2.54 cm)

For the use of duplex HSSS 2205 strands, a higher area of strands was selected to account for the lower UTS compared to conventional steel as discussed further in Section 5.3.1. The diameter of these HSSS strands was increased from $^{7}/_{16}$-in. (11.1 mm) to ½-in. (12.7 mm), which represents an increase of 30% of the nominal area of steel. Additionally, to avoid the galvanic corrosion of the spiral wire with the duplex HSSS 2205 strand, the No. 5 Birmingham wire was replaced by austenitic SS 304 wire, with the same diameter and the same spacing distribution shown in Figure 5.4. Austenitic SS 304 wire was selected due to its lower cost and good corrosion resistance, and because duplex HSSS 2205 wire reduced to the 0.226-in. (5.74 mm) diameter was brittle and could not be

bent to radii required for the spiral transverse reinforcement. Separate tests indicated no galvanic corrosion between the 304 and 2205 steels.

5.2.2 Piles Fabrication and Instrumentation

The piles were built using two rigid parallel metallic beds or forms, one for prestressed concrete elements using duplex HSSS 2205 strands and austenitic SS 304 spiral wire, and the other one for AISI 1080 steel specimens. The same construction procedure was used for both types of prestressed concrete elements.

The forms were cleaned and sprayed with lubricant to ease the removal of the piles, and metallic spacers were used to divide each element (Figure 5.5). The strands were anchored to one end of the forms (dead end) and jacked from the other one.

Figure 5.5 Prestressing forms and metallic spacers.

The durability specimens were positioned closest to the jacking end, followed by the 27-ft. (8.23 m) piles. The 70-ft. (21.3 m) piles were positioned closer to the dead end of the forms. The prestressing cables were fixed at the dead end using anchorage chucks, composed by restraining rings to secure the position of the strands (see Figure 5.6).

Figure 5.6 Anchorage chucks at the dead end of the strands.

The strands were individually loaded using a hydraulic jack (see Figure 5.7). An average jacking load of 22.5 kips (100 kN) was applied to each strand, which represents an initial prestressing stress (f_{si}) of 70% and 61% of the UTS for AISI 1080 conventional steel and duplex HSSS 2205 strands (281 [1,937 MPa] and 242 ksi [1,669 MPa]), respectively.

After strand prestressing, the spiral reinforcement was distributed along the specimens (see Figure 5.8). In the piles using stainless steel, plastic ties were used to attach the spiral wire to the strands and to fix the spacing in order to avoid the occurrence of galvanic corrosion.

Figure 5.7 Loading of strands.

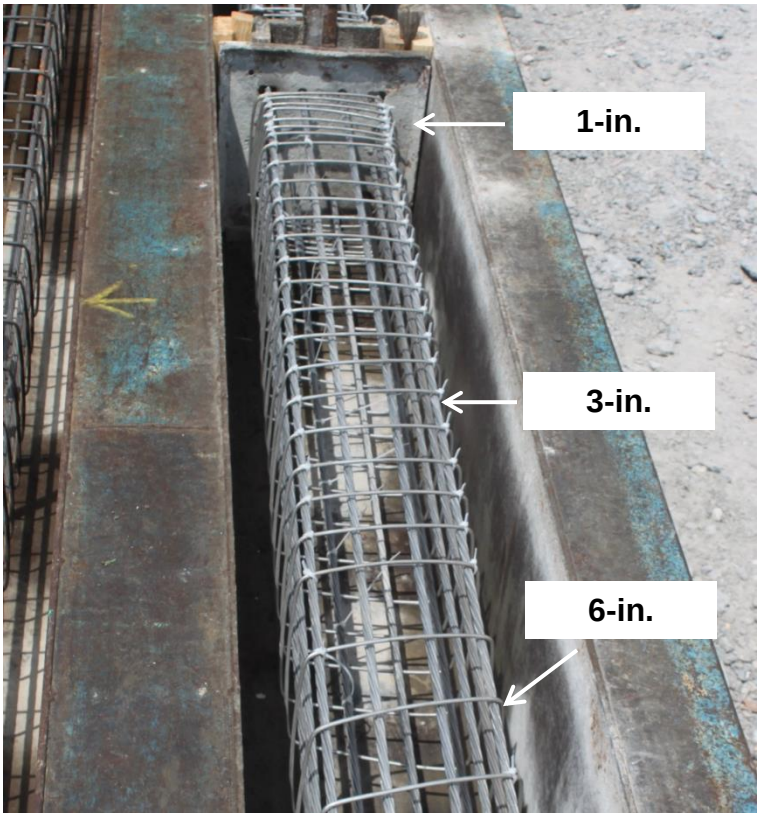

Figure 5.8 Spiral wire distribution. (1-in. = 2.54 cm)

Before concrete placement, four Geokon Model 4200 vibrating wire strain gauges (VWSG) were installed in each 70-ft. (21.3 m) pile for the determination of prestress losses. The VWSGs were placed at the mid-height of the piles, at approximately 17.5 ft. (5.3 m) from each end and on both sides of the piles. The sensors in piles using stainless steel were tied to the middle strands using austenitic SS 304 wire pieces and plastic ties (Figure 5.9).

VWSG consists on a tensioned wire connected to end blocks and an electromagnetic coil that excites and helps to obtain the resonant frequency of the wire. Changes on the wire tension by relative movements of the blocks will produce changes on the resonant frequency of the wire that can be translated to strain units by the readout.

VWSGs used in the piles had a gauge length of 6-in. (15.24 cm), a nominal range of 3,000 με, a resolution of 1 με, an operational temperature range from -4 to 176 °F (-20 to 80 °C), and they included a thermistor to monitor the internal temperature of concrete. The thermistor had an operational temperature range from -112 to 302 °F (-80 to 150 °C) and an accuracy of ± 0.9 °F (± 0.5 °C).

Figure 5.9 Vibrating wire strain gauge for prestress losses measurement.

The instrument cables of the VWSGs were run along the length of the prestressing strands to one end of the piles, where the cables were numbered and kept inside embedded terminal boxes for protection of the lead wires (Figure 5.10). Strain measurements were collected using a Geokon GK-404 manual readout. The zero measurement was taken the morning after concrete placement, before the release of the strands (Figure 5.11).

Figure 5.10 Instrument cables for prestress losses measurement**.**

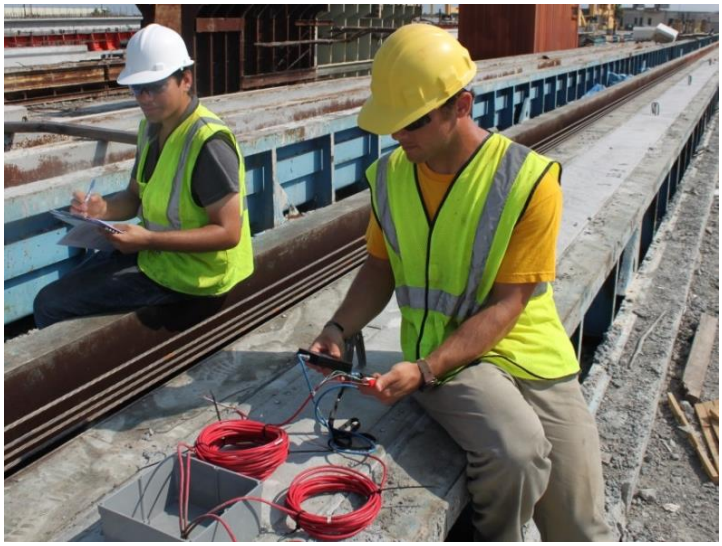

Figure 5.11 Prestress losses measurements.

Concrete was prepared in the plant using nine batches, limited by the capacity of the nonagitating truck that transported the material to the zone where the piles were constructed. Cylinders samples (dimensions 4×8-in. [10.2×20.3 cm] and 6×12-in. [15.2×30.5-cm]) were prepared with concrete from the first eight batches. Slump of 8-in. (20.3 cm) and air content of 5% were measured for the first batch.

The concrete was deposited in the forms by the truck using a chute, spread with shovels, and compacted with portable internal vibrators, while the surface was finished with manual darbies (Figure 5.12). Then, concrete surface was covered with plastic sheets. The ambient temperature during placing of concrete was 92 °F (33.3 °C), and the relative humidity was close to 100%.

The properties of concrete are presented in Section 5.3.2.

Figure 5.12 Concrete placing and compaction.

For the determination of the transfer length, the concrete surface strain profile was measured using a detachable mechanical strain gauge (DEMEC gauge). DEMEC points were fixed on the concrete surface at the end of each pile using two embedded metal strips (Figures 5.13 and 5.14). DEMEC points were spaced at 2-in. (5.1 cm); a 10-in. (25.4 cm) gauge length reader with a precision of ±0.0001-in. (±0.00254 mm) was used for each reading.

Figure 5.13 Strips for embedment of DEMEC points for transfer length measurement.

Steel nuts and brass pieces were screwed to the metal strips to create the embedded DEMEC measurement points. The surface of the metal strips was sprayed with demolding oil. Transverse wood strips were used to fix the distance between metal strips

and to position the strips at the end of the piles, immediately after the finishing of concrete surface.

After 15 hours, the metal strips were removed from the piles and the DEMEC points remained for the determination of the transfer length (Figure 5.14). The initial measurement (zero measurement) was taken before the release of the strands. The following measurements were taken after release and then before sunrise on the following days to avoid the influence of temperature changes between measurements.

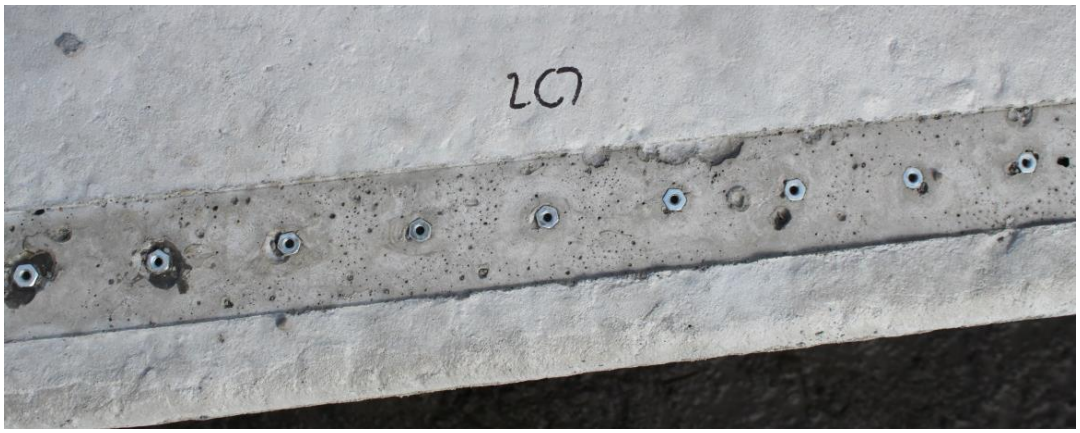

Figure 5.14 DEMEC points in pile concrete surface.

One day after concrete placement, the strands were released by cutting them using a gas torch (Figure 5.15). The required compressive strength of concrete before strand release was 4,000 psi (27.6 MPa), and an average value of 4,018 psi (27.7 MPa) was measured in cast cylinders.

After strand release, the piles and specimens were removed from the prestressing beds to an adjacent position (Figure 5.16).

Figure 5.15 Strand release.

Figure 5.16 Piles removal from the prestressing forms.

5.2.3 Composite Beam Construction

Two 27-ft. (8.23 m) piles per type of steel were built in order to evaluate the development length (l_d) of the strands. The l_d is the required length from the end of the pile over which the strand and concrete should be effectively bonded in order to develop the nominal strength of the prestressing steel.

An additional 27-in. (68.6 cm) top section was added to the piles to assure a strain in the prestressing strand greater than 2% to test the l_d. To provide an appropriate bond between the pile and the top section, the surface of the pile was roughed, and #5 bar stirrup reinforcement, spaced 6-in. (15.2 cm) along the pile, was embedded during pile's construction (see Figure 5.17).

Figure 5.17 27-ft. (8.23 m) piles for development length evaluation.

These short piles were transported to the Georgia Tech Structures and Materials Lab, where the top section was placed. Details regarding the construction of the development length specimens are presented in Appendix H.

Concrete of the top section of the beams was ready-mixed concrete with design strength of 6,000 psi (41.4 MPa) at 28 days. Water addition was required to reach proper workability. Concrete was placed on different dates for piles containing stainless and conventional steel strands. Companion 4×8-in. (10.2×20.3 cm) cylinder samples were prepared and fogroom cured until compressive strength testing.

The compressive strengths of the top concrete sections are shown in Figure 5.18, where the final point in each curve corresponds to the strength of concrete at the time of flexural testing of beams for development length determination. Variable addition of water before placing can explain differences in compressive strength.

The final condition of 27-ft. (8.23 m) piles after the addition of the top section is shown in Figure 5.19.

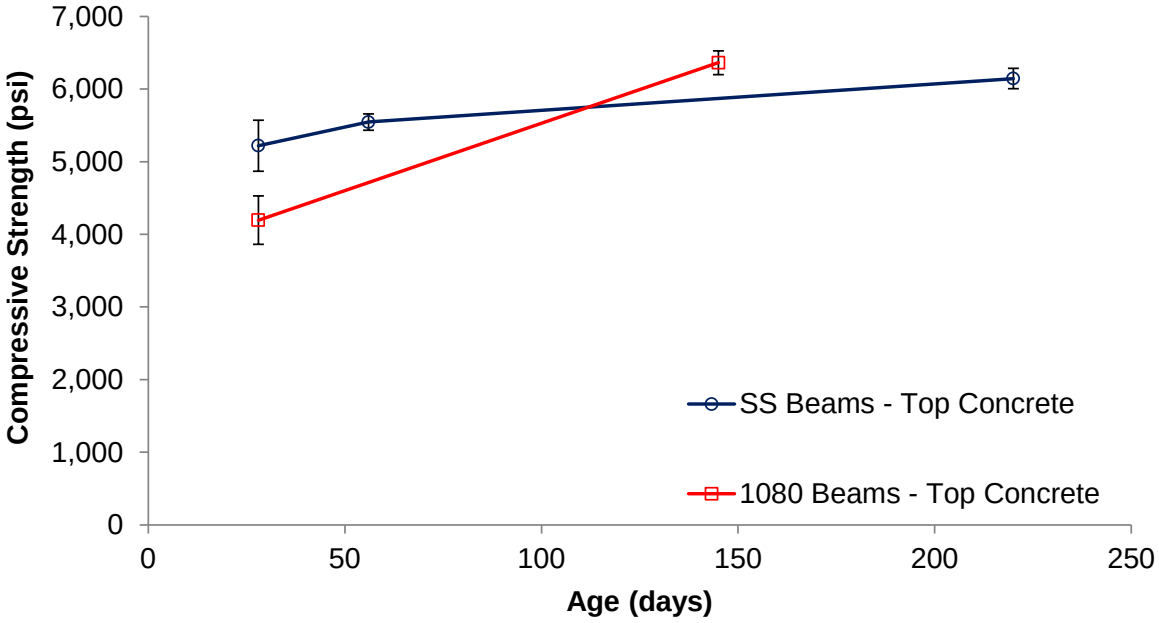

Figure 5.18 Compressive strength of concrete used in top section of beams. (1,000 psi = 6.9 MPa)

Figure 5.19 Development length testing specimen.

5.3 Properties of Materials Used in Prestressed Piles

The material property test results of concrete compressive strength, elastic modulus, splitting tensile strength, creep, and rapid chloride permeability, and of the steel reinforcement, duplex HSSS 2205, SS 304, and AISI 1080, are presented in this section.

5.3.1 Steel Properties

Moser et al. (2012) studied the corrosion resistance of AISI 1080 steel, duplex HSSS 2205, and austenitic SS 304, while Schuetz (2013) investigated the mechanical behavior of AISI 1080 and duplex HSSS 2205 strands. A summary of those findings is presented in this section.

Additionally, the mechanical properties of SS 304 wire and the galvanic corrosion evaluation between duplex HSSS 2205 strands and SS 304 wire are included.

5.3.1.1 Duplex high-strength stainless steel 2205

Duplex HSSS 2205 (ASTM A276 grade UNS S31803), ½ in. (12.7 mm) diameter 7–wire prestressing strands were produced at Sumiden Wire Products Corporation in

Dickson, TN, using the same equipment and production techniques used for conventional AISI 1080, low relaxation prestressing strands (see Figure 5.20). More information about the production process of SS strands can be found in Chapter 7 of Moser et al. (2012).

Figure 5.20 Duplex HSSS 2205 strand and austenitic SS 304 wire samples.

The mechanical properties of the strands tested by Schuetz (2013) are given in Table 5.1 and in Figure 5.21. Duplex HSSS 2205 strands have a lower ultimate tensile strength (UTS), elastic modulus, and yield stress compared to conventional strands. To account for lower mechanical properties, the area of the strand was increased about 30% in the case of duplex HSSS 2205 (diameter of ½-in. [12.7 mm] instead of the commonly used $^{7}/_{16}$-in. [11.1 mm]). Also, the ultimate strain of HSSS 2205 is only 27% of the value for conventional AISI 1080 steel, which indicates a lower ductility of duplex HSSS 2205 strands (Figure 5.21).

Table 5.1 Mechanical properties of duplex HSSS 2205 and conventional steel strands. 1 ksi = 6.9 MPa.

	Duplex HSSS 2205		**AISI 1080 Steel**	
	Average	Std Dev	**Average**	Std Dev
UTS (ksi)	**241.5**	1.6	**281.8**	2.0
Ultimate strain (in/in)	**1.60%**	0.07%	**5.89%**	0.59%
Elastic modulus (ksi)	**23,500**	190	**29,400**	130
Yield Stress (ksi, 0.2% offset criterion)	**228.7**	2.4	**254.7**	0.6
Stress-relaxation 70% UTS – 1,000 h	**2.49%**	0.24%	**2.40%**	

Schuetz (2013) observed a stress relaxation loss of 2.49% when testing duplex HSSS 2205 strands following standard ASTM E328 (1,000 hours of test duration, temperature controlled room, at 70% UTS), while Moser et al. (2012) estimated a stress loss of 2.40% in AISI 1080 wires from 200 hours results. The limit for low relaxation prestressing strand according to ASTM A416 is 2.5% for 1,000 h tests with strands loaded at 70% of UTS.

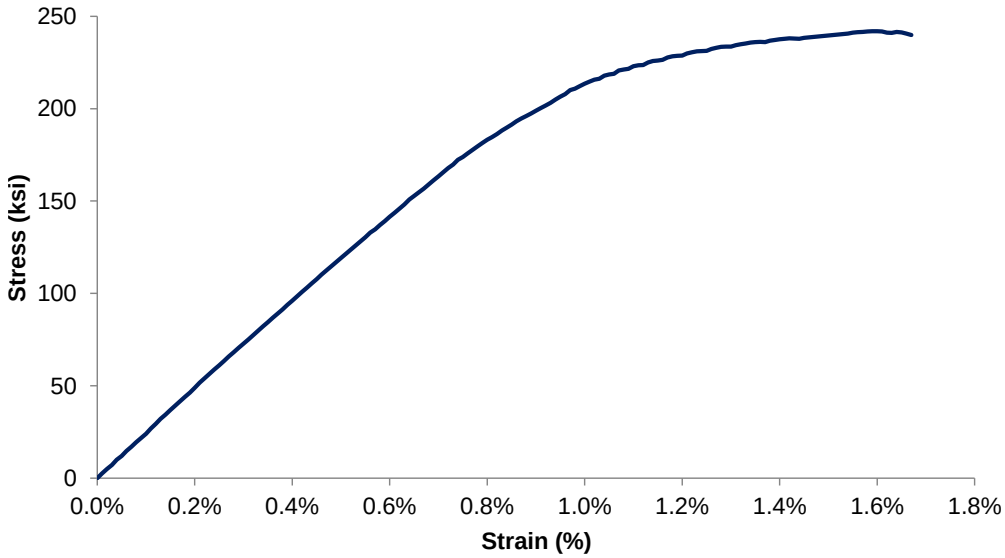

Figure 5.21 Stress-strain curve of duplex HSSS 2205 strand. 1 ksi = 6.9 MPa.

Moser et al. (2012) analyzed the corrosion behavior of the steels included in this document. Using electrochemical cyclic potentiodynamic polarization techniques in simulated concrete alkaline and carbonated environments contaminated by chloride ions, they found the results given in Table 5.2, where the higher corrosion resistance of duplex 2205 is evidenced.

Table 5.2 Corrosion behavior of different steel alloys (modified from Moser et al. [2012]).

	Alkaline (pH = 12.5)				**Carbonated** (pH = 9.5)			
Cl^- content (M)	0.00	0.25	0.50	1.00	0.00	0.25	0.50	1.00
Duplex 2205	**NC**	**NC**	**NC**	**NC**	**NC**	**NC**	**NC**	**NC**
Austenitic 304	**NC**	**NC**	**MP**	**SP**	**NC**	**MP**	**SP**	**SP**
AISI 1080	**NC**	**SP**	**SP**	**SP**	**MP**	**SP**	**SP**	**SP**

Note: **NC**: no corrosion initiated - **MP**: metastable pitting - **SP**: stable pitting

5.3.1.2 Austenitic stainless steel 304

Austenitic SS 304 wire (ASTM A276 grade UNS 30400), with a diameter of 0.226-in. (5.74 mm), was selected for the transverse confinement and shear spiral reinforcement of piles using duplex HSSS 2205 strands. Higher CTL and lower time to corrosion initiation were observed in wires compared with prestressing strands, due to the presence of crevices and surface imperfections that provide initiation sites for corrosion.

One of the main concerns in order to test the suitability of the wire is the potential formation of a galvanic couple when in contact with the strands. Two dissimilar metals electronically connected in a conductive environment can undergo galvanic corrosion. In this case, the anodic member of the couple will present local accelerated corrosion, while the other metal will be cathodically protected. This reaction is not necessarily related with the difference in standard half-cell potential from the electromotive force (emf) Series, and its occurrence and kinetics depend on the composition of every member of the galvanic couple, the exposed area of the cathode and the anode, and the environmental conditions (e.g., temperature, pH) under which both metals are in contact (Zhang, 2011).

To evaluate the occurrence of galvanic corrosion, samples of HSSS 2205 strand and SS 304 spiral wire were tested following the standard ASTM G71. The description and results of the test are detailed in Appendix I. In summary, in a seawater solution, the current measured between both metals did not indicate the formation of a galvanic couple. Thus, the combined use of both types of stainless steels will not compromise the durability of the prestressed concrete piles due to localized accelerated galvanic corrosion.

The tensile capacity of the wires was tested in an electromechanical universal testing machine. Three samples obtained from the spiral wire reinforcement, with gauge lengths of approximately 4.3-in. (10.9 cm), were tested individually under direct tension. A typical stress-strain curve of the SS 304 wire is shown in Figure 5.22, and a summary of the results of the tensile strength test is given in Table 5.3.

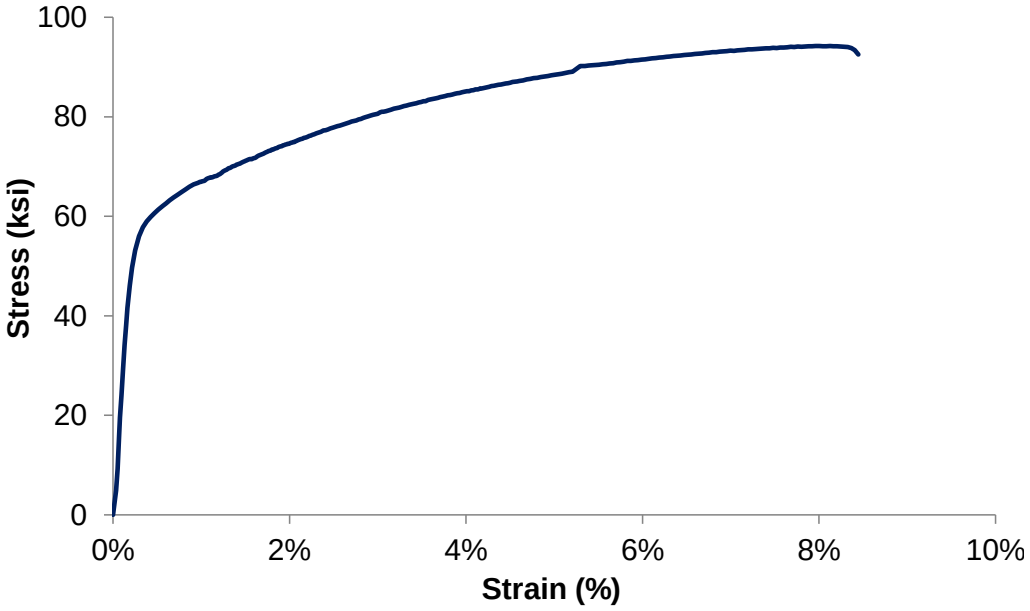

Figure 5.22 Stress-strain curve for austenitic SS 304 wire. 1 ksi = 6.9 MPa.

Table 5.3 Mechanical properties of austenitic SS 304 wire. 1 ksi = 6.9 MPa.

	Average	**Std Dev**
UTS (ksi)	**91.8**	3.5
Yield stress (ksi, 0.2% offset)	**61.9**	---------
Ultimate strain (in/in)	**7.8%**	0.2%
Elastic modulus (ksi)	**26,182**	394

For the determination of the yield point, a 2-in. (5.1 cm) SATEC extensometer was attached to the wire during the test and removed when an 80% of the UTS was reached. The calculation of the yield point according to the 0.2% offset and the 1% strain criteria is shown in Figure 5.23. For calculation of the shear capacity of the piles, the lower yield stress value was used in order to perform a conservative evaluation.

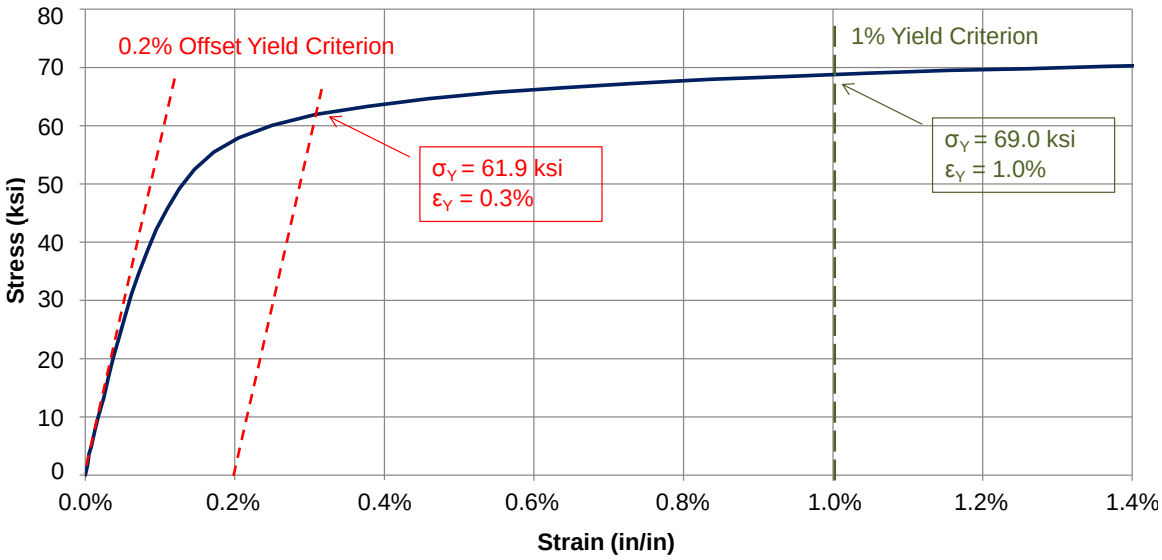

Figure 5.23 Yield point calculation for austenitic SS 304 wire. (1 ksi = 6.9 MPa)

5.3.2 Concrete Properties

Concrete was prepared in the plant, using nine consecutive batches to fill the forms. Cylinders of two different sizes (dimensions 4×8-in. [10.2×20.3 cm] and 6×12-in. [15.2×30.5 cm]) were prepared using the first eight batches of concrete in order to determine the mechanical properties, the chloride permeability, and to assess the variability within the piles. Samples from the ninth batch accidentally were not taken. The excellent consistency in batches two through eight indicates that batch nine would be similar. Batch one was a little weaker than the others for reasons unknown.

5.3.2.1 Concrete mixture composition

GDOT Class AAA HPC mixture was used in the piles to assure a chloride ion permeability less than 2000 coulombs. The specified design compressive strength at 28 days (f_c') was 5,000 psi (34.5 MPa). The mixture proportions are given in Table 5.4.

A 14.8% mass substitution of cement by ASTM C618 Class F fly ash was used (replacement of 19.5% by volume). The water-to-cementitious material ratio (*w/cm*) was 0.23 and a coarse aggregate size #67 was used (maximum size of aggregate, MSA = ¾" [19.1 mm]). The aggregate volumetric fraction corresponded to 71.4%, and the design air content was 4.0%. The measured slump for the first batch was 8 inches (20.3 cm).

Table 5.4 Mixture design of concrete.

	Specific Gravity	**Mix Design (lbs./yd^3)**	**Mix Design (kg/m^3)**
Type I Cement	3.14	687	408
Water	1.00	188	112
Class F Fly Ash	2.26	119	71
Coarse Aggregate	2.65	1,870	1,109
Fine Aggregate	2.62	1,305	774
Design air content:		4.0%	
Retarder (Goulston Chupol N20):		2.36 fl. oz./cwt	479.5 ml
HRWR (Goulston Chupol N60):		6.45 fl. oz./cwt	1,310.5 ml
AEA (Goulston Chupol FA-10):		0.46 fl. oz./cwt	93.5 ml

The chemical composition of the cement (ASTM C150 Type I/II cement) is given in Table 5.5. The composition was obtained by quantitative X-ray diffraction (QXRD) refinement.

Table 5.5 QXRD analysis of cement type I/II used.

C_3S	C_2S	C_3A	C_4AF	Free CaO	Free MgO	Quartz	K_2SO_4
62.5%	16.1%	3.8%	11.1%	0.2%	0.2%	0.1%	0.2%

Gypsum	Hemihydrate	Anhydrate	$CaCO_3$	$Ca(OH)_2$
1.3%	0.6%	0.2%	1.1%	2.7%

5.3.2.2 Variability of concrete

Different batches of concrete were used for each pile and durability specimens. Considering that differences in concrete composition can produce differences during pile testing, Table 5.6 shows the variability of concrete strength measured at 28 and at 438 days.

Table 5.6 Variability of concrete strength of prestressed concrete elements at 28 and 438 days (time of flexure and shear testing). (1,000 psi = 6.9 MPa)

Prestressed Concrete Elements	Compressive Strength (psi)	Std Dev (psi)	Number of Cylinders
28 Days			
Durability Specimens	6,475	101	2
Pile AISI 1080 #1	8,795	---------	1
Pile AISI 1080 #2	6,761	500	3
Pile HSSS 2205 #1	7,801	500	2
Pile HSSS 2205 #2	7,905	398	3
Pile HSSS 2205 #3	8,139	33	2
438 Days			
Durability Specimens	8,819	94	2
Pile AISI 1080 #1	12,064	318	5
Pile AISI 1080 #2	9,678	814	5
Pile HSSS 2205 #1	10,611	328	6
Pile HSSS 2205 #2	10,686	292	9
Pile HSSS 2205 #3	10,931	179	5

The statistical similarity of piles and specimens was analyzed using the results of concrete strength at 438 days, given that they are a better representation of the long-term strength of concrete and that a larger number of cylinders were used for their determination (see Table 5.6).

Table 5.7 shows the results of the statistical analysis performed for the results summarized in Table 5.6. The hypotheses of similarity of means (H_0) for the whole set of cylinders and for concrete cylinders of piles using conventional steel are rejected for an α = 5% significance level. In the case of concrete cylinders representing the strength of piles using duplex HSSS 2205, there is no evidence to reject H_0. The p-value, the conditional probability of rejecting H_0 given that H_0 is true, is also included for every statistical hypothesis test; μ_i is the mean of the sampling distribution for each selected subset *i*.

Table 5.7 Statistical analysis of compressive strength results at 438 days.

Test	**Decision** (α = 5%)	**p-value**
H_0: $\mu_i = \mu$	Reject H_0	2.41×10^{-8}
H_0: $\mu_{2205\text{-}1} = \mu_{2205\text{-}2}$	Fail to Reject H_0	65.19%
H_0: $\mu_{2205} = \mu$	Fail to Reject H_0	17.63%
H_0: $\mu_{1080} = \mu$	Reject H_0	0.02%

Even when piles using duplex HSSS 2205 were built with different batches of concrete, their long-term strength can be considered statistically similar. In the case of piles using conventional steel, strength of concrete in pile AISI 1080 #1 is higher than concrete in pile AISI 1080 #2.

5.3.2.3 Strength of concrete

Strength of concrete was tested using 4×8-in. (10.2×20.3 cm) cylinders at 4, 7, 28, and 91 days from casting, following standard ASTM C39. Two cylinders were tested at the plant just before release to assure adequate release strength. This "one-day" strength was not included in Figure 5.24 because cylinders were tested under different conditions at the plant. The strength was also tested at 243 days during the flexure test for development length evaluation, and at 438 days during the flexural and shear capacity testing. The results of strength vs. time are shown in Figure 5.24, where the error bars indicate ± one standard deviation. It should be noted that only specimens from batches 2 to 8 are considered for the calculation of the average strength. Individual results per cylinder at every age of testing are included in Appendix J.

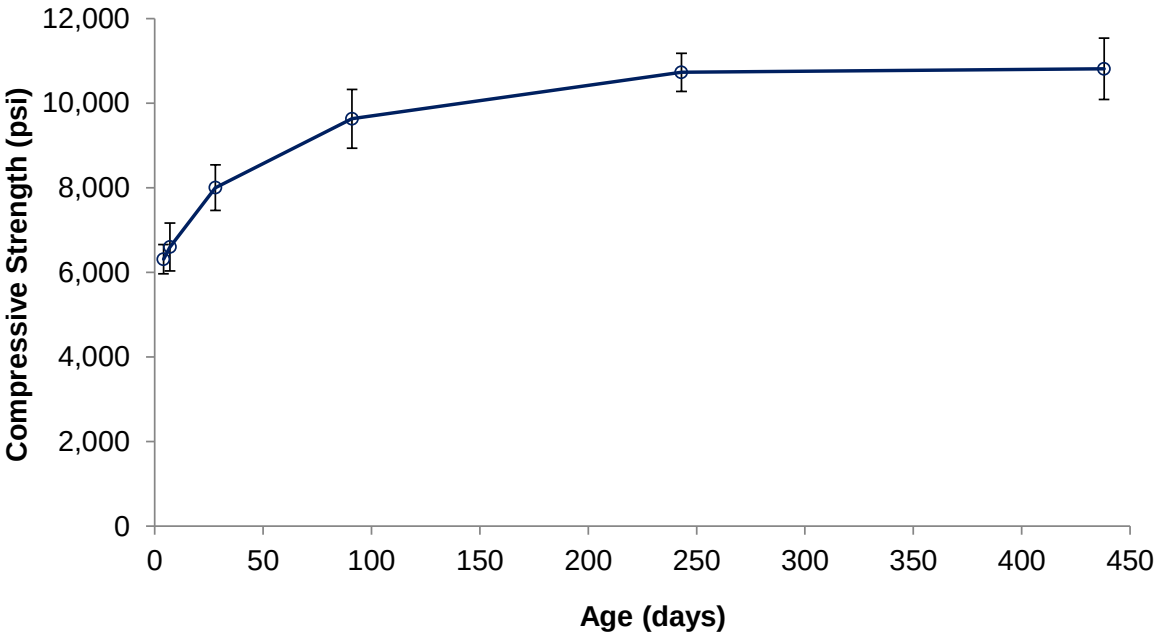

Figure 5.24 Compressive strength of concrete at 4, 7, 28, 91, 243, and 438 days from casting. Average do not consider batch 1, which was not used in the piles. (1,000 psi = 6.9 MPa)

GDOT requires a minimum compressive strength of 5,000 psi (34.5 MPa) at 28 days for the concrete piles. The measured average strength at 28 days was 8,001 psi (55.2 MPa), and the average strength for every pile or specimen was also higher than the requirement (see Table 5.6). Also, the strength of concrete was tested before strand release in the plant at 1 day from casting, and an average value of 4,018 psi (27.7 MPa) was measured (result not included in Figure 5.24). A minimum compressive strength of concrete of 4,000 psi (27.6 MPa) is required to release the strands. The relationship of strength-time of concrete can be represented by Equation 5.1 (t in days, R^2=98.7%).

$$f_c^{'} = 1{,}046.8 \cdot \ln(t) + 4{,}710 \quad 1 \le t \le 438 \tag{5.1}$$

ACI 363R: Report on High Strength Concrete (2010) defines the term *high-strength concrete* as "concrete that has a specified compressive strength for design of 8000 psi (55.2 MPa) or greater". Even considering that the report recognizes that there is no definitive limit that determines a dramatic change on the mechanical properties of concrete, the equations of reports ACI 363.R and ACI 318 to predict the elastic modulus and splitting tensile strength are compared with the results obtained experimentally. Design strength is commonly considered at 28 days of age; in this case, 8,001 psi (55.2 MPa).

5.3.2.4 Stress-strain behavior of concrete

The modulus of elasticity and Poisson's modulus were obtained according to standard ASTM C469 at 4, 28, 91, and 445 days. Cylinders of dimensions 6×12-in.

(15.2×30.5 cm) were selected from batches 2 to 8. Three cylinders were tested at every age, and the deformations until 40% of the ultimate load were used for the calculation of the elastic modulus. Individual results and individual stress-strain curves up to approximately 60% of the maximum load are given in Appendix J. A summary of the results is shown in Table 5.8, where they are compared with estimations suggested by ACI reports 318 and 363.R, and AASHTO LRFD.

Table 5.8 Elastic modulus and Poisson's ratio of concrete at 4, 28, 91, and 445 days. 1 ksi = 6.9 MPa.

Age (days)	**Elastic Modulus** (ksi) Average (Std Dev)	**Poisson's Ratio** Average (Std Dev)	**Exp. Estimation** (Eq. 4.5, ksi)	**Estimation ACI-318** (Eq. 4.3, ksi)	**Estimation ACI-363R** (Eq. 4.2, ksi)	**Estimation AASHTO** (Eq. 4.4, ksi)
4	**6,138** (354)	**0.17** (0.01)	6,195	4,322	5,007	4,460
28	**6,683** (677)	**0.20** (0.02)	6,607	4,976	5,445	5,134
91	**6,892** (423)	**0.22** (0.02)	6,857	5,594	5,859	5,772
445	**7,138** (448)	**0.17** (0.01)	7,193	5,927	6,082	6,115

The ACI 363.R proposed estimation of the elastic modulus for ASTM moist-cured cylinders is shown in Equation 5.2 (compressive strength in psi).

$$E_c = 38{,}200 \cdot \left(f_c^{'}\right)^{0.50} + 2{,}110{,}000 \qquad (5.2)$$

Equation 5.2 is an empirical relationship developed by Myers and Carrasquillo (1998) that considers the use of fly ash in high-performance mixtures.

ACI 318 (2011) proposes an estimated elastic modulus of normalweight concrete, shown in Equation 5.3 (compressive strength in psi).

$$E_c = 57{,}000\sqrt{f_c'} \tag{5.3}$$

Alternatively, AASHTO LRFD estimates the elastic modulus of concrete using the compressive strength of concrete f_c', in ksi, and the unit weight of concrete w_c, in kcf (Equation 5.4).

$$E_c = 33{,}000 \cdot w_c^{1.5} \cdot \sqrt{f_c'} \tag{5.4}$$

Experimental results are given in Table 5.8. The relationship elastic modulus-time of concrete can be represented by Equation 5.5 (t in days, R^2=97.6%).

$$E_c = 211.9 \cdot \ln(t) + 5{,}900.8 \quad 1 \le t \le 438 \tag{5.5}$$

Table 5.8 shows that Equation 5.2 is a better estimation than the equation obtained from ACI 318 (Equation 5.3), but both equations fail to estimate the experimental value at every age of testing. AASHTO LRFD estimation (Equation 5.4) is also highly inaccurate compared to experimental results, although it is a better estimation than the ACI 318 equation. Estimations from the codes are compared with estimated values using the expression derived from experimental results (Equation 5.5).

5.3.2.5 Splitting tensile strength

The tensile strength of concrete was indirectly measured using the splitting tensile strength test described in ASTM C496. A summary of results is shown in Table 5.9. At every age, three 4×8-in. (10.2×20.3 cm) cylinders were tested and the development of a crack in the direction of the application of the load was checked in order to calculate the splitting tensile strength according to the standard.

Results obtained from this method are generally higher than the ones obtained from direct tensile strength and lower than the modulus of rupture (ASTM C78 or C293).

Table 5.9 Splitting tensile strength of concrete at 7, 28, and 445 days. (1,000 psi = 6.9 MPa)

Age (days)	**Splitting Tensile Strength** (psi)			$\frac{f_{sp}}{f'_c}$	**Estimation ACI-318** (psi)	**Estimation ACI-363R** (psi)
	Average	Std Dev				
7	**670**	41	$8.5\sqrt{f'_c}$	10.9%	526	581
28	**697**	20	$8.0\sqrt{f'_c}$	9.2%	585	646
445	**797**	48	$7.7\sqrt{f'_c}$	7.4%	697	769

Similar to the estimation of the elastic modulus, the equation from ACI 363.R ($7.4\sqrt{f'_c}$) is closer to the experimental value than the estimation of ACI 318 ($6.7\sqrt{f'_c}$) at every age. At 28 days, the splitting tensile strength of the pile concrete had a mean of 8.0 $\sqrt{f'_c}$. Also, it is observed that the ratio between splitting tensile strength and compressive strength decreases with time. This behavior is related to the reduced extensibility and the higher cracking potential of high-strength concrete. The rate of tensile strength evolution over time is lower compared to compressive strength. At a given strain, stresses in

concrete will be proportional to the elastic modulus, considerably higher than the predictions as seen in Table 5.8. The combination of these two factors produces a concrete more prone to cracking.

5.3.2.6 Creep of concrete

Creep testing was performed according to ASTM C512, beginning at 28 days from casting. Three 6×12-in. (15.2×30.5 cm) cylinders, cured in fogroom until testing and obtained from different batches, were placed in the creep loading frame, while two additional cylinders were kept in the same temperature and humidity controlled room during the duration of the tests to evaluate drying shrinkage. The cylinder ends were ground smooth with a water grinder (Figure 5.25).

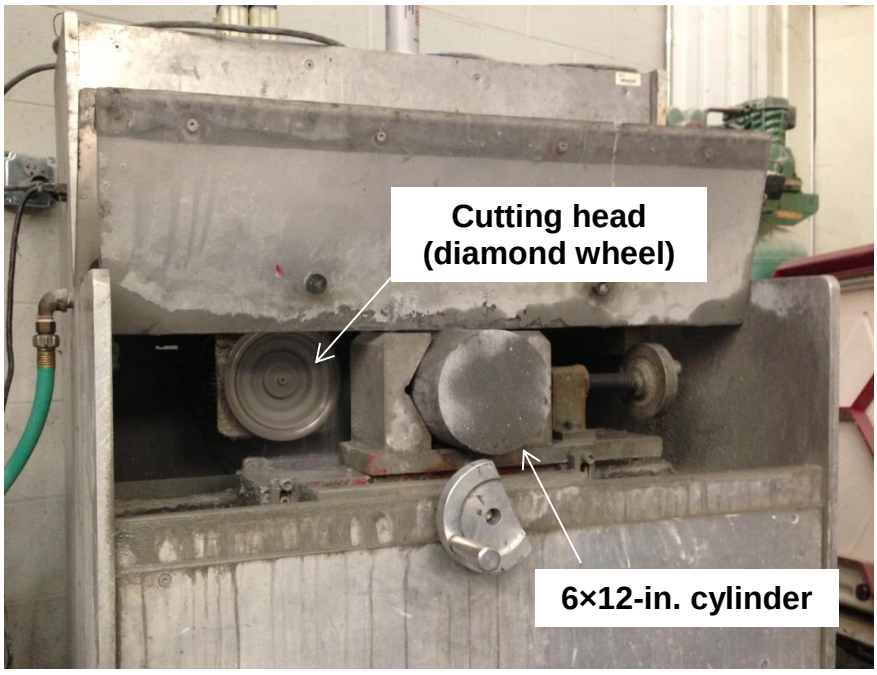

Figure 5.25 Cylinder end grinding machine. (1-in. = 2.54 cm)

DEMEC points were epoxied to the cylinders for creep and shrinkage evaluation at two opposite sides of the cylinders. The measurements were made by the same person, using the same DEMEC gauge equipment to minimize the variability of the test. The test was performed inside a conditioned room, where the temperature and relative humidity were kept at constant values of 73±1 °F (23±0.6 °C) and 50±2%, respectively.

The test setup is shown in Figure 5.26. The load was applied using a hydraulic jack and controlled by a load cell. The top loading plate was fixed to the loading bars of the frame, while the bottom loading plate was allowed to move upwards. At 28 days from casting, the cylinders were loaded to 40% of their ultimate strength. Before every measurement, the applied load was adjusted to account for pressure losses. Losses not higher than 10 lbf (44 N) were observed during the testing period. The nuts fixing the position of the bottom loading plate were also adjusted before every measurement.

After 52 days from the start of the test, several cracks appeared at the top and bottom cylinders and dummy samples. The cracks extended to the mid-height of the cylinders after one day. The test was terminated.

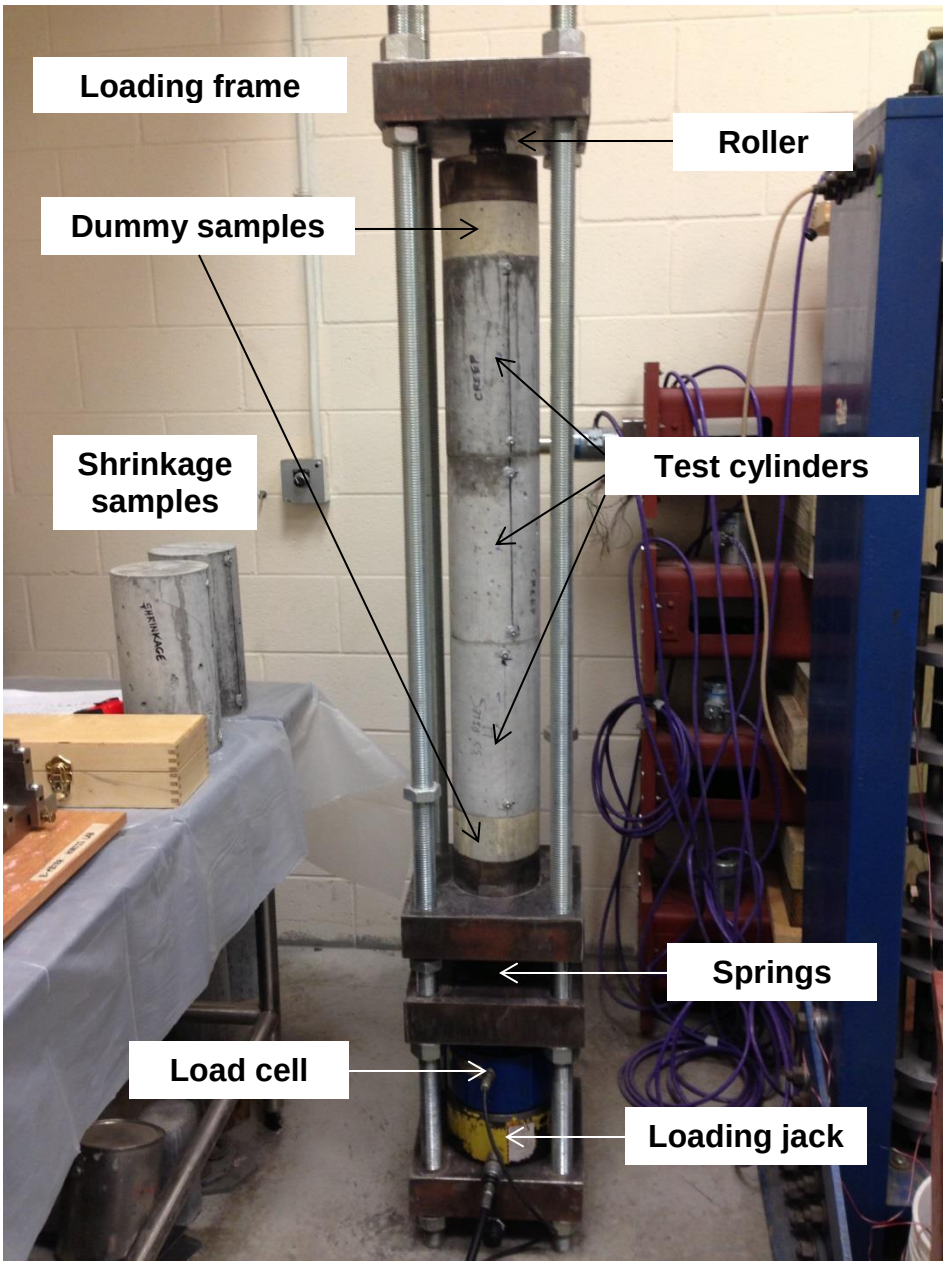

Figure 5.26 Creep test set up (ASTM C512).

The results of the creep test, including the deformations due to shrinkage, during the first 1,247 hours are shown in Figure 5.27. A logarithmic correlation of the results is shown in Equation 5.6 (t in hours, R^2=97.7%).

$$\varepsilon_{c,sh} = 59.68 \cdot \ln(t) + 116.78 \quad 1 \le t \le 438 \tag{5.6}$$

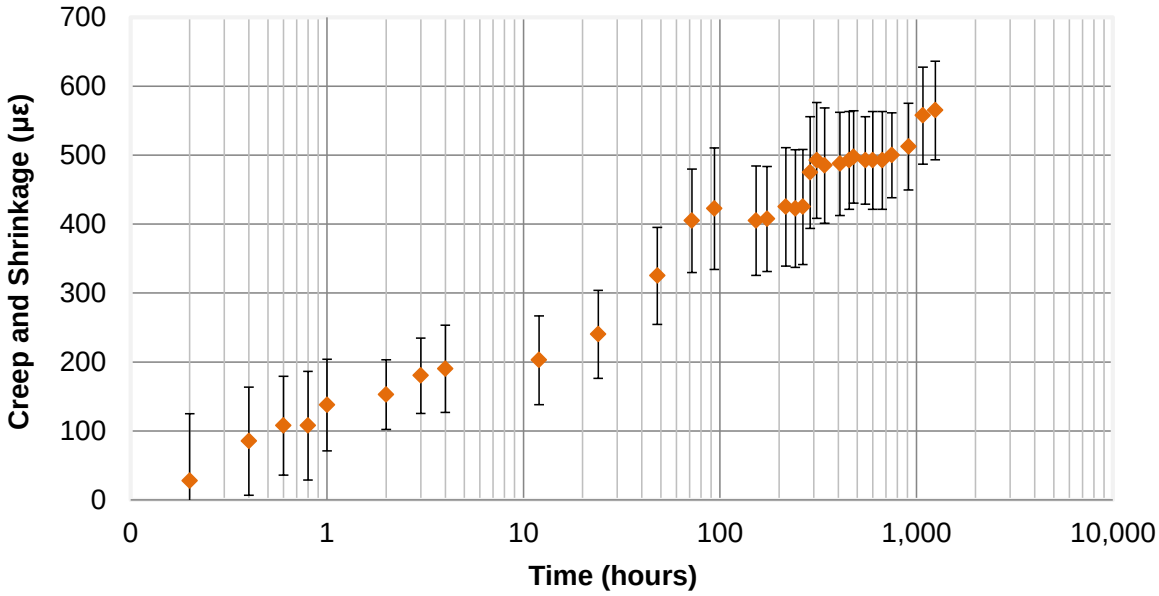

Figure 5.27 Creep and shrinkage measurements during the first 1,247 hours.

Using the measurements on the cylinder samples for shrinkage evaluation, the deformation due to creep was isolated from results shown in Figure 5.27. Creep deformations increased logarithmically for around 100 hours, and remained at an approximately constant value for later ages. The average creep strain after 100 hours was 341.7 με (Figure 5.28).

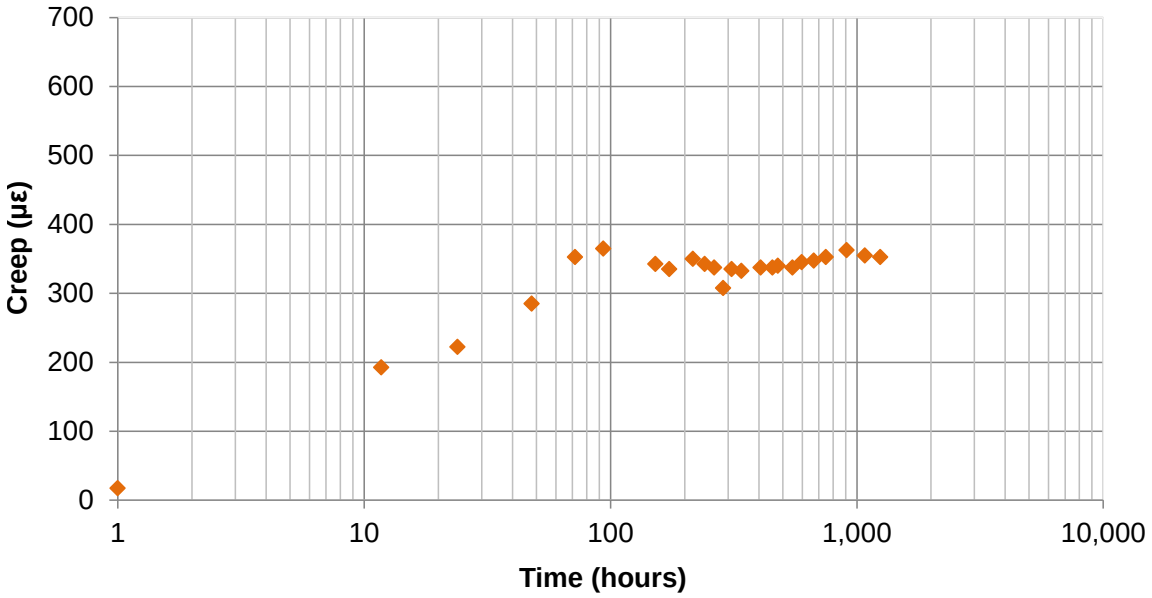

Figure 5.28 Creep calculation during the first 1,247 hours.

In order to compare the results with previous creep testing of high-strength and high-performance concrete (Kahn et al., 2005), the specific creep (strain relative to applied stress) and the creep coefficient (ratio of creep strain to initial elastic strain) were calculated. The previous 2005 study used a higher cementitious content (cement plus silica fume plus fly ash) than the concrete used for the piles. The concrete compressive strengths in the previous study ranged from 14.14 ksi (97.5 MPa) to 16.38 ksi (112.9 MPa) at 28 days; and the specimens were loaded when the concrete was 28 days old. Those specimens had creep coefficients of 0.752 and 0.690 measured at 376 days, respectively; the specific creep values at 376 days were of 0.197 με/psi (28.57 με/MPa) for every concrete.

Calculated specific creep for the pile specimens concrete is shown in Figure 5.29. The regression for these results is given in Equation 5.7 (t in days, R^2=97.7%), which predicts a specific creep of 0.217 με/psi (31.47 με/MPa) at 376 days.

$$\varepsilon' = 0.0196 \cdot \ln(t) + 0.1005 \quad (5.7)$$

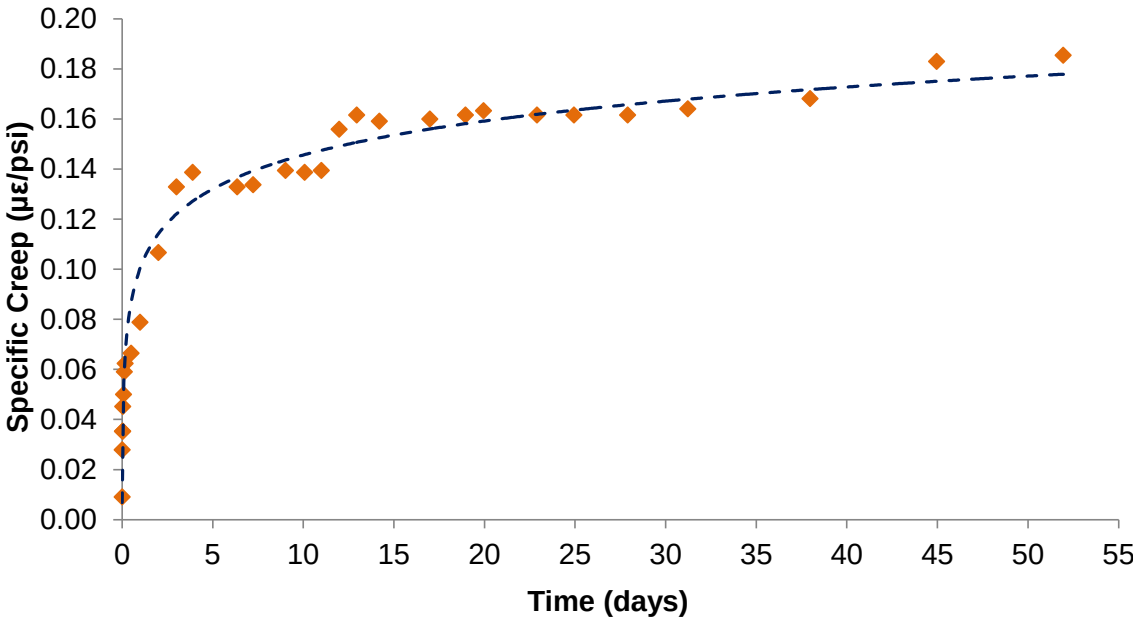

Figure 5.29 Specific creep calculation during the first 52 days. Blue dashed line shows correlation expressed in Equation 4.7. (1 με/psi = 145 με/MPa)

Calculated creep coefficient, ϕ, for the pile concrete is shown in Figure 5.30. The regression for these results is given in Equation 5.8 (t in days, R^2=97.8%), which predicts a creep coefficient of 1.56 at 376 days.

$$\phi = 0.1468 \cdot \ln(t) + 0.6862 \quad (5.8)$$

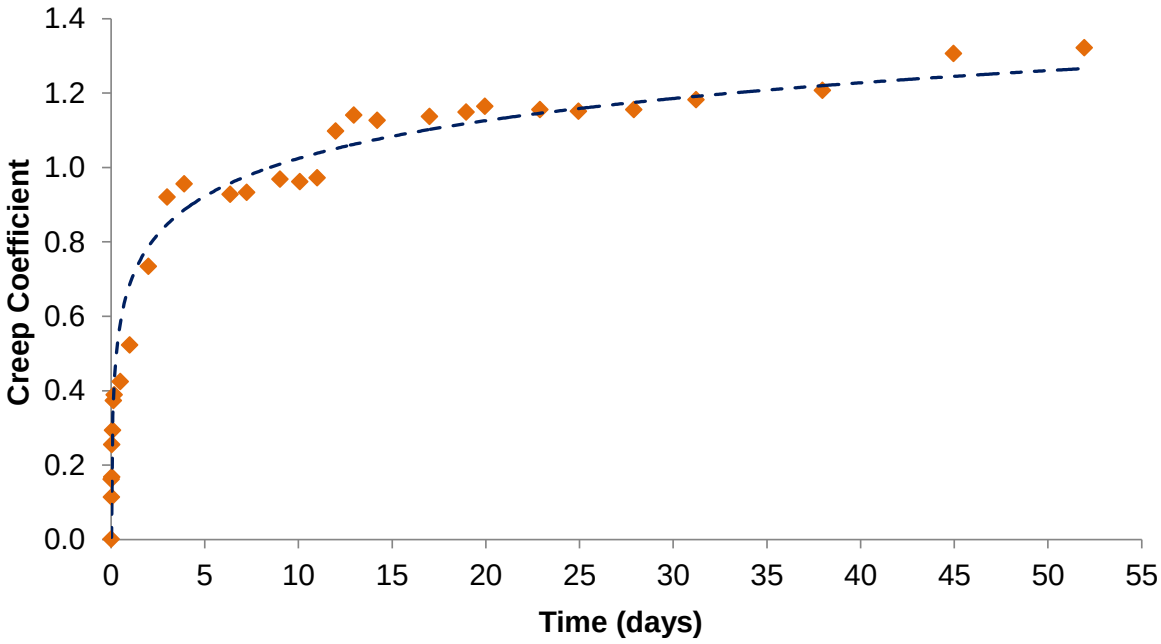

Figure 5.30 Creep coefficient calculation during the first 52 days. Blue dashed line shows correlation expressed in Equation 4.8.

ACI 209.R-92: Prediction of Creep, Shrinkage, and Temperature Effects in Concrete Structures (1992, reapproved in 1997) provides equations to predict creep and shrinkage deformations of concrete. Creep strains can be calculated from the prediction of the creep coefficient (Equation 5.9), while an expression for prediction of shrinkage strains is provided in the report (Equation 5.10).

$$\phi = \frac{t^{\psi}}{d + t^{\psi}} \cdot \phi_{\mathrm{u}} \tag{5.9}$$

$$\varepsilon_{sh} = \frac{t^{\alpha}}{f + t^{\alpha}} \cdot \left(\varepsilon_{sh}\right)_{\mathrm{u}} \tag{5.10}$$

where t is the time from loading for Equation 5.9 and the time from the beginning of drying for Equation 5.10, ϕ is the creep coefficient at time t, ϕ_u is the ultimate creep

coefficient, ε_{sh} is the shrinkage strain at time t, and $(\varepsilon_{sh})_u$ is the ultimate shrinkage strain. ψ, d, α, and f are constants that depend on member shape and size.

The value of ϕ_u depends on the age of loading, the ambient relative humidity, the volume-to-surface area ratio, the slump, fine aggregate-to-total aggregate ratio, and air content. The value of $(\varepsilon_{sh})_u$ depends on the cementitious material content, the ambient relative humidity, the volume-to-surface area ratio, the slump, fine aggregate-to-total aggregate ratio, and air content. ACI 209 recommends expressions to calculate ϕ_u and $(\varepsilon_{sh})_u$, and values for ψ, d, α, and f. They are not included in this document.

Values obtained from Equations 5.9 and 5.10 overestimate experimental creep and shrinkage strains (Figure 5.31) for the concrete studied in this research.

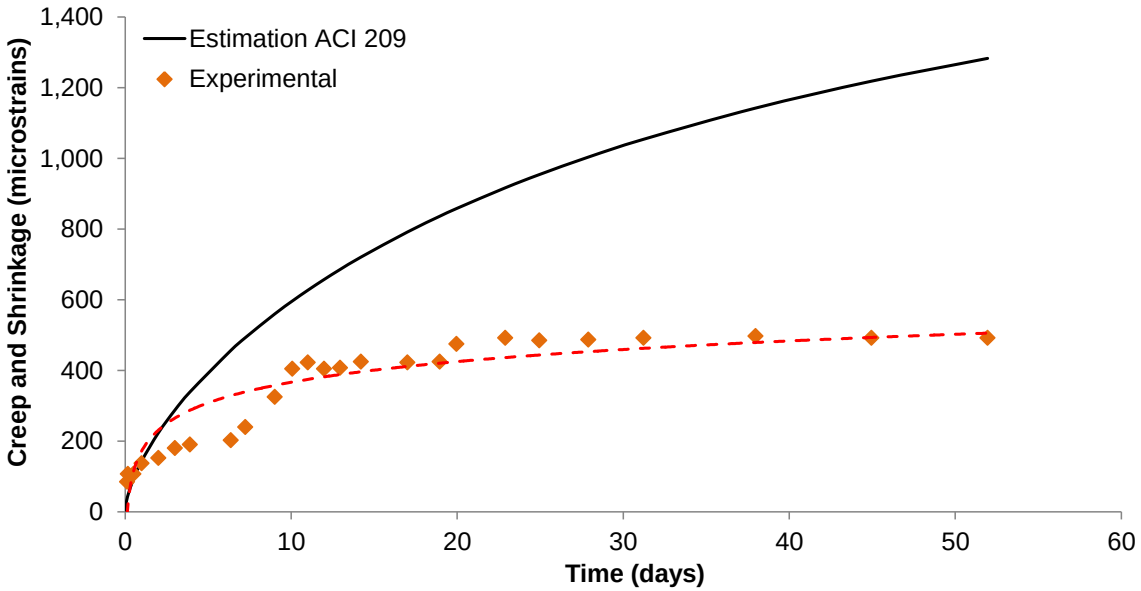

Figure 5.31 Creep plus shrinkage results compared to ACI 209 estimations. Red dashed line shows logarithmic correlation of experimental results.

Overall, the long-term creep response of the high-performance concrete used for the piles is much less than predicted using standard models and it is similar to the

behavior of very high-performance concrete used for long-span bridge girders in Georgia. Such lower creep deformations are expected to lead to reduced prestress losses in marine piles.

5.3.2.7 Rapid chloride permeability test (RCPT)

To evaluate the permeability to chloride ions of concrete, the standard ASTM C1202 test was performed on 2-in. (5.1 cm) long sections of 4×8-in. (10.2×20.3 cm) cylinders at 56 days. Three cylinders cured in fogroom were sawed to obtain the testing specimens. An average charge of 2,850 C (standard deviation of 156 C) passed during the test period of 6 hours. According to the standard, the chloride penetrability of this concrete can be categorized as "moderate."

Special Provision for GDOT Standard Specification 500 specifies a maximum chloride permeability at 56 days of 2,000 C for HPC, but Holland et al. (2012) proposed a maximum charge of 1,000 C passed during the test for a concrete to be considered a high-performance mixture for prestressed concrete piles exposed to marine environments. The two recommended ternary concrete mixtures given by Holland et al. (2012) for marine piles showed a total charge passed of 354 and 273 C, at 56 days.

5.4 Driving and Extraction of Piles

The driving capacity of piles using duplex HSSS 2205 strands was tested six months after the pile construction, and the driving performance was compared to that of piles constructed with conventional steel strands. Overdriving and reflective cracking of piles may be a concern in coastal zones, and they can compromise the durability of the structure. Reflective cracking can be produced by impact stress wave reflection when piles are driven into soft soils underneath hard soils; thin transverse cracks can be generated by the tensile stresses produced after the reflective wave (Holland et al., 2012). The three HSSS 2205 piles and two conventional AISI 1080 piles were driven to refusal into the Savannah River, and then they were extracted by use of a water jet to erode the soil next to the pile. In order to evaluate the ability of the piles to resist the impact loading during driving, the piles were examined for damage and cracking after pile extraction.

As a result of the driving operation, piles using duplex HSSS 2205 showed no spalling, visible damage or cracks. Also, the bearing capacity of these piles averaged 27% more than the design requirement, and the HSSS 2205 piles performed similarly to those using conventional steel strands. It was concluded that piles built with duplex HSSS 2205 strands can withstand the applied impact loading and be successfully driven without damage.

Section 5.4 details the driving operation and summarizes the driving capacity and behavior exhibited by the piles. The piles were driven at age 174 days and they were extracted the following day on the advice of the geotechnical engineer and the pile driving contractor; those experts explained that the river bottom soil would adhere so

tightly to the piles within two weeks that the piles could not be extracted. The flexural and shear testing of the piles were performed beginning 180 days after extraction.

5.4.1 Driving Operation and Procedures

Piles were driven into the Savannah River, in a space adjacent to an old dock at the Standard Concrete Products Company plant in Savannah, Georgia. The driving operation was performed by TIC Marine & Heavy Civil Corporation 174 days after the construction of the piles. They were extracted the following day. Figures 5.32 to 5.38 show the driving and extraction operations.

Piles were loaded onto a barge equipped with a crane and transported to a location about 50 ft. (15.2 m) from the river bank. A steel template was installed to place the piles and to assure vertical displacement during driving. A D-30 single-acting diesel hammer was used to drive the piles to refusal. A "refusal criterion", defined by the pile driving contractor as 10 blows of the hammer per ½-in. (12.7 mm), was selected to determine the end of the operation. Pile diving log, hammer specifications, and hammer bearing chart based on GDOT formula are given in Appendix K.

Figure 5.32 Piles being loaded onto a barge.

Figure 5.33 Barge, crane, and pile template in Savannah River, GA.

Figure 5.34 Lifting of pile SS #2 off the barge (left), and placing of pile SS #2 in the template (right).

Figure 5.35 Driving of pile SS #2 (left), and blow counting of pile SS #2 (right).

Figure 5.36 Final condition of piles after driving operation.

Figure 5.37 Positioning of the water jet (left) and extraction of pile SS #1 (right).

Figure 5.38 Preparation to extract pile SS #1 (left), and extraction of pile SS #1 (right).

At the end of the driving operation, piles were extracted using a water jet system and carefully monitored to find reflective cracks, spalling, and other evidences of damage due to pile driving or extraction.

Then, piles were cut in halves in order to be transported to Georgia Tech Structures and Materials Lab for flexural and shear testing of piles (Figure 5.39). Description and results of these tests are presented in Sections 5.5 and 5.6, respectively.

Figure 5.39 70-feet long piles were cut in halves and transported to Georgia Tech Structures and Materials Lab in Atlanta, GA.

5.4.2 Results

Pile driving was stopped by the contractor after the required capacity was greatly exceeded. The bearing capacity of the piles, estimated at the end of the driving operation, can be observed in Table 5.10. The capacity of the piles was 18% to 37% higher than the required design capacity (82 tons, 10 blows per ½-in. [12.7 mm]).

Table 5.10 Pile driving results for AISI 1080 steel and duplex HSSS 2205 strands. 1-in. = 2.54 cm.

	Penetration per 10 Blows (in.)	**Bearing Capacity** (ton)	**Bearing to Design Capacity**
Pile AISI 1080 #1	1.75	97	1.18
Pile AISI 1080 #2	1.25	112	1.37
Pile HSSS 2205 #1	1.50	104	1.27
Pile HSSS 2205 #2	1.50	104	1.27
Pile HSSS 2205 #3	1.50	104	1.27

Additionally, no damage, spalling or visible cracking was observed after driving in piles using duplex HSSS 2205 strands, while one of the piles including conventional steel exhibited a small hairline crack.

5.5 Flexural Capacity of Piles

Flexural behavior of piles was tested using the 70-ft. (21.3 m) long specimens, cut into two 35-ft. (10.7 m) long sections after the pile driving operation described in Chapter 5. The ten 35-ft. (10.7 m) sections were transported to Georgia Tech Structures and Materials Lab.

Six piles using duplex HSSS 2205 strands and four piles using conventional AISI 1080 steel strands were tested in a four-point flexure setup (see Figure 5.40).

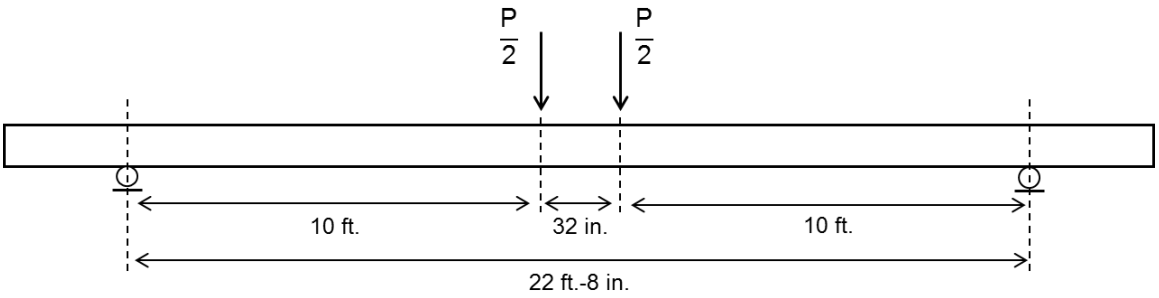

Figure 5.40 Diagram of flexure test. **(**1-in. = 2.54 cm, 1-ft. = 30.5 cm)

This chapter presents a description of the flexure test, a summary of the results, and a comparison with the behavior predicted by ACI 318 and AASHTO LRFD.

5.5.1 Flexure Test Setup

The piles were supported by rollers and loaded at their mid-length by a 2-point load system. The load was applied by a 500 ton hydraulic ram and recorded using a 200 kip (890 kN) load cell. A steel beam supported by rollers was used to transfer the load from the hydraulic ram to the piles as illustrated in Figure 5.41. The mid-length deflection of the piles was measured using a string potentiometer. Three digital gauge dials were attached to one side of the piles, in order to estimate the strains in the prestressing strands at pile failure. Two dials were attached to the pile at 1-in. (2.54 cm) from the top and from the bottom, while a third was installed at the mid-height of the pile. Initially, a gauge length of 13-in. (33.0 cm) was used for the first four tests (pile 1080-1 Bottom, pile HSSS-1 Bottom and Top, and pile HSSS-3 Bottom); the gauge length was increased to 18-in. (45.7 cm) for the rest of the tests in order to cover the more extensive flexural cracking region. Strains were similar for both gauge lengths. The load was applied monotonically and was paused to mark crack patterns.

While the load-deflection data were recorded even after crushing of the concrete, the dial gauges were removed before the ultimate load to avoid damage. As a consequence, load-deflection curves show the behavior of the piles along the whole duration of the test, but some moment-curvature results calculated from strain and load measurements do not represent the complete behavior of the piles before failure. In these cases, the ultimate point was estimated from the load-deflection data, using a moment-area technique. The application of the moment-area method for the calculation of the ultimate curvatures is given and calculated ultimate curvatures are shown in Appendix L.

Average concrete compressive strength of individual piles (see Section 5.3.2) and the actual position of the strands (Appendix G) were used in the calculation of the flexural nominal strength. Also, a Todeschini stress block was assumed for the estimation of concrete compressive stresses (Wight and MacGregor, 2011) for ACI 318 method and a rectangular stress block was assumed for AASHTO calculations. ACI 318 and AASHTO calculations are given in Appendix M.

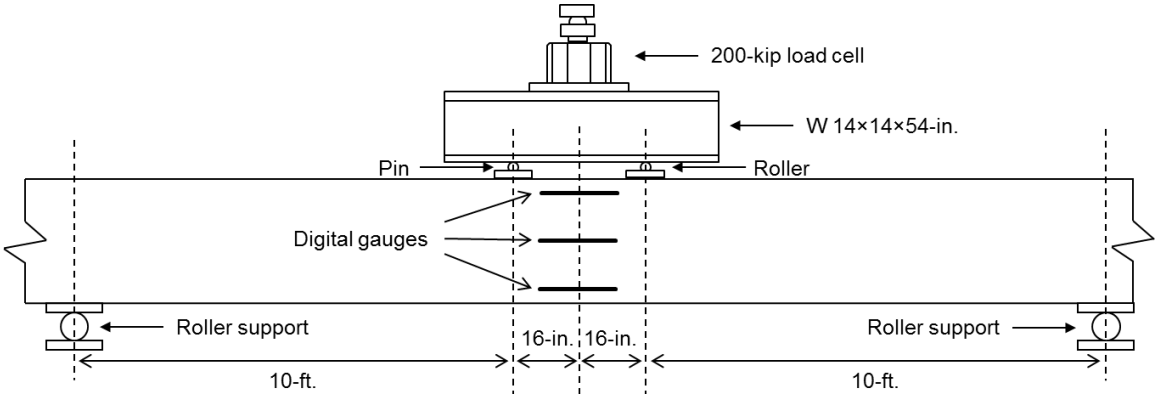

(a)

(b)

Figure 5.41 Flexure test setup. (1-in. = 2.54 cm, 1-ft. = 30.5 cm)

5.5.2 Results

Flexure tests of piles exhibited typical flexure, concrete crushing failures, with flexural cracks approximately evenly distributed every 10-in. (25.4 cm) and propagating from the bottom of the pile. The maximum crack widths were about 0.06-in. (1.52 mm). First crack was observed at an applied load between 15 (66.7 kN) to 20 kips (89.0 kN). Failure by concrete crushing at the top of the pile was observed in all the tests, as predicted by calculations in Appendix M. The calculated moments and curvatures, the load-deflection and moment-curvature curves compared to predicted curves, the changes of the strain distribution along the depth of the pile during the test, and the crack pattern close to failure of each tested pile are detailed in Appendix N and they are summarized in Tables 5.11 and 5.12. Errors in the strain gauge measurements occurred in piles HSSS 2205 #1 – bottom half, HSSS 2205 #3 – bottom half, and AISI 1080 #2 – top half. Only the load-deflection curve and the crack pattern are presented in these cases.

Table 5.11 Experimental and calculated ultimate moments. (1 kip·in = 113 N·m)

Pile	M_{exp} (kip·in)	$M_{u,ACI}$ (kip·in)	$M_{u,AASHTO}$ (kip·in)	$\frac{M_{u,exp}}{M_{u,ACI}}$	$\frac{M_{u,exp}}{M_{u,AASHTO}}$
AISI 1080 #1 – Top	2,585	2,436	2,406	1.06	1.07
AISI 1080 #1 – Bottom	2,507	2,436	2,419	1.03	1.04
AISI 1080 #2 – Top	2,654	2,530	2,313	1.05	1.15
AISI 1080 #2 – Bottom	2,686	2,530	2,321	1.06	1.16
HSSS 2205 #1 – Top	2,872	2,634	2,560	1.09	1.12
HSSS 2205 #1 – Bottom	2,835	2,634	2,564	1.08	1.11
HSSS 2205 #2 – Top	2,954	2,908	2,615	1.02	1.13
HSSS 2205 #2 – Bottom	3,044	2,877	2,560	1.06	1.19
HSSS 2205 #3 – Top	2,920	2,856	2,606	1.02	1.12
HSSS 2205 #3 – Bottom	2,868	2,866	2,606	1.00	1.10

Table 5.12 Experimental and calculated ultimate curvatures. (1 rad/in = 39.37 rad/m)

Pile	φ_{exp} (rad/in)	$\varphi_{u,ACI}$ (rad/in)	$\varphi_{u,AASHTO}$ (rad/in)	$\frac{\varphi_{exp}}{\varphi_{u,ACI}}$	$\frac{\varphi_{exp}}{\varphi_{u,AASHTO}}$
AISI 1080 #1 – Top*	1.073×10^{-3}	1.043×10^{-3}	8.819×10^{-4}	1.03	1.22
AISI 1080 #1 – Bottom	1.235×10^{-3}	1.043×10^{-3}	8.849×10^{-4}	1.18	1.40
AISI 1080 #2 – Top	--------	8.876×10^{-4}	7.190×10^{-4}	--------	--------
AISI 1080 #2 – Bottom*	1.013×10^{-3}	8.876×10^{-4}	7.190×10^{-4}	1.14	1.41
HSSS 2205 #1 – Top*	9.071×10^{-4}	9.146×10^{-4}	6.960×10^{-4}	0.99	1.30
HSSS 2205 #1 – Bottom	--------	9.146×10^{-4}	6.960×10^{-4}	--------	--------
HSSS 2205 #2 – Top	8.738×10^{-4}	8.873×10^{-4}	7.005×10^{-4}	0.98	1.25
HSSS 2205 #2 – Bottom	8.488×10^{-4}	8.921×10^{-4}	6.989×10^{-4}	0.95	1.21
HSSS 2205 #3 – Top	7.956×10^{-4}	9.042×10^{-4}	7.157×10^{-4}	0.88	1.11
HSSS 2205 #3 – Bottom	--------	9.018×10^{-4}	7.131×10^{-4}	--------	--------

* $\varphi_{u,exp}$ estimated using moment-area method.

Experimental ultimate moments were calculated using the load and actual distances between supports and applied load. Ultimate curvatures were calculated using strain measurements and corrected, when possible, by the moment-area method. Differences in calculated ultimate moments were caused by differences in concrete strengths and small differences in measured locations of the prestressing strands through the length of the piles.

Figure 6.3 shows the load-deflection curves of the flexure tests. At lower loads, close to the cracking point, greater deflections are observed in piles with the duplex HSSS 2205 strands compared to those with the conventional strand. This behavior can be attributed to the lower flexural stiffness as a result of the lower elastic modulus of stainless steel compared to conventional steel. Piles using stainless steel reinforcement

exhibited higher ultimate loads, which were expected due to the greater area of prestressing strand used.

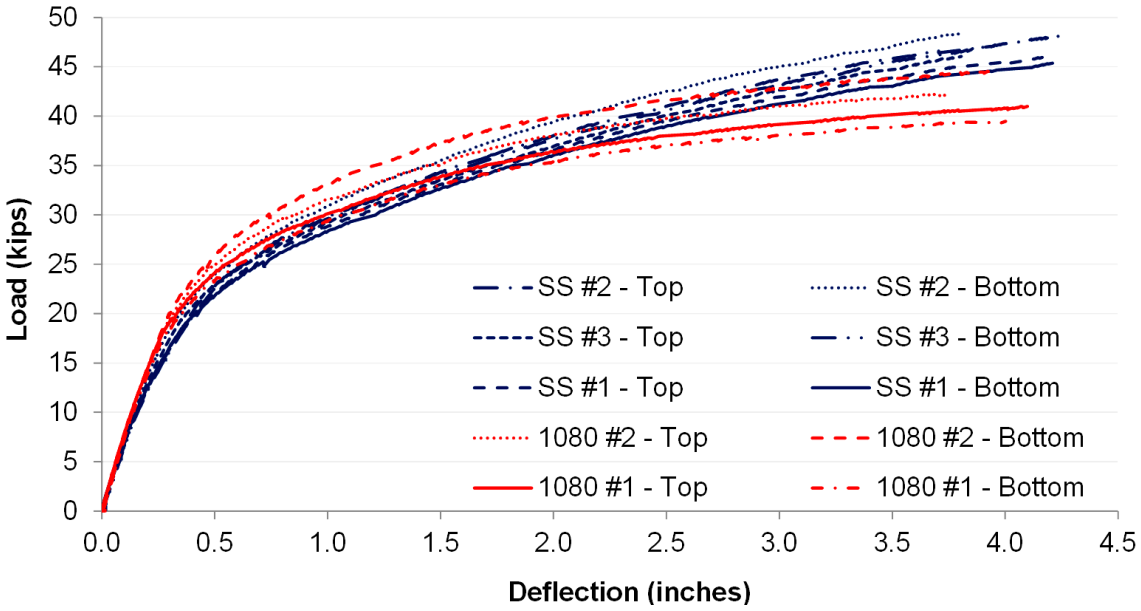

Figure 5.42 Summary of load-deflection (P-δ curves) for HSSS 2205 (blue) and AISI 1080 steel (red). (1 kip = 4.45 kN)

Figures 5.43 and 5.44 show moment-curvature results obtained from experimental data and the theoretical behavior, predicted by ACI 318. The moment at each point was calculated from the recorded applied load, while the curvature was calculated from the deformations measured by the dial gauges. When possible, the ultimate curvature was estimated using the moment-area method. In these cases, a dashed line shows the extended moment-curvature response after the strain gauges were removed.

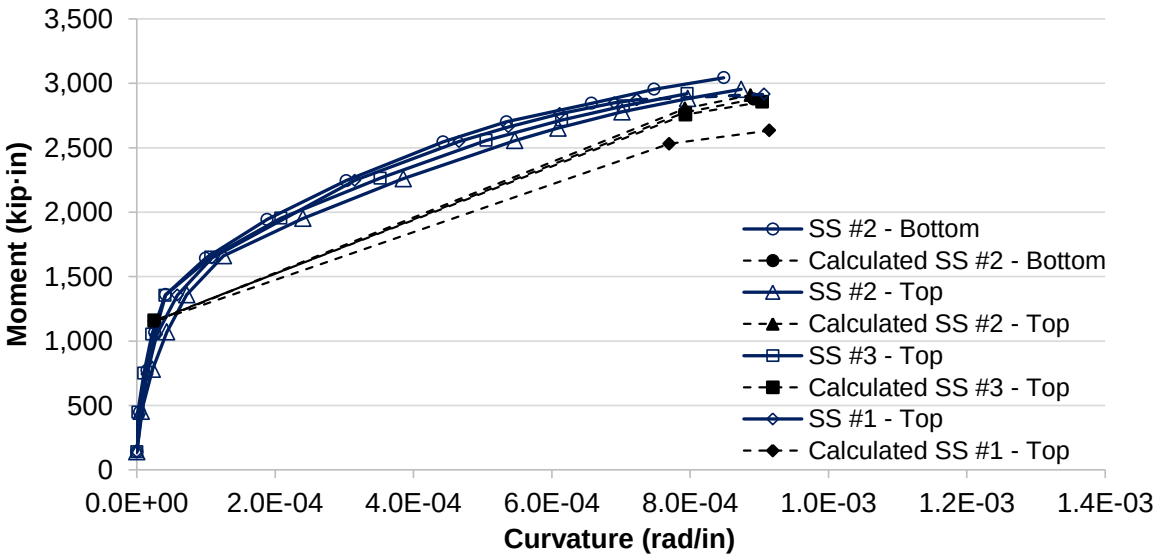

Figure 5.43 Summary of moment-curvature curves for piles using duplex HSSS 2205. Results are compared with calculated curves using ACI 318.
(1 kip·in = 113 N·m)

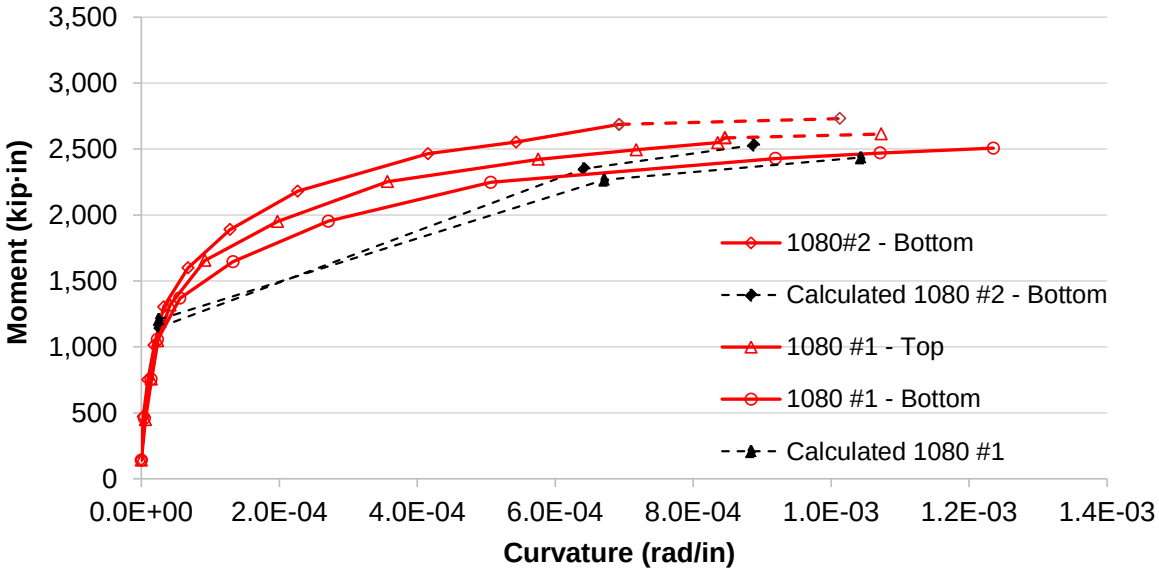

Figure 5.44 Summary of moment-curvature curves for piles using AISI 1080 steel. Results are compared with calculated curves using ACI 318.
(1 kip·in = 113 N·m)

Figures 5.45 and 5.46 show the comparison of moment-curvature results with the predicted behavior by AASHTO LRFD.

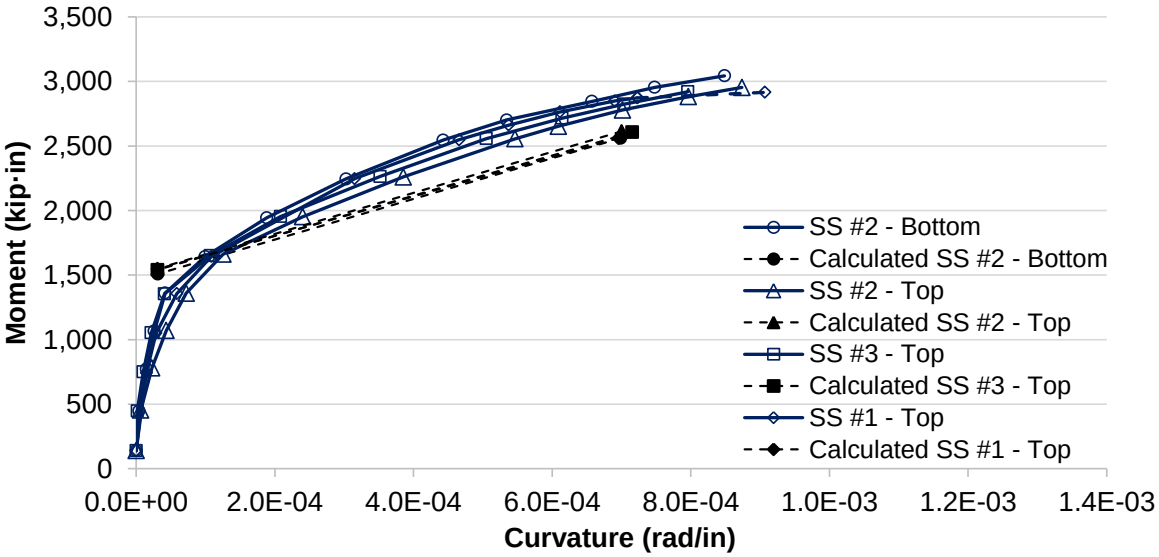

Figure 5.45 Summary of moment-curvature curves for piles using duplex HSSS 2205. Results are compared with calculated curves using AASHTO LRFD. (1 kip·in = 113 N·m)

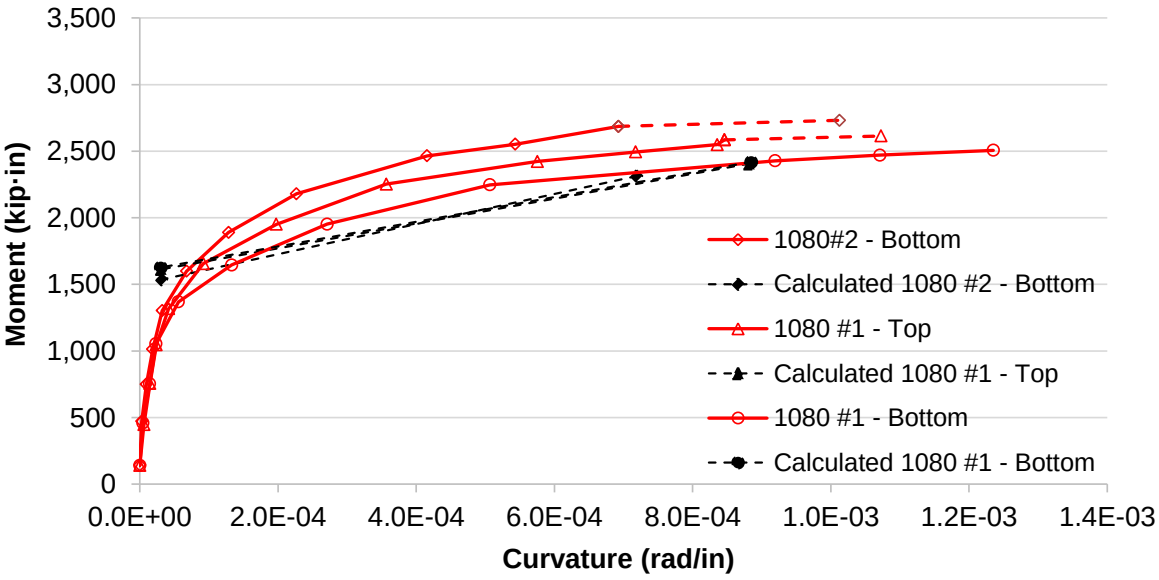

Figure 5.46 Summary of moment-curvature curves for piles using AISI 1080 steel. Results are compared with calculated curves using AASHTO LRFD. (1 kip·in = 113 N·m)

5.5.2.1 Comparison of results with ACI 318 and AASHTO LRFD

All the piles exhibited a higher ultimate moment than the predicted values using conventional analysis based on AASHTO LRFD and ACI 318.

Piles using duplex HSSS 2205 strands showed lower ultimate curvatures than the predicted values using ACI 318 and higher ultimate curvatures using AASHTO LRFD. This lower ductility is a consequence of the smaller plastic deformation range of duplex HSSS 2205 compared to AISI 1080 steel. The ultimate strains of duplex HSSS 2205 and conventional steel strands from direct tension tests were 1.60% and 5.89%, respectively.

5.5.2.2 Effect of type of steel

Piles using duplex HSSS 2205 strands showed a lower ultimate curvature and a higher ultimate moment compared to piles with conventional steel strands.

In the case of piles using conventional steel, the higher ultimate curvature of pile 1080 #1 compared to 1080 #2 can be attributed to the higher compressive strength of concrete used in pile 1080 #1 (see Section 5.3.2.2).

Additionally, at the moment of failure due to concrete crushing at the top of the pile, at least the bottom layer of stainless and conventional steel strands was yielding. Then, small increments of the load produced the breakage of duplex HSSS 2205 strands, while conventional strands were able to deform without failing for a considerably higher load increase.

5.5.2.3 Concrete at failure

The ultimate strain of concrete at the top section, calculated from the dial gauge measurements, ranged between 0.2% and 0.23%, lower than the assumed value of 0.3% used in ACI 318 and AASHTO LRFD. The lower extensibility of high-strength concrete, as mentioned in Section 5.3.2.5, is thought to be responsible for this difference.

5.6 Shear Capacity of Piles

The shear capacities of the piles were tested at each end of each 35-ft. (10.7 m) long pile segment; testing was conducted after the pile driving and extraction. Simply supported piles were loaded at a shear span approximately two times the pile height as illustrated in Figure 5.47. Through this configuration, two different spiral reinforcement spacings, 3-in. (7.6 cm) and 6-in. (15.2 cm), were tested per pile segment.

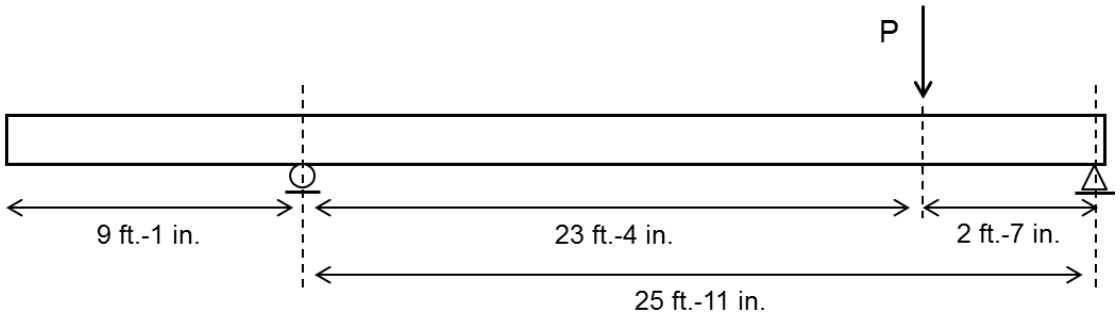

Figure 5.47 Diagram of shear test. **(**1-in. = 2.54 cm, 1-ft. = 30.5 cm)

Shear tests were performed on twelve pile segments reinforced with austenitic SS 304 transverse spiral reinforcement and eight pile segments reinforced with AISI 1080 transverse spiral reinforcement.

Shear failure of the piles was observed in every test, and no significant statistical difference was found in the ultimate shear and deflection of the piles, regardless of the spacing and type of transverse or longitudinal reinforcement tested. It was concluded that the replacement of conventional wire shear reinforcement with SS 304 wire spiral reinforcement in prestressed concrete piles produces equivalent shear capacity.

This section describes the shear tests and provides the analysis of the results.

5.6.1 Shear Test Setup

Figure 5.48 shows the detailed setup of the shear test. Piles 35-ft. (10.7 m) long were simply supported and a load was applied at 31-in. (78.7 cm) from the pin support. The load was applied using a 500 ton hydraulic ram and recorded every 0.5 seconds using a 200 kip (890 kN) load cell. The deflection was recorded using a wire potentiometer epoxied to the bottom of the pile at the same distance to the support from the applied load.

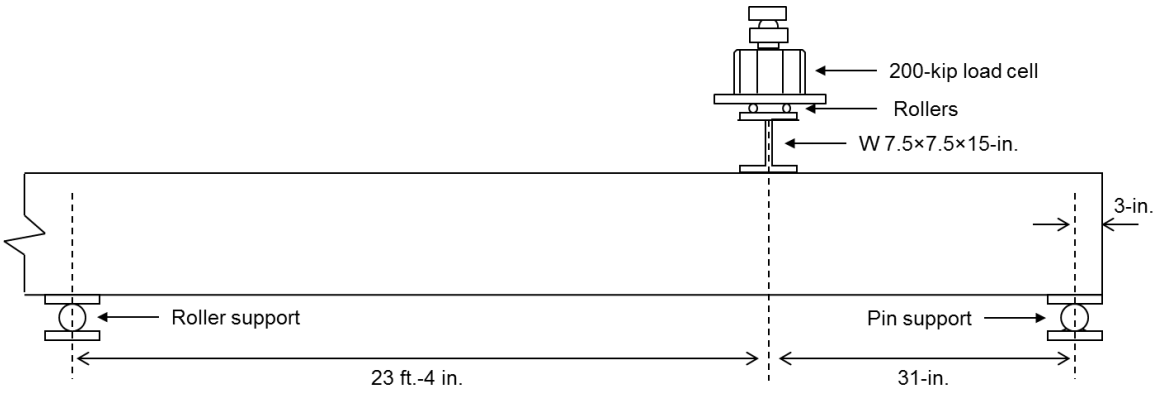

Figure 5.48 Shear test setup. (1-in. = 2.54 cm, 1-ft. = 30.5 cm)

In order to calculate the shear from the load measurements, the actual value of the nominal distances shown in Figure 5.48 were measured before every test. Actual shear

span of 31.00-in. (78.74 cm) was measured in 65% of the tests and deviations no higher than 1 inch from this value were observed in the rest of the tests; the actual shear span was considered in the analysis of results. Rollers at the load application beam assured no longitudinal restraint of the pile (Figure 5.49).

Errors in test set-up and loading procedures occurred in tests of piles HSSS #2 and #3, top halves, and their results were not considered for the analysis of the results.

Figure 5.49 Load application system.

5.6.2 Results and Discussion

The first crack appeared when the shear at the loading point reached 45 (200 kN) to 50 kips (222.4 kN) and the deflection was close to 0.2-in. (5.08 mm). A shear crack propagated from the bottom of the pile, at a distance of 15-in. (38.1 cm) to 20-in. (50.8 cm) from the support, in the direction of the applied load with an angle close to 45°.

Evidence of concrete crushing at the top of the beam and initiation of bond failure was observed at the end of the test (see Figure 5.50).

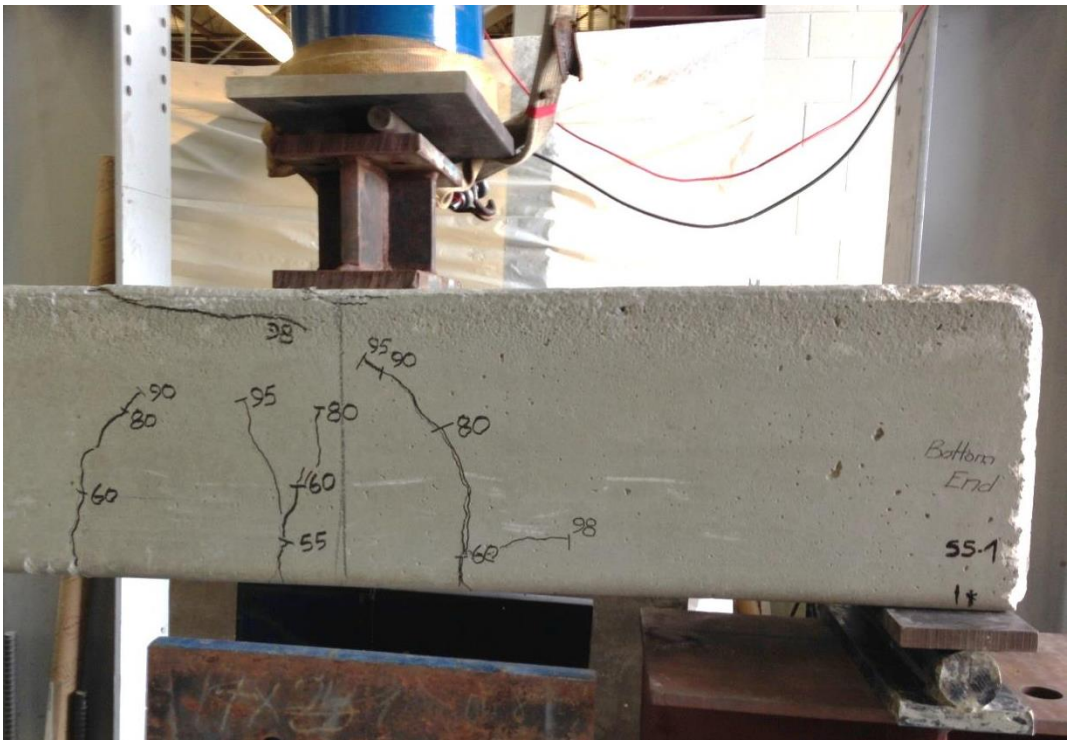

Figure 5.50 Typical crack pattern at failure. Numbers on the pile indicate the applied load when cracks appeared. (1 kip = 4.45 kN)

Examples of nominal shear strength calculations according to ACI 318 and AASHTO LRFD are given in Appendix O.

A summary of the experimental and calculated ultimate shear capacities of the piles is given in Table 5.13. A summary of the ultimate shear of every tested pile is given in Appendix P.

Table 5.13 Comparison of average ultimate shear with ACI 318 and AASHTO LRFD nominal shear strengths. (1 kip = 4.45 kN, 1-in. = 2.54 cm)

Pile – Spacing	$\mathbf{V}_{u,exp}$ (kips)	$\mathbf{V}_{u,ACI}$ (kips)	$\mathbf{V}_{u,AASHTO}$ (kips)	$\frac{V_{u,exp}}{V_{u,ACI}}$	$\frac{V_{u,exp}}{V_{u,AASHTO}}$
HSSS 2205 – 3-in.	88.8	68.6	72.9	1.29	1.22
HSSS 2205 – 6-in.	93.4	58.2	62.4	1.61	1.50
AISI 1080 – 3-in.	87.1	70.9	75.3	1.23	1.16
AISI 1080 – 6-in.	88.9	59.6	63.9	1.49	1.39

It can be observed that the use of SS 304 spiral wire reinforcement is conservative with respect to ACI 318 and AASHTO LRFD provisions. In piles using stainless steel, ACI 318 predicts a nominal shear strength 23% and 38% lower than the average value obtained experimentally for spacings 3-in. (7.6 cm) and 6-in. (15.2 cm), respectively, while AASHTO LRFD predicts a nominal shear strength 18% and 33% lower than the average value obtained experimentally for spacings of 3-in. (7.6 cm) and 6-in. (15.2 cm), respectively.

5.6.2.1 Shear-deflection curves

Figures 5.51 and 5.52 show the shear-deflection curves of the piles until failure. For the HSSS 2205 piles, the black lines are used for the 3-in. (7.6 cm) spiral spacing and blue lines for the 6-in. (15.2 cm) spiral wire spacing. For the AISI 1080 piles, the red lines are used for the 3-in. (7.6 cm) spiral spacing and green lines for the 6-in. (15.2 cm) spiral wire spacing.

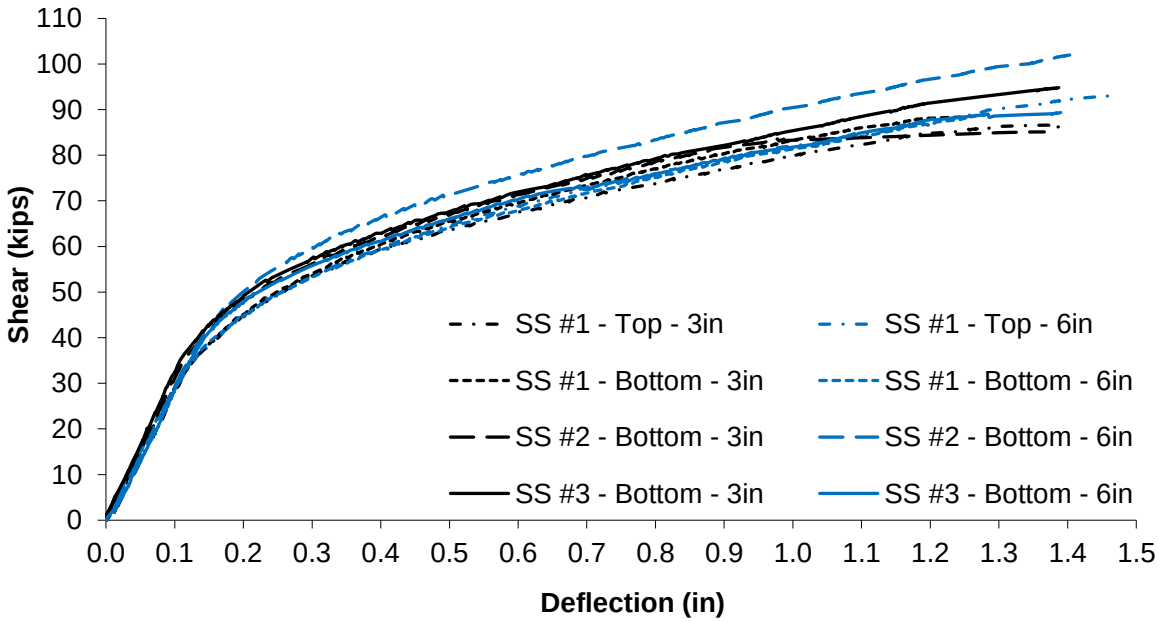

Figure 5.51 Shear-deflection curves for HSSS 2205 piles (spacings 3-in. [7.6 cm] and 6-in. [15.2 cm]).

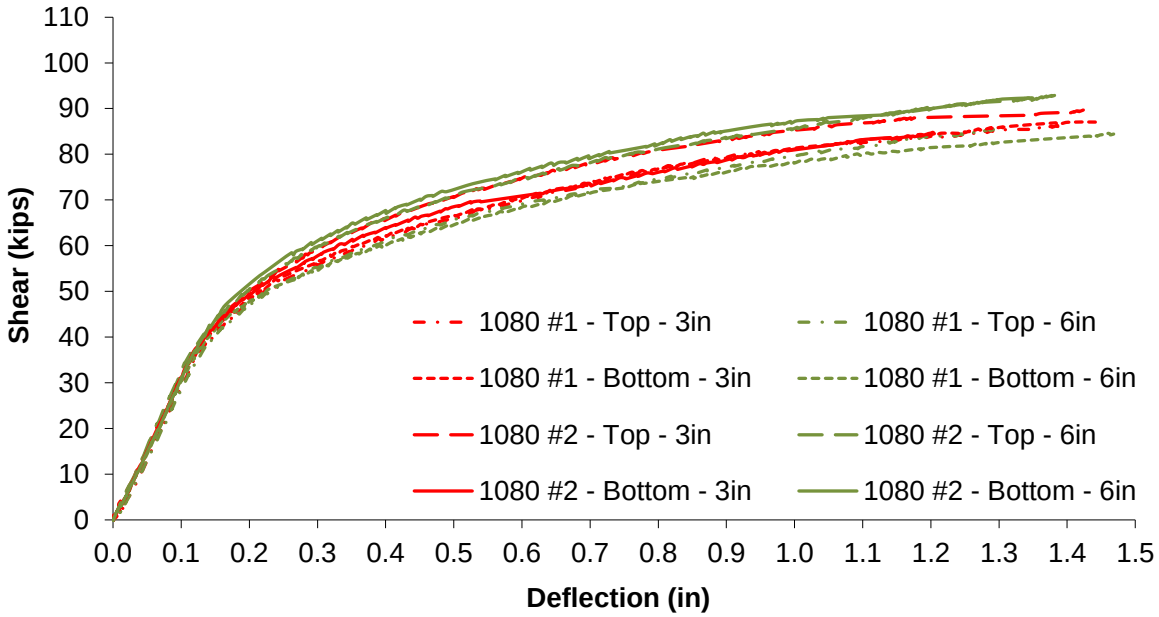

Figure 5.52 Shear-deflection curves for AISI 1080 piles (spacings 3-in. [7.6 cm] and 6-in. [15.2 cm]).

Figure 5.53 and 5.54 gives the shear force divided by $\sqrt{f'_c}$ for the HSSS 2205 piles and the AISI 1080 piles with 3-in. and with 6-in. spiral spacing, respectively.

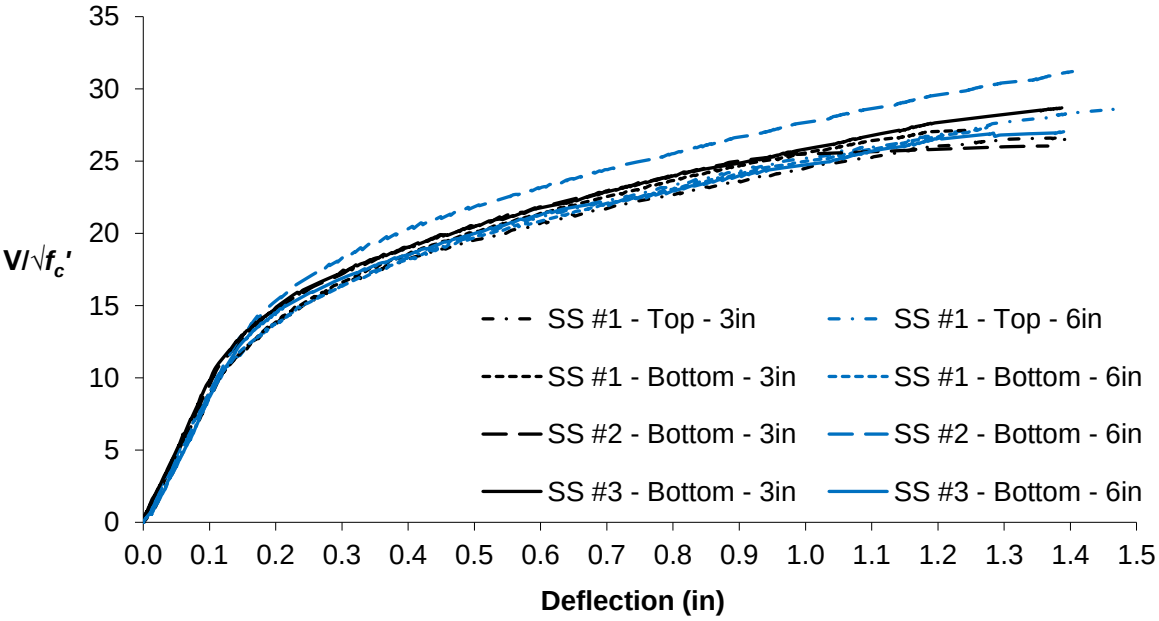

Figure 5.53 Shear divided by $\sqrt{f'_c}$ for HSSS 2205 piles (spacings 3-in. and 6-in.).

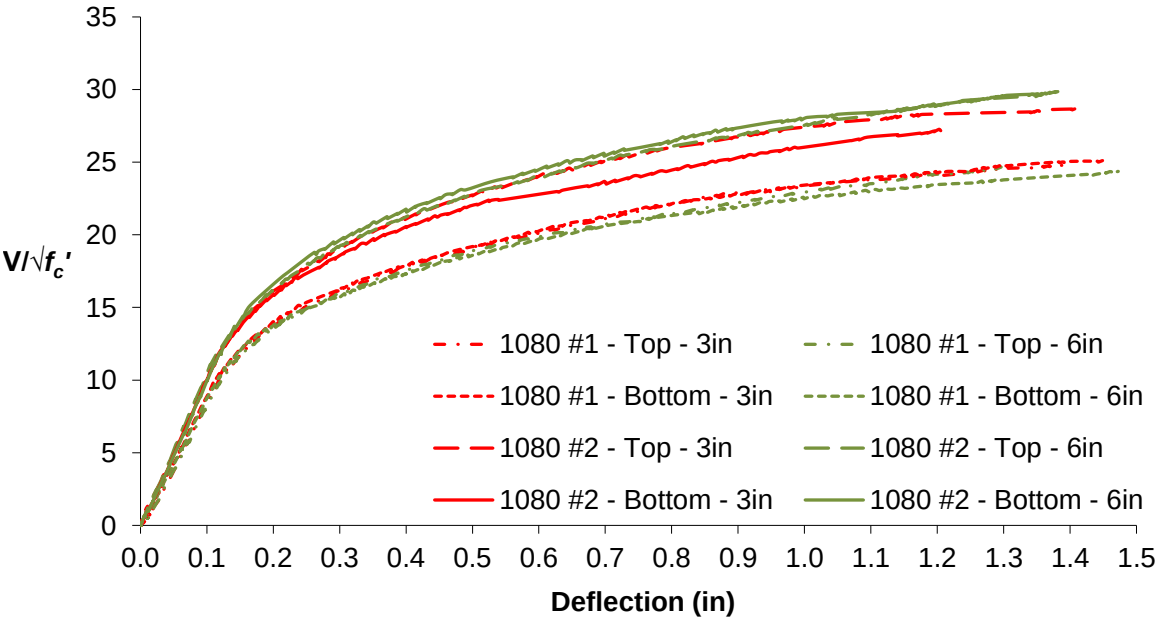

Figure 5.54 Shear divided by $\sqrt{f'_c}$ for AISI 1080 piles (spacings 3-in. and 6-in.).

Normalized shear by $\sqrt{f'_c}$ shows different trends depending on the type of prestressing steel. For piles using stainless steel, the strength of concrete shows no important effect on total shear, while the contribution of concrete to total shear on piles using conventional steel is different for both tested piles. The same observation is obtained for the calculated contribution of concrete by ACI 318 and AASHTO LRFD (Table 5.14).

Table 5.14 Shear strength provided by concrete, V_c, according to ACI 318 and AASHTO LRFD. (1 kip = 4.45 kN)

Pile	$\mathbf{V_{c,ACI}}$ (kips)	$\mathbf{V_{c,AASHTO}}$ (kips)
HSSS 2205 #1	47.65	51.94
HSSS 2205 #2	47.74	52.05
HSSS 2205 #3	48.04	52.40
AISI 1080 #1	49.75	54.33
AISI 1080 #2	46.65	50.94

5.6.2.2 Statistical analysis of results

In Figures 5.51 and 5.52, no clear difference is observed in the shear behavior of the piles using 3-in. (7.6 cm) and 6-in. (15.2 cm) spacing. Thus, statistical similarity of the ultimate shear and deflection was tested using ANOVA. The results of the statistical analysis are shown in Tables 5.15 and 5.16.

Table 5.15 Statistical analysis of ultimate shear results.

Test	Decision ($\alpha = 5\%$)	p-value
H_0: $\mu_{1080} = \mu$	Fail to Reject H_0	47.24%
H_0: $\mu_{2205} = \mu$	Fail to Reject H_0	25.20%
H_0: $\mu_i = \mu$	Fail to Reject H_0	25.64%
H_0: $\mu_{1080\text{-}1} = \mu_{1080\text{-}2}$	Fail to Reject H_0	8.89%

Table 5.16 Statistical analysis of ultimate deflection results.

Test	Decision ($\alpha = 5\%$)	p-value
H_0: $\mu_{1080} = \mu$	Fail to Reject H_0	91.15%
H_0: $\mu_{2205} = \mu$	Fail to Reject H_0	58.10%
H_0: $\mu_i = \mu$	Fail to Reject H_0	95.15%

No significant difference is found between piles using conventional transverse reinforcement and piles reinforced with SS 304 spiral wire, for an α=5% significance level. Also, similarity of means is observed between tests performed on different spiral wire spacing.

5.7 Prestress Losses of Piles

As described in Section 5.2.2, prestress losses were measured using VWSGs embedded at 17.5 ft. (5.3 m) from each end of each pile. VWSGs were installed before concrete placement (Figure 5.55). The "zero," initial measurement was taken immediately before strand release, and subsequent measurements were taken right after strand release, before and after pile driving, and at intermediate times (Figure 8.1). The final measurement was performed before shear and flexural testing of the piles, 335 days after the initial measurement.

Figure 5.55 Strain gauge installation (left) and measurement of strains (right).

Experimental results were compared with the refined and lump-sum estimation methods described in AASHTO LRFD (2013) and as illustrated in Appendix Q. The

refined method calculates the total prestress loss in pretensioned elements as the sum of the losses due to elastic shortening at jacking, relaxation of steel, and shrinkage and creep of concrete. The lump-sum method estimates long-term losses (creep and shrinkage of concrete and relaxation of steel stress) using a single formula.

Losses predicted by the AASHTO LRFD refined method were 59% higher than the measured values. It was concluded that the use of AASHTO LRFD for the estimation of prestress losses of duplex HSSS 2205 strands is conservative.

Also, duplex HSSS 2205 strands exhibited similar early loss of the initial prestress and higher losses at later ages compared to conventional strands. GDOT Standard 3215 specifies a maximum loss of 22% of the initial pretension force. At 335 days, losses of the initial prestressing load of 7.84% and 9.39% were measured for AISI 1080 steel and duplex HSSS 2205 strands, respectively. The AASHTO refined method predicts that losses at 335 days are approximately 90% of the total losses considering a service life of 100 years for the analyzed prestressed concrete piles. Thus, it is very unlikely that prestress losses in prestressed concrete piles will surpass the GDOT Standard 3215 limit for loss of pretension force.

5.7.1 Results

Using vibrating wire strain gauges, the strains of the concrete over time and the internal temperature were obtained. Perfect bond between the strands and concrete was assumed so that the change in strain of the concrete equaled the change in strain of the prestressing strands. Variations in concrete internal temperature were accounted for by calculating the relative thermal deformation of the steel vibrating wire with respect to

concrete. The assumed coefficients of thermal expansion for steel and concrete were 12.2 and 10.2 με/°C (6.78 and 5.67 με/°F), respectively. Using the elastic modulus of the strands, obtained from tensile strength tests (Section 5.3.1), the prestress losses were calculated from the strain readings.

5.7.1.1 Experimental losses compared with the AASHTO refined method

Prestress losses during the first 335 days are shown in Figure 5.56 for conventional steel and duplex HSSS 2205 strands. Measured prestress losses are compared with AASHTO estimated values (black lines in the figure), calculated with the refined method (see calculations given in Appendix Q).

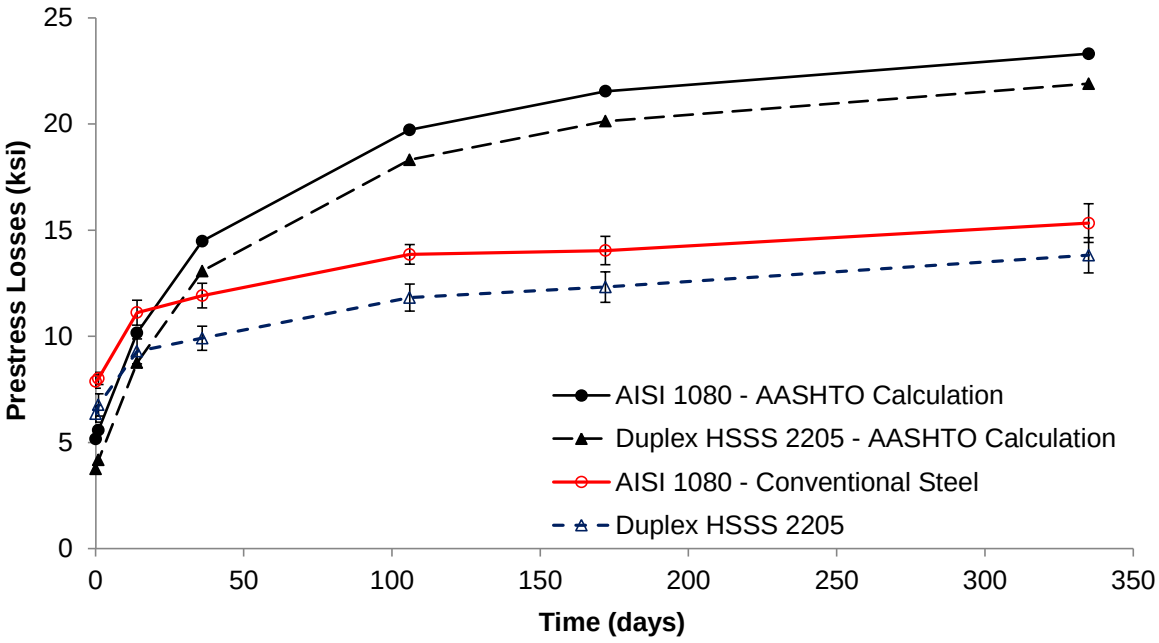

Figure 5.56 Prestress losses during the first 335 days. (1 ksi = 6.9 MPa)

The measured losses during the first 14 days were higher than the predicted AASHTO values, while at later ages the values predicted by AASHTO were significantly larger than the experimental results.

In Table 5.17, the influence of each source of prestress loss in total experimental losses is compared with the corresponding AASHTO predictions at 335 days. Relaxation of steel stress was estimated from experimental results (Schuetz, 2013) and added to losses measured using embedded strain gauges.

Table 5.17 Comparison between experimental and predicted prestress losses at 335 days. (1 ksi = 6.9 MPa)

	Duplex HSSS 2205		**AISI 1080 Steel**	
	Experimental (ksi)	AASHTO predictions (ksi)	Experimental (ksi)	AASHTO predictions (ksi)
Jacking Stress	144.9	144.9	196.8	196.8
Elastic Shortening (ES)	6.3	3.6	7.9	4.5
Stress Relaxation (RE)	4.2*	0.073	4.7*	0.567
Creep plus Shrinkage (ASTM C512)	15.5**	18.2	19.4**	18.2
Creep plus Shrinkage (Measured, CR + SH)	7.5	18.2	7.4	18.2
Total Losses (ES + CR + SH + RE)	18.0	21.9	20.1	23.3

* Experimental stress relaxation calculated from experimental values obtained by Schuetz (2013) for initial stress of 70% UTS.
** Experimental creep and shrinkage losses estimated from results of ASTM C512 standard test.

Experimental elastic shortening corresponds to the first measurement of prestress losses on the piles, performed after strand release. The values are approximately 75% higher than AASHTO predicted values, but it is expected that part of the stress relaxation of the prestressing strands occurred at the time of the first reading. Schuetz (2013)

determined that as much as a 25% of the stress relaxation measured at 1,000 hours for HSSS 2205 strands can occur in one hour after the application of the prestressing force.

Time-dependent losses (creep, shrinkage, and stress relaxation losses) show a higher difference between experimental and predicted values. This difference corresponds mostly to creep and shrinkage losses estimation. Even though estimated creep and shrinkage losses from ASTM C512 test results (Section 5.3.2.6) are relatively closer to AASHTO predictions, experimental time-dependent losses measured in the piles, which correspond to the measurements after the first reading, are approximately 60% lower than predicted values. It is noted that the creep and shrinkage tests were performed under a relative humidity of 50% while the piles were at relative humidity between 70% (Savannah, Georgia) and 100% (Savannah River and exposed to rain). The higher humidity would reduce the combined creep and shrinkage strains.

At 335 days, predicted losses were approximately 22% higher than experimental results, including stress relaxation estimation, for duplex HSSS 2205. Additionally, if a service life of 100 years for the piles is considered, the AASHTO refined method predicts that losses at 335 days represent about 90% of total, 100-year losses for both types of strands (Table 5.18).

Table 5.18 Ratio of experimental to calculated losses at 335 days and estimated losses at 100 years.

Pile	**Calc/Exp at 335 days**	**AASHTO Losses 100 years** (ksi)	**AASHTO Losses 100 years** (MPa)	**AASHTO Losses 100 years** (με)
AISI 1080 Steel	1.16	25.61	176.57	871
Duplex HSSS 2205	1.22	24.20	166.85	1,030

5.7.1.2 Effect of pile driving and type of prestressing steel

The pile-driving operation was performed at day 174 from initial prestress application. As a result, no significant effect on prestress losses due to driving was observed.

Also, when prestress losses in each end of the piles are analyzed (see separated graphs in Appendix R), no clear differences are observed. Two piles using duplex HSSS 2205 strands and one pile using conventional steel strands exhibit similar prestress loss values, at both ends. On the contrary, piles AISI 1080 #1 and HSSS 2205 #3 show higher prestress losses on the end closer to the jacking end of the prestressing form.

It was also observed in Table 5.17 that higher average values of prestress losses are obtained with the AISI 1080 steel strands. This difference is properly predicted by AASHTO. However, considering the lower elastic modulus of duplex HSSS 2205 strands, these prestress losses represent lower strains than in conventional steel.

Since duplex HSSS 2205 and conventional steel strands were prestressed at 60% and 70% of the UTS, respectively, a proper comparison should include the loss of the initial prestress of each type of strand. It is noted that the relaxation loss of prestressing force in each strand type was about 2.5% if loaded to 70% of UTS.

Figure 5.57 shows the loss of initial prestress with time. The initial elastic loss in the piles with HSSS 2205 and in piles with conventional strands was similar. The long-term loss in piles with duplex HSSS 2205 strands is slightly larger than the loss in piles with conventional strand. Considering the initial prestress of each strand (60% UTS vs. 70% UTS), the relaxation of duplex HSSS 2205 strands is slightly less than that of conventional steel strands. Given that the initial prestressing force is the same, a higher

force is applied by the duplex HSSS 2205 strands over time. This greater force would lead to greater creep of the piles, and consequently to higher prestress losses.

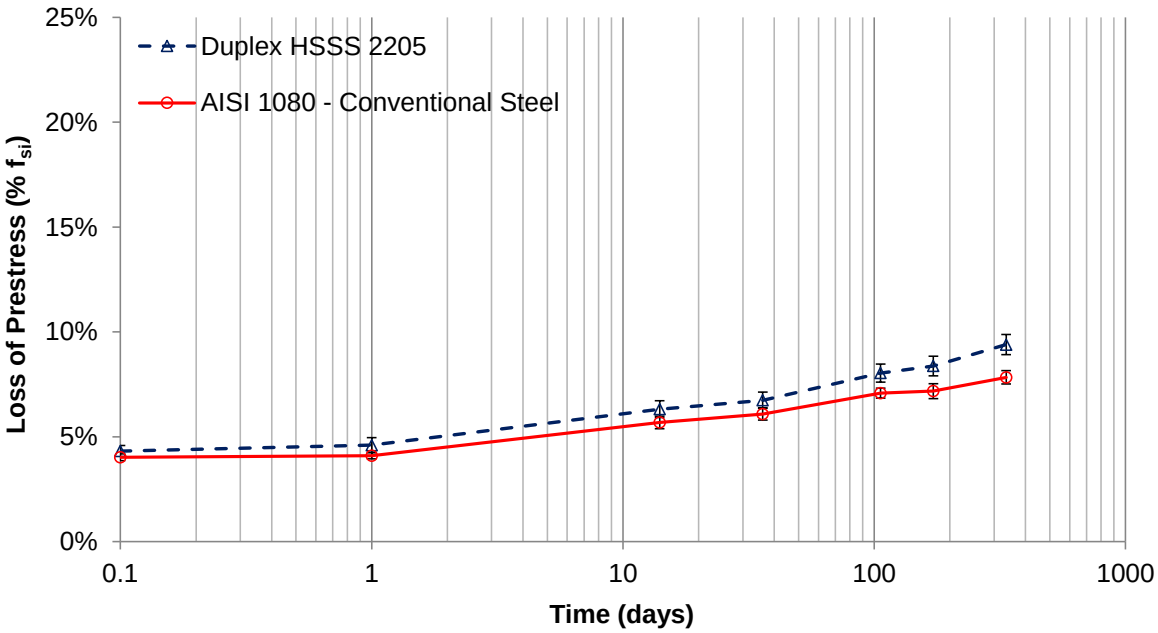

Figure 5.57 Loss of initial prestress for the first 335 days. Error bars correspond to standard deviation of losses.

A maximum loss of initial prestressing of 22% is required by GDOT Standard 3215. Regardless of the type of prestressing steel, losses at 335 days are predicted to be 90% of the total losses at the end of a service life of 100 years. Thus, it is unlikely that the loss of prestress of the piles will exceed the specified limit.

5.7.1.3 Experimental losses compared with AASHTO lump-sum method

Table 5.19 shows the comparison between experimental losses, including strain gauge measurements and stress relaxation estimation, and prestress losses calculated with the AASHTO lump-sum method (see calculations given in Appendix Q). The calculated

lump-sum losses at 335 days approximately equal the measured losses for piles with HSSS 2205 strands, and they are 95% of those measured for piles with conventional strand.

Table 5.19 Comparison of measured losses at 335 days and calculated losses with the AASHTO lump-sum method.

Pile	**Experimental Losses at 335 days** (ksi)	**Experimental Losses at 335 days** (MPa)	**AASHTO Lump-Sum Losses** (ksi)	**AASHTO Lump-Sum Losses** (MPa)
AISI 1080 Steel	20.1	138.3	19.0	131.3
Duplex HSSS 2205	18.0	124.2	18.1	124.9

5.8 Durability Assessment

Eight 20-in. (50.8 cm) long specimens were placed in the tidal zone of the Savannah River to evaluate the long-term performance of prestressed concrete piles, using duplex HSSS 2205 and conventional steel, exposed to marine environments. Periodic extraction of cores and evaluation of the specimens were used to determine the rate of chloride ingress as well as the extent of steel corrosion and concrete degradation due to sulfate attack, abrasion, or carbonation. Such damage to existing concrete substructure elements in coastal Georgia bridges has been described in a previous report presented to GDOT (Moser et al., 2011a).

5.8.1 Durability Samples

The durability specimens were prestressed in the same conditions as the piles and kept in a location adjacent to the prestressing forms for about one month (Figure 5.58).

No cover was provided on two sides of each specimen in order to accelerate corrosion of the strands on those two sides. The selected location for durability assessment is the old dock at Standard Concrete Products plant in Savannah, GA, latitude 32.07876° N, longitude 81.05012° W (see Figure 5.59). Average high and low annual temperatures were 77.4 °F (25.2 °C) and 56.1 °F (13.4 °C), respectively, and average monthly humidity ranged between 69% and 79% during the year. The Savannah River exhibits a combination of fresh and seawater and has two tidal cycles per day according to the Center for Operational Oceanographic Products and Services, NOAA (2014). The presence of algae and mollusks were observed at the dock, a pH of 6.78 was measured using a Thermo Scientific Orion 3-Star Plus pH Portable Meter. Chloride ion concentration of 4,552 mg/L and sulfate ion concentration of 554 mg/L were measured on water samples obtained at high tide, following ASTM D4458 and D4130, respectively. Thus, ACI 318 exposure classes are S1 (sulfate) and C2 (corrosion).

Figure 5.58 Construction of small specimens for long term evaluation of concrete and steel.

Figure 5.59 Placement of specimens in the Savannah River.

5.8.2 Results

Before placing the samples in the river, five cores were drilled from different specimens at 42 days from piles construction, following the guidance of ASTM C42. A drilling head with a nominal diameter of 3-in. (76.2 mm) was used, and samples of prestressing strands and spiral wire were included on the drilled cores. The cores were transported to Georgia Tech Structures and Materials Lab in closed plastic bags, where three samples were sawed from the cores for determination of the compressive strength and were kept under fogroom conditions (73.5±3.5 °F [23.0±2.0 °C], RH > 98%) for five days before testing. These compressive strength samples were obtained from core regions without steel strands or wires (Figure 5.60).

Figure 5.60 Core drilling operation.

After 20 months (620 days) from pile construction, one specimen made with conventional reinforcement and one made with stainless steel reinforcement were retrieved from the river, cleaned to remove the river mud, and transported to Georgia Tech Structures and Materials Lab (Figure 5.61). At high tide, specimens were completely submerged; while at low tide (6 to 7-ft. [1.83 to 2.13 m] lower), part of the specimens was exposed. Also, due to the difficulty to lift the specimens from the bottom of the river and the surface condition before cleaning, it is believed that the bottom section of the specimens was partially buried in the soft soil present in the dock.

In each specimen, one core was taken in the top-to-bottom direction, at the position of one of the middle strands of the top layer, and another core was taken transversally. These cores were kept in closed plastic bags at constant temperature

(73.5±3.5 °F [23.0±2.0 °C]). Two compressive strength samples were cut from the cores taken from 620-day old samples.

(a) (b)

Figure 5.61 (a) Removal of specimens from the river and (b) stainless steel specimen after cleaning.

5.8.2.1 Compressive strength of cores

The compressive strengths of cores were compared with the strength obtained from cylinder samples corresponding to the first batch, given that this first batch was used for the small durability specimens. All of the 4×8-in. (10.2×20.3 cm) cylinder samples were kept in the fogroom until the time of testing. The ends of the core cut compression samples were smoothed with a manual rubbing stone, and unbonded rubber pad caps were used during testing. The average length-to-diameter ratio (*l/d*) of the 42-day old samples was 2.19, and the apparent density of the saturated cores was 147 pcf (2,355 kg/m^3). The average *l/d* of the 620-day old samples was 2.02, and the apparent density of the saturated cores was 144 pcf (2,307 kg/m^3). Table 5.20 shows the results

obtained for both sets of samples at 42 and 620 days from casting. Following procedures from ACI 214.4R (2010), the average strength of the cores was compared to 85% of the average strength $(\overline{f}_c)$ of 4×8-in. (10.2×20.3 cm) control concrete cylinders, and individual strength of cores was compared with the 75% of the average strength of cylinders (Table 5.20).

Table 5.20 Compressive strength of cores and cylinders of batch #1 at 42 days. (1,000 psi = 6.9 MPa, $\overline{f}_c$ = average strength of cylinders)

Age of Testing	**Sample**	**Compressive Strength** (psi)		Average of cores (psi) > 85% $\overline{f}_c$	Individual cores (psi) > 75% $\overline{f}_c$
		Average	Std Dev		
42 days	Cores	**6,696**	542	YES	YES
	Cylinders	**6,886**	72		
620 days	Cores	**11,908**	1,154	YES	YES
	Cylinders	**9,186**	867		

The higher strength observed in cylinders at 42 days is attributed to the use of fogroom curing conditions (Gonnerman and Shuman, 1928) or to the use of an *l/d* of the cores which was slightly higher than the specified maximum value in ASTM C42 (*l/d* = 2.1). Cylinders were demolded at the Georgia Tech Structures and Materials Lab three days after casting and kept inside the fogroom until testing, while the 42-day old cores were exposed to air curing in a coastal environment after removal from the prestressing beds. However, the objective of the determination of the compressive strength of cores was not the estimation of the strength of concrete in the piles, but to establish a baseline

for future evaluations. Decrease of compressive strength typically indicates deterioration of concrete due to environmental exposure.

At 620 days, the average compressive strength of the cores was about 30% higher than the strength of the companion test cylinders.

5.8.2.2 Chloride content

Powder samples were obtained by drilling the cores at three different depth intervals, 0 to 1-in. (0 to 2.54 cm), 1-in. to 2-in. (2.54 cm to 5.08 cm), and 2-in. to 3-in. (5.08 to 7.62 cm) from the top surface (Figure 5.62)..

Figure 5.62 Drilled core at different depths for chloride content determination.

Collection of pulverized concrete in 620-days cores was performed on cores obtained in the top-bottom direction, in order to determine the chloride content at the top strand position. Four measurements were made at each depth range.

Powder samples were kept in separate sealed containers, and only the fraction passing sieve No. 20 (< 850 μm) was conserved for testing. Then, the acid-soluble content of chloride was determined by potentiometric titration (Figure 5.63), following the procedure in ASTM C1152.

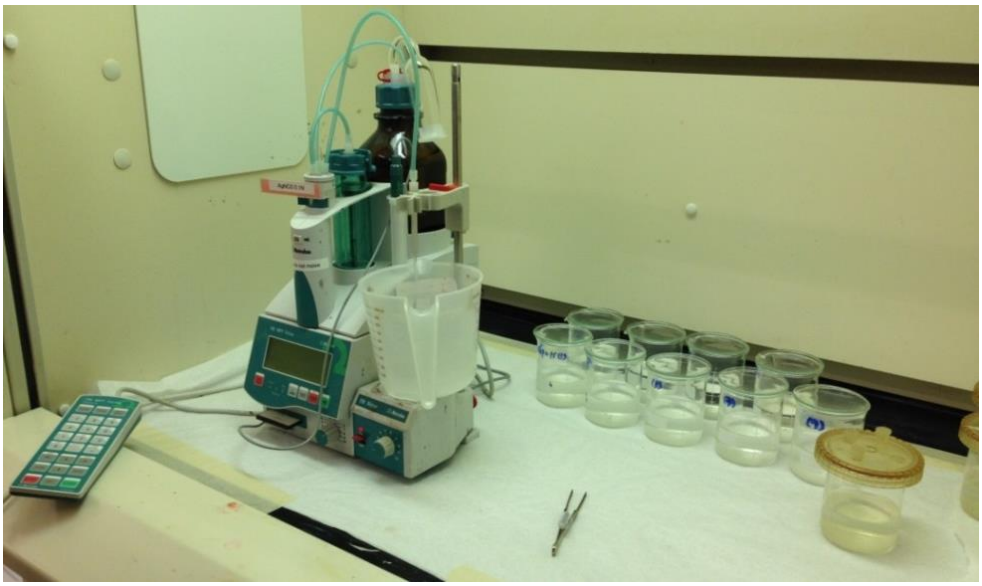

Figure 5.63 Autotitrator for chloride content determination.

Concrete powder was dissolved in (1:1) nitric acid, boiled for 10 seconds, and filtered using a Buchner funnel and filtration flask with suction through a Grade 41 coarse-textured filter paper. Then, the sample was stirred in the presence of an indicator silver/silver chloride standard electrode on a Metrohm 798 MPT Titrino autotitrator. The electrode was used to measure the change of potential during the addition of a titrant (silver nitrate solution, 0.1 N $AgNO_3$) to the sample. The equipment determines and

graphs the relationship between the potential of Ag^+ (calculated from the change of potential) and the added amount of titrate. The amount of silver nitrate needed to stabilize the reaction, identified from the inflection point of the curve, is used to calculate the chloride content of the sample. The results are compared with a blank measurement performed with deionized (DI) water (electrical resistivity $\rho = 18.2\ M\Omega \cdot cm$).

The determination of the percentage of chloride that initiates steel corrosion (chloride threshold limit, CTL) is of interest, but various CTL values have been reported in the literature and various values are found in standards. For prestressed concrete using conventional steel, the British standard BS 8110 set the maximum chloride content of 0.10% by mass of cement, while ACI 357 and ACI 222 use 0.06% and 0.08% for the same CTL estimation, respectively (Ann and Song, 2007). In a previous report (Holland et al., 2012), a value of 0.05% of chloride content by mass of concrete was chosen as a reference for corrosion initiation. This number is the default chloride threshold for corrosion initiation used in Life-365 software (Bentz, 2003), and it was selected as a representative value of the suggested range of chloride threshold levels to initiate corrosion by Glass and Buenfeld (1997). Chloride content of 0.05% by mass of concrete is used as the CTL for durability assessment in this research.

The results of the test at 42 and 620 days are given in Table 5.21.

Table 5.21 Acid-soluble chloride content of cores, obtained by titration (ASTM C1152). (1-in. = 2.54 cm)

Age of Testing	Distance from Surface	%Cl by Mass of Concrete
42 days	0 - 1 inches	0.000
	1 - 2 inches	0.000
	2 - 3 inches	0.000
620 days	0 - 1 inches	0.008
	1 - 2 inches	0.006
	2 - 3 inches	0.019

A negligible amount of acid-soluble chloride was found in the 42-days cores. In the case of 620-days samples results, the chloride content at every depth was lower than the CTL. The higher concentration in the sample obtained at 2 to 3-in. from the top surface can be explained by the chloride ingress from the side of the specimen. Top middle prestressing strands of durability specimens are at a similar distance from top and side surfaces.

5.8.2.3 Corrosion of prestressing strands

After the compressive strength samples were sawed from the cores, the rest of the samples were kept in an air-dried condition inside closed plastic bags. The condition of the prestressing strands was inspected using a stereo microscope.

Since corrosion of prestressing strands is typically initiated at impingement sites between prestressing wires by the influence of surface imperfections (Moser et al., 2011b), two or three wires of the strands were removed, and the crevice regions were exposed (Figure 5.64). Assessment of strand corrosion included the cores obtained from

the top surface and from the side of the specimen, for both types of steel – the side samples had about 0.2-in. (5 mm) cover while the top and bottom had about 3.2-in. (81 mm) cover.

Figure 5.64 Presence of corrosion products at AISI 1080 prestressing steel (top surface core), after 620 days from casting.

(a) AISI 1080 steel.

The condition of the conventional steel strands was compared with an AISI 1080 prestressing strand exposed to room conditions for several years. In this control sample, mild chemical action is evidenced by uniform discoloration of the impingement sites (Figure 5.65). In contrast, both AISI 1080 strand samples (top and side surface cores) show indications that suggest the initiation of localized active corrosion. Micrographs of strand taken from the top of the top surface core are shown in Figures 5.66 to 5.68; the presence of corrosion products is observed next to regions where loss of material is appreciable, and growth of tubular corrosion products from the steel surface are noted.

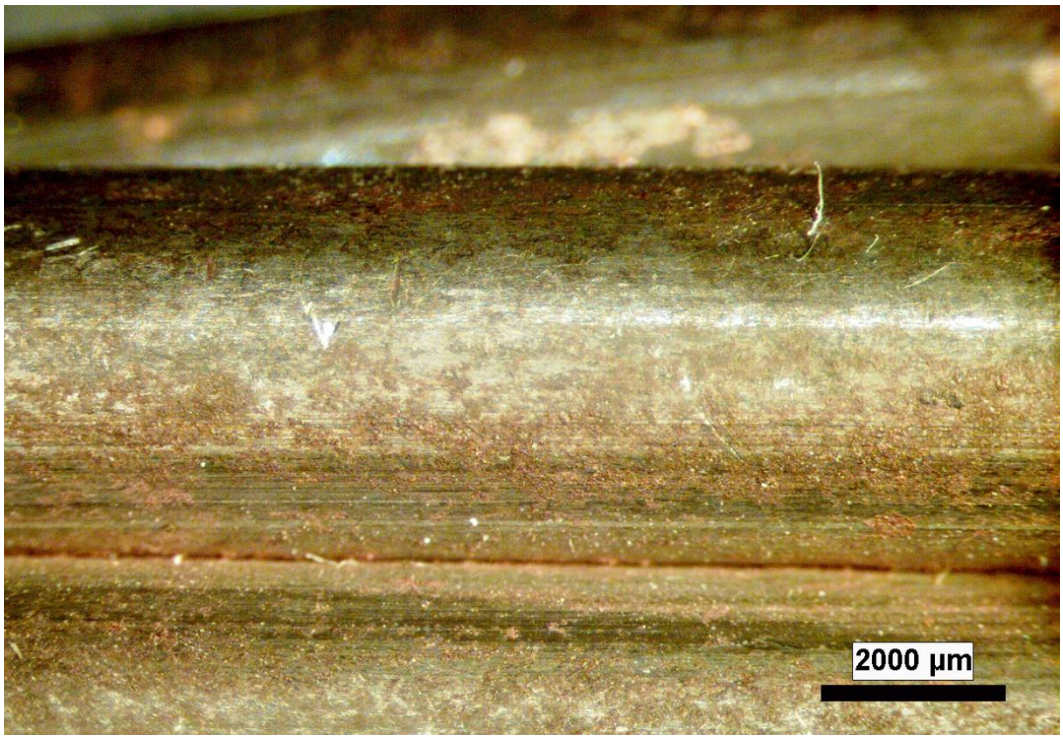

Figure 5.65 Surface of control AISI 1080 prestressing strand, exposed to room conditions (X6.5).

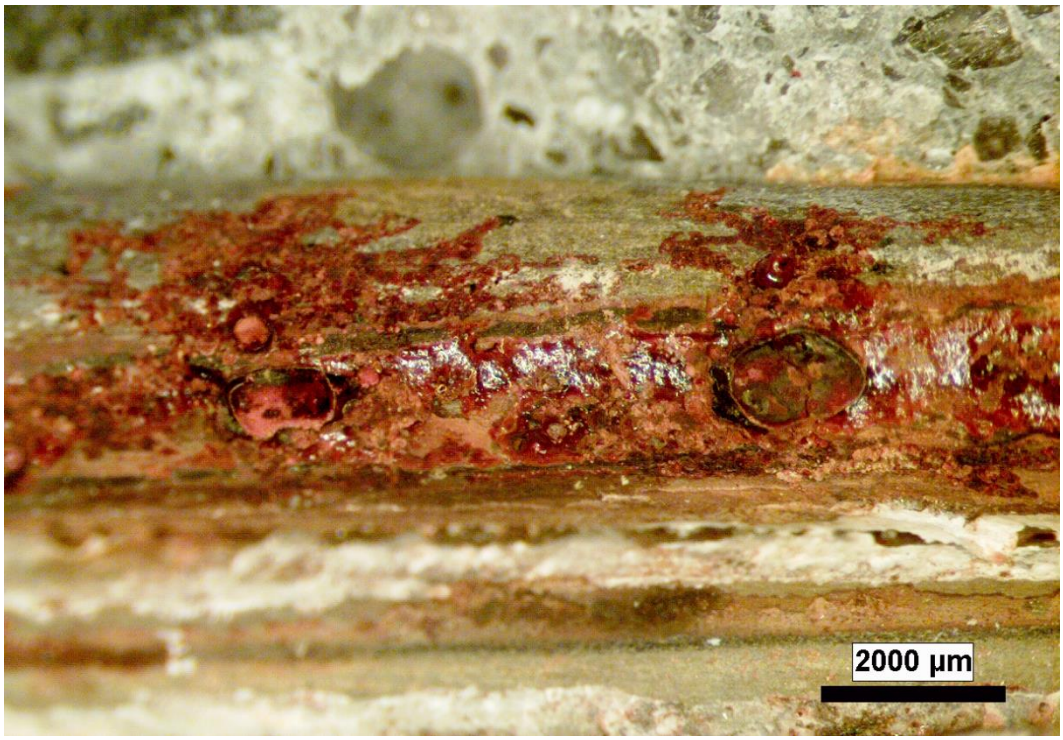

Figure 5.66 Surface of AISI 1080 prestressing strand from top surface core (X6.5).

Figure 5.67 Corrosion products in AISI 1080 prestressing strand surface (top surface core, X6.5).

Figure 5.68 Surface of AISI 1080 prestressing strand from top surface core (X10).

Core samples were taken from the side surface of the durability specimens where there was about ¼-in. (6.4 mm) of cover. AISI 1080 strand samples from the side surface core show similar, though more extensive, deterioration as the top surface strand (Figure 5.69). The presence of localized corrosion activity in prestressing strands at chloride concentrations lower than the CTL of 0.05% suggests that this parameter should be lower than the conventional 0.05% limit when used for conventional prestressing strand.

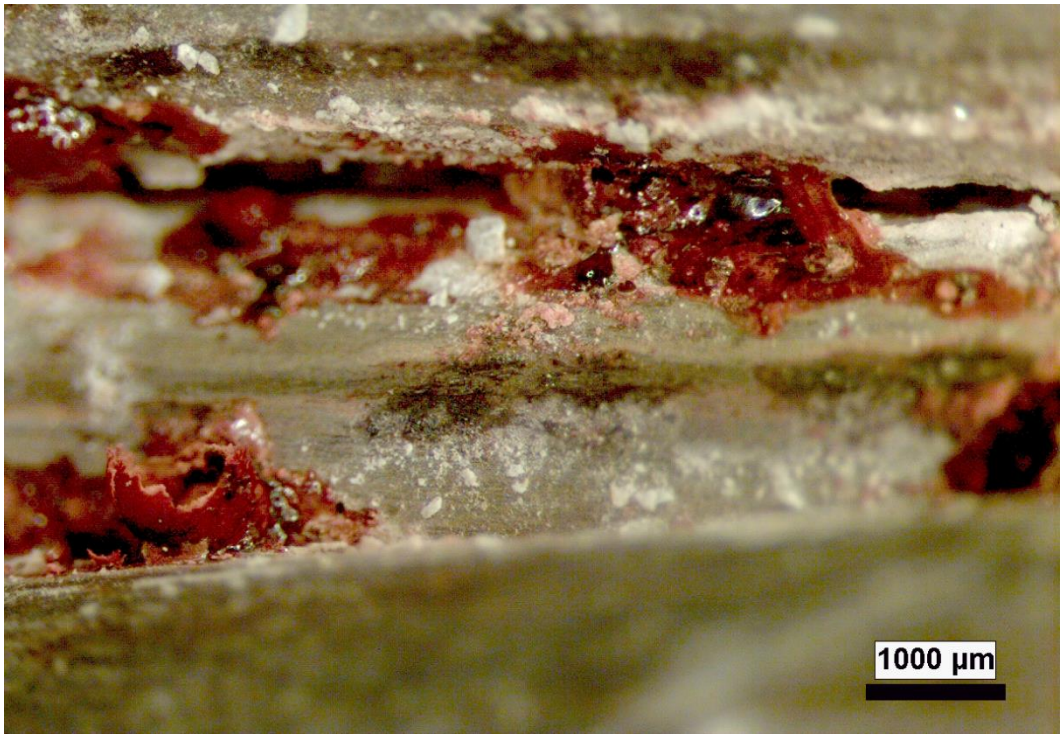

Figure 5.69 Surface of AISI 1080 prestressing strand from side surface core (X10).

(b) Duplex HSSS 2205 strands and austenitic SS 304 spiral wire.

Similar to the AISI 1080 case, the condition of duplex HSSS 2205 strands was compared with a strand sample obtained from the pile construction. The control sample was kept at Georgia Tech Structures and Materials Lab. Figure 5.70 shows an excellent

condition of the surface of the control strand, no evidence of corrosion initiation, or chemical activity at the impingement sites.

Figure 5.70 Surface of control duplex HSSS 2205 prestressing strand (X6.5).

Micrographs of top surface duplex HSSS 2205 strand show a general good condition (Figures 5.71 and 5.72), but uniform discoloration at some of the contact regions between adjacent strands evidences chemical activity occurring at these sites. A similar condition is observed in strand samples obtained from the core drilled at the specimen side (Figures 5.73 and 5.74). Overall, the condition of the stainless steel strand was considered excellent.

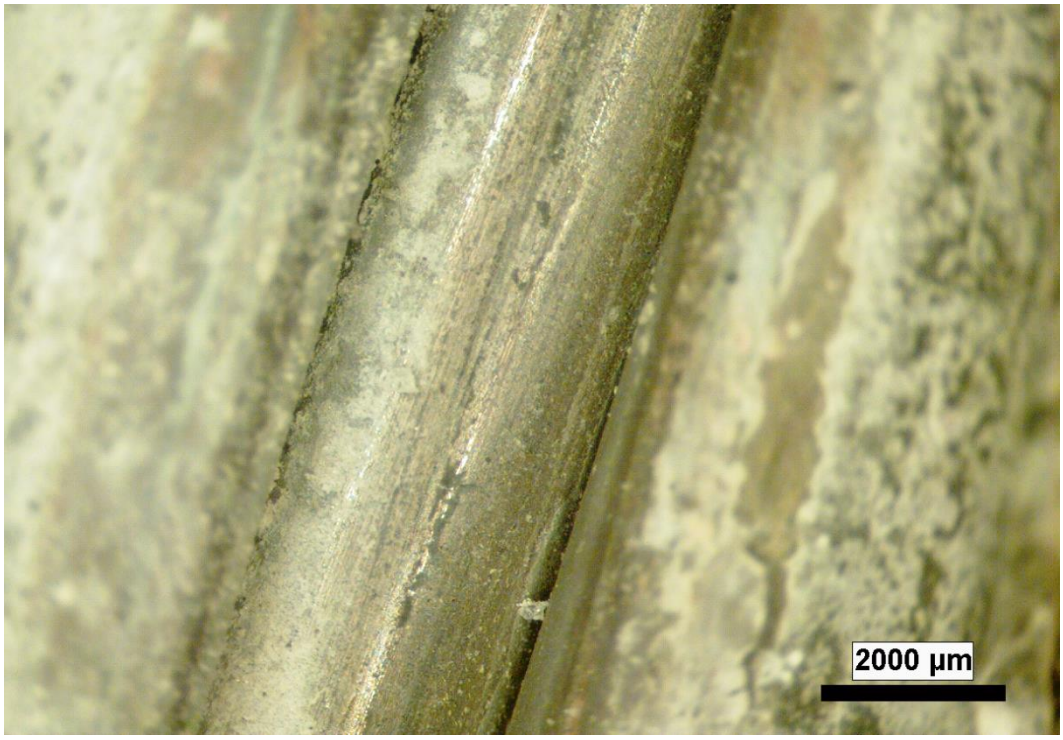

Figure 5.71 Surface of duplex HSSS 2205 prestressing strand (top surface core, X6.5).

Figure 5.72 Surface of duplex HSSS 2205 prestressing strand (top surface core, X6.5).

Figure 5.73 Surface of duplex HSSS 2205 prestressing strand (side surface core, X6.5).

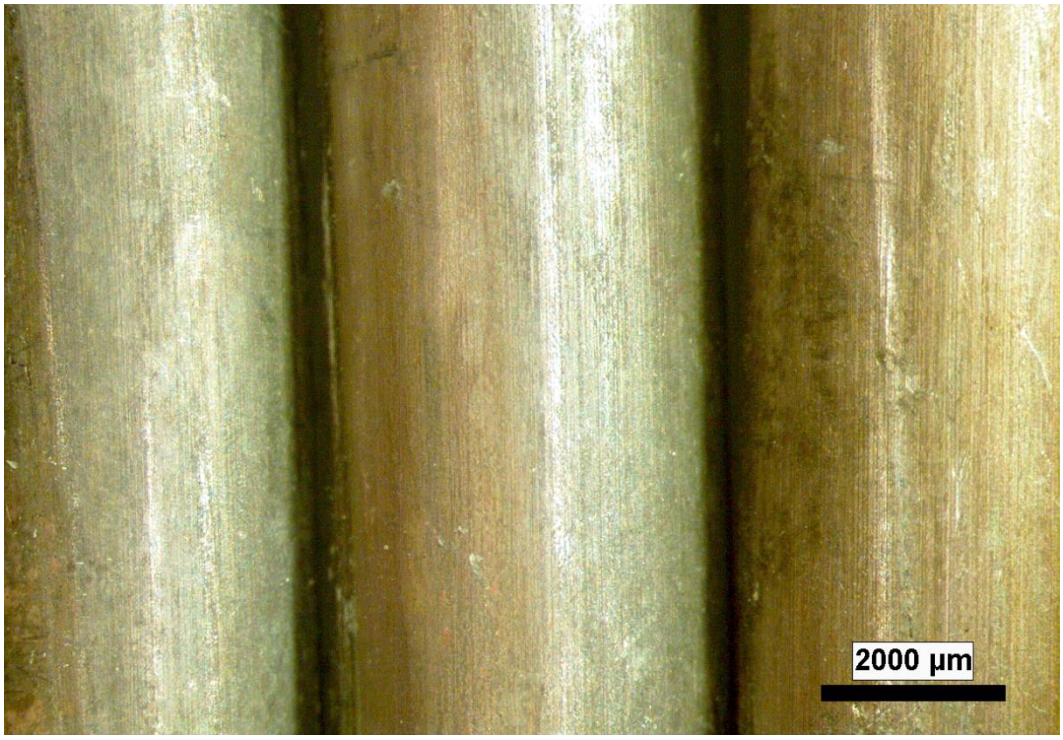

Figure 5.74 Surface of duplex HSSS 2205 prestressing strand (side surface core, X6.5).

5.9 Conclusions of the Chapter

It can be concluded that piles using duplex HSSS 2205 strands and austenitic SS 304 spiral wire can be successfully driven to refusal without visible damage.

Additionally, the results of the flexure tests show that the flexural capacity of prestressed concrete piles using duplex HSSS 2205 strands may be conservatively predicted using AASHTO LRFD specifications and using provisions of ACI 318-11. However, the post-yield ductility of piles with HSSS 2205 strand is much less than that of piles with conventional prestressing strand. When a higher inelastic deformation energy dissipation capacity is required as needed for fender piles, the lower ductility of these piles should be considered. For stainless steel reinforced piles used as fender piles, a lower strength reduction factor (ϕ) as used for compression-controlled members is recommended.

Shear strength provided by austenitic SS 304 wire spiral reinforcement was 29% and 61% higher than predicted nominal shear strength by ACI 318 for spacings of 3-in. (7.6 cm) and 6-in. (15.2 cm), respectively, and 22% and 50% higher than the predicted nominal shear strength by AASHTO LRFD for spacings of 3-in. (7.6 cm) and 6-in. (15.2 cm), respectively. The use of austenitic SS 304 wire spiral reinforcement provides shear strength equivalent to that of conventional wire spiral reinforcement.

The use of AASHTO refined method for the estimation of prestress losses is conservative for duplex HSSS 2205 strands. Experimental losses equaled 82.3% of those predicted by the refined method, and 99% of those predicted by the lump-sum method. Also, losses of prestressed concrete piles built using duplex HSSS 2205 strands comply with current GDOT requirements.

CHAPTER 6

TRANSFER AND DEVELOPMENT LENGTH OF PRESTRESSED CONCRETE PILES USING DUPLEX HSSS 2205 STRANDS

6.1 Introduction

The bond performance of prestressed concrete piles using stainless steel reinforcement is assessed by the experimental determination of the transfer and development lengths. The transfer length is used in the design process to check the stresses at the end of the prestressed concrete member at early stages, and the flexural and shear strengths later in the service life of the member (Mitchell et al., 1993), while the development length impacts the bending and shear strengths of pretensioned members (Zia and Mostafa, 1977). Experimental results are compared to ACI and AASHTO requirements and to estimation expressions proposed by previous studies.

6.2 Description of Tests

6.2.1 Transfer Length

Transfer length (l_t) is defined by ACI 318 (2011) as the "length of embedded pretensioned strand required to transfer the effective prestress to the concrete," while AASHTO LRFD (2013) defines it as "the length over which the pretensioning force is transferred to the concrete by bond and friction in a pretensioned member." An idealized diagram of the steel stresses is illustrated in Figure 6.1 (Russell and Burns, 1993). It is assumed that, after strand release, the stresses transferred to the concrete increase linearly

from zero at the end of the pile to a point where the prestress force is fully transferred. This distance is the transfer length.

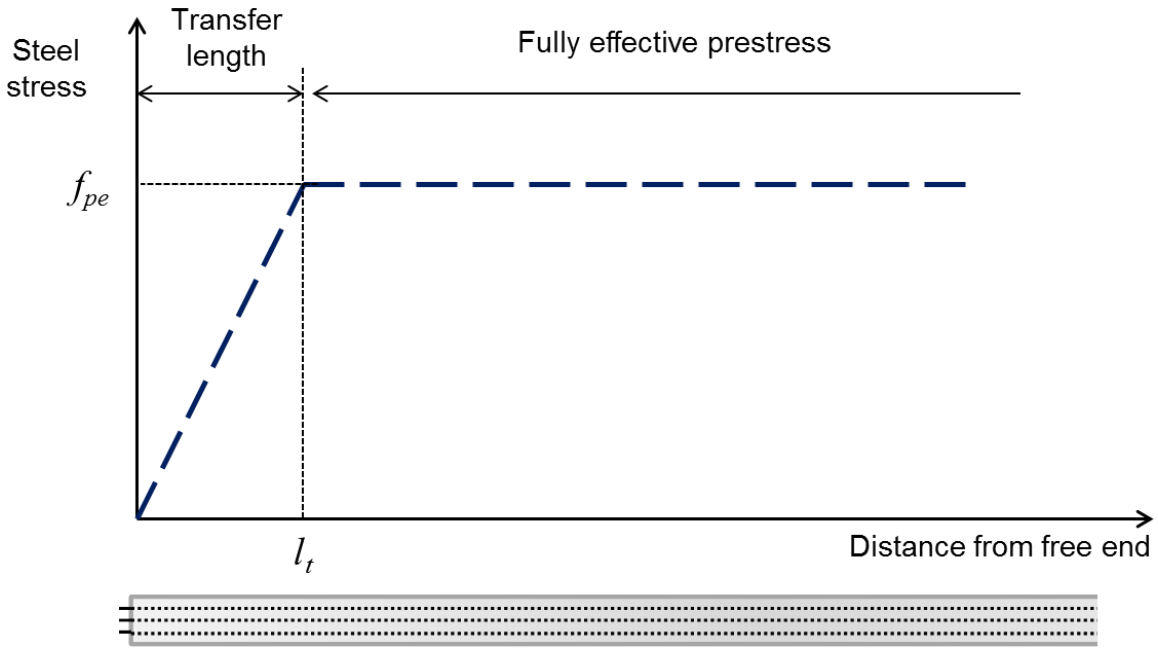

Figure 6.1 Idealization of strand stresses along the pile (modified from Russell and Burns (1993)).

Transfer length of the prestressed concrete piles was measured at each end of the piles, using the concrete surface strain (CSS) method (Russell and Burns, 1993). As a result of the prestressing force transferred from the steel strands to the concrete, strains and compressive stresses are induced. By equilibrium, these compressive stresses in the concrete balance the tensile stresses in the prestressing strands. Thus, the measurement of the concrete surface strains mirrors the strain profile of the prestressing strands (Reutlinger, 1999; Kahn et al., 2002).

The average transfer lengths of the piles using duplex HSSS 2205 and conventional steel strands were shorter than the predicted values using AASHTO LRFD

and ACI 318. After pile driving and extraction, the average transfer lengths of the piles remained the same or shorter than before driving and less than the AASHTO LRFD and ACI 318 predictions.

This chapter describes the determination of the transfer length of the piles by the CSS method. Also, results before and after driving are compared with estimated transfer lengths according to ACI 318, AASHTO LRFD, and expressions proposed in the literature and described in Section 2.3.1.2.

6.2.2 Transfer Length Measurements

The CSS method was used by Russell (1992) to determine the transfer length of 0.6-in. (15.2 mm) diameter, 7-wire strands of prestressed concrete girders. This technique considers that 1) stress of prestressing strand varies linearly from zero at the end of the pretensioned element to a maximum value where full prestressing force is transferred to the concrete, 2) prestress transfer to the concrete depends on bond strength developed by Hoyer's effect and, with a lower contribution, mechanical interlocking, and 3) equilibrium of compressive stresses in concrete and tensile stresses in the prestressing strands allows the determination of strand strains along the prestressed concrete element by the measurement of concrete surface strains.

As described in Section 5.2.2, two rows of embedded DEMEC points were installed at the surface of each end of each pile. DEMEC points were placed along 8-ft. (2.44 m) at the ends of the piles; the points were spaced at 2-in. (5.1 cm) on centers, starting at 1-in. (2.54 cm) from the end. The measurements were performed using a DEMEC gauge with a gauge length of 8-in. (20.3 cm) and a precision of ±0.0001-in.

(±0.00254 mm), which allowed 86 readings at each end (Figure 6.2). The same person performed the measurements along the piles, using the same DEMEC gauge. Before measurements were taken, the DEMEC tool was zeroed using an INVAR reference bar to account for temperature variations.

Figure 6.2 Concrete surface strain measurements. Note the two parallel rows of DEMEC gauge points on each side of the top surface of the pile.

The first measurements were taken before the release of the strands. Then, an initial reading was performed after strand release, while the rest of the measurements were performed before sunrise beginning the following morning to avoid significant deformations in the concrete due to solar radiation and resulting temperature gradients.

In order to describe the CSS method in detail, results for pile 1080 #1, jacking end (i.e., the end of pile closer to the jacking end of the prestressing bed during construction) is presented. Figure 6.3 shows the raw concrete strain profile along pile 1080 #1, jacking end. Measurements of both rows of DEMEC points were averaged. It can be observed

that at 14 days, less variable measurements were obtained compared to readings after release and at 1 day from release. Thus, measurements taken at 14 days were considered for the calculation of the transfer length before driving. The deformation of the pile at release was thought to be restrained by the prestressing bed.

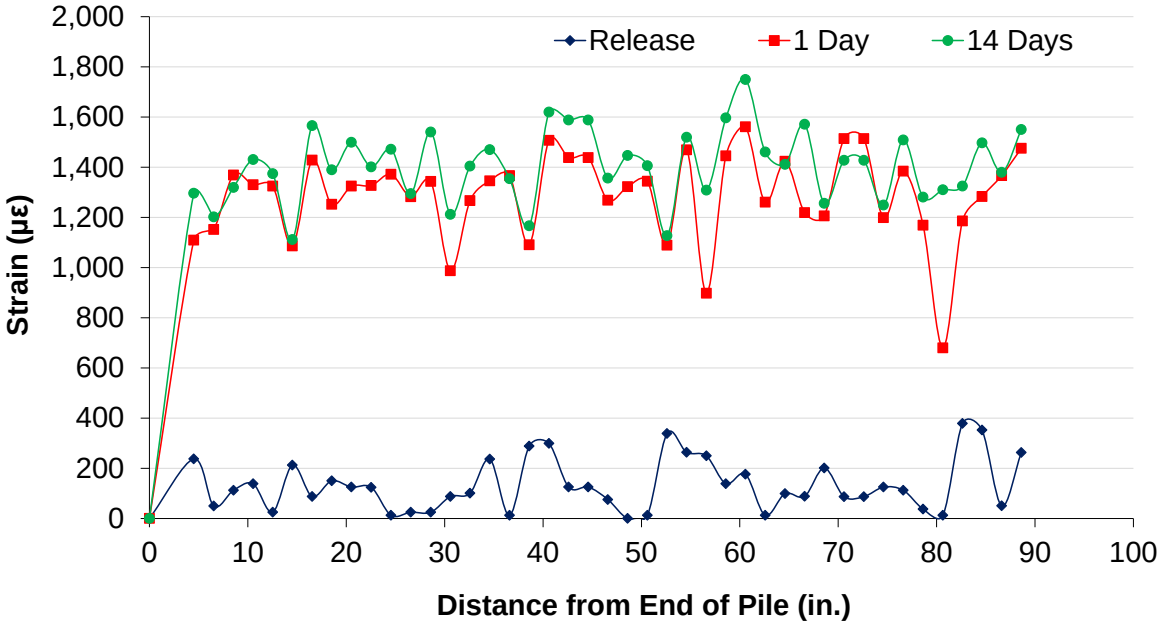

Figure 6.3 Raw concrete surface strain profile for Pile 1080 #1 – Jacking End. (1-in. = 2.54 cm)

The CSS method smooths the raw strain profile shown in Figure 6.3 by averaging every three consecutive readings. The objective of the smoothening of the curve is to reduce anomalies and remove part of the noise associated with the measurement acquisition. Equation 6.1 was used for smoothening of raw data (Russell and Burns, 1993).

$$\varepsilon_i = \frac{\varepsilon_{i-1} + \varepsilon_i + \varepsilon_{i+1}}{3} \tag{6.1}$$

where ε_i is the i-th strain for $i = 2,\ldots, 42$ in the case of the prestressed concrete piles.

As a result, the profile in Figure 6.4 was obtained by the smoothening of raw strain profiles. The smoothed strain profile was used to determine the transfer length of the prestressed concrete element. It should be noted that the distances of the reading points are also averaged in the smoothed profile. Thus, the initial strain of the raw profile (Figure 6.3) is located at 4.51-in. (11.46 cm) from the end of the pile, while the first averaged strain of the smoothed profile is positioned at 6.53-in (16.59 cm) from the end of the pile.

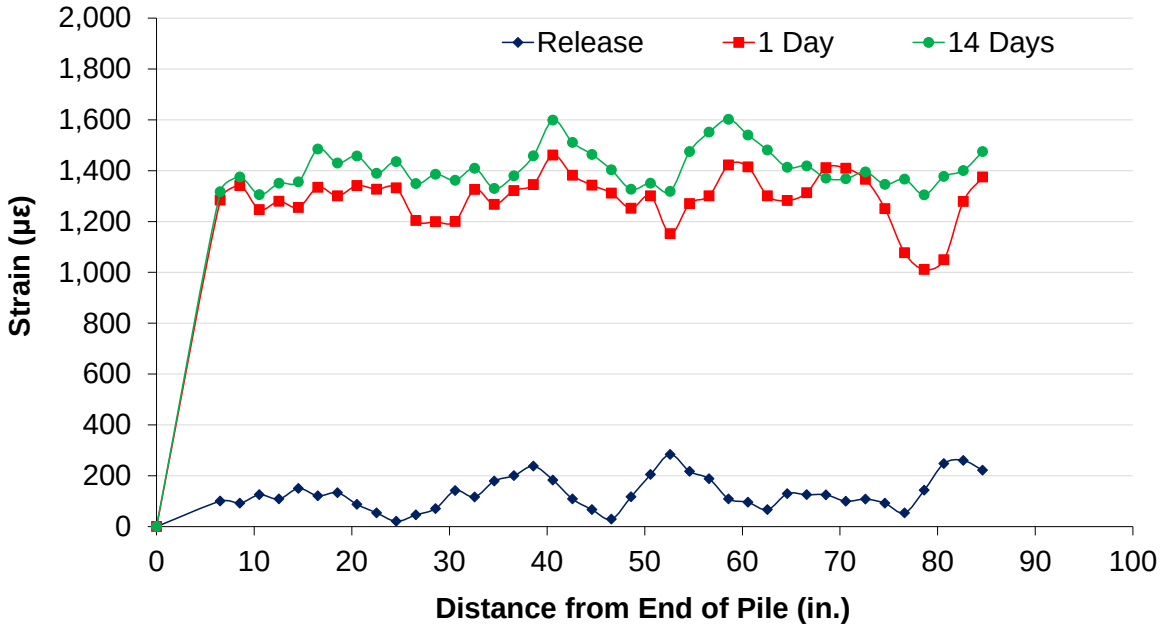

Figure 6.4 Smoothed concrete surface strain profile for Pile 1080 #1 – Jacking End. (1-in. = 2.54 cm)

As mentioned by Russell and Burns (1993), DEMEC readings determine the average deformation of the concrete surface along the gauge length. In combination with the smoothening process, the averaged strain along the pile length shows a reduction of the slope around the position of the transfer length and the profile deviates from the

assumed transferred strain profile (Figure 6.1), which usually artificially increases the calculated transfer length.

Following the smoothening of raw data, the calculation of the transfer length is performed by the 95% average maximum strain (AMS) method. In this method, the average maximum strain is calculated as the average of the strains in the constant strain plateau (section of the profile corresponding to the full transfer of the prestressing force). Then, a line corresponding to 95% of this value is intersected with the initial linear trend of the smoothed curve to obtain the transfer length of the element, as seen in Figure 6.5. The use of the 95% AMS method corrects part of the inaccuracies introduced by the smoothening of the curve, and the obtained transfer length is still conservative compared with the one calculated if a bilinear strain profile is used.

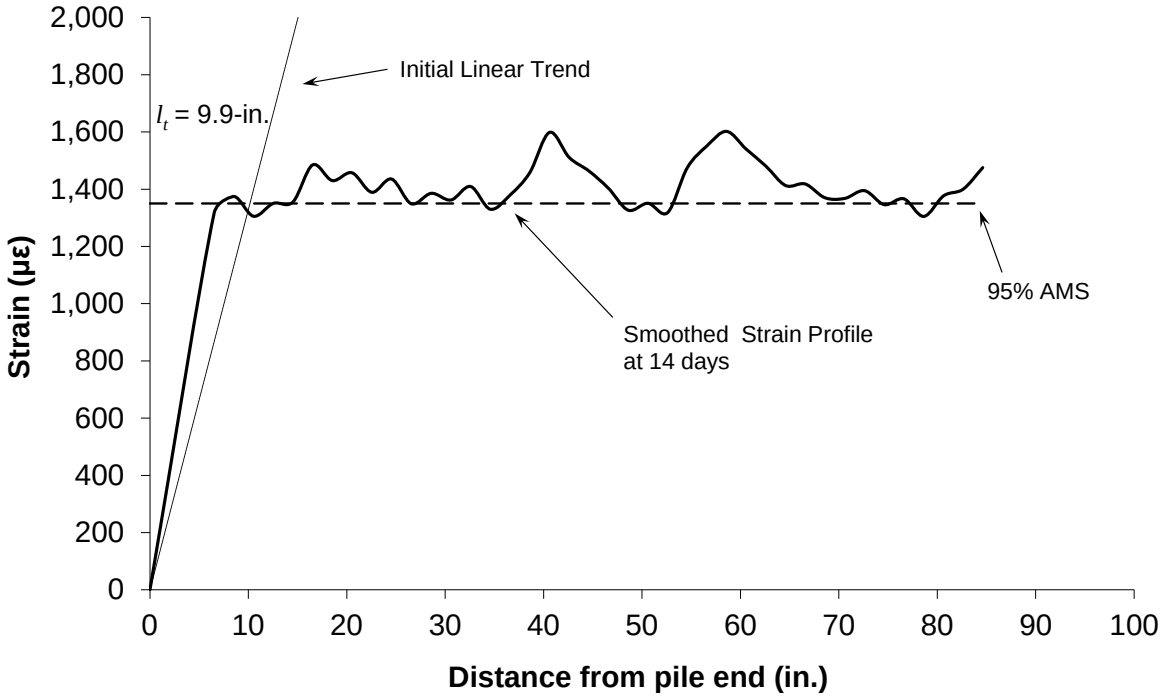

Figure 6.5 Determination of transfer length from the smoothed strain profile for Pile 1080 #1 – Jacking End at 14-days after release. (1-in. = 2.54 cm)

Given that some of the piles showed strains before the constant strain plateau that are not clearly represented by a straight line and to avoid arbitrary interpretation of the data, the initial linear trend was calculated by the ordinary least squares method with a zero intercept.

To understand the effect of driving on the transfer length of prestressed concrete piles, the same procedure was repeated after the driving and extraction operation. Smoothed strain profiles and transfer length determination of the piles before and after driving can be observed in Appendix S.

6.2.3 Development Length

The development length of the ½-in. (12.7 mm) diameter HSSS 2205 prestressing strand was determined experimentally by testing the 27-ft. (8.23 m) long composite pile specimens. Development length is the length of prestressing strand required to develop the design strength of the prestressing strand, f_{ps}. When the tension in the strand increases by the action of external forces, the bond stress also increases to maintain the equilibrium and to anchor the strand (Russell and Burns, 1993). Thus, the development length can be defined as the minimum embedment required to avoid strand slip when the design stress of the strand is reached (Buckner, 1995). Figure 6.6 shows an idealized model of the steel stress buildup, starting from the free end of the pile, until the design stress f_{ps} is reached at l_d.

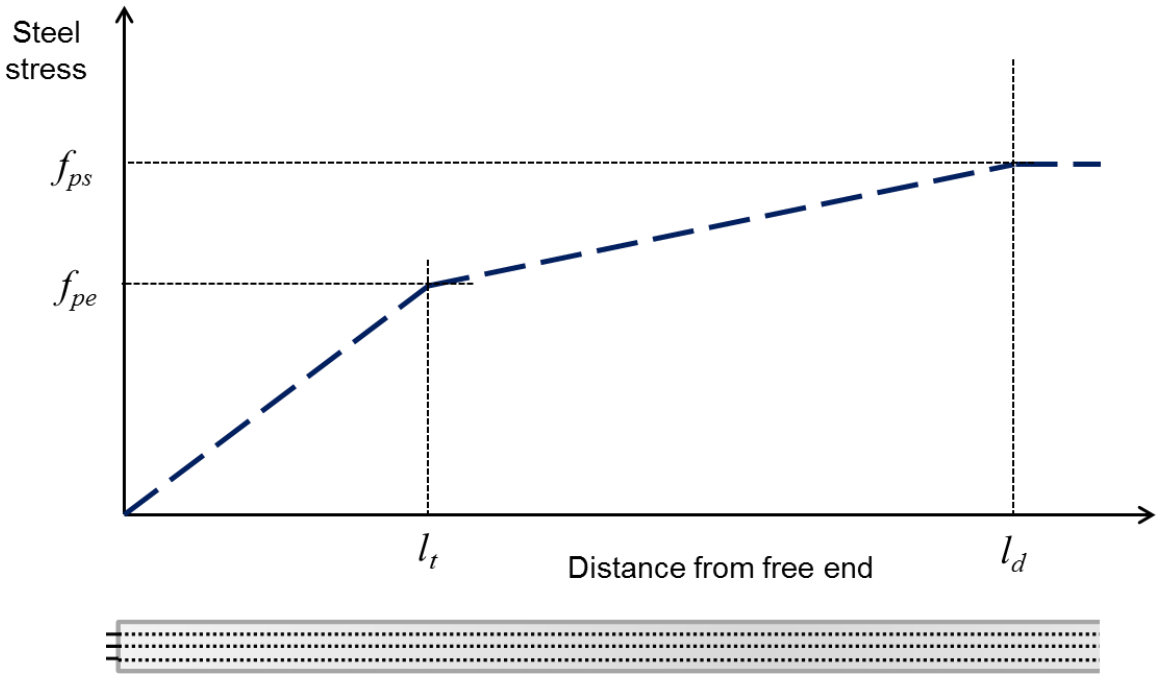

Figure 6.6 Idealized steel stress along the pile.

ACI 318 (2011) and AASHTO LRFD (2013) define the development length required for bonded prestressing strands in pretensioned members using the expressions given in Equations 6.2 and 6.3, respectively. For pretensioned members with a depth greater than 24-in. (61.0 cm), the AASHTO equation increases the calculated l_d by 60% using the 1.6 factor shown in Equation 6.3.

ACI: $$l_d \geq \left(\frac{f_{se}}{3{,}000}\right) \cdot d_b + \left(\frac{f_{ps} - f_{se}}{1{,}000}\right) \cdot d_b \qquad (6.2)$$

AASHTO: $$l_d \geq 1.6 \cdot \left(f_{ps} - \frac{2}{3} f_{pe}\right) \cdot d_b \qquad (6.3)$$

where d_b is the nominal diameter of strands, f_{ps} is the stress in the prestressing steel at the time of the nominal resistance (experimental failure) of the pile, and f_{pe} (f_{se} in ACI 318) is the effective stress in the prestressing strand after losses.

The development length of duplex HSSS 2205 strands was evaluated by loading the composite 27-ft. (8.23 m) piles in flexure. Embedment length (distance between pile end and applied load) at which strand slip was greater than 0.01-in. (0.254 mm) was considered lower than l_d. Experimental results of piles constructed using duplex HSSS 2205 and conventional steel strands showed development lengths 85% to 88% of the value predicted by ACI 318, and 53% to 55% of the value predicted by AASHTO LRFD.

It was concluded that the use of ACI 318 and AASHTO LRFD to predict the development length of duplex HSSS 2205 strands is conservative.

The setup of the flexural test used for development length determination is discussed below. The results of the tests are compared with the predicted values from the codes and expressions proposed in the literature.

6.2.4 Development Length Test

A flexural test for the determination of the development length was performed on 27-ft. (8.23 m) long piles, after the addition of a top concrete section that increased the depth of the section to 43-in. (109.2 cm). During testing, the average compressive strength of concrete in the piles was 10,728 psi (74.0 MPa), while the compressive strength of the top, composite concrete section of the piles using duplex HSSS 2205 and conventional steel strands was 5,925 and 6,251 psi (40.9 and 43.1 MPa), respectively. Details of the construction of the specimens are given in Section 5.2 and in Appendix H.

The 27-ft. (8.23 m) composite pile sections were simply supported and loaded at a variable embedment length with two point loads spaced 4-in. (10.16 cm) apart. The load was applied by a 500 ton hydraulic ram, equipped with a 1,000 kip (4.45 MN) load cell.

A W10×77×24-in. (25.4×195.6×61 cm) long steel beam with stiffeners was placed under the load cell, supported by two 1-in. (2.54 cm) diameter rollers. The displacement of the pile at the position of load was recorded using a string potentiometer. The diagram in Figure 6.7 shows the test setup.

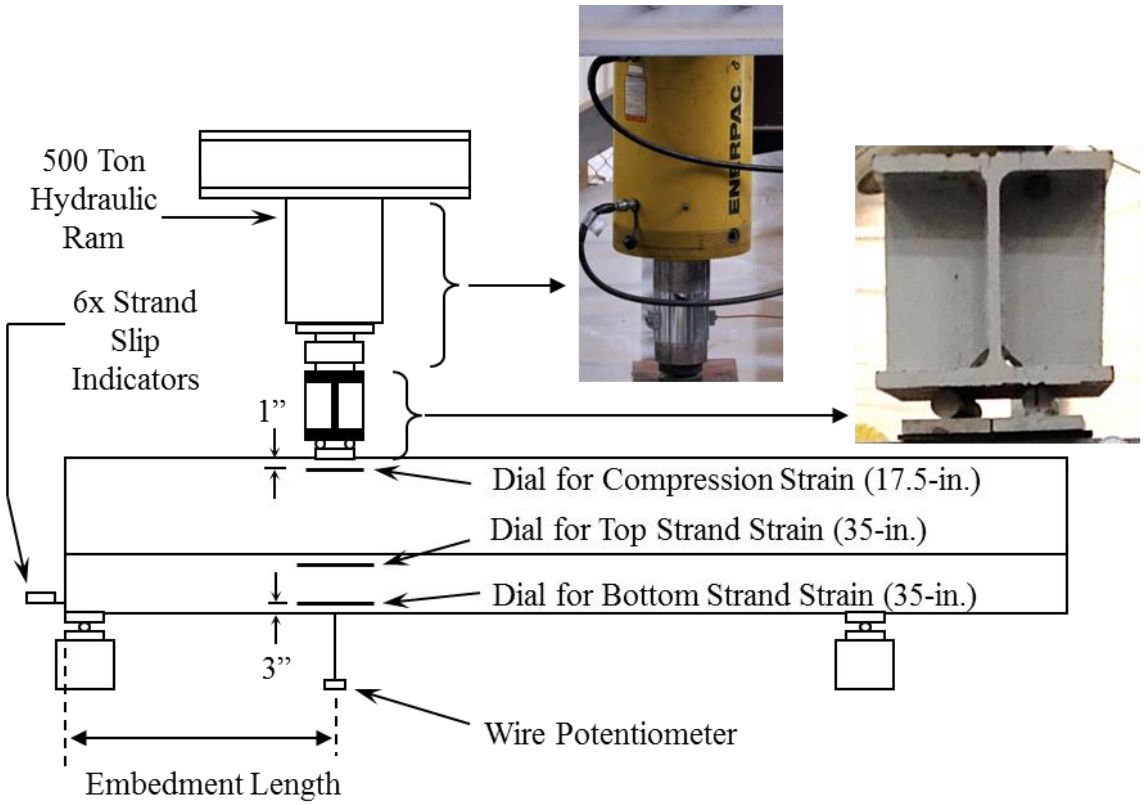

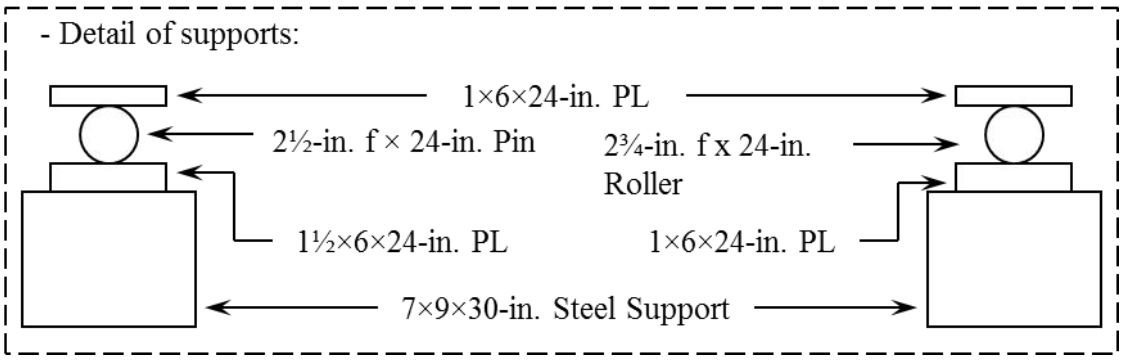

Figure 6.7 Setup for development length test. (1-in. = 2.54 cm)

Three dial gauges were attached at each side of the piles to estimate the strains in the prestressing strands and at the top section. Gauge lengths of 35-in. (89 cm) and 17.5-in. (44.5 cm) were used for the measurement of the strains in the strands and at 1-in. (2.54 cm) below the top of the composite section, respectively, as shown in Figure 6.8.

At the end of the pile closer to the applied load, four dial gauges were epoxied to the bottom row of strands and two additional dial gauges were attached to the pile in order to determine strand slip (Figure 6.9). A strand slip higher than 0.01-in. (0.254 mm) indicated slip and that the bond stress capacity was not able to counteract the increasing stress in the prestressing steel, meaning that the embedment length was lower than the development length.

Load was applied monotonically and was intermittently paused to mark crack patterns and to record dial gauge measurements.

Figure 6.8 Development length test. Opposite side of the pile was equipped with analog dial strain gauges, in the same way as shown in the picture.

Figure 6.9 Analog dial gauges were epoxied to bottom strands for slip determination.

In order to identify the minimum embedment length that provided development of the strands, the initial test was performed using the value predicted by the ACI Equation 6.2, where f_{ps} was defined as the ultimate stress of the strand. Then, the embedment length was progressively reduced until shear failure or strand slip occurred (74% of the predicted development length); Table 6.1 shows the embedment length tested for every pile and their ratio with respect to the predicted development length. Eight development length tests were performed, four for each type of prestressing steel.

Table 6.1 Embedment lengths used for development length determination.
(1-in. = 2.54 cm)

Pile	**Embedment Length** (in.)	**% l_d** ACI Eq. 10.1	**% l_d** AASHTO Eq. 10.2	**Failure Mode**
AISI 1080 Steel	53.50	74%	46%	shear/bond
	57.00	79%	49%	shear/bond
	61.00	85%	53%	flexure
	72.00	100%	62%	flexure
Duplex HSSS 2205	57.00	73%	46%	shear/bond
	61.75	79%	49%	shear/bond
	69.00	88%	55%	flexure
	79.75	102%	64%	flexure

6.3 Results and Analysis

6.3.1 Transfer Length Results

Table 6.2 shows the calculated transfer length before and after driving for each pile end, using the CSS method. Experimental transfer lengths are compared with predicted values by AASHTO LRFD and ACI 318. In each case, the jacking end of the pile was the one which was hit by the pile driver hammer.

Table 6.2 Summary of transfer lengths of piles before and after driving. The percentage of the value given by AASHTO LRFD is shown in parenthesis. (1-in. = 2.54 cm)

Pile End	**Day 14**	**Average Day 14**	**Day 273**, after driving	**Average Day 273**	**AASHTO LRFD** (2013)	**ACI 318** (2011)
1080 #1 Jacking End	9.9-in. (38%)	**17.8-in. (68%)**	10.0-in. (38%)	**15.2-in. (58%)**	26.3-in.	25.5-in.
1080 #1 Dead End	22.2-in. (85%)		22.0-in. (84%)			
1080 #2 Jacking End	13.4-in. (51%)		12.3-in. (47%)			
1080 #2 Dead End	25.5-in. (97%)		16.4-in. (62%)			
HSSS 2205 #1 Jacking End	9.8-in. (33%)	**17.1-in. (57%)**	10.3-in. (34%)	**17.3-in. (58%)**	30.0-in.	21.2-in.
HSSS 2205 #1 Dead End	15.6-in. (52%)		11.5-in. (38%)			
HSSS 2205 #2 Jacking End	17.3-in. (58%)		23.7-in. (79%)			
HSSS 2205 #2 Dead End	24.7-in. (82%)		24.0-in. (80%)			
HSSS 2205 #3 Jacking End	13.6-in. (45%)		13.3-in. (44%)			
HSSS 2205 #3 Dead End	21.7-in. (72%)		20.9-in. (70%)			

The average transfer length of HSSS 2205 ½-in. (12.7 mm) strands and AISI 1080 conventional 7/16-in. (11.1 mm) strands are lower than the respective AASHTO and ACI

calculated values. At 14 days for the AISI 1080 strands, the average transfer lengths were 68% and 66% of the AASHTO and ACI 318 lengths, respectively. At 14 days for the duplex HSSS 2205 strands, the average transfer lengths were 57% and 74% of the AASHTO and ACI 318 lengths, respectively. Also, individual results at 14 and 273 days ranged between 33% and 97% of the AASHTO prediction. Conversely, the transfer lengths of conventional steel strands were less than the ACI equation, but not all of the duplex HSSS 2205 strand lengths were.

In the case of pile HSSS 2205 #2, one end showed a transfer length higher than the ACI 318 prediction before driving, while both ends showed a higher transfer length after driving. Pile HSSS 2205 #2 was not easily removed from the form bed during fabrication and additional mechanical hammering was required. This early disturbance and vibration of the pile may have contributed to the relatively higher transfer length values.

Transfer length results present an important variability, with values ranging from 9.8-in. (24.9 cm) to 25.5-in. (64.8 cm). Transfer length of pretensioned elements may be influenced by strand diameter, specimen cover, concrete strength at strand release, and is usually higher at the cut end (Oh and Kim, 2000; Oh et al., 2006). As mentioned in Chapter 4, the use of concrete mixtures from different batches introduced variability in the strength of concrete for different specimens. Even when concrete strength measured in cylinders before strand release was 4,018 psi (27.7 MPa), it is expected that concrete strength varied among the piles. Additionally, results show that the tested end of the pile has a high influence on the obtained transfer length. Calculated transfer length at the jacking end was lower than the dead end (anchorage end) in all cases. The anchorage end

had approximately 100 ft. (30.5 m) of free strand compared to about 10 ft. (3 m) at the jacking end.

Pile driving had little effect on calculated transfer length. While Figures S.1 to S.10 in Appendix S show an increase of the overall compressive strain after driving, the transfer lengths remained the same.

6.3.2 Comparison of Transfer Length Results with Proposed Expressions

Expressions for transfer length reported by previous studies and detailed in Section 2.3.1.2 are compared with experimental results in Table 6.3. Calculation of transfer lengths considers prestress losses obtained by the AASHTO refined estimation method. Percentage difference was calculated using Equation 6.4. Thus, a positive difference between experimental l_t and a proposed equation indicated that the equation is a conservative prediction.

$$Difference = \frac{l_{t,proposed} - l_{t,experimental}}{l_{t,experimental}} \tag{6.4}$$

Experimental results are conservative compared to most of the expressions. The equation described by Buckner (1995) for the best fit for transfer length results, calculated using the 95% AMS method from data originated in many research programs, is the only non-conservative expression for both types of steel.

Equations based only on the diameter of the prestressing strand (AASHTO LRFD [2013] and Martin and Scott [1976]) are overly conservative for duplex HSSS 2205 strand. These equations consider the increase of the transfer length when strands with

higher diameter are used. In this case, the same jacking force was applied to the piles, therefore a lower initial prestress was applied to duplex HSSS 2205 strands.

Table 6.3 Comparison of experimental transfer length with code values and research proposed expressions. (1-in. = 2.54 cm)

	Duplex HSSS 2205		**AISI 1080 Steel**	
	l_t (in)	Difference	l_t (in)	Difference
Experimental	**17.1**	---------	**17.8**	---------
AASHTO LRFD	**30.0**	+ 75.2%	**26.3**	+ 47.9%
ACI 318	**21.2**	+ 24.1%	**25.5**	+ 43.5%
Zia and Mostafa	**22.3**	+ 30.2%	**26.8**	+ 50.7%
Martin and Scott	**40.0**	+ 133.6%	**35.0**	+ 97.2%
Russell and Burns	**31.9**	+ 86.1%	**38.2**	+ 115.2%
Deatherage et al.	**23.9**	+ 39.6%	**27.9**	+ 57.0%
Mitchell et al.	**20.5**	+ 19.7%	**23.9**	+ 34.6%
Buckner – Design	**23.9**	+ 39.6%	**27.9**	+ 57.0%
Buckner – Best Fit	**14.6**	– 14.7%	**17.0**	– 4.1%
Lane	**32.0**	+ 87.2%	**42.1**	+ 137.2%
Meyer – Design	**30.6**	+ 78.8%	**26.8**	+ 50.9%
Meyer – Best Fit	**25.0**	+ 46.0%	**21.9**	+ 23.2%
Ramirez and Russell	**20.0**	+ 16.8%	**17.5**	– 1.4%

Expressions using stress in prestressing strand after release, $f_{si,}$ (i.e., stress after losses due to elastic shortening) and concrete strength at release, f_{ci}', provide better

agreement with experimental transfer lengths than the predictions using the effective stress at the prestressing strand after all losses, f_{se}. It has been observed previously that transfer length of pretensioned members is directly related to the stress of prestressing strand right after or at release and inversely related to the strength of concrete at release (Oh and Kim, 2000; Barnes et al., 2003). The use of these parameters can account for the use of non-conventional strands.

6.3.3 Development Length Results

In all the tests, the first flexural crack appeared when the load was about 60% of the ultimate load and the tests were stopped when the beam failed in either a flexural mode or shear/bond mode.

Load-deflection curve, strain distribution of the section during the test, moment-curvature curve, and shear-strand slip curve for each individual development length test are given in Appendix T.

6.3.3.1 Strand slip results

Displacements measured by the dials epoxied to the strands were subtracted from that measured by the dials epoxied to the end of the pile. The relative displacement of the strand with respect to the pile was the strand slip. Figure 6.10 shows the results of shear vs. average slip for each test, and Figure 6.11 shows the slip at failure for each embedment length.

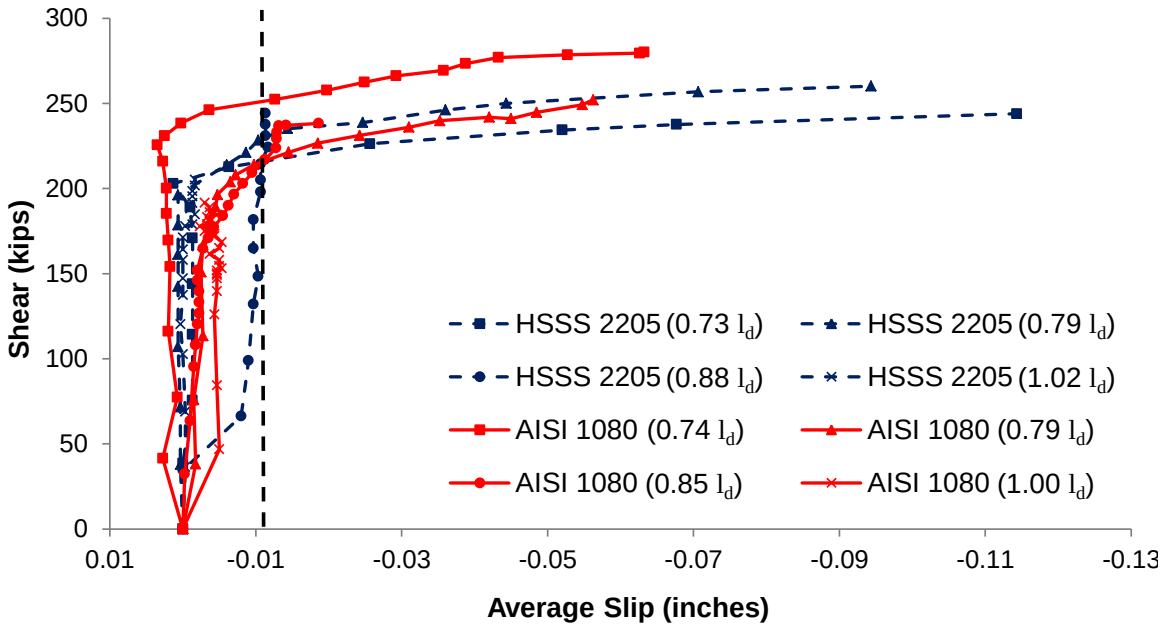

Figure 6.10 Average strand slip with shear increase during testing. Dashed, vertical line shows limit of 0.01-in. (0.254 mm) for strand slip at failure. (1-in. = 2.54 cm)

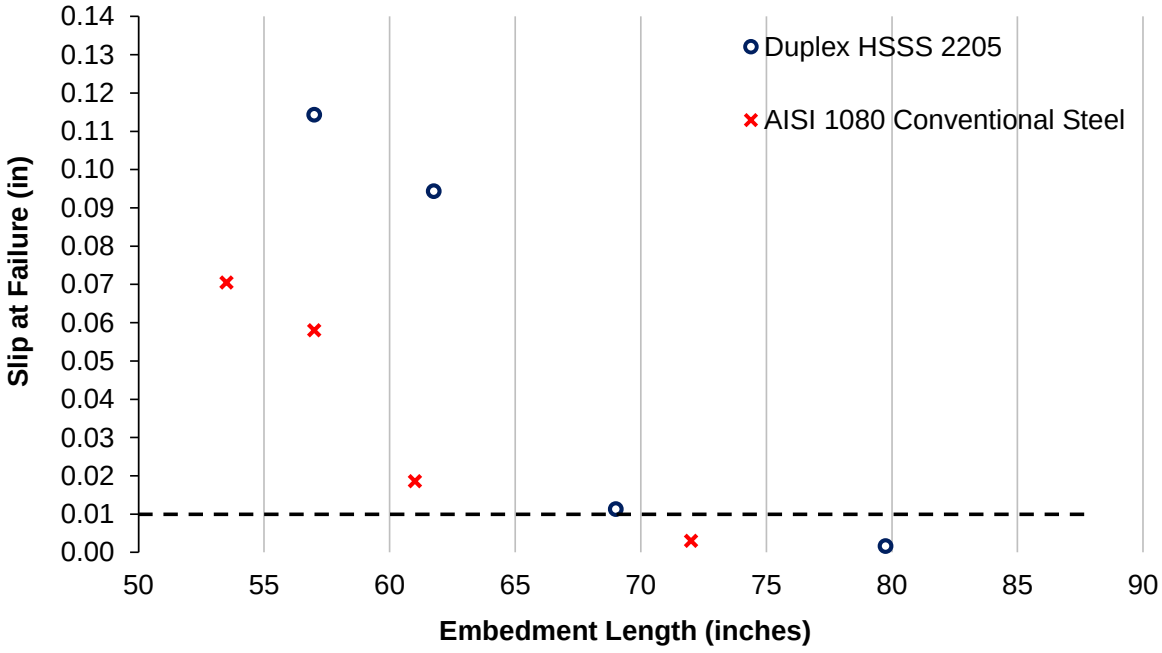

Figure 6.11 Slip at failure. Dashed line shows the assumed slip failure limit and defined flexure and shear failure of piles. The calculated l_d by Equation 10.1 for duplex HSSS 2205 and conventional steel are 78.3 and 72.0-in., respectively. Using Equation 10.2, these values are 125.2 and 115.3-in., respectively. (1-in. = 2.54 cm)

When the theoretical l_d calculated using Equation 10.1 was used as embedment length, negligible strand slips were observed (0.002-in. [0.0508 mm] and 0.003-in. [0.0762 mm] for duplex HSSS 2205 and conventional steel strands, respectively). Embedment lengths corresponding to a 79% and 74% of the predicted l_d by Equation 10.1 exhibited strand slip that exceeded the 0.01-in. (0.254 mm) limit. Embedment length of 85% l_d for conventional steel strands and 88% l_d for duplex HSSS 2205 strands corresponded to strand slip at failure closest to 0.01-in. (0.254 mm).

Figure 6.12 shows the strain and stress at the bottom layer of strands during the test. The initial stress corresponds to the effective stress of the prestressing strands (f_{se} or f_{pe}) at start of testing. This value was calculated by subtracting the experimental losses measured with internal vibrating wire strain gauges from the initial jacking stress. Increasing strains in the strands during the test were measured using the external strain gauges located at the depth of the bottom layer. The measured stress-strain curves of the prestressing strands were used to determine the strand stress based on the measured strand strains.

Figure 6.13 shows the stress at the bottom layer of strands vs. average slip. It is observed that the use of an embedment length of 73% l_d for duplex HSSS 2205 strands was the only test where the ultimate estimated stress was lower than 97% of the UTS.

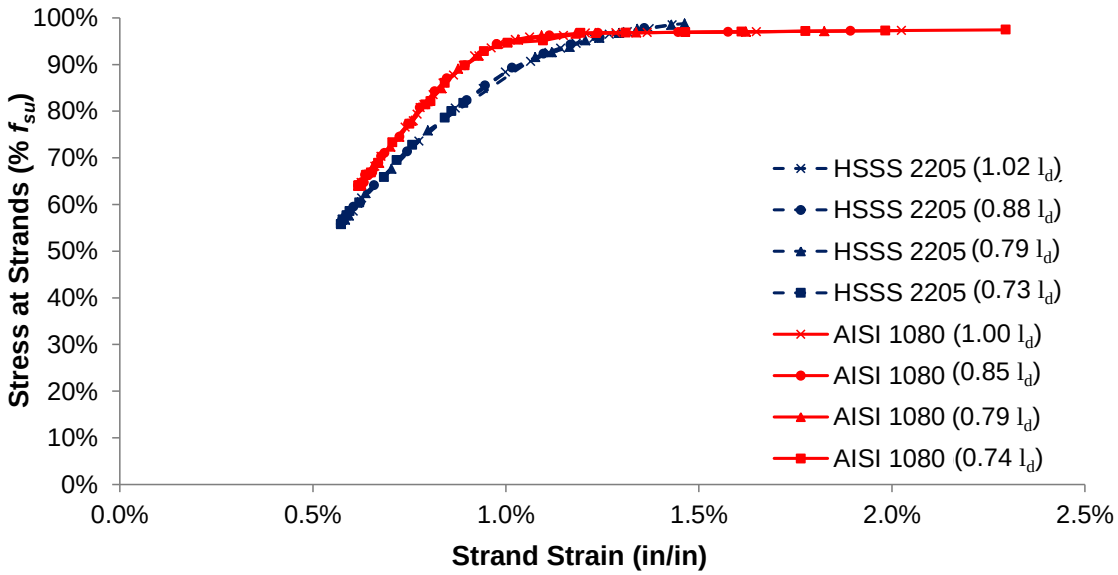

Figure 6.12 Stress and strain of bottom layer of strands during testing. Stress is shown as percentage of the UTS of the strand.

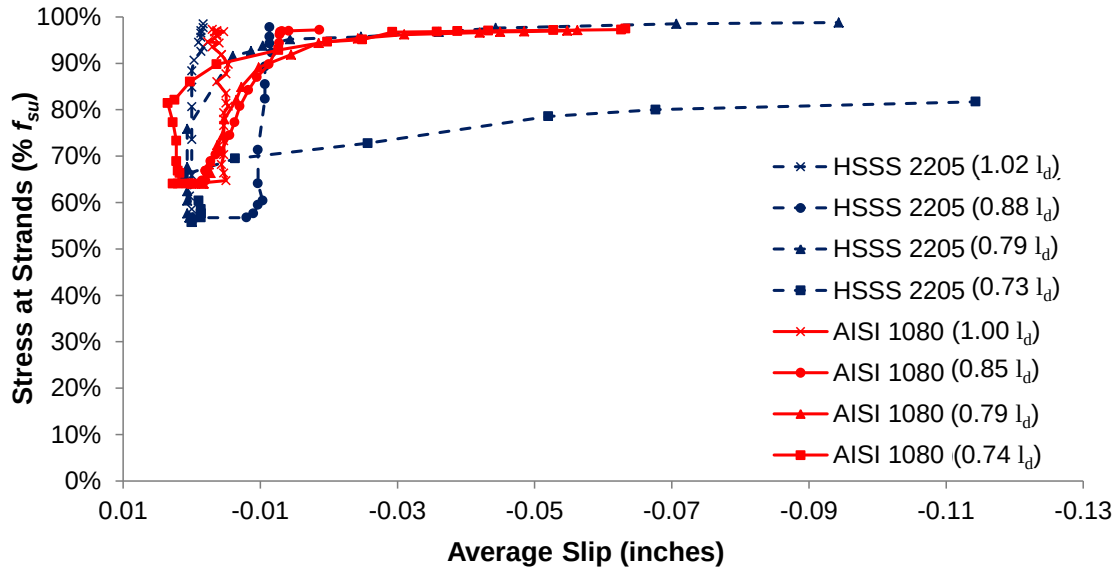

Figure 6.13 Average strand slip with stress increase in the bottom layer of strands. Stress is shown as percentage of the UTS of the strand. (1-in. = 2.54 cm)

For conventional steel strands, ultimate stress estimated in all the tests ranged between 97.2% and 97.4% of f_{su}. Ultimate strains ranged between 1.83% and 2.29%; the test with shortest embedment length (0.74 l_d) was the one with the highest strand strains.

In the case of duplex HSSS 2205 strands, ultimate stresses and strains of the bottom strands for embedment lengths 102%, 88%, and 79% l_d ranged between 97.8% and 98.8% of the UTS, and between 1.36% and 1.46%, respectively. However, for the test with the shorter embedment length (73% l_d) the ultimate stress was only 81.7% of the UTS at strand slip.

The differences between both types of steel can be explained by the higher ductility of conventional steel strands compared to duplex HSSS 2205 strands given in Table 4.1 (ε_u of 5.89% vs. 1.60%).

The experimental development length was selected as the lowest embedment length in which the strand slip was less than 0.01-in (0.254 mm) and in which the member failed in a flexural rather than shear or bond mode. From Table 10.1, the shortest embedment length which led to a flexural failure with no strand slip was 61-in. (154.9 cm) for piles made with conventional 1080 strand and was 69-in. (175.3 cm) for piles made with HSSS 2205 strand. This meant that the experimental development length of conventional 1080 strand was 85% of the predicted value by ACI 318 and 53% of the predicted value by AASHTO LRFD. The experimental development length of duplex HSSS 2205 strand was 88% of the predicted value by ACI 318 and 55% of the predicted value by AASHTO LRFD. Thus, the use of ACI 318 Equation 10.1 and AASHTO LRFD Equation 10.2 to estimate the development length of duplex HSSS 2205 strands gave values which were greater than the experimental values; therefore, the equations are conservative.

6.3.3.2 Failure type

Crack pattern observed in both types of failure is shown in Figure 6.14, where the number next to the crack corresponds to the recorded load at the time that the crack was at the cross-mark position. Loads in Figure 6.14 are different than the shears given in Figure 6.10.

(a)

Figure 6.14 Typical crack pattern exhibited after (a) flexural failure when the strands ruptured, and (b) shear/bond failure of piles. (1 kip = 4.45 kN)

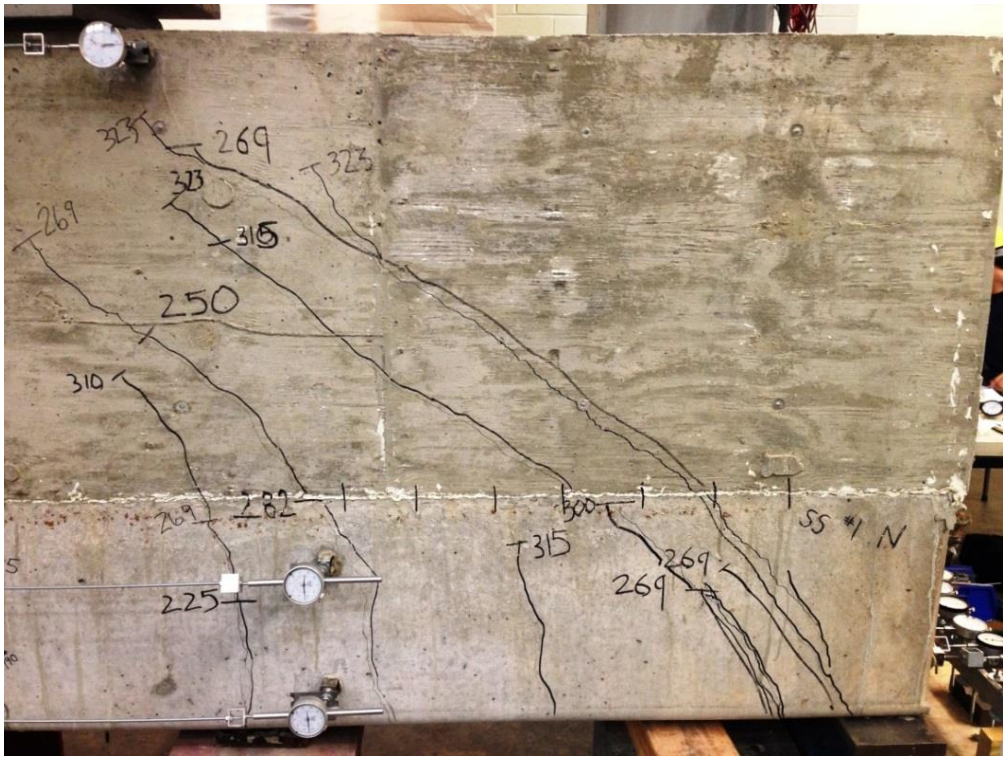

(b)

Figure 6.14 (cont.) Typical crack pattern exhibited after (a) flexural failure when the strands ruptured, and (b) shear/bond failure of piles. (1 kip = 4.45 kN)

Good composite behavior was evidenced by the continuity of the cracks between the precast pile and poured-in-place top section.

Piles loaded at an embedment length around 102% and 88% of l_d predicted by ACI 318 exhibited a typical flexural failure (Figure 6.14a) with the HSSS 2205 strand breaking at the end of the test and with strand slips lower or similar to the 0.01-in. (0.254 mm) limit. After strand breaking, the rupture of the whole section was observed at the location of the applied load.

Piles loaded at embedment lengths of 79% and 73% of l_d predicted by ACI 318 showed shear failure (Figure 6.14b). Shear cracks initiated at 2 to 8-in. (5 to 23 cm) from the pin support at a moment that coincided with the onset of slip of the strands (see

Figure 6.10). Large increases of strand slip after initiation of shear cracks in the transfer length zone have also been reported by Meyer (2002) and Russell (1992).

The first shear crack extended from the bottom of the pile to the mid-height of the original pile, passing through at least two rows of strands at an angle approximately 45° from the horizontal. Tests that exhibited shear failures were stopped after a sudden drop of the recorded load was observed, which corresponded to strand slip and before a general rupture of the section.

6.3.3.3 Moment-curvature behavior

The experimental curvature was estimated using the strain distributions included in Appendix T, which were determined from the strain gauges attached to the sides of the composite pile specimens; the experimental moment was estimated using the applied load and the actual position of the load with respect to the supports.

Figure 6.15 shows the experimental moment curvature for duplex HSSS 2205 (blue lines) and conventional steel (red lines) piles. Black lines show the predicted, theoretical behavior using a Todeschini concrete stress block (Wight and MacGregor, 2011).

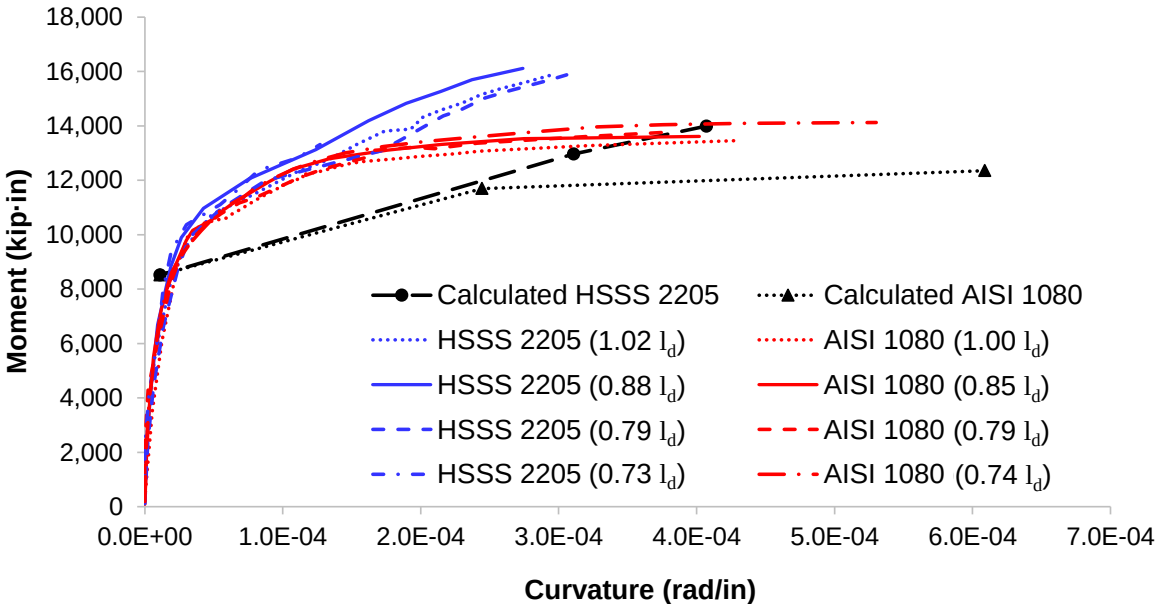

Figure 6.15 Experimental and predicted moment-curvature results. The ratio of the actual embedment length to predicted development lengths from Equation 10.1 are given in parentheses. (1 kip·in = 113 N·m, 1 rad/in = 39.37 rad/m)

Piles, using conventional and stainless steel, showed higher ultimate moments than predicted values. It is noted that the comparison of the nominal capacity of the piles should be made with experimental results that showed no strand slip, given that this assumption is made on the theoretical calculation.

In the case of conventional steel strand, the ultimate moment is similar for every test. However, the test that showed highest strand slip (0.071-in. [1.8 mm]) also exhibited an ultimate curvature 32% higher than the average of the rest of the tests. The difference in ultimate curvature can be attributed to a higher deformation of the horizontal strain gauges due to the combined effect of the applied load and the slip of the strands. However, using the measurement of the deformations of the pile, an estimated ultimate stress in the bottom strands of about 273.5 ksi (1,886 MPa) was calculated in each case.

For the piles using duplex HSSS 2205 strands, similar behavior was observed on tests with the three higher embedment lengths, but the test with the lowest embedment length and highest strand slip (0.114-in. [2.9 mm]) present an ultimate moment and curvature 17% and 57% lower than the average of the rest of the tests, respectively. Also, the estimated ultimate stress in the bottom strands dropped from 237.9 ksi (l_e = 1.02 l_d, [1,640 MPa]) to 197.4 ksi (l_e = 0.73 l_d, [1,361 MPa]).

6.3.3.4 Evaluation of development length using experimental prestress losses

The calculation of f_{pe} and f_{se} in Equations 6.2 and 6.3 was performed by the estimation of prestress losses at testing time using the AASHTO refined method (Section 5.7 and Appendix Q). However, the measured losses were lower than the predicted ones. Thus, the use of experimental losses leads to lower calculated development lengths for the piles.

Estimated prestress losses during testing were 21.0 and 19.6 ksi (145 MPa and 135 MPa) for piles using conventional steel and duplex HSSS 2205 strands, respectively; measured prestress losses closest to testing time were 14.0 and 12.3 ksi (96.5 MPa and 84.8 MPa). Using the latter values for the estimation of the development length in Equation 6.2, l_d changes from 72.0-in. to 70.0-in. (182.9 to 177.8 cm) for piles using conventional steel, and from 78.3-in. to 75.8-in. (198.9 to 192.5 cm) for piles using duplex HSSS 2205.

Considering this change, embedment lengths that exhibited strand slips close to 0.01-in. (0.254 mm) correspond to 87% and 91% of l_d based on Equation 6.2 for piles using conventional steel and duplex HSSS 2205 strands, respectively. Thus, the

experimental estimations of development length remain conservative when actual losses are considered in the calculation of l_d.

6.3.4 Comparison of Results with Proposed Expressions

Table 6.4 shows the experimental estimation of the development length compared to expressions proposed in the literature. The difference was calculated with respect to the experimental estimation, according to Equation 6.5.

$$Difference = \frac{l_{d,proposed} - l_{d,experimental}}{l_{d,experimental}} \tag{6.5}$$

Expressions with positive difference were considered conservative. Thus, equations proposed by Russell and Burns (1993), Mitchell et al. (1993), and Ramirez and Russell (2008) are non-conservative expressions for the estimation of l_d.

Good approximations of development length consider the nominal diameter of strand, d_b, the stress in the strand after transfer, f_{si}, the effective stress after prestress losses, f_{pe} or f_{se}, and the stress in the strand at nominal strength of member, f_{ps}. Concrete strength at strand release is also considered by some of the theoretical relations.

Table 6.4 Comparison of experimental l_d with codes values and research proposed expressions for development length. (1-in. = 2.54 cm)

	Duplex HSSS 2205		**AISI 1080 Steel**	
	l_d (in)	Difference	l_d (in)	Difference
Experimental	**69.0**	---------	**61.0**	---------
ACI 318	**78.3**	+ 13.4%	**72.0**	+ 18.1%
AASHTO LRFD	**125.2**	+ 81.4%	**115.3**	+ 89.0%
Zia and Mostafa	**93.5**	+ 35.6%	**85.0**	+ 39.3%
Martin and Scott	**115.3**	+ 67.1%	**141.5**	+ 132.0%
Russell and Burns	**52.3**	– 24.2%	**55.4**	– 9.2%
Deatherage et al.	**109.4**	+ 58.6%	**97.7**	+ 60.2%
Mitchell et al.	**59.5**	– 13.8%	**55.7**	– 8.6%
Buckner	**94.6**	+ 37.1%	**165.5**	+ 171.4%
Lane	**93.0**	+ 34.8%	**88.5**	+ 44.3%
Meyer – Design	**84.9**	+ 23.1%	**71.0**	+ 16.4%
Meyer – Best Fit	**76.7**	+ 11.2%	**63.9**	+ 4.7%
Ramirez and Russell	**50.0**	– 27.5%	**43.8**	– 28.3%

Equations included in ACI 318 (2011) and AASHTO LRFD (2013) provided conservative estimations for transfer and development length. Additionally, Table 6.5 shows the expressions proposed in the literature that gave closer approximations of experimental transfer and development length for piles using duplex HSSS 2205 and conventional steel strands. The selection of the best proposed equations other than ACI

and AASHTO are those which gave a ratio of experimental-to-predicted development length and a ratio of experimental-to-predicted transfer length less than 1.0.

Table 6.5 Expressions closer to experimental values.

Zia and Mostafa (1977)	l_t	$l_t = 1.5\frac{f_{si}}{f_{ci}^{'}} d_b - 4.6$
	l_d	$l_d = \left(1.5\frac{f_{si}}{f_{ci}^{'}} d_b - 4.6\right) + 1.25\left(f_{su} - f_{se}\right)\cdot d_b$
Deatherage et al. (1994)	l_t	$l_t = \frac{f_{si}\cdot d_b}{3}$
	l_d	$l_d = \frac{f_{si}\cdot d_b}{3} + 1.50\left(f_{su} - f_{se}\right)\cdot d_b$
Meyer (2002)	l_t	$l_t = 50\cdot \mathrm{d_b}\sqrt{\frac{6{,}000}{f_{ci}^{'}}}$
	l_d	$l_d = \left(50\sqrt{\frac{5{,}000}{f_{ci}^{'}}} + f_{ps} - f_{se}\right)\cdot \mathrm{d_b}$

6.4 Conclusions of the Chapter

Transfer length of prestressed concrete piles using duplex HSSS 2205 strands can be conservatively estimated using predicted values by AASHTO LRFD and ACI 318. Additionally, pile driving does not affect the transfer length of prestressed concrete piles.

Experimental development length of duplex HSSS 2205 strands were found to be 88% of the specified value computed by ACI 318, and 55% of the specified value computed by AASHTO LRFD. Thus, development length of prestressed concrete piles using duplex HSSS 2205 strands can be conservatively estimated using equations given by AASHTO LRFD and ACI 318.

CHAPTER 7

CONCLUSIONS AND RECOMMENDATIONS

The research described in this document investigated the impact of the use of acidic sands and of stainless steel reinforcement on coastal prestressed concrete structures, in order to improve their long-term performance and to comply with existent requirements of service life. Conclusions and recommendations of this thesis are shown separately for the study of acidic sands and stainless steel reinforcement.

7.1 Conclusions

7.1.1 Acidic Sands

The use of sulfide- and sulfate-bearing aggregates in concrete and mortar was found to produce measureable effects on early age behavior, mechanical properties, and factors influencing long-term performance. Both acidic sands tested behaved in a different way with respect to a siliceous control sand, approved by GDOT for its use as concrete fine aggregate. Furthermore, sands obtained from the same deposit, at different times, also presented dissimilar performance in terms of early-age and mechanical properties. These results evidence the variability of the sand deposit and the lack of consistency of the extracted sand. Conclusions of the analysis of acidic sands are given as follows.

- Isothermal calorimetry results show that for a range of cement compositions delays in early cement hydration can be expected in the presence of Site D or Site H sand, compared to the GDOT-approved sand source. The magnitude of the delay is dependent

on the cement composition and the sand, with Site H producing generally greater delays, presumably due to a greater sulfate content in that source.

- Vicat setting time tested on five different cement compositions showed that the use of acidic sands generally delays the setting time of mortar compared to Control sand. Site H sand showed greater delay in every mortar mixture, while Site D sand showed earlier setting than Control sand only when Type V cement was used. Minor differences among the sands were observed on the cumulative heat of hydration at 4 days.

- A moderate increase in compressive strength and dynamic modulus of elasticity is observed in concrete containing Site H sand when compared to that with Control sand or Site D sand, when examined in GDOT Class AA1 concrete. Statistical analysis shows that the compressive strength and dynamic modulus of Site H concrete are higher compared to Site D samples at every age of testing, except for the strength at 7 days when no statistical difference was found between the three sands. Despite the higher values obtained for the Site H concrete, because Site D and H sand were obtained from the same source, the variability in the concrete mechanical properties is a concern.

- All tested sands produced concretes with moderate chloride permeability, according to 56-day rapid chloride permeability test and 2-year surface resistivity results.

- No evidence of expansion due to internal sulfate attack initiated by the presence of sulfates or sulfides in the aggregate sources was observed in mortar samples over a testing period of more than 400 days.

- When examining the potential for Site H sand to participate in reactions leading to DEF-induced expansion in mortar mixtures exposed to a high temperature curing, dependence on cement composition was noted. For Type I and Type I/II cements, the

presence of Site H sand accelerates the onset and rate of DEF expansion; in Type III cement mortars, Site H sand generates higher ultimate expansion. Mortar containing Site H sand and Type V cement showed potentially damaging DEF-expansion, while mortar containing Control sand and Type V cement showed no DEF-expansion. This effect can be attributed to alkali release from feldspar mineral and to the higher and more distributed sulfate content present in Site H sand samples.

- Degree of microcracking and DEF-damage increased when higher expansions were measured and for cement with higher amount of C_3A and sulfate.

- The use of the Site H and Site D sands leads to earlier corrosion of reinforced steel bars embedded in concrete, compared to Control sand. The initiation of active corrosion occurred at an earlier age, and more extensive cracking and damage due to corrosion was observed when the Site D or H sands were used.

7.1.2 Stainless Steel Reinforcement

The use of duplex HSSS 2205 (ASTM A276 grade UNS S31803) to replace conventional AISI 1080 steel prestressing strands is proposed to increase the durability and provide a 100+ year service life of precast, prestressed concrete bridge piles exposed to marine environments. Further, special wire made using an austenitic stainless steel grade 304 (ASTM A276, UNS 30400) was investigated as a replacement for conventional wire spiral (AASHTO M32) and proved satisfactory. The investigation drew the following conclusions.

- Prestressed concrete piles reinforced with duplex HSSS 2205 strands can be built using the conventional precast concrete plant construction procedures.

- Duplex HSSS 2205 strand does not form a galvanic couple with austenitic SS 304 wire samples under alkaline, carbonated, and seawater conditions. Thus, these two different stainless steel alloys may be used together to reinforce prestressed concrete piles.

- Total prestress loss in piles with duplex HSSS 2205 was 18.0 ksi which represented a 12.4% loss from the initial jacking stress at 335 days. Total prestress loss in piles with conventional 1080 strand was 20.1 ksi which represented a 10.2% loss from the initial jacking stress at 335 days. The lower relaxation of duplex HSSS 2205 strands resulted in higher compressive stresses in the piles with the HSSS 2205 strand which caused higher creep strains and increased total loss. A loss of prestressing force lower than the GDOT specified limit is expected at the end of the service life.

- Prestress losses of duplex HSSS 2205 are 82.3% and 99.4% of the value predicted by AASHTO LRFD refined and lump-sum methods at 335 days, respectively. It is concluded than the use of AASHTO LRFD refined method for the calculation of prestress losses of duplex HSSS 2205 strands is conservative.

- Prestress losses of duplex HSSS 2205 and conventional steel strands were not affected by pile driving and extraction.

- The transfer lengths (l_t) of duplex HSSS 2205 and conventional steel obtained by concrete surface strain measurements at 14 days were shorter than the l_t predicted using AASHTO LRFD and ACI 318. Compared to calculations of transfer length following AASHTO LRFD, AISI 1080 steel and duplex HSSS 2205 presented average experimental values that were 68% and 57% of the predicted value, respectively.

- Prestressed concrete piles using duplex HSSS 2205 can be driven until refusal following GDOT requirements, without appreciable damage or visible cracking. The bearing capacity of piles using duplex HSSS 2205 was at least 27% higher than the design capacity.

- The transfer lengths of duplex HSSS 2205 and conventional steel strands were not significantly affected by pile driving and extraction. After driving, the l_t of AISI 1080 steel and duplex HSSS 2205 strands were 58% and 58% of the value predicted by AASHTO LRFD, respectively.

- The shortest embedment length which led to a flexural failure with no strand slip was 61 in. for piles made with conventional 1080 strand. Based on this experimental development length (l_d), the l_d of conventional AISI 1080 strands was found to be 53% of the value computed by AASHTO LRFD and 85% of the value computed by ACI 318.

- The shortest embedment length which led to a flexural failure with no strand slip was 69 in. for piles made with HSSS 2205 strand. Based on this experimental development length (l_d), the l_d of duplex HSSS 2205 strands was found to be 55% of the value computed by AASHTO LRFD and 88% of the value computed by ACI 318.

- Development and transfer length results demonstrated that duplex HSSS 2205 strands may be designed using current AASHTO LRFD and ACI 318 standards.

- For piles made with duplex HSSS 2205 strands, ultimate moment strengths obtained experimentally were 10 to 19% higher than those calculated using AASHTO LRFD provisions, and they were 0 to 9% higher than those calculated using ACI 318 provisions. For piles made with conventional AISI 1080 strands, ultimate moment strengths obtained experimentally were 4 to 16% higher than those calculated using

AASHTO LRFD provisions, and they were 3 to 6% higher than those calculated using ACI 318 provisions.

- Piles using duplex HSSS 2205 and with spiral, transverse reinforcement made using SS 304 showed statistically similar ultimate shear strengths as the piles made with conventional steel. There was no significant difference in pile strengths with spiral reinforcement spaced between 3 in. and 6 in.

Considering the conclusions stated above, duplex HSSS 2205 can be used in prestressing strands in combination with austenitic SS 304 for the transverse confinement and shear reinforcement for prestressed concrete piles, using the same design requirements and construction procedures used for conventional AISI 1080 steel.

7.2 Recommendations for Practice

7.2.1 Acidic Sands

Coastal lowland sources of aggregates should be tested in order to identify contamination by sulfates, sulfides, alkali feldspar or other potentially deleterious components and to assess pH. Testing should be performed routinely, to quantify variations in the same source or stockpile over time and variations during production and storage.

Due to concerns related to DEF, the use of sand containing sulfate, sulfide, or alkali feldspar is not recommended for mass, prestressed concrete, precast operations, or other applications where early high temperature could produce DEF. The use of supplementary cementitious materials (SCMs) may provide some benefit when general

use cements must be used, but the appropriate SCM type and use rate must be established.

The use of sulfide- and sulfate-bearing aggregate is not recommended for marine environments, given that concrete containing acidic sands is more prone to corrosion. This is particularly sensible in the case of prestressed concrete elements, where the chloride threshold limit (CTL) is lower due to the presence of crevices located at the impingement sites between adjoining prestressing wires.

7.2.2 Stainless Steel Reinforcement

It is recommended that duplex HSSS 2205 prestressing strand be used to reinforce precast prestressed concrete piles in marine environments and that austenitic SS 304 be used as transverse, spiral reinforcement in these same piles.

Until further studies are completed, it is recommended that the HSSS 2205 be initially stressed to not greater than 70% of the ultimate tensile strength.

7.3 Recommendations for Further Research

7.3.1 Acidic Sands

The impact of aggregates from questionable coastal sources on concrete performance has not been well-addressed in the literature or current codes. However, there is growing awareness of the importance of such materials. Further research should address at least the following topics.

- Quantification of the composition and variation in composition of sand deposits in coastal regions, in order to establish their range and variability.

- Statistical analysis, for a range of sands and a range of concrete compositions with varying binder (i.e., cement and SCM) compositions, to appreciate the range of mechanical behavior to better appreciate the influence of the inconsistency of sand source.

- The combination of cements with SCMs such as fly ash, silica fume or metakaolin, for the mitigation of DEF to determine appropriate SCMs compositions and their level of cement replacement. Currently, there is limited research showing the efficiency of SCM replacement in order to reduce or avoid expansion.

- The effect of the use of Type V cement on the corrosion resistance of reinforced concrete should be analyzed. Friedel's salt formation product of the reaction of C_3A and chloride ions may be minimized in the case of Type V cement. As a result, an even lower corrosion resistance could be obtained.

7.3.2 Stainless Steel Reinforcement

Further research is recommended in order to develop a heat treatment for the 2205 alloy or to develop a new alloy which has greater ductility than the current 2205 strand studied herein.

APPENDIX A: VP-SEM and EDS analysis of acidic sands

- Micrographs and EDS analysis of Control sand particles.

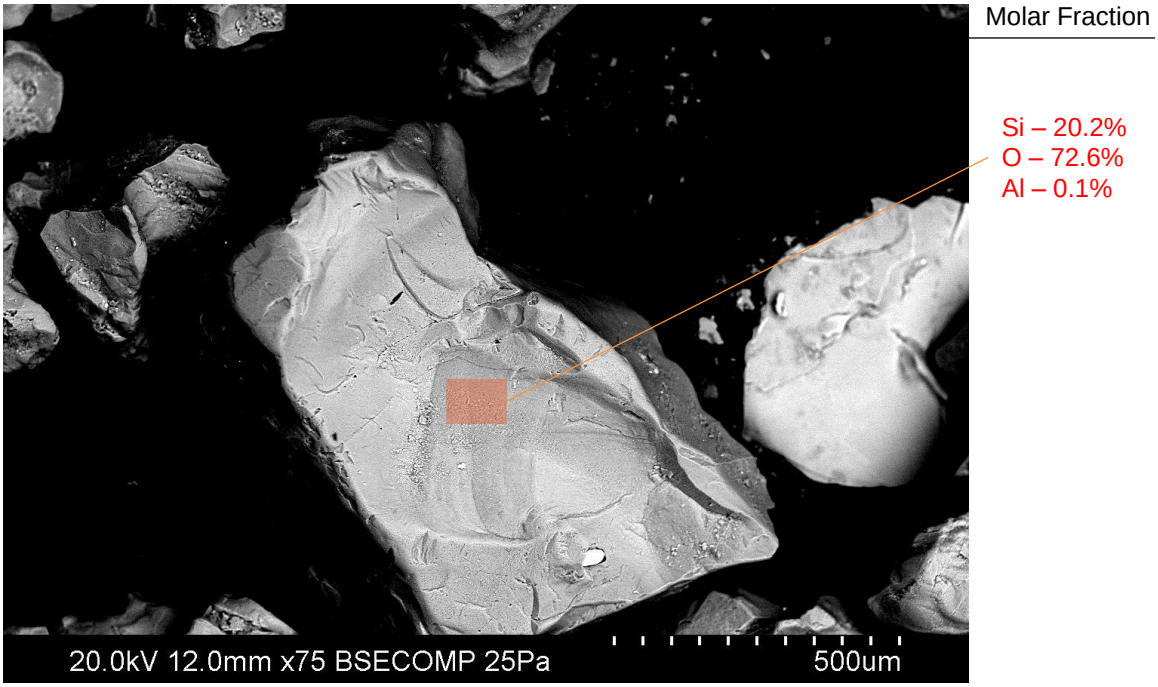

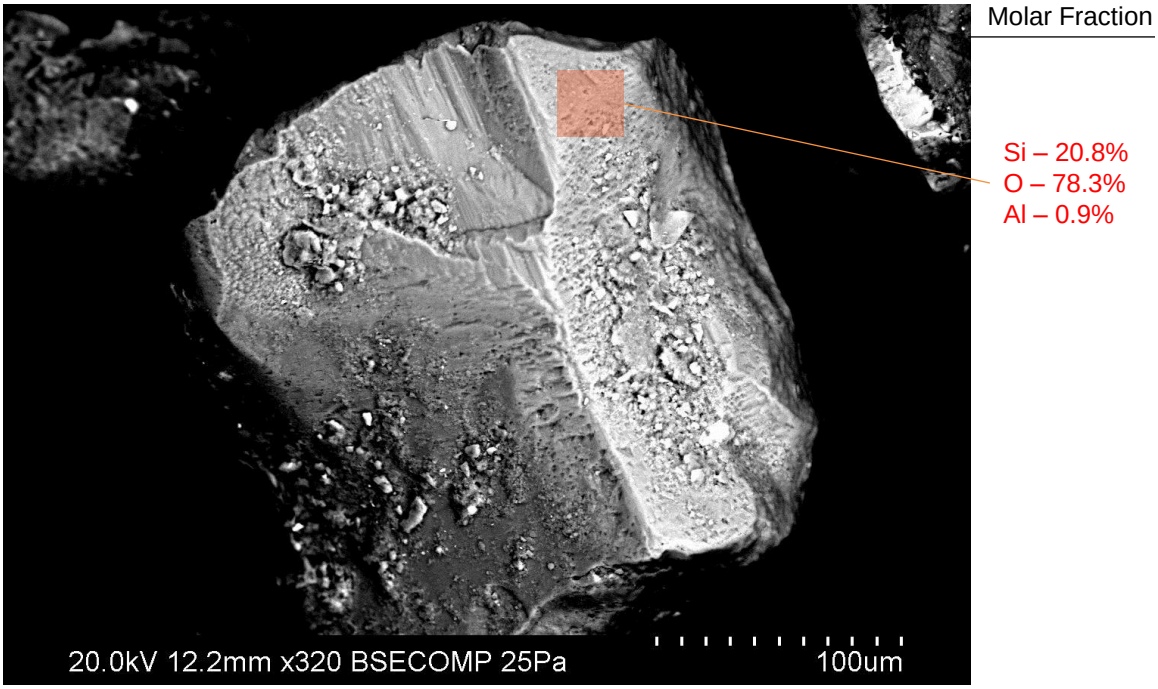

- Micrographs and EDS analysis of Site H sand particles.

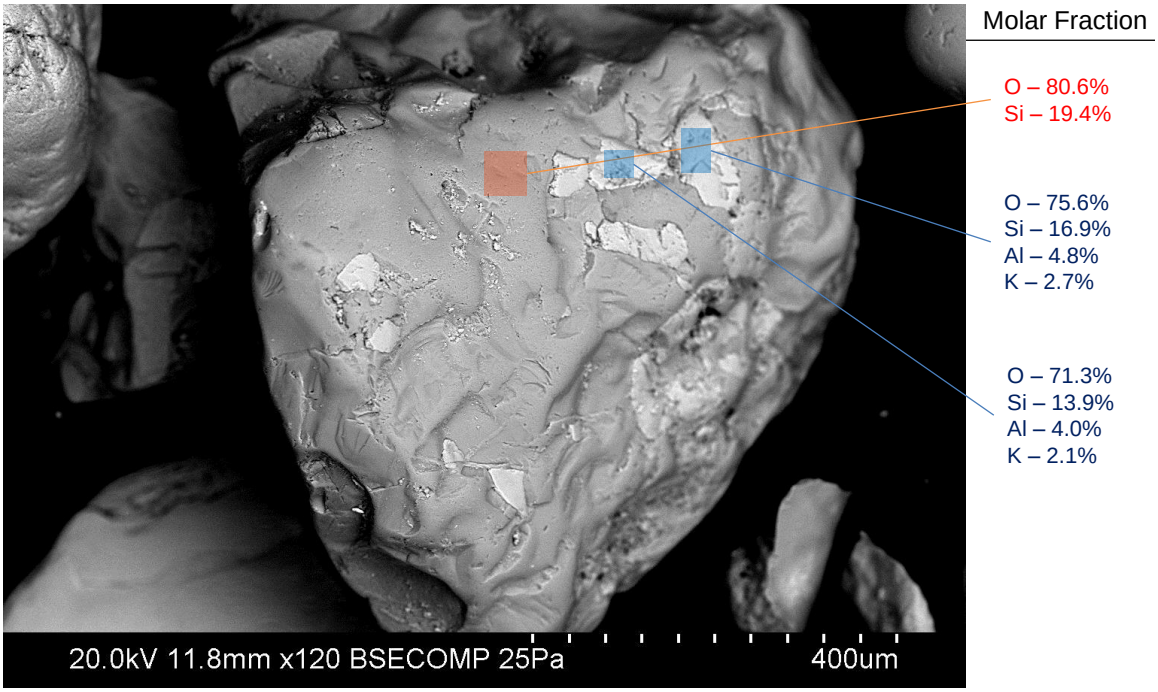

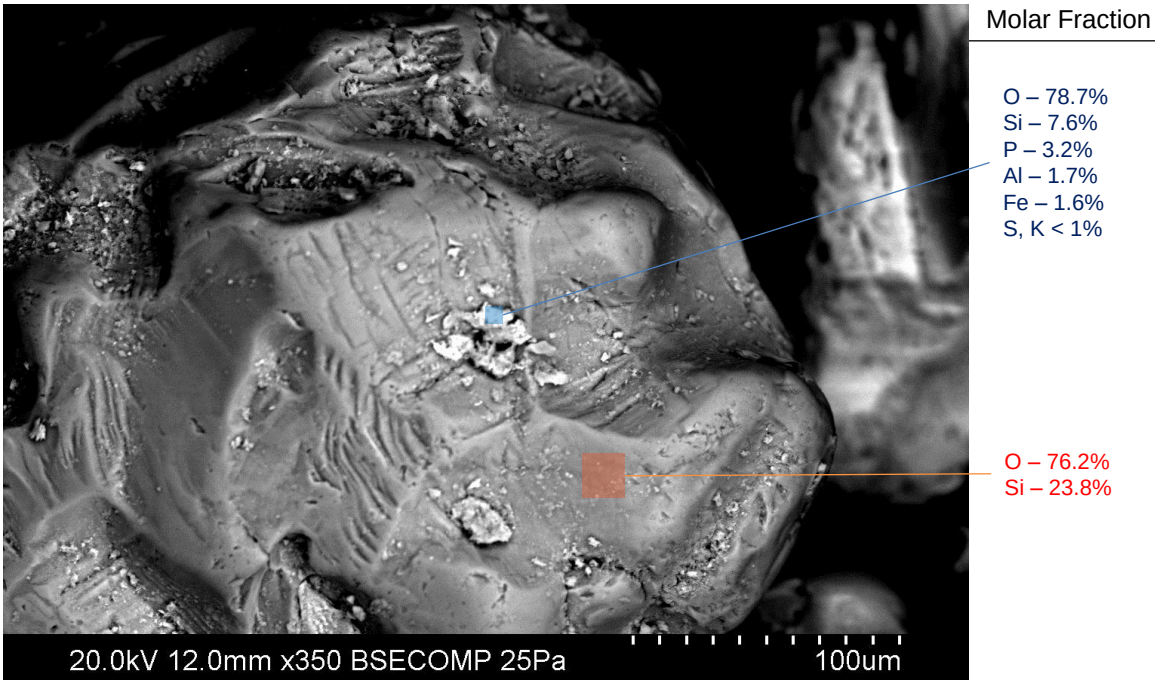

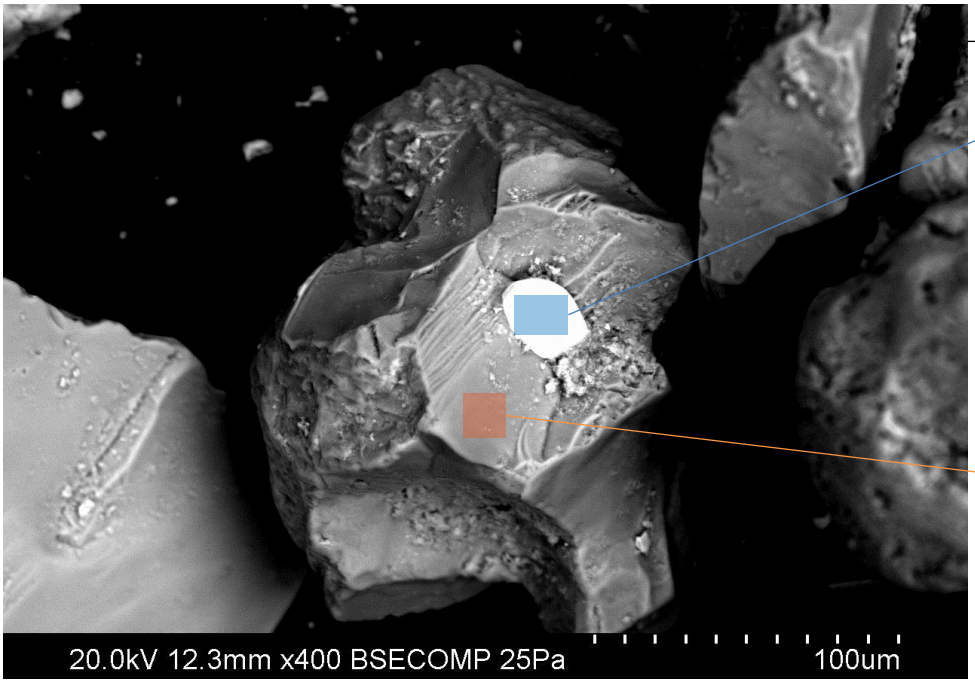
Molar Fraction
O – 66.7%
Si – 7.9%
Zr – 4.6%
Al – 0.3%
O – 79.0%
Si – 20.9%
20.0kV 12.3mm x400 BSECOMP 25Pa
100um

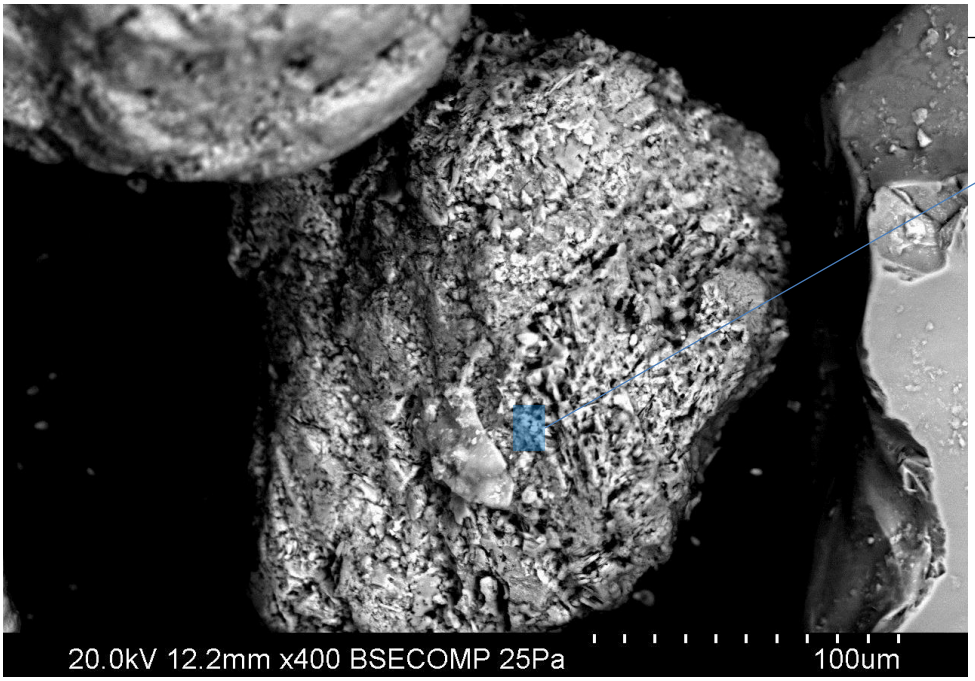
Molar Fraction
O – 76.0%
Si – 14.2%
Al – 6.6%
Na – 2.2%
K, Fe, Ca < 1%
20.0kV 12.2mm x400 BSECOMP 25Pa
100um

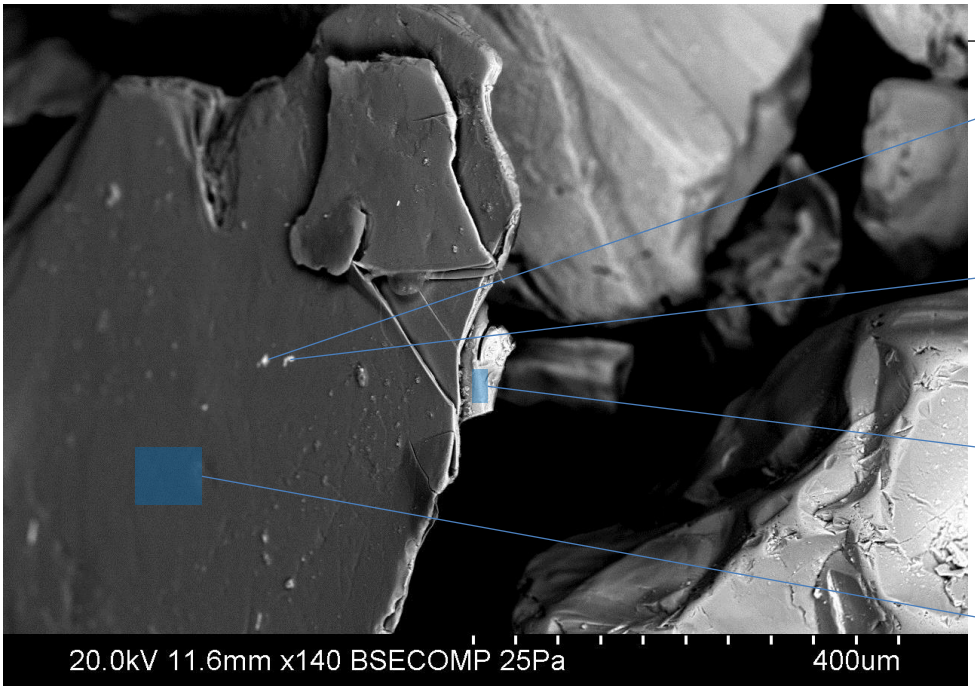

Molar Fraction

O – 79.2%
Si – 10.1%
Zr – 7.1%
Al – 2.3%
K, Fe, Mg < 1%

O – 76.0%
Si – 8.2%
Zr – 5.4%
Al – 2.5%
K, Fe < 1%

O – 73.7%
Si – 13.6%
Al – 9.3%
K – 2.2%
Mg – 1.1%
Fe – 0.1%

O – 75.3%
Si – 12.6%
Al – 9.2%
K – 2.0%
Mg – 0.8%

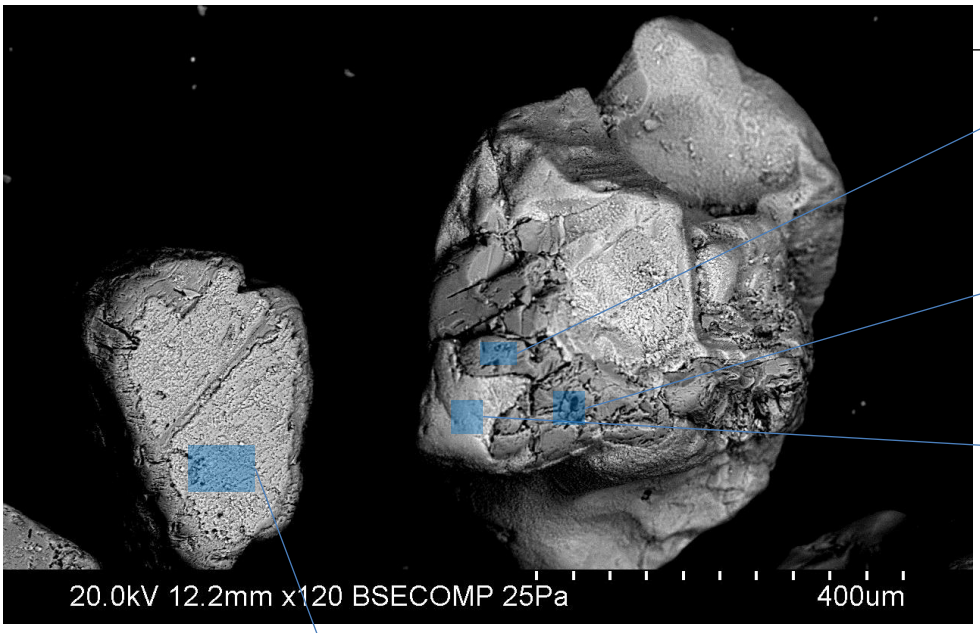

Molar Fraction

O – 64.0%
Si – 10.9%
Na – 5.0%
Al – 4.3%
K, Ca < 1%

O – 59.5%
Si – 11.1%
Al – 3.9%
Na – 3.6%
K, Ca < 1%

O – 61.9%
Si – 13.2%
Al – 4.2%
K – 2.6%
Na – 0.3%

O – 70.9%
Si – 12.1%
Al – 4.2%
K – 1.9%
Fe, Ti, Mg, Ca < 1%

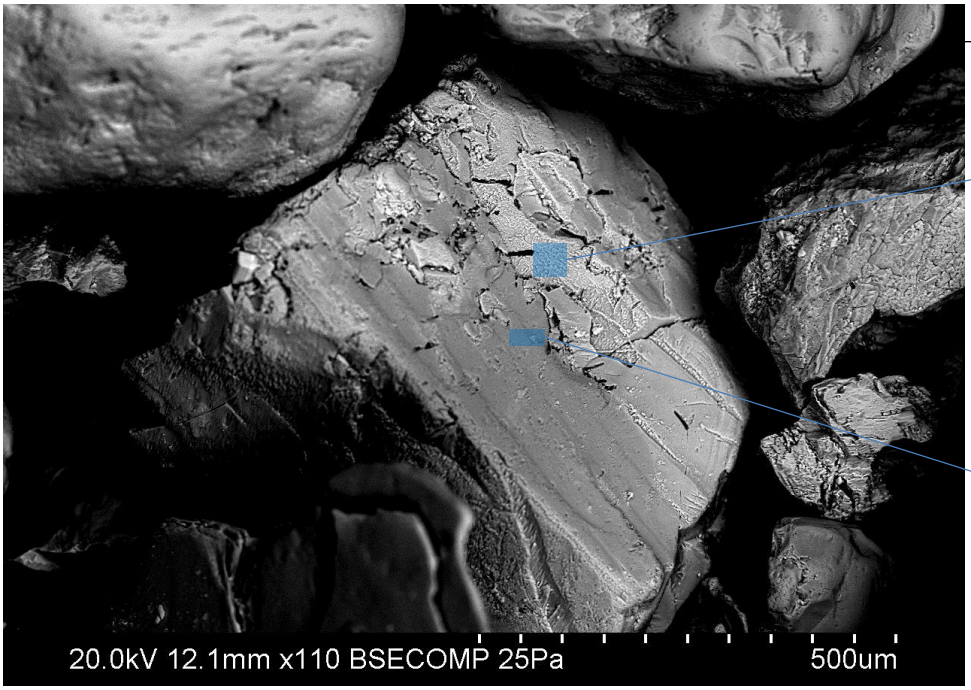

Molar Fraction

O – 71.3%
Si – 16.1%
Al – 6.6%
Na – 5.1%
Ca, P < 1%

O – 74.0%
Si – 13.5%
Al – 6.0%
Na – 5.9%
Ca, P, Mg < 1%

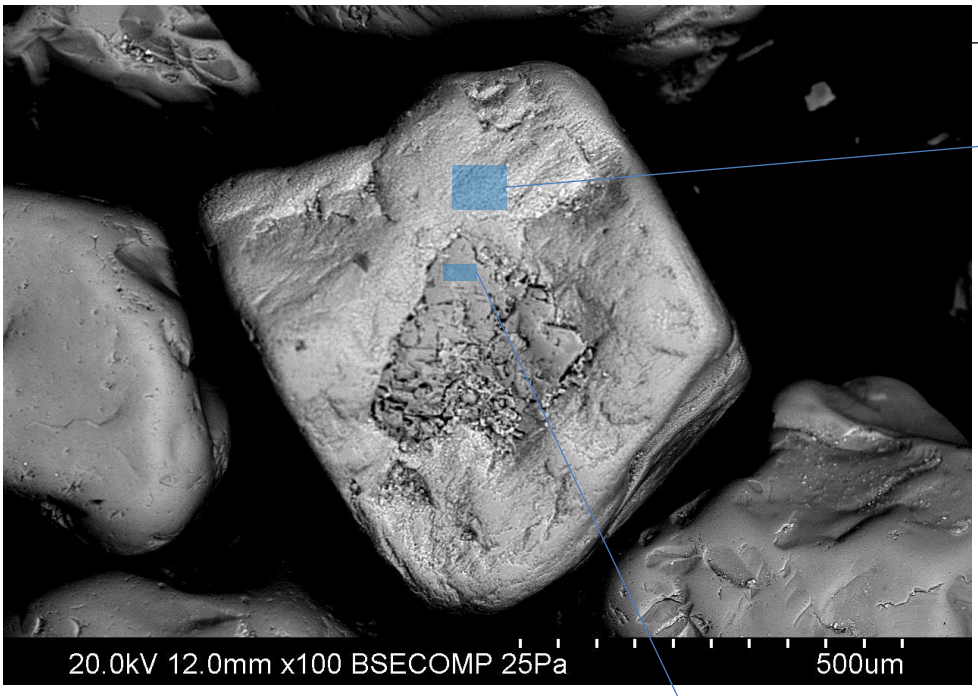

Molar Fraction

O – 76.9%
Si – 15.1%
Al – 5.0%
K – 2.4%
Na, S < 1%

O – 72.8%
Si – 15.2%
Na – 6.4%
Al – 5.2%
S, K, Fe, Mg < 1%

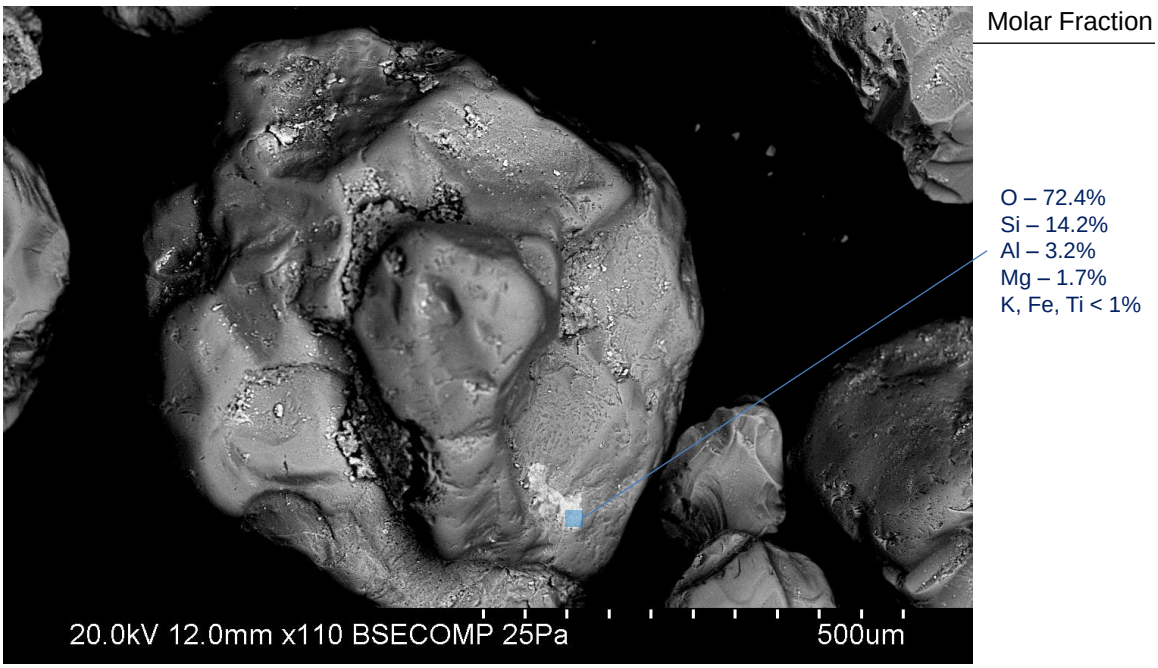

- Micrographs and EDS analysis of Site D sand particles.

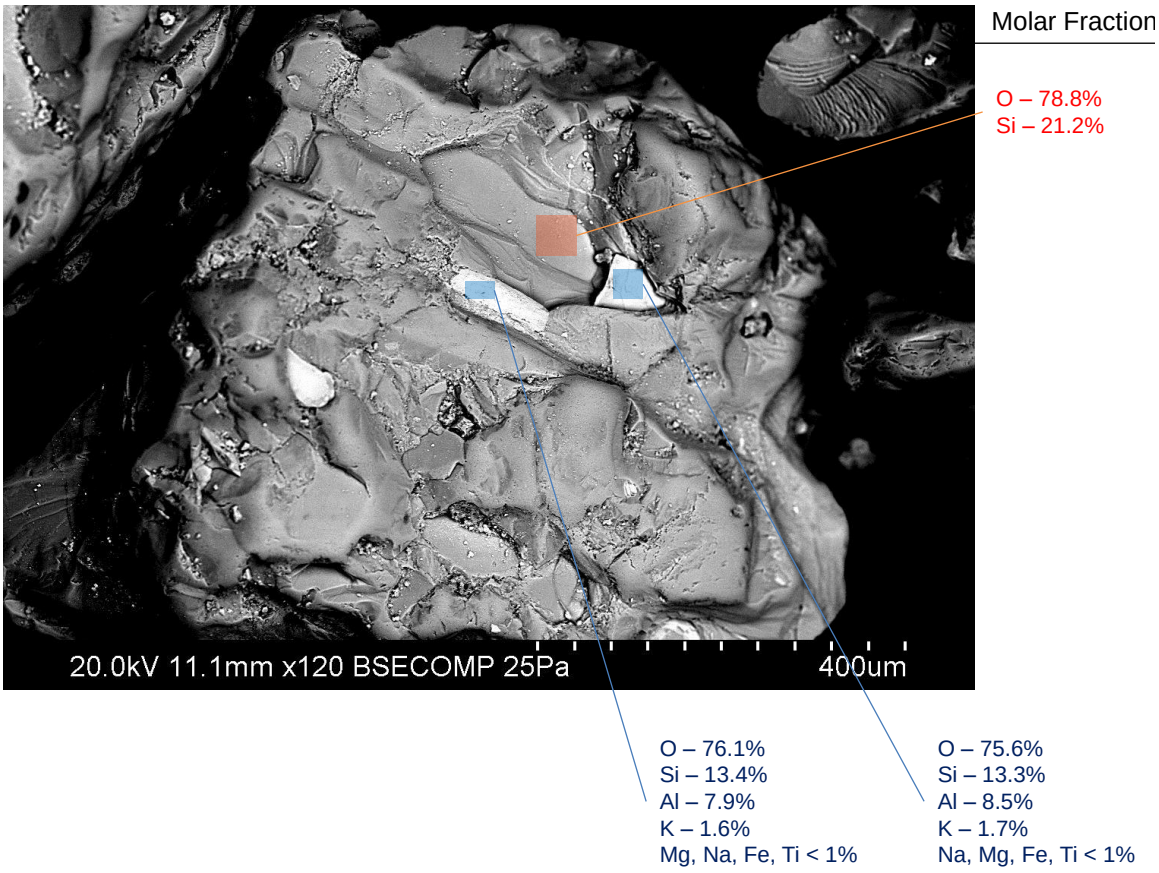

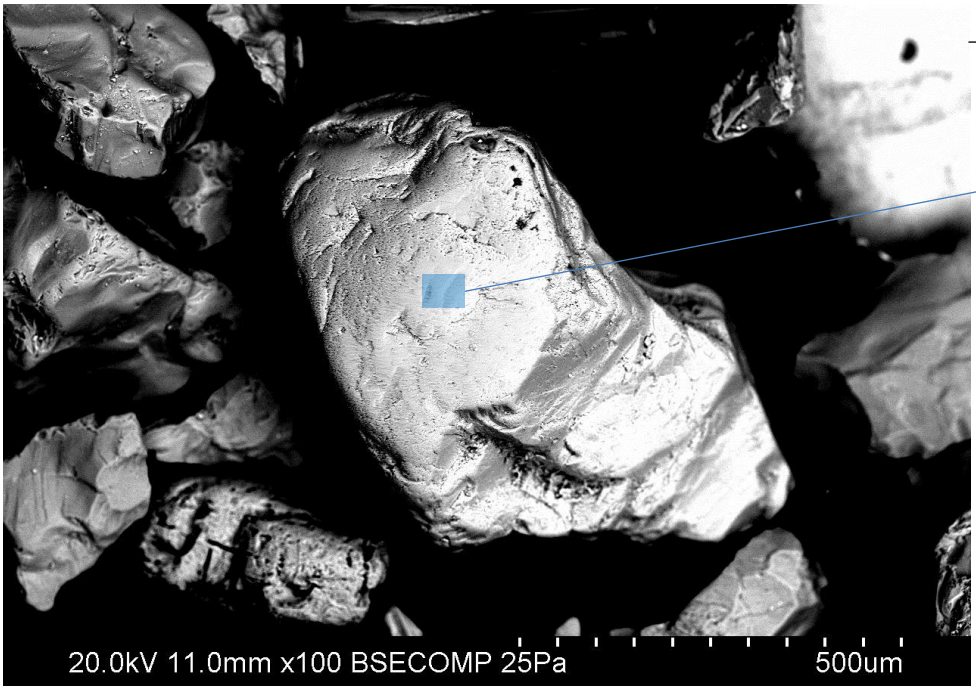

Molar Fraction

O – 70.6%
Si – 19.3%
Al – 5.9%
K – 3.8%
Na, Ca < 1%

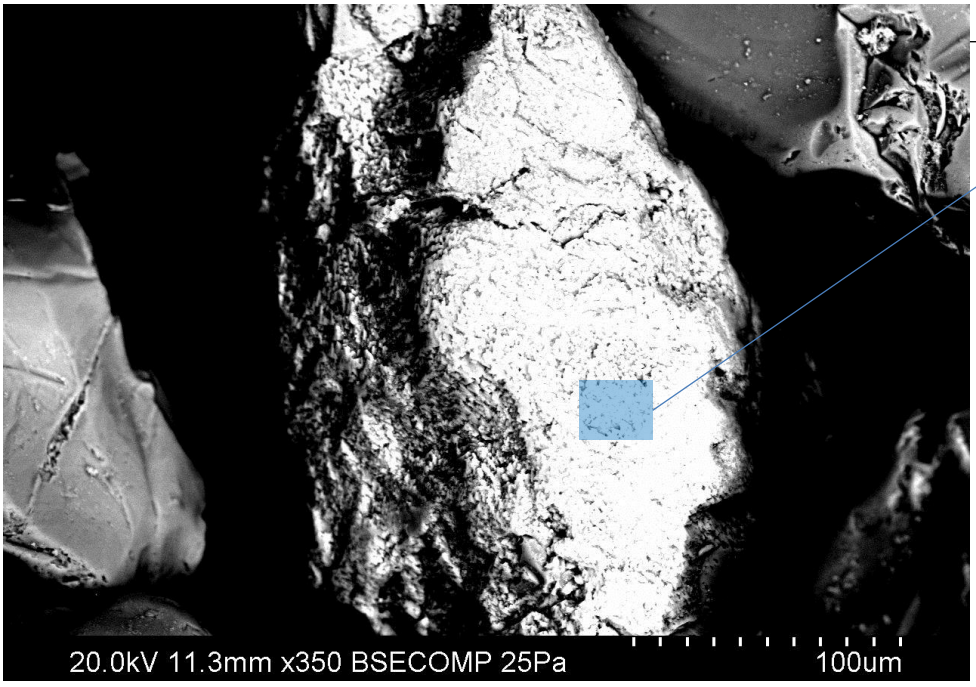

Molar Fraction

O – 74.6%
Si – 16.8%
Al – 5.5%
K – 2.7%
Na – 0.4%

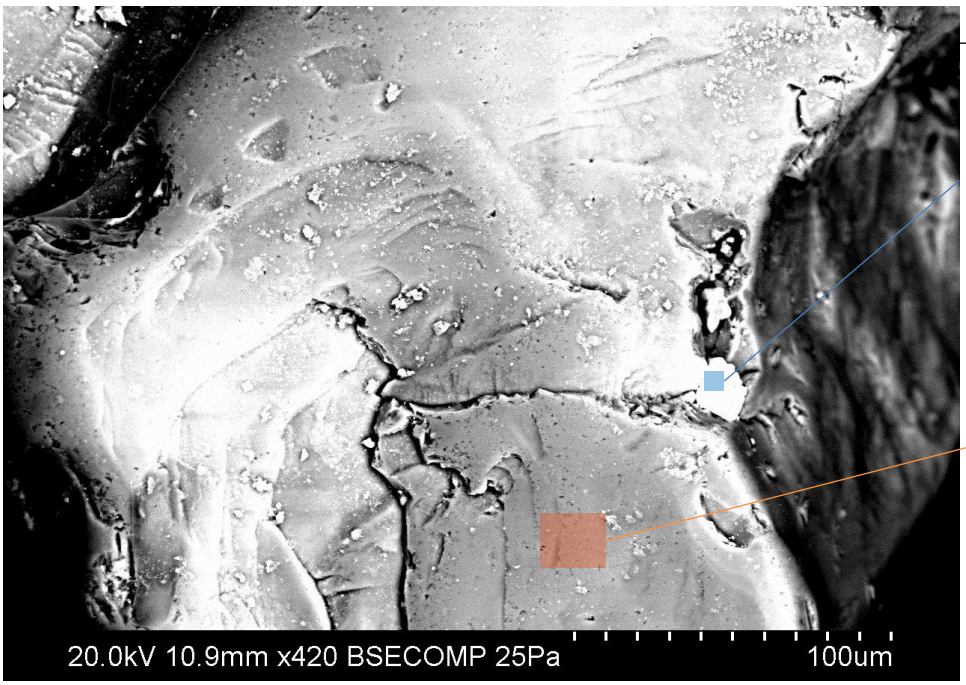

Molar Fraction

O – 74.4%
Si – 8.8%
Zr – 5.8%
Al, Fe, Na, K < 1%

O – 76.0%
Si – 24.0%

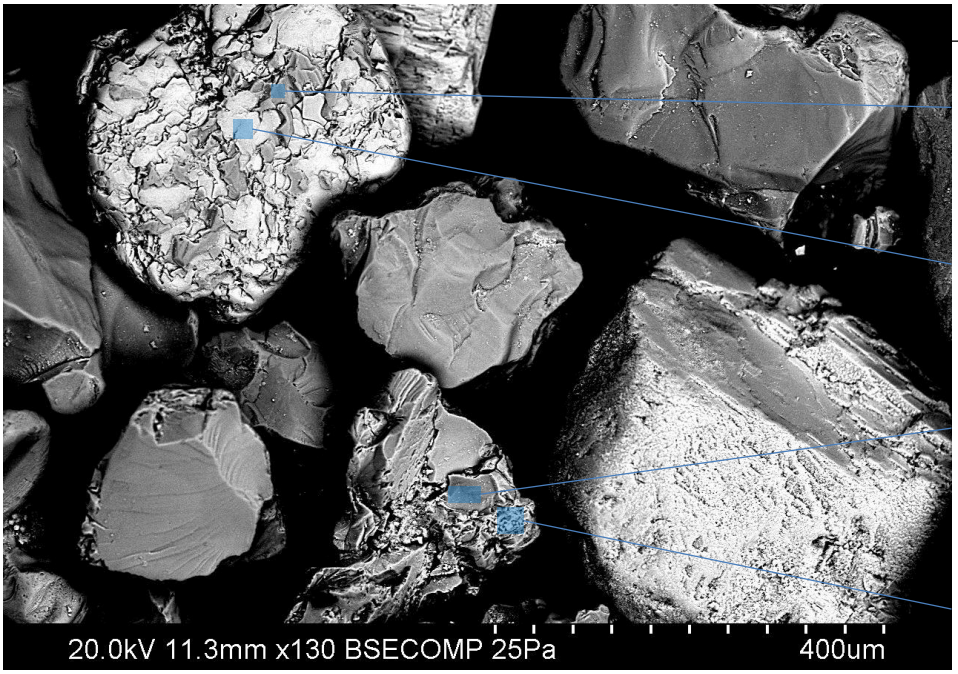

Molar Fraction

O – 77.9%
Si – 18.7%
Al – 2.2%
K, Na, Fe, Mg < 1%

O – 64.5%
Si – 10.8%
Al – 1.7%
K, Na, Fe, Mg < 1%

O – 70.2%
Si – 16.7%
Al – 6.8%
Na – 5.4%
Ca, K < 1%

O – 72.4%
Si – 15.4%
Al – 6.1%
Na – 4.5%
Ca, Ti, Fe, K < 1%


Molar Fraction
O – 74.0%
Si – 17.6%
Al – 5.2%
K – 3.1%
20.0kV 11.4mm x270 BSECOMP 25Pa
200um

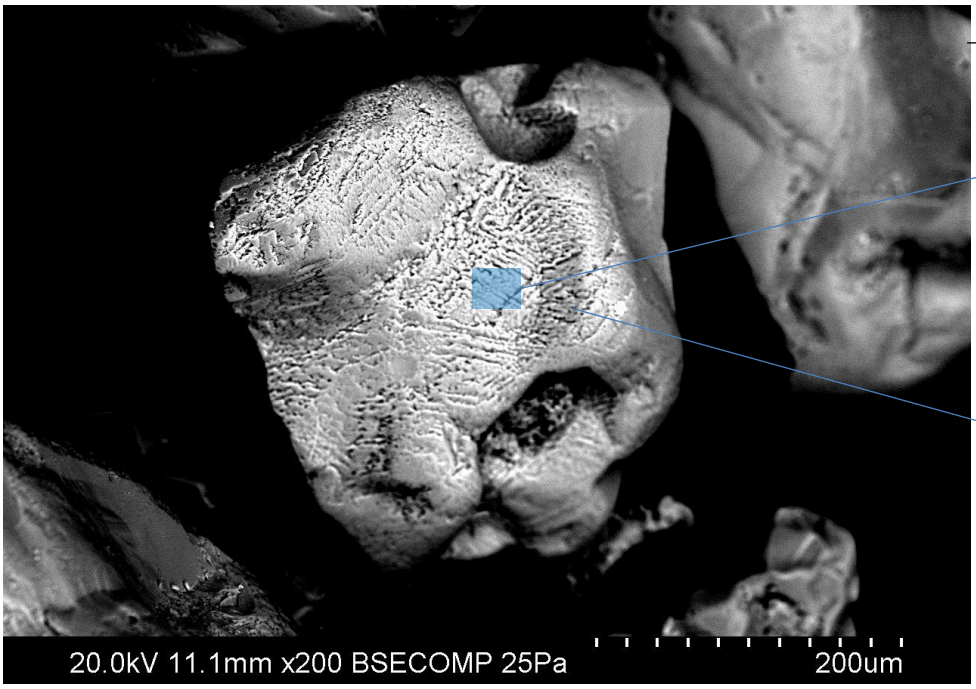
Molar Fraction
O – 72.8%
Si – 18.3%
Al – 5.3%
K – 3.6%
O – 64.3%
Si – 8.8%
Zr – 5.3%
Al, K, Ti < 1%
20.0kV 11.1mm x200 BSECOMP 25Pa
200um

APPENDIX B: Modeled Degree of Hydration on Time

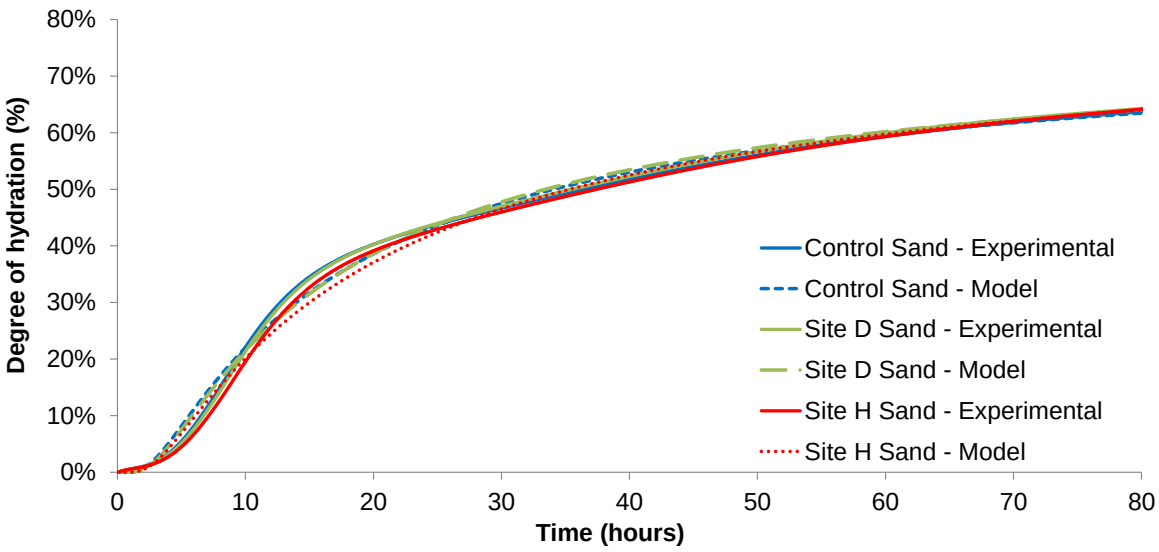

Figure B.1 Experimental and modeled degree of hydration for mortars using Cement A (Type I/II).

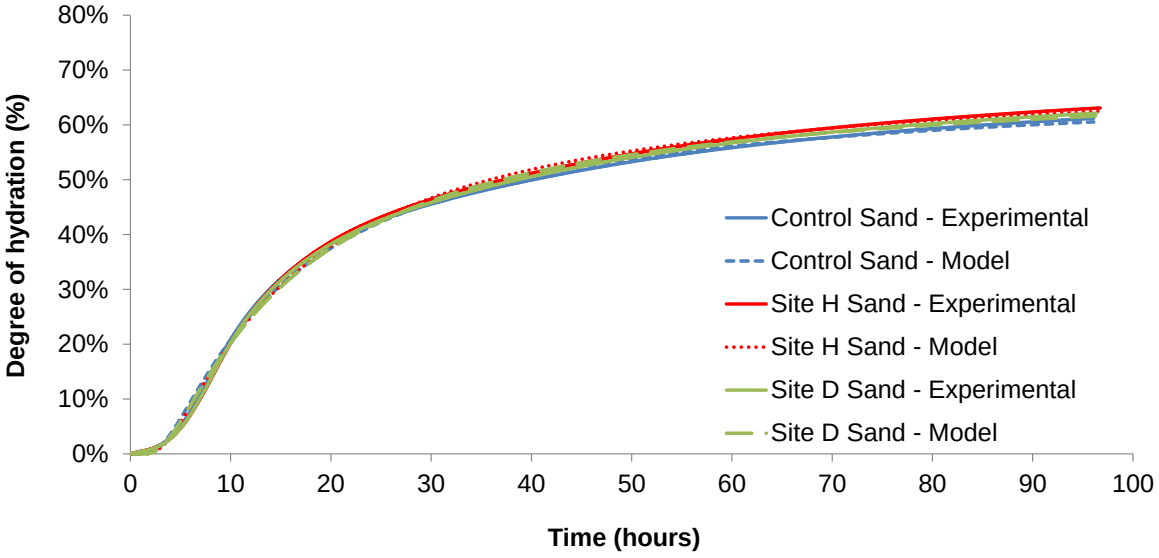

Figure B.2 Experimental and modeled degree of hydration for mortars using Cement B (Type V).

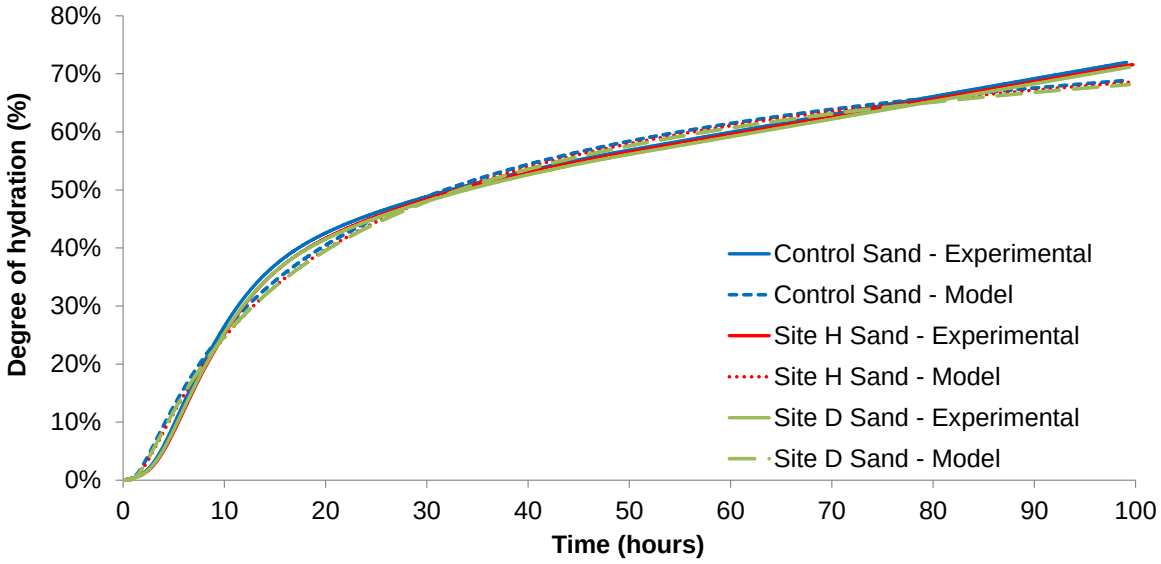

Figure B.3 Experimental and modeled degree of hydration for mortars using Cement C (Type I/II).

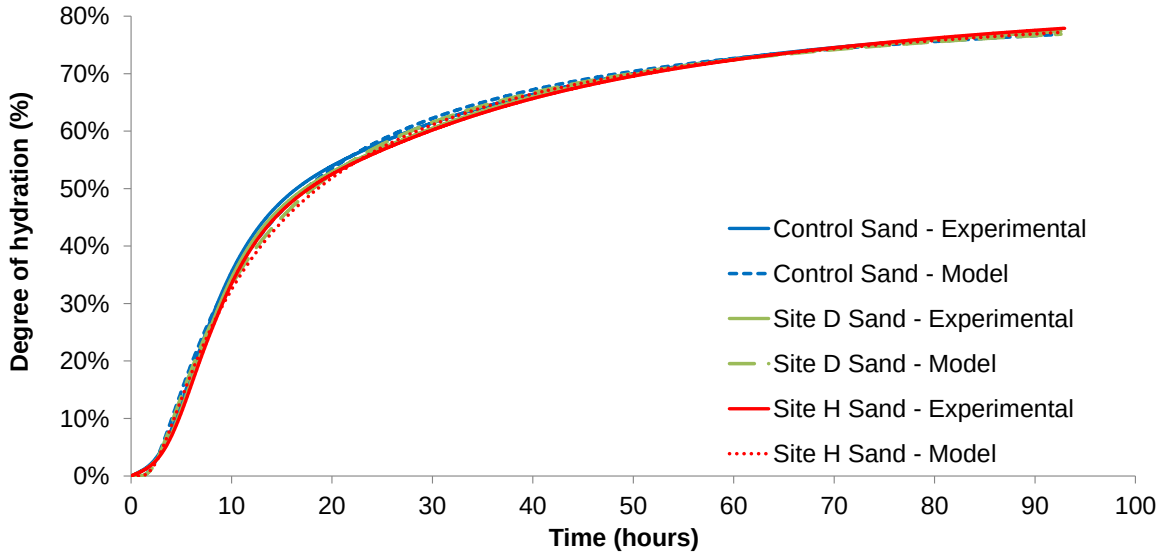

Figure B.4 Experimental and modeled degree of hydration for mortars using Cement D (Type III).

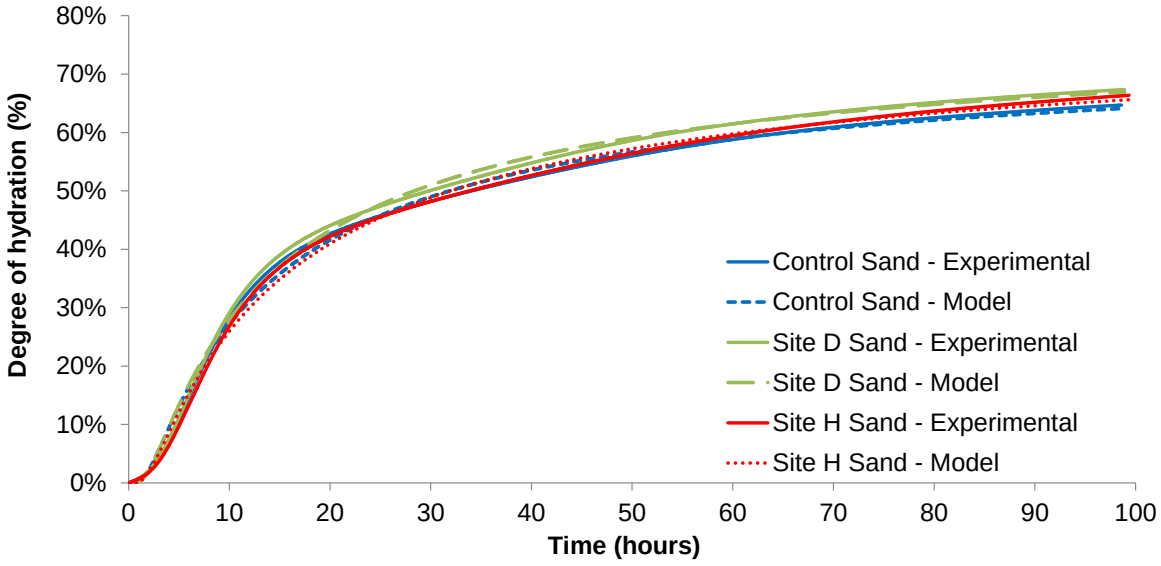

Figure B.5 Experimental and modeled degree of hydration for mortars using Cement E (Type I).

APPENDIX C: Individual Results of Compressive Strength of Concrete

Table C.1. Individual results of compressive strength test for Control sand specimens.

	Age	Compressive Strength (psi)	Rounded Compressive Strength (psi)	Average (psi)	Standard Deviation (psi)
CONTROL SAND	1 day	2,428.8	2,430	**2,533**	280
		2,324.2	2,320		
		2,847.5	2,850		
	3 days	3,192.6	3,190	**3,137**	76
		3,052.6	3,050		
		3,168.8	3,170		
	7 days	5,171.7	5,170	**4,850**	288
		4,765.9	4,770		
		4,613.9	4,610		
	28 days	4,835.9	4,840	**5,533**	621
		5,720.0	5,720		
		6,039.9	6,040		
	56 days	5,480.5	5,480	**5,797**	275
		5,966.7	5,970		
		5,940.5	5,940		
	90 days	6,407.6	6,410	**6,233**	159
		6,098.8	6,100		
		6,186.4	6,190		

Table C.2. Individual results of compressive strength test for Site H sand specimens.

	Age	Compressive Strength (psi)	Rounded Compressive Strength (psi)	Average (psi)	Standard Deviation (psi)
SITE H SAND	1 day	3,604.1	3,600	**3,650**	87
		3,602.5	3,600		
		3,750.5	3,750		
	3 days	4,006.7	4,000	**4,123**	188
		4,033.8	4,030		
		4,343.3	4,340		
	7 days	5,104.9	5,100	**5,480**	344
		5,566.4	5,570		
		5,766.2	5,770		
	28 days	6,642.3	6,640	**6,637**	55
		6,584.2	6,580		
		6,689.3	6,690		
	56 days	7,188.2	7,190	**7,670**	423
		7,991.2	7,990		
		7,832.0	7,830		
	90 days	----------	wrong failure	**7,895**	92
		7,832.0	7,830		
		7,960.9	7,960		

Table C.3. Individual results of compressive strength test for Site D sand specimens.

	Age	Compressive Strength (psi)	Rounded Compressive Strength (psi)	Average (psi)	Standard Deviation (psi)
SITE D SAND	1 day	2,819.4	2,820	**2,590**	252
		2,324.5	2,320		
		2,633.2	2,630		
	3 days	3,775.2	3,780	**3,557**	225
		3,325.5	3,330		
		3,561.1	3,560		
	7 days	4,221.6	4,220	**4,447**	575
		4,018.7	4,020		
		5,103.3	5,100		
	28 days	5,552.9	5,550	**5,647**	249
		5,928.5	5,930		
		5,457.4	5,460		
	56 days	6,835.7	6,840	**6,710**	225
		6,449.8	6,450		
		6,836.5	6,840		
	90 days	6,659.8	6,660	**6,790**	184
		6,920.9	6,920		
		----------	wrong failure		

APPENDIX D: Variability of Results - Accelerated Corrosion Testing

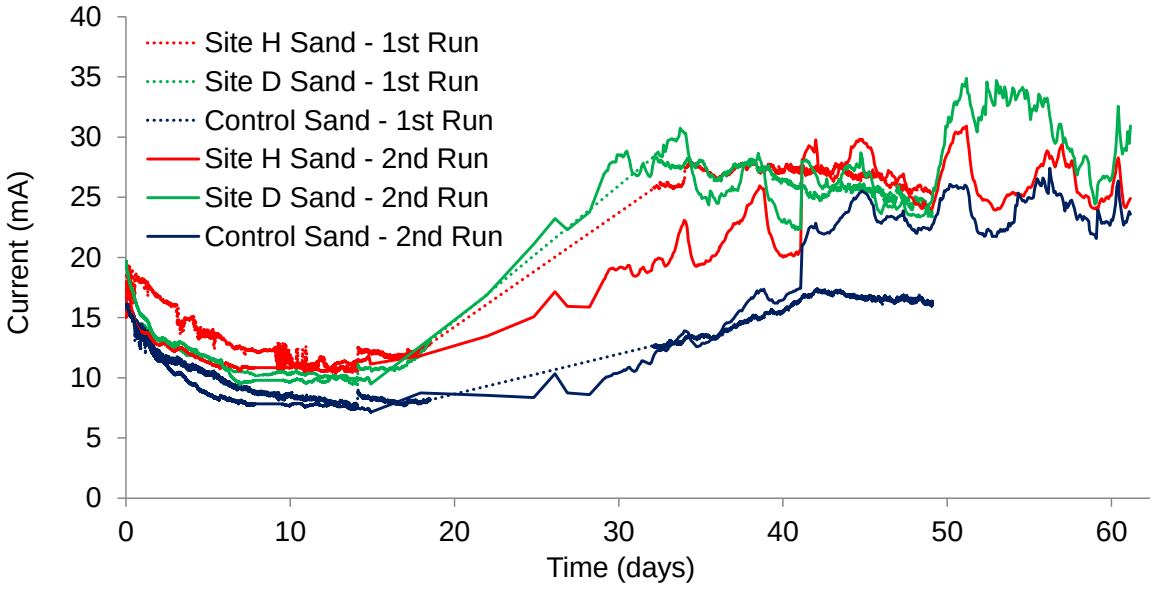

Figure D.1 Evolution of current during the test for Control sand specimens.

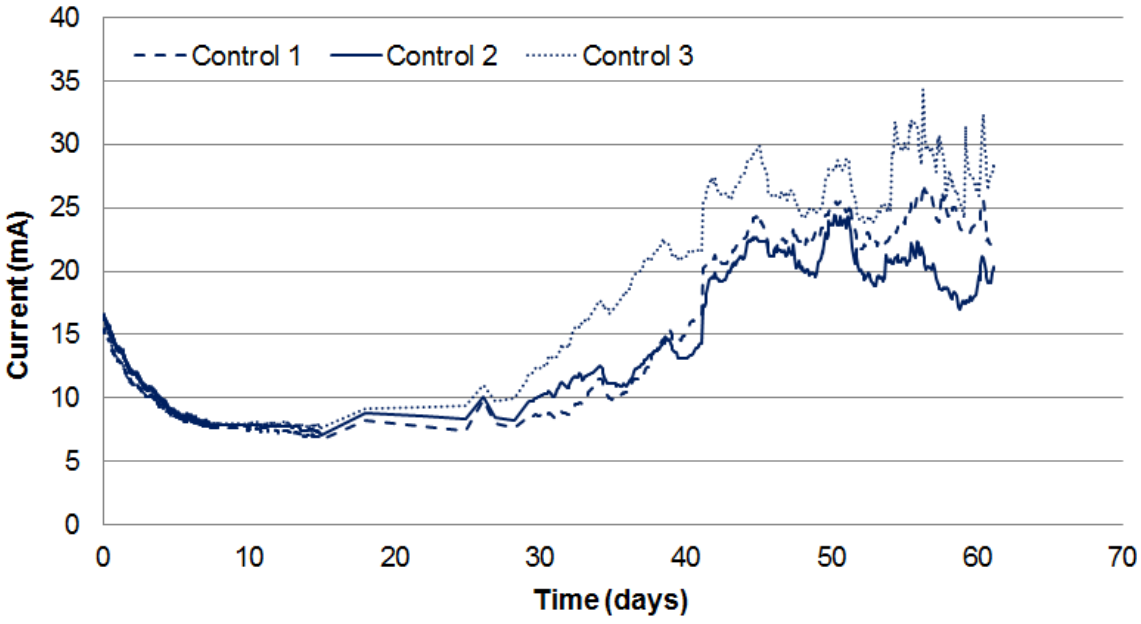

Figure D.2 Evolution of current during the test for Control sand specimens.

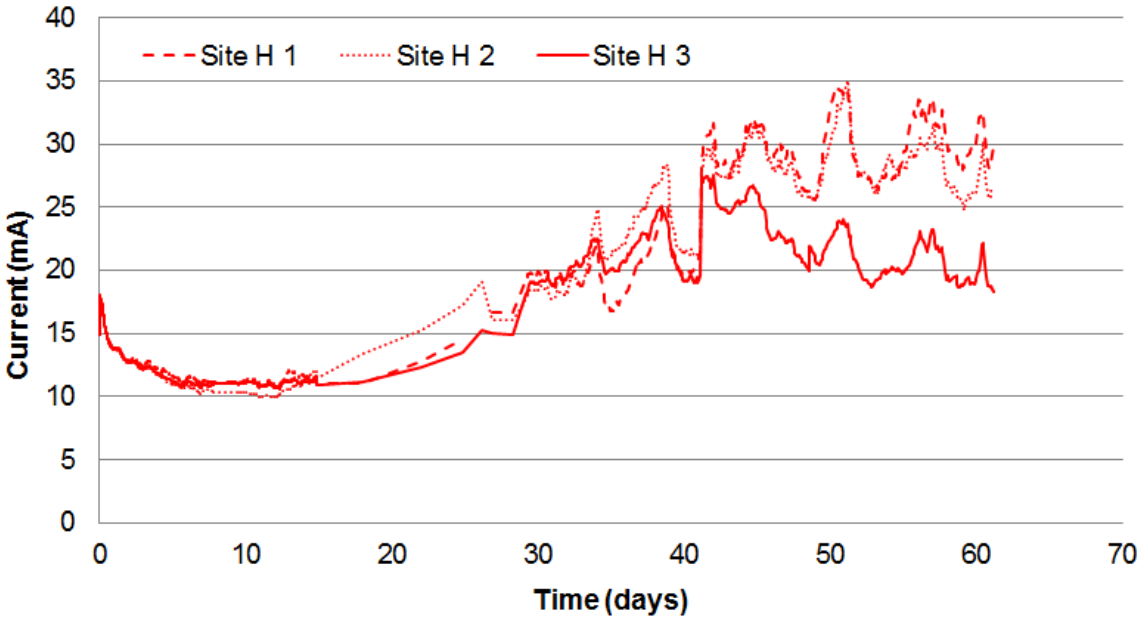

Figure D.3 Evolution of current during the test for Site H sand specimens.

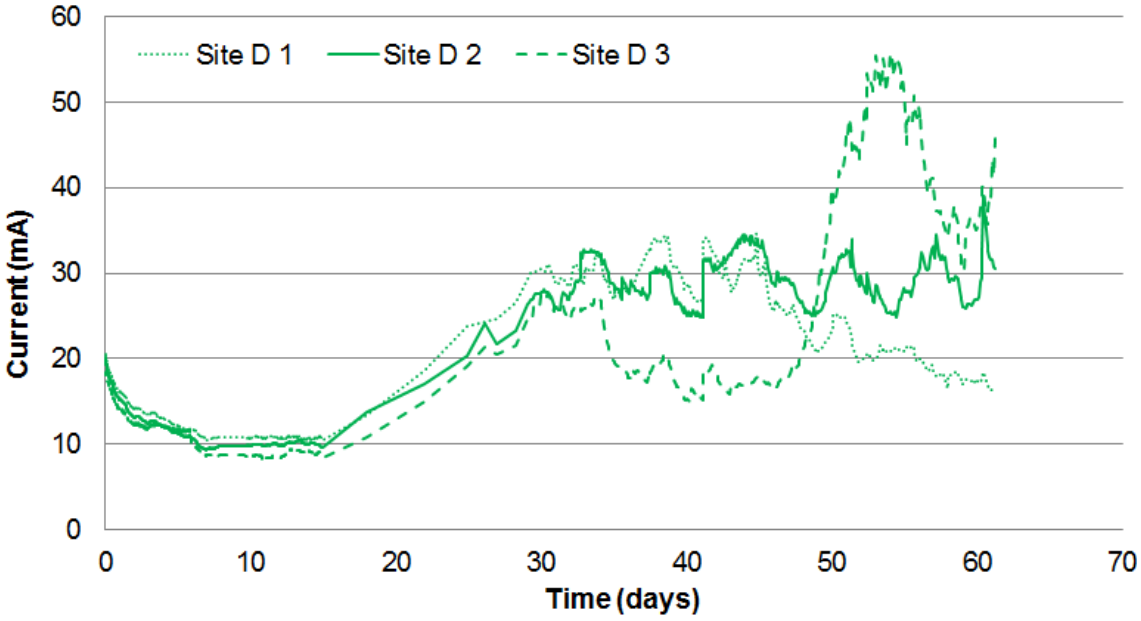

Figure D.4 Evolution of current during the test for Site D sand specimens.

APPENDIX E: VP-SEM Micrographs of Heat-Cured Mortars

Micrographs included in this appendix are separated by mortar mixture. Days from casting and expansion at the time of sample preparation are included for each mixture. Micrographs show the most common features of DEF-damage, the higher variability on the composition of Site H sand, the higher deterioration of samples using Cement D (Type III) compared to Cement B (Type V) samples, and the good condition of mortar sample containing Cement B (Type V) and Control sand.

- Cement D - Site H sand (442 days, 2.611% expansion).

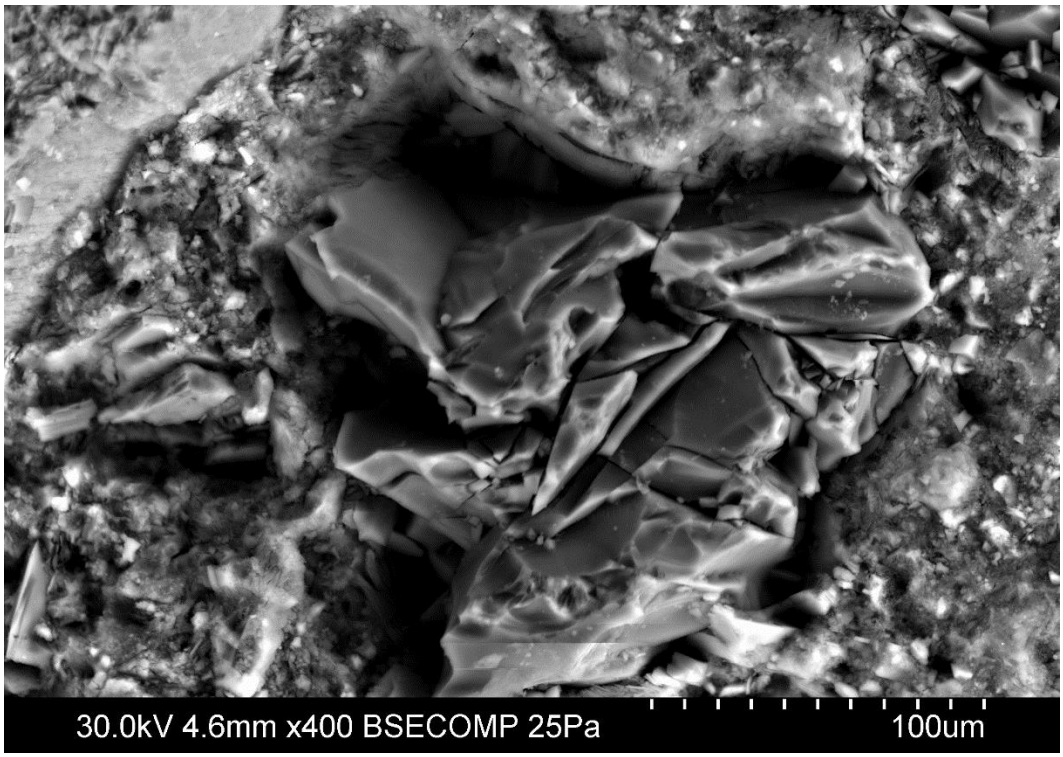

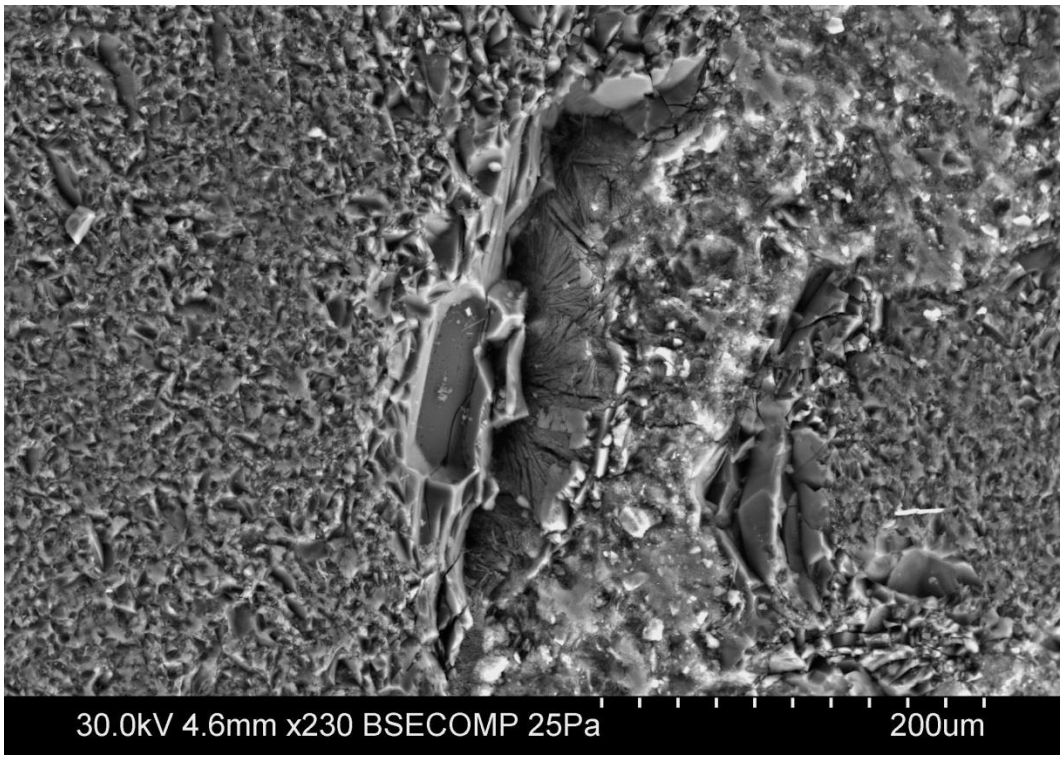
30.0kV 4.6mm x230 BSECOMP 25Pa
200um

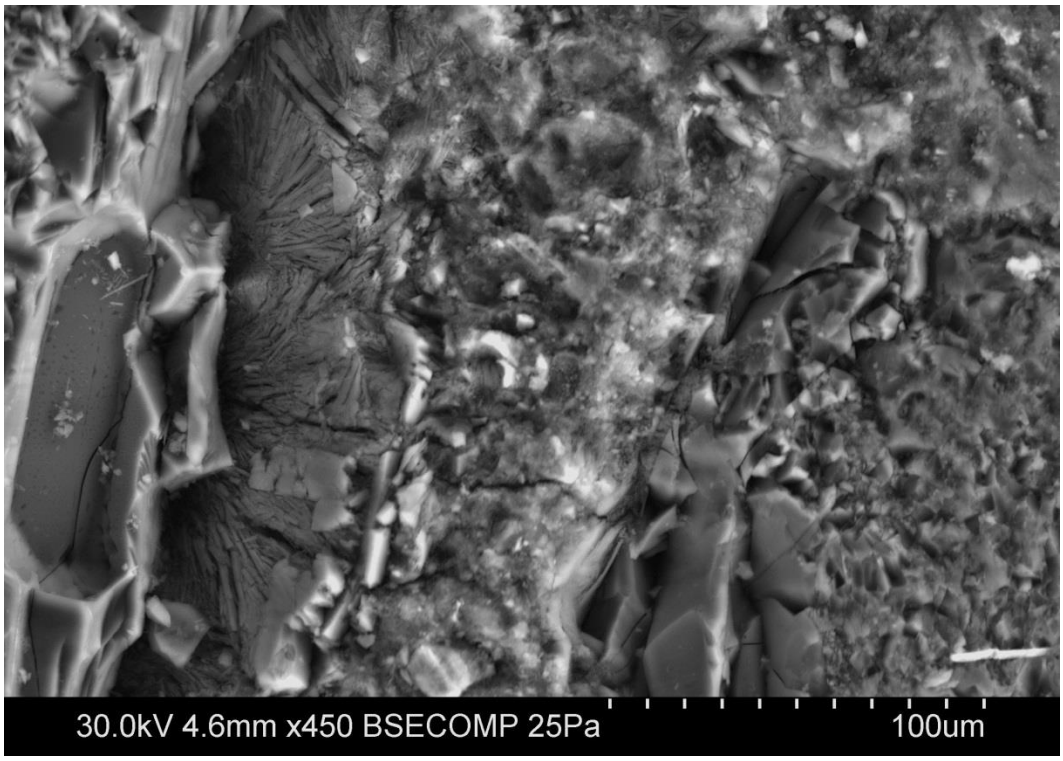
30.0kV 4.6mm x450 BSECOMP 25Pa
100um

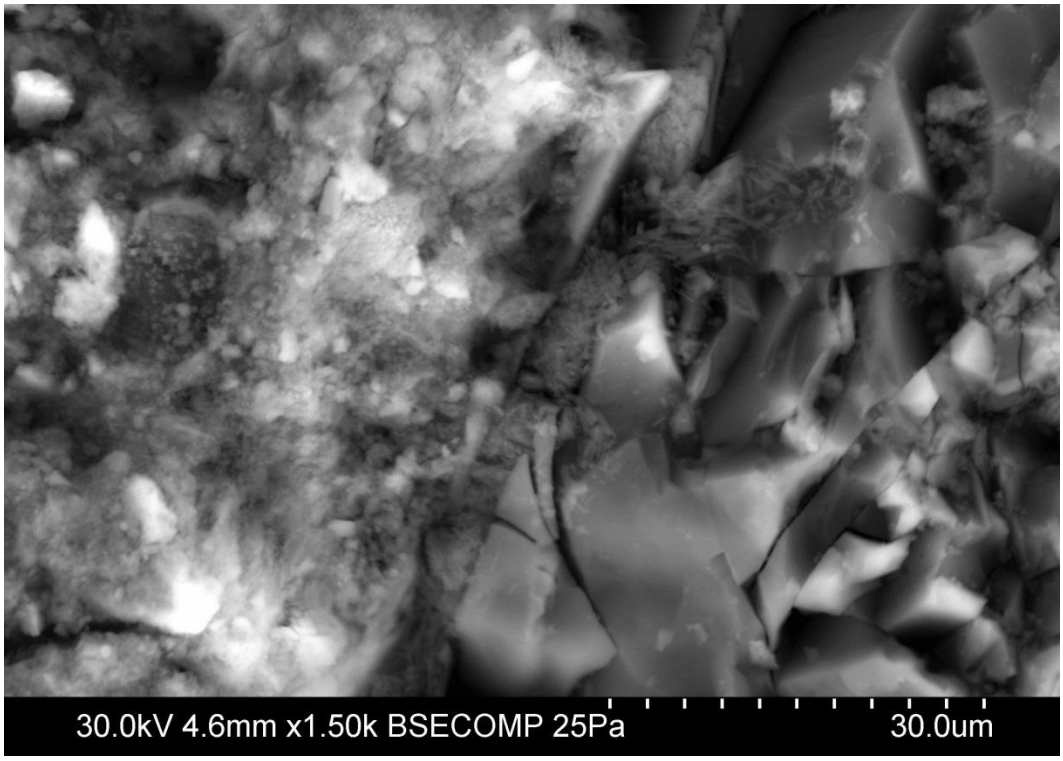
30.0kV 4.6mm x1.50k BSECOMP 25Pa
30.0um

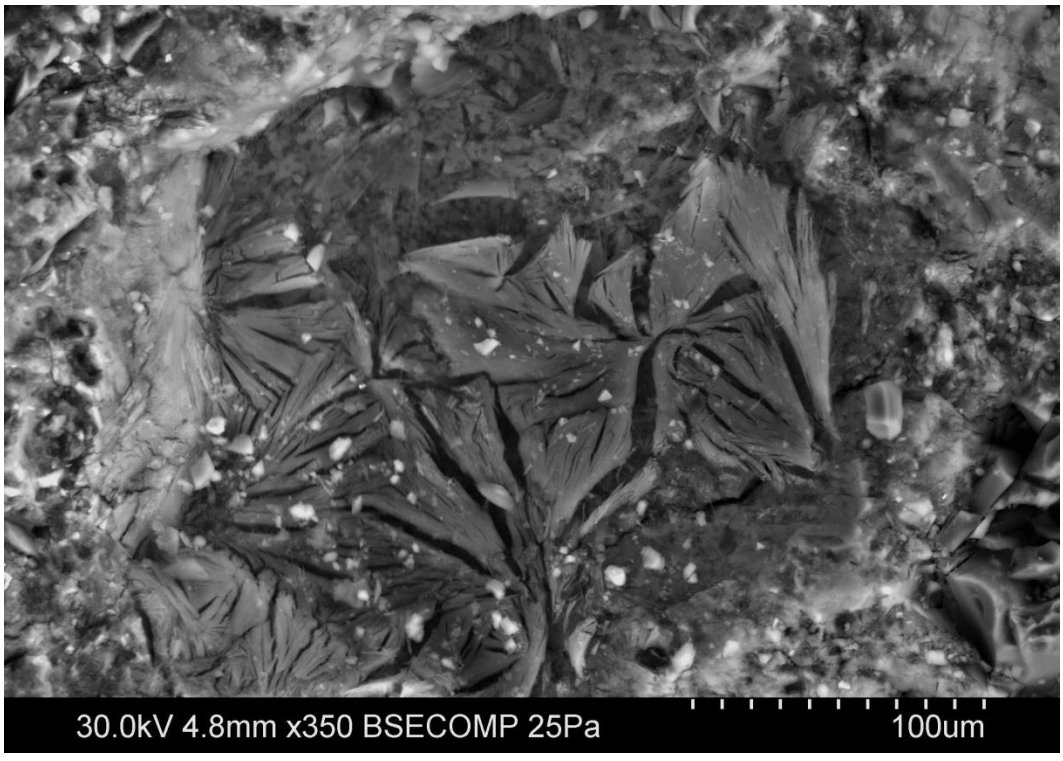
30.0kV 4.8mm x350 BSECOMP 25Pa
100um

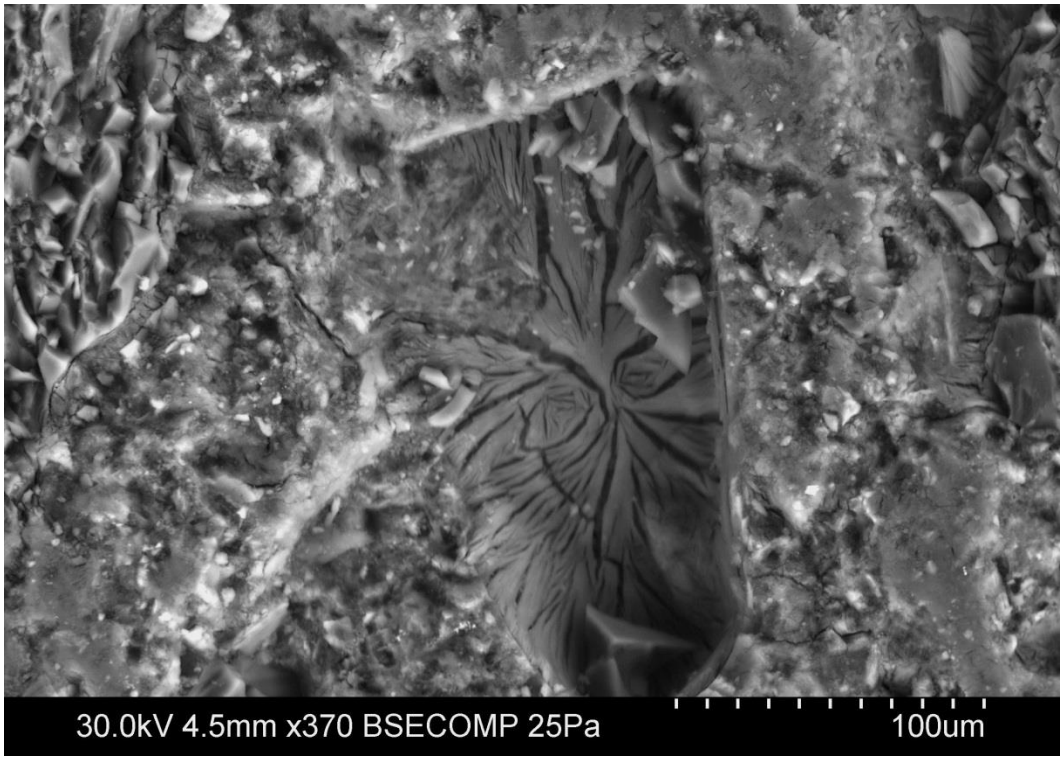
30.0kV 4.5mm x370 BSECOMP 25Pa
100um

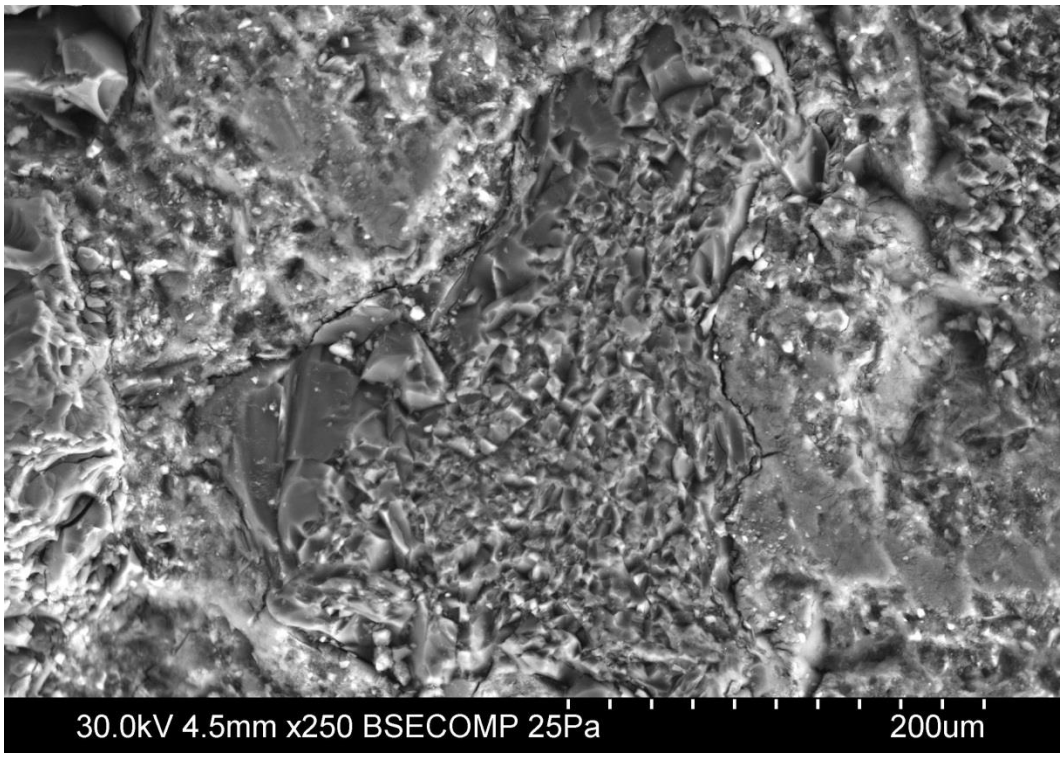
30.0kV 4.5mm x250 BSECOMP 25Pa
200um

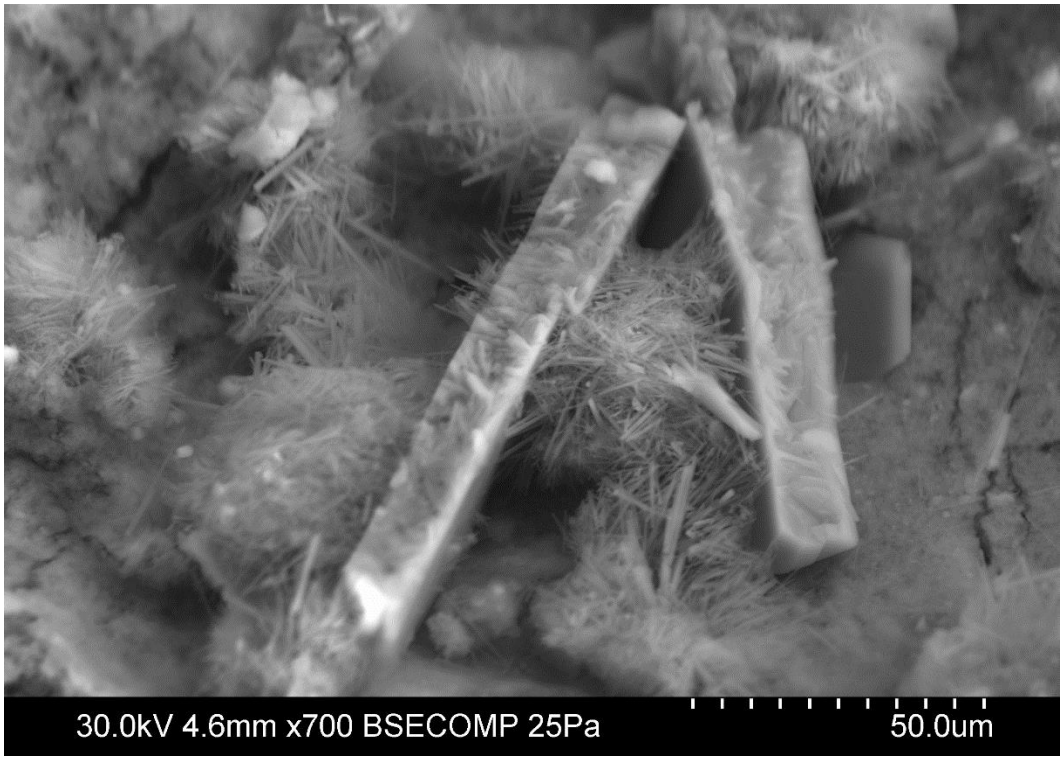
30.0kV 4.6mm x700 BSECOMP 25Pa
50.0um

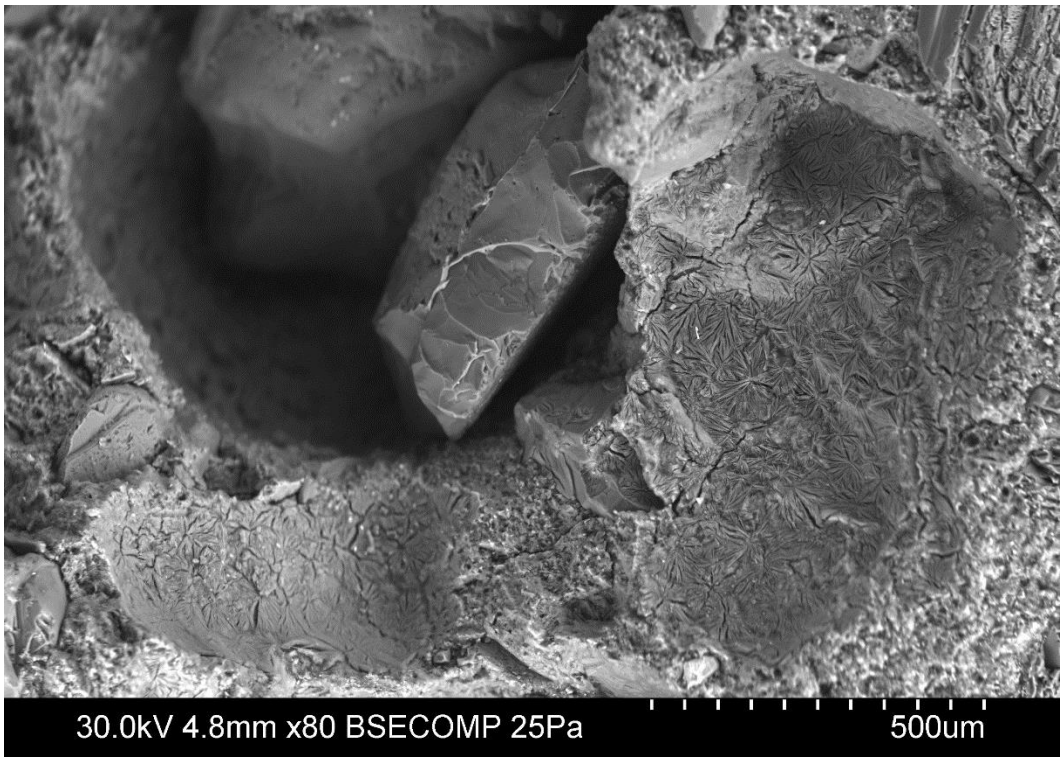
30.0kV 4.8mm x80 BSECOMP 25Pa
500um

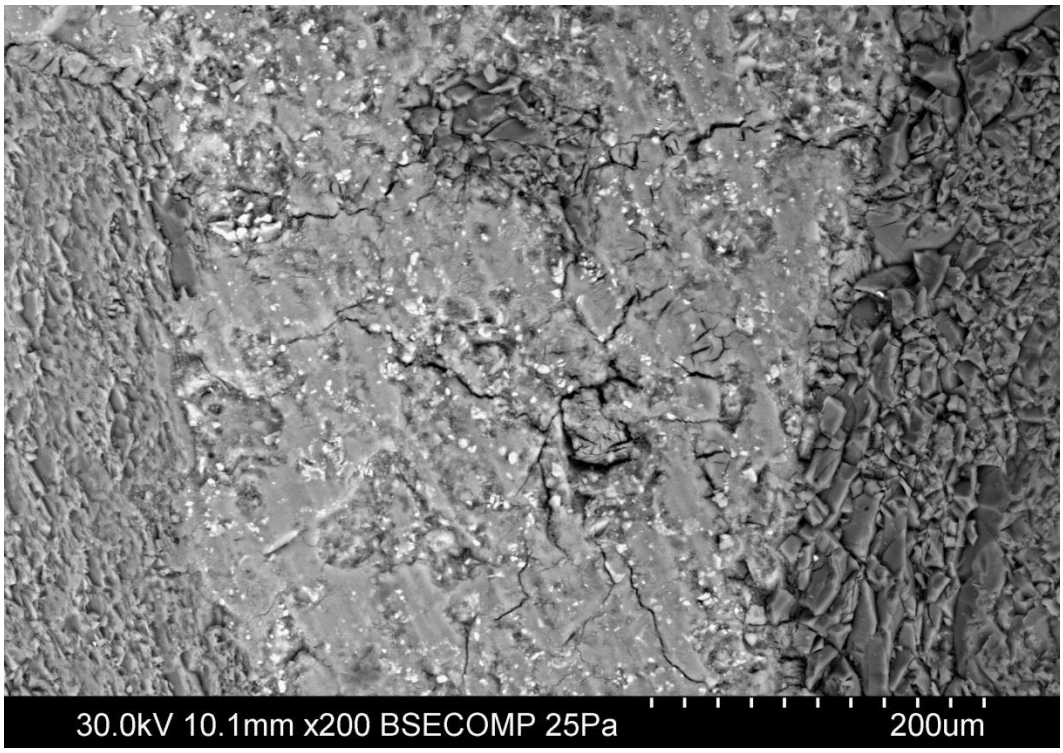
30.0kV 10.1mm x200 BSECOMP 25Pa
200um

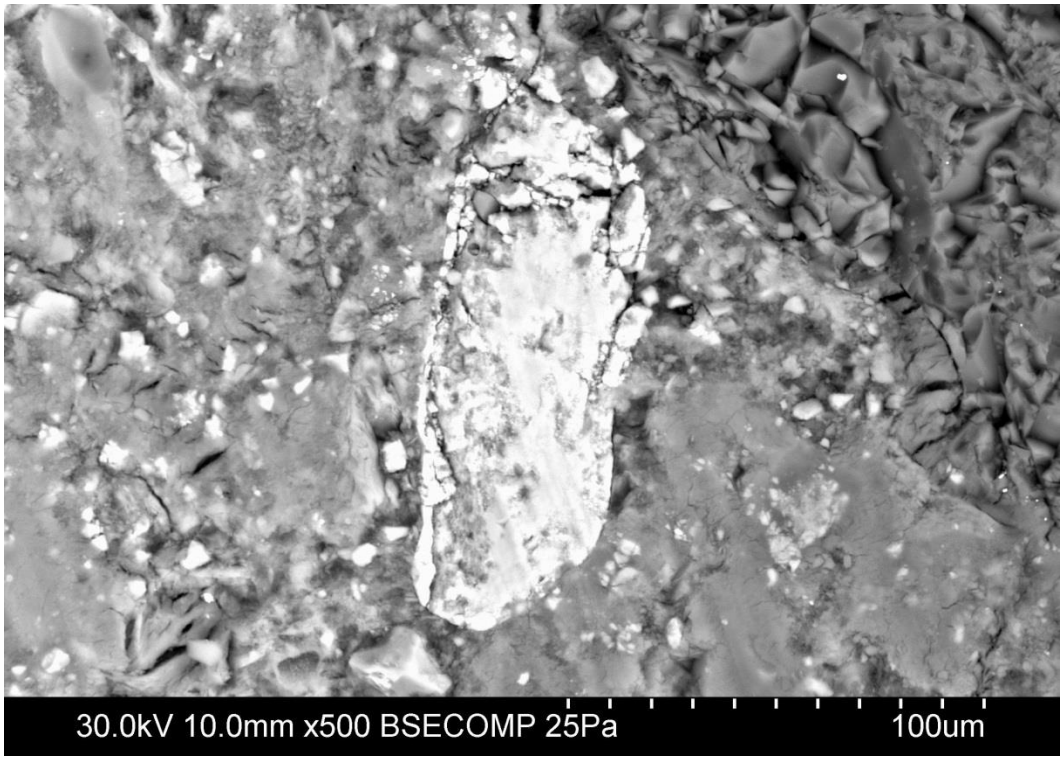
30.0kV 10.0mm x500 BSECOMP 25Pa
100um

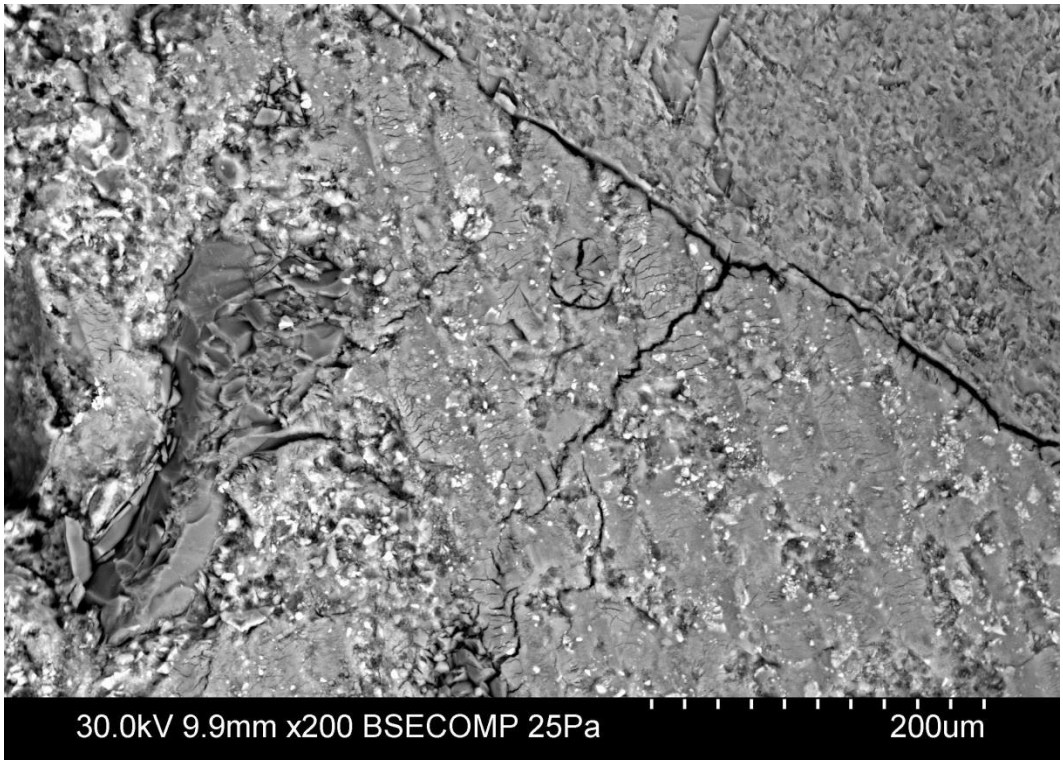
30.0kV 9.9mm x200 BSECOMP 25Pa
200um

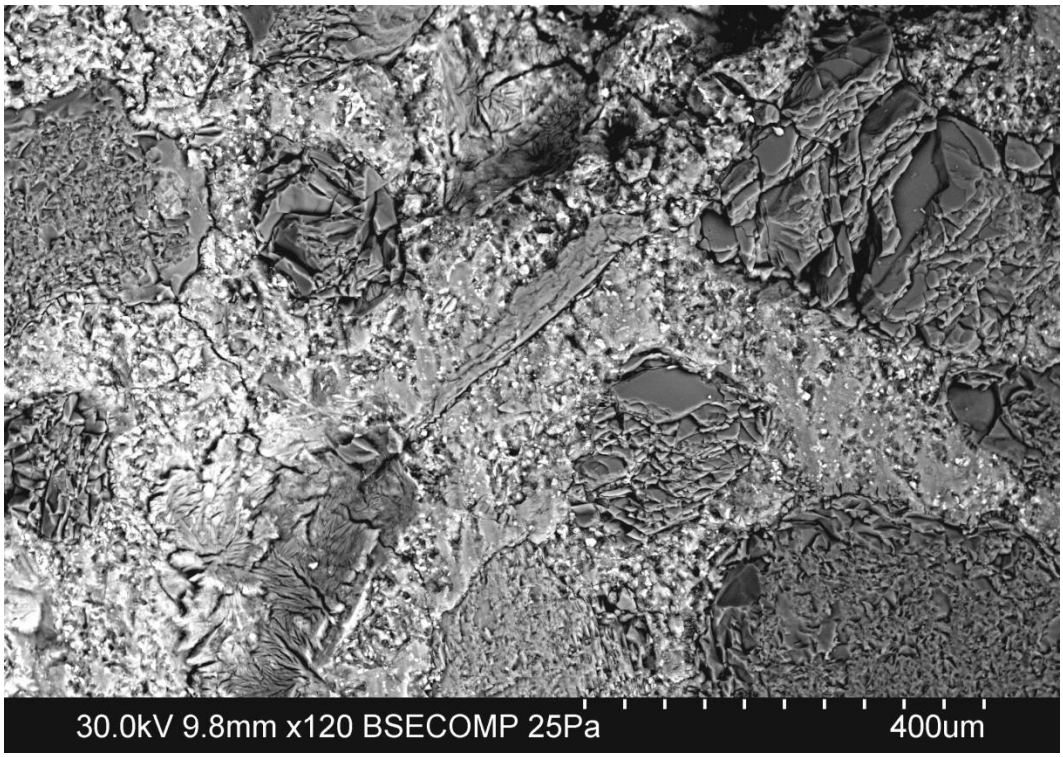
30.0kV 9.8mm x120 BSECOMP 25Pa
400um

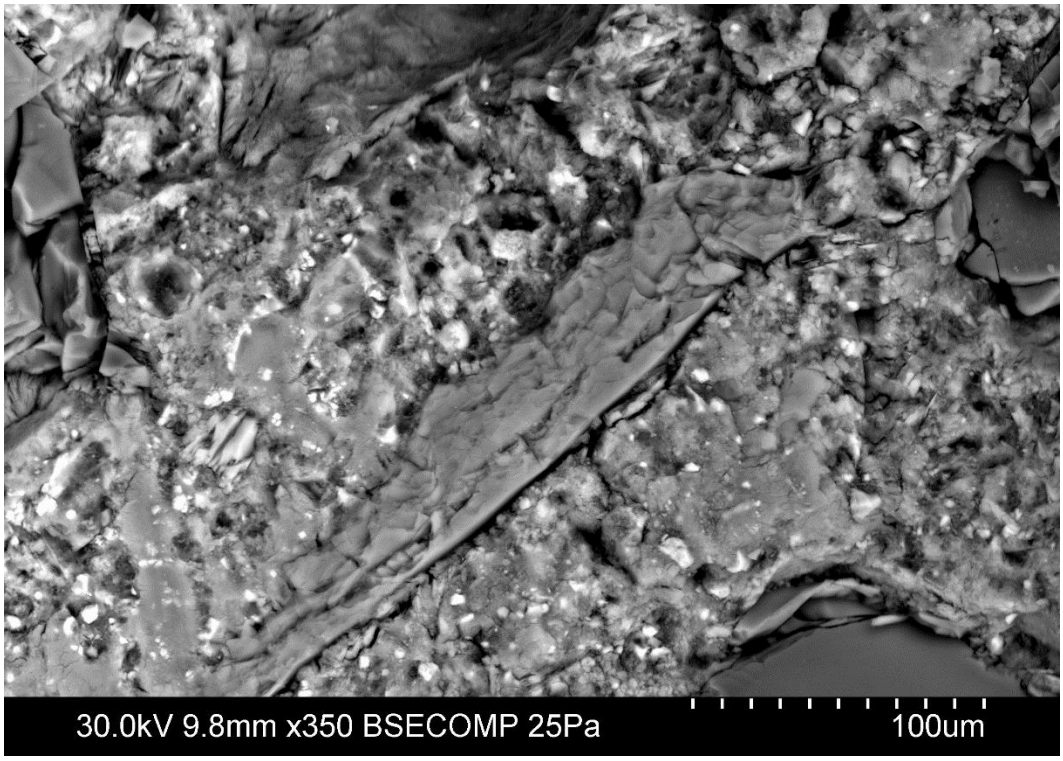
30.0kV 9.8mm x350 BSECOMP 25Pa
100um

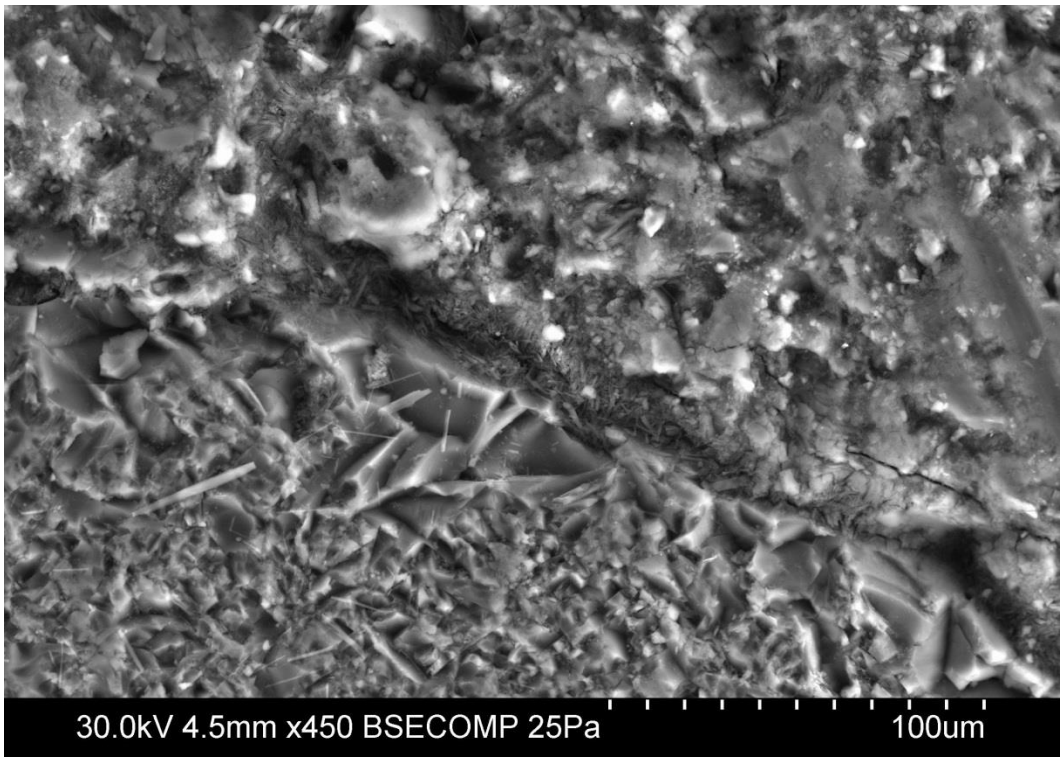
30.0kV 4.5mm x450 BSECOMP 25Pa
100um

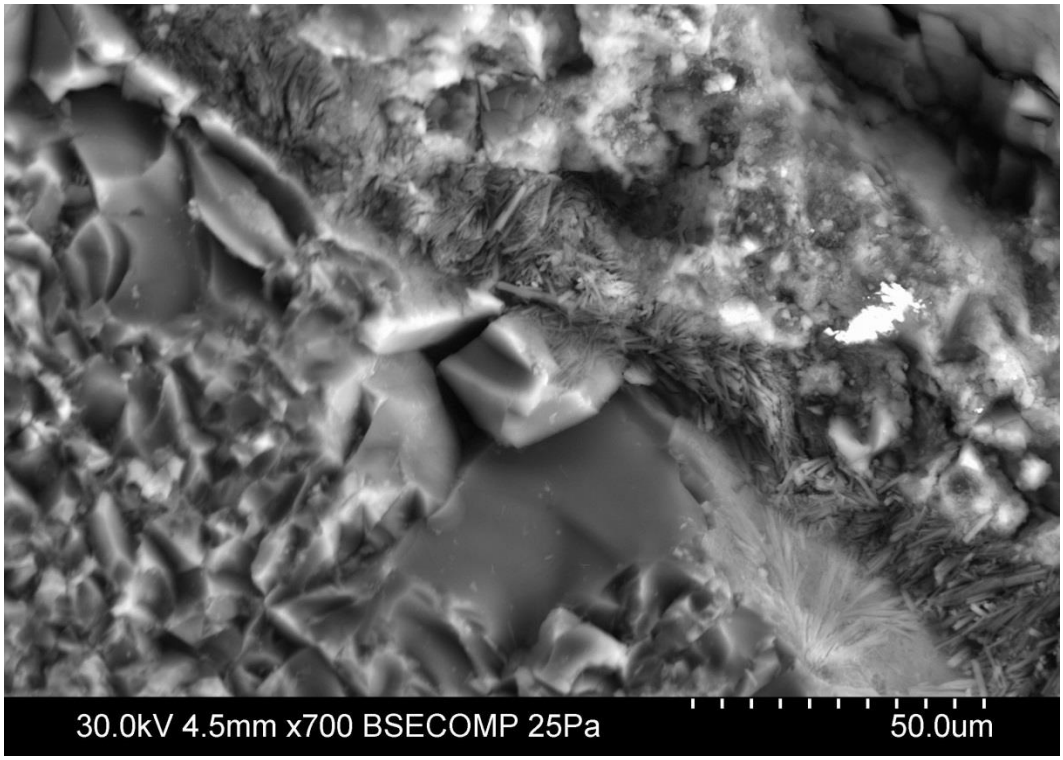
30.0kV 4.5mm x700 BSECOMP 25Pa
50.0um

- Cement D - Control sand (298 days, 2.235% expansion).

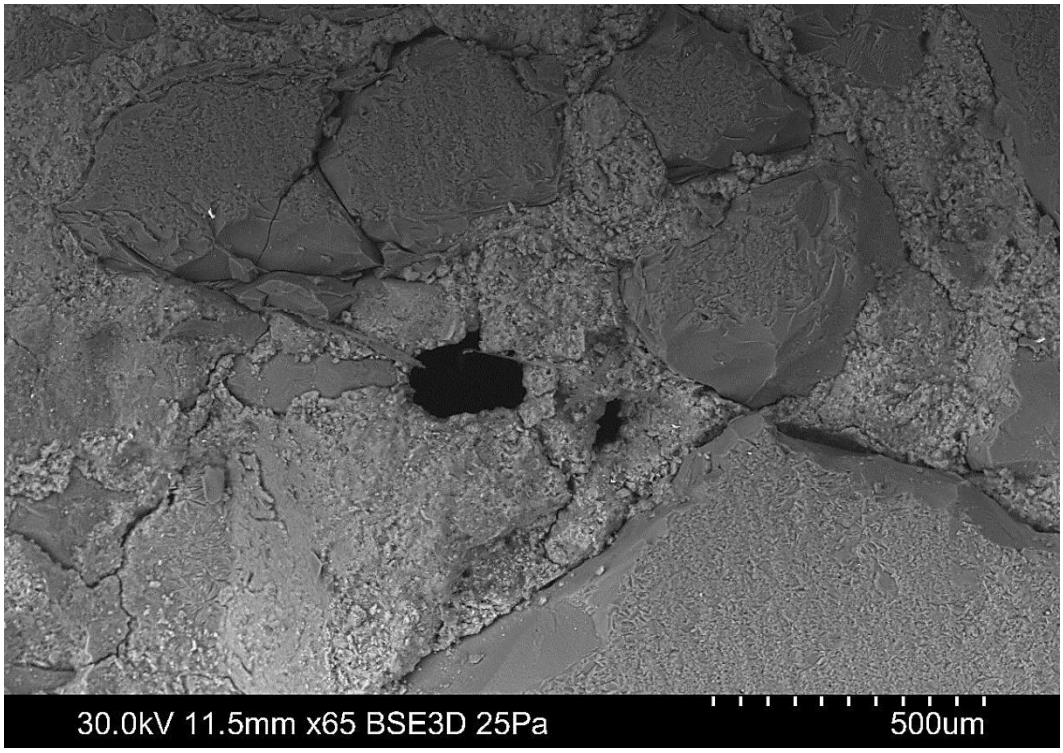

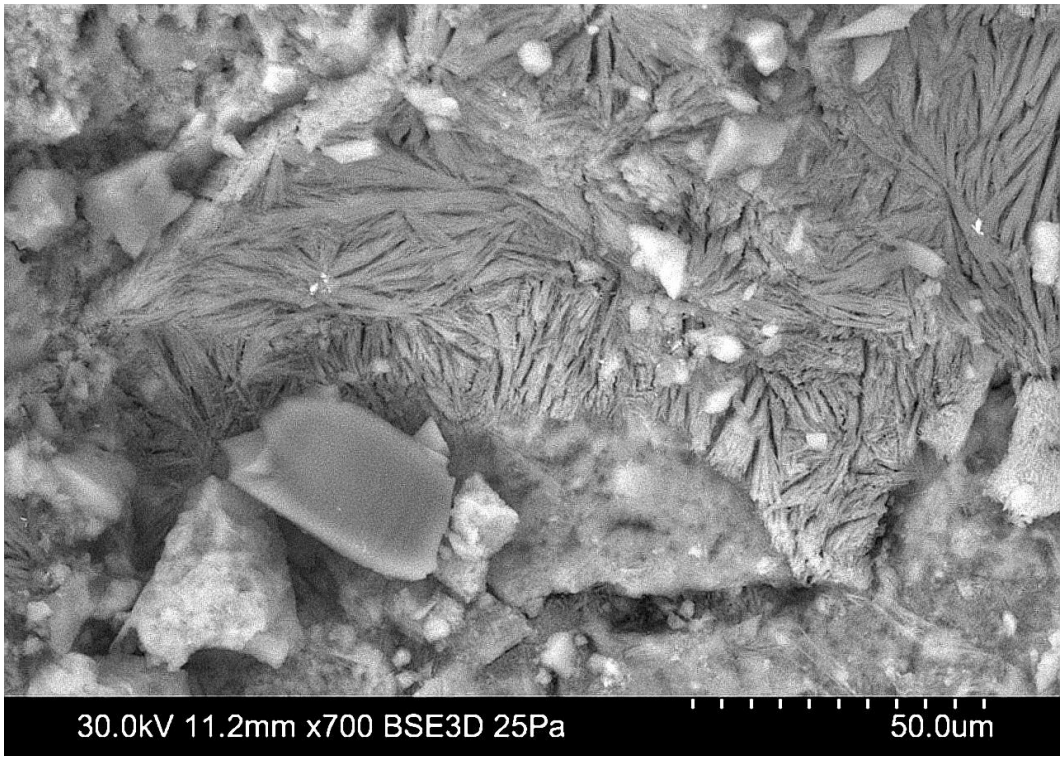

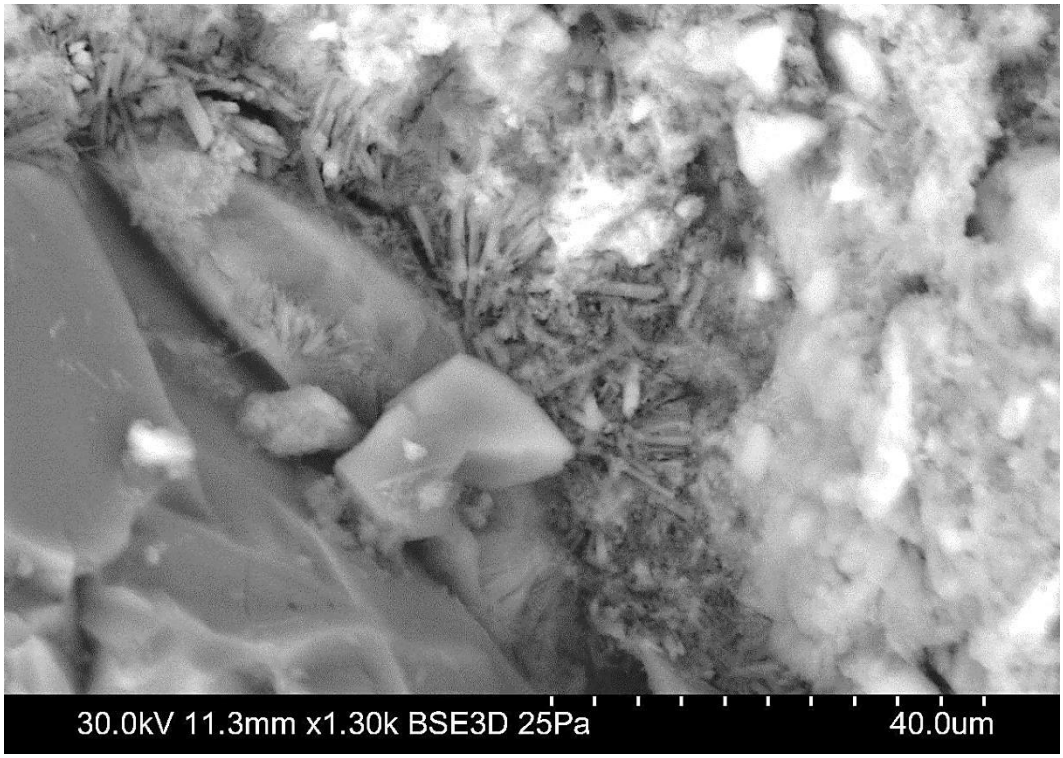
30.0kV 11.3mm x1.30k BSE3D 25Pa
40.0um

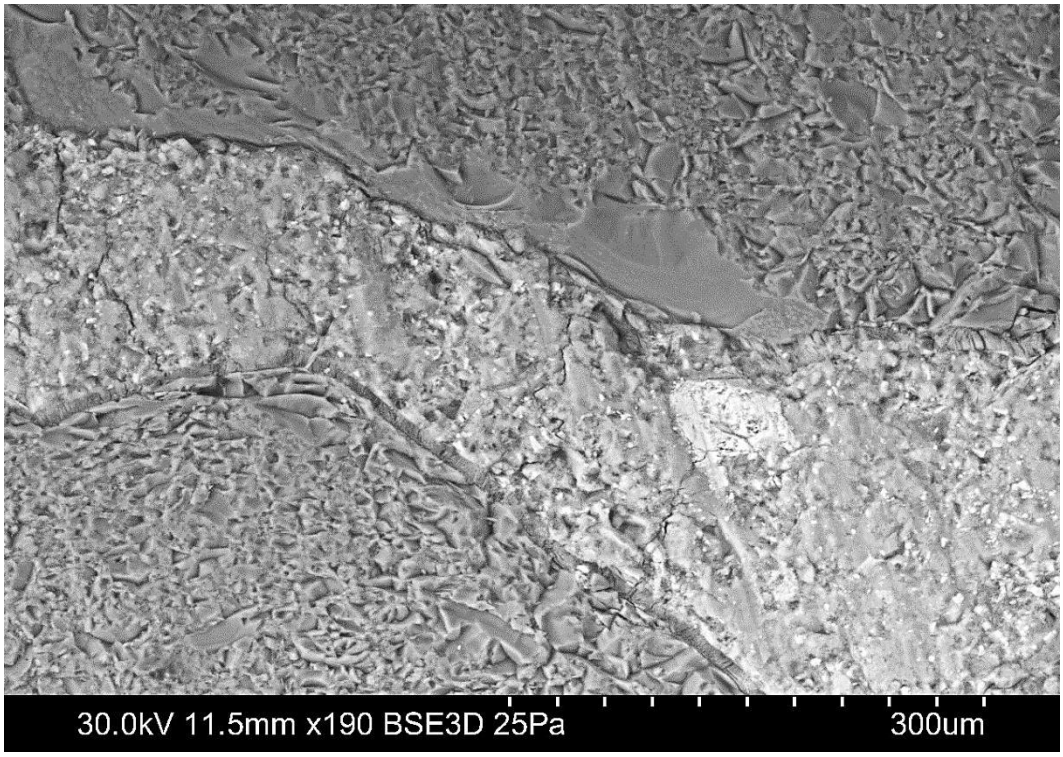
30.0kV 11.5mm x190 BSE3D 25Pa
300um

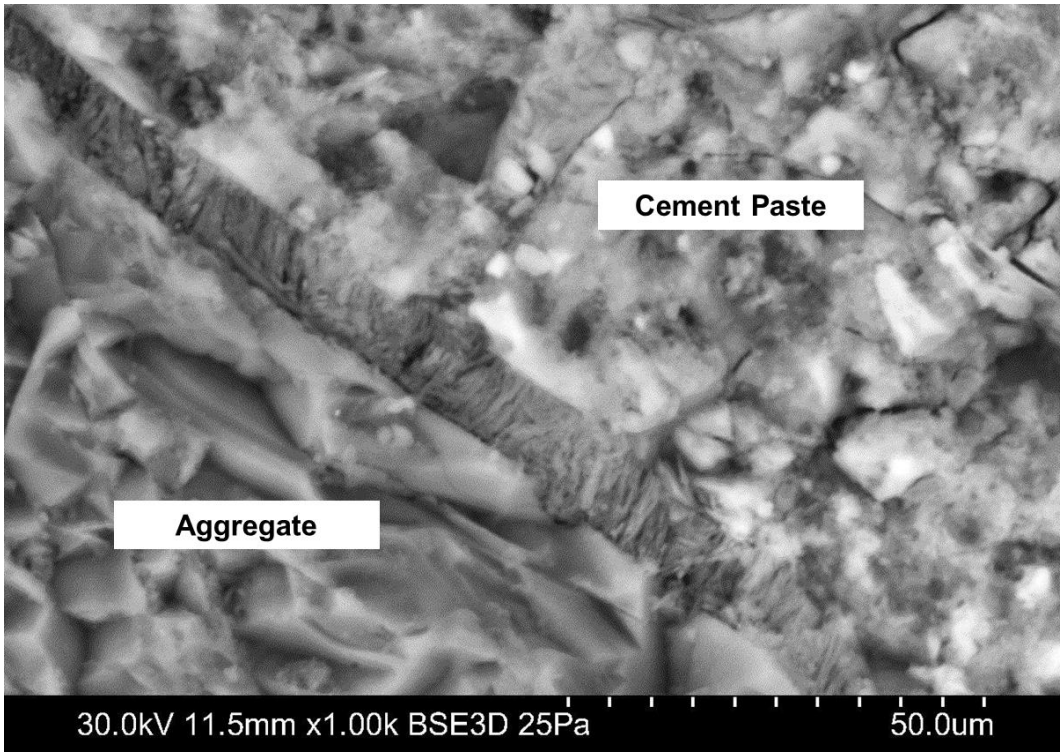
Cement Paste
Aggregate
30.0kV 11.5mm x1.00k BSE3D 25Pa
50.0um

- Cement A - Site H sand (674 days, 0.793% expansion).

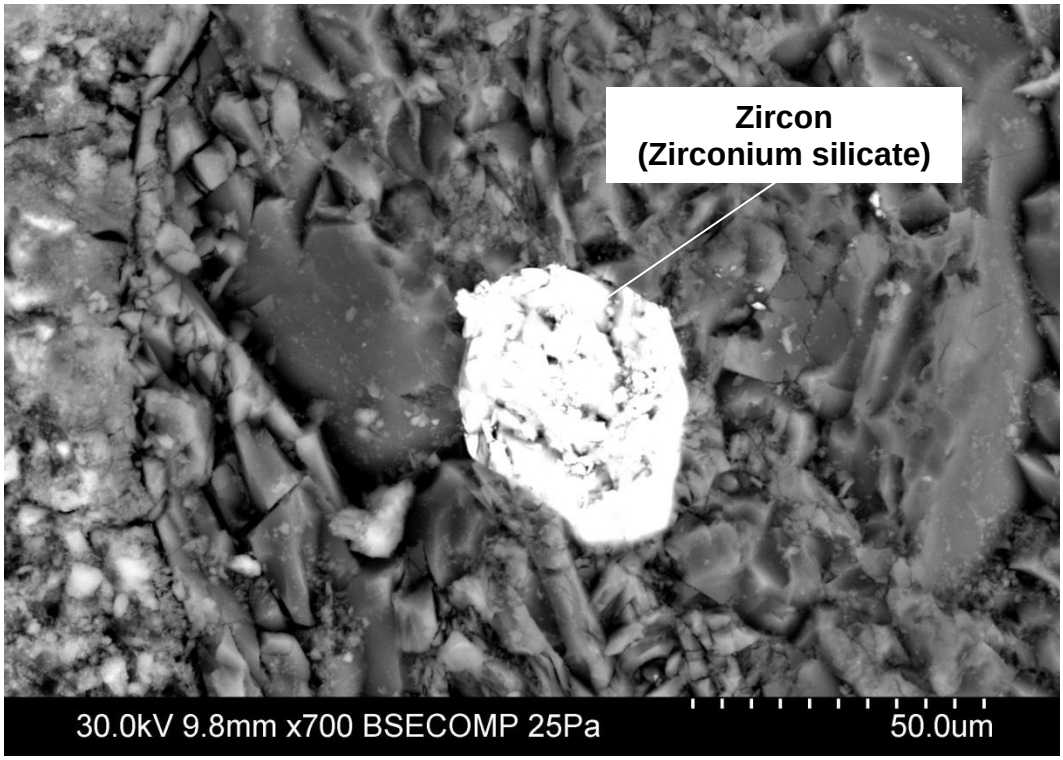

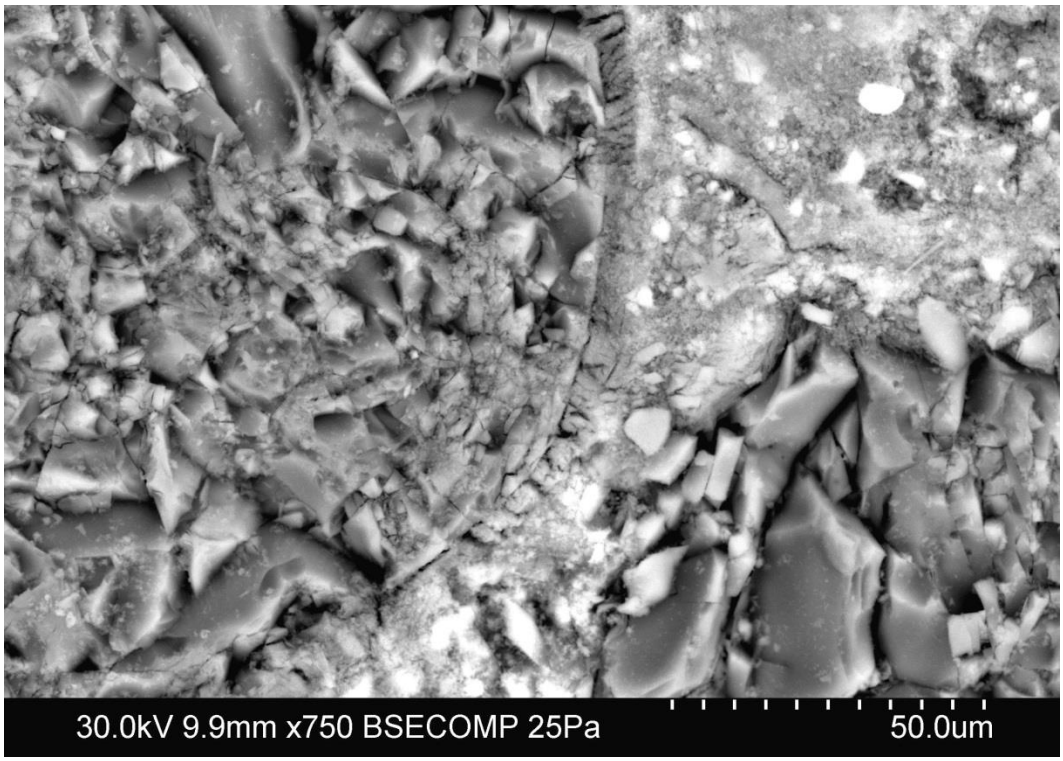

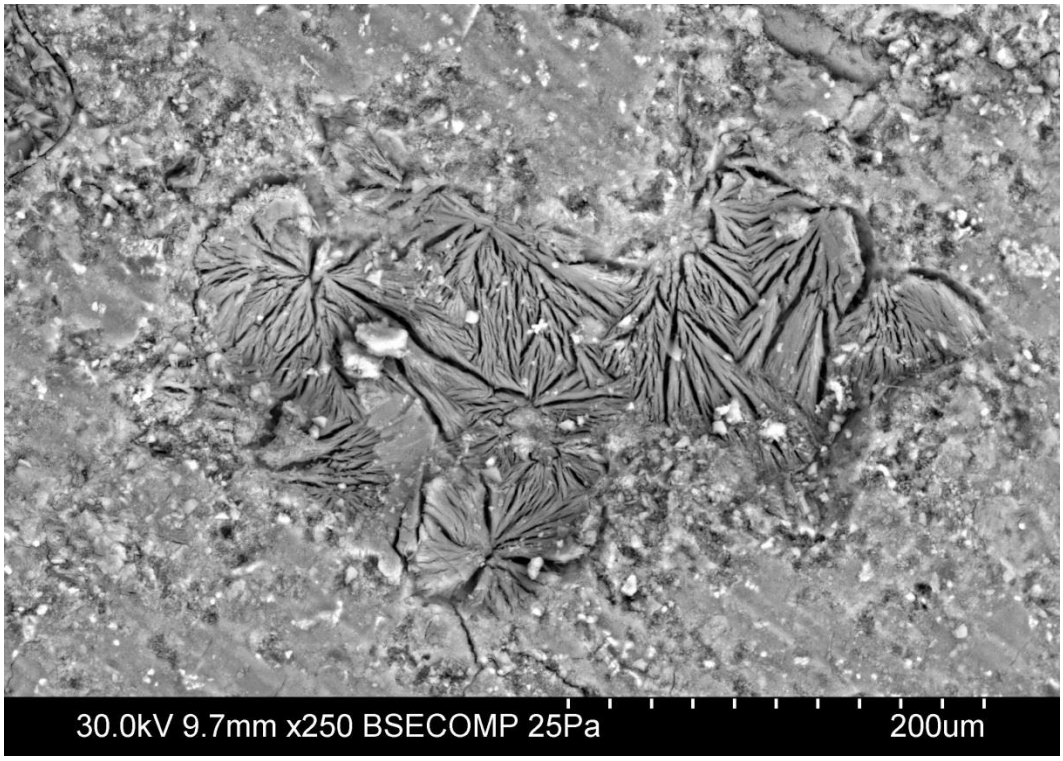
30.0kV 9.7mm x250 BSECOMP 25Pa
200um

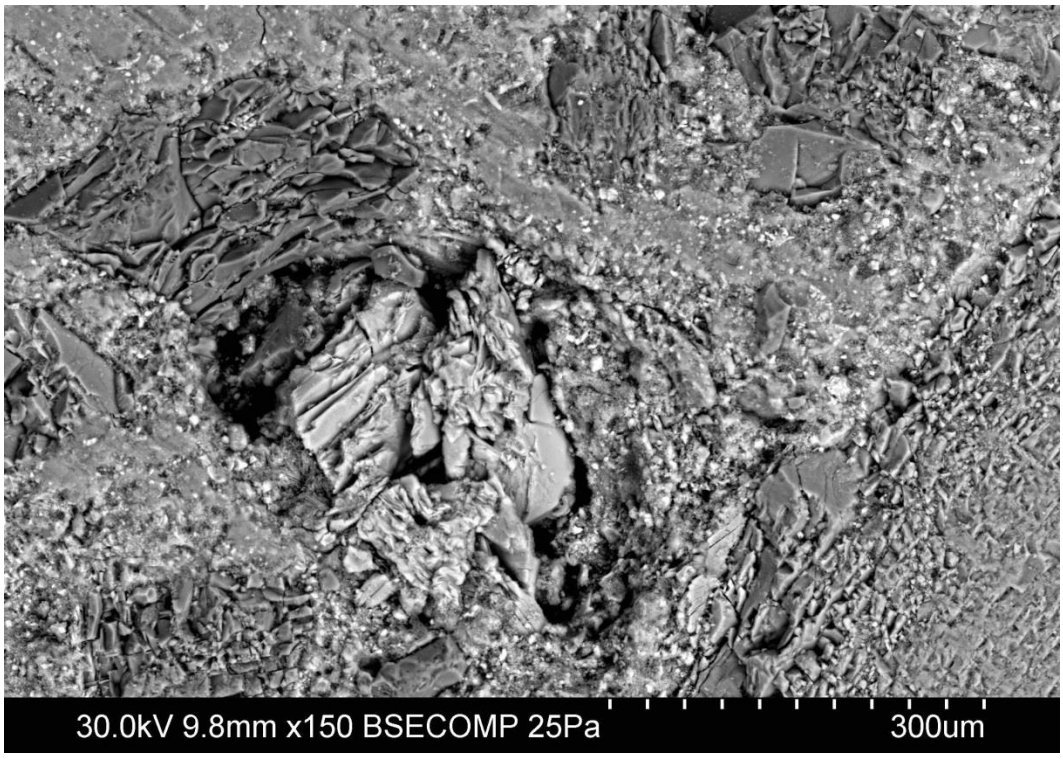
30.0kV 9.8mm x150 BSECOMP 25Pa
300um

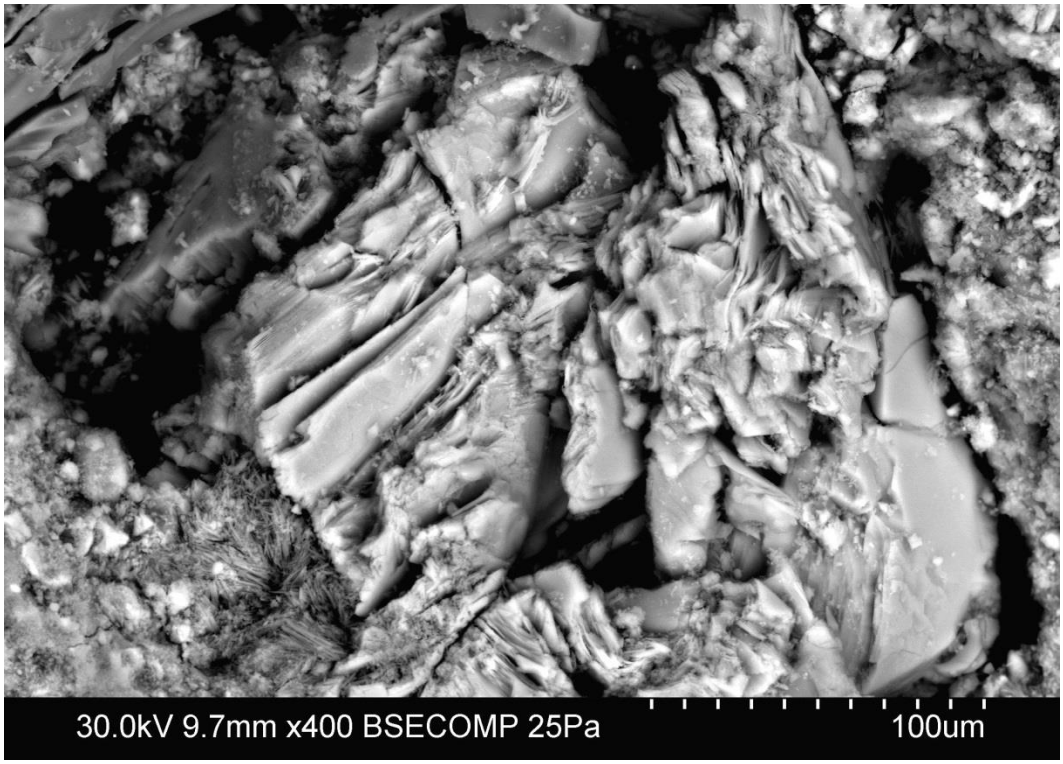
30.0kV 9.7mm x400 BSECOMP 25Pa
100um

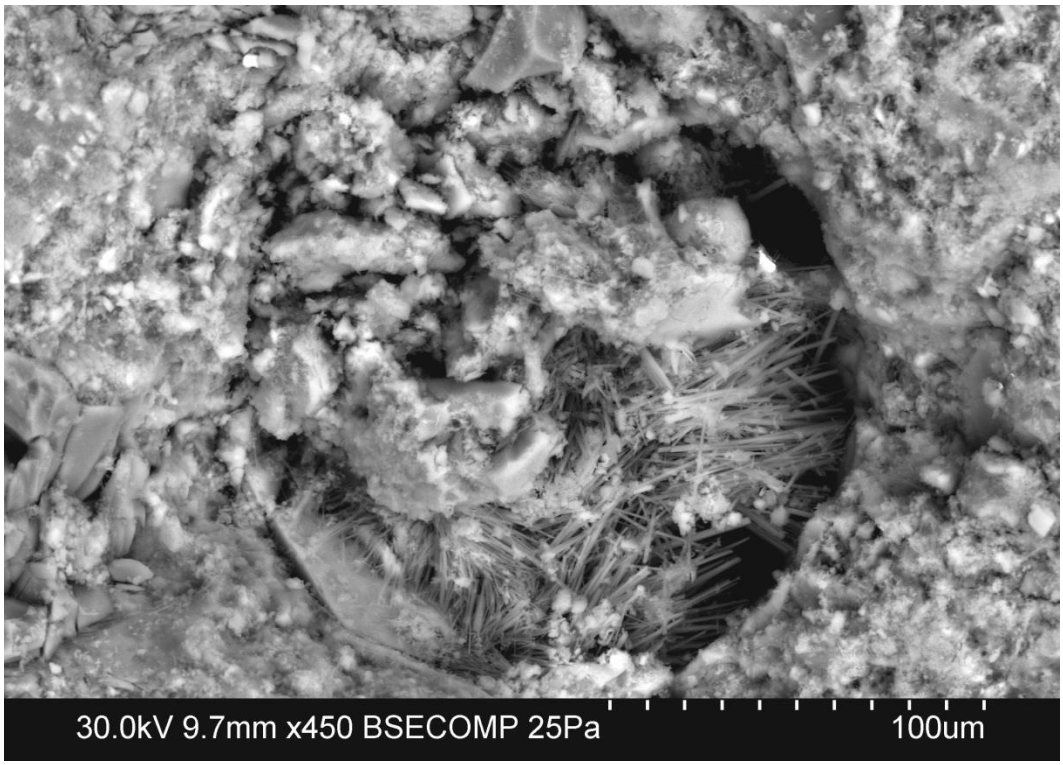
30.0kV 9.7mm x450 BSECOMP 25Pa
100um

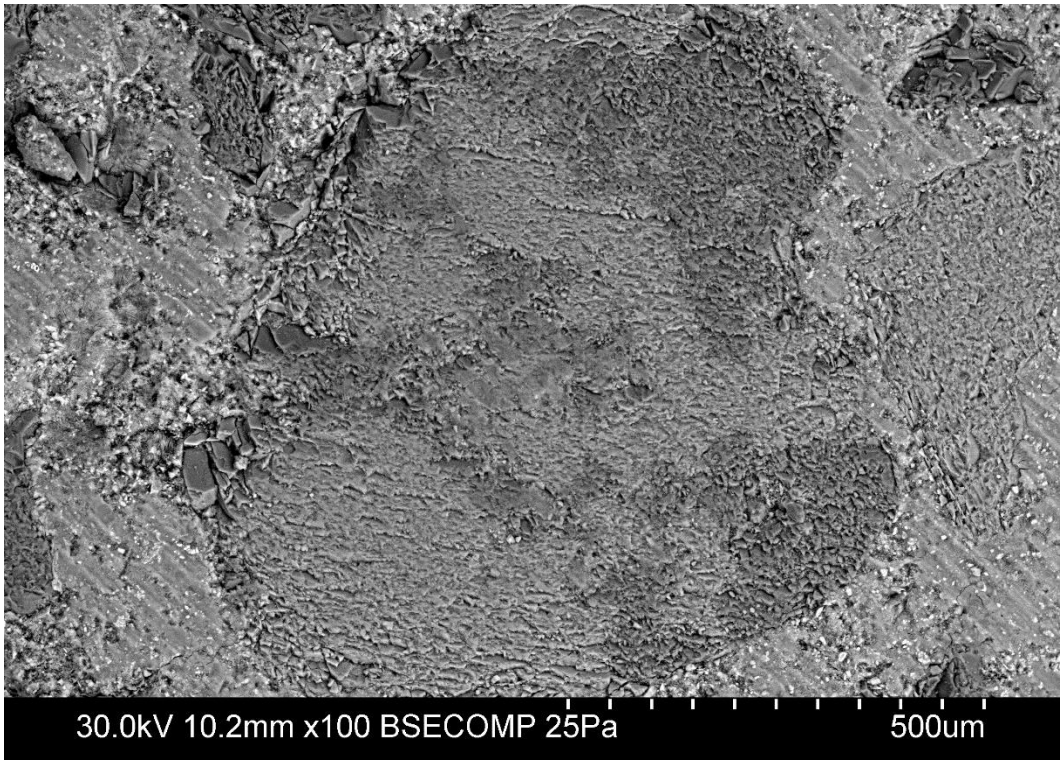
30.0kV 10.2mm x100 BSECOMP 25Pa
500um

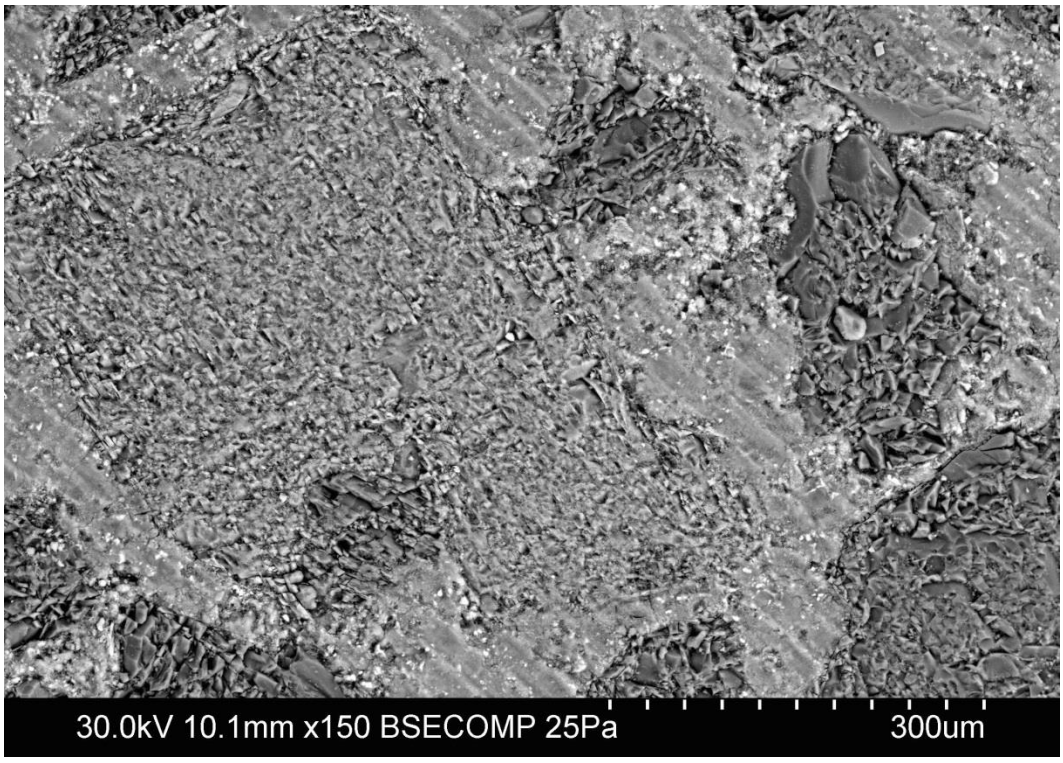
30.0kV 10.1mm x150 BSECOMP 25Pa
300um

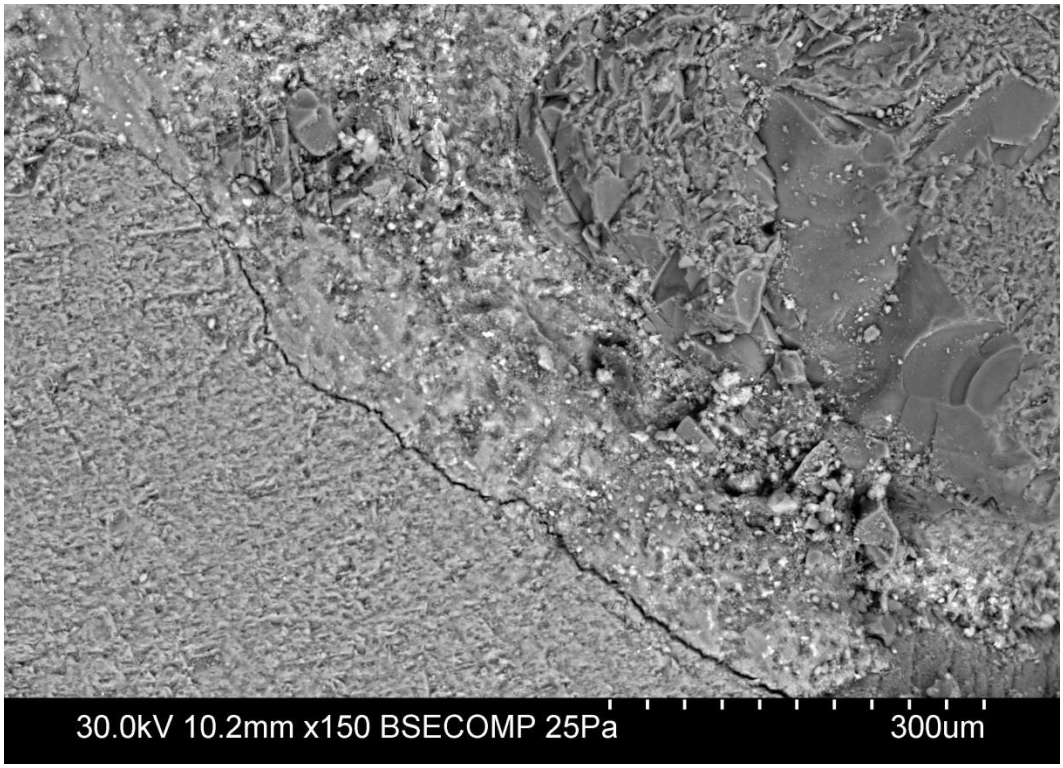
30.0kV 10.2mm x150 BSECOMP 25Pa
300um

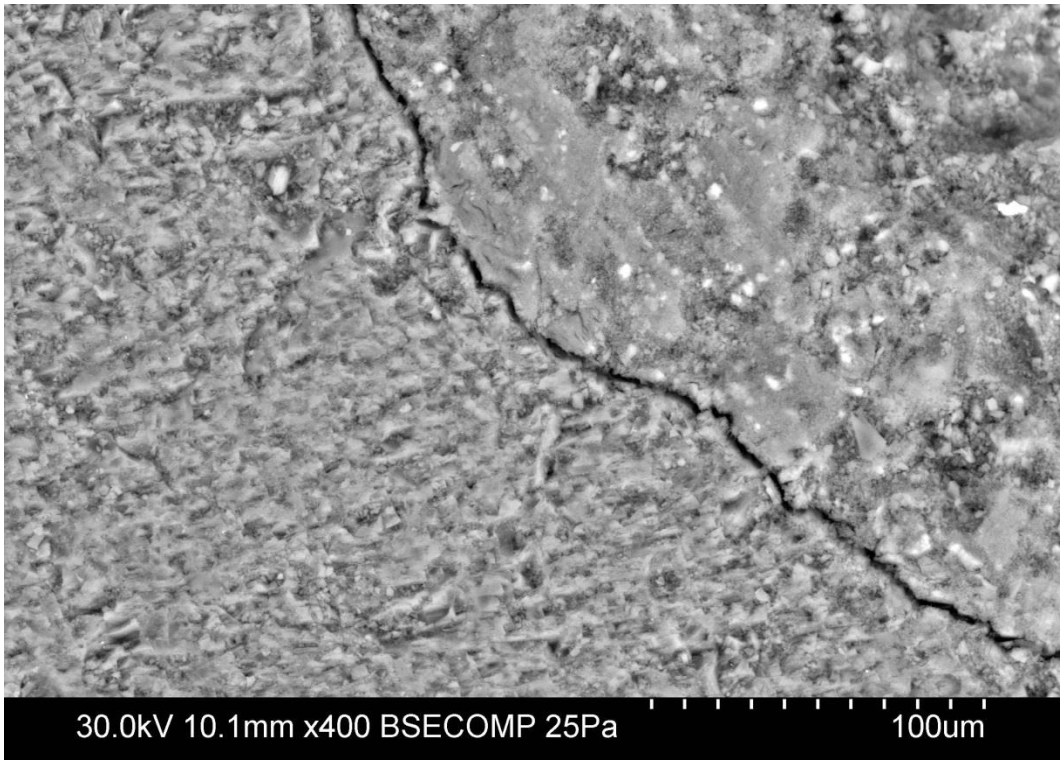
30.0kV 10.1mm x400 BSECOMP 25Pa
100um

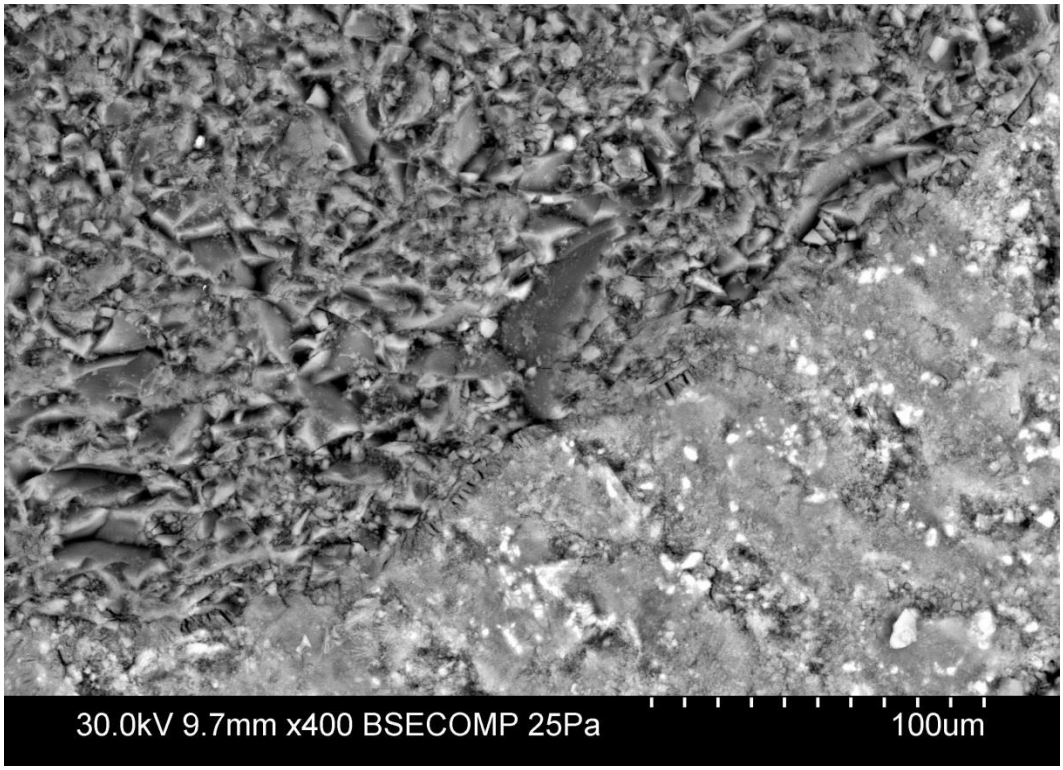
30.0kV 9.7mm x400 BSECOMP 25Pa
100um

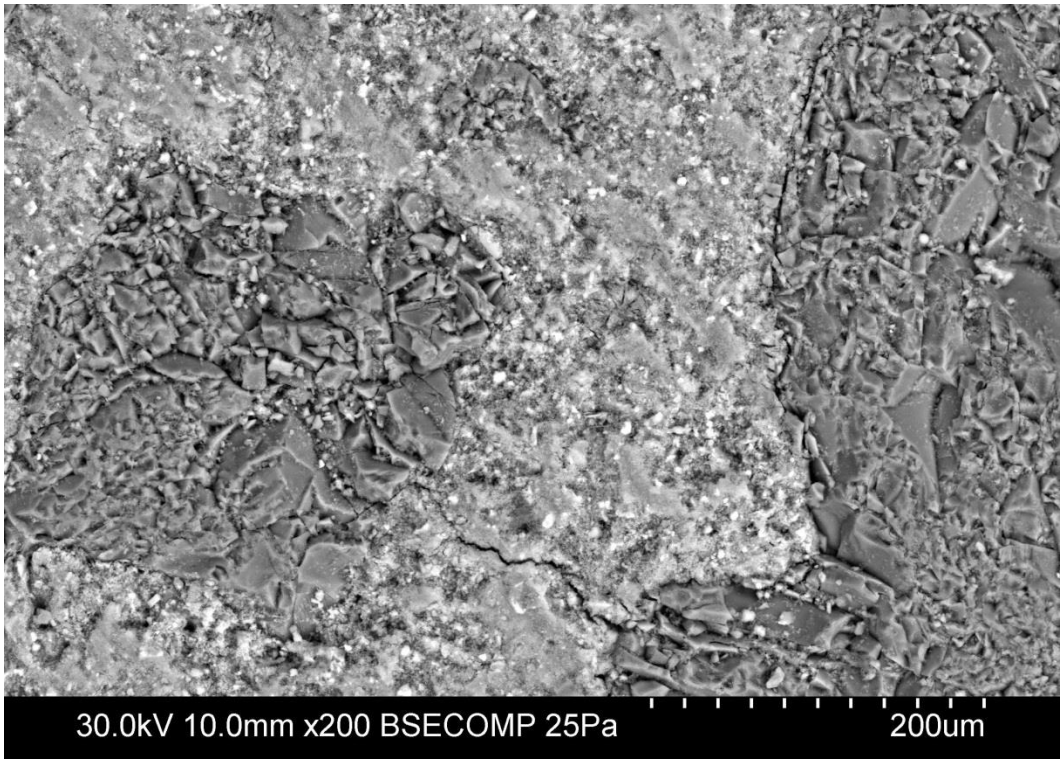
30.0kV 10.0mm x200 BSECOMP 25Pa
200um

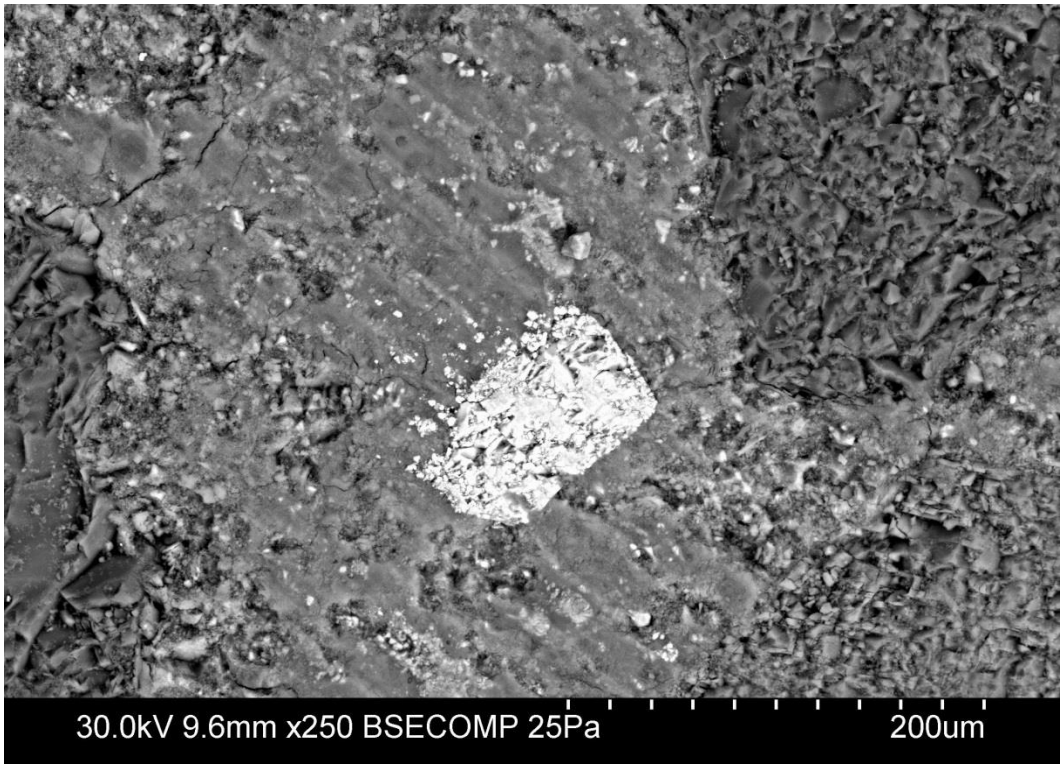
30.0kV 9.6mm x250 BSECOMP 25Pa
200um

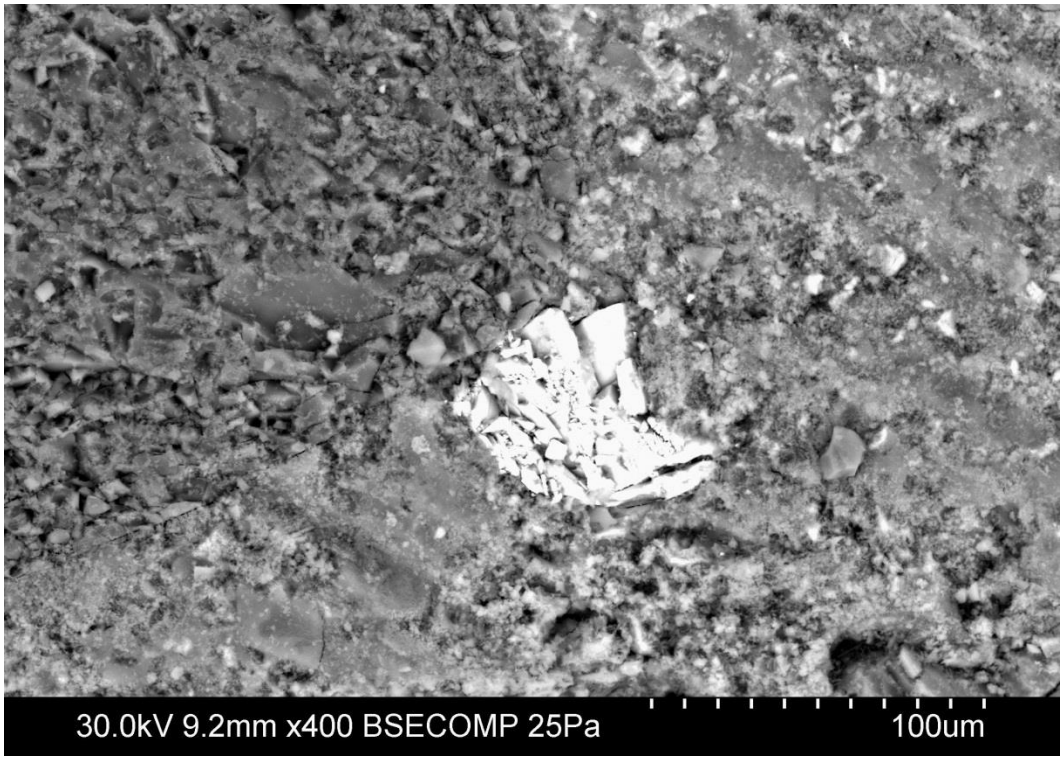
30.0kV 9.2mm x400 BSECOMP 25Pa
100um

- Cement A - Control sand (481 days, 0.845% expansion).

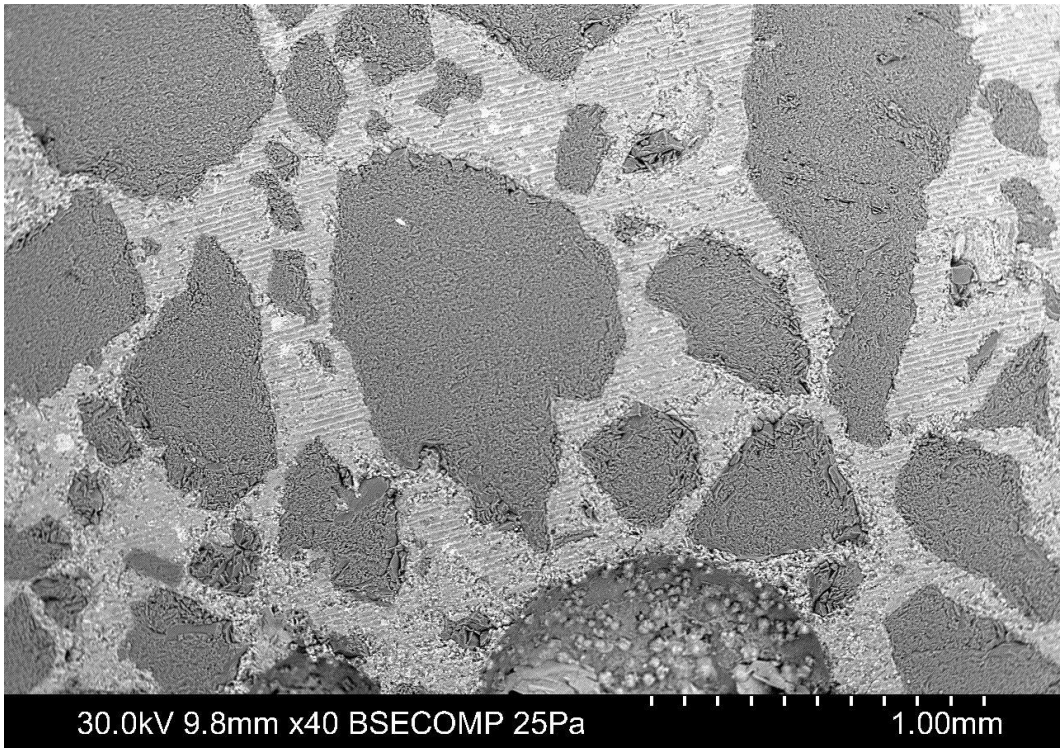

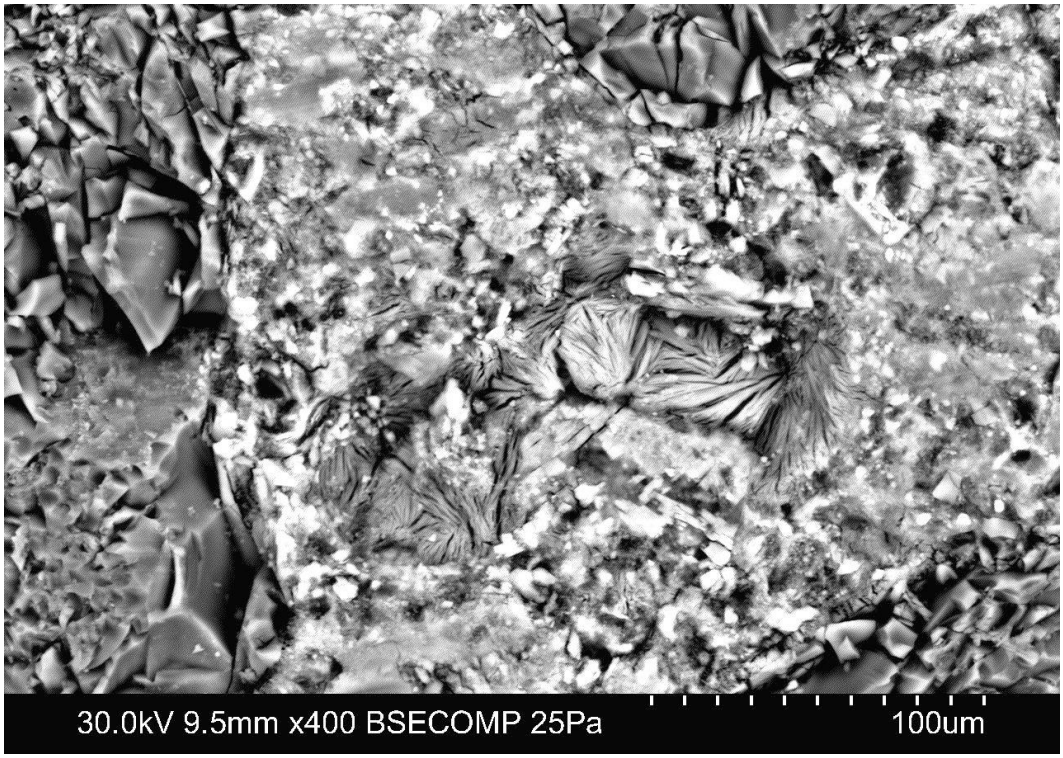

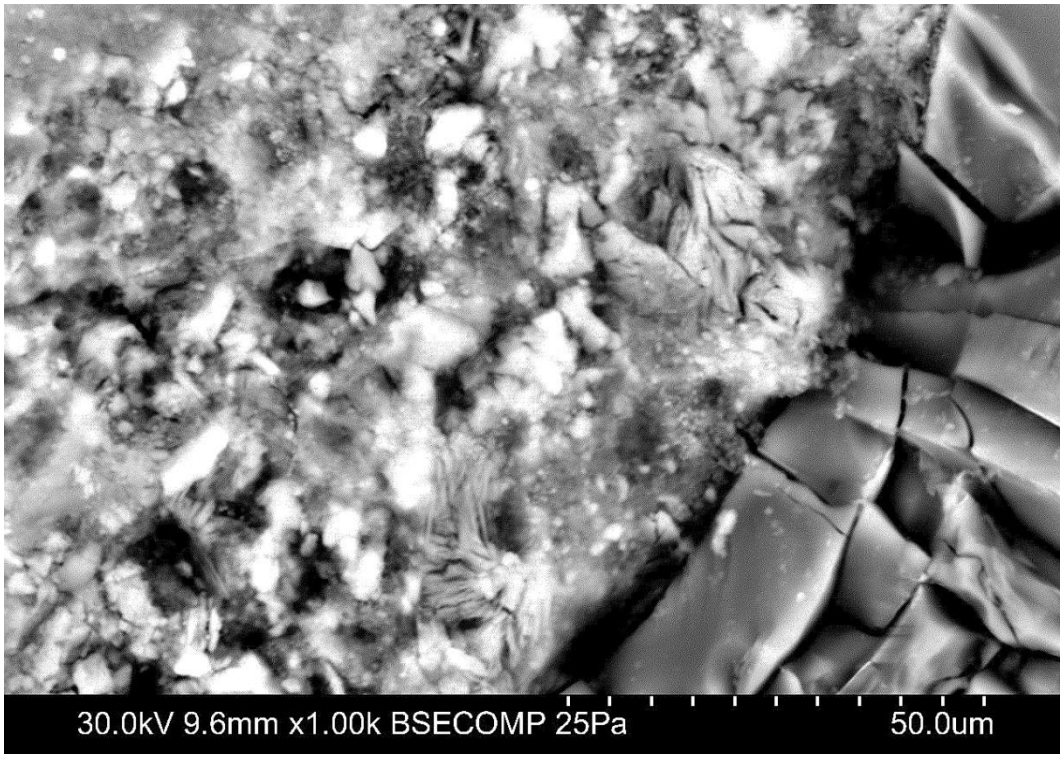
30.0kV 9.6mm x1.00k BSECOMP 25Pa
50.0um

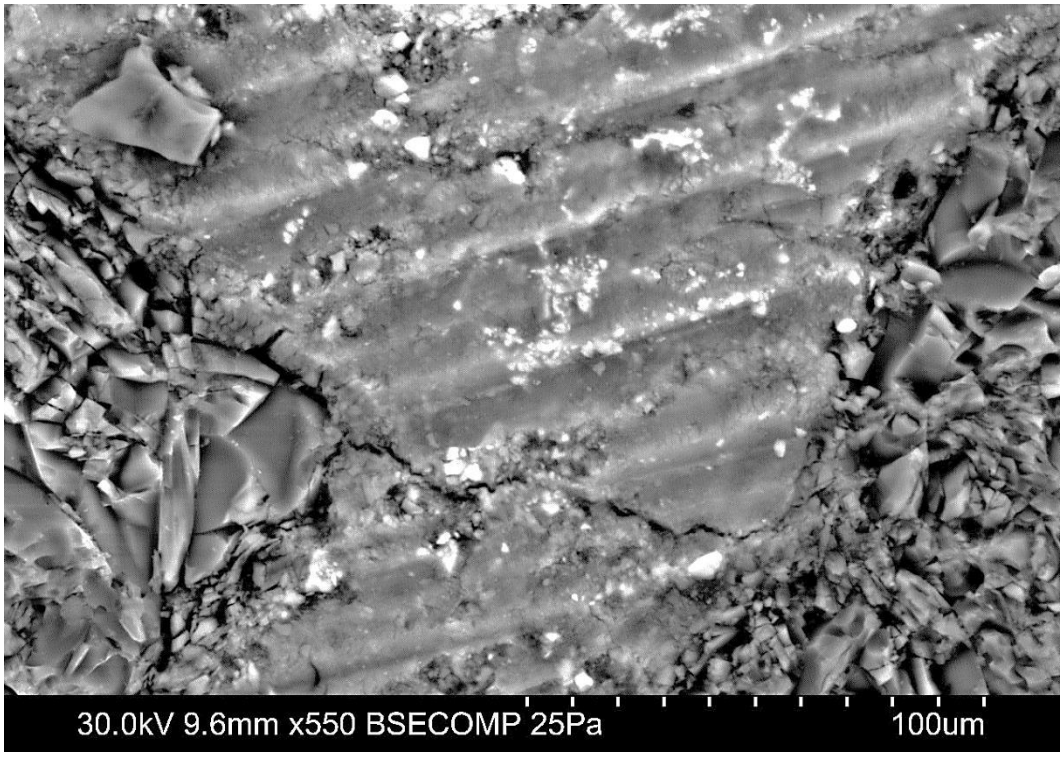
30.0kV 9.6mm x550 BSECOMP 25Pa
100um

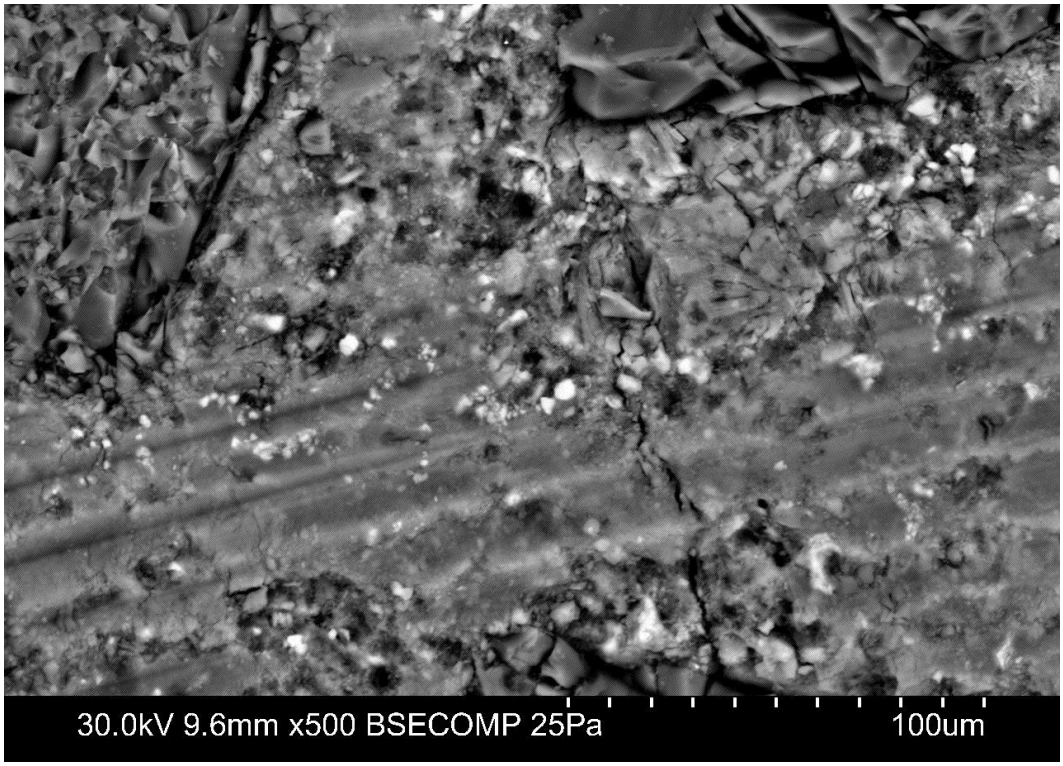
30.0kV 9.6mm x500 BSECOMP 25Pa
100um


30.0kV 10.0mm x250 BSECOMP 25Pa
200um

- Cement B - Site H sand (663 days, 0.205% expansion).

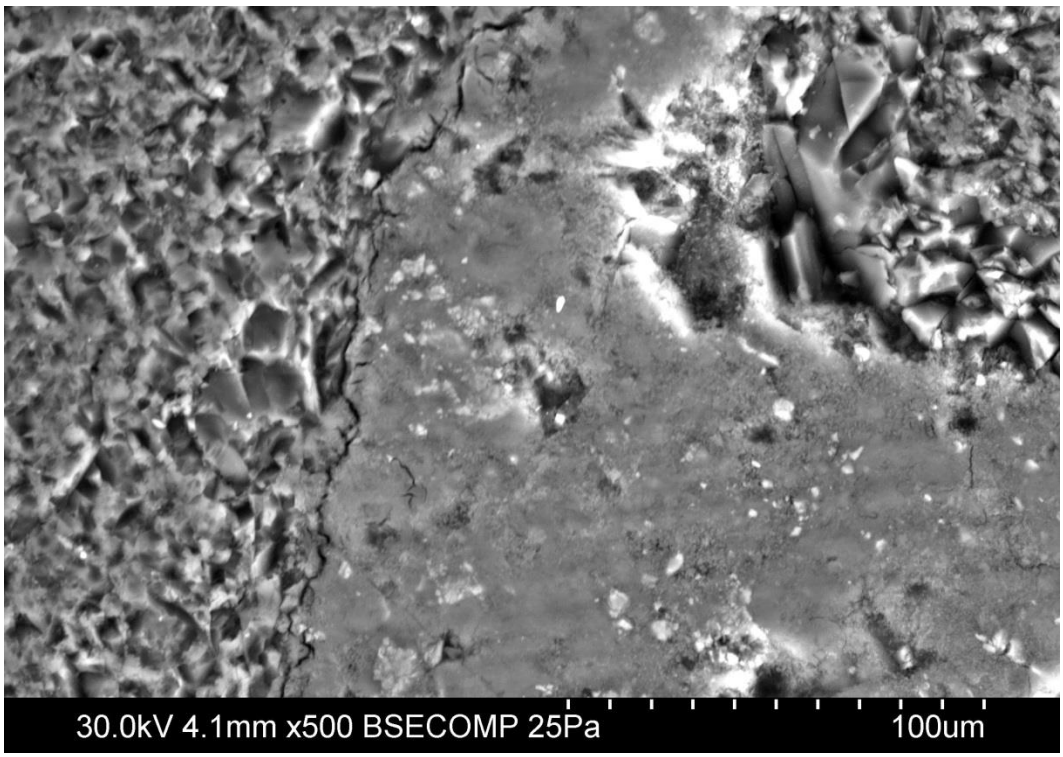

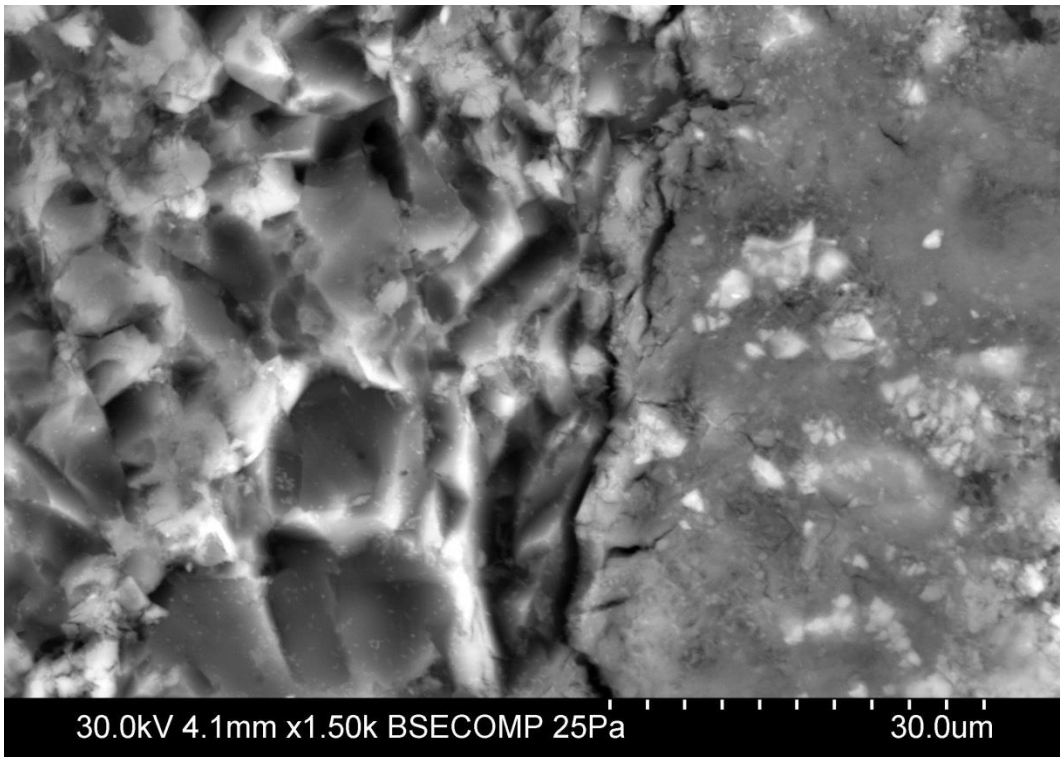

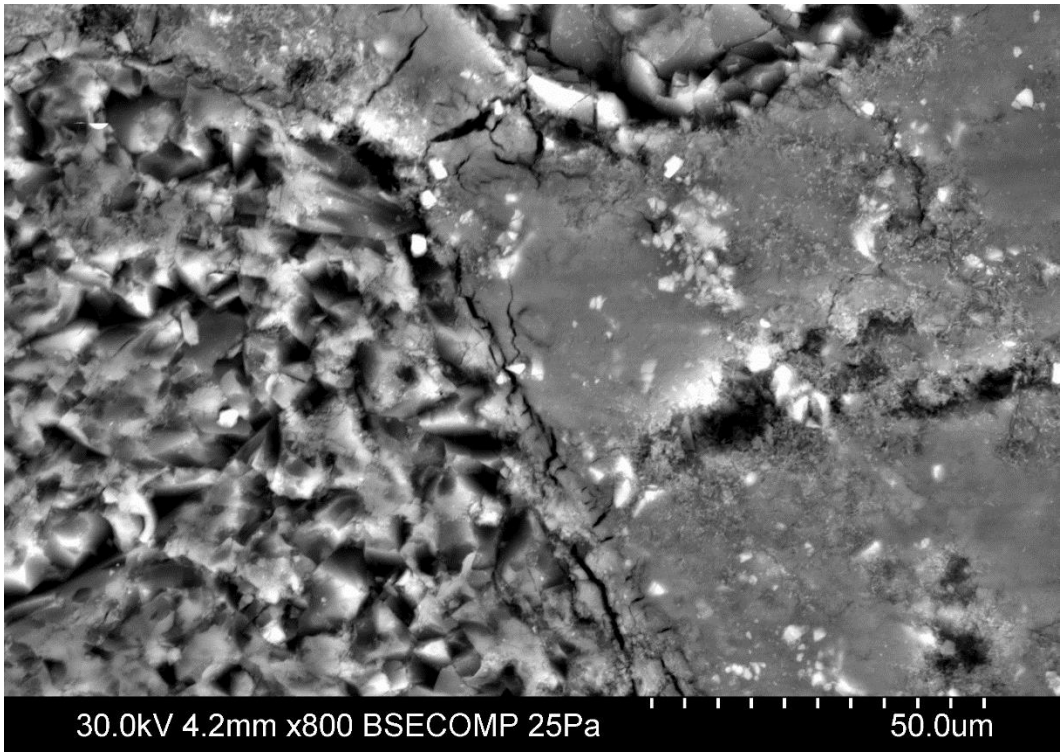
30.0kV 4.2mm x800 BSECOMP 25Pa
50.0um

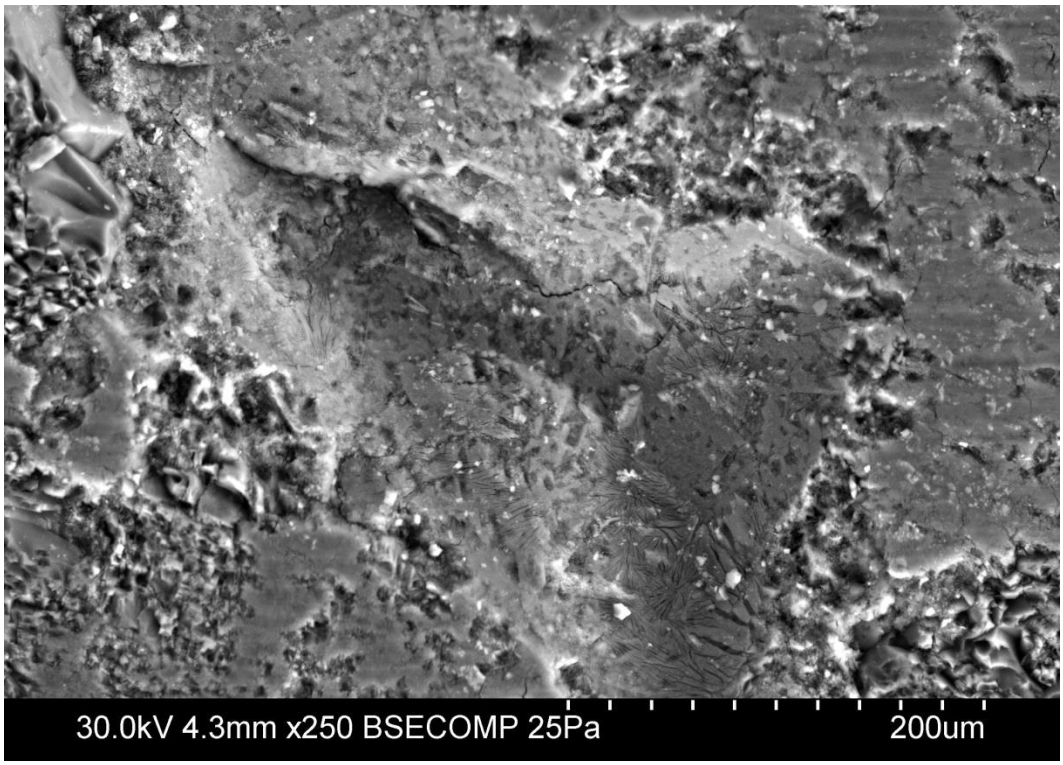
30.0kV 4.3mm x250 BSECOMP 25Pa
200um

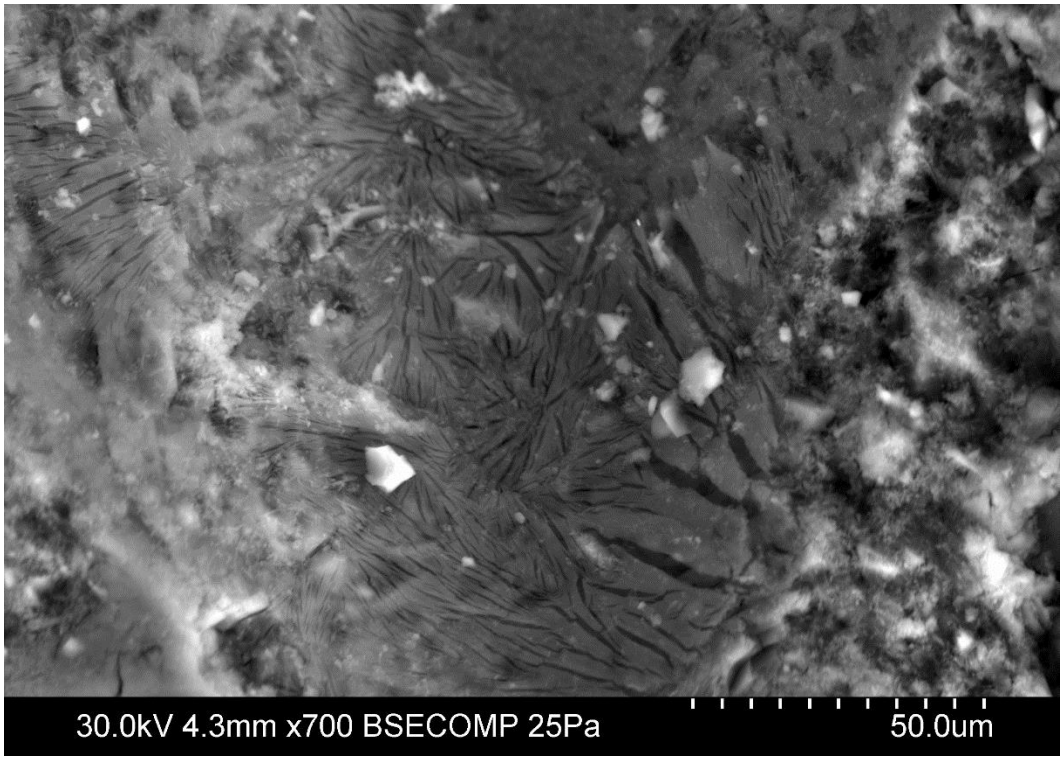
30.0kV 4.3mm x700 BSECOMP 25Pa
50.0um

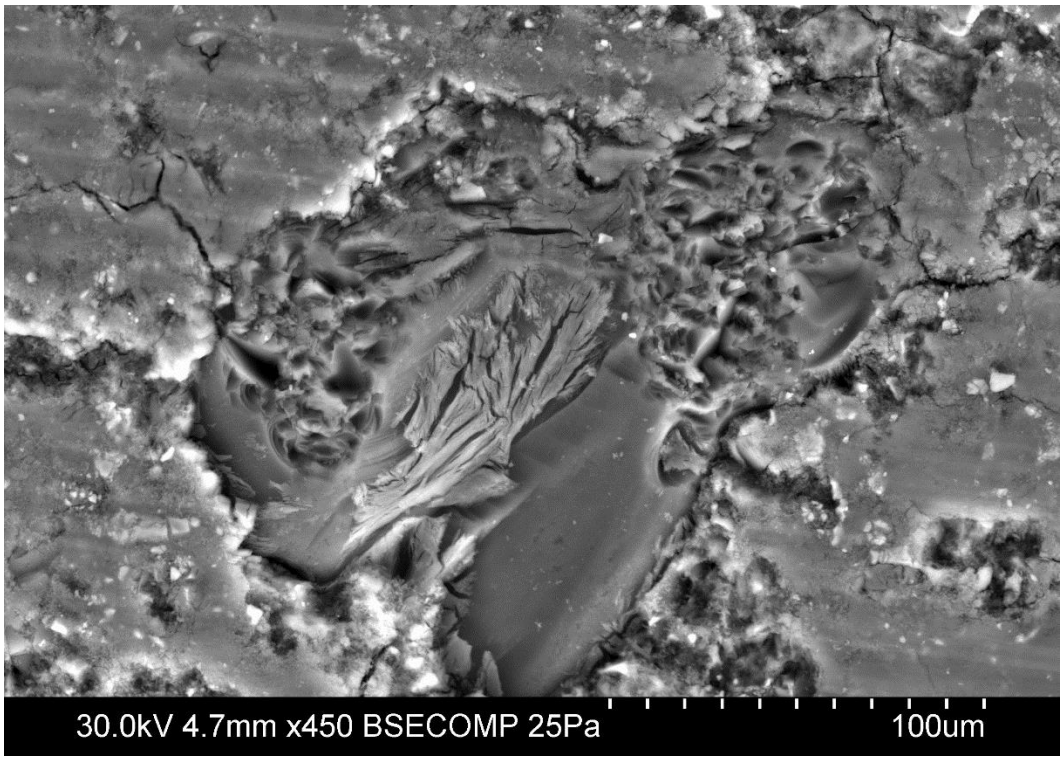
30.0kV 4.7mm x450 BSECOMP 25Pa
100um

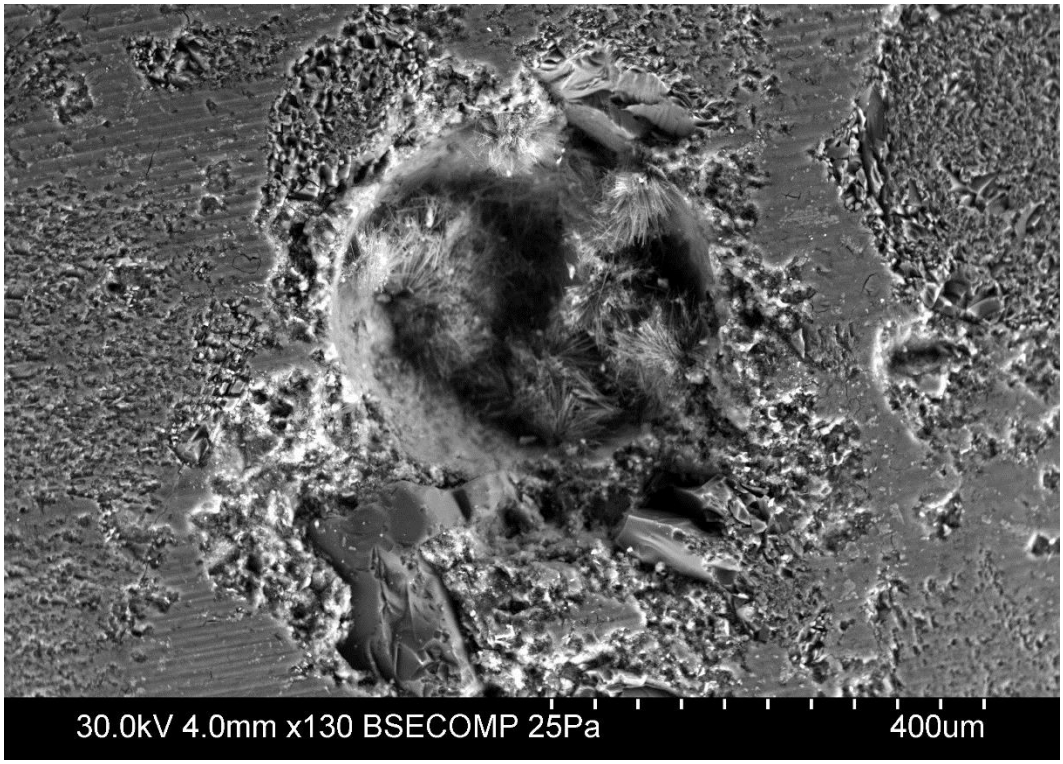
30.0kV 4.0mm x130 BSECOMP 25Pa
400um

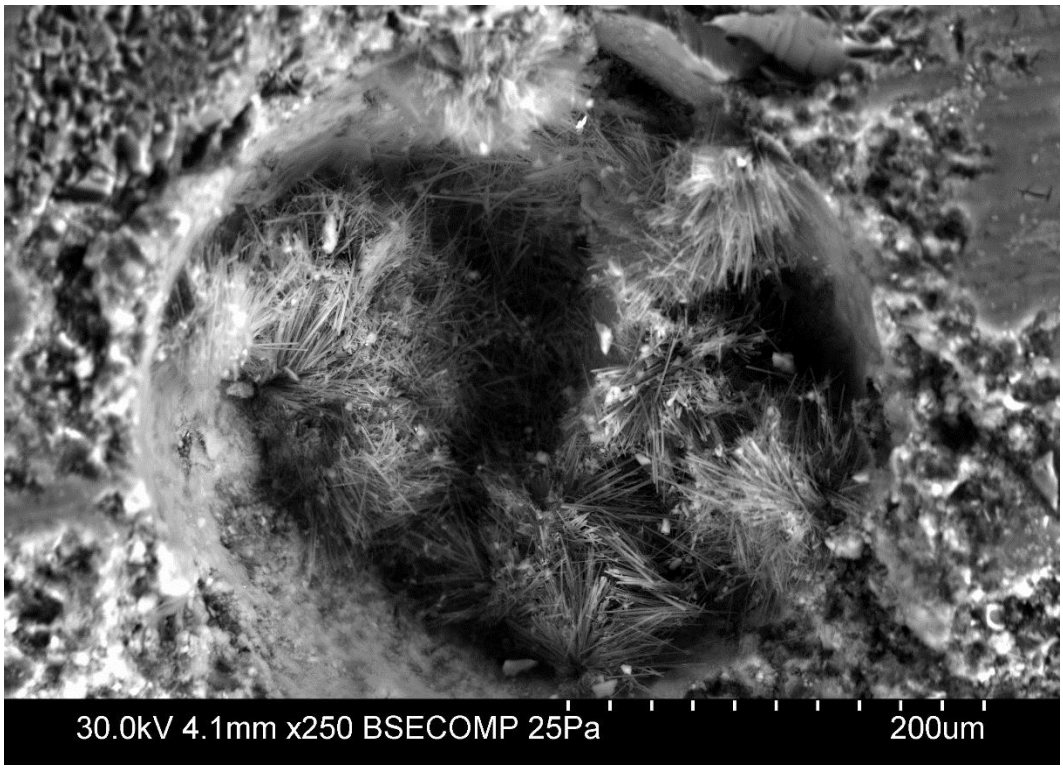
30.0kV 4.1mm x250 BSECOMP 25Pa
200um

- Cement B - Control sand (383 days, 0.009% expansion).

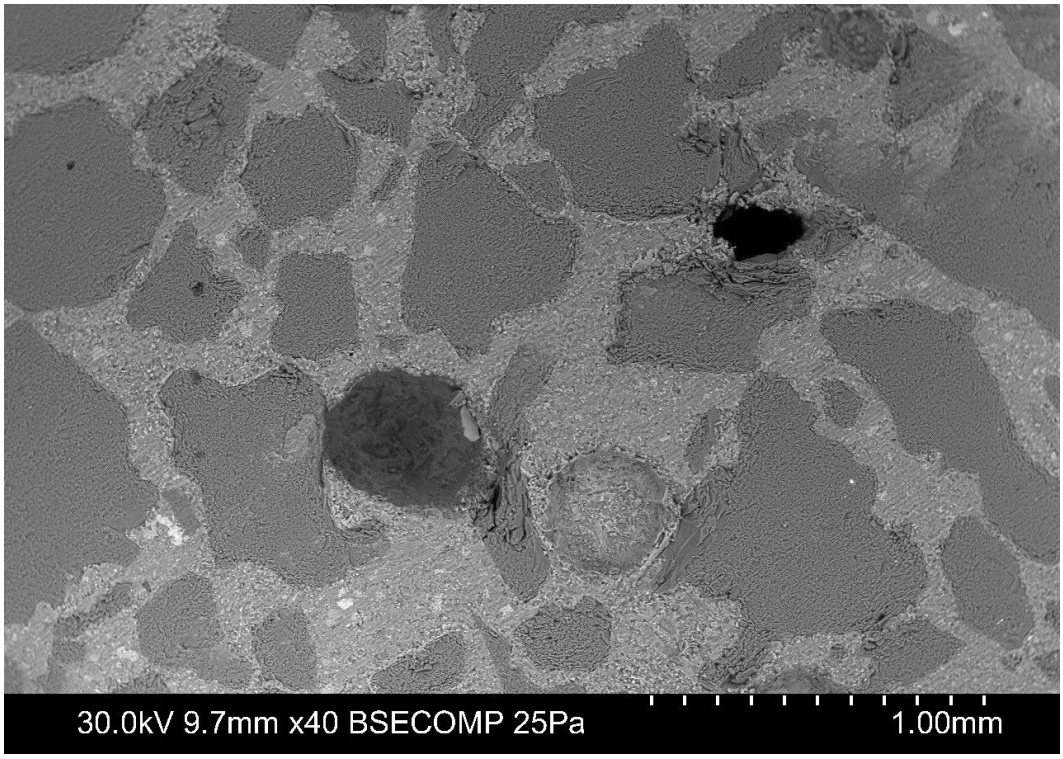

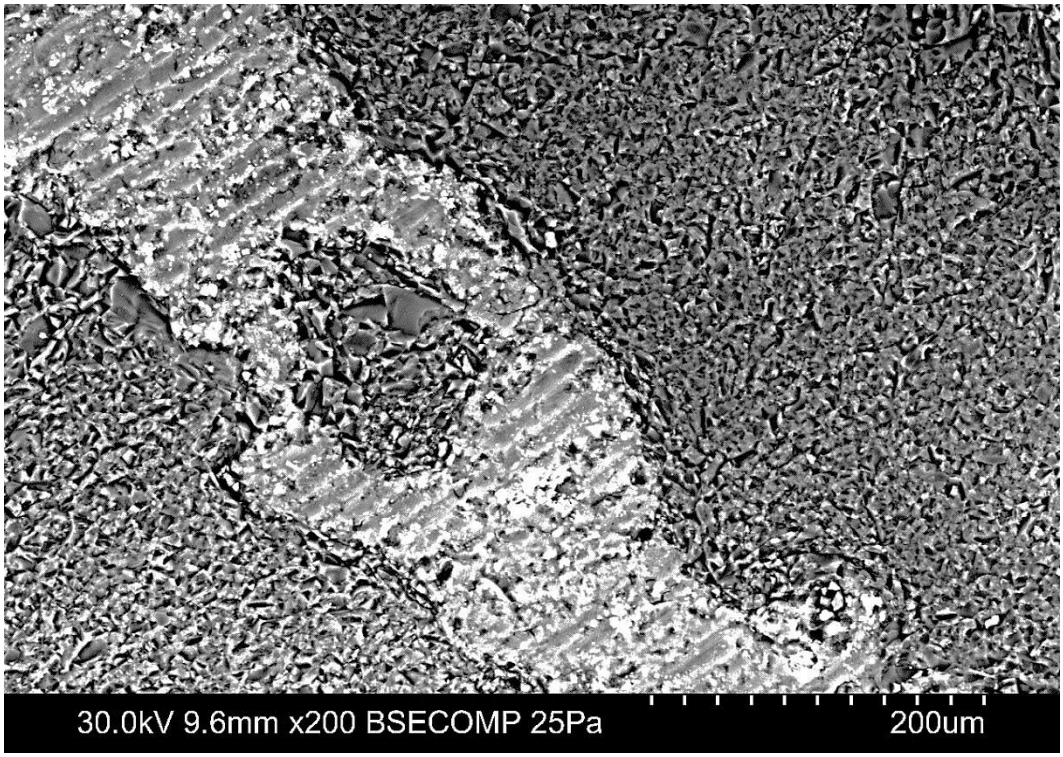

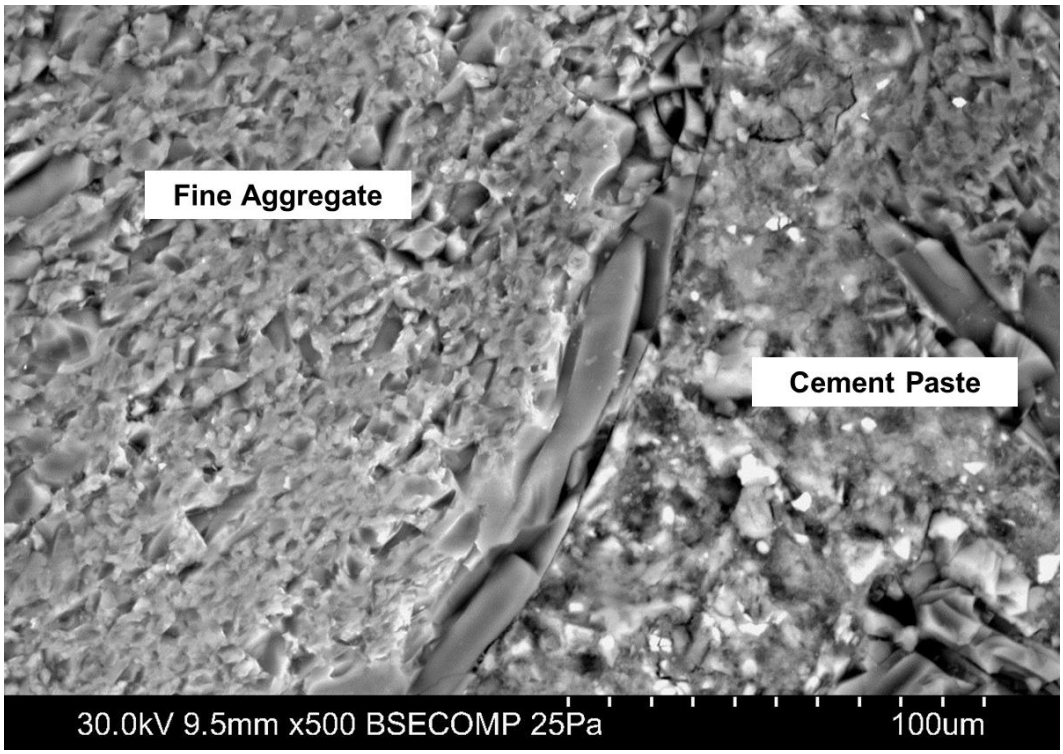
Fine Aggregate
Cement Paste
30.0kV 9.5mm x500 BSECOMP 25Pa
100um

APPENDIX F: Life-Cycle Cost Analysis of the Use of Stainless Steel Reinforcement

An estimation of the life-cycle cost of prestressed concrete piles using duplex HSSS 2205 prestressing strands was performed using software Life-365, version 2.2.1 (http://www.life-365.org/). A similar analysis performed by Azizinamini et al. (2013) for urban highway bridges in Boston, MA estimated a lower life-cycle cost when stainless steel reinforcement was included compared to the use of high-performance concrete incorporating 5% silica fume, increased cover (3.5-in. [8.9 cm] vs. 2.5-in. [6.4 cm] in the alternative using stainless steel), and the use of a membrane and overlay.

Life-365 estimates the service life of a reinforced concrete element by the calculation of the time to chloride-induced corrosion initiation in the reinforcement. Chloride concentration profiles are estimated using 2D Fickian diffusion modelling in the case of square columns and beams. Time to repair is defined as the time to corrosion initiation plus 6 years (assumed propagation period) when conventional or stainless steel is used in the project. The cost, extent, and frequency of repairs after first repair are defined by the user or by default.

A limitation of the software estimation is that duplex HSSS 2205 is not included as a steel reinforcement alternative and only reinforced concrete elements can be analyzed. For this reason, austenitic stainless steel grade 316, with a lower corrosion resistance, was used in the estimation. Prestressing strands have lower CTLs than reinforcing steel (Moser et al., 2011) and Hurley and Scully (2013) suggested longer corrosion propagation periods of stainless steel grades compared to conventional steel.

Thus, the estimation of the service life of conventional prestressing steel using Life-365 may possibly be overestimated.

The following inputs and assumptions were used in the life-cycle cost estimation:

- Location: Savannah, GA.
- Chloride exposure levels and temperature cycle correspond to default values for Savannah, GA.
- Exposure: marine tidal zone.
- Analysis period: 100 years (base year: 2013).
- Element: 70-ft. long, 20-in. (50.8 cm) square column/beam (20-in. [50.8 cm] is the minimum width allowed by Life-365 for square columns).
- Concrete mixture proportions correspond to the actual mixture design used in the piles.
- Reinforcement ratio calculated from pile design.
- Cover: 3-in. (7.62 cm) in every surface.
- Stainless steel grade: austenitic 316 (CTL=0.50% vs. 0.05% in conventional steel). Unit cost of stainless steel was increased to eight times the cost of conventional steel (3.6 $/lb. vs. 0.45 $/lb.).
- U.S. inflation rate (year 2014): 1.61%.
- Real discount rate: 1.4%, used for benefit-cost analysis of federal programs in programs of more than 30 years (from Appendix C: Discount Rates for Cost-Effectiveness, Lease Purchase, and Related Analyses, in Energy Price Indices and Discount Factors for Life-Cycle Cost Analysis – 2014 Annual Supplement to NIST Handbook 135).
- Default cost, extent, and interval of repairs were assumed. A 10% of the element area is repaired every 10 years starting from the first repair, at a unit cost of 37.16 $/ft.

Results of the estimation are shown in Table F.1, where service life correspond to the sum of the time to corrosion initiation and the propagation period, and the life-cycle cost corresponds to a project period of 100 years.

Table F.1 Life-cycle cost and service life estimation.

	Duplex HSSS 2205	**AISI 1080 Steel**
Service life (years)	100+	27.7
Life-cycle cost ($/ft.)	42.8	236.7

The results of the estimation indicate that the use of duplex HSSS 2205 prestressing strands can improve the durability of prestressed concrete piles in marine environments. However, differences in some of the parameters considered in the estimation may affect the calculated life-cycle cost and the conditions under which the use of duplex HSSS 2205 strands can be considered a superior alternative to conventional steel. In order to account for the variation of these parameters, variability analyses were performed using Life-365.

Figure F.1 shows a summary of the analysis of variation in steels cost and the repair area, cost, and interval time. The impact of the percentage change, from –100% to +100% of the initially assumed value, on the life-cycle cost of piles using conventional steel (red lines in Figure F.1) and duplex HSSS 2205 (blue lines) indicates than the use of duplex HSSS 2205 strands gives lower life-cycle costs in most of the cases. Only when repair cost or area is reduced in about 90%, estimated life-cycle cost of conventional steel is lower than duplex HSSS 2205.

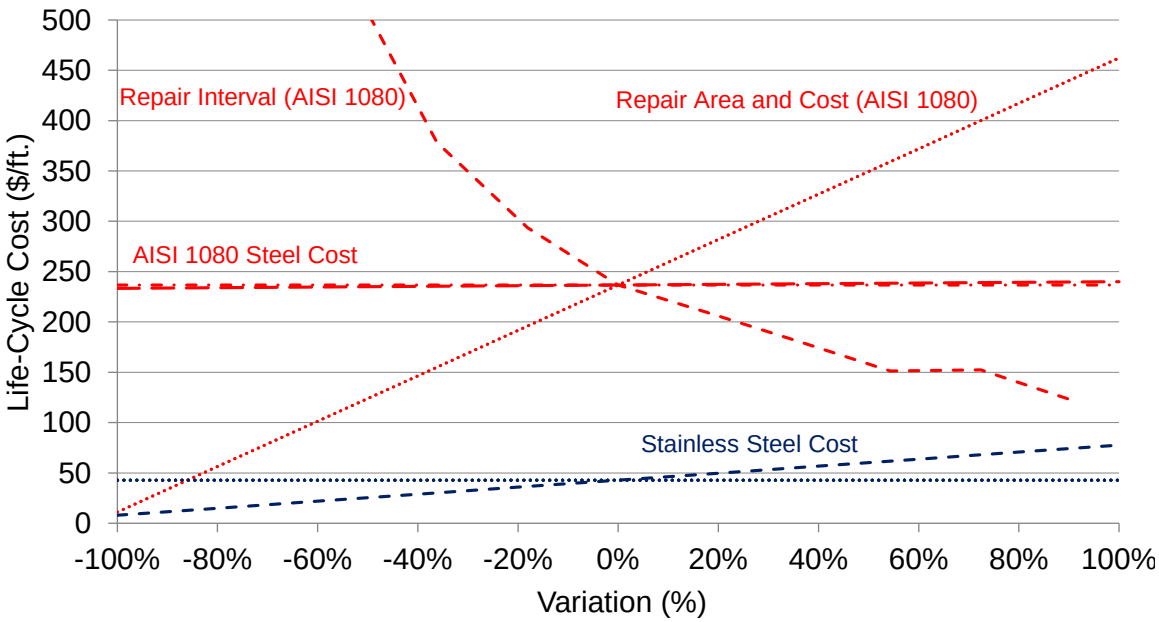

Figure F.1 Variability analysis of LCC estimation.

APPENDIX G: Actual Dimensions of Pile Sections

- Pile AISI 1080 #1 – Top Half:

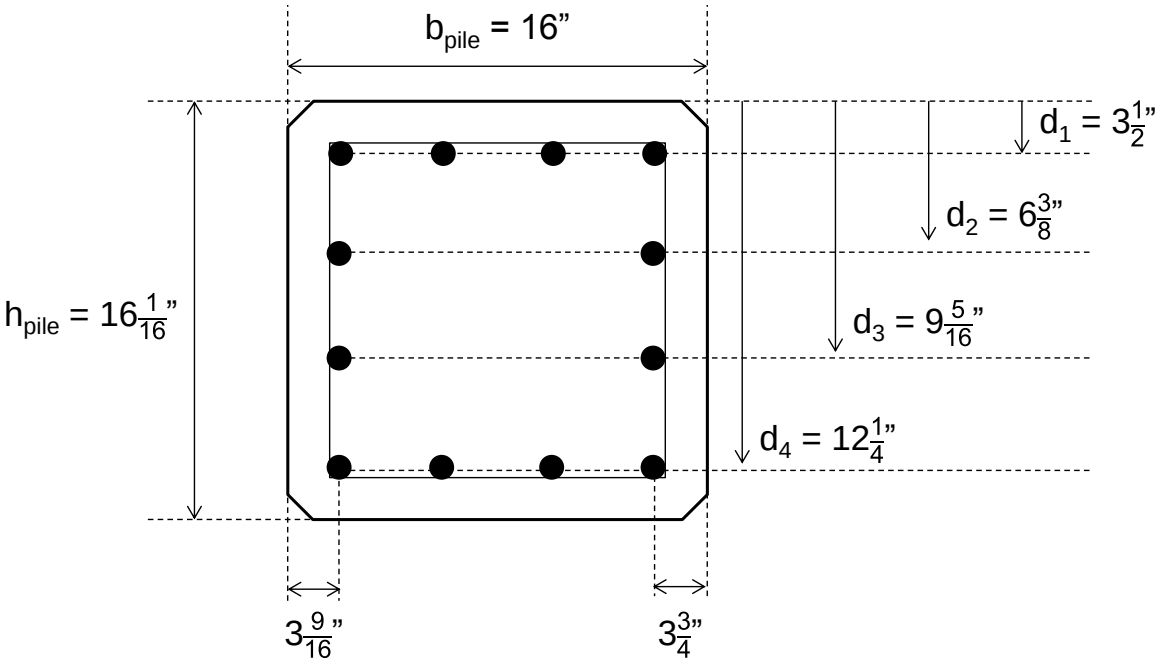

- Pile AISI 1080 #1 – Bottom Half:

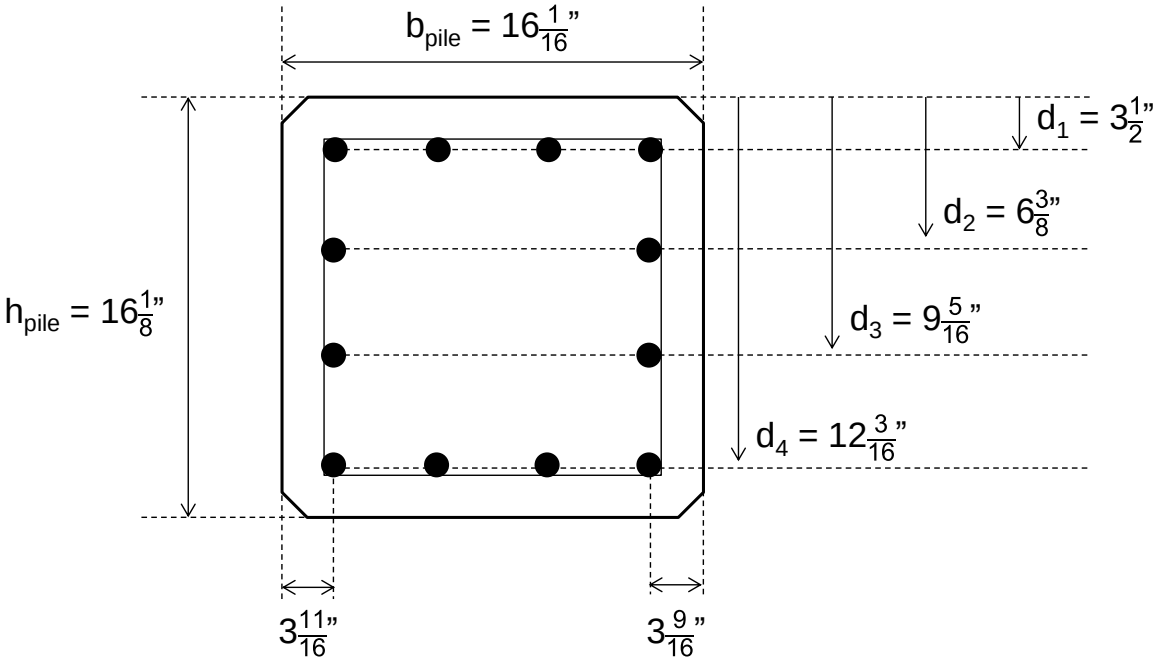

- Pile AISI 1080 #2 – Top Half:

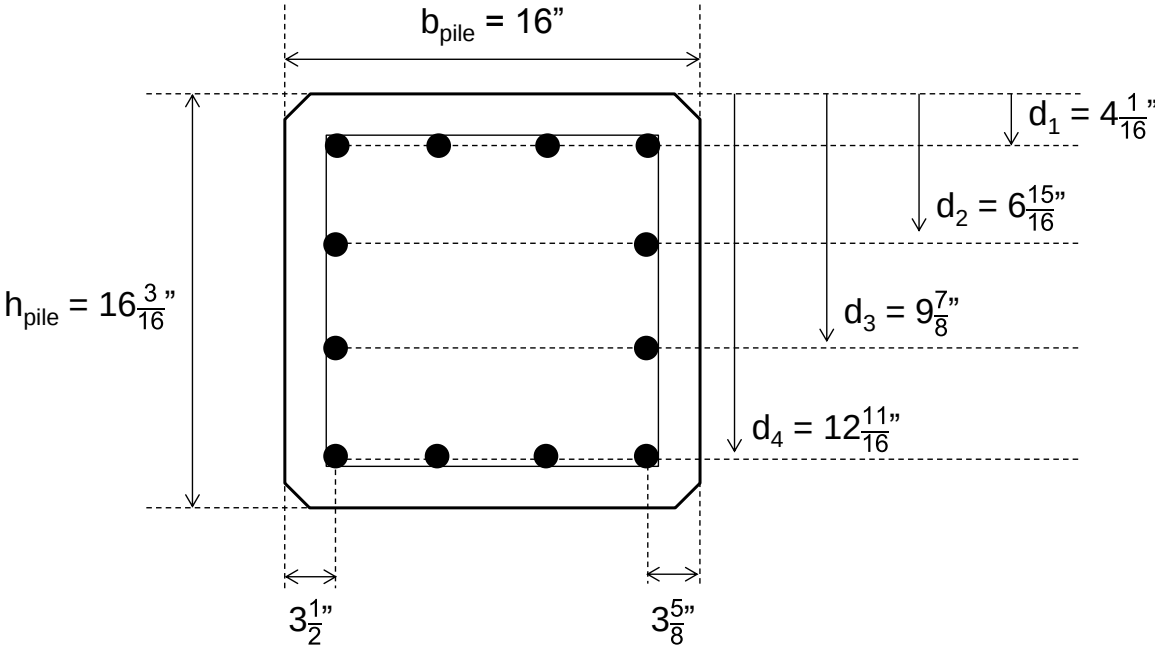

- Pile AISI 1080 #2 – Bottom Half:

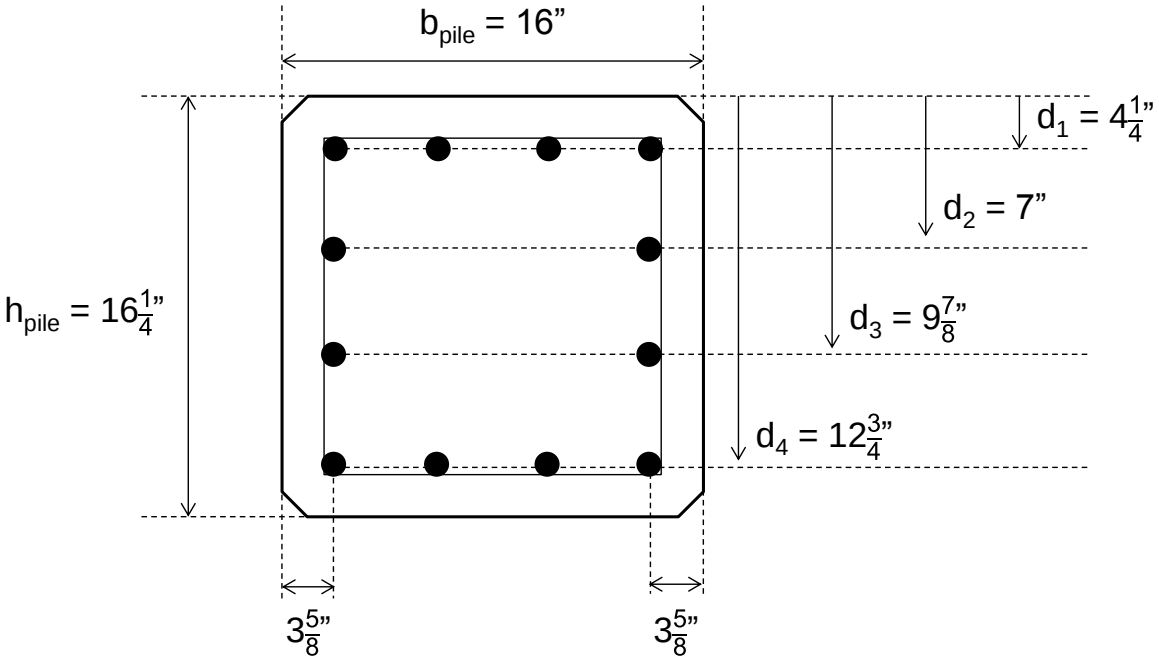

- Pile HSSS 2205 #1 – Top Half:

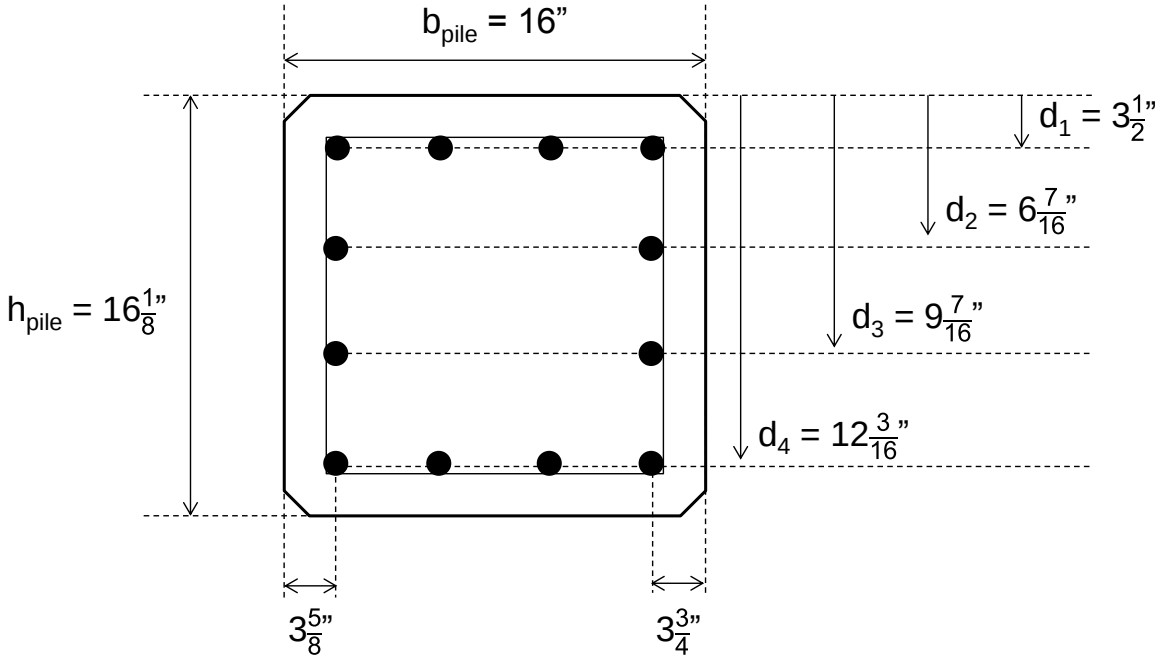

- Pile HSSS 2205 #1 – Bottom Half:

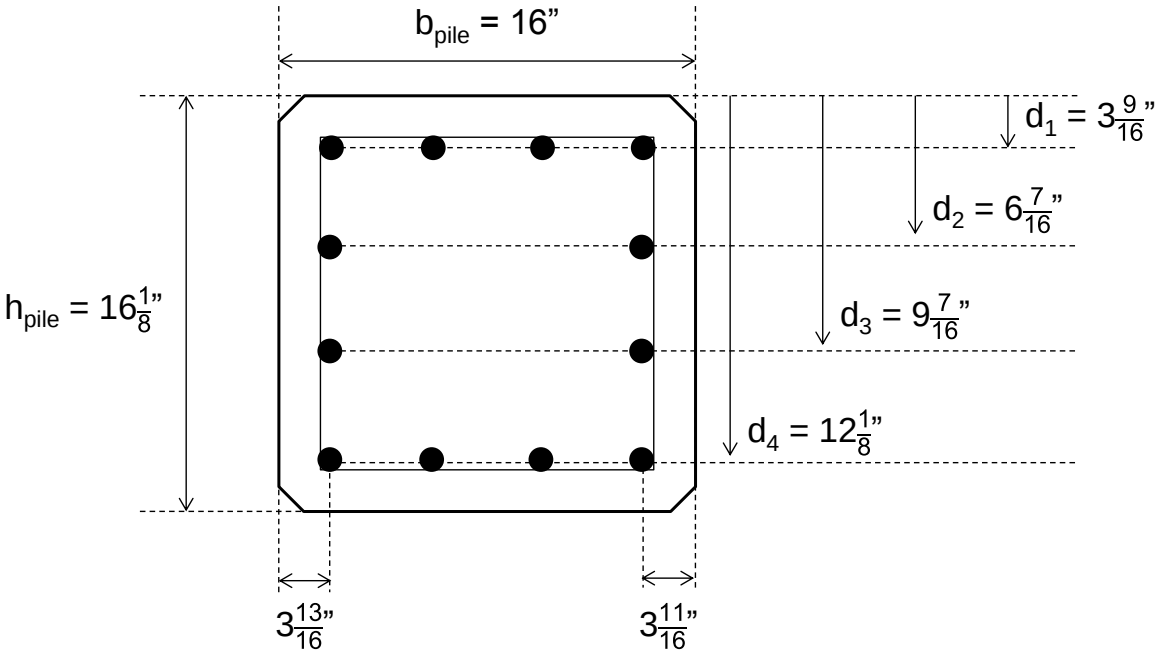

- Pile HSSS 2205 #2 – Top Half:

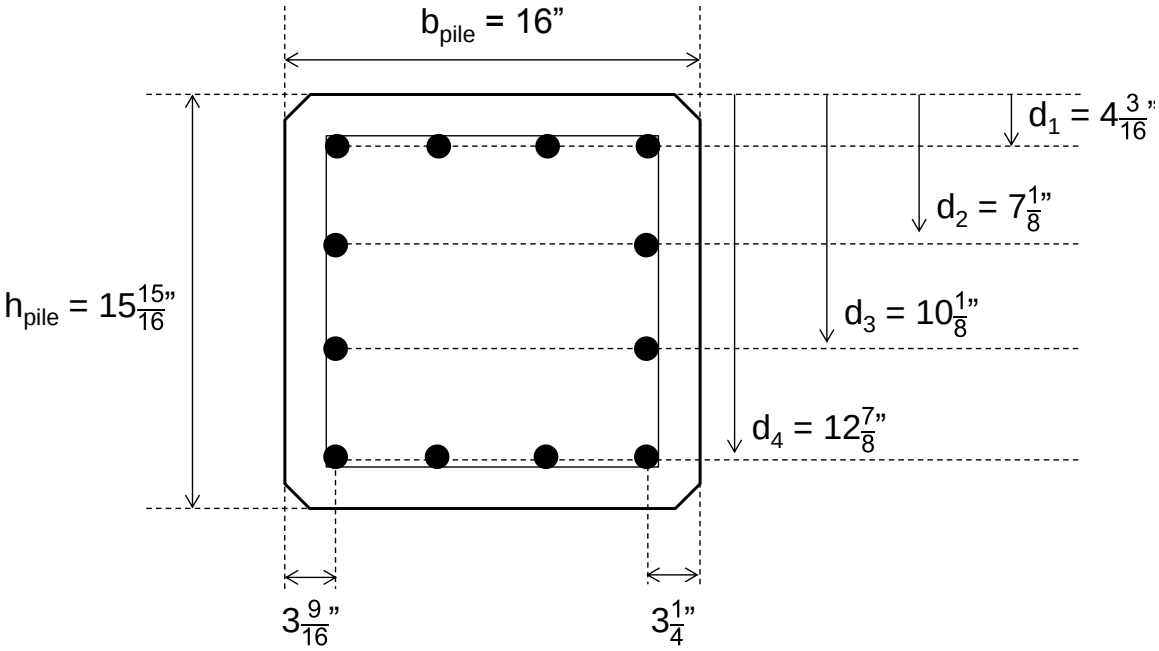

- Pile HSSS 2205 #2 – Bottom Half:

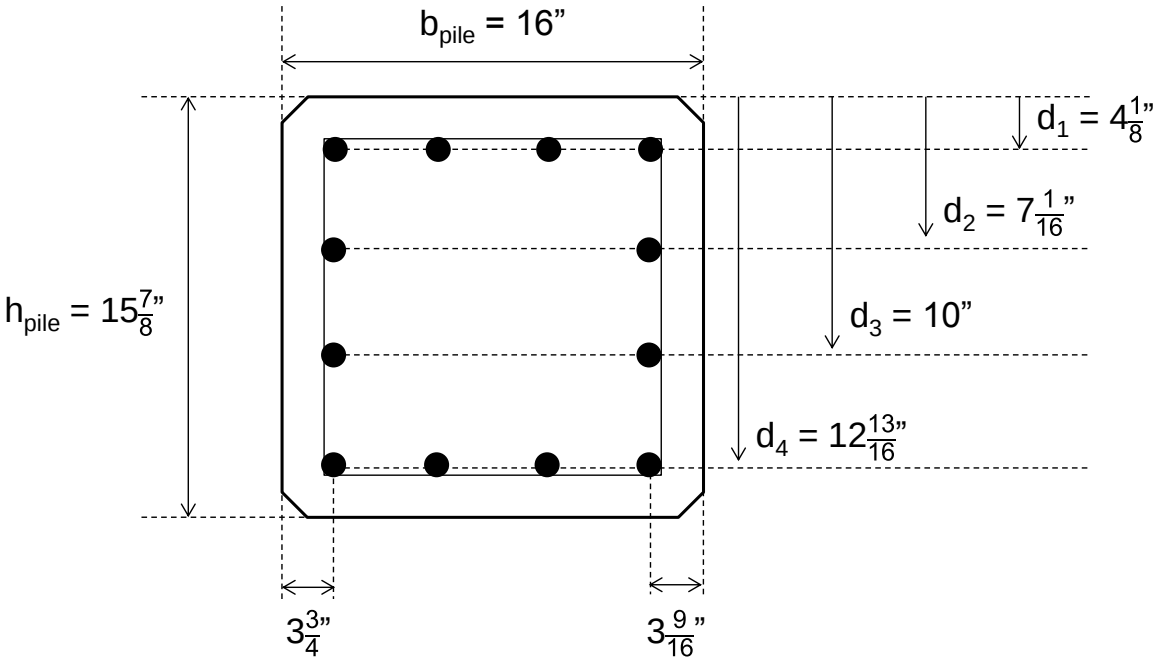

- Pile HSSS 2205 #3 – Top Half:

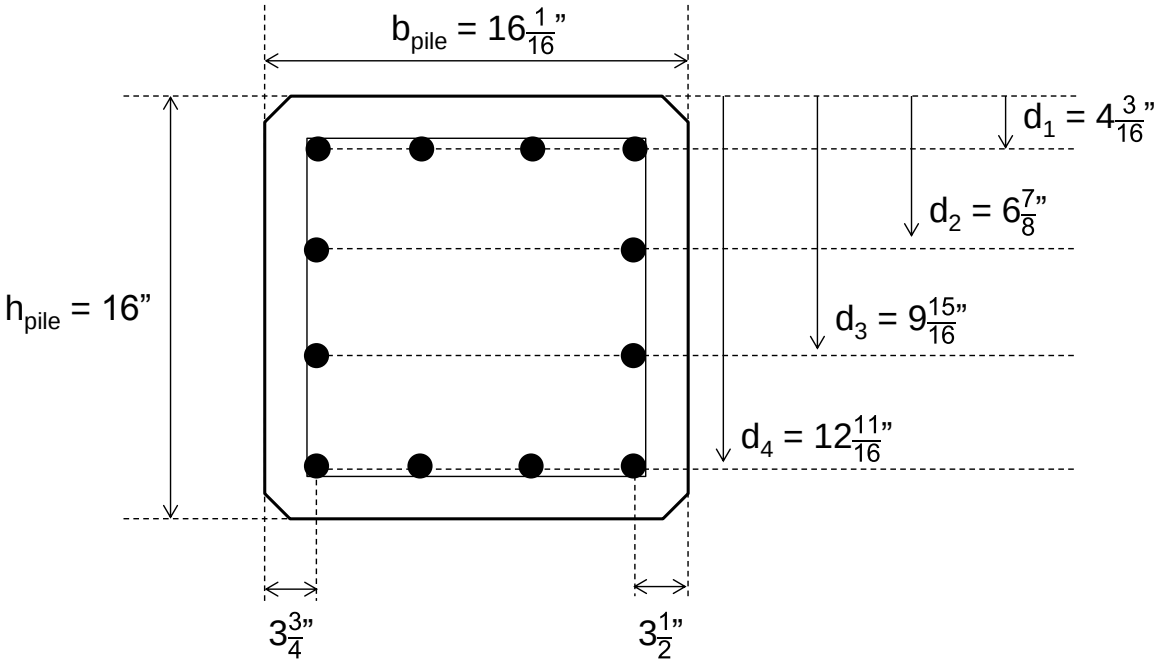

- Pile HSSS 2205 #3 – Bottom Half:

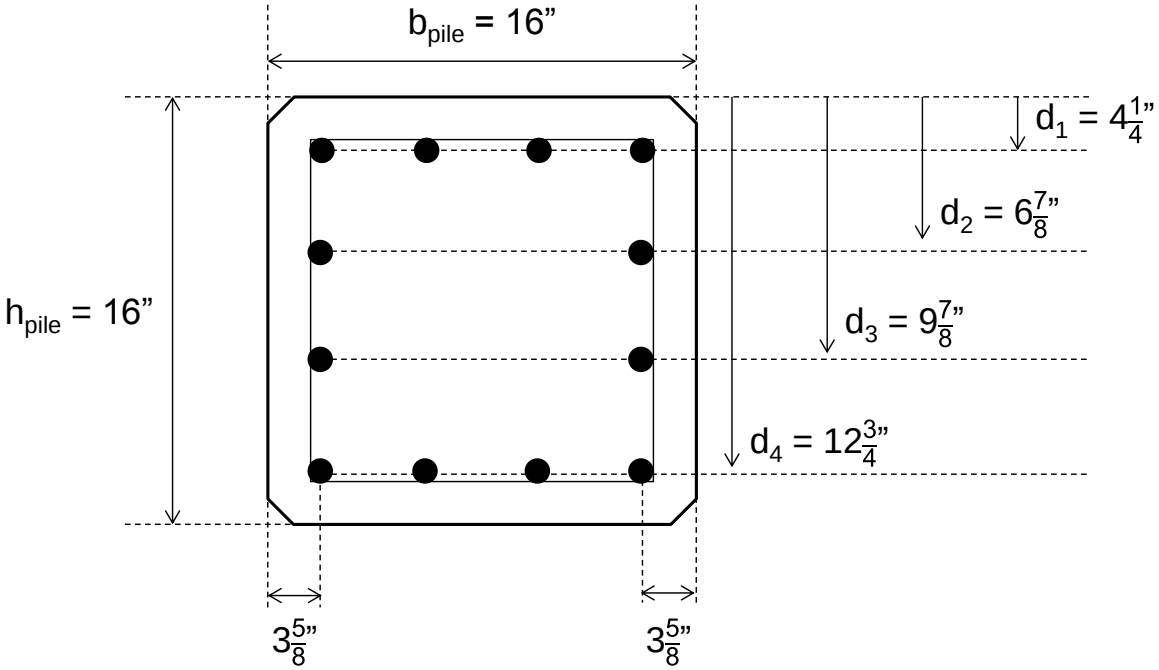

APPENDIX H: Formwork Design and Construction

The determination of the development length of the piles was performed by flexural testing of the 27-ft. (8.23 m) long piles. In order to produce pile failure by having a strain in the strands greater than 2% or the breaking of the strands themselves, the depth of the specimens was increased by the addition of a top section of concrete to get a final 16×43-in. (40.6×109.2 cm) rectangular section. The top surface of the piles was roughened after screeding the surface; #5 U-shaped stirrups were embedded to provide good bonding between the hardened concrete of the pile and the fresh concrete from added section and to assure development failure of the strands rather than shear failure of the specimens.

The 27-ft. (8.23 m) long piles were transported to the Georgia Tech Structures and Materials Lab, where the placement of the top section took place. The formwork designed for the construction of the top section consisted of plywood ¾-in. (19.1 mm) sheathing, supported by horizontal 2×4-in. (5.1×10.2 cm) studs. The forms were drilled at the positions shown in Figure H.1 to position tie rods to hold the formwork panels at the 16.5-in. (41.9 cm) width of the top of the piles.

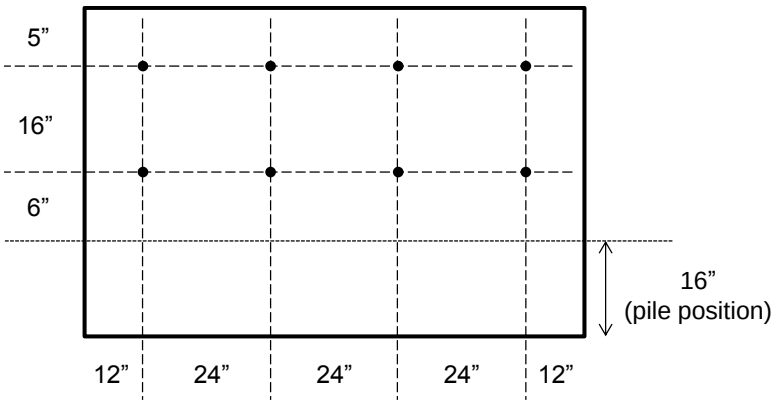

Figure H.1 Diagram of plywood panel and position of the drilled holes. (1-in. = 2.54 cm)

Two layers of acrylic latex paint were applied at the side of the panels facing concrete, to seal the surface of plywood in order to avoid moisture absorption from fresh concrete (see Figure H.2). Then, a wax release agent was sprayed on the same surface.

Vertical 2×4-in. (5.1×10.2 cm) wood studs were nailed to plywood in order to provide stiffness and strength to formwork during concrete placement (see Figure H.3).

Figure H.2 Surface coating application.

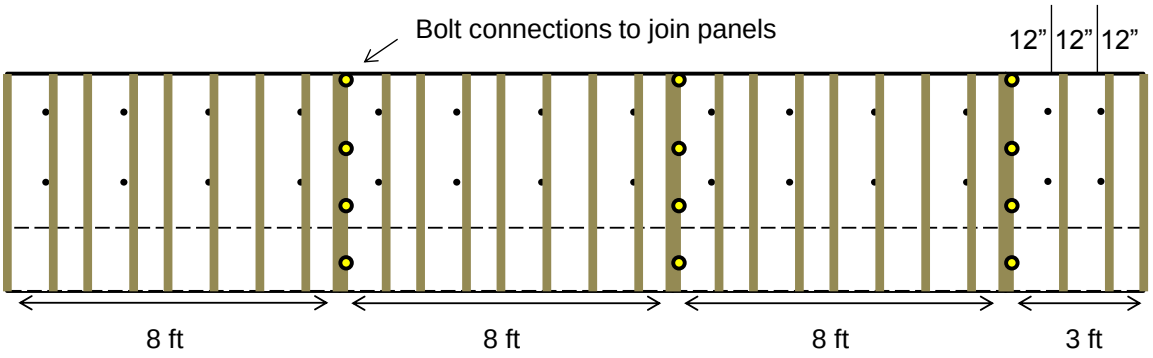

Figure H.3 Distribution of studs on the formwork sheathing. (1-in. = 2.54 cm)

Horizontal 8-ft. (2.44 m) long 2×4-in. (5.1×10.2 cm) double wales were nailed to the studs at the position of the drilled holes (Figure H.4). The end panels were joined to the side panels using ¼-in. (6.35 mm) bolts. The ¼-in. (6.35 mm) diameter threaded rods were attached to the wales by nuts and washers, and a constant distance between opposing panels of 16.5-in. (41.9 cm) was fixed along the pile. After positioning of the panels (see Figure H.5), the joints were caulked with silicone.

Concrete was placed directly from the ready-mix truck, and then consolidated with an internal spud vibrator (Figure H.6). The surface was screeded and floated with wood boards, and the surface was covered with plastic sheets (Figure H.7).

Formwork panels were removed after one week from casting (Figure H.8).

Figure H.4 Formwork panel before positioning on the piles.

Figure H.5 Formwork sheathing before concrete placing.

Figure H.6 Placing (left) and vibration (right) of the top section of concrete.

Figure H.7 Curing and protection of concrete after placing.

Figure H.8 27-ft piles with top concrete section.

APPENDIX I: Galvanic Corrosion Evaluation (SS 304–HSSS 2205)

The use of dissimilar metals for prestressing strands and transverse shear reinforcement in the piles can create the conditions under which a galvanic couple and accelerated corrosion of the more active metal (anode) could happen. To evaluate the occurrence of galvanic corrosion between the couple duplex HSSS 2205 (strands) – austenitic SS 304 (shear reinforcement), the standard test ASTM G71 was performed under three exposures representing potential environments for the metallic couple during service life: seawater, alkaline and carbonated conditions.

I.1 Test Procedure

To represent each environmental exposure, the following solutions were used:

a) Seawater: 0.5M Cl^- solution (pH=6.5).

b) Carbonated: 0.3M $NaHCO_3$ + 0.1M Na_2CO_3 (pH=9.5).

c) Alkaline: 4 g/l $Ca(OH)_2$ (pH=12.5).

Standard ASTM G71 suggests the use of 40 cm^3 of solution for every 1 cm^2 of exposed surface area of the couple. Thus, 2 cm (0.787-in.) long samples for duplex 2205 strands and austenitic 304 wires were cut using a precision water saw (Figures I.1 and I.2). Strand and shear reinforcement samples had approximately 22.87 cm^2 (3.545 in^2) and 4.12 cm^2 (0.639 in^2) of exposed area, respectively. Following the suggestion of the standard, a volume of 1 liter (33.814 oz.) was used for every condition. Additionally, the anode-to-cathode area ratio was kept constant at 0.18 and the surfaces were used as-received.

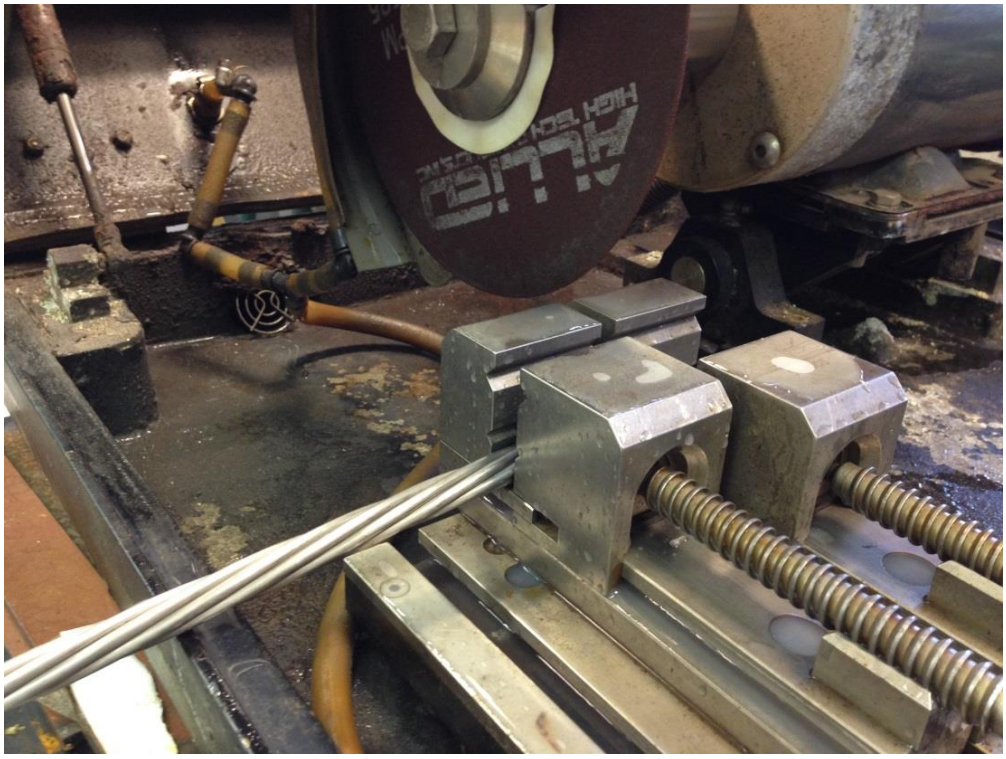

Figure I.1 Sample preparation.

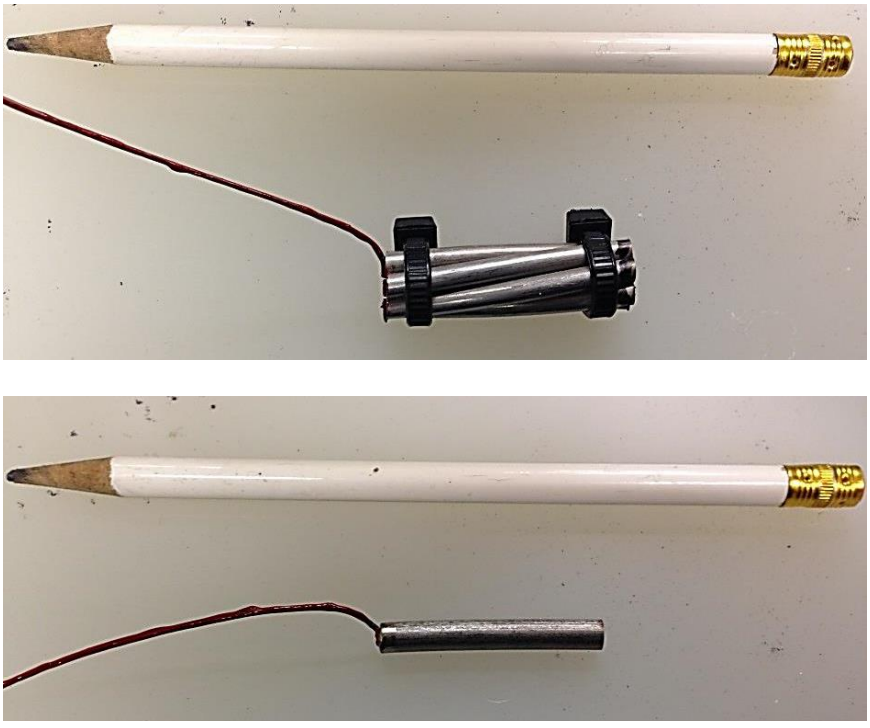

Figure I.2 Duplex HSSS 2205 (top) and austenitic SS 304 (bottom) samples.

Then, the samples were welded to a stainless steel austenitic 316 wire to apply the required potential during the test. To avoid the electrochemical reaction of the SS 316 wire with any of the metals in the couple, an insulating epoxy coating was applied at the connection between the samples and the SS 316 wire, which was also covered with the epoxy coating (see Figure I.3). The area covered by the epoxy coating was not considered in the calculation of the exposed area.

Figure I.3 Epoxy coating application.

Every cell included of a couple composed by samples of HSSS 2205 strand and SS 304 wire, and a reference electrode calibrated before the test. They were connected to a potentiostat to keep the potential of the working electrode (anode, in this case the SS 304 wire) at a constant value. Every cell was submerged in 1 liter of solution and the system was connected to an 8-channel electrochemical multiplexer that provided the

current between both stainless steel alloys (Figures I.4 and I.5). Two replicates were prepared per solution. One measurement was obtained every minute for 60 hours.

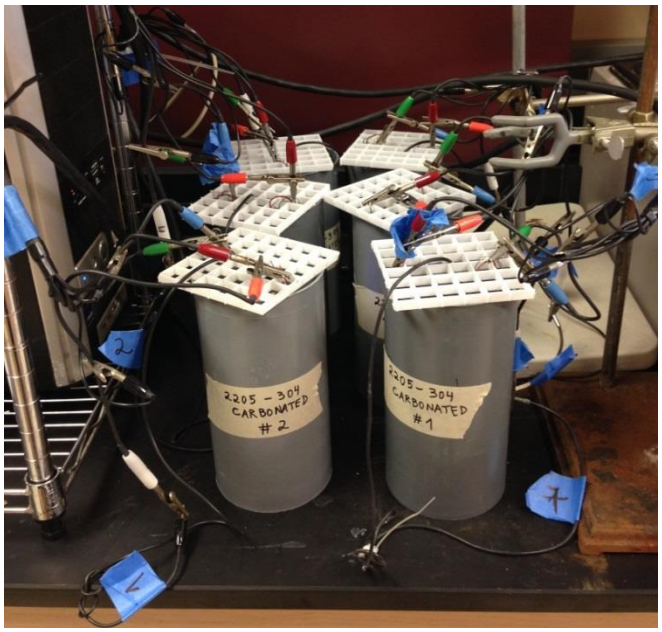

Figure I.4 System of 6 cells (three solutions, two replicates per solution).

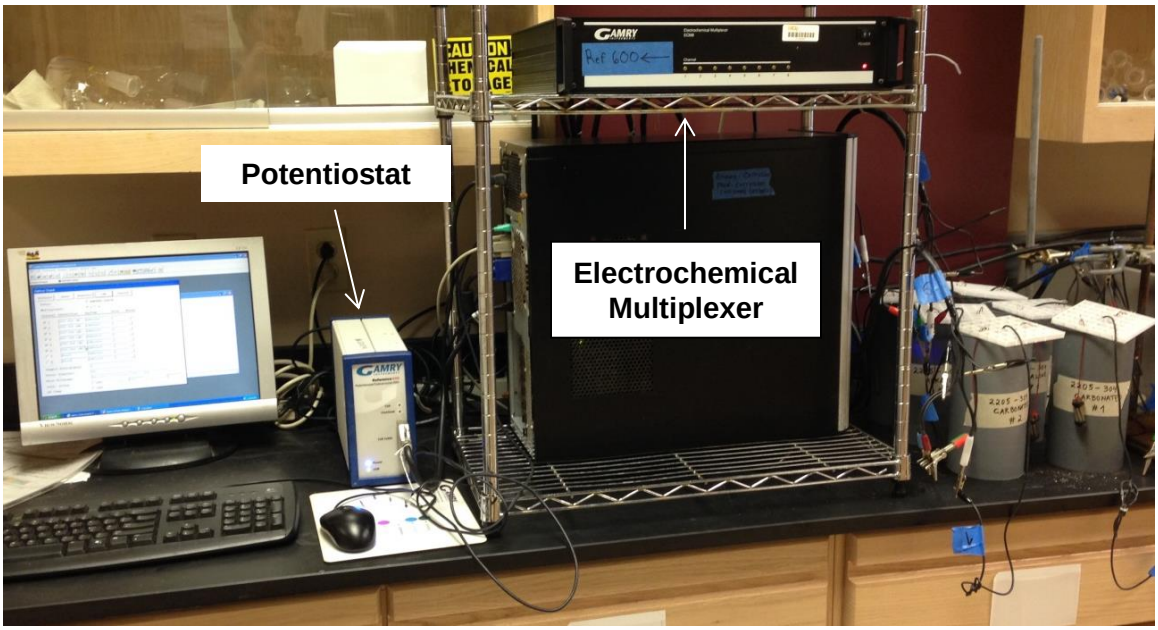

Figure I.5 Galvanic corrosion test set up.

I.2 Results of Galvanic Corrosion Test

The average current developed between the two stainless steels during the galvanic corrosion test is given in Figures I.6 and I.7. For every cell, the current between both samples (HSSS 2205 vs. SS 304) goes to values close to zero before 2 hours from the start of the test. The most extreme case, seawater condition, started with an average current of ~300 μA, but this value decreased quickly to 34.6 μA after 1 hour and 1.1 μA after 2 hours from the start of the test.

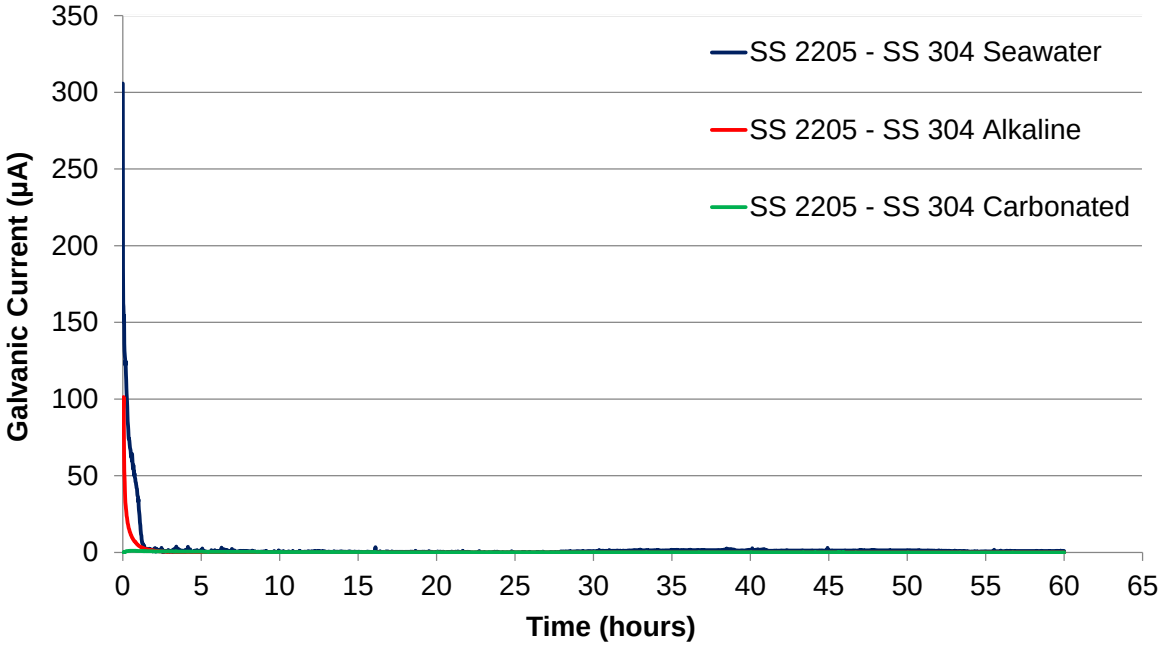

Figure I.6 Current evolution during galvanic corrosion test.

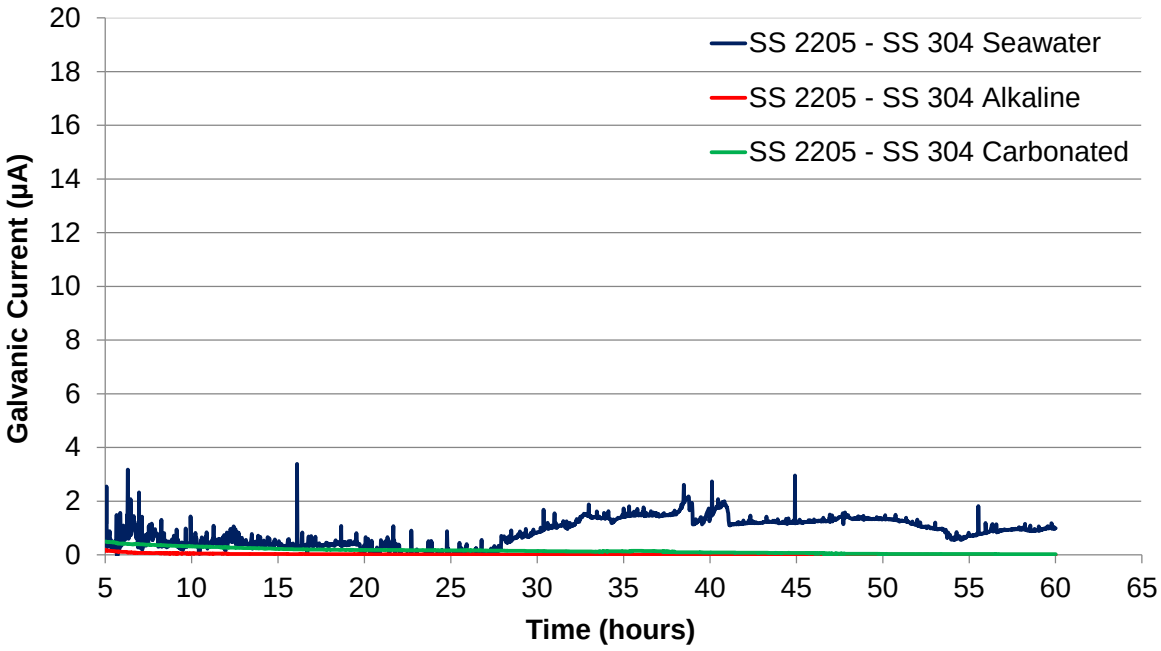

Figure I.7 Current evolution from 5 to 60 hours.

The occurrence of a galvanic couple produces a current flowing between the anode and the cathode, an accelerated corrosion of the anode, and an electrochemical protection for the cathodic member.

The measured current can be converted to corrosion rate using Faraday's law (Equation I.1).

$$r = 0.129\frac{ia}{nF} \tag{I.1}$$

where r is the corrosion rate in mpy (mils per year), i is the current density, a is the atomic weight, F is Faraday's constant (96,500 C/equivalents), and n is the number of equivalents (electrons) exchanged.

In the case of alloys, the number of equivalents can be calculated using Equation I.2.

$$N_{eq} = \sum\left(\frac{f_i \cdot n_i}{a_i}\right) \quad \text{(I.2)}$$

where f_i is the mass fraction, a_i is the atomic weight, and n_i is the numbers of electrons exchanged, for every *i* element in the alloy.

For austenitic SS 304 (anode), N_{eq} = 0.03981. The rate of corrosion for the anode was calculated using the average current of the last 10 hours of the test (Figure I.6) and Equation I.1. The rate of corrosion calculated for each condition can be observed in Table I.1. Commonly, rates of corrosion below 1 mpy are considered negligible and are indication of an excellent corrosion resistance (Jones, 1996).

Table I.1 Rate of galvanic corrosion under tested conditions.

Testing Condition	**Rate of Corrosion** (mpy)
Seawater	0.095775
Alkaline	0.000230
Carbonated	0.002832

Results observed in Figure I.6 and Table I.1 indicate that, in the case of a couple formed by HSSS duplex 2205 and austenitic SS 304 under tested conditions, both samples will passivate and the development of galvanic corrosion is highly unlikely.

APPENDIX J: Properties of Concrete

- Compressive strength of concrete:

Age of Testing (days)	**Batch***	**Maximum Load** (lbs.)	**Compressive Strength** (psi)	**Average** (psi)	**Std Dev** (psi)
4	**2**	83,960	6,681.3	**5,750**	1,155
	1	51,160	4,071.2		
	6	75,260	5,989.0		
	7	78,660	6,259.6		
7	**8**	77,880	6,197.5	**6,173**	836
	2	87,910	6,995.7		
	1	66,909	5,324.4		
28	**2**	110,520	8,794.9	**7,619**	841
	4	92,140	7,332.3		
	7	102,470	8,154.3		
	6	101,980	8,115.3		
	1	82,260	6,546.0		
	8	93,580	7,446.9		
	5	102,570	8,162.3		
	1	80,470	6,403.6		
91	**2**	124,810	9,932.1	**9,630**	696
	3	127,220	10,123.8		
	4	111,000	8,833.1		
243	**3**	140,600	11,188.6	**10,728**	450
	2	134,550	10,707.1		
	5	129,290	10,288.6		
438	**1**	109,990	8,752.7	**10,811**	956
	1	111,660	8,885.6		
	2	147,980	11,775.9		
	2	149,100	11,865.0		
	2	156,220	12,431.6		
	3	149,030	11,859.4		
	3	155,660	12,387.0		
	4	124,580	9,913.8		
	4	129,900	10,337.1		
	4	131,940	10,499.5		
	5	138,150	10,993.6		
	5	140,230	11,159.1		
	6	134,010	10,664.2		
	6	137,100	10,910.1		
	6	137,340	10,929.2		
	7	131,590	10,471.6		
	7	136,580	10,868.7		
	7	137,720	10,959.4		
	8	127,110	10,115.1		
	8	130,970	10,422.3		
	8	136,090	10,829.7		

- Compressive strength of pile's concrete (excluding batch #1*):

Age of Testing (days)	**Average** (psi)	**Std Dev** (psi)
4	**6,310**	349
7	**6,597**	564
28	**8,001**	538
91	**9,630**	696
243	**10,728**	450
438	**11,021**	727

- Additional compressive strength test results of batch #1 cylinders and compressive strength of cores obtained from durability specimens:

Age of Testing (days)	**Sample**	**Maximum Load** (lbs.)	**Diameter** (in)	**Length** (in)	**L/d**	**Compressive Strength** (psi)
42	Cores	41,820	2.73	6.01	2.2	7,145
		35,670	2.73	6.02	2.2	6,094
		40,090	2.73	5.90	2.2	6,849
42	Cylinders	85,850	4.00	8.00	2.0	6,832
		86,170	4.00	8.00	2.0	6,857
		87,560	4.00	8.00	2.0	6,968
624	Cores	74,480	2.73	5.51	2.0	12,724
		64,740	2.73	5.50	2.0	11,093
620	Cylinders	104,460	4.00	8.00	2.0	8,313
		115,600	4.00	8.00	2.0	9,199
		126,240	4.00	8.00	2.0	10,046

***Note:** Batch #1 was used for the material evaluation blocks and 27-ft. long piles used for development length tests.

- Elastic modulus and Poisson's ratio of concrete:

Age of Testing (days)	**Batch***	**Poisson's Ratio**	**Average ν**	**Std Dev ν**	**Modulus of Elasticity** (ksi)	**Average E_c** (ksi)	**Std Dev E_c** (ksi)
	7	0.19			6,428.4		
4	**6**	0.19	**0.19**	0.05	5,920.6	**6,138**	354
	7	0.21			6,065.8		
	3	0.20			6,655.3		
28	**6**	0.21	**0.20**	0.02	7,136.1	**6,683**	677
	8	0.20			6,256.9		
	3	0.21			6,831.8		
91	**5**	0.23	**0.22**	0.02	6,676.9	**6,892**	423
	8	0.24			7,235.1		
	7	0.18			7,428.8		
445	**8**	0.16	**0.17**	0.01	7,228.7	**7,138**	448
	5	0.17			6,733.7		

- Stress-strain curves (ASTM C469):

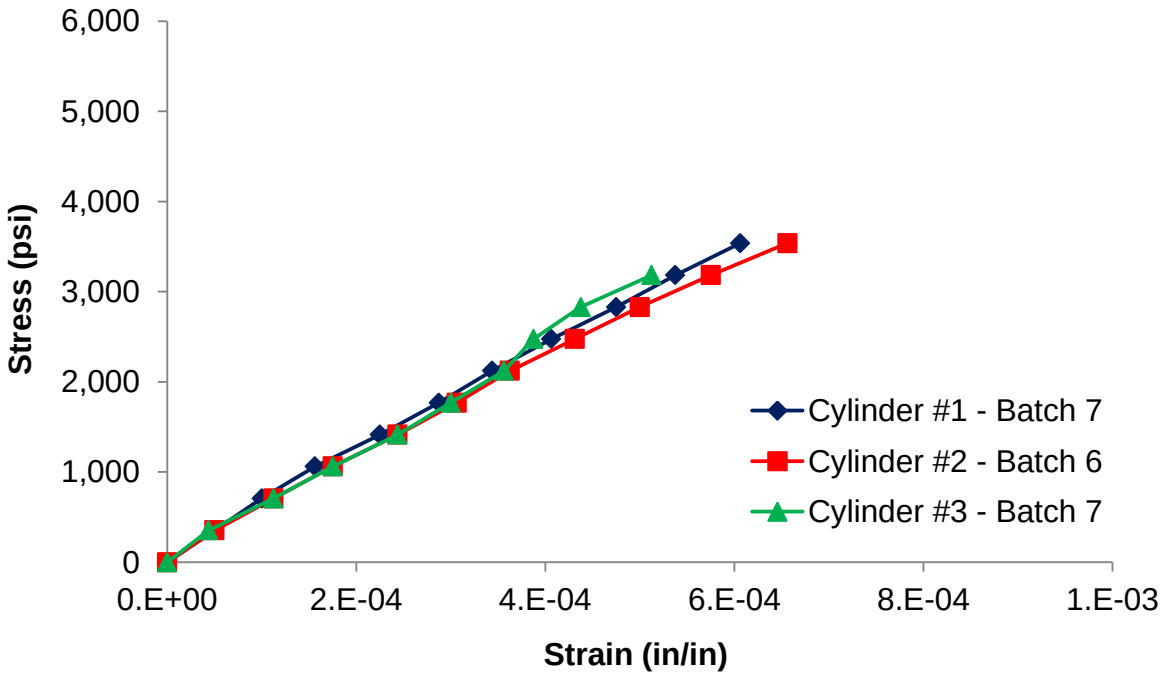

Figure J.1 Stress-strain curve of concrete at 4 days (ASTM C469).

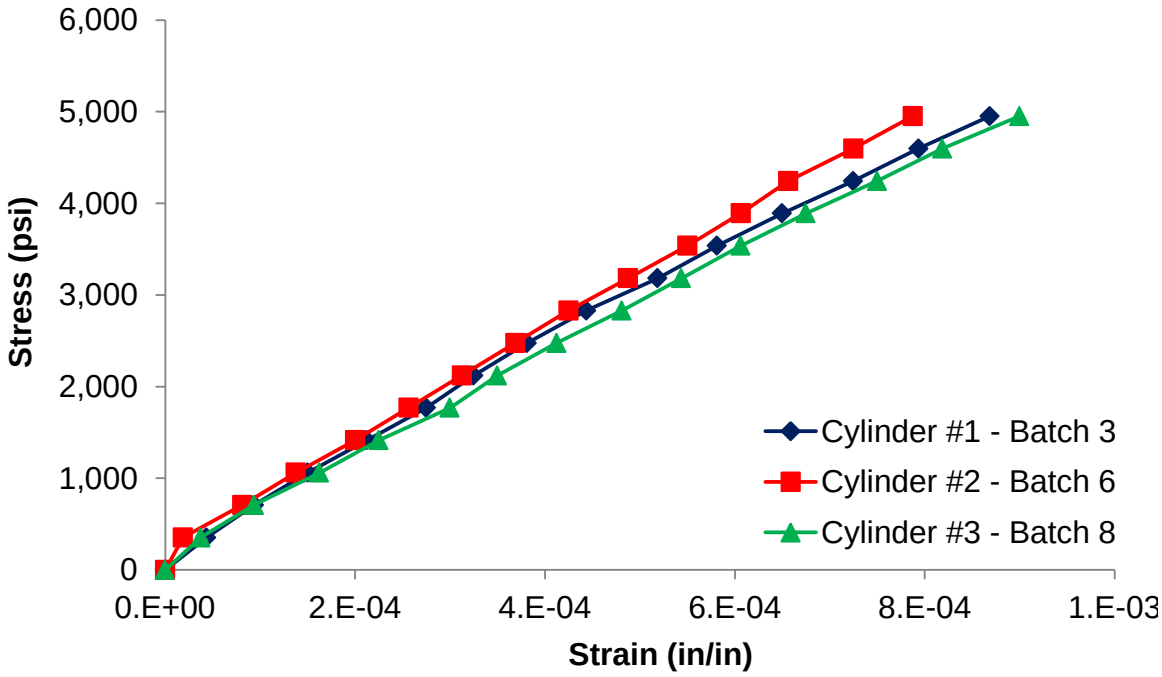

Figure J.2 Stress-strain curve of concrete at 28 days (ASTM C469).

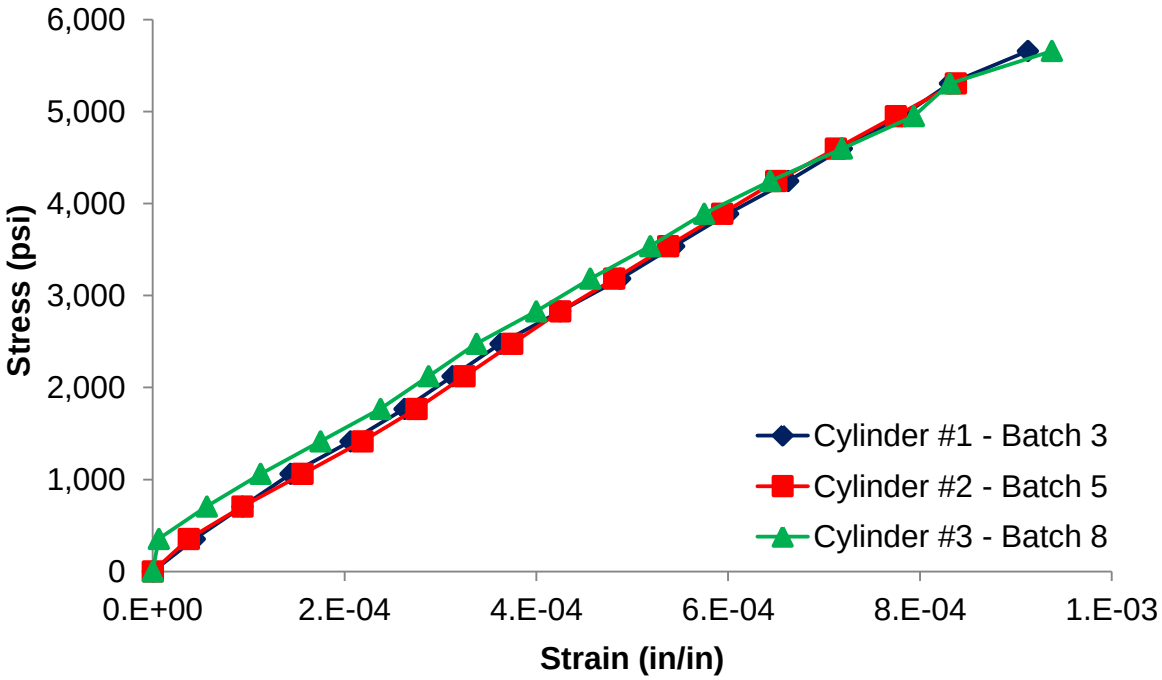

Figure J.3 Stress-strain curve of concrete at 91 days (ASTM C469).

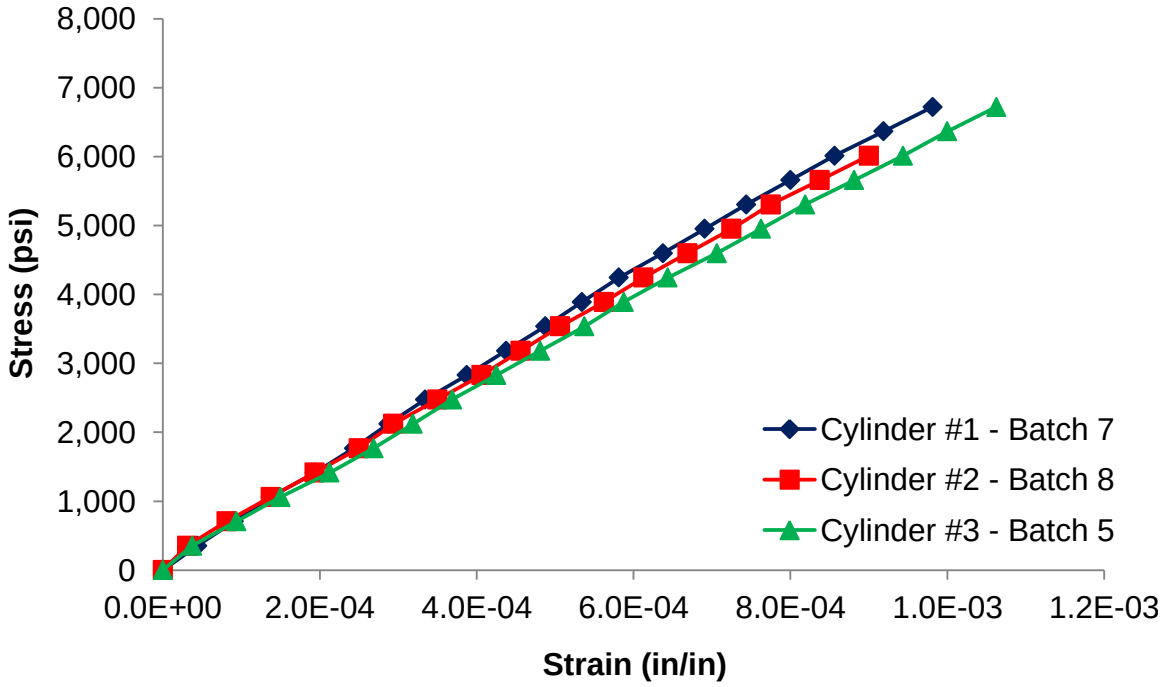

Figure J.4 Stress-strain curve of concrete at 445 days (ASTM C469).

APPENDIX K: Pile Driving Information

- Hammer specification provided by American Pile Driving Equipment, Inc. [https://www.apevibro.com/]:

APE Model D30-32 Diesel Hammer

PRINT (OPENS UP NEW WINDOW)

Batter Pile Energy Reduction Chart Batter Pile Angle Chart Bearing Chart: D30-32

Maximum rated energy	91,088 ft-lbs
Maximum obtainable stroke	165 inches
Pump setting 1: (minimum)	35,381 ft-lbs
Pump setting 2:	51,662 ft-lbs
Pump setting 3:	62,950 ft-lbs
Pump setting 4: (maximum)	69,458 ft-lbs
**Optional variable throttle gives infinte stroke control.	
Stroke at rated energy	126 inches
Energy at rated stroke	76,000 ft-lbs
Speed (blows per minute)	36-52
Ram	6,615 lbs
Avil	1,360 lbs
Hammer weight (includes trip device)	14,991 lbs
Typical operating (weight with drive cap)	17,076 lbs
Weight (D X 3.14/4 X 6 X .283=	675 lbs
Diameter	22.5 inches
Thickness (the 6 in above equation is thickness of plate)	6 inches
Type	Aluminum/Micarta
Diameter	22.5 inches
Thickness	2 inches
Elastic-Modulus	285 kips per square inch
Coeff. of Restitution	0.8
Weight (fits 8 by 26 leads)	1,166 lbs
Weight (fits 8 by 26 inch leads)	1,350 lbs
Square box inserts size 10 through 20 inch:	1,400 lbs
Pipe inserts for pipe size 12 to 24 diameter:	2,545 lbs

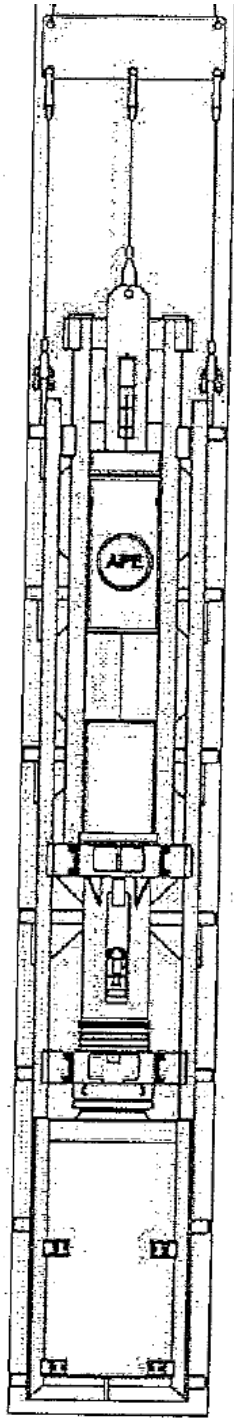

Fuel tank (runs on diesel or bio-diesel)	17.70 gal
Oil tank	2.4 gal
Diesel or Bio-diesel fuel	2.64 gal/hr
Lubrication oil	0.26 gal/hr
**Grease twice per day or after 45 minutes of continous driving	
Length overall	207.1 inches
Length over cylinder extension	246.4 inches
Impact block diameter	22.0 inches
Hammer width overall	28.3 inches
Minimum clearance for leads	19.7 inches
Note: if using 32 inch leads the drive cap will weigh:	1,550 lbs

Specifications may vary due to site conditions or hammer conditions or set up. Specifications may change without notice. Consult the factory for details on any specific hammer.

- APE diesel pile hammer bearing chart (based on GDOT formula) provided by The Industrial Company (TIC), Savannah, Georgia:

Ram Weight (#)													
6615													
Penetration for	Bearing in tons when H, in feet, equals												
10 blows	4.0	4.5	5.0	5.5	6.0	6.5	7.0	7.5	8.0	8.5	9.0	9.5	10.0
(in)													
0.5	106	119	132	146	159	172	185	198	212	225	238	251	265
0.625	101	113	126	139	151	164	176	189	202	214	227	239	252
0.75	96	108	120	132	144	156	168	180	192	204	216	229	241
0.875	92	104	115	127	138	150	161	173	184	196	207	219	230
1	88	99	110	121	132	143	154	165	176	187	198	209	221
1.125	85	95	106	116	127	138	148	159	169	180	191	201	212
1.25	81	92	102	112	122	132	142	153	163	173	183	193	204
1.375	78	88	98	108	118	127	137	147	157	167	176	186	196
1.5	76	85	95	104	113	123	132	142	151	161	170	180	189
1.625	73	82	91	100	109	119	128	137	146	155	164	173	182
1.75	71	79	88	97	106	115	123	132	141	150	159	168	176
1.875	68	77	85	94	102	111	119	128	137	145	154	162	171
2	66	74	83	91	99	107	116	124	132	141	149	157	165
2.125	64	72	80	88	96	104	112	120	128	136	144	152	160
2.25	62	70	78	86	93	101	109	117	125	132	140	148	156
2.375	60	68	76	83	91	98	106	113	121	129	136	144	151
2.5	59	66	74	81	88	96	103	110	118	125	132	140	147
2.625	57	64	72	79	86	93	100	107	114	122	129	136	143
2.75	56	63	70	77	84	91	97	104	111	118	125	132	139
2.875	54	61	68	75	81	88	95	102	109	115	122	129	136
3	53	60	66	73	79	86	93	99	106	112	119	126	132
3.125	52	58	65	71	77	84	90	97	103	110	116	123	129
3.25	50	57	63	69	76	82	88	95	101	107	113	120	126
3.375	49	55	62	68	74	80	86	92	98	105	111	117	123
3.5	48	54	60	66	72	78	84	90	96	102	108	114	120
3.625	47	53	59	65	71	76	82	88	94	100	106	112	118
3.75	46	52	58	63	69	75	81	86	92	98	104	109	115
3.875	45	51	56	62	68	73	79	84	90	96	101	107	113
4	44	50	55	61	66	72	77	83	88	94	99	105	110
4.125	43	49	54	59	65	70	76	81	86	92	97	103	108
4.25	42	48	53	58	64	69	74	79	85	90	95	101	106
4.375	42	47	52	57	62	67	73	78	83	88	93	99	104
4.5	41	46	51	56	61	66	71	76	81	87	92	97	102
4.625	40	45	50	55	60	65	70	75	80	85	90	95	100
4.75	39	44	49	54	59	64	69	74	78	83	88	93	98
4.875	38	43	48	53	58	63	67	72	77	82	87	91	96
5	38	43	47	52	57	61	66	71	76	80	85	90	95
5.125	37	42	46	51	56	60	65	70	74	79	84	88	93
5.25	36	41	46	50	55	59	64	68	73	78	82	87	91
5.375	36	40	45	49	54	58	63	67	72	76	81	85	90
5.5	35	40	44	49	53	57	62	66	71	75	79	84	88
5.625	35	39	43	48	52	56	61	65	69	74	78	82	87
5.75	34	38	43	47	51	55	60	64	68	73	77	81	85
5.875	34	38	42	46	50	55	59	63	67	71	76	80	84
6	33	37	41	45	50	54	58	62	66	70	74	79	83
6.125	33	37	41	45	49	53	57	61	65	69	73	77	81
6.25	32	36	40	44	48	52	56	60	64	68	72	76	80
6.375	32	36	39	43	47	51	55	59	63	67	71	75	79
6.5	31	35	39	43	47	51	54	58	62	66	70	74	78

Pile Bearing (TN) = 2WH / (S + 0.2) WH = Hammer Energy (ft-lbs) S = Pile Pentration per blow

- Pile driving log provided by The Industrial Company (TIC), Savannah, Georgia:

TIC PILE LOG

Hammer	D-30	Datum	Top of Template	Pile size	16"	Date	18-Dec-13
Fuel setting	#3	Elevation	~ +8 MHW	Type	PSC	By	WBJ
Cushion	6" plywood	⟷	Run of the pile	Pile length	70'		
		⟷	Weight of the hammer	Design Capacity	82 Tons		

Georgia Tech SS Test Pile Program

Pile 2 (cold hammer)			Pile 1 (PDA)			Pile S3 (PDA)			Pile S2			Pile S1		
Elev. (ft)	Depth (ft)	Blows	Elev. (ft)	Depth (ft)	Blows	Elev. (ft)	Depth (ft)	Blows	Elev. (ft)	Depth (ft)	Blows	Elev. (ft)	Depth (ft)	Blows
	1			1			1			1			1	
	2			2			2			2			2	
	3			3			3			3			3	
	4			4			4			4			4	
	5			5			5			5			5	
	6			6			6			6			6	
	7			7			7			7			7	
	8			8			8			8			8	
	9			9			9			9			9	
	10			10			10			10			10	
	11			11			11			11			11	
	12			12			12			12			12	
	13			13			13			13			13	
	14			14			14			14			14	
	15			15			15			15			15	
	16			16			16			16			16	
	17			17			17			17			17	
	18			18			18			18			18	
	19			19			19			19			19	
	20			20			20			20			20	
	21			21			21			21			21	
	22			22			22			22			22	
	23			23			23			23			23	
	24			24			24			24			24	
	25			25			25			25			25	
	26			26			26			26			26	
	27			27			27			27			27	
	28			28			28			28			28	
	29			29			29			29			29	
	30			30			30			30			30	
	31			31			31			31			31	
	32			32			32			32			32	
	33			33			33			33			33	
	34			34			34			34			34	
	35			35			35			35			35	
	36			36			36			36			36	
	37			37			37			37			37	
	38			38			38			38			38	
	39			39			39			39			39	
	40			40			40			40			40	
	41			41			41			41			41	
	42			42			42			42			42	
	43			43			43			43			43	
	44			44	8		44			44	3		44	
	45	1		45	22		45	8		45	7		45	
	46	3		46	32		46	18		46	17		46	8
	47	18		47	37		47	36		47	26		47	24
	48	27		48	36		48	46		48	28		48	26
	49	33		49	43		49	53		49	34		49	28
	50	35		50	44		50	50		50	40		50	33
	51	36		51	49		51	50		51	44		51	38
	52	41		52	53		52	52		52	54		52	41
	53	51		53	56		53	52		53	59		53	48
	54	51		54	56		54	56	-46	54	stop		54	50
	55	52	-47	55	stop	-47	55	stop		55			55	61
	56	63		56			56			56		-48	56	stop
-49	57	stop		57			57			57			57	
	58			58			58			58			58	
	59	1 1/4"-5.5'		59	1 3/4"-5.5'		59	1 1/2"-5.5'		59	1 1/2"-5.5'		59	1 1/2"-5.5'
	60	112T		60	97T		60	104T		60	104T		60	104T

Note: Top of the marl was indicated at ~ EL -50 with the jet stopping penetration during extraction

Piles 1 and 2 were construction with conventional 270 ksi 7/16 strand and 5-gauge spiral
Piles S1, S2 and S3 were constructed with 2205 stainless steel 250 ksi 1/2 in. strand and stainless steel 5-gauge spiral

APPENDIX L: Calculation of Ultimate Curvature by Moment-Area Method

The dial gauges, used for strain measurements during the flexure test, were removed before failure of the piles. However, the applied load and deflection at the mid-length were recorded during the complete duration of the test. Based on the ultimate load and deflection, the moment-area method was used for the estimation of the ultimate curvature.

Figure L.1 shows the applied symmetric curvature diagram, from a roller support to the mid-length of the pile. The length of the plastic hinge was assumed equal to the depth of the pile, 16-in. (40.6 cm), and Equation L.1 was used for the estimation of the ultimate curvature.

$$\Delta_u = \sum_{i=1}^{6} \left(A_i \times \bar{x}_i \right) \tag{L.1}$$

where A_i is the area of the region of the curvature diagram shown in Figure F.1, and $\bar{x}_i$ is the distance from the centroid of A_i to the roller support.

The ultimate moment was determined using the recorded ultimate load, while the moments and curvatures at cracking and yield points were obtained from calculated values using the actual position of strands and compressive strength of concrete of the piles. Cracking and yield moments were used to calculate the position of φ_{cr} and φ_y in the curvature diagram where φ is the curvature at the maximum moment section in radians/inch.

Given that the ultimate deflection was known from the flexure test data, Equation L.1 was solved for φ_u. The values of φ_u per each pile can be observed in Table L.1.

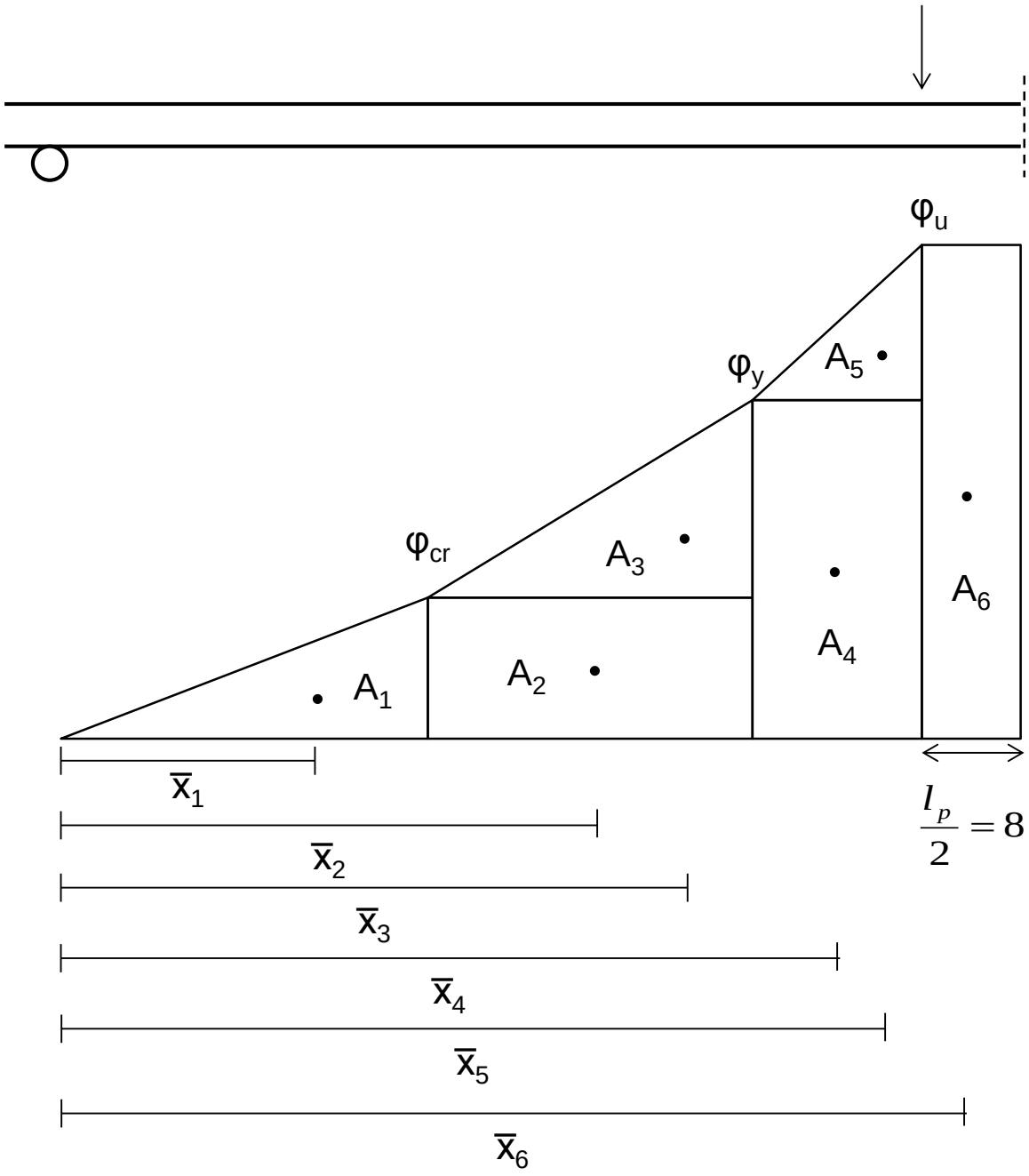

Figure L.1 Curvature diagram for ultimate curvature calculation where l_p is the plastic hinge length assumed as the distance between load points.

Table L.1 Ultimate curvature calculated by moment-area method. 1 rad/in = 39.37 rad/m.

	Ultimate curvature (rad/in)
Pile 1080 #1 - Top Half	1.073×10^{-3}
Pile 1080 #2 - Bottom Half	1.013×10^{-3}
Pile HSSS 2205 #1 - Top Half	9.071×10^{-4}

For piles 1080 #1 (bottom half), HSSS 2205 #2 (top half), HSSS 2205 #2 (bottom half), and HSSS 2205 #3 (top half) the calculated ultimate curvature was lower than the one obtained from test measurements. This can be attributed to a removal of the dial strain gauges close to the failure point in the case of pile 1080 #1 (bottom half), and to a brittle behavior that did not develop the assumed curvature diagram in Figure L.1, in the case of piles using duplex HSSS 2205 strands.

For piles 1080 #2 (top half), HSSS 2205 #1 (bottom half), and HSSS 2205 #3 (bottom half), the strain measurements were inappropriate for curvature calculations, due to failure of the dials during the test or mistakes in readings. Thus, the moment-curvature diagrams were not able to be calculated for these piles.

APPENDIX M: Calculation of Flexural Capacity of Piles

M.1 ACI 318 Moment-Curvature Calculation for Pile SS #2 – Top Half.

Pile Properties:

$L := 35ft \qquad \gamma := 150pcf \qquad \phi := 1.0$

$f'_c := 10686psi \qquad f'_{ci} := 4100psi$

$$\beta_1 := \begin{cases} 0.85 \text{ if } 2500psi \le f'_c \le 4000psi \\ 0.65 \text{ if } f'_c \ge 8000psi \\ 1.05 - 0.05 \cdot \frac{f'_c}{1000psi} \text{ otherwise} \end{cases} = 0.65$$

$E_i := 57000 \cdot \sqrt{f'_{ci} \cdot psi} = 3649.781 \cdot ksi$

$E := 57000 \cdot \sqrt{f'_c \cdot psi} \qquad E = 5892.267 \cdot ksi$

$f_r := 7.5 \cdot \sqrt{f'_c \cdot psi} = 0.775 \cdot ksi$

$b := 16.063in \qquad h := 16.125in \qquad A := b \cdot h = 259.016 \cdot in^2 \qquad I := \frac{1}{12} \cdot b \cdot h^3 = 5612.348 \cdot in^4$

$y_t := \frac{h}{2} = 8.063 \cdot in \qquad y_b := -y_t \qquad k_t := \frac{I}{A \cdot y_b} = -2.687 \cdot in \qquad k_b := \frac{-I}{A \cdot y_t} = -2.687 \cdot in$

Stainless Steel 2205 Strand Properties:

$A_{strand} := 0.153in^2 \qquad f_{pu} := 241.5ksi \qquad \varepsilon_{us} := 0.016 \qquad d_b := \frac{1}{2}in = 0.5 \cdot in \qquad E_{ps} := 23500ksi$

$f_{py} := 228.7ksi \qquad \varepsilon_{ys} := 0.012 \qquad cover := 3.5in + \frac{d_b}{2} = 3.75 \cdot in \qquad P_{strand} := 22.5kip$

$f_{si} := \frac{P_{strand}}{A_{strand}} = 147.059 \cdot ksi \qquad e_{mid} := \frac{h - 2 \cdot cover}{6} = 1.438 \cdot in \qquad n := 12$

$$num := \begin{pmatrix} 4 \\ 2 \\ 2 \\ 4 \end{pmatrix} \qquad e_p := \begin{pmatrix} \frac{h}{2} - cover \\ e_{mid} \\ -e_{mid} \\ cover - \frac{h}{2} \end{pmatrix} = \begin{pmatrix} 4.313 \\ 1.438 \\ -1.438 \\ -4.313 \end{pmatrix} \cdot in \qquad d_p := \begin{pmatrix} 4.188 \\ 7.125 \\ 10.125 \\ 12.875 \end{pmatrix} in$$

$P_i := f_{si} \cdot num \cdot A_{strand} \qquad P_{tot} := \sum P_i = 270 \cdot kip \qquad \frac{f_{si}}{f_{pu}} = 60.894 \cdot \%$

Calculated Prestress Losses (AASHTO): from mathcad spreadsheet.

$Losses := -22.686ksi \qquad \Delta f_{ps} := Losses = -22.686 \cdot ksi \qquad f_{se} := f_{si} + \Delta f_{ps} = 124.373 \cdot ksi$

$\varepsilon_{calc} := \frac{\Delta f_{ps}}{E_{ps}} = -965.362 \cdot 10^{-6} \qquad F_i := f_{se} \cdot num \cdot A_{strand} \qquad F_{se} := \sum F_i = 228.349 \cdot kip$

Cracking condition:

$$M_{cr} := -\left(\frac{F_{se}}{A} + f_r\right)\cdot\frac{I}{y_b} \qquad f_b := f_r \qquad f_t := \frac{-M_{cr}\cdot y_t}{I} = -1.657\cdot ksi$$

$$\varepsilon_b := \frac{f_b}{E} = 1.316\times 10^{-4} \qquad \varepsilon_t := \frac{f_t}{E} = -2.812\times 10^{-4} \qquad \phi_{cr} := \frac{\varepsilon_b - \varepsilon_t}{h}$$

$$M_{cr} = 1153.376\cdot kip\cdot in \qquad \phi_{cr} = 2.56\times 10^{-5}\cdot\frac{rad}{in}$$

Yield condition:

$$\varepsilon_{tf} := 0.00241 \qquad \varepsilon_0 := 1.71\cdot\frac{f'_c}{E} = 0.003$$

$$\beta_{1y} := \frac{\ln\left[1 + \left(\frac{\varepsilon_{tf}}{\varepsilon_0}\right)^2\right]}{\frac{\varepsilon_{tf}}{\varepsilon_0}} = 0.608 \qquad k_2 := 1 - 2\cdot\frac{\left(\frac{\varepsilon_{tf}}{\varepsilon_0} - \operatorname{atan}\left(\frac{\varepsilon_{tf}}{\varepsilon_0}\right)\right)}{\left(\frac{\varepsilon_{tf}}{\varepsilon_0}\right)^2\cdot\beta_{1y}} = 0.365$$

$$\varepsilon_{se} := \frac{f_{se}}{E_{ps}} = 0.005292 \qquad f_{cgs} := \frac{-F_{se}}{A} = -0.882\cdot ksi \qquad \varepsilon_{ce} := \frac{f_{cgs}}{E} = -0.0001496$$

$c := 3.313in$ Manually adjust so T=C $\qquad C := \beta_{1y}\cdot f'_c\cdot c\cdot b = 345.724\cdot kip$

$$\varepsilon_c := \frac{\varepsilon_{tf}}{c}\cdot(d_p - c) = \begin{pmatrix}0.00064\\0.00277\\0.00496\\0.00696\end{pmatrix} \qquad \varepsilon_s := \varepsilon_c + \varepsilon_{se} + \varepsilon_{ce} = \begin{pmatrix}0.0058\\0.0079\\0.0101\\0.0121\end{pmatrix}$$

Note: Strand yields at 0.012 and ruptures at 0.016

$$f_s := \begin{pmatrix}137.014ksi\\181.356ksi\\214.660ksi\\229.896ksi\end{pmatrix}$$

Data from stress-strain test

$$i := 0..3 \qquad P_i := f_{s_i}\cdot num_i\cdot A_{strand} \qquad P = \begin{pmatrix}83.853\\55.495\\65.686\\140.696\end{pmatrix}\cdot kip$$

$T := f_s\cdot num\cdot A_{strand} = 345.73\cdot kip \qquad C = 345.72\cdot kip \qquad M_y := -C\cdot k_2\cdot c + P\cdot d_p$

$$f_t := \frac{-M_y\cdot y_t}{I} = -4.029\cdot ksi \qquad \varepsilon_t := \frac{f_t}{E} = -6.838\times 10^{-4} \qquad \varepsilon_b := \varepsilon_{s_3} = 0.0121$$

$$\phi_y := \frac{\varepsilon_b - \varepsilon_t}{h} \qquad M_y = 2804.53\cdot kip\cdot in \qquad \phi_y = 7.927\times 10^{-4}\cdot\frac{rad}{in}$$

Ultimate capacity:

$f''_c := 0.9 \cdot f_c = 9.617 \cdot ksi$ $\varepsilon_u := 0.003$

$$\beta_1 := \frac{\ln\left[1 + \left(\frac{\varepsilon_u}{\varepsilon_0}\right)^2\right]}{\frac{\varepsilon_u}{\varepsilon_0}} = 0.683 \qquad k_2 := 1 - 2 \cdot \frac{\left(\frac{\varepsilon_u}{\varepsilon_0} - \operatorname{atan}\left(\frac{\varepsilon_u}{\varepsilon_0}\right)\right)}{\left(\frac{\varepsilon_u}{\varepsilon_0}\right)^2 \cdot \beta_1} = 0.347$$

$\varepsilon_{se} := \frac{f_{se}}{E_{ps}} = 0.005292$ $f_{cgs} := \frac{-F_{se}}{A} = -0.882 \cdot ksi$ $\varepsilon_{ce} := \frac{f_{cgs}}{E} = -0.0001496$

$c := 3.381in$ Manually adjust so T=C $C := \beta_1 \cdot f''_c \cdot c \cdot b = 356.636 \cdot kip$

$$\varepsilon_c := \frac{\varepsilon_u}{c} \cdot (d_p - c) = \begin{pmatrix} 0.00072 \\ 0.00332 \\ 0.00598 \\ 0.00842 \end{pmatrix} \qquad \varepsilon_s := \varepsilon_c + \varepsilon_{se} + \varepsilon_{ce} = \begin{pmatrix} 0.0059 \\ 0.0085 \\ 0.0111 \\ 0.0136 \end{pmatrix}$$

Note:
Strand yields at 0.012
and ruptures at 0.016

$$f_s := \begin{pmatrix} 139.155ksi \\ 191.415ksi \\ 223.511ksi \\ 236.097ksi \end{pmatrix}$$

Data from
stress-strain test

$i := 0..3$

$P_i := f_{s_i} \cdot num_i \cdot A_{strand} \qquad P = \begin{pmatrix} 85.163 \\ 58.573 \\ 68.394 \\ 144.491 \end{pmatrix} \cdot kip$

$T := f_s \cdot num \cdot A_{strand} = 356.622 \cdot kip$ $C = 356.636 \cdot kip$

$M_u := -C \cdot k_2 \cdot c + P \cdot d_p$ $\phi_u := \frac{\varepsilon_u}{c}$ $M_u = 2908.23 \cdot kip \cdot in$ $\phi_u = 8.873 \times 10^{-4} \cdot \frac{rad}{in}$

M.2 ACI 318 Moment-Curvature Calculation for Pile 1080 #1 – Bottom Half.

Pile Properties:

$L := 35ft \qquad \gamma := 150pcf \qquad \phi := 1.0$

$f'_c := 12064psi \qquad f'_{ci} := 4100psi$

$$\beta_1 := \begin{cases} 0.85 & \text{if } 2500psi \le f'_c \le 4000psi \\ 0.65 & \text{if } f'_c \ge 8000psi \\ 1.05 - 0.05 \cdot \dfrac{f'_c}{1000psi} & \text{otherwise} \end{cases} = 0.65$$

$E_i := 57000 \cdot \sqrt{f'_{ci} \cdot psi} = 3649.781 \cdot ksi$

$E := 57000 \cdot \sqrt{f'_c \cdot psi} \qquad E = 6260.666 \cdot ksi$

$f_r := 7.5 \cdot \sqrt{f'_c \cdot psi} = 0.824 \cdot ksi$

$b := 16.063in \qquad h := 16.125in \qquad A := b \cdot h = 259.016 \cdot in^2 \qquad I := \frac{1}{12} \cdot b \cdot h^3 = 5612.348 \cdot in^4$

$y_t := \frac{h}{2} = 8.063 \cdot in \qquad y_b := -y_t \qquad k_t := \frac{I}{A \cdot y_b} = -2.687 \cdot in \qquad k_b := \frac{-I}{A \cdot y_t} = -2.687 \cdot in$

High Strength Steel AISI 1080 Strand Properties:

$A_{strand} := 0.1155in^2 \qquad f_{pu} := 281.1ksi \qquad \varepsilon_{us} := 0.0547 \qquad d_b := \frac{7}{16}in = 0.438 \cdot in \qquad E_{ps} := 29400ksi$

$f_{py} := 265.47ksi \qquad \varepsilon_{ys} := 0.01 \qquad cover := 3.5in + \frac{d_b}{2} = 3.719 \cdot in \qquad P_{strand} := 22.5kip$

$f_{si} := \frac{P_{strand}}{A_{strand}} = 194.805 \cdot ksi \qquad e_{mid} := \frac{h - 2 \cdot cover}{6} = 1.448 \cdot in \qquad n := 12$

$$num := \begin{pmatrix} 4 \\ 2 \\ 2 \\ 4 \end{pmatrix} \qquad e_p := \begin{pmatrix} \frac{h}{2} - cover \\ e_{mid} \\ -e_{mid} \\ cover - \frac{h}{2} \end{pmatrix} = \begin{pmatrix} 4.344 \\ 1.448 \\ -1.448 \\ -4.344 \end{pmatrix} \cdot in \qquad d_p := \begin{pmatrix} 3.5 \\ 6.375 \\ 9.313 \\ 12.188 \end{pmatrix} in$$

$P_i := f_{si} \cdot num \cdot A_{strand} \qquad P_{tot} := \sum P_i = 270 \cdot kip \qquad \frac{f_{si}}{f_{pu}} = 69.301 \cdot \%$

Calculated Prestress Losses (AASHTO): from mathcad spreadsheet.

$Losses := -24.42ksi \qquad \Delta f_{ps} := Losses = -24.42 \cdot ksi \qquad f_{se} := f_{si} + \Delta f_{ps} = 170.385 \cdot ksi$

$\varepsilon_{calc} := \frac{\Delta f_{ps}}{E_{ps}} = -830.612 \cdot 10^{-6} \qquad F_i := f_{se} \cdot num \cdot A_{strand} \qquad F_{se} := \sum F_i = 236.154 \cdot kip$

Cracking condition:

$$M_{cr} := -\left(\frac{F_{se}}{A} + f_r\right)\cdot\frac{I}{y_b} \qquad f_b := f_r \qquad f_t := \frac{-M_{cr}\cdot y_t}{I} = -1.736\cdot ksi$$

$$\varepsilon_b := \frac{f_b}{E} = 1.316\times 10^{-4} \qquad \varepsilon_t := \frac{f_t}{E} = -2.772\times 10^{-4} \qquad \phi_{cr} := \frac{\varepsilon_b - \varepsilon_t}{h}$$

$M_{cr} = 1208.095\cdot kip\cdot in$ $\qquad \phi_{cr} = 2.535\times 10^{-5}\cdot\frac{rad}{in}$

Yield condition:

$$\varepsilon_{tf} := 0.00177 \qquad \varepsilon_0 := 1.71\cdot\frac{f'_c}{E} = 0.003$$

$$\beta_{1y} := \frac{\ln\left[1 + \left(\frac{\varepsilon_{tf}}{\varepsilon_0}\right)^2\right]}{\frac{\varepsilon_{tf}}{\varepsilon_0}} = 0.472 \qquad k_2 := 1 - 2\cdot\frac{\left(\frac{\varepsilon_{tf}}{\varepsilon_0} - \operatorname{atan}\left(\frac{\varepsilon_{tf}}{\varepsilon_0}\right)\right)}{\left(\frac{\varepsilon_{tf}}{\varepsilon_0}\right)^2\cdot\beta_{1y}} = 0.35$$

$$\varepsilon_{se} := \frac{f_{se}}{E_{ps}} = 0.005795 \qquad f_{cgs} := \frac{-F_{se}}{A} = -0.912\cdot ksi \qquad \varepsilon_{ce} := \frac{f_{cgs}}{E} = -0.0001456$$

$c := 3.359in$ Manually adjust so T=C $\qquad C := \beta_{1y}\cdot f'_c\cdot c\cdot b = 307.201\cdot kip$

$$\varepsilon_c := \frac{\varepsilon_{tf}}{c}\cdot(d_p - c) = \begin{pmatrix}0.00007\\0.00159\\0.00314\\0.00465\end{pmatrix} \qquad \varepsilon_s := \varepsilon_c + \varepsilon_{se} + \varepsilon_{ce} = \begin{pmatrix}0.0057\\0.0072\\0.0088\\0.0103\end{pmatrix}$$

Note:
Strand yields at 0.010
and ruptures at 0.0547

$$f_s := \begin{pmatrix}166.304ksi\\209.348ksi\\251.726ksi\\268.009ksi\end{pmatrix}$$

Data from stress-strain test

$i := 0..3$

$$P_i := f_{s_i}\cdot num_i\cdot A_{strand} \qquad P = \begin{pmatrix}76.832\\48.359\\58.149\\123.82\end{pmatrix}\cdot kip$$

$T := f_s\cdot num\cdot A_{strand} = 307.16\cdot kip$ $\qquad C = 307.2\cdot kip$ $\qquad M_y := -C\cdot k_2\cdot c + P\cdot d_p$

$$f_t := \frac{-M_y\cdot y_t}{I} = -3.256\cdot ksi \qquad \varepsilon_t := \frac{f_t}{E} = -5.2\times 10^{-4} \qquad \varepsilon_b := \varepsilon_{s_3} = 0.0103$$

$$\phi_y := \frac{\varepsilon_b - \varepsilon_t}{h}$$

$M_y = 2266.26\cdot kip\cdot in$ $\qquad \phi_y = 6.711\times 10^{-4}\cdot\frac{rad}{in}$

Ultimate capacity:

$f'_c := 0.9 \cdot f_c = 10.858 \cdot ksi$ $\varepsilon_u := 0.003$

$$\beta_{1u} := \frac{\ln\left[1 + \left(\frac{\varepsilon_u}{\varepsilon_0}\right)^2\right]}{\frac{\varepsilon_u}{\varepsilon_0}} = 0.663 \qquad k_2 := 1 - 2 \cdot \frac{\left(\frac{\varepsilon_u}{\varepsilon_0} - \operatorname{atan}\left(\frac{\varepsilon_u}{\varepsilon_0}\right)\right)}{\left(\frac{\varepsilon_u}{\varepsilon_0}\right)^2 \cdot \beta_{1u}} = 0.375$$

$\varepsilon_{se} := \frac{f_{se}}{E_{ps}} = 0.005795$ $f_{cgs} := \frac{-F_{se}}{A} = -0.912 \cdot ksi$ $\varepsilon_{ce} := \frac{f_{cgs}}{E} = -0.0001456$

$c := 2.876in$ Manually adjust so T=C $C := \beta_{1u} \cdot f'_c \cdot c \cdot b = 332.607 \cdot kip$

$$\varepsilon_c := \frac{\varepsilon_u}{c} \cdot (d_p - c) = \begin{pmatrix} 0.00065 \\ 0.00365 \\ 0.00671 \\ 0.00971 \end{pmatrix} \qquad \varepsilon_s := \varepsilon_c + \varepsilon_{se} + \varepsilon_{ce} = \begin{pmatrix} 0.0063 \\ 0.0093 \\ 0.0124 \\ 0.0154 \end{pmatrix}$$

Note:
Strand yields at 0.010
and ruptures at 0.0547

$$f_s := \begin{pmatrix} 181.957ksi \\ 260.217ksi \\ 271.957ksi \\ 271.957ksi \end{pmatrix}$$

Data from
stress-strain test

$i := 0..3$

$P_i := f_{s_i} \cdot num_i \cdot A_{strand}$ $P = \begin{pmatrix} 84.064 \\ 60.11 \\ 62.822 \\ 125.644 \end{pmatrix} \cdot kip$

$T := f_s \cdot num \cdot A_{strand} = 332.64 \cdot kip$ $C = 332.61 \cdot kip$

$M_u := -C \cdot k_2 \cdot c + P \cdot d_p$ $\phi_u := \frac{\varepsilon_u}{c}$ $M_u = 2435.55 \cdot kip \cdot in$ $\phi_u = 1.043 \times 10^{-3} \cdot \frac{rad}{in}$

M.3 AASHTO Moment-Curvature Calculation for Pile SS #2 – Top Half.

Pile Properties:

$L := 35ft$ $\phi := 1.0$

$f'_c := 10686psi$ $f'_{ci} := 4100psi$

$\beta_1 := \begin{cases} 0.85 \text{ if } 2500psi \le f'_c \le 4000psi \\ 0.65 \text{ if } f'_c \ge 8000psi \\ 1.05 - 0.05 \cdot \frac{f'_c}{1000psi} \text{ otherwise} \end{cases} = 0.65$

$E_i := 33000 \cdot (0.147)^{1.5} \cdot \sqrt{f'_{ci} \cdot ksi} = 3766 \cdot ksi$

$E := 33000 \cdot (0.147)^{1.5} \cdot \sqrt{f'_c \cdot ksi} = 6080 \cdot ksi$

$f_r := 0.24 \cdot \sqrt{f'_c \cdot ksi} = 0.785 \cdot ksi$

$b := 16.063in$ $h := 16.125in$ $A := b \cdot h = 259.016 \cdot in^2$ $I := \frac{1}{12} \cdot b \cdot h^3 = 5612.348 \cdot in^4$

$y_t := \frac{h}{2} = 8.063 \cdot in$ $y_b := -y_t$ $k_t := \frac{I}{A \cdot y_b} = -2.687 \cdot in$ $k_b := \frac{-I}{A \cdot y_t} = -2.687 \cdot in$

Stainless Steel 2205 Strand Properties:

$A_{strand} := 0.153in^2$ $f_{pu} := 241.5ksi$ $\varepsilon_{us} := 0.016$ $d_b := \frac{1}{2}in = 0.5 \cdot in$ $E_{ps} := 23500ksi$

$f_{py} := 228.7ksi$ $\varepsilon_{ys} := 0.012$ $cover := 3.5in + \frac{d_b}{2} = 3.75 \cdot in$ $P_{strand} := 22.5kip$

$f_{si} := \frac{P_{strand}}{A_{strand}} = 147.059 \cdot ksi$ $e_{mid} := \frac{h - 2 \cdot cover}{6} = 1.438 \cdot in$ $n := 12$

$num := \begin{pmatrix} 4 \\ 2 \\ 2 \\ 4 \end{pmatrix}$ $e_p := \begin{pmatrix} \frac{h}{2} - cover \\ e_{mid} \\ -e_{mid} \\ cover - \frac{h}{2} \end{pmatrix} = \begin{pmatrix} 4.313 \\ 1.438 \\ -1.438 \\ -4.313 \end{pmatrix} \cdot in$ $d_p := \begin{pmatrix} 4.188 \\ 7.125 \\ 10.125 \\ 12.875 \end{pmatrix} in$

$P_i := f_{si} \cdot num \cdot A_{strand}$ $P_{tot} := \sum P_i = 270 \cdot kip$ $\frac{f_{si}}{f_{pu}} = 60.894 \cdot \%$

Calculated Prestress Losses (AASHTO): from mathcad spreadsheet.

$Losses := -22.686ksi$ $\Delta f_{ps} := Losses = -22.686 \cdot ksi$ $f_{se} := f_{si} + \Delta f_{ps} = 124.373 \cdot ksi$

$\varepsilon_{calc} := \frac{\Delta f_{ps}}{E_{ps}} = -965.362 \cdot 10^{-6}$ $F_i := f_{se} \cdot num \cdot A_{strand}$ $F_{se} := \sum F_i = 228.349 \cdot kip$

Cracking condition:

$\gamma_1 := 1.6 \qquad \gamma_2 := 1.1 \qquad \gamma_3 := 1.0 \qquad S_c := \frac{b \cdot h^2}{6}$

$M_{cr} := \gamma_3 \cdot \left[\left(\gamma_1 \cdot f_r + \gamma_2 \cdot \frac{F_{se}}{A} \right) \cdot S_c \right]$

$f_b := f_r \qquad f_t := \frac{-M_{cr} \cdot y_t}{I} = -2.225 \cdot ksi$

$\varepsilon_b := \frac{f_b}{E} = 1.29 \times 10^{-4} \qquad \varepsilon_t := \frac{f_t}{E} = -3.66 \times 10^{-4} \qquad \phi_{cr} := \frac{\varepsilon_b - \varepsilon_t}{h}$

$M_{cr} = 1548.859 \cdot kip \cdot in \qquad \phi_{cr} = 3.07 \times 10^{-5} \cdot \frac{rad}{in}$

Ultimate capacity:

$\varepsilon_u := 0.003 \qquad k := 2 \cdot \left(1.04 - \frac{f_{py}}{f_{pu}} \right) \qquad A_{ps} := n \cdot A_{strand} \qquad d := \frac{h}{2}$

$c := \frac{A_{ps} \cdot f_{pu}}{0.85 \cdot \left(f'_c \cdot \beta_1 \cdot b + k \cdot A_{ps} \cdot \frac{f_{pu}}{d} \right)} = 4.283 \cdot in \qquad a := \beta_1 \cdot c$

$f_{ps} := f_{pu} \cdot \left(1 - k \cdot \frac{c}{d_p} \right) = \begin{pmatrix} 195.564 \\ 214.499 \\ 222.5 \\ 226.558 \end{pmatrix} \cdot ksi$

$M_u := \sum_{i=0}^{3} \left(f_{ps_i} \cdot num_i \cdot A_{strand} \right) \cdot \left(d - \frac{a}{2} \right) \qquad \phi_u := \frac{\varepsilon_u}{c}$

$M_u = 2615.284 \cdot kip \cdot in \qquad \phi_u = 7.005 \times 10^{-4} \cdot \frac{rad}{in}$

M.4 AASHTO Moment-Curvature Calculation for Pile 1080 #1 – Bottom Half.

Pile Properties:

$L := 35ft$ $\phi := 1.0$

$f_c := 12064psi$ $f_{ci} := 4100psi$

$\beta_1 := \begin{cases} 0.85 \text{ if } 2500psi \le f_c \le 4000psi = 0.65 \\ 0.65 \text{ if } f_c \ge 8000psi \\ 1.05 - 0.05 \cdot \frac{f_c}{1000psi} \text{ otherwise} \end{cases}$

$E_i := 33000 \cdot (0.147)^{1.5} \cdot \sqrt{f_{ci} \cdot ksi} = 3766 \cdot ksi$

$E := 33000 \cdot (0.147)^{1.5} \cdot \sqrt{f_c \cdot ksi} = 6460 \cdot ksi$

$f_r := 0.24 \cdot \sqrt{f_c \cdot ksi} = 0.834 \cdot ksi$

$b := 16.063in$ $h := 16.125in$ $A := b \cdot h = 259.016 \cdot in^2$ $I := \frac{1}{12} \cdot b \cdot h^3 = 5612.348 \cdot in^4$

$y_t := \frac{h}{2} = 8.063 \cdot in$ $y_b := -y_t$ $k_t := \frac{I}{A \cdot y_b} = -2.687 \cdot in$ $k_b := \frac{-I}{A \cdot y_t} = -2.687 \cdot in$

High Strength Steel AISI 1080 Strand Properties:

$A_{strand} := 0.1155in^2$ $f_{pu} := 281.1ksi$ $\varepsilon_{us} := 0.0547$ $d_b := \frac{7}{16}in = 0.438 \cdot in$ $E_{ps} := 29400ksi$

$f_{py} := 265.47ksi$ $\varepsilon_{ys} := 0.01$ $cover := 3.5in + \frac{d_b}{2} = 3.719 \cdot in$ $P_{strand} := 22.5kip$

$f_{si} := \frac{P_{strand}}{A_{strand}} = 194.805 \cdot ksi$ $e_{mid} := \frac{h - 2 \cdot cover}{6} = 1.448 \cdot in$ $n := 12$

$num := \begin{pmatrix} 4 \\ 2 \\ 2 \\ 4 \end{pmatrix}$ $e_p := \begin{pmatrix} \frac{h}{2} - cover \\ e_{mid} \\ -e_{mid} \\ cover - \frac{h}{2} \end{pmatrix} = \begin{pmatrix} 4.344 \\ 1.448 \\ -1.448 \\ -4.344 \end{pmatrix} \cdot in$ $d_p := \begin{pmatrix} 3.5 \\ 6.375 \\ 9.313 \\ 12.188 \end{pmatrix} in$

$P_i := f_{si} \cdot num \cdot A_{strand}$ $P_{tot} := \sum P_i = 270 \cdot kip$ $\frac{f_{si}}{f_{pu}} = 69.301 \cdot \%$

Calculated Prestress Losses (AASHTO): from mathcad spreadsheet.

$Losses := -24.42ksi$ $\Delta f_{ps} := Losses = -24.42 \cdot ksi$ $f_{se} := f_{si} + \Delta f_{ps} = 170.385 \cdot ksi$

$\varepsilon_{calc} := \frac{\Delta f_{ps}}{E_{ps}} = -830.612 \cdot 10^{-6}$ $F_i := f_{se} \cdot num \cdot A_{strand}$ $F_{se} := \sum F_i = 236.154 \cdot kip$

Cracking condition:

$\gamma_1 := 1.6 \qquad \gamma_2 := 1.1 \qquad \gamma_3 := 1.0 \qquad S_c := \frac{b \cdot h^2}{6}$

$M_{cr} := \gamma_3 \cdot \left[\left(\gamma_1 \cdot f_r + \gamma_2 \cdot \frac{F_{se}}{A} \right) \cdot S_c \right]$

$f_b := f_r \qquad f_t := \frac{-M_{cr} \cdot y_t}{I} = -2.337 \cdot ksi$

$\varepsilon_b := \frac{f_b}{E} = 1.29 \times 10^{-4} \qquad \varepsilon_t := \frac{f_t}{E} = -3.617 \times 10^{-4} \qquad \phi_{cr} := \frac{\varepsilon_b - \varepsilon_t}{h}$

$M_{cr} = 1626.565 \cdot kip \cdot in \qquad \phi_{cr} = 3.043 \times 10^{-5} \cdot \frac{rad}{in}$

Ultimate capacity:

$\varepsilon_u := 0.003 \qquad k := 2 \cdot \left(1.04 - \frac{f_{py}}{f_{pu}} \right) \qquad A_{ps} := n \cdot A_{strand} \qquad d := \frac{h}{2}$

$c := \frac{A_{ps} \cdot f_{pu}}{0.85 \cdot \left(f'_c \cdot \beta_1 \cdot b + k \cdot A_{ps} \cdot \frac{f_{pu}}{d} \right)} = 3.39 \cdot in \qquad a := \beta_1 \cdot c$

$f_{ps} := f_{pu} \cdot \left(1 - k \cdot \frac{c}{d_p} \right) = \begin{pmatrix} 229.037 \\ 252.517 \\ 261.534 \\ 266.149 \end{pmatrix} \cdot ksi$

$M_u := \sum_{i=0}^{3} \left(f_{ps_i} \cdot num_i \cdot A_{strand} \right) \cdot \left(d - \frac{a}{2} \right) \qquad \phi_u := \frac{\varepsilon_u}{c}$

$M_u = 2418.986 \cdot kip \cdot in \qquad \phi_u = 8.849 \times 10^{-4} \cdot \frac{rad}{in}$

APPENDIX N: Individual Results of Flexure Test

Table N.1 Calculated moments and curvatures at cracking, yield, and ultimate condition for piles using AISI 1080 steel strands (ACI 318).

	$M_{crack,calc}$ (kip·in)	$\varphi_{crack,calc}$ (rad/in)	$M_{yield,calc}$ (kip·in)	$\varphi_{yield,calc}$ (rad/in)	$M_{ult,calc}$ (kip·in)	$\varphi_{ult,calc}$ (rad/in)
Pile 1080 #1 Top Half	1,208	2.54×10^{-5}	2,266	6.71×10^{-4}	2,436	1.04×10^{-3}
Pile 1080 #1 Bottom Half	1,208	2.54×10^{-5}	2,266	6.71×10^{-4}	2,436	1.04×10^{-3}
Pile 1080 #2 Top Half	1,148	2.64×10^{-5}	2,351	6.42×10^{-4}	2,531	8.88×10^{-4}
Pile 1080 #2 Bottom Half	1,148	2.64×10^{-5}	2,351	6.42×10^{-4}	2,531	8.88×10^{-4}

Table N.2 Calculated moments and curvatures at cracking, yield, and ultimate condition for piles using duplex HSSS 2205 strands (ACI 318).

	$M_{crack,calc}$ (kip·in)	$\varphi_{crack,calc}$ (rad/in)	$M_{yield,calc}$ (kip·in)	$\varphi_{yield,calc}$ (rad/in)	$M_{ult,calc}$ (kip·in)	$\varphi_{ult,calc}$ (rad/in)
Pile 2205 #1 Top Half	1,151	2.56×10^{-5}	2,530	7.70×10^{-4}	2,633	9.15×10^{-4}
Pile 2205 #1 Bottom Half	1,151	2.56×10^{-5}	2,530	7.70×10^{-4}	2,633	9.15×10^{-4}
Pile 2205 #2 Top Half	1,153	2.56×10^{-5}	2,805	7.93×10^{-4}	2,908	8.87×10^{-4}
Pile 2205 #2 Bottom Half	1,153	2.56×10^{-5}	2,774	7.92×10^{-4}	2,877	8.92×10^{-4}
Pile 2205 #3 Top Half	1,160	2.55×10^{-5}	2,757	7.93×10^{-4}	2,856	9.04×10^{-4}
Pile 2205 #3 Bottom Half	1,160	2.55×10^{-5}	2,773	7.96×10^{-4}	2,866	9.02×10^{-4}

Table N.3 Calculated moments and curvatures at cracking and ultimate condition for piles using AISI 1080 steel strands (AASHTO LRFD).

	$M_{crack,calc}$ (kip·in)	$\varphi_{crack,calc}$ (rad/in)	$M_{ult,calc}$ (kip·in)	$\varphi_{ult,calc}$ (rad/in)
Pile 1080 #1 Top Half	1,613	3.06×10^{-5}	2,406	8.82×10^{-4}
Pile 1080 #1 Bottom Half	1,627	3.04×10^{-5}	2,419	8.85×10^{-4}
Pile 1080 #2 Top Half	1,536	3.14×10^{-5}	2,313	7.19×10^{-4}
Pile 1080 #2 Bottom Half	1,536	3.14×10^{-5}	2,321	7.19×10^{-4}

Table N.4 Calculated moments and curvatures at cracking and ultimate condition for piles using duplex HSSS 2205 strands (AASHTO LRFD).

	$M_{crack,calc}$ (kip·in)	$\varphi_{crack,calc}$ (rad/in)	$M_{ult,calc}$ (kip·in)	$\varphi_{ult,calc}$ (rad/in)
Pile 2205 #1 Top Half	1,546	3.07×10^{-5}	2,560	6.96×10^{-4}
Pile 2205 #1 Bottom Half	1,546	3.07×10^{-5}	2,564	6.96×10^{-4}
Pile 2205 #2 Top Half	1,549	3.07×10^{-5}	2,615	7.01×10^{-4}
Pile 2205 #2 Bottom Half	1,508	3.14×10^{-5}	2,560	6.99×10^{-4}
Pile 2205 #3 Top Half	1,540	3.09×10^{-5}	2,606	7.16×10^{-4}
Pile 2205 #3 Bottom Half	1,537	3.09×10^{-5}	2,606	7.13×10^{-4}

- Pile AISI 1080 #1 – Top Half:

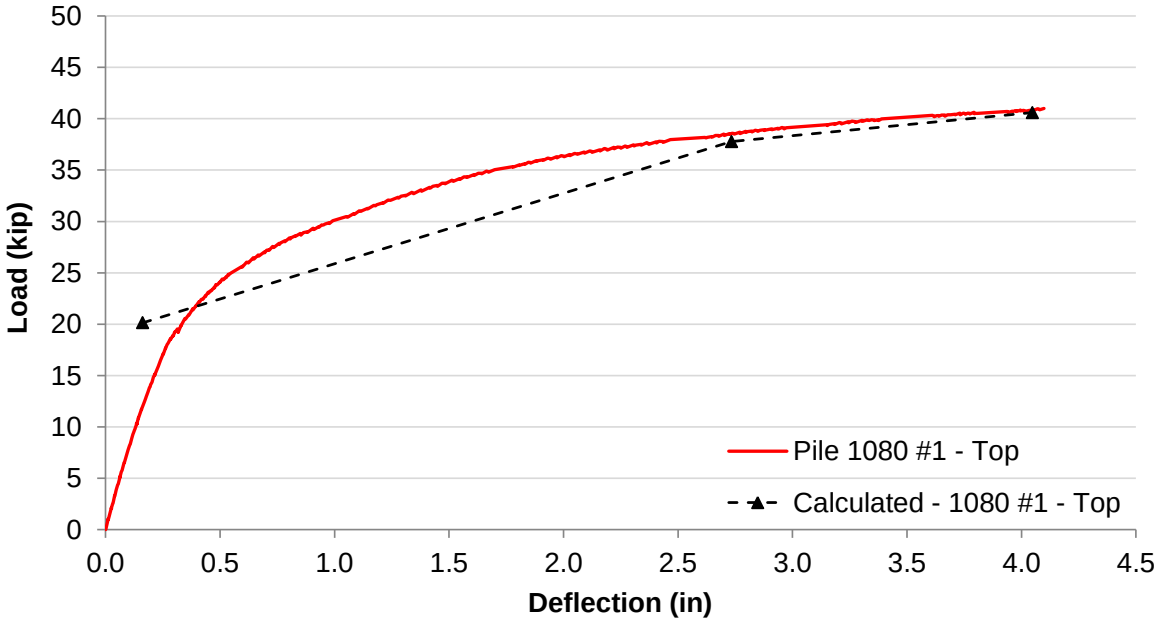

Figure N.1 Load-deflection curve for top half of pile 1080 #1, from flexure test. Dashed line shows calculations following ACI 318 requirements.

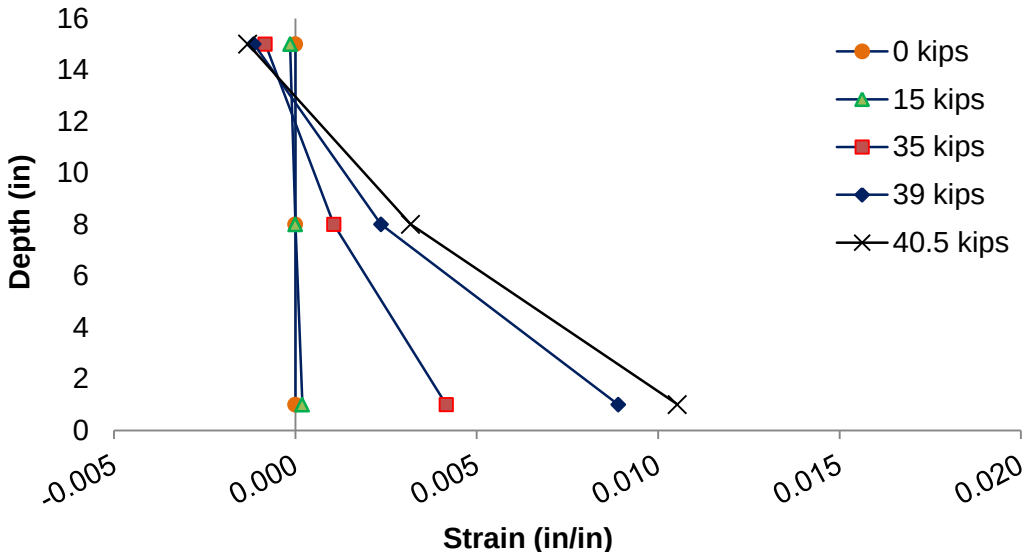

Figure N.2 Strain distributions of top half of pile 1080 #1.

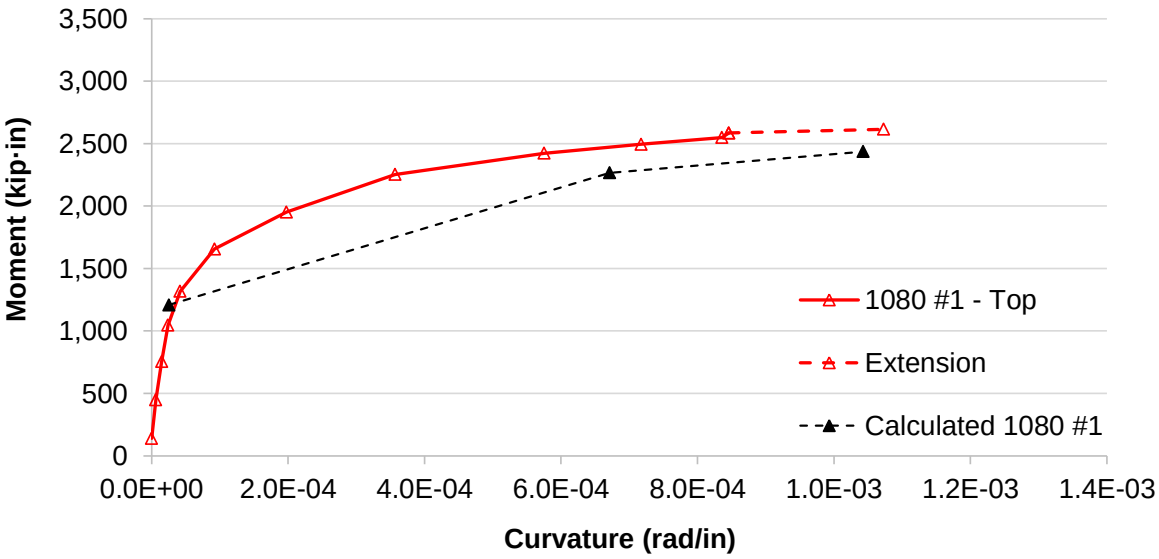

Figure N.3 Moment-curvature curve for top half of pile 1080 #1. Extension (dashed line) includes estimated ultimate curvature and moment. Dashed line shows calculations following ACI 318 requirements.

Figure N.4 Cracking pattern of top half of pile 1080 #1 before failure.

- Pile AISI 1080 #1 – Bottom Half:

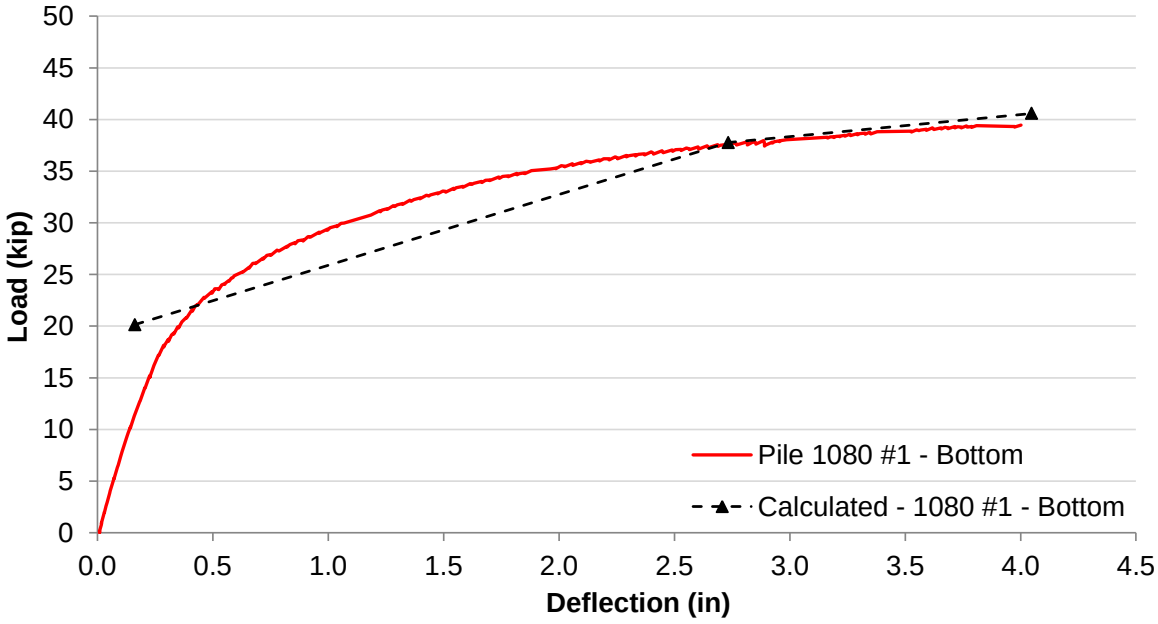

Figure N.5 Load-deflection curve for bottom half of pile 1080 #1, from flexure test. Dashed line shows calculations following ACI 318 requirements.

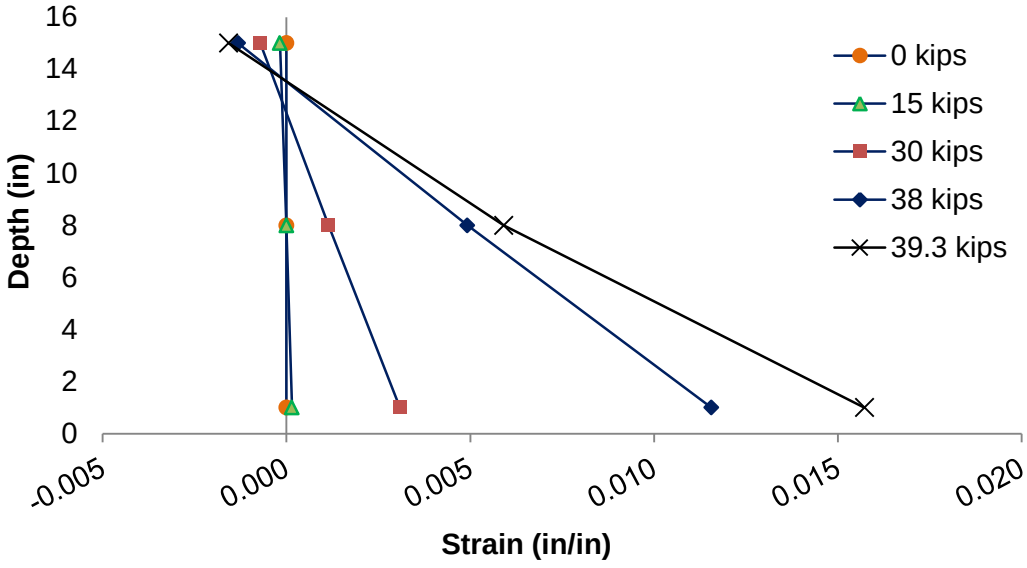

Figure N.6 Strain distributions of bottom half of pile 1080 #1.

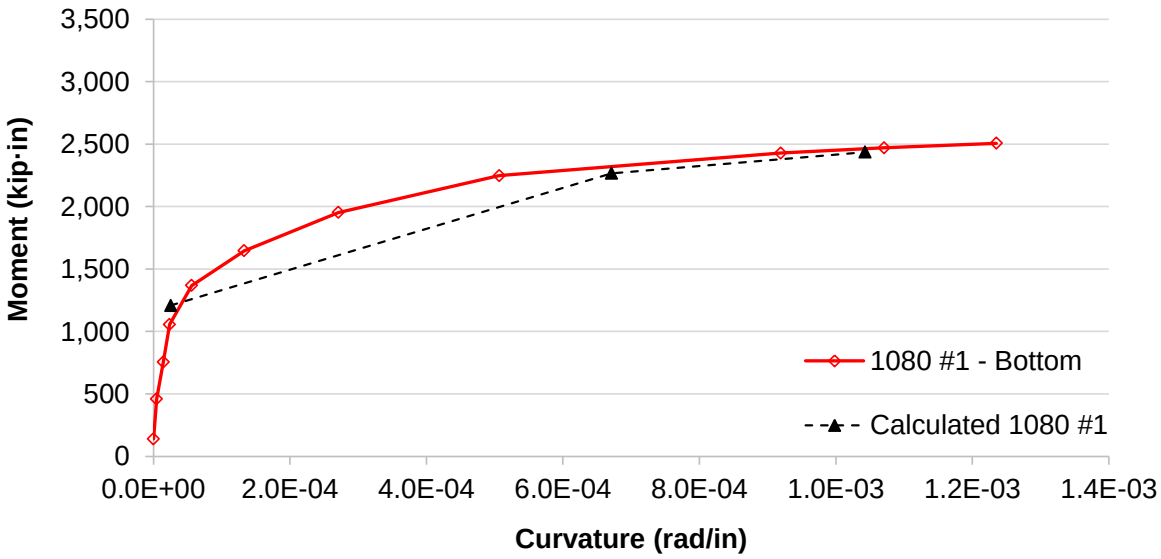

Figure N.7 Moment-curvature curve for bottom half of pile 1080 #1. Dashed line shows calculations following ACI 318 requirements.

Figure N.8 Cracking pattern of bottom half of pile 1080 #1 before failure.

- Pile AISI 1080 #2 – Top Half:

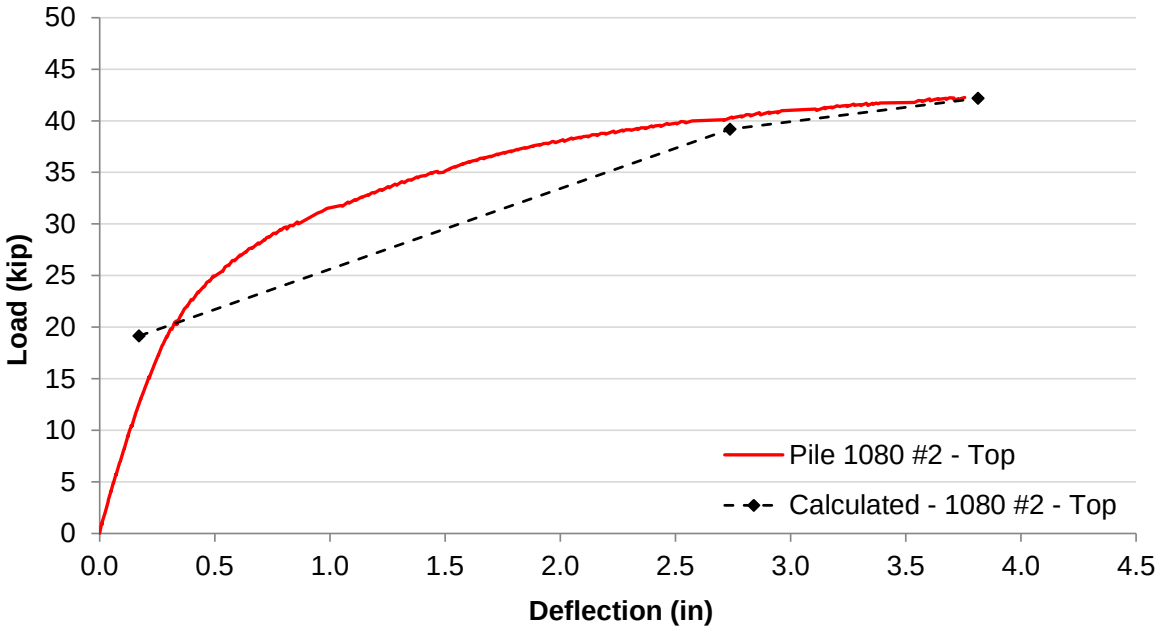

Figure N.9 Load-deflection curve for top half of pile 1080 #2, obtained from flexure test. Dashed line shows calculations following ACI 318 requirements.

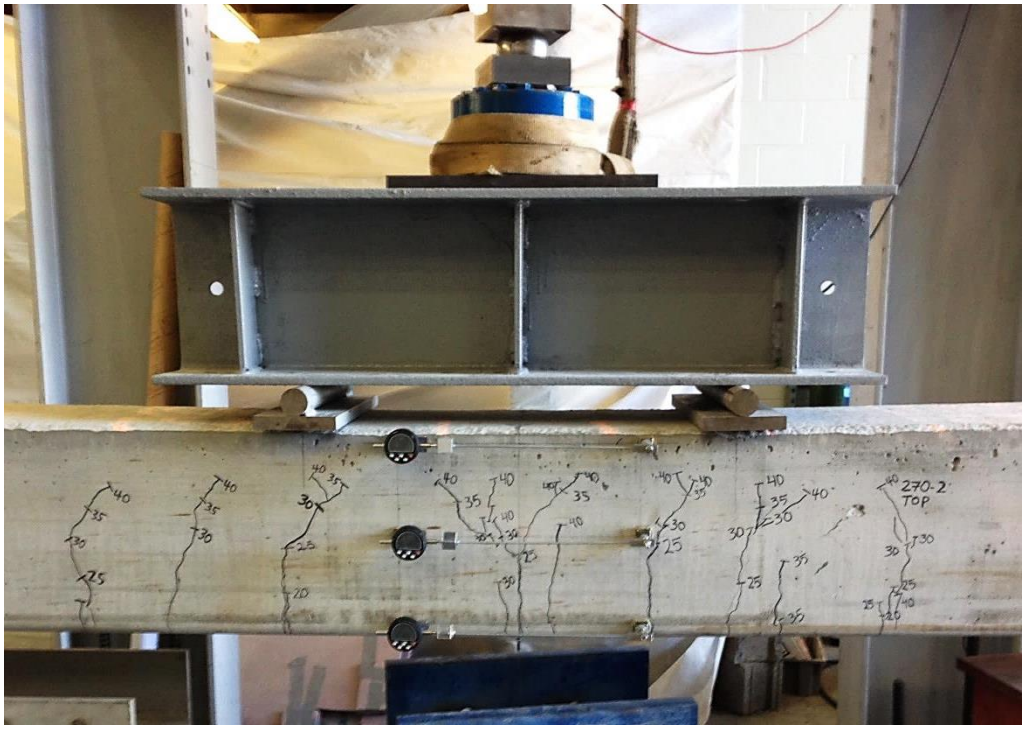

Figure N.10 Cracking pattern of top half of pile 1080 #2 before failure.

- Pile AISI 1080 #2 – Bottom Half:

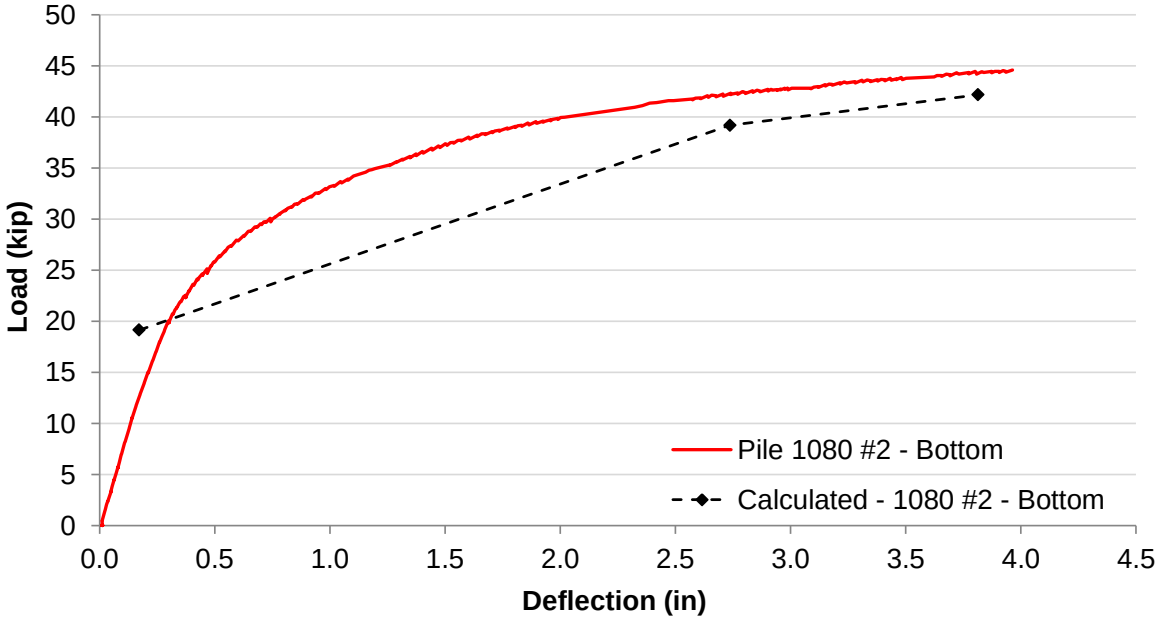

Figure N.11 Load-deflection curve for bottom half of pile 1080 #2, from flexure test. Dashed line shows calculations following ACI 318 requirements.

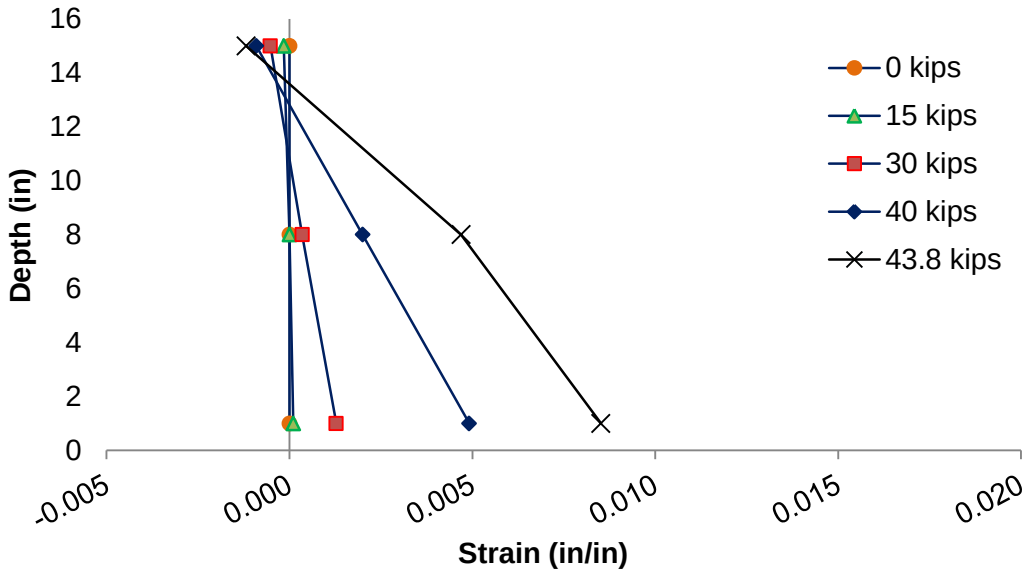

Figure N.12 Strain distributions of bottom half of pile 1080 #2.

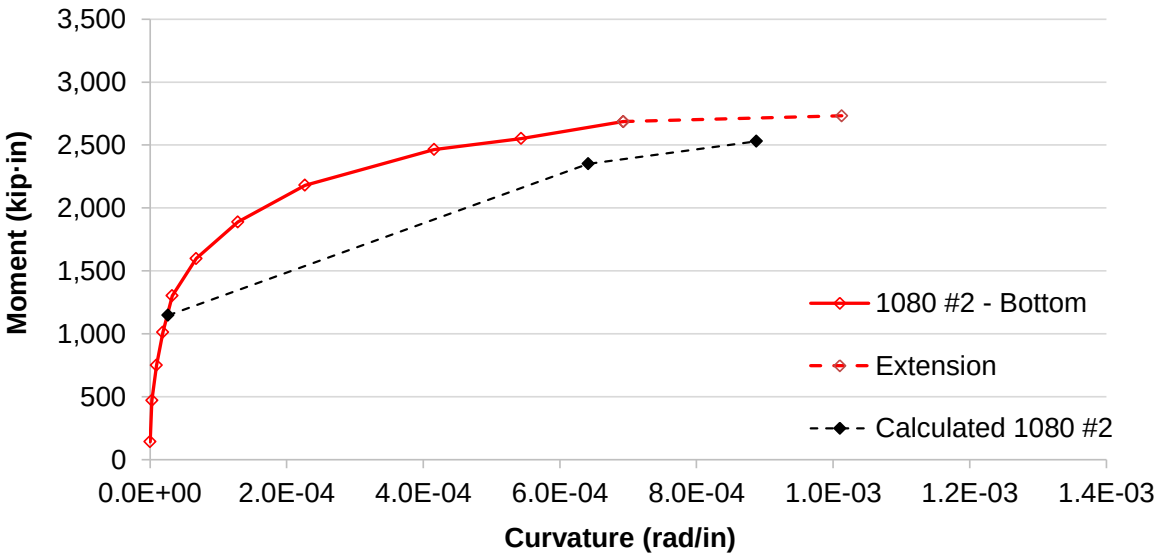

Figure N.13 Moment-curvature curve for bottom half of pile 1080 #2. Dashed line shows calculations following ACI 318 requirements.

Figure N.14 Cracking pattern of bottom half of pile 1080 #2 after failure.

- Pile HSSS 2205 #1 – Top Half:

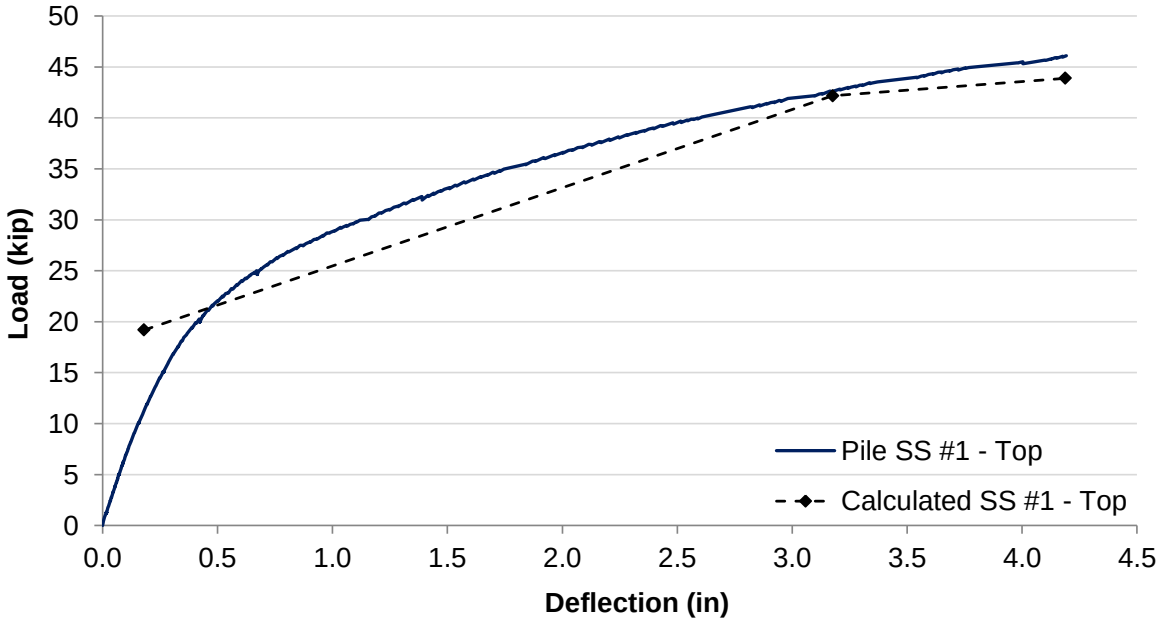

Figure N.15 Load-deflection curve for top half of pile HSSS 2205 #1, from flexure test. Dashed line shows calculations following ACI 318 requirements.

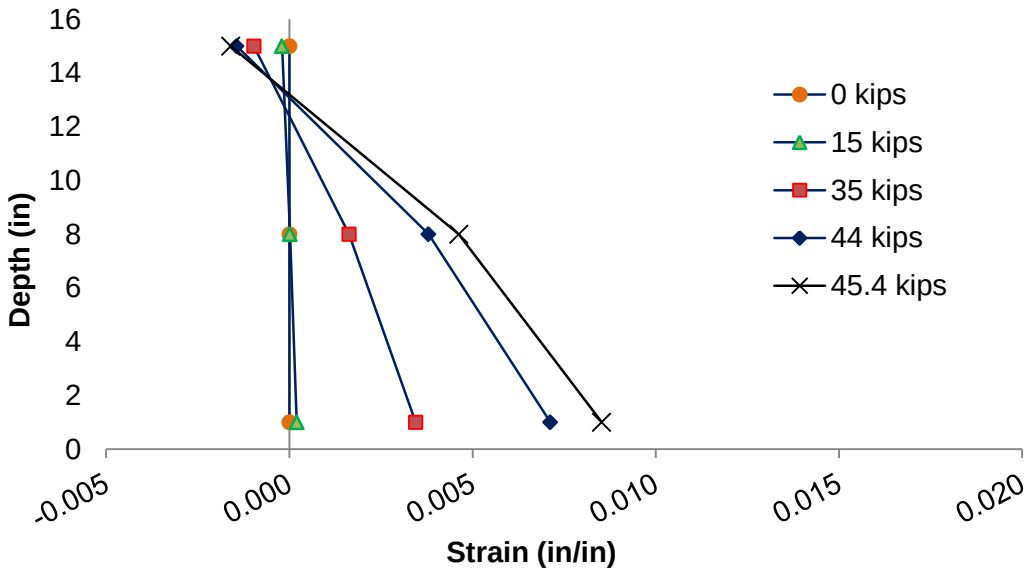

Figure N.16 Strain distributions of top half of pile HSSS 2205 #1.

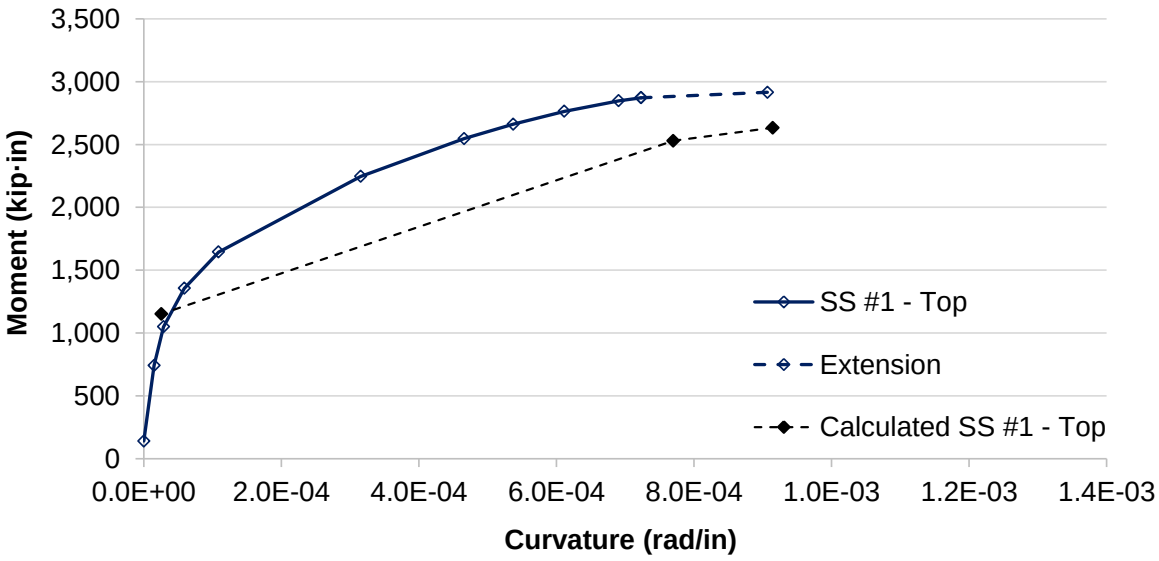

Figure N.17 Moment-curvature curve for top half of pile HSSS 2205 #1. Dashed line shows calculations following ACI 318 requirements.

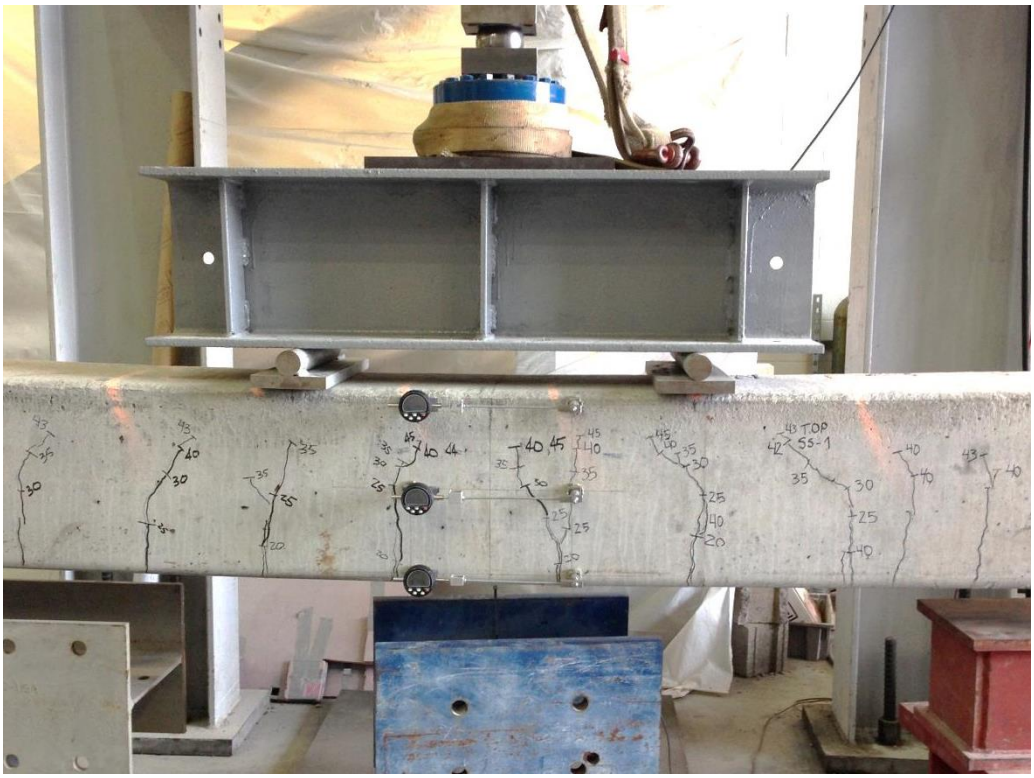

Figure N.18 Cracking pattern of top half of pile HSSS 2205 #1 before failure.

- Pile HSSS 2205 #1 – Bottom Half:

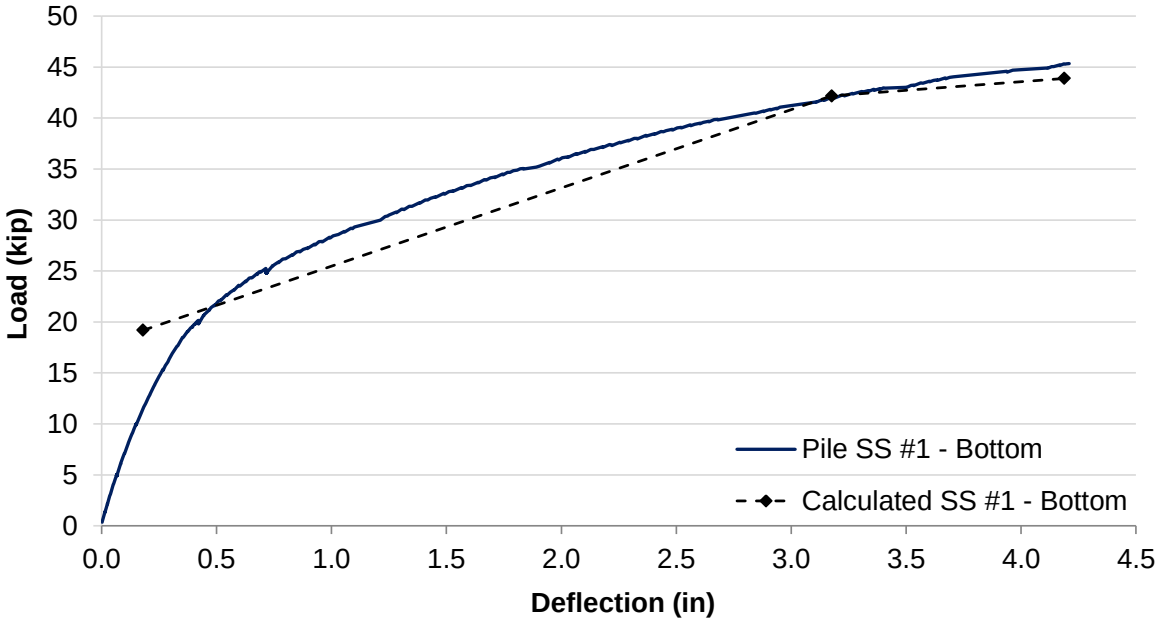

Figure N.19 Load-deflection curve for bottom half of pile HSSS 2205 #1, from flexure test. Dashed line shows calculations following ACI 318 requirements.

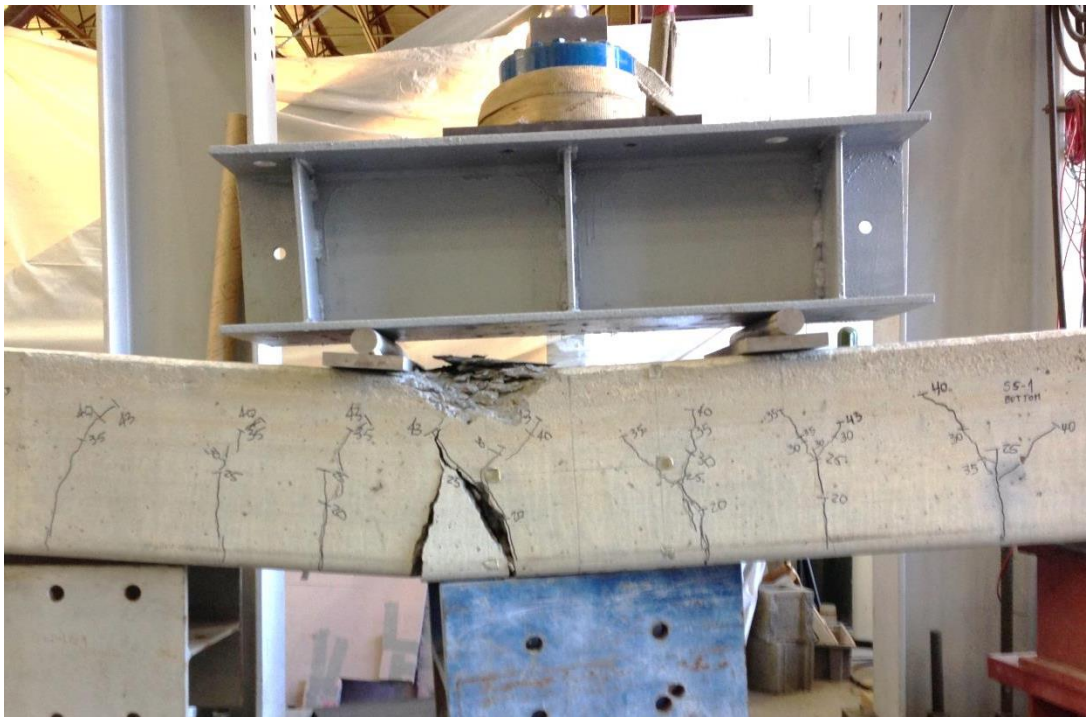

Figure N.20 Cracking pattern of bottom half of pile HSSS 2205 #1 after failure.

- Pile HSSS 2205 #2 – Top Half:

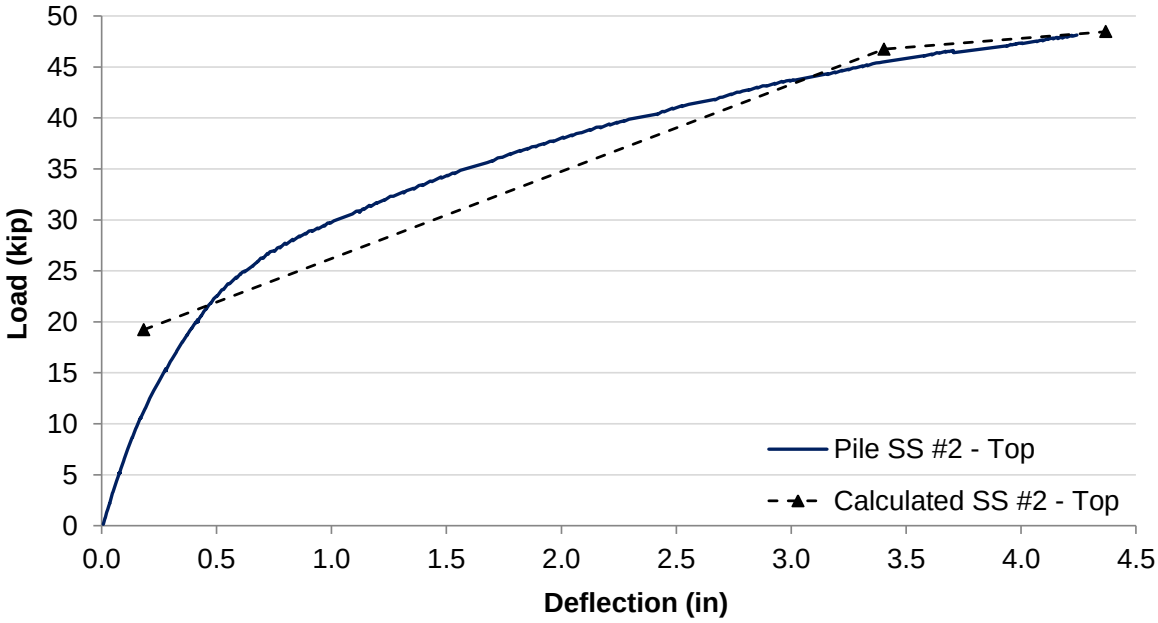

Figure N.21 Load-deflection curve for top half of pile HSSS 2205 #2, from flexure test. Dashed line shows calculations following ACI 318 requirements.

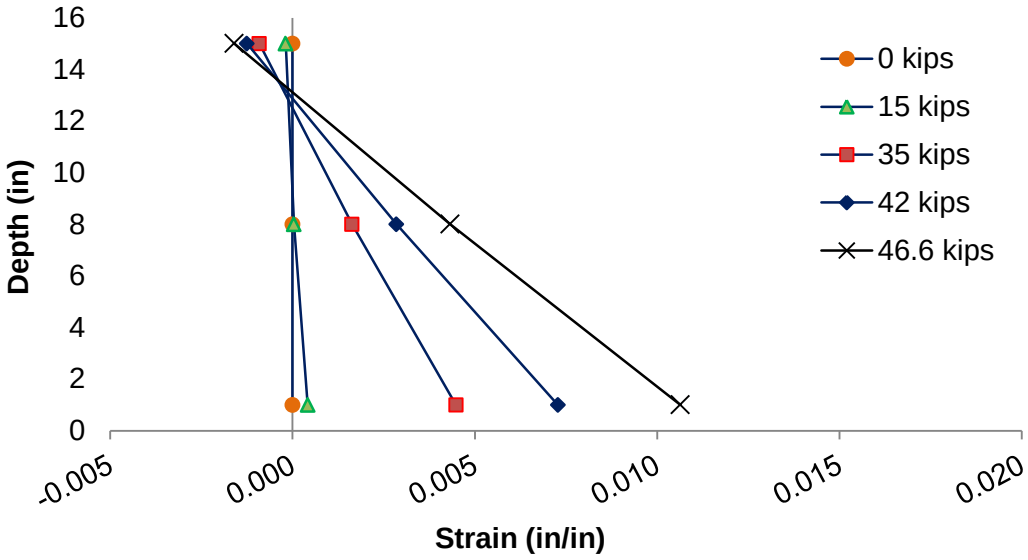

Figure N.22 Strain distributions of top half of pile HSSS 2205 #2.

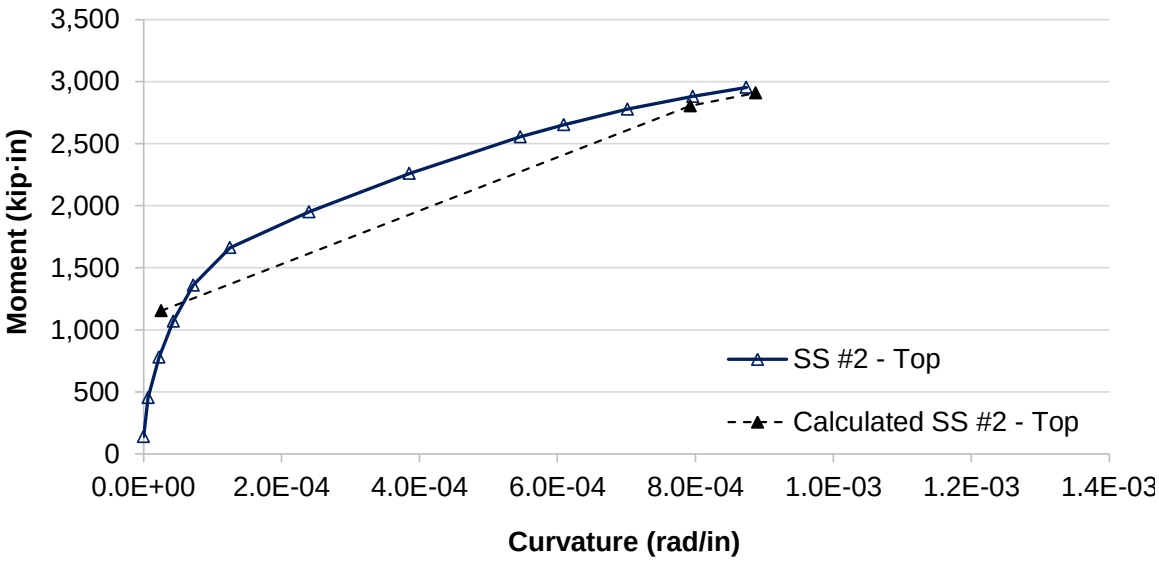

Figure N.23 Moment-curvature curve for top half of pile HSSS 2205 #2. Dashed line shows calculations following ACI 318 requirements.

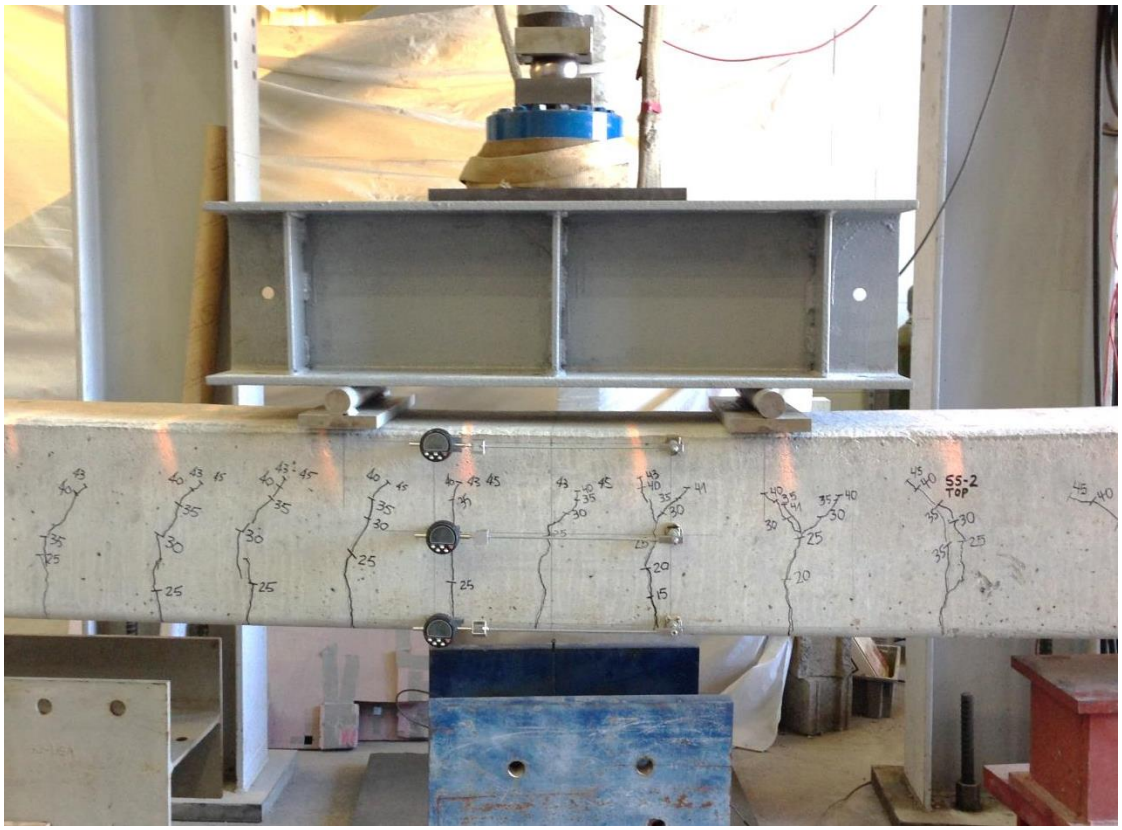

Figure N.24 Cracking pattern of top half of pile HSSS 2205 #2 before failure.

- Pile HSSS 2205 #2 – Bottom Half:

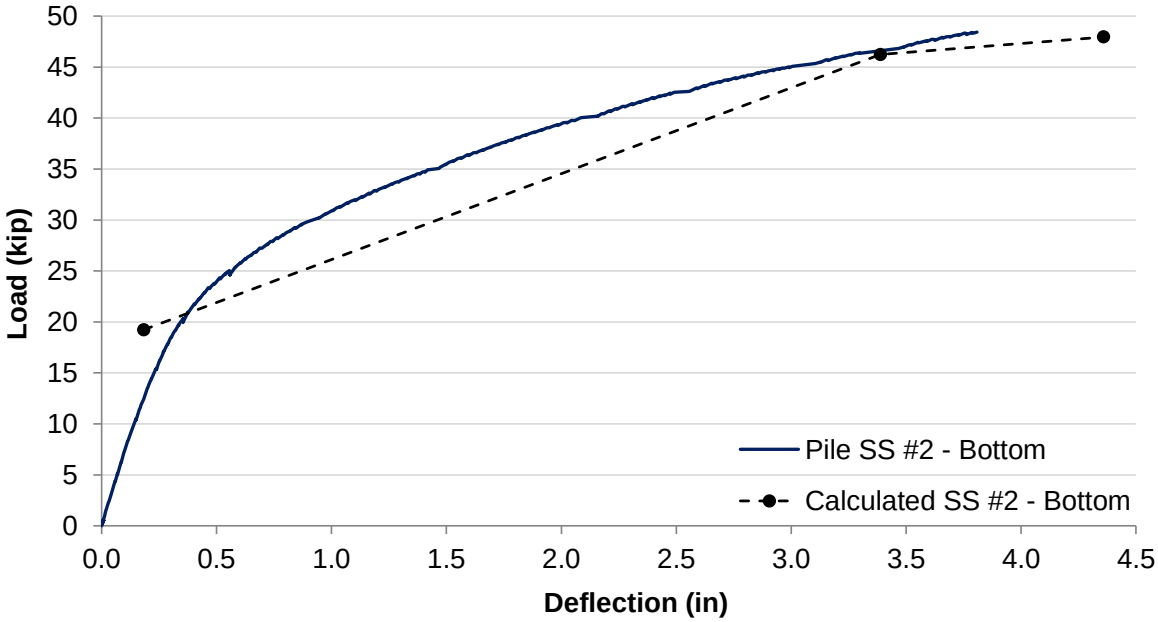

Figure N.25 Load-deflection curve for bottom half of pile HSSS 2205 #2, from flexure test. Dashed line shows calculations following ACI 318 requirements.

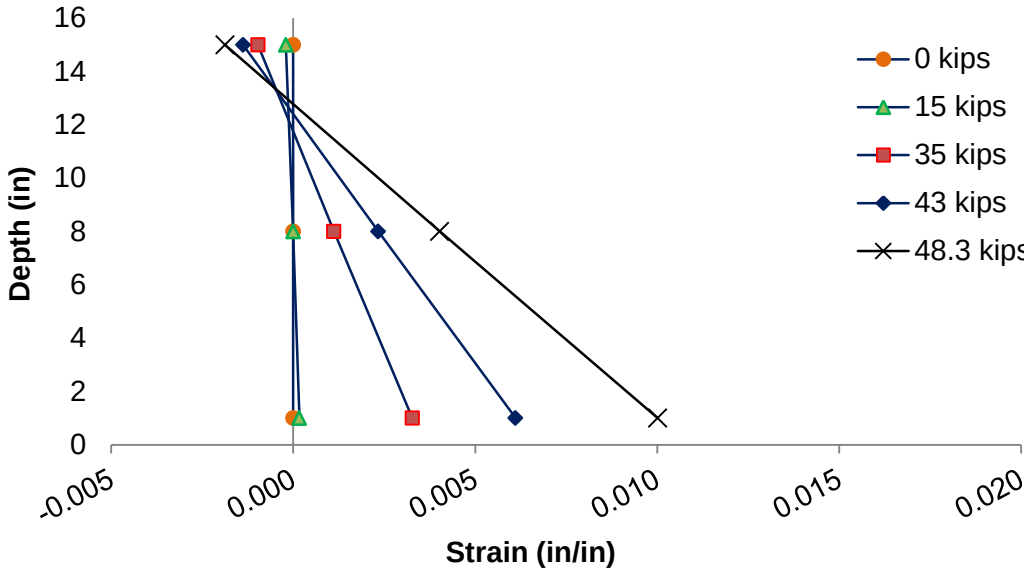

Figure N.26 Strain distributions of bottom half of pile HSSS 2205 #2.

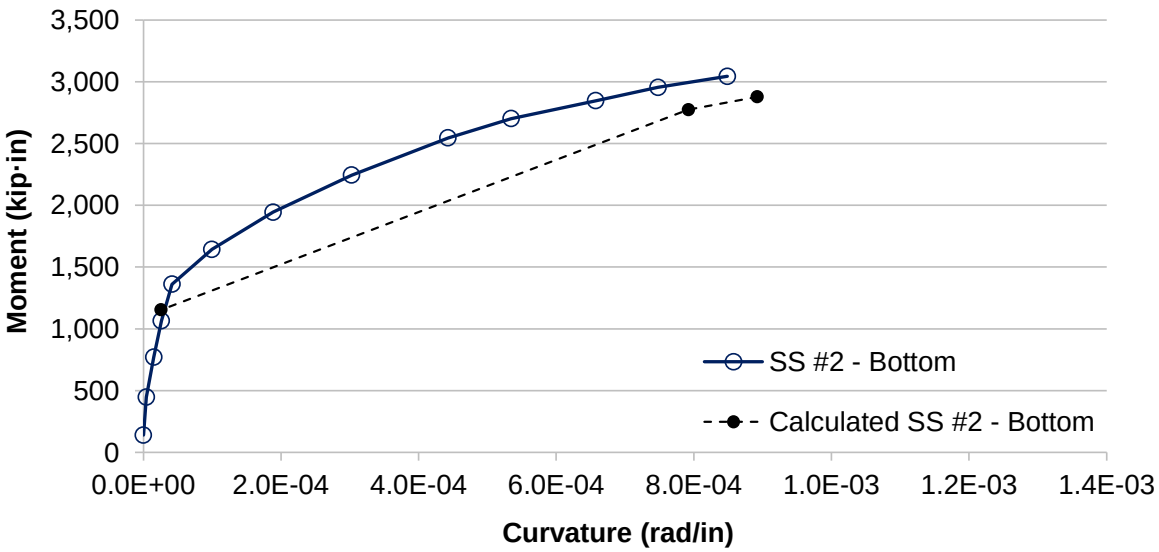

Figure N.27 Moment-curvature curve for bottom half of pile HSSS 2205 #2. Dashed line shows calculations following ACI 318 requirements.

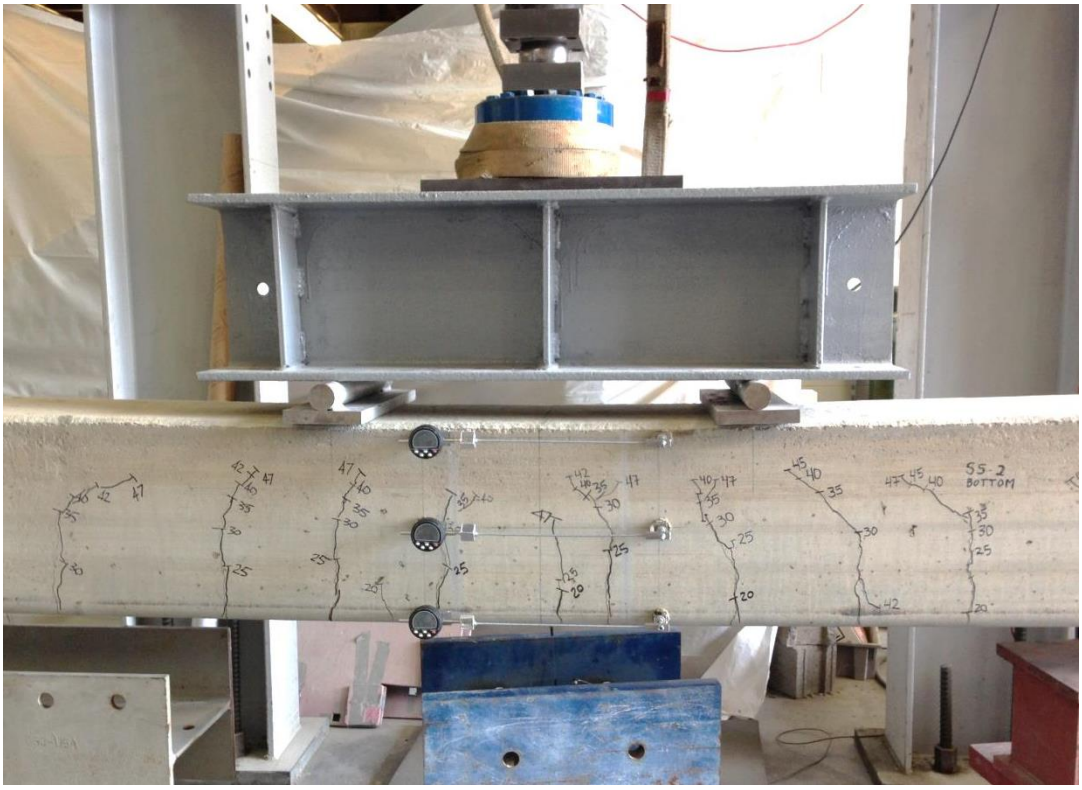

Figure N.28 Cracking pattern of bottom half of pile HSSS 2205 #2 before failure.

- Pile HSSS 2205 #3 – Top Half:

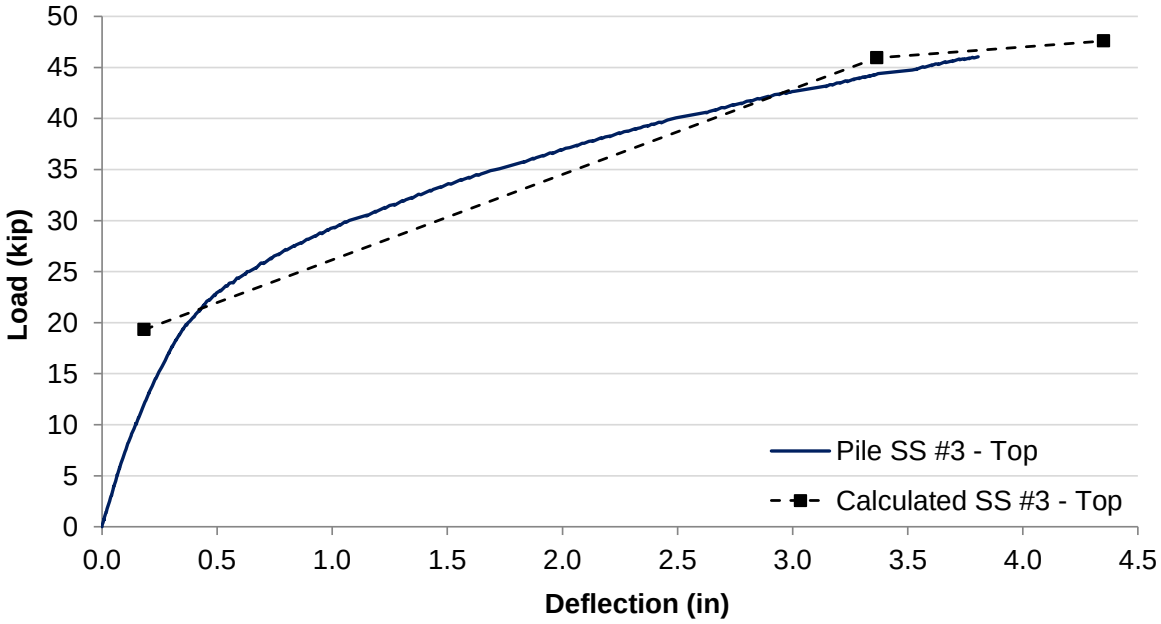

Figure N.29 Load-deflection curve for top half of pile HSSS 2205 #3, from flexure test. Dashed line shows calculations following ACI 318 requirements.

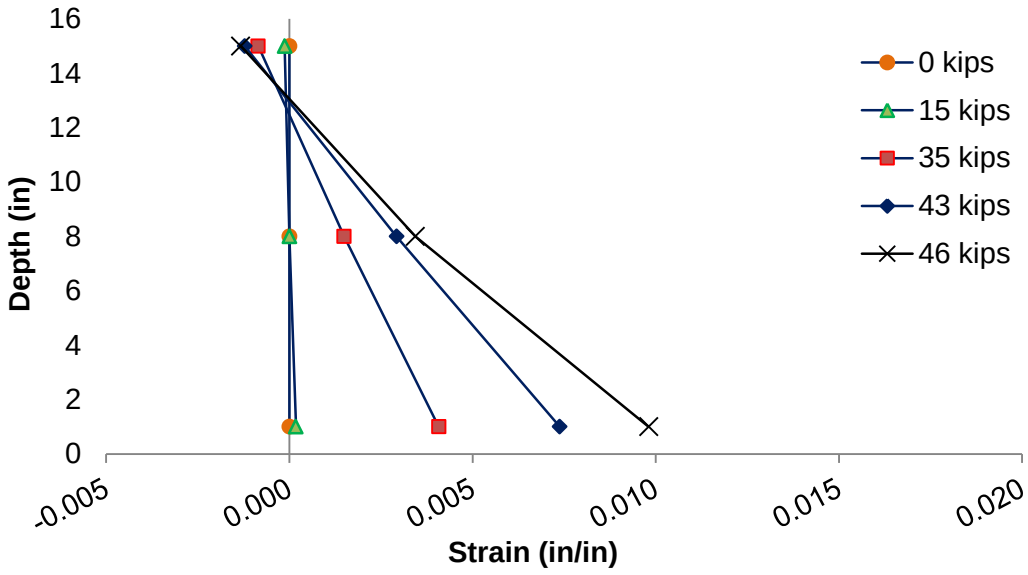

Figure N.30 Strain distributions of top half of pile HSSS 2205 #3.

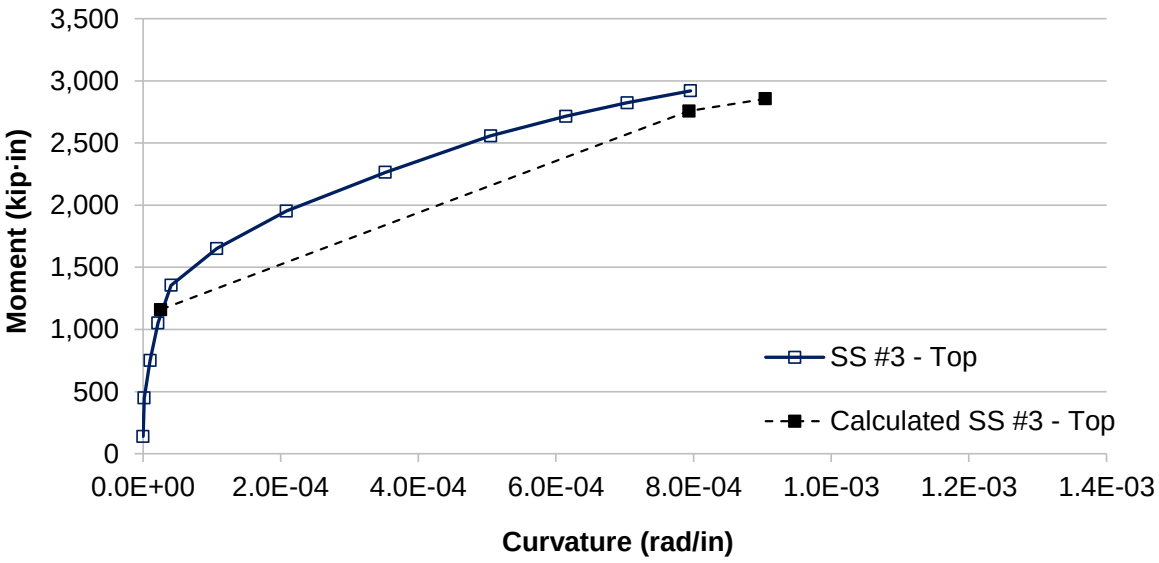

Figure N.31 Moment-curvature curve for top half of pile HSSS 2205 #3. Dashed line shows calculations following ACI 318 requirements.

Figure N.32 Cracking pattern of top half of pile HSSS 2205 #3 after failure.

- Pile HSSS 2205 #3 – Bottom Half:

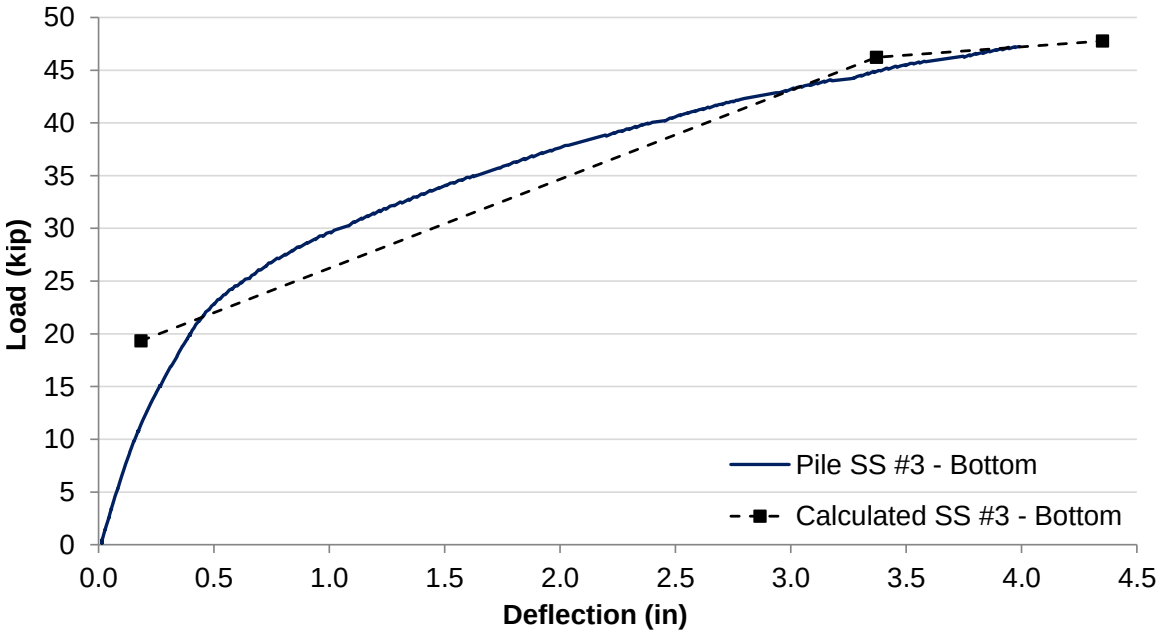

Figure N.33 Load-deflection curve for bottom half of pile HSSS 2205 #3, from flexure test. Dashed line shows calculations following ACI 318 requirements.

Figure N.34 Cracking pattern of bottom half of pile HSSS 2205 #3 after failure.

APPENDIX O: Calculation of Nominal Shear Strength

O.1 ACI 318 Nominal Shear Strength for Piles Using Conventional Steel.

– Piles AISI 1080, spiral wire spacing of 6 inches.

- Pile properties.

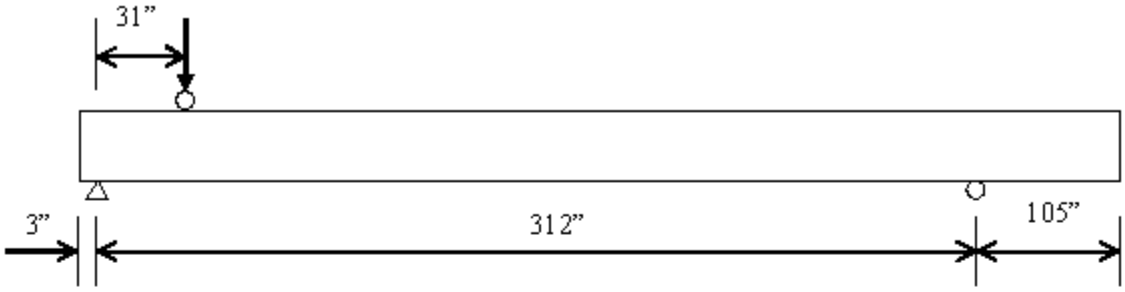

$f_c := 10800psi$ $f_{pu} := 281.1ksi$ $E_{ps} := 29400psi$ $f_{se} := 195.7ksi$

$b_w := 16in$ $h := 16in$ $y_t := 8in$ $y_b := -8in$ $Area := b_w \cdot h = 256 \cdot in^2$

$A_{ps} := 1.386in^2$ $I_g := \frac{1}{12} b_w \cdot h^3$ $P_e := 270kip$ $e := -0in$ $w_{sw} := 21.667 \frac{lbf}{in}$

$L_1 := 311in$ $L_2 := 106in$ $L := L_1 + L_2 + 3in = 35 \cdot ft$ $x_1 := 31in$ $d := 0.8 \cdot h = 12.8 \cdot in$

$DL := w_{sw} \cdot L = 9100.14 \cdot lbf$ $V_D := \frac{1}{L_1} \cdot \left[DL \cdot \left(\frac{L}{2} - L_2 \right) \right]$ $V_D = 3.043 \cdot kip$

$P_L := 62.8kip$ Value adjusted in order to have $V_n = V_D + V_L$

$F_{se} := P_e - 21.16kip = 248.84 \cdot kip$

$V_L := \frac{1}{L_1} \cdot \left[P_L \cdot (L_1 - x_1) \right]$ $V_L = 56.54 \cdot kip$ $V_p := 0kip$

$M_D := V_D \cdot x_1 - \frac{w_{sw} \cdot x_1^2}{2}$ $M_D = 6.994 \cdot kip \cdot ft$ $M_L := V_L \cdot x_1$ $M_L = 146.062 \cdot kip \cdot ft$

$M_{cre} := \frac{-I_g}{y_b} \cdot \left(6 \cdot \sqrt{f_c \cdot psi} + \frac{F_{se}}{Area} + \frac{F_{se} \cdot e \cdot y_b}{I_g} + \frac{M_D \cdot y_b}{I_g} \right)$ $M_{cre} = 83.776 \cdot kip \cdot ft$

- **Web and flexural shear.**

$$V_{ci} := \max\left(\left|0.6\cdot\sqrt{f_c\cdot psi}\cdot b_w\cdot d\right| + \left|V_D\right| + \left|\frac{V_L\cdot M_{cre}}{M_L}\right|, \left|1.7\sqrt{f_c\cdot psi}\cdot b_w\cdot d\right|\right) \qquad V_{ci} = 48.243\cdot kip$$

$$V_{cw} := \left(3.5\sqrt{f_c\cdot psi} + \frac{0.3\cdot F_{se}}{Area}\right)\cdot b_w\cdot d + V_p \qquad V_{cw} = 134.21\cdot kip$$

$$V_c := \min\left(V_{ci}, V_{cw}\right) = 48.243\cdot kip$$

- **Shear reinforcement.**

$$A_v := 0.076in^2 \qquad f_y := 70ksi \qquad sp := 6in$$

$$V_s := \frac{A_v\cdot f_y\cdot d}{sp} = 11.349\cdot kip$$

- **Total shear.**

$$V_n := V_c + V_s = 59.592\cdot kip$$

O.2 ACI 318 Nominal Shear Strength for Piles Using Stainless Steel

– Piles HSSS 2205, spiral wire spacing of 6 inches.

- Pile properties.

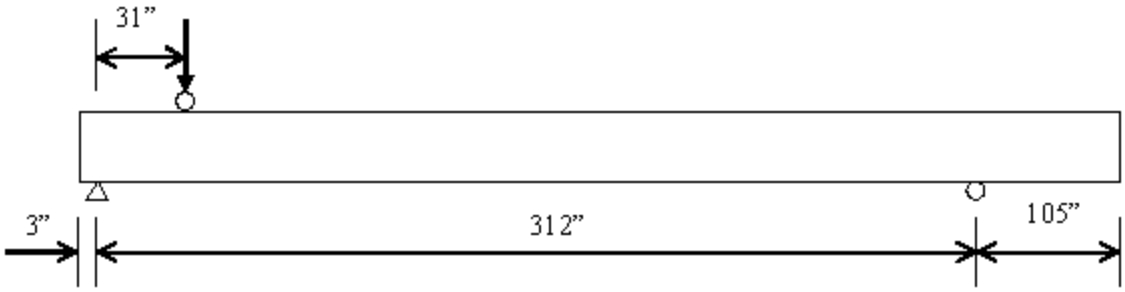

$f_c := 10700psi$ $f_{pu} := 241.5ksi$ $E_{ps} := 23500psi$ $f_{se} := 147.1ksi$

$b_w := 16in$ $h := 16in$ $y_t := 8in$ $y_b := -8in$ $Area := b_w \cdot h = 256 \cdot in^2$

$A_{ps} := 1.848in^2$ $I_g := \frac{1}{12} b_w \cdot h^3$ $P_e := 270kip$ $e := -0in$ $w_{sw} := 21.667 \frac{lbf}{in}$

$L_1 := 311in$ $L_2 := 106in$ $L := L_1 + L_2 + 3in = 35 \cdot ft$ $x_1 := 31in$ $d := 0.8 \cdot h = 12.8 \cdot in$

$DL := w_{sw} \cdot L = 9100.14 \cdot lbf$ $V_D := \frac{1}{L_1} \cdot \left[DL \cdot \left(\frac{L}{2} - L_2 \right) \right]$ $V_D = 3.043 \cdot kip$

$P_L := 61.2kip$ Value adjusted in order to have $V_n = V_D + V_L$

$F_{se} := P_e - 25.37kip = 244.63 \cdot kip$

$V_L := \frac{1}{L_1} \cdot \left[P_L \cdot (L_1 - x_1) \right]$ $V_L = 55.1 \cdot kip$ $V_p := 0kip$

$M_D := V_D \cdot x_1 - \frac{w_{sw} \cdot x_1^2}{2}$ $M_D = 6.994 \cdot kip \cdot ft$ $M_L := V_L \cdot x_1$ $M_L = 142.341 \cdot kip \cdot ft$

$M_{cre} := \frac{-I_g}{y_b} \cdot \left(6 \cdot \sqrt{f_c \cdot psi} + \frac{F_{se}}{Area} + \frac{F_{se} \cdot e \cdot y_b}{I_g} + \frac{M_D \cdot y_b}{I_g} \right)$ $M_{cre} = 82.676 \cdot kip \cdot ft$

- **Web and flexural shear.**

$$V_{ci} := \max\left(\left|0.6\cdot\sqrt{f_c\cdot psi}\cdot b_w\cdot d\right| + \left|V_D\right| + \left|\frac{V_L\cdot M_{cre}}{M_L}\right|, \left|1.7\sqrt{f_c\cdot psi}\cdot b_w\cdot d\right|\right) \qquad V_{ci} = 47.758\cdot kip$$

$$V_{cw} := \left(3.5\sqrt{f_c\cdot psi} + \frac{0.3\cdot F_{se}}{Area}\right)\cdot b_w\cdot d + V_p \qquad V_{cw} = 132.86\cdot kip$$

$$V_c := \min\left(V_{ci}, V_{cw}\right) = 47.758\cdot kip$$

- **Shear reinforcement.**

$$A_v := 0.08in^2 \qquad f_y := 61ksi \qquad sp := 6in$$

$$V_s := \frac{A_v\cdot f_y\cdot d}{sp} = 10.411\cdot kip$$

- **Total shear.**

$$V_n := V_c + V_s = 58.168\cdot kip$$

O.3 AASHTO LRFD Nominal Shear Strength for Piles Using Conventional Steel.

– Piles AISI 1080, spiral wire spacing of 6 inches.

- Pile properties.

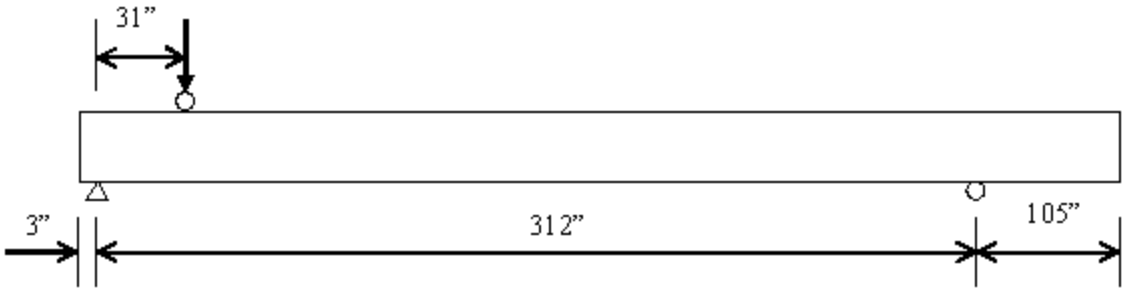

$f_c := 10800psi$ $f_{pu} := 281.1ksi$ $E_{ps} := 29400psi$ $f_{se} := 195.7ksi$

$b_w := 16in$ $h := 16in$ $y_t := 8in$ $y_b := -8in$ $Area := b_w \cdot h = 256 \cdot in^2$

$A_{ps} := 1.386in^2$ $I_g := \frac{1}{12} b_w \cdot h^3$ $P_e := 270kip$ $e := -0in$ $w_{sw} := 21.667 \frac{lbf}{in}$

$L_1 := 311in$ $L_2 := 106in$ $L := L_1 + L_2 + 3in = 35 \cdot ft$ $x_1 := 31in$ $d := 0.8 \cdot h = 12.8 \cdot in$

$DL := w_{sw} \cdot L = 9100.14 \cdot lbf$ $V_D := \frac{1}{L_1} \cdot \left[DL \cdot \left(\frac{L}{2} - L_2 \right) \right]$ $V_D = 3.043 \cdot kip$

$P_L := 67.7kip$ Value adjusted in order to have $V_n = V_D + V_L$

$F_{se} := P_e - 21.16kip = 248.84 \cdot kip$

$V_L := \frac{1}{L_1} \cdot \left[P_L \cdot (L_1 - x_1) \right]$ $V_L = 60.952 \cdot kip$ $V_p := 0kip$

$M_D := V_D \cdot x_1 - \frac{w_{sw} \cdot x_1^2}{2}$ $M_D = 6.994 \cdot kip \cdot ft$ $M_L := V_L \cdot x_1$ $M_L = 157.459 \cdot kip \cdot ft$

$M_{cre} := \frac{-I_g}{y_b} \cdot \left(0.24 \cdot \sqrt{f_c \cdot ksi} + \frac{F_{se}}{Area} + \frac{F_{se} \cdot e \cdot y_b}{I_g} + \frac{M_D \cdot y_b}{I_g} \right)$ $M_{cre} = 93.173 \cdot kip \cdot ft$

- **Web and flexural shear.**

$$V_{ci} := \max\left(\left|0.02\cdot\sqrt{f_c\cdot ksi}\cdot b_w\cdot d\right| + \left|V_D\right| + \left|\frac{V_L\cdot M_{cre}}{M_L}\right|, \left|0.06\sqrt{f_c\cdot ksi}\cdot b_w\cdot d\right|\right) \qquad V_{ci} = 52.571\cdot kip$$

$$V_{cw} := \left(0.06\sqrt{f_c\cdot ksi} + \frac{0.3\cdot F_{se}}{Area}\right)\cdot b_w\cdot d + V_p \qquad V_{cw} = 100.1\cdot kip$$

$$V_c := \min\left(V_{ci}, V_{cw}\right) = 52.571\cdot kip$$

- **Shear reinforcement.**

$$A_v := 0.076in^2 \qquad f_y := 70ksi \qquad sp := 6in$$

$$V_s := \frac{A_v\cdot f_y\cdot d}{sp} = 11.349\cdot kip$$

- **Total shear.**

$$V_n := V_c + V_s = 63.92\cdot kip$$

O.4 AASHTO LRFD Nominal Shear Strength for Piles Using Stainless Steel.

– Piles HSSS 2205, spiral wire spacing of 6 inches.

- Pile properties.

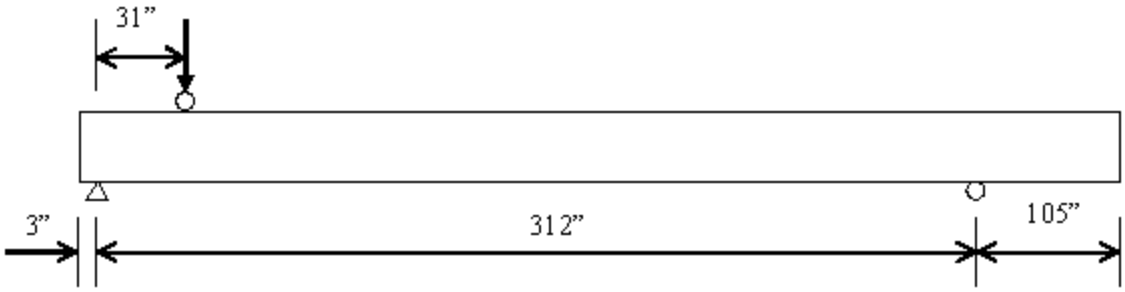

$f_c := 10700psi$ $f_{pu} := 241.5ksi$ $E_{ps} := 23500psi$ $f_{se} := 147.1ksi$

$b_w := 16in$ $h := 16in$ $y_t := 8in$ $y_b := -8in$ $Area := b_w \cdot h = 256 \cdot in^2$

$A_{ps} := 1.848in^2$ $I_g := \frac{1}{12} b_w \cdot h^3$ $P_e := 270kip$ $e := -0in$ $w_{sw} := 21.667 \frac{lbf}{in}$

$L_1 := 311in$ $L_2 := 106in$ $L := L_1 + L_2 + 3in = 35 \cdot ft$ $x_1 := 31in$ $d := 0.8 \cdot h = 12.8 \cdot in$

$DL := w_{sw} \cdot L = 9100.14 \cdot lbf$ $V_D := \frac{1}{L_1} \cdot \left[DL \cdot \left(\frac{L}{2} - L_2 \right) \right]$ $V_D = 3.043 \cdot kip$

$P_L := 66kip$ Value adjusted in order to have $V_n = V_D + V_L$

$F_{se} := P_e - 25.37kip = 244.63 \cdot kip$

$V_L := \frac{1}{L_1} \cdot \left[P_L \cdot (L_1 - x_1) \right]$ $V_L = 59.421 \cdot kip$ $V_p := 0kip$

$M_D := V_D \cdot x_1 - \frac{w_{sw} \cdot x_1^2}{2}$ $M_D = 6.994 \cdot kip \cdot ft$ $M_L := V_L \cdot x_1$ $M_L = 153.505 \cdot kip \cdot ft$

$M_{cre} := \frac{-I_g}{y_b} \cdot \left(0.24 \cdot \sqrt{f_c \cdot ksi} + \frac{F_{se}}{Area} + \frac{F_{se} \cdot e \cdot y_b}{I_g} + \frac{M_D \cdot y_b}{I_g} \right)$ $M_{cre} = 92.03 \cdot kip \cdot ft$

- **Web and flexural shear.**

$$V_{ci} := \max\left(\left|0.02\cdot\sqrt{f_c\cdot ksi}\cdot b_w\cdot d\right| + \left|V_D\right| + \left|\frac{V_L\cdot M_{cre}}{M_L}\right|, \left|0.06\sqrt{f_c\cdot ksi}\cdot b_w\cdot d\right|\right) \qquad V_{ci} = 52.066\cdot kip$$

$$V_{cw} := \left(0.06\sqrt{f_c\cdot ksi} + \frac{0.3\cdot F_{se}}{Area}\right)\cdot b_w\cdot d + V_p \qquad V_{cw} = 98.91\cdot kip$$

$$V_c := \min\left(V_{ci}, V_{cw}\right) = 52.066\cdot kip$$

- **Shear reinforcement.**

$$A_v := 0.08in^2 \qquad f_y := 61ksi \qquad sp := 6in$$

$$V_s := \frac{A_v\cdot f_y\cdot d}{sp} = 10.411\cdot kip$$

- **Total shear.**

$$V_n := V_c + V_s = 62.477\cdot kip$$

APPENDIX P: Summary of Shear Tests

Table P.1 Experimental ultimate shear for piles using conventional steel.

Pile	**Ultimate shear** (kips)
1080 #1 – Top – 3-in.	86.6
1080 #1 – Top – 6-in.	85.7
1080 #1 – Bottom – 3-in.	87.2
1080 #1 – Bottom – 6-in.	84.6
1080 #2 – Top – 3-in.	89.7
1080 #2 – Top – 6-in.	92.5
1080 #2 – Bottom – 3-in.	84.8
1080 #2 – Bottom – 6-in.	92.9
Average 1080 – 3-in.	87.1 (2.0)*
Average 1080 – 6-in.	88.9 (4.4)*
Average 1080	88.0 (3.3)*

* Number in parenthesis shows standard deviation.

Table P.2 Experimental ultimate shear for piles using stainless steel.

Pile	**Ultimate shear** (kips)
HSSS 2205 #1 – Top – 3-in.	86.8
HSSS 2205 #1 – Top – 6-in.	93.4
HSSS 2205 #1 – Bottom – 3-in.	88.4
HSSS 2205 #1 – Bottom – 6-in.	89.0
HSSS 2205 #2 – Bottom – 3-in.	85.1
HSSS 2205 #2 – Bottom – 6-in.	102.0
HSSS 2205 #3 – Bottom – 3-in.	94.8
HSSS 2205 #3 – Bottom – 6-in.	89.4
Average HSSS 2205 – 3-in.	88.8 (4.3)*
Average HSSS 2205 – 6-in.	93.4 (6.0)*
Average HSSS 2205	91.1 (5.4)*

* Number in parenthesis shows standard deviation.

APPENDIX Q: AASHTO LRFD Prestress Losses Calculation

- AASHTO Refined and AASHTO Lump-sum Methods:

Pile Information:

$f_c := 10.8ksi$ $f_{ci} := 4.018ksi$

Measured f_c at 1 day = 4.02 ksi (at SCP plant)

Measured f_c at 438 days = 10.81 ksi

$E_c := 7138ksi$ $E_{ci} := 6138ksi$

Measured E_c at 4 days = 6,138 ksi

Measured E_c at 445 days = 7,138 ksi

$h := 16in$ $y_t := \frac{h}{2}$ $y_b := y_t$ $L_1 := 70ft$ $Area := h^2$ $I := \frac{h^4}{12}$ $cover := 3.5in$

$P_{jack} := 22.5kip$ $\Delta f_{ANC} := 0ksi$ $n := 12$

Duplex HSSS 2205 Strands Properties:

$f_{u.ss} := 241.5ksi$ $E_{ps.ss} := 23500ksi$ $f_{se.ss} := 0.6 \cdot f_{u.ss} = 144.9 \cdot ksi$ $A_{ps.ss} := 0.153in^2$

AISI 1080 Steel Strands Properties:

$f_u := 281.1ksi$ $E_{ps} := 29400ksi$ $f_{se} := 0.7 \cdot f_u = 196.77 \cdot ksi$ $A_{ps} := 0.115in^2$

Strands Configuration:

$$e_{mid} := \frac{h - 2 \cdot cover}{6} \qquad bars := \begin{pmatrix} 4 \\ 2 \\ 2 \\ 4 \end{pmatrix} \qquad e_p := \begin{pmatrix} \frac{h}{2} - cover \\ e_{mid} \\ -e_{mid} \\ cover - \frac{h}{2} \end{pmatrix} \qquad d_p := -e_p + \frac{h}{2}$$

$$P_i := P_{jack} \cdot bars = \begin{pmatrix} 90 \\ 45 \\ 45 \\ 90 \end{pmatrix} \cdot kip \qquad P_1 := P_{i_0} + P_{i_1} + P_{i_2} + P_{i_3} = 270 \cdot kip$$

Savannah RH: average annual high, according to the Southeast Regional Climate Center = 87%.

$RH := 75$

Note: AASHTO LRFD equation number is shown in parenthesis.

Elastic Shortening:

$P_2 := 0.9\left(P_1 + \Delta f_{ANC} \cdot A_{ps}\right) = 243 \cdot kip \qquad e_2 := 0$

$f_2 := \frac{P_2}{n \cdot A_{ps}} = 176.087 \cdot ksi \qquad f_{2.ss} := \frac{P_2}{n \cdot A_{ps.ss}} = 132.353 \cdot ksi \qquad f_{cgp} := \frac{-P_2}{Area} = -0.949 \cdot ksi$

$\Delta f_{pES} := \frac{E_{ps}}{E_{ci}} \cdot f_{cgp} = -4.547 \cdot ksi$ **(5.9.5.2.3a-1)**

$f_2 + \Delta f_{pES} = 171.54 \cdot ksi < 0.7 \cdot f_u = 196.77 \cdot ksi$

$\Delta f_{pES.ss} := \frac{E_{ps.ss}}{E_{ci}} \cdot f_{cgp} = -3.634 \cdot ksi$ **(5.9.5.2.3a-1)**

$f_{2.ss} + \Delta f_{pES.ss} = 128.719 \cdot ksi < 0.7 \cdot f_{u.ss} = 169.05 \cdot ksi$

- **AASHTO Refined Method.**

Shrinkage and Creep Losses:

$V_2 := h^2 \qquad S_2 := 4 \cdot h \qquad k_s := \max\left(1.45 - 0.13 \frac{1}{in} \frac{V_2}{S_2}, 1.0\right)$ **(5.4.2.3.2-2)**

$k_{hs} := 2.0 - 0.014 \cdot RH = 0.95$ **(5.4.2.3.3-2)**

$t := 9125$ change time according to required time span (days)

$k_f := \frac{5ksi}{1ksi + f_{ci}} = 0.996$ **(5.4.2.3.2-4)** $\qquad k_{td} := \frac{t}{61 - 4 \cdot 4.5 + t} = 0.995$ **(5.4.2.3.2-5)**

$\varepsilon_{sh} := -k_s \cdot k_{hs} \cdot k_f \cdot k_{td} \cdot 0.48 \cdot 10^{-3} = -4.522 \times 10^{-4}$ **(5.4.2.3.3-1)**

$k_{hc} := 1.56 - 0.008 \cdot RH = 0.96$ **(5.4.2.3.2-3)** $\qquad \psi_{tf.ti} := 1.9 \cdot k_s \cdot k_{hc} \cdot k_f \cdot k_{td} \cdot 3^{-0.118} = 1.589$ **(5.4.2.3.2-1)**

$K_{id} := \frac{1}{1 + \frac{E_{ps}}{E_{ci}} \cdot \frac{A_{ps}}{Area} \cdot \left(1 + \frac{Area \cdot e_2 \cdot e_2}{I}\right) \cdot \left(1 + 0.7 \cdot \psi_{tf.ti}\right)} = 0.995$ **(5.9.5.4.2a-2)**

$K_{id.ss} := \frac{1}{1 + \frac{E_{ps.ss}}{E_{ci}} \cdot \frac{A_{ps.ss}}{Area} \cdot \left(1 + \frac{Area \cdot e_2 \cdot e_2}{I}\right) \cdot \left(1 + 0.7 \cdot \psi_{tf.ti}\right)} = 0.995$ **(5.9.5.4.2a-2)**

$\Delta f_{pSR} := \varepsilon_{sh} \cdot E_{ps} \cdot K_{id} = -13.236 \cdot ksi$ $\Delta f_{pSR.ss} := \varepsilon_{sh} \cdot E_{ps} \cdot K_{id.ss} = -13.232 \cdot ksi$

(5.9.5.4.2a-1)

$\Delta f_{pCR} := \frac{E_{ps}}{E_{ci}} \cdot f_{cgp} \cdot \psi_{tf.ti} \cdot K_{id} = -7.192 \cdot ksi$ $\Delta f_{pCR.ss} := \frac{E_{ps}}{E_{ci}} \cdot f_{cgp} \cdot \psi_{tf.ti} \cdot K_{id.ss} = -7.19 \cdot ksi$

(5.9.5.4.2b-1)

Stress Relaxation:

$f_{py} := 0.94 \cdot f_u = 264.234 \cdot ksi$ $K_L := 30$

$f_{py.ss} := 0.94 \cdot f_{u.ss} = 227.01 \cdot ksi$

$f_{pi} := f_2 + \Delta f_{pES} = 171.54 \cdot ksi > 0.55 \cdot f_{py} = 145.329 \cdot ksi$

$f_{pi.ss} := f_{2.ss} + \Delta f_{pES.ss} = 128.719 \cdot ksi > 0.55 \cdot f_{py.ss} = 124.855 \cdot ksi$

$f_{pt} := f_{pi}$ $f_{pt.ss} := f_{pi.ss}$

$\Delta f_{pRE} := \frac{-f_{pt}}{K_L} \cdot \left(\frac{f_{pt}}{f_{py}} - 0.55 \right) = -0.567 \cdot ksi$ **(5.9.5.4.2c-1)**

$\Delta f_{pRE.ss} := \frac{-f_{pt.ss}}{K_L} \cdot \left(\frac{f_{pt.ss}}{f_{py.ss}} - 0.55 \right) = -0.073 \cdot ksi$ **(5.9.5.4.2c-1)**

Total Stress Losses Refined Method - Conventional Steel:

$Losses := \Delta f_{pES} + \Delta f_{pSR} + \Delta f_{pCR} + \Delta f_{pRE} + \Delta f_{ANC}$ $Losses = -25.541 \cdot ksi$

$f_s := f_2 + Losses = 150.546 \cdot ksi$

$F_{se} := f_s \cdot A_{ps}$ $F_{se} = 17.313 \cdot kip$

$\varepsilon_{se} := \frac{Losses}{E_{ps}}$ $\varepsilon_{se} = -8.6875 \times 10^{-4}$

Total Stress Losses Refined Method - Stainless Steel:

$$Losses_{ss} := \Delta f_{pES.ss} + \Delta f_{pSR.ss} + \Delta f_{pCR.ss} + \Delta f_{pRE.ss} + \Delta f_{ANC}$$

$Losses_{ss} = -24.129 \cdot ksi$

$f_{s.ss} := f_{2.ss} + Losses_{ss} = 108.224 \cdot ksi$

$F_{se.ss} := f_{s.ss} \cdot A_{ps.ss}$ $F_{se.ss} = 16.558 \cdot kip$

$\varepsilon_{se.ss} := \frac{Losses_{ss}}{E_{ps.ss}}$ $\varepsilon_{se.ss} = -1.0268 \times 10^{-3}$

- **AASHTO Lump-Sum Method.**

Shrinkage, Creep, and Stress Relaxation Losses:

$\Delta f_{pR} := 2.4ksi$ $\gamma_h := 1.7 - 0.01 \cdot RH = 0.95$ **(5.9.5.3-2)**

$\gamma_{st} := k_f$ **(5.9.5.3-3)**

$$\Delta f_{pLT} := -\left(10 \cdot \frac{f_{pi} \cdot A_{ps}}{Area} \cdot \gamma_h \cdot \gamma_{st} + 12 \cdot \gamma_h \cdot \gamma_{st} \cdot ksi + \Delta f_{pR}\right) \quad \textbf{(5.9.5.3-1)}$$

$$\Delta f_{pLT.ss} := -\left(10 \cdot \frac{f_{pi.ss} \cdot A_{ps.ss}}{Area} \cdot \gamma_h \cdot \gamma_{st} + 12 \cdot \gamma_h \cdot \gamma_{st} \cdot ksi + \Delta f_{pR}\right) \quad \textbf{(5.9.5.3-1)}$$

Total Stress Losses Lump-Sum Method - Conventional Steel:

$Losses_{LS} := \Delta f_{pES} + \Delta f_{pLT}$ $Losses_{LS} = -19.035 \cdot ksi$

$f_{s.LS} := f_2 + Losses_{LS} = 157.052 \cdot ksi$

$F_{se.LS} := f_{s.LS} \cdot A_{ps}$ $F_{se.LS} = 18.061 \cdot kip$

$\varepsilon_{se.LS} := \frac{Losses_{LS}}{E_{ps}}$ $\varepsilon_{se.LS} = -6.4745 \times 10^{-4}$

Total Stress Losses Lump-Sum Method - Stainless Steel:

$Losses_{LS.ss} := \Delta f_{pES.ss} + \Delta f_{pLT.ss}$ $\quad Losses_{LS.ss} = -18.122 \cdot ksi$

$f_{s.LS.ss} := f_{2.ss} + Losses_{LS.ss} = 114.231 \cdot ksi$

$F_{se.LS.ss} := f_{s.LS.ss} \cdot A_{ps.ss}$ $\quad F_{se.LS.ss} = 17.477 \cdot kip$

$\varepsilon_{se.LS.ss} := \dfrac{Losses_{LS.ss}}{E_{ps.ss}}$ $\quad \varepsilon_{se.LS.ss} = -7.7113 \times 10^{-4}$

APPENDIX R: Individual Prestress Losses

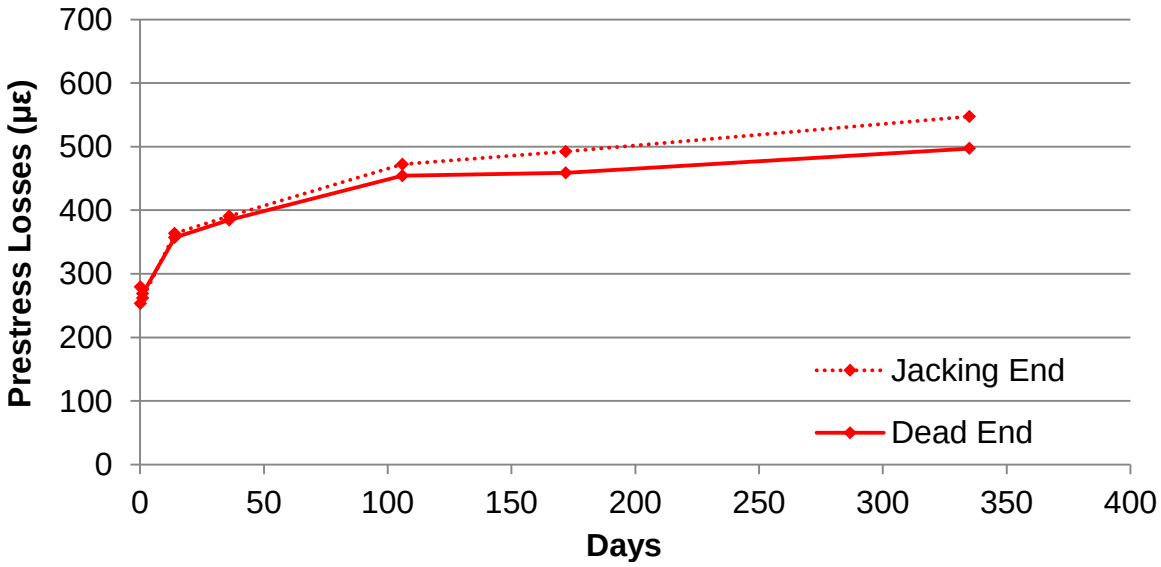

Figure R.1 Prestress losses of pile 1080 #1. Wires 3 and 4 correspond to vibrating wire sensors closer to the jacking end of the pile.

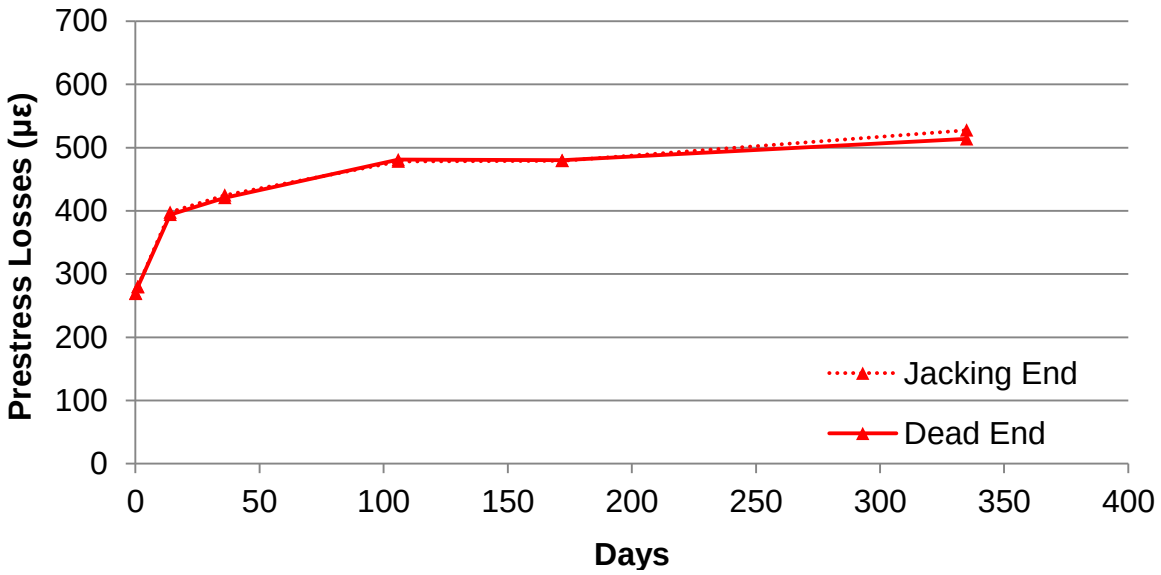

Figure R.2 Prestress losses of pile 1080 #2. Wires 3 and 4 correspond to vibrating wire sensors closer to the jacking end of the pile.

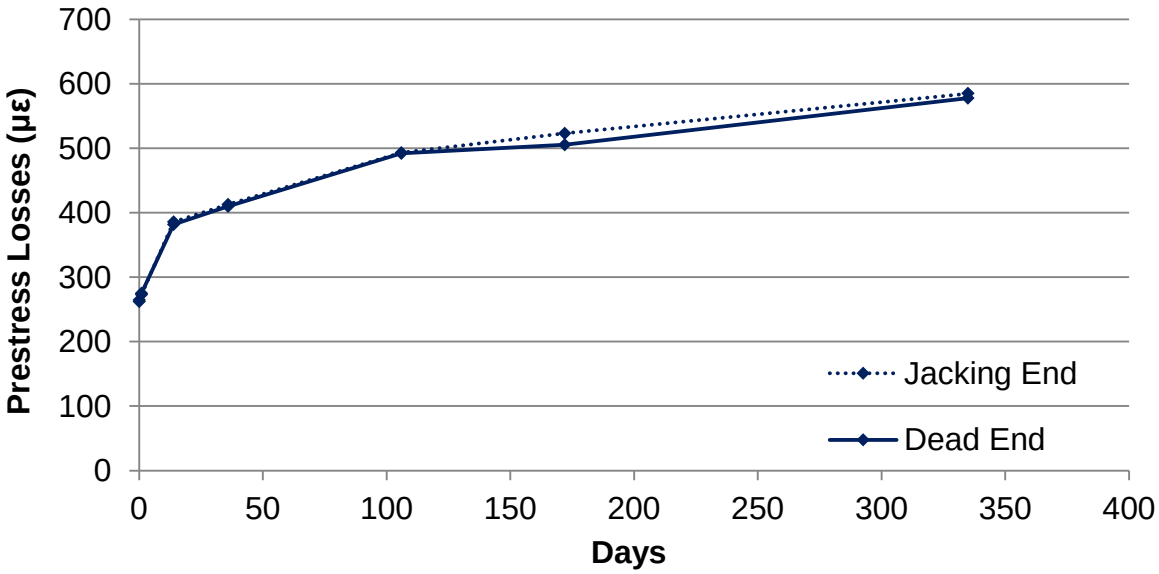

Figure R.3 Prestress losses of pile HSSS 2205 #1. Wires 3 and 4 correspond to vibrating wire sensors closer to the jacking end of the pile.

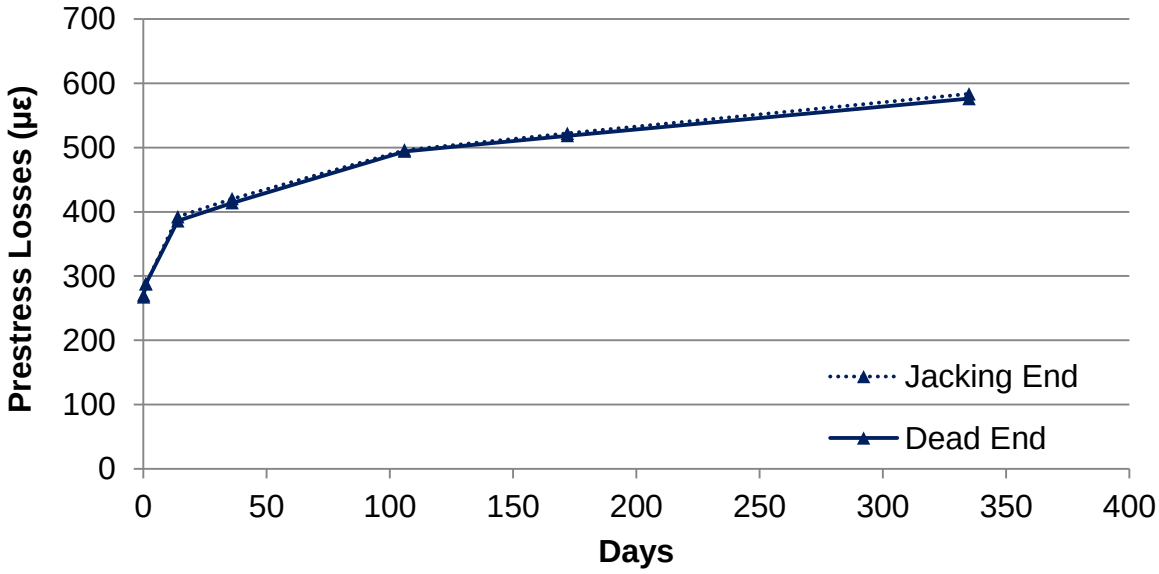

Figure R.4 Prestress losses of pile HSSS 2205 #2. Wires 3 and 4 correspond to vibrating wire sensors closer to the jacking end of the pile.

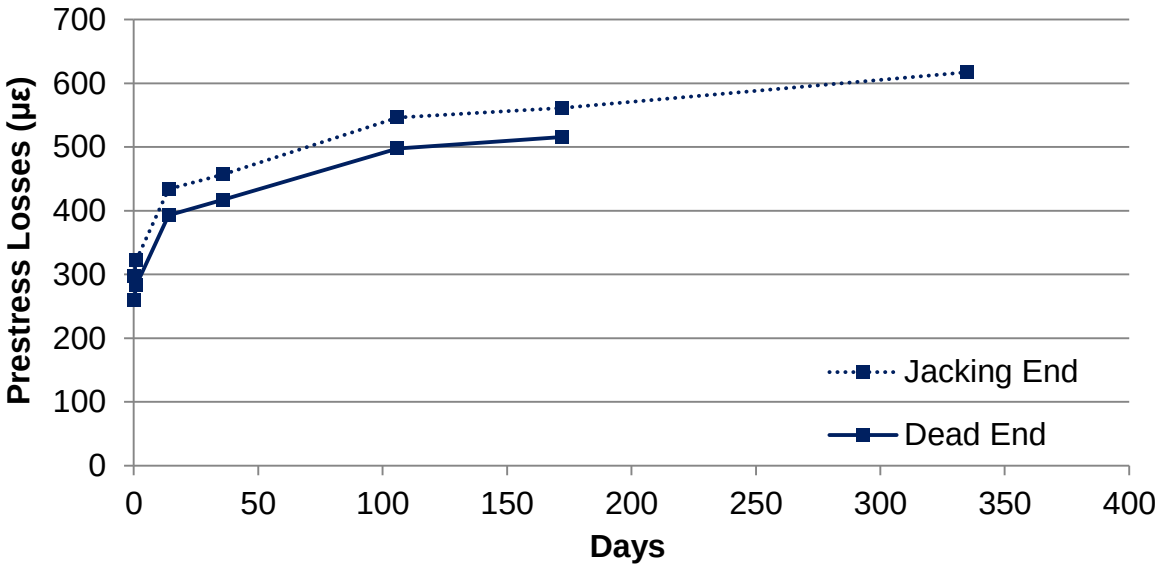

Figure R.5 Prestress losses of pile HSSS 2205 #3. Wires 3 and 4 correspond to vibrating wire sensors closer to the jacking end of the pile.

APPENDIX S: Concrete Surface Strain Profiles

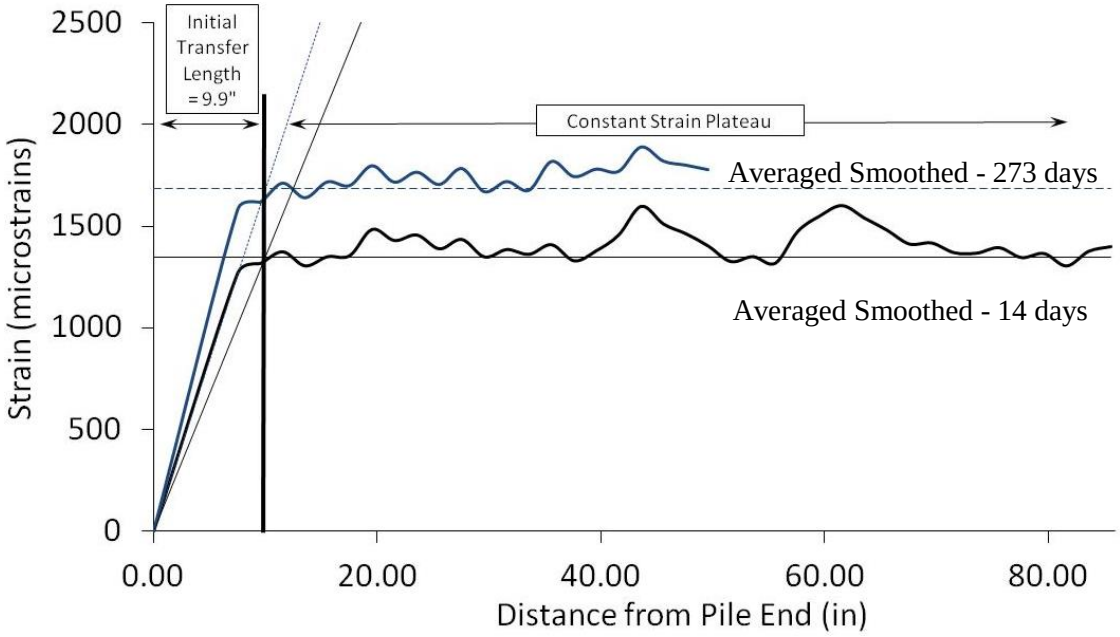

Figure S.1 Smoothed concrete surface strain profiles of pile 1080 #1, jacking end.

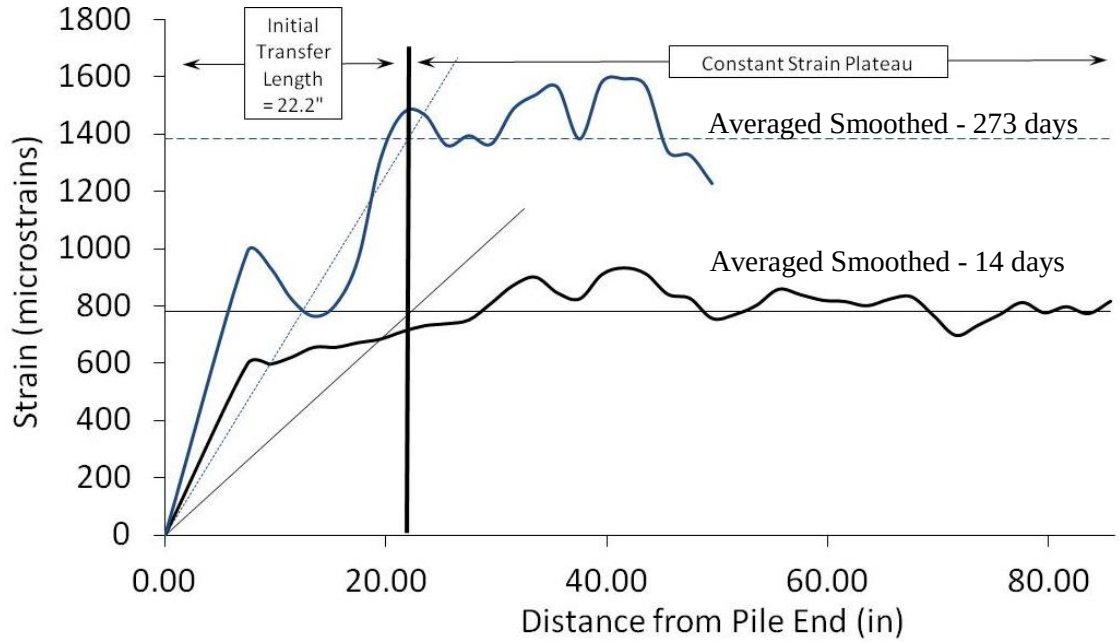

Figure S.2 Smoothed concrete surface strain profiles of pile 1080 #1, dead end.

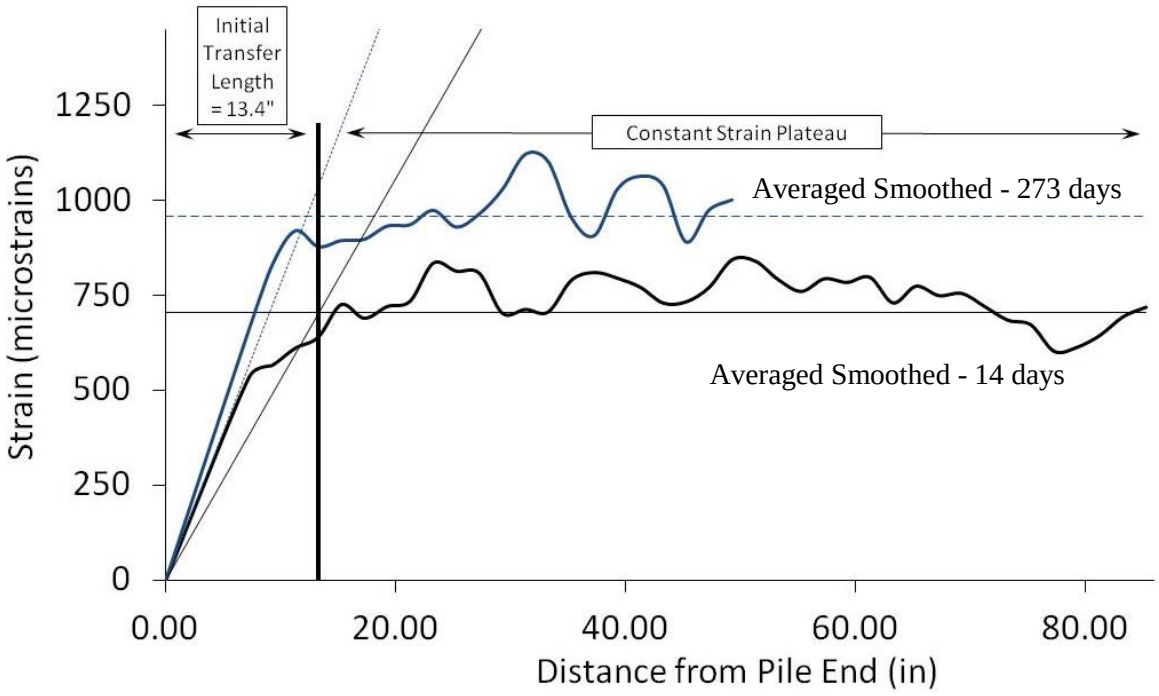

Figure S.3 Smoothed concrete surface strain profiles of pile 1080 #2, jacking end.

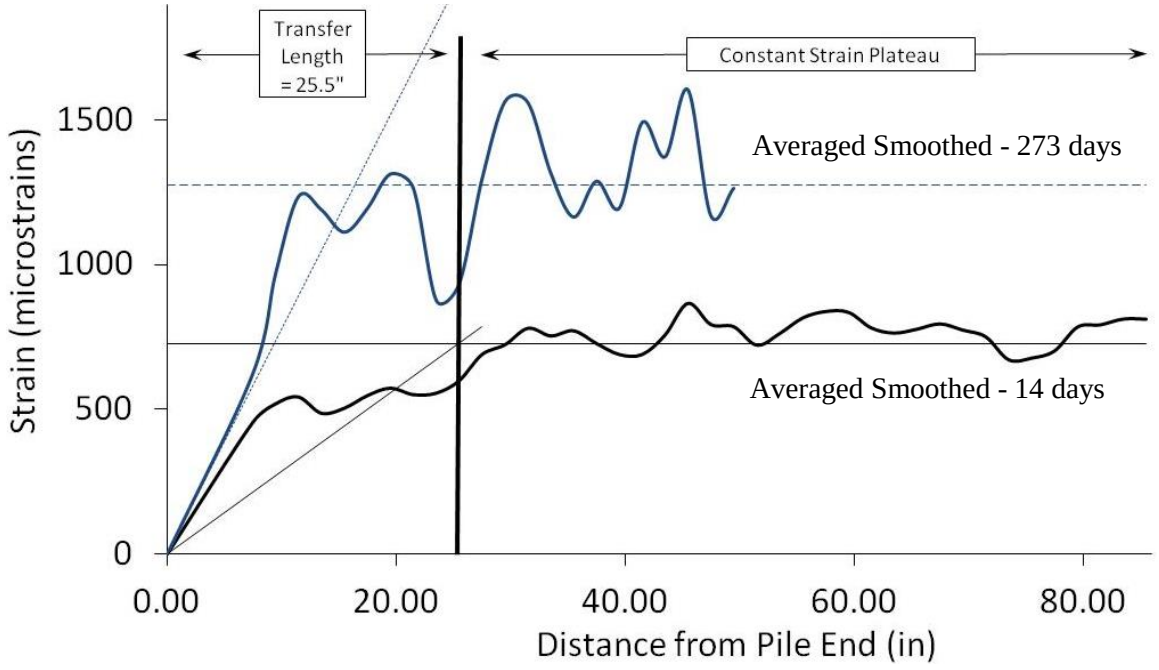

Figure S.4 Smoothed concrete surface strain profiles of pile 1080 #2, dead end.

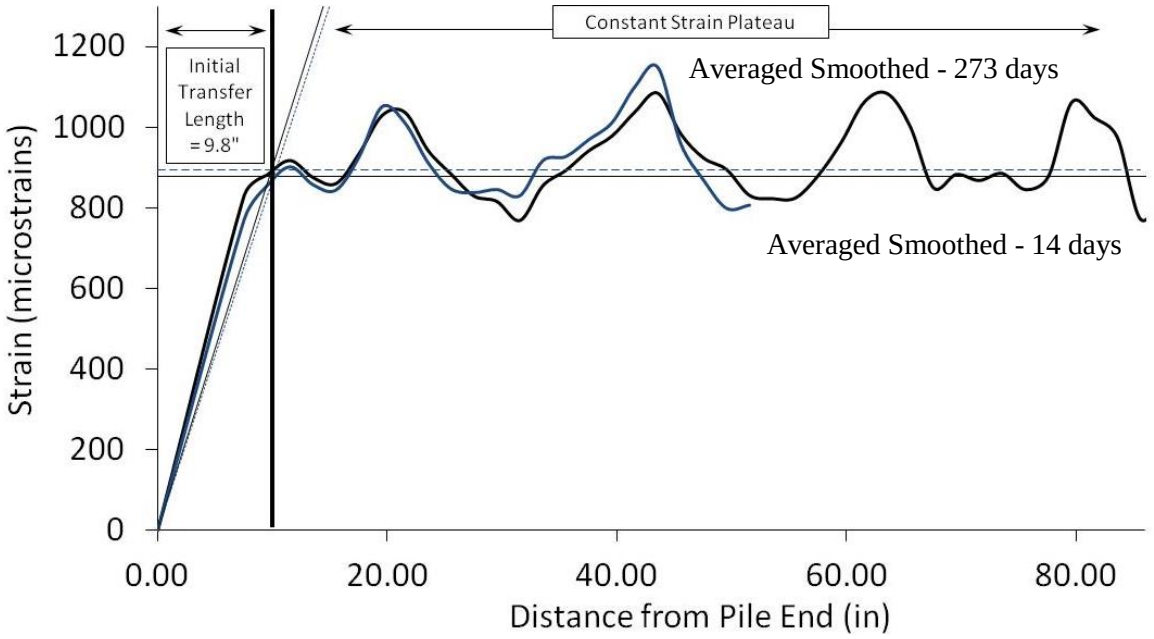

Figure S.5 Smoothed concrete surface strain profiles of pile HSSS 2205 #1, jacking end.

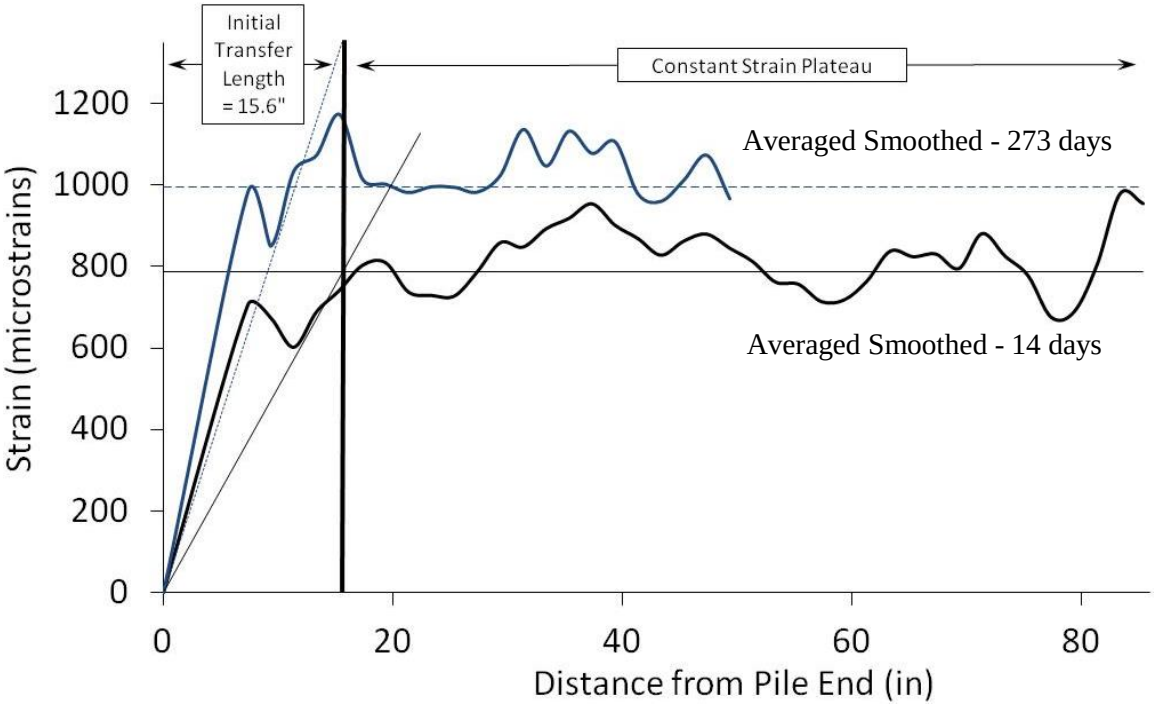

Figure S.6 Smoothed concrete surface strain profiles of pile HSSS 2205 #1, dead end.

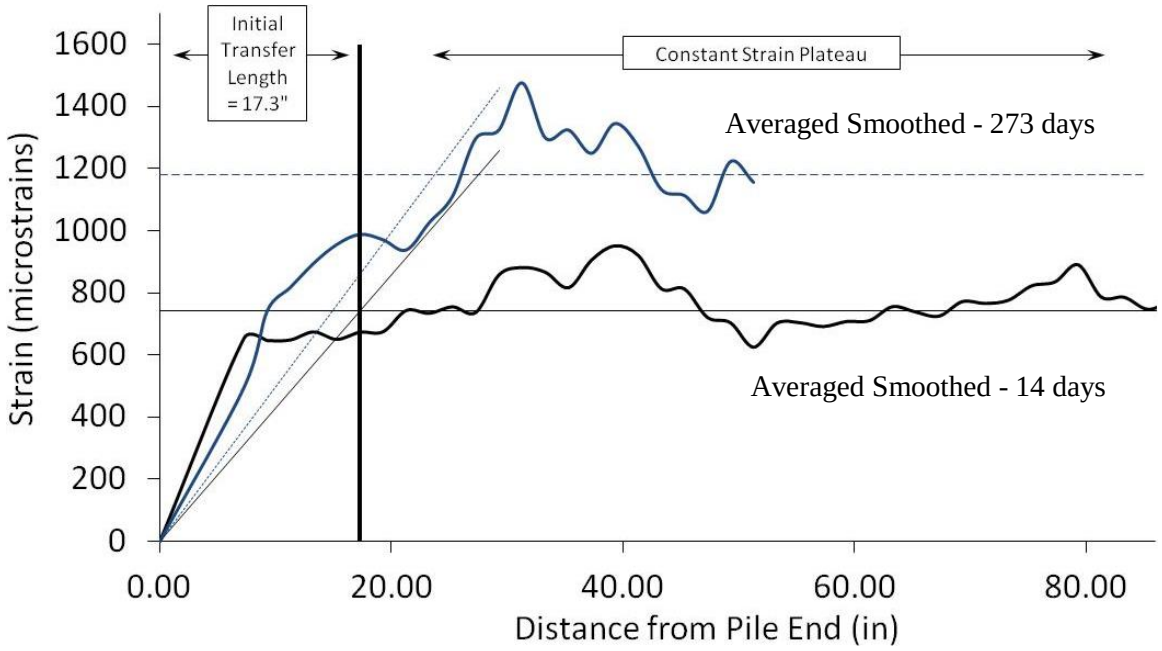

Figure S.7 Smoothed concrete surface strain profiles of pile HSSS 2205 #2, jacking end.

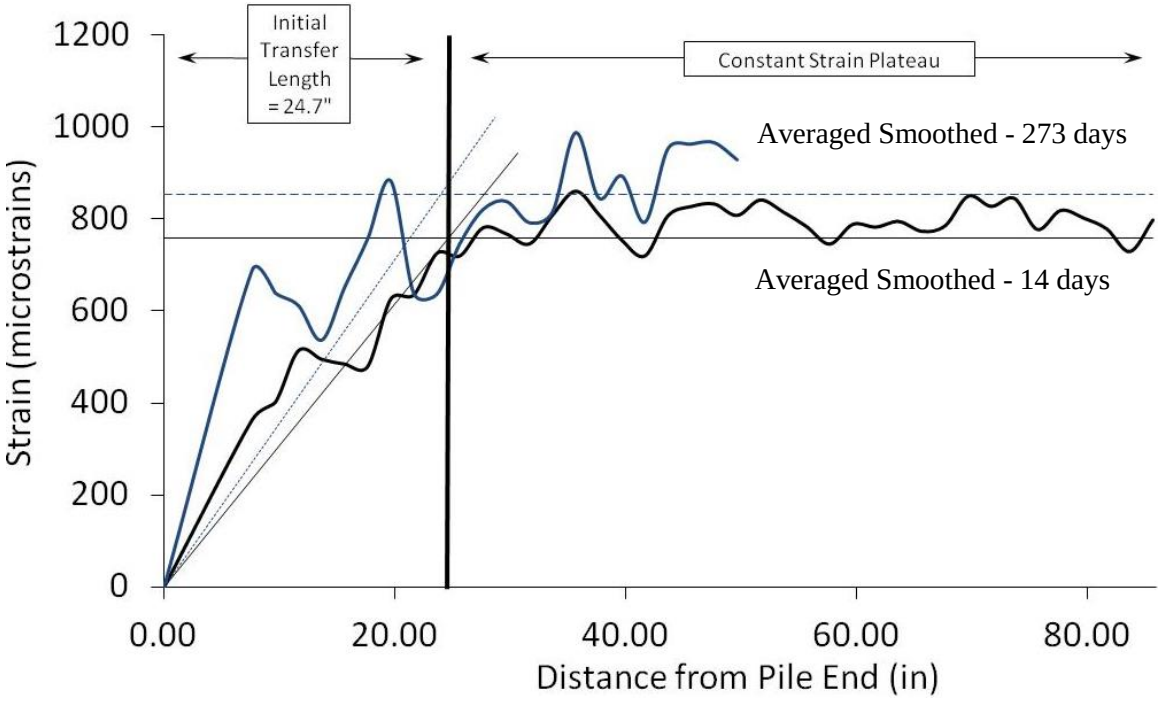

Figure S.8 Smoothed concrete surface strain profiles of pile HSSS 2205 #2, dead end.

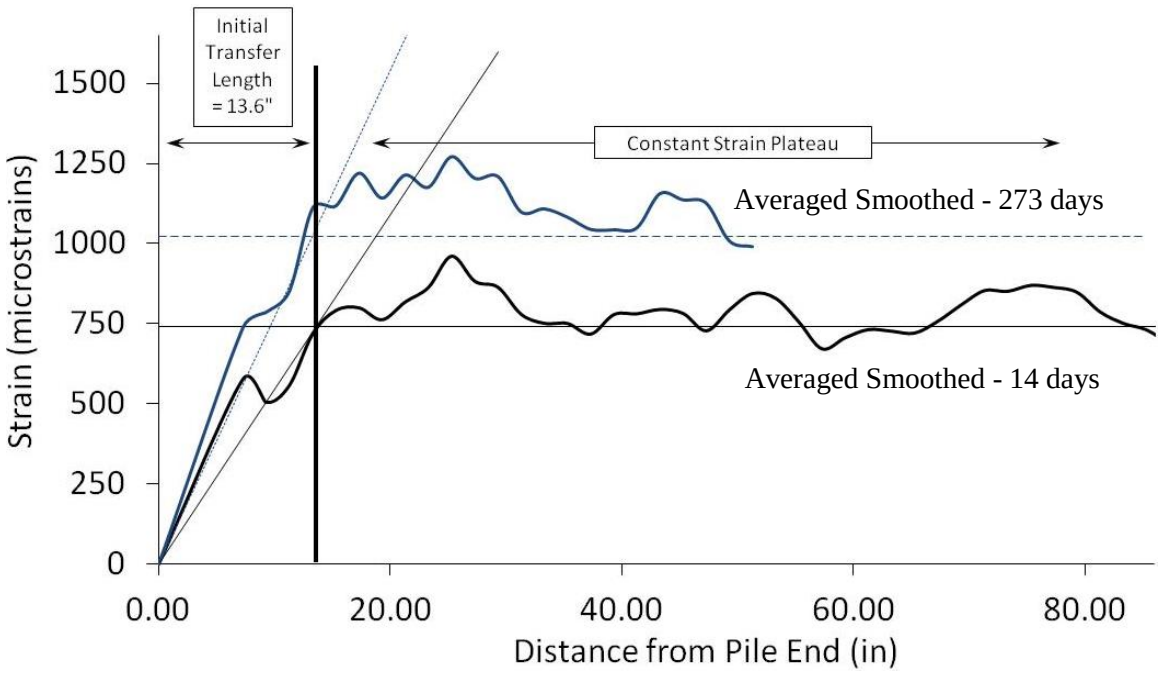

Figure S.9 Smoothed concrete surface strain profiles of pile HSSS 2205 #3, jacking end.

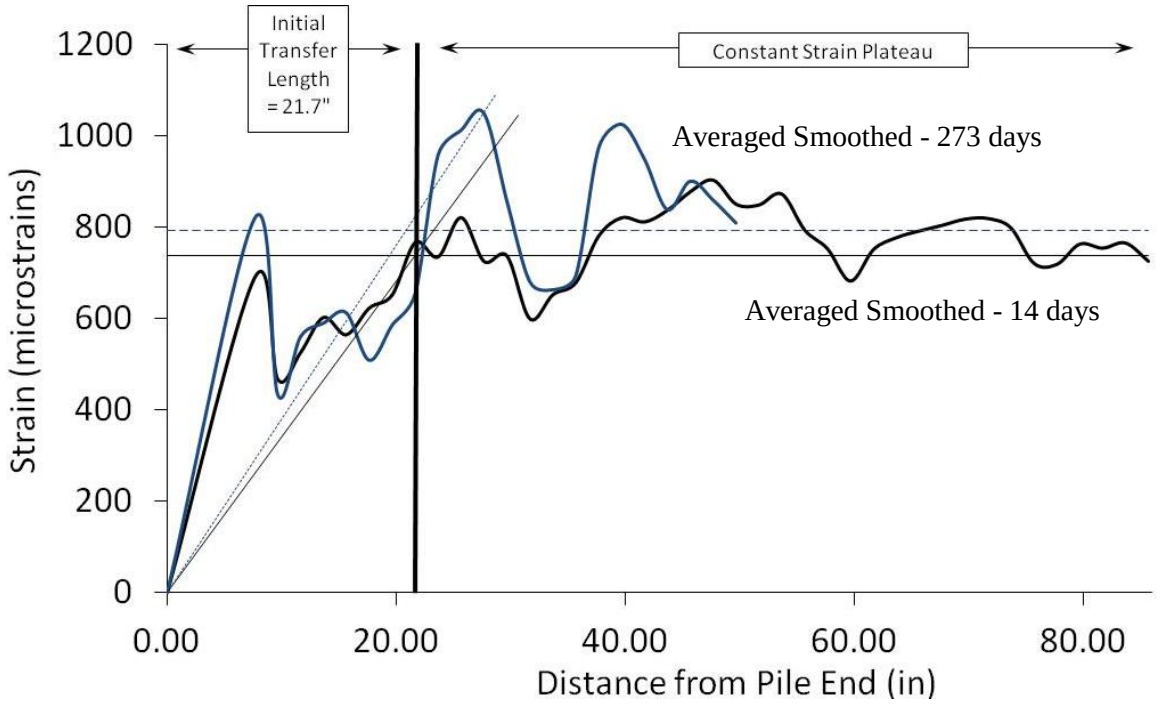

Figure S.10 Smoothed concrete surface strain profiles of pile HSSS 2205 #3, dead end.

APPENDIX T: Development Length Test – Individual Results

- Pile 1080 – Embedment length: 72 inches.

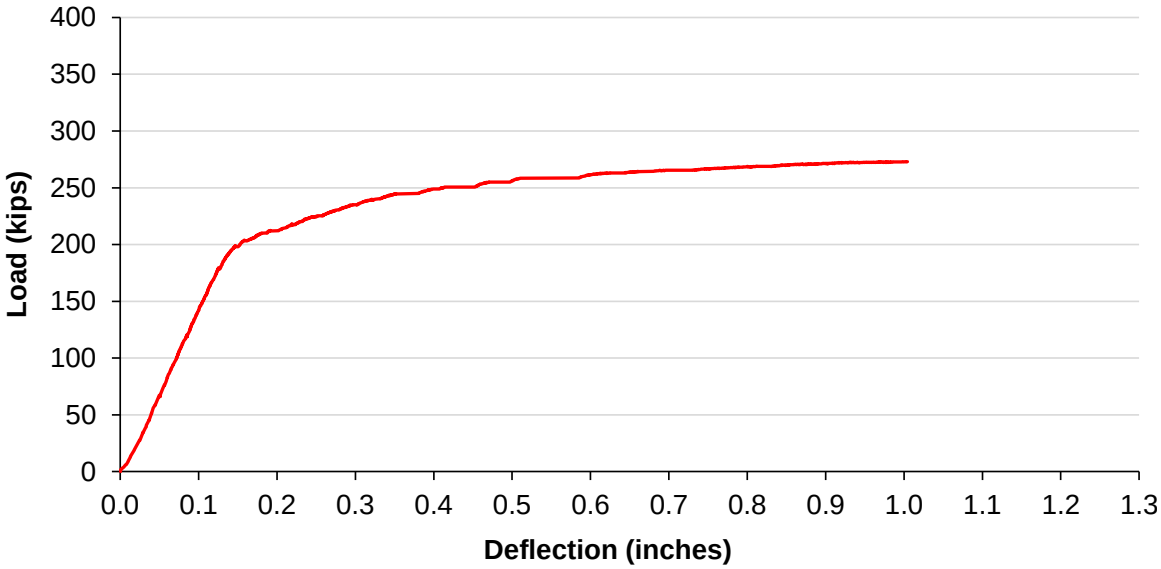

Figure T.1 Load-deflection curve for pile 1080 (l_e = 72-in.).

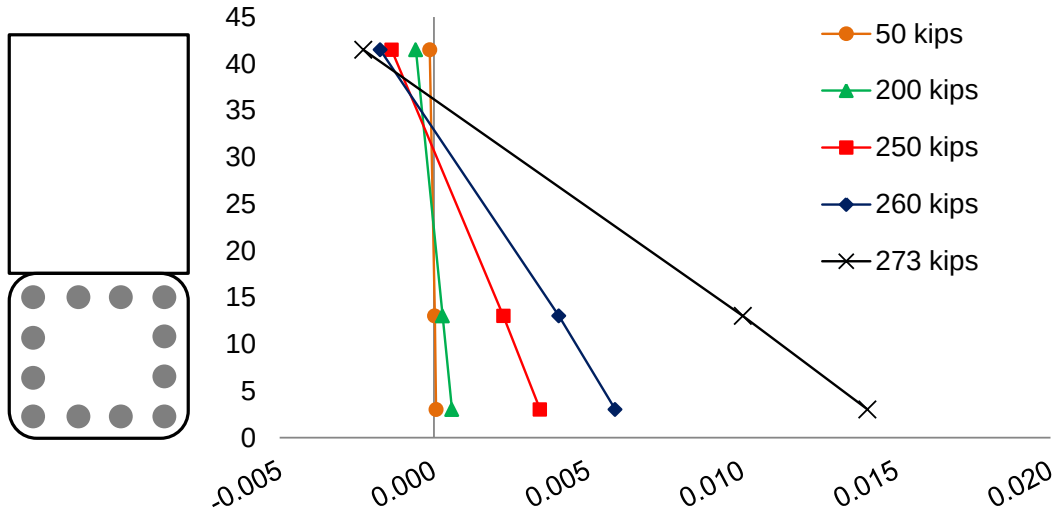

Figure T.2 Strain distribution for pile 1080 (l_e = 72-in.).

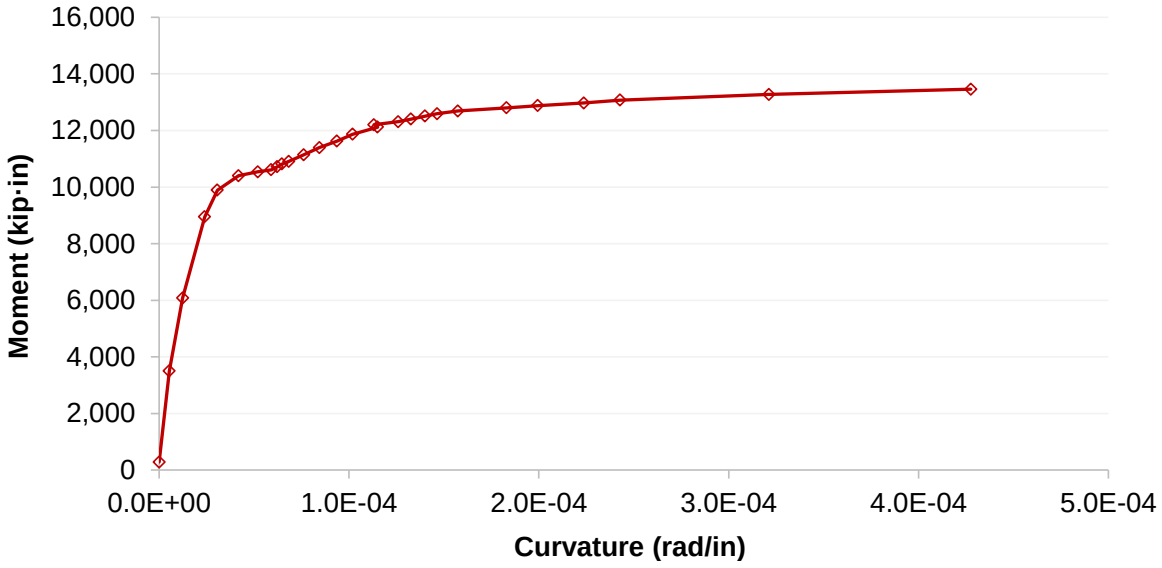

Figure T.3 Moment-curvature curve for pile 1080 (l_e = 72-in.).

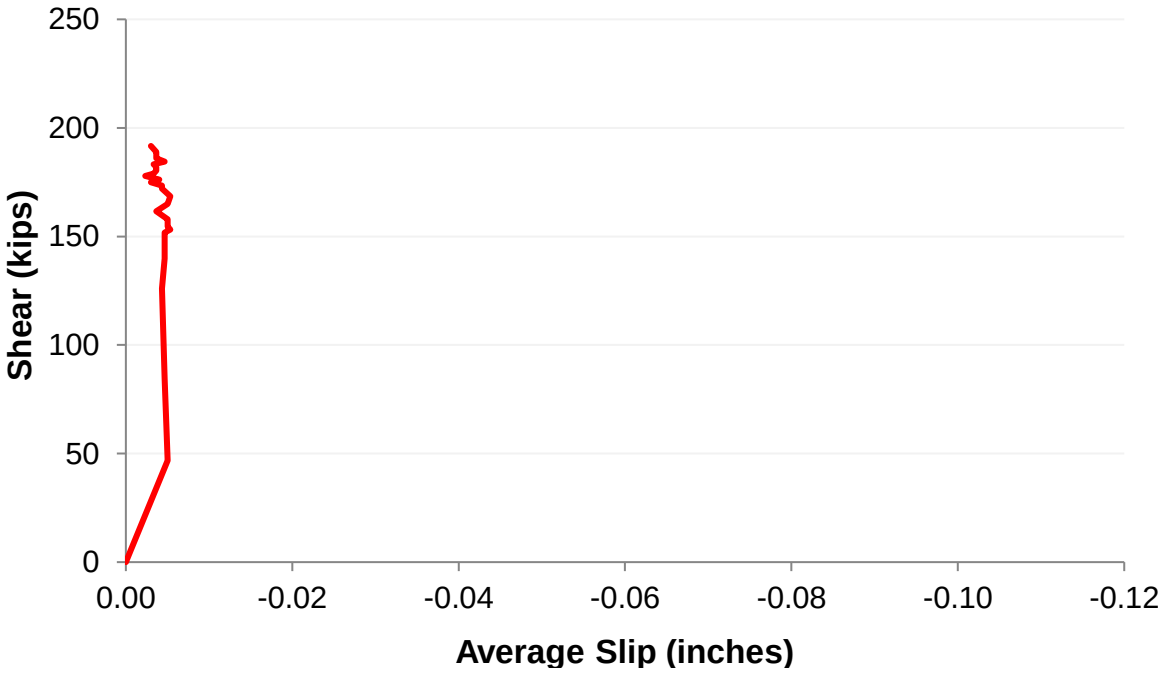

Figure T.4 Strand slip for pile 1080 (l_e = 72-in.).

- Pile 1080 – Embedment length: 61 inches.

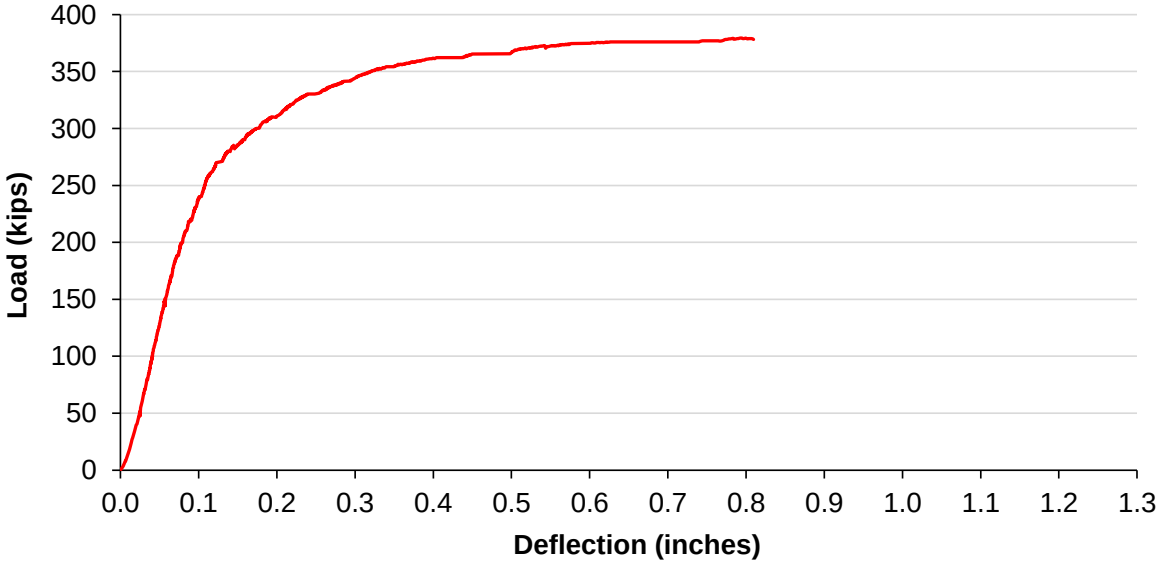

Figure T.5 Load-deflection curve for pile 1080 (l_e = 61-in.).

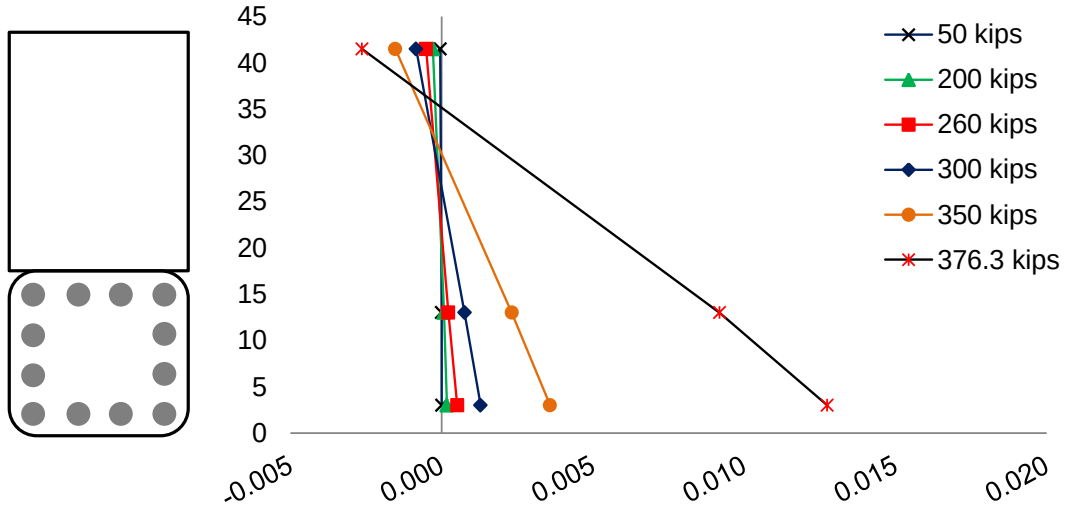

Figure T.6 Strain distribution for pile 1080 (l_e = 61-in.).

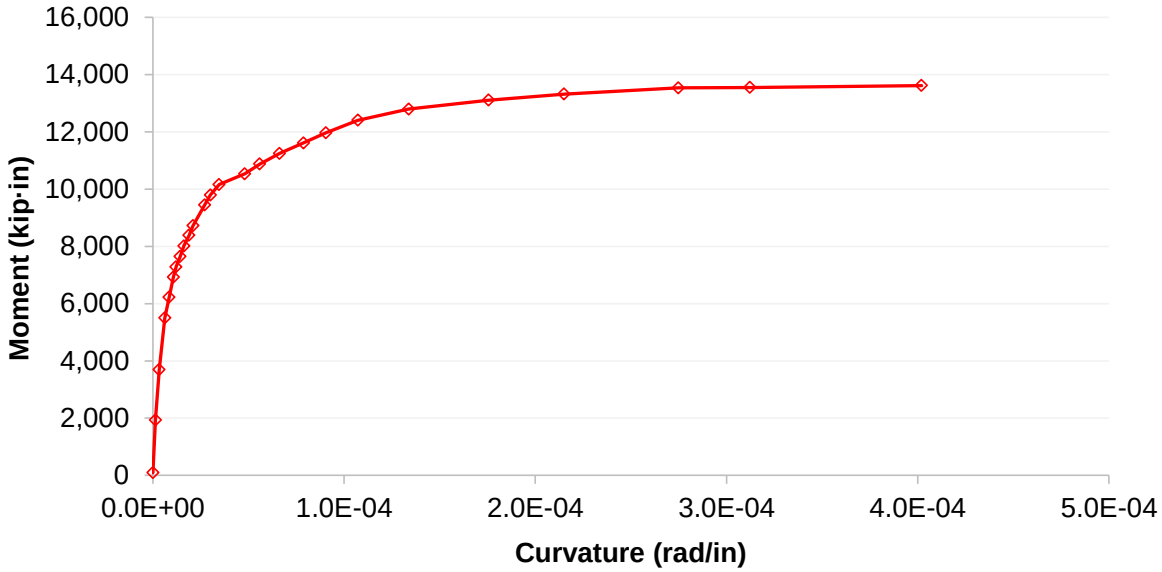

Figure N.7 Moment-curvature curve for pile 1080 (l_e = 61-in.).

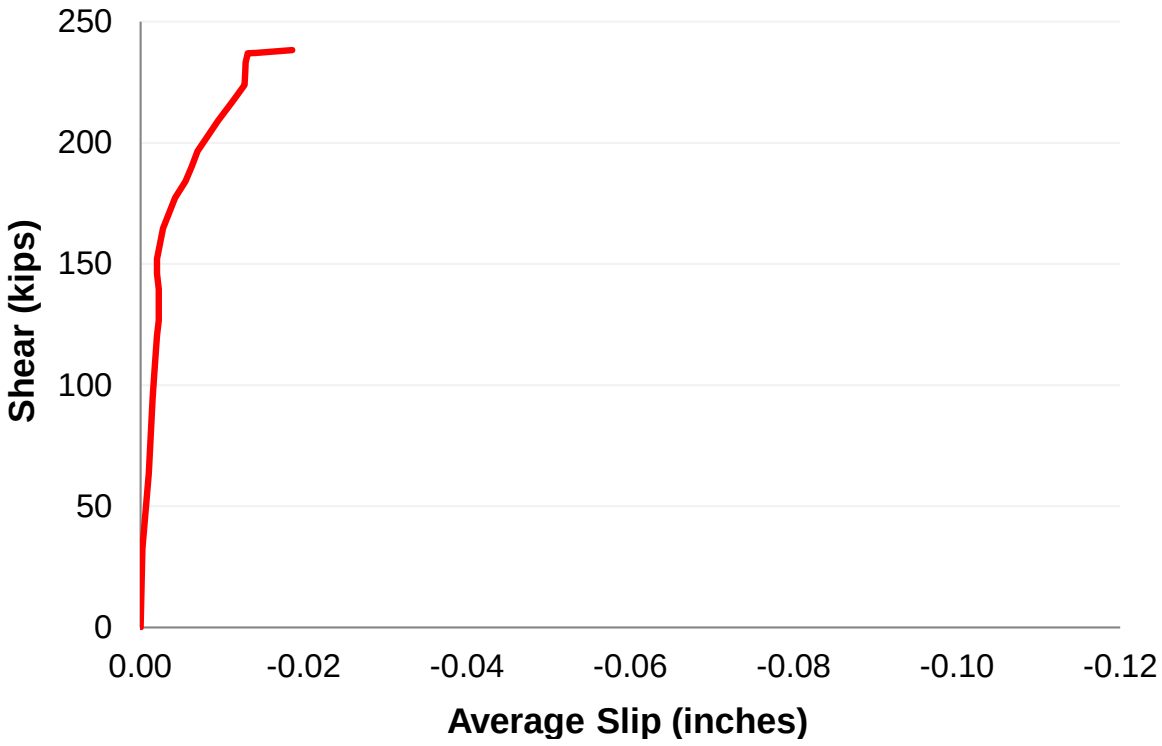

Figure T.8 Strand slip for pile 1080 (l_e = 61-in.).

- Pile 1080 – Embedment length: 57 inches.

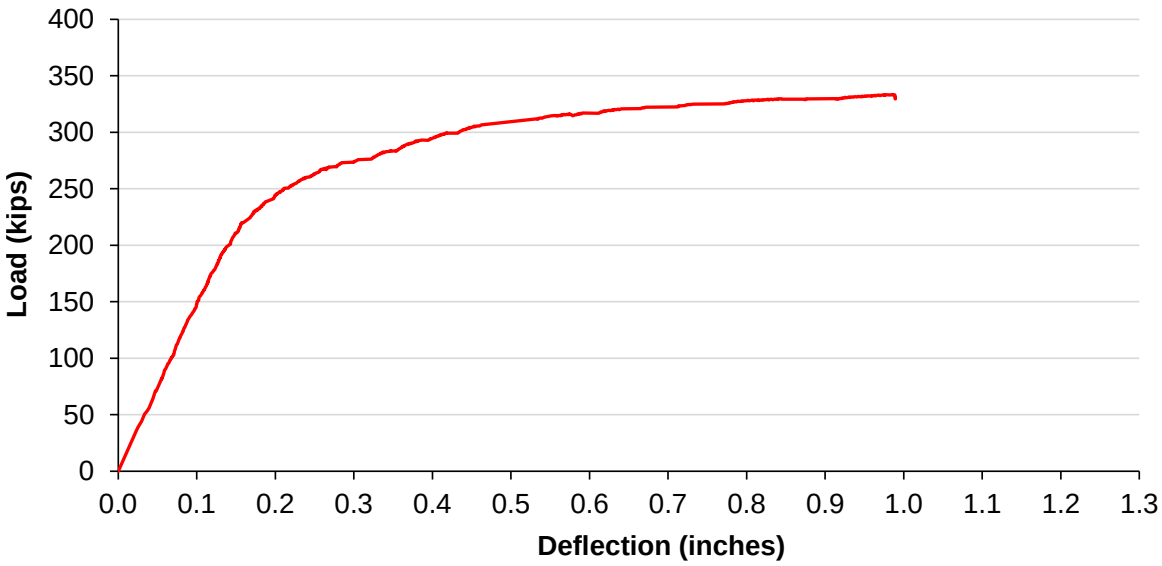

Figure T.9 Load-deflection curve for pile 1080 (l_e = 57-in.).

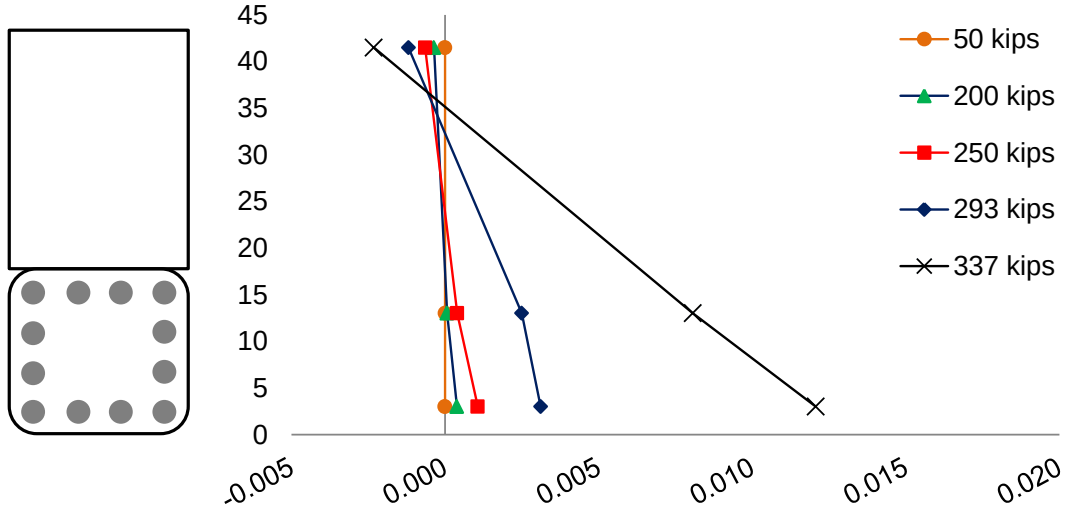

Figure T.10 Strain distribution for pile 1080 (l_e = 57-in.).

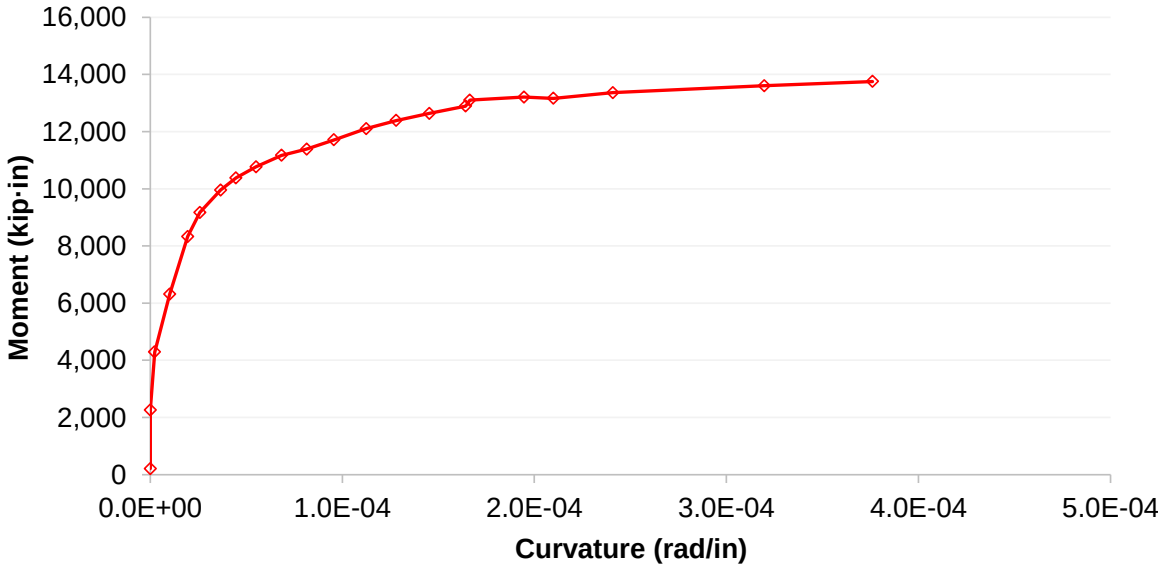

Figure N.11 Moment-curvature curve for pile 1080 (l_e = 57-in.).

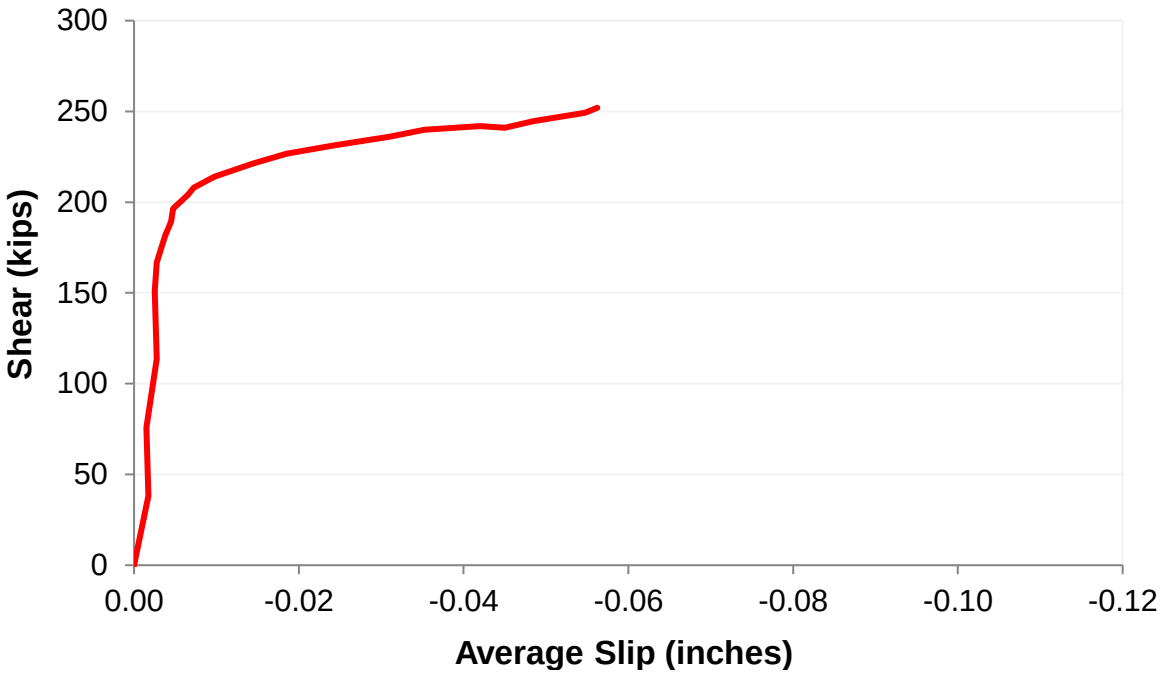

Figure T.12 Strand slip for pile 1080 (l_e = 57-in.).

- Pile 1080 – Embedment length: 53.5 inches.

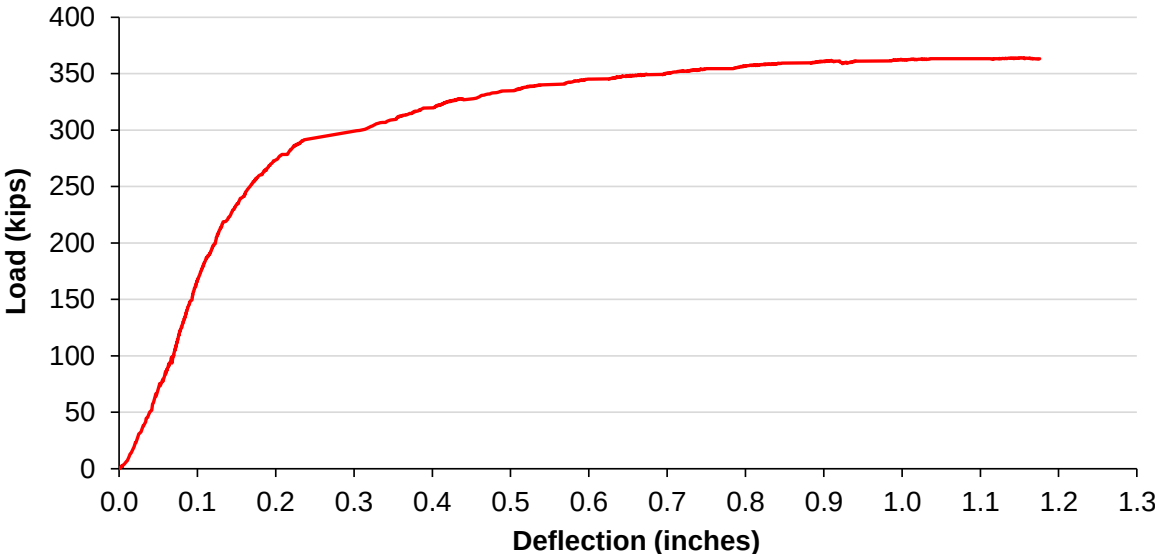

Figure T.13 Load-deflection curve for pile 1080 (l_e = 53.5-in.).

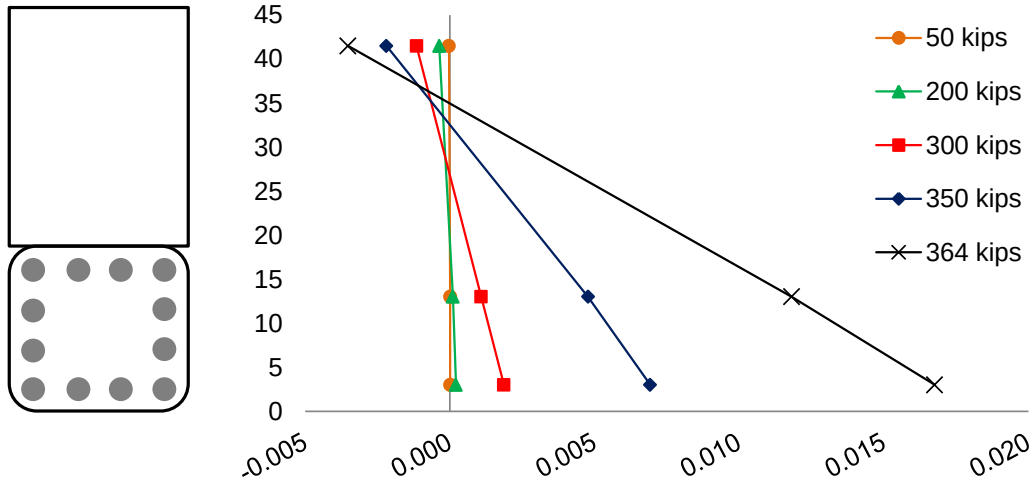

Figure T.14 Strain distribution for pile 1080 (l_e = 53.5-in.).

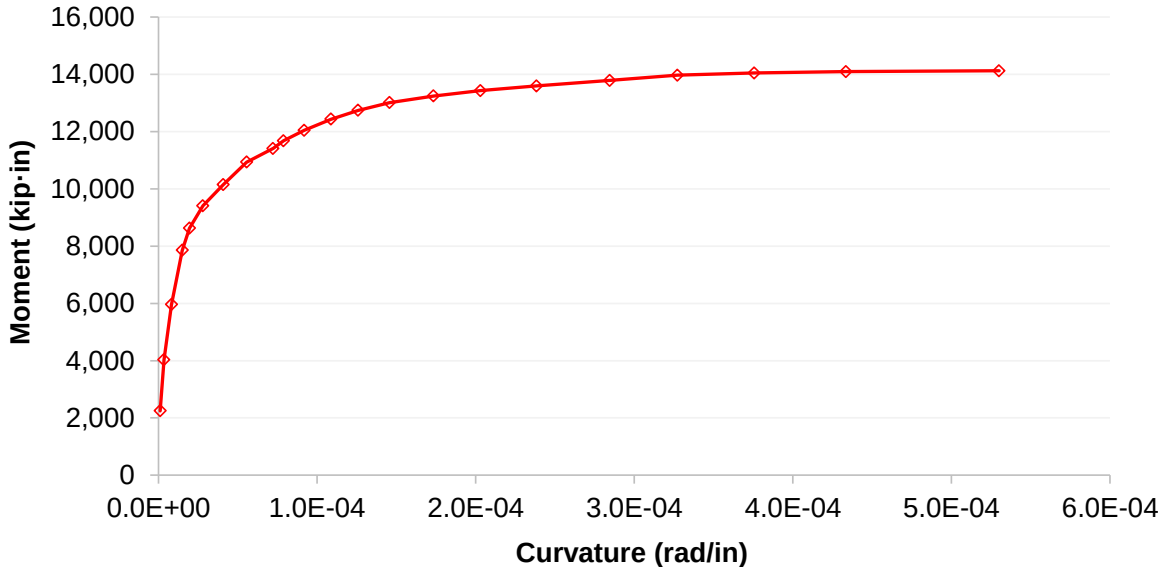

Figure T.15 Moment-curvature curve for pile 1080 (l_e = 53.5-in.).

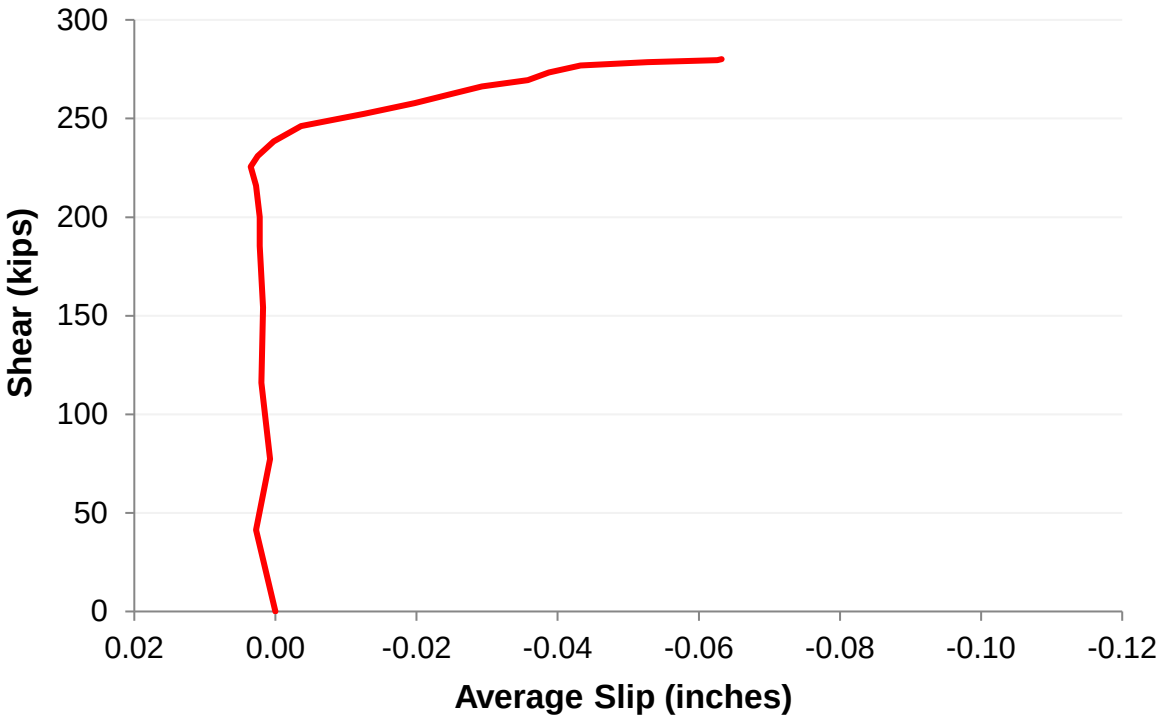

Figure T.16 Strand slip for pile 1080 (l_e = 53.5-in.).

- Pile HSSS 2205 – Embedment length: 79.75 inches.

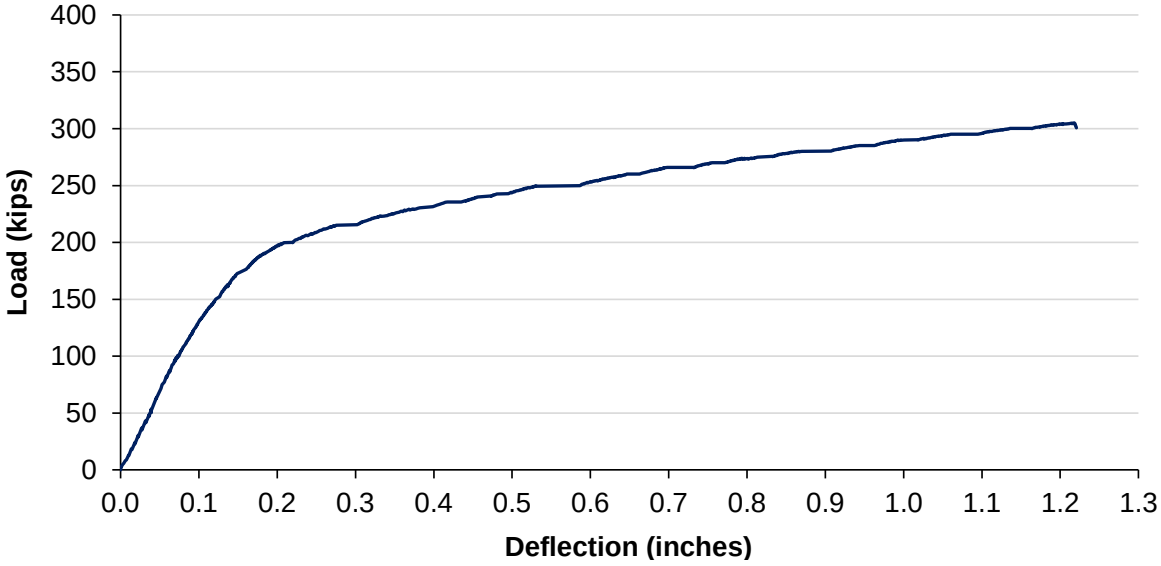

Figure T.17 Load-deflection curve for pile HSSS 2205 (l_e = 79.75-in.).

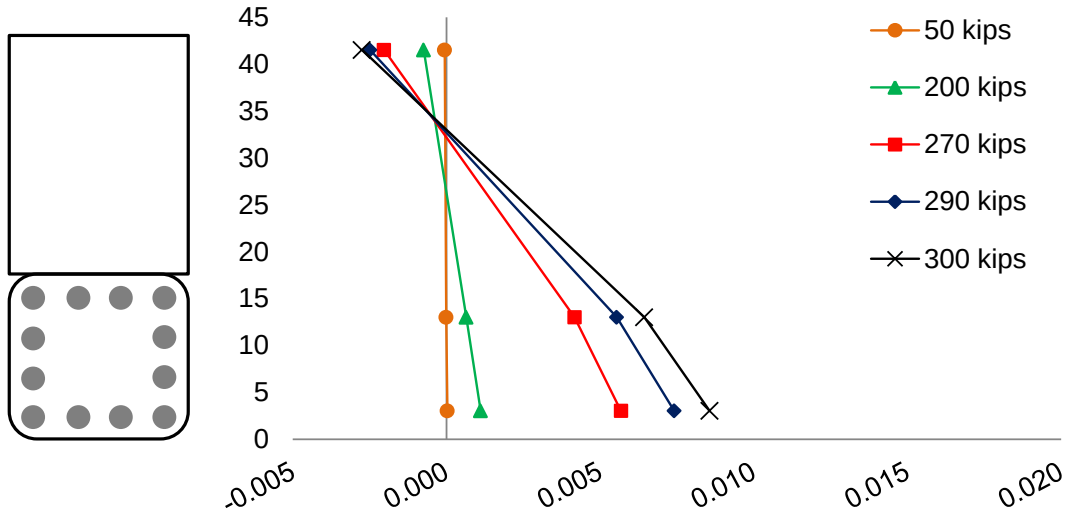

Figure T.18 Strain distribution for pile HSSS 2205 (l_e = 79.75-in.).

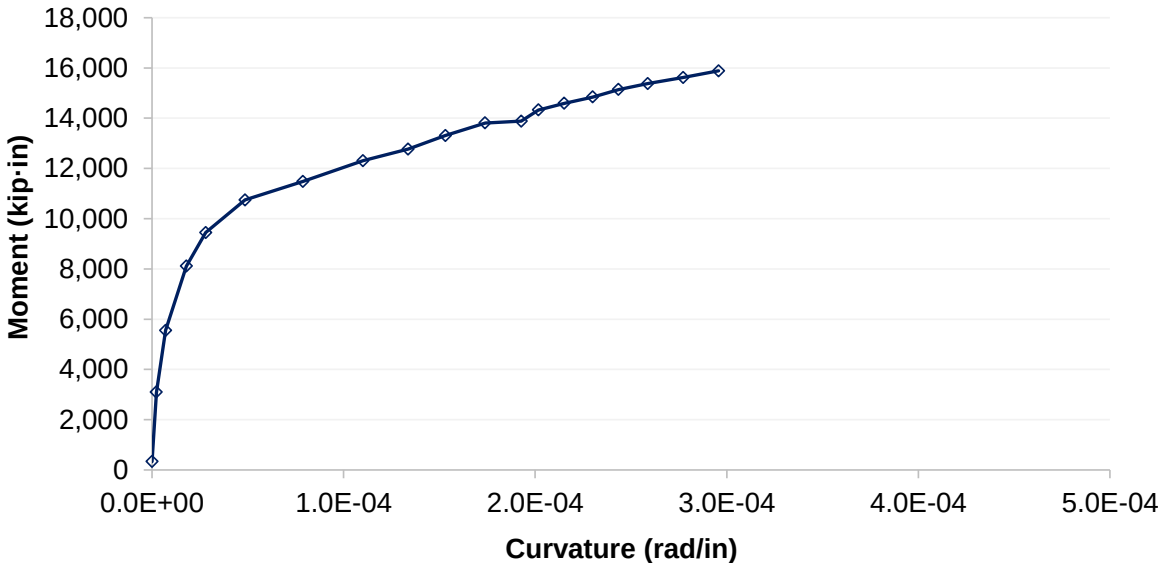

Figure T.19 Moment-curvature curve for pile HSSS 2205 (l_e = 79.75-in.).

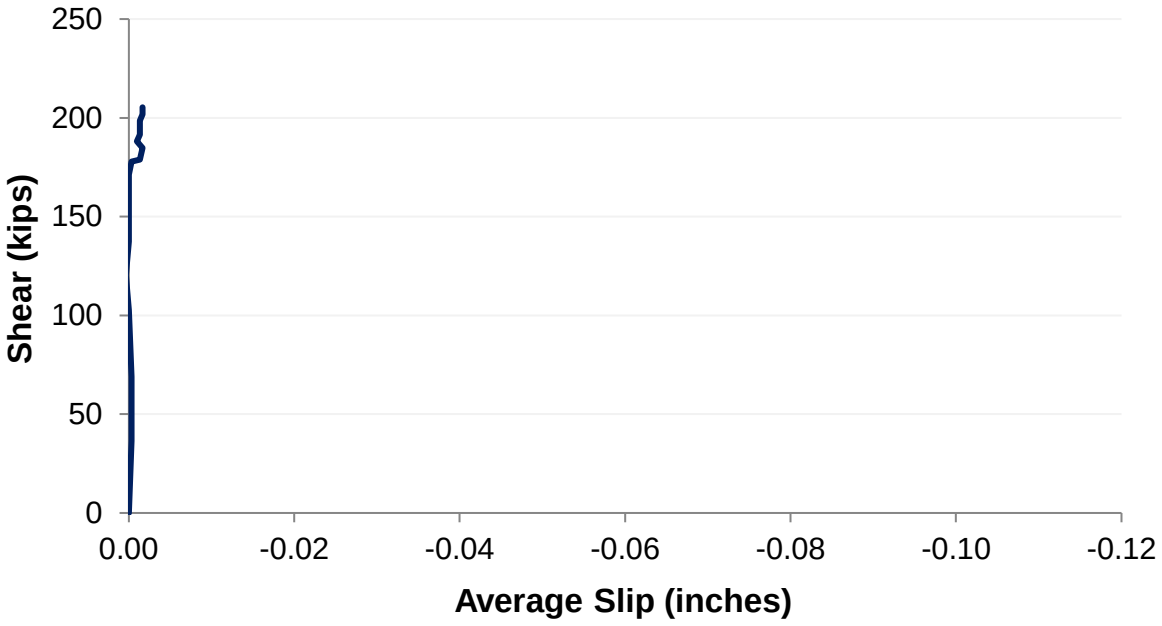

Figure T.20 Strand slip for pile HSSS 2205 (l_e = 79.75-in.).

- Pile HSSS 2205 – Embedment length: 69 inches.

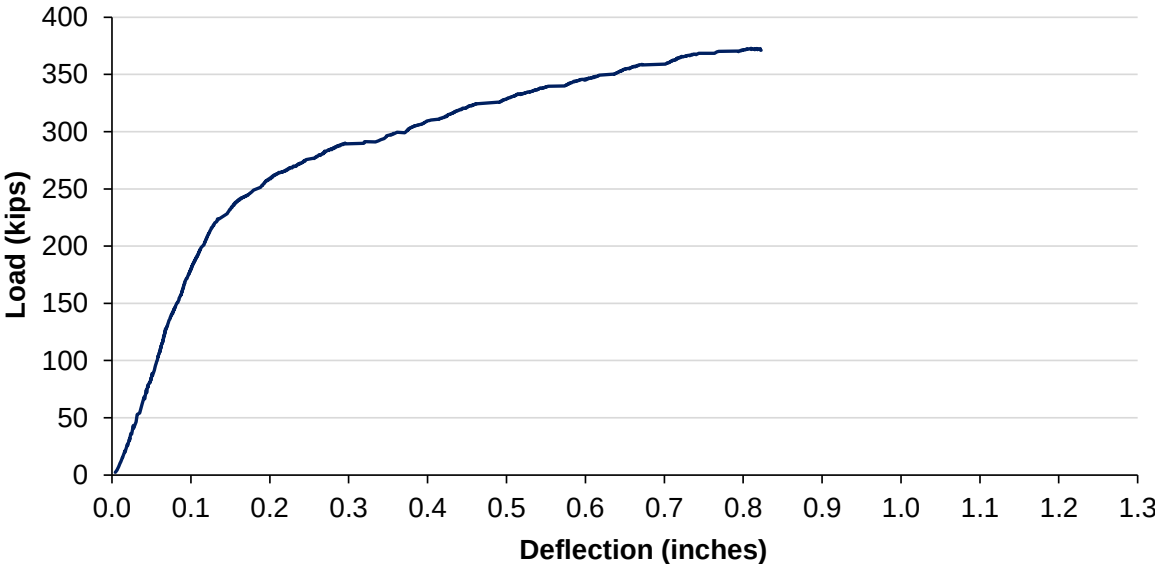

Figure T.21 Load-deflection curve for pile HSSS 2205 (l_e = 69-in.).

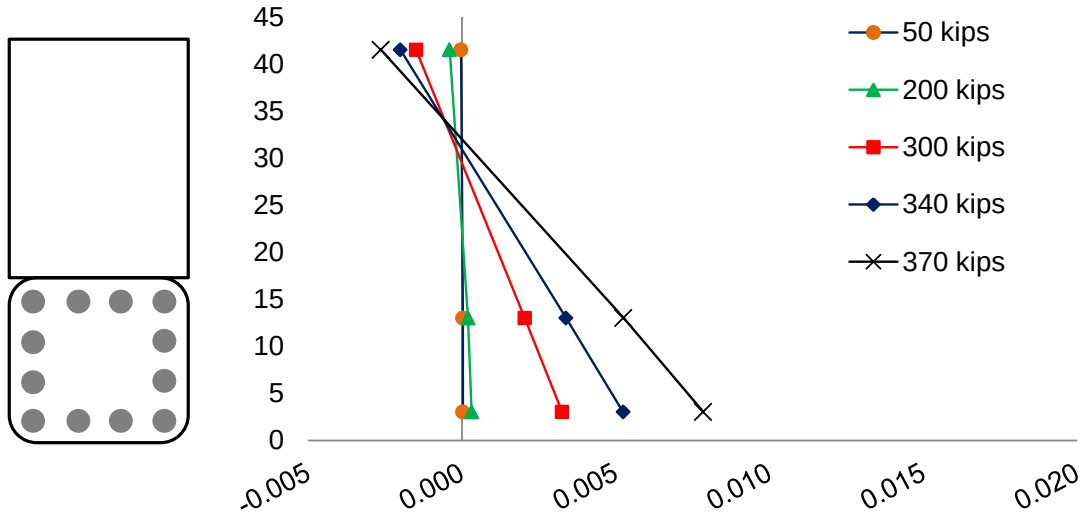

Figure T.22 Strain distribution for pile HSSS 2205 (l_e = 69-in.).

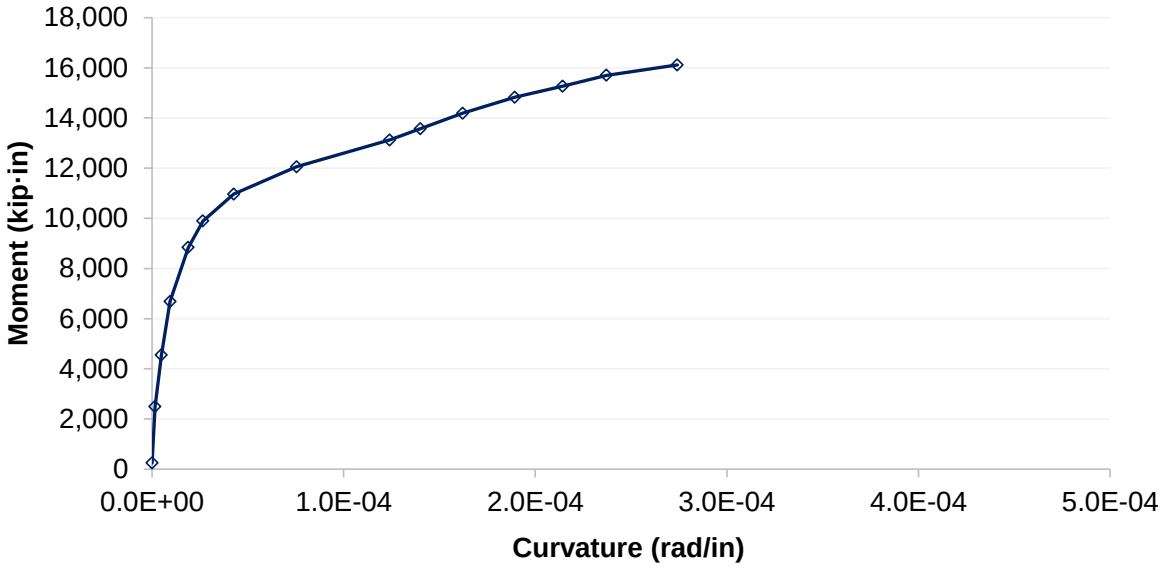

Figure T.23 Moment-curvature curve for pile HSSS 2205 (l_e = 69-in.).

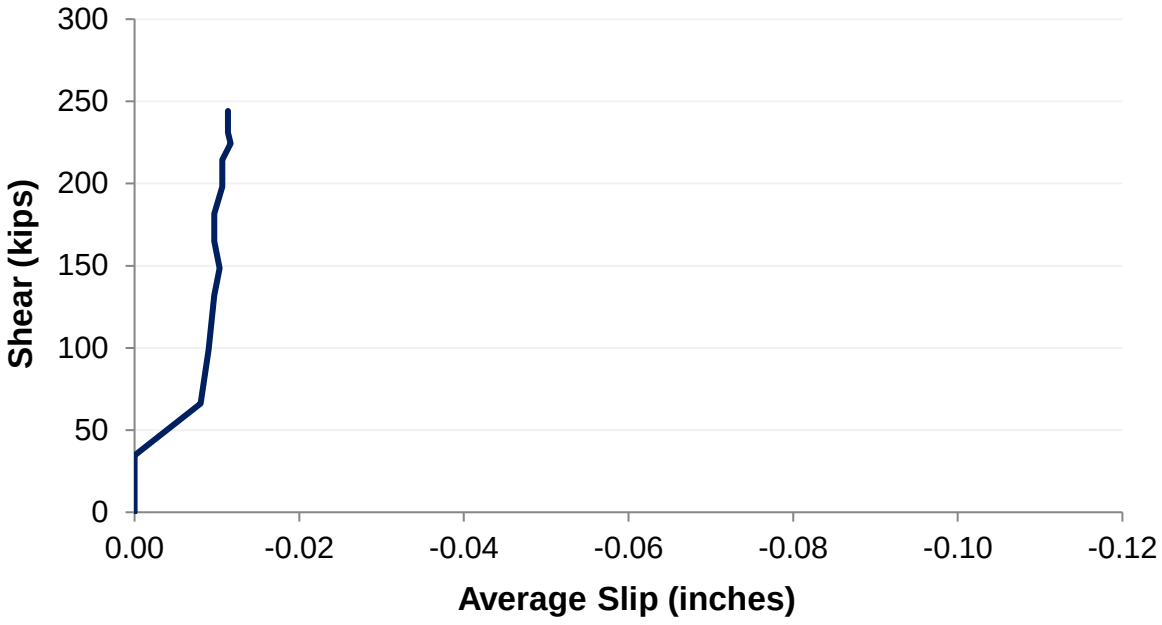

Figure T.24 Strand slip for pile HSSS 2205 (l_e = 69-in.).

- Pile HSSS 2205 – Embedment length: 61.75 inches.

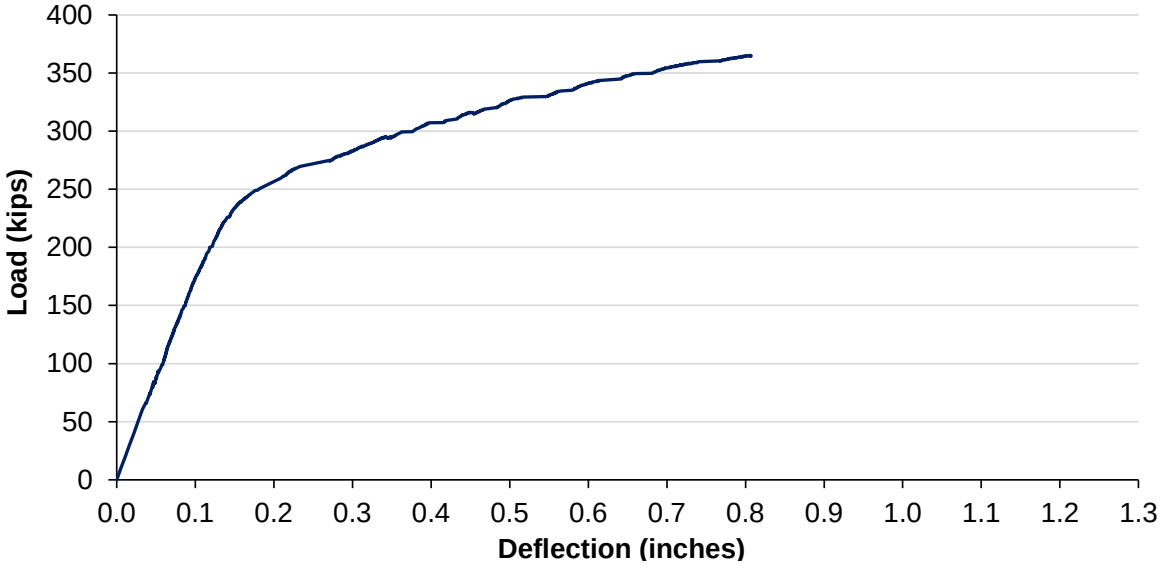

Figure T.25 Load-deflection curve for pile HSSS 2205 (l_e = 61.75-in.).

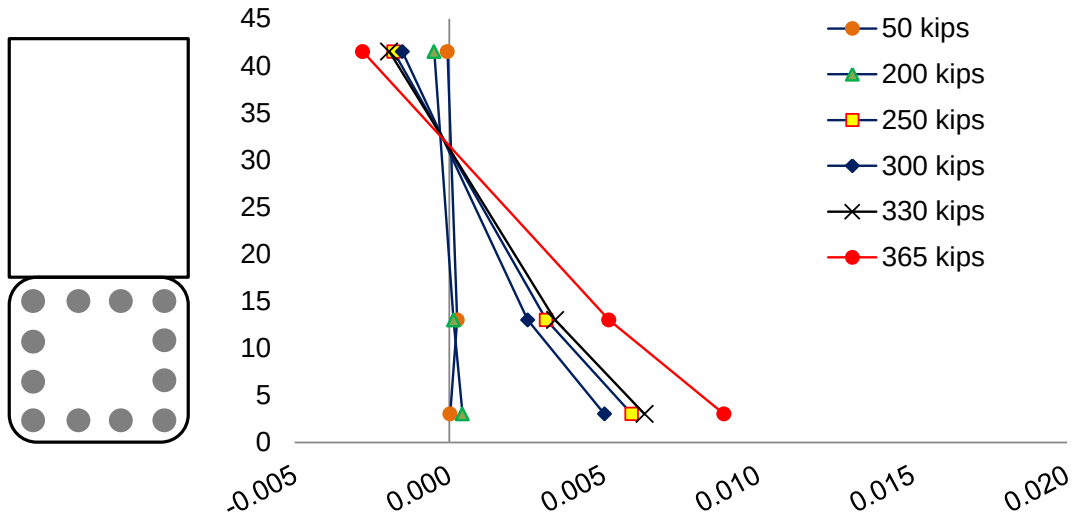

Figure T.26 Strain distribution for pile HSSS 2205 (l_e = 61.75-in.).

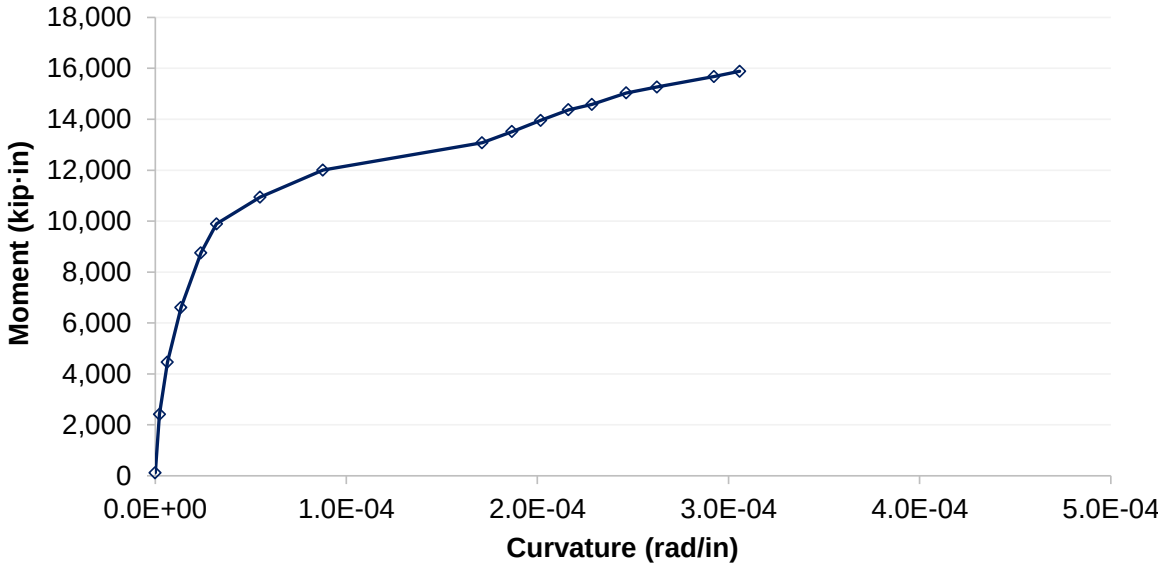

Figure T.27 Moment-curvature curve for pile HSSS 2205 (l_e = 61.75-in.).

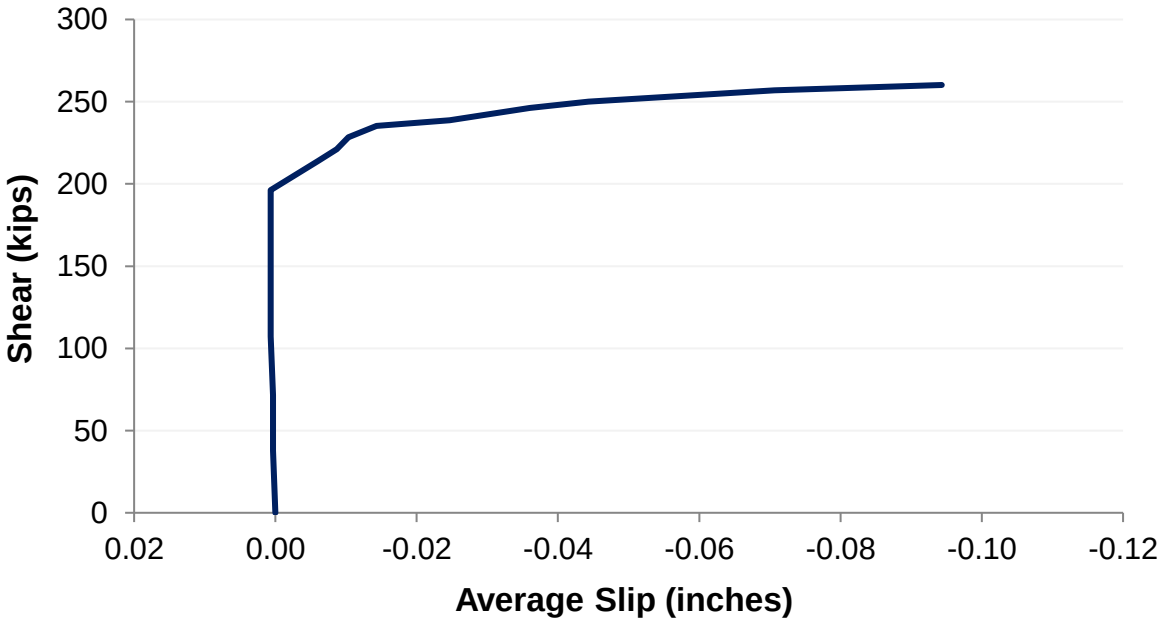

Figure T.28 Strand slip for pile HSSS 2205 (l_e = 61.75-in.).

- Pile HSSS 2205 – Embedment length: 57 inches.

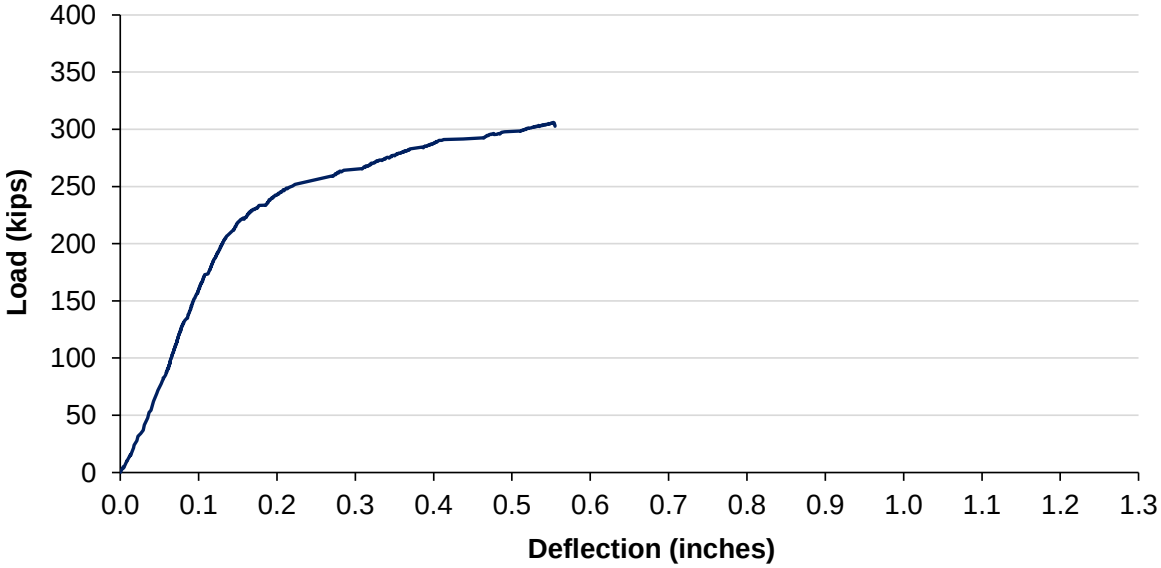

Figure T.29 Load-deflection curve for pile HSSS 2205 (l_e = 57-in.).

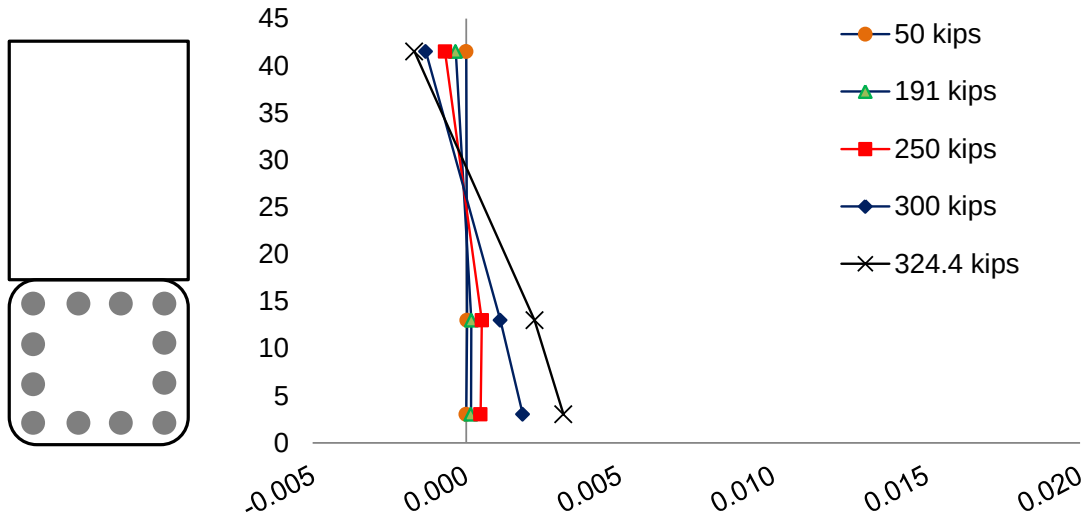

Figure T.30 Strain distribution for pile HSSS 2205 (l_e = 57-in.).

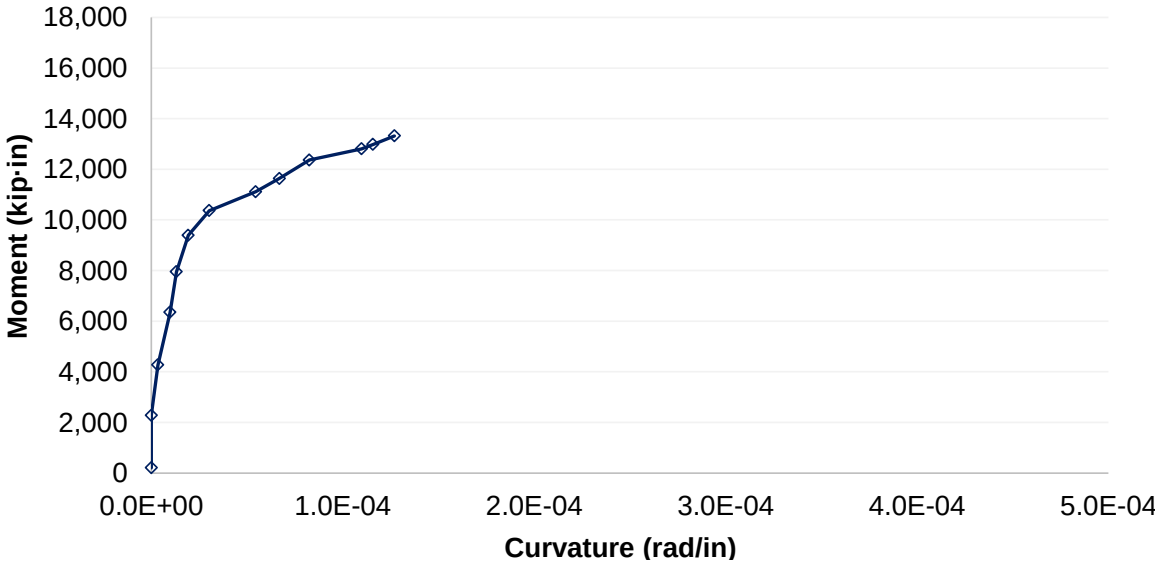

Figure T.31 Moment-curvature curve for pile HSSS 2205 (l_e = 57-in.).

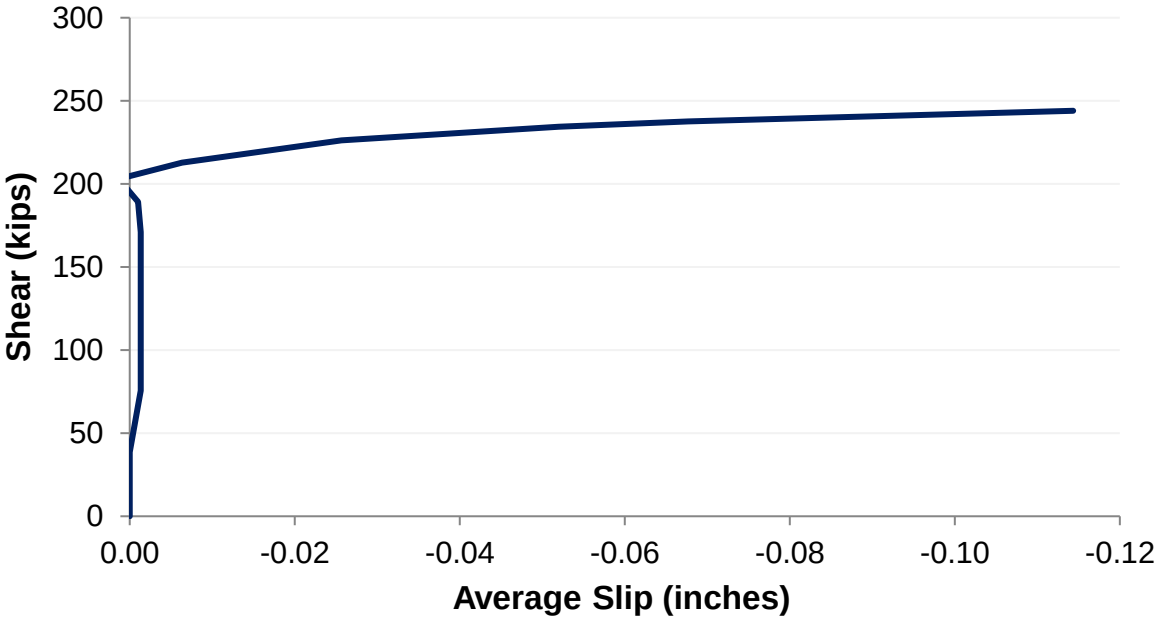

Figure T.32 Strand slip for pile HSSS 2205 (l_e = 57-in.).

REFERENCES

AASHTO LRFD (2013). "AASHTO LRFD Bridge Design Specifications (6th Edition) with 2012 and 2013 Interim Revisions," American Association of State Highway and Transportation Officials, Washington, DC, USA.

AASHTO TP 95 (2011). "Standard Method of Test for Surface Resistivity Indication of Concrete's Ability to Resist Chloride Ion Penetration (TP 95-11)," American Association of State Highway and Transportation Officials, Washington, DC, USA.

ACI Committee 201 (2008). "Guide to Durable Concrete (ACI 201.2R-08)," American Concrete Institute, Farmington Hills, MI, USA.

ACI Committee 209 (1992). "Prediction of Creep, Shrinkage, and Temperature Effects in Concrete Structures (ACI 209.R-92)," American Concrete Institute, Farmington Hills, MI, USA.

ACI Committee 214 (2010). "Guide for Obtaining Cores and Interpreting Compressive Strength Results (ACI 214.4R-10)," American Concrete Institute, Farmington Hills, MI, USA.

ACI Committee 222 (2001). "Corrosion of Prestressing Steels (ACI 222.2R-01)," American Concrete Institute, Farmington Hills, MI, USA.

ACI Committee 318 (2011). "Building Code Requirements for Structural Concrete (ACI 318-11) and Commentary," American Concrete Institute, Farmington Hills, MI, USA.

ACI Committee 357 (2014). "Guide for Design and Construction of Waterfront and Coastal Concrete Marine Structures (ACI 357.3R-14)," American Concrete Institute, Farmington Hills, MI, USA.

ACI Committee 363 (2010). "Report on High-Strength Concrete (ACI 363.R-10)," American Concrete Institute, Farmington Hills, MI, USA.

Al-Abidien, H.M.Z. (1987), Aggregates in Saudi Arabia: A Survey of Their Properties and Suitability for Concrete, *Materials and Structures* 20 (4), 260–264.

Al-Amoudi, O.S.B., and Maslehuddin, M. (1993), The Effect of Chloride and Sulfate Ions on Reinforcement Corrosion, *Cement and Concrete Research* 23 (1), 139−146.

Al Shamaa, M., Lavaud, S., Divet, L., Nahas, G., and Torrenti, J.M. (2015), Influence of Relative Humidity on Delayed Ettringite Formation, *Cement and Concrete Composites* 58, 14–22.

Alvarez-Armas, I. (2008), Duplex Stainless Steels: Brief History and Some Recent Alloys, *Recent Patents on Mechanical Engineering* 1 (1), 51−57.

Aïtcin, P.C. (2003), The Durability Characteristics of High Performance Concrete: A Review, *Cement and Concrete Composites* 25 (4), 409−420.

Ann, K.Y., and Song, H.-W. (2007), Chloride Threshold Level for Corrosion of Steel in Concrete, *Corrosion Science* 49 (11), 4113−4133.

ASTM A276/A276M (2015). "Standard Specification for Stainless Steel Bars and Shapes," American Society for Testing and Materials, West Conshohocken, PA, USA.

ASTM A416/A416M (2012). "Standard Specification for Steel Strand, Uncoated Seven-Wire for Prestressed Concrete," American Society for Testing and Materials, West Conshohocken, PA, USA.

ASTM A580/A580M (2014). "Standard Specification for Stainless Steel Wire," American Society for Testing and Materials, West Conshohocken, PA, USA.

ASTM A1064/A1064M (2015). "Standard Specification for Carbon-Steel Wire and Welded Wire Reinforcement, Plain and Deformed, for Concrete," American Society for Testing and Materials, West Conshohocken, PA, USA.

ASTM C31/C31M (2015). "Standard Practice for Making and Curing Concrete Test Specimens in the Field," American Society for Testing and Materials, West Conshohocken, PA, USA.

ASTM C33/C33M (2013). "Standard Specification for Concrete Aggregates," American Society for Testing and Materials, West Conshohocken, PA, USA.

ASTM C39/C39M (2014). "Standard Test Method for Compressive Strength of Cylindrical Concrete Specimens," American Society for Testing and Materials, West Conshohocken, PA, USA.

ASTM C109/C109M (2013). "Standard Test Method for Compressive Strength of Hydraulic Cement Mortars (Using 2-in. or [50-mm] Cube Specimens)," American Society for Testing and Materials, West Conshohocken, PA, USA.

ASTM C127 (2012). "Standard Test Method for Density, Relative Density (Specific Gravity), and Absorption of Coarse Aggregate," American Society for Testing and Materials, West Conshohocken, PA, USA.

ASTM C128 (2012). "Standard Test Method for Density, Relative Density (Specific Gravity), and Absorption of Fine Aggregate," American Society for Testing and Materials, West Conshohocken, PA, USA.

ASTM C136/C136M (2014). "Standard Test Method for Sieve Analysis of Fine and Coarse Aggregates," American Society for Testing and Materials, West Conshohocken, PA, USA.

ASTM C143/C143M (2012). “Standard Test Method for Slump of Hydraulic-Cement Concrete,” American Society for Testing and Materials, West Conshohocken, PA, USA.

ASTM C150 (2012). “Standard Specification for Portland Cement,” American Society for Testing and Materials, West Conshohocken, PA, USA.

ASTM C215 (2014). “Standard Test Method for Fundamental Transverse, Longitudinal, and Torsional Resonant Frequencies of Concrete Specimens,” American Society for Testing and Materials, West Conshohocken, PA, USA.

ASTM C231/C231M (2014). “Standard Test Method for Air Content of Freshly Mixed Concrete by the Pressure Method,” American Society for Testing and Materials, West Conshohocken, PA, USA.

ASTM C305 (2014). “Standard Practice for Mechanical Mixing of Hydraulic Cement Pastes and Mortars of Plastic Consistency,” American Society for Testing and Materials, West Conshohocken, PA, USA.

ASTM C469/C469M (2014). “Standard Test Method for Static Modulus of Elasticity and Poisson's Ratio of Concrete in Compression,” American Society for Testing and Materials, West Conshohocken, PA, USA.

ASTM C490/C490M (2011). “Standard Practice for Use of Apparatus for the Determination of Length Change of Hardened Cement Paste, Mortar, and Concrete,” American Society for Testing and Materials, West Conshohocken, PA, USA.

ASTM C618 (2012). “Standard Specification for Coal Fly Ash and Raw or Calcined Natural Pozzolan for Use in Concrete,” American Society for Testing and Materials, West Conshohocken, PA, USA.

ASTM C1012/C1012M (2013). “Standard Test Method for Length Change of Hydraulic-Cement Mortars Exposed to a Sulfate Solution,” American Society for Testing and Materials, West Conshohocken, PA, USA.

ASTM C1038/C1038M (2014). “Standard Test Method for Expansion of Hydraulic Cement Mortar Bars Stored in Water,” American Society for Testing and Materials, West Conshohocken, PA, USA.

ASTM C1202 (2012). “Standard Test Method for Electrical Indication of Concrete's Ability to Resist Chloride Ion Penetration,” American Society for Testing and Materials, West Conshohocken, PA, USA.

ASTM C1260 (2014). “Standard Test Method for Potential Alkali Reactivity of Aggregates (Mortar-Bar Method),” American Society for Testing and Materials, West Conshohocken, PA, USA.

ASTM C1679 (2014). "Standard Practice for Measuring Hydration Kinetics of Hydraulic Cementitious Mixtures Using Isothermal Calorimetry," American Society for Testing and Materials, West Conshohocken, PA, USA.

ASTM D4130 (2015). "Standard Test Method for Sulfate Ion in Brackish Water, Seawater, and Brines," American Society for Testing and Materials, West Conshohocken, PA, USA.

ASTM D4458 (2015). "Standard Test Method for Chloride Ions in Brackish Water, Seawater, and Brines," American Society for Testing and Materials, West Conshohocken, PA, USA.

ASTM E328 (2013). "Standard Test Methods for Stress Relaxation for Materials and Structures," American Society for Testing and Materials, West Conshohocken, PA, USA.

ASTM G71 (2014). "Standard Guide for Conducting and Evaluating Galvanic Corrosion Tests in Electrolytes," American Society for Testing and Materials, West Conshohocken, PA, USA.

Atahan, H.N., and Dikme, D. (2010), "Improving Sulfate Resistance of Mortars Produced with Sands Contaminated by Natural Sulfate," in: W. Brameshuber (Ed.), International RILEM Conference on Material Science, RILEM Publications SARL.

Atahan, H.N., and Dikme, D. (2011), Use of mineral admixtures for enhanced resistance against sulfate attack, *Construction and Building Materials* 25 (8), 3450–3457.

Azizinamini, A., Ozyildirim, H.C., Power, E.H., Kline, E.S., Mertz, D.R., Myers, G.F., and Whitmore, D.W. (2013). "Design Guide for Bridges for Service Life," Prepublication Draft Report No. SHRP 2 Renewal Project R19A, Transportation Research Board, National Academy of Sciences, 744 pp.

Bandyopadhyay, T.K., and Sengupta, B. (1986), Determining Time Dependent Losses of Prestress with due Consideration of Aging Coefficient and Percentage of Steel, *ACI Journal Proceedings* 83 (2), 236–243.

Barnes, R.W., Grove, J.W., and Burns, N.H. (2003), Experimental Assessment of Factors Affecting Transfer Length, *ACI Structural Journal* 100 (6), 740-748.

Baroghel-Bouny, V., Thiéry, M., and Wang, X. (2011), Modelling of Isothermal Coupled Moisture–Ion Transport in Cementitious Materials, *Cement and Concrete Research* 41 (8), 828–841.

Bauer, S., Cornell, B., Figurski, D., Ley, T., Miralles, J., and Folliard, K.J. (2006). "Alkali-Silica Reaction and Delayed Ettringite Formation in Concrete: A Literature Review," Report No. FHWA/TX-06/0-4085-1, Center for Transportation Research, The University of Texas at Austin, Austin, Texas, 73 pp.

Bautista, A., and Gonzalez, J.A. (1996), Analysis of the Protective Efficiency of Galvanizing Against Corrosion of Reinforcements Embedded In Chloride Contaminated Concrete, *Cement and Concrete Research* 26 (2), 215–224.

Beddoe, R.E., and Dorner, H.W. (2005), Modelling Acid Attack on Concrete: Part I. The Essential Mechanisms, *Cement and Concrete Research* 35 (12), 2333–2339.

Bensted, J. (1983), Chemical Aspects of Normal Setting of Portland Cement, in: J.F. Young (Ed.), *Characterization and Performance Prediction of Cement and Concrete*, Proceedings of the Second Engineering Foundation Conference, Henniker, NH, USA, 69–86.

Bentz, E.C. (2003), Probabilistic Modeling of Service Life for Structures Subjected to Chlorides, *ACI Materials Journal* 100 (5), 391–397.

Bentz, D.P., Bognacki, C.J., Riding, K.A., and Villarreal, V.H. (2011), Hotter Cements, Cooler Concretes, *Concrete International* 33 (1), 41–48.

Bentz, D.P., Guthrie, W.S., Jones, S.Z., and Martys, N.S. (2014), Predicting Service Life of Steel-Reinforced Concrete Exposed to Chlorides, *Concrete International* 36 (9), 55–64.

Berkeley, K.G.C., and Pathmanaban, S. (1990). *Cathodic Protection of Reinforcement Steel in Concrete*, Sevenoaks, Kent, England: Butterworths and Company Publishers, Limited.

Berner, R.A. (1984), Sedimentary Pyrite Formation: An Update, *Geochimica et Cosmochimica Acta* 48 (4), 605–615.

Bérubé, M.-A., Duchesne, J., Dorion, J.F., and Rivest, M. (2002), Laboratory Assessment of Alkali Contribution by Aggregates to Concrete and Application to Concrete Structures Affected by Alkali–Silica Reactivity, *Cement and Concrete Research* 32 (8), 1215–1227.

Bertolini, L., Elsener, B., Pedeferri, P., Redaelli, E., and Polder, R (2013). *Corrosion of Steel in Concrete: Prevention, Diagnosis, Repair (2nd Edition)*, Weinheim, Germany: Wiley-VCH.

Bohni, H. (2005). *Corrosion in Reinforced Concrete Structures*, Cambridge, England: Woodhead Publishing Limited.

Bogue, R.H. (1947). *The Chemistry of Portland Cement*, New York, USA: Reinhold Publishing Corp.

Bolen, W.P. (2014), "Sand and Gravel, Construction", in: USGS Minerals Yearbook 2012, U.S. Geological Survey, U.S. Department of the Interior.

Böttcher, M.E. (2011), "Sulfur Cycle," in: V. Reitner, J. Thiel (Eds.), Encyclopedia of Geobiology, Springer: Heidelberg, pp 856.

Brimblecombe, P. (2003), "The Global Sulfur Cycle," in: W. Schlesinger (Ed.), Treatise on Geochemistry, Biogeochemistry, Amsterdam: Elsevier, Vol. 8, pp. 645.

Broekmans, M.A.T.M. (2012), Deleterious Reactions of Aggregate with Alkalis in Concrete, *Reviews in Mineralogy & Geochemistry* 74 (1), 279–364.

Brown, P.W., and Bothe, J.V. (1993), The Stability of Ettringite, *Advances in Cement Research* 5 (18), 47–63.

Buckner, C.D. (1995), A Review of Strand Development Length for Pretensioned Concrete Members, *PCI Journal* 40 (2), 84–105.

Bullard, J.W., Jennings, H.M., Livingston, R.A., Nonat, A., Scherer, G.W., Schweitzer, J.S., Scrivener, K.L., and Thomas, J.J. (2011), Mechanisms of Cement Hydration, *Cement and Concrete Research* 41 (12), 1208–1223.

Cannon, E., Lewinger, C., Abi, C., and Hamilton, H.R. (2006). "St. George Island Bridge Pile Testing," Final Report, UF Project No. 00051711, Florida Department of Transportation, 113 pp.

Center for Operational Oceanographic Products and Services, National Oceanic and Atmospheric Administration (NOAA), November 6th, 2014 (website update date: October 15th, 2013), from http://tidesandcurrents.noaa.gov/

Chaix, O., Hartt, W.H., Kessler, R., and Powers, R. (1995), Localized Cathodic Protection of Simulated Prestressed Concrete Pilings in Seawater, *Corrosion Science* 51 (5), 386–398.

Chandra, A.P., and Gerson, A.R. (2010), The Mechanisms of Pyrite Oxidation and Leaching: A Fundamental Perspective, *Surface Science Reports* 65 (9), 293–315.

Chinchón-Payá, S., Aguado, A., and Chinchón, S. (2012), A Comparative Investigation of the Degradation of Pyrite and Pyrrhotite under Simulated Laboratory Conditions, *Engineering Geology* 127 (24), 75–80.

Clinkenbeard, J.P. (2012), "Aggregate Sustainability in California," California Geological Survey, Department of Conservation.

Constantiner, D., and Diamond, S. (2003), Alkali Release from Feldspars into Pore Solutions, *Cement and Concrete Research* 33 (4), 549–554.

Cousins, T.E., Johnston, D.W., and Zia, P. (1986). "Alkali-Silica Reaction and Delayed Ettringite Formation in Concrete: A Literature Review," Report No. FHWA/NC/87-005, Center for Transportation Engineering Studies, North Carolina State University, Raleigh, North Carolina, 191 pp.

Crammond, N.J. (1984), Examination of Mortar Bars Containing Varying Percentages of Coarsely Crystalline Gypsum as Aggregate, *Cement and Concrete Research* 14 (2), 225–230.

Damidot, D., and Glasser, F.P. (1992), "Sulphate Attack on Concrete: Prediction of the AFt Stability from Phase Equilibria," in: Proceedings of the 9th International Congress on the Chemistry of Cement, New Delhi, India, Vol. 5, pp 316–321.

Darmawan, M.S., and Stewart, M.G. (2007), Effect of Pitting Corrosion on Capacity of Prestressing Wires, *Magazine of Concrete Research* 59 (2), 131–139.

Darwin, D. (2007), It's Time to Invest, *Concrete International* 29 (10), 7.

Deatherage, J.H., Burdette, E.G., and Chew, C.K. (1994), Development Length and Lateral Spacing Requirements of Prestressing Strand for Prestressed Concrete Bridge Girders, *PCI Journal* 39 (1), 70-83.

Dehwah, H.A.F., Maslehuddin, M., and Austin, S.A. (2002), Long-Term Effect of Sulfate Ions and Associated Cation Type on Chloride-Induced Reinforcement Corrosion in Portland Cement Concretes, *Cement and Concrete Composites* 23 (1), 139–146.

Demis, S., Efstathiou, M.P., and Papadakis, V.G. (2014), Computer-Aided Modeling of Concrete Service Life, *Cement and Concrete Composites* 47, 9–18.

Ehlen, M.A., Thomas, M.D.A., and Bentz, E.C. (2009), Life-365 Service Life Prediction Model™ Version 2.0, *Concrete International*, 31 (5), 41–46.

Ekolu, S.O., Thomas, M.D.A., and Hooton, R.D. (2006), Pessimum Effect of Externally Applied Chlorides on Expansion Due To Delayed Ettringite Formation: Proposed Mechanism, *Cement and Concrete Research* 36 (4), 688–696.

FIB, Bulletin No 34 (2006). "Model Code for Service Life Design," fib-fédération internationale du béton (International Federation for Structural Concrete), Lausanne, Switzerland.

Fitzpatrick, R.W., Shand, P., and Merry, R.H. (2009), "Acid Sulfate Soils," in: J.T. Jennings (Ed.), Natural History of the Riverland and Murraylands, Royal Society of South Australia: Adelaide, Australia, pp 65–111.

Flatt, R.J., and Scherer, G.W. (2008), Thermodynamics of Crystallization Stresses in DEF, *Cement and Concrete Research* 38 (3), 325–336.

Florida DOT (2000), "Florida Method of Test for an Accelerated Laboratory Method for Corrosion Testing of Reinforced Concrete Using Impressed Current (FM 5-522)," Florida Department of Transportation, Tallahassee, FL, USA.

Folliard, K.J., Barborak, R., Drimalas, T., Du, L., Garber, S., Ideker, J., Ley, T., Williams, S., Juenger, M., Fournier, B., and Thomas, M.D.A. (2006), "Preventing

ASR/DEF in New Concrete: Final Report," Final Report, No. FHWA/TX-06/0-4085-5, Center for Transportation Research, The University of Texas at Austin, Austin, TX, 254 pp.

Fontana, M. (1986). *Corrosion Engineering, 3rd Edition*, New York, USA: McGraw-Hill.

Frankel, G.S. (1998), Pitting Corrosion of Metals, A Review of the Critical Factors, *Journal of the Electrochemical Society* 145 (6), 2186–2198.

Gardner, L. (2005), The Use of Stainless Steel in Structures, *Progress in Structural Engineering and Materials* 7 (2), 45–55.

Geng, J., Easterbrook D., Li, L.-Y., and Mo, L-W (2015), The Stability of Bound Chlorides in Cement Paste with Sulfate Attack, *Cement and Concrete Research* 68, 211–222.

Ghods, P., Isgor, O.B., McRae, G., and Miller, T. (2009), The Effect of Concrete Pore Solution Composition on the Quality of Passive Oxide Films on Black Steel Reinforcement, *Cement and Concrete Composites* 33 (1), 2–11.

Ghods, P. (2010). Multi-Scale Investigation of the Formation and Breakdown of Passive Films on Carbon Steel Rebar in Concrete. Doctoral Thesis, Carleton University, 322 pp.

Ghods, P., Isgor, O.B., Bensebaa, F., and Kingston, D. (2012), Angle-Resolved XPS Study of Carbon Steel Passivity and Chloride-Induced Depassivation in Simulated Concrete Pore Solution, *Corrosion Science* 58, 159–167.

Gjørv, O.E. (2014). *Durability Design of Concrete Structures in Severe Environments*, Boca Raton, FL, USA: CRC Press, Taylor & Francis Group.

Glass, G.K., and Buenfeld, N.R. (1997), Chloride Threshold Levels for Corrosion Induced Deterioration of Steel in Concrete, in: L.O. Nilsson and J. Ollivier (Eds.), *Chloride Penetration into Concrete*, Proceedings of the RILEM International Workshop on Chloride Penetration into Concrete, RILEM Paris, 429–452.

Glasser, F.P. (2004), "The Stability of Ettringite," in K.L. Scrivener and J. Scrivener (Eds.), Internal Sulfate Attack: Proceedings of RILEM Workshop on Delayed Ettringite Formation, RILEM Paris.

Goguel, R. (1995), Alkali Release by Volcanic Aggregates In Concrete, *Cement and Concrete Research* 25 (4), 841–852.

Gonnerman, H.F., and Shuman, E.C. (1928), Flexure and Tension Tests of Plain Concrete, *Major Series* 171 (209), 149.

Grabowski, E., Czarnecki, B., Gillott, J.E., Duggan, C.R., and Scott, J.F. (1992), Rapid Test of Concrete Expansivity Due to Internal Sulfate Attack, *ACI Materials Journal* 89 (5), 469–480.

Griess, J.C., and Naus, D.J. (1980), "Corrosion of Steel Tendons Used in Prestressed Concrete Pressure Vessels," in: D.E. Tonini and J.M. Gaidis (Eds.), Corrosion of Reinforcing Steel in Concrete, ASTM STP 713, American Society for Testing and Materials, pp. 32–50.

Gunay, H.B., Ghods, P., Isgor, O.B., Carpenter, G.J.C., and Wu, X. (2012), Angle-Resolved XPS Study of Carbon Steel Passivity and Chloride-Induced Depassivation in Simulated Concrete Pore Solution, *Corrosion Science* 58, 159–167.

Gunay, H.B., Isgor, O.B., and Ghods, P. (2015), Kinetics of Passivation and Chloride-Induced Depassivation of Iron in Simulated Concrete Pore Solutions Using Electrochemical Quartz Crystal Nanobalance, *Corrosion* 71 (5), 615–627.

Hails, J.R., and Hoyt, J.H. (1969), An Appraisal of the Evolution of the Lower Atlantic Coastal Plain of Georgia, USA, *Transactions of the Institute of British Geographers* 46, 53–68.

Hanson, N.W., and Kaar, P.H (1959), Flexural Bond Tests of Pretensioned Prestressed Beams, *ACI Journal* 55 (1), 783–802.

Hansson, C.M. (1984), Comments on Electrochemical Measurements of the Rate of Corrosion of Steel in Concrete, *Cement and Concrete Research* 14 (4), 574–584.

Hartt, W.H., and Rosenberg, A.M. (1980), Influence of $Ca(NO_2)_2$ on Sea Water Corrosion of Reinforcing Steel in Concrete, *ACI Special Publication 65*, 609–622.

Hartt, W.H., Powers, R.G., Lysogorski, D.K., Paredes, M., and Virmani, Y.P. (2006). "Job Site Evaluation of Corrosion-Resistant Alloys for Use as Reinforcement in Concrete," Final Report, No. FHWA-HRT-06-078, Federal Highway Administration, 92 pp.

Hawkins, A.B. (2014), "Engineering Implications of the Oxidation of Pyrite: An Overview, with Particular Reference to Ireland", in: A.B. Hawkins (Ed.), Implications of Pyrite Oxidation for Engineering Works, Switzerland: Springer International Publishing.

Herrick, S.M., and Vorhis, R.C. (1963), Subsurface Geology of the Georgia Coastal Plain, The Geological Survey, *Information Circular 25*.

Holland, R.B., Moser, R.D., Kahn, L.F., Singh, P., and Kurtis, K.E. (2012). "Durability of Precast Prestressed Concrete Piles in Marine Environment, Part 2 Volume 1: Concrete," Final Report, No. FHWA-GA-12-1026, Georgia Institute of Technology, Atlanta, GA, 338 pp.

Holland, R.B. (2012). Durability of Precast Prestressed Concrete Piles in Marine Environments. Doctoral Thesis, Georgia Institute of Technology, 426 pp.

Holland, R.B., Kurtis, K.E., Moser, R.D., Kahn, L.F., Aguayo, F., and Singh, P.M. (2014), Multiple Deterioration Mechanisms in Coastal Concrete Piles, *Concrete International* 36 (7), 45–52.

Hoyer, E., and Friedrich, E. (1939), Beitrag zur Frage der Haftspannung in Eisenbetonbauteilen, *Beton und Eisen* 50 (9), 717–736.

Hurley, M.F., and Scully, J.R. (2006), Threshold Chloride Concentrations of Selected Corrosion-Resistant Rebar Materials Compared to Carbon Steel, *Corrosion* 62 (10), 892–904.

Hurley, M.F., and Scully, J.R. (2013), Lateral and Radial Corrosion Propagation Behavior of 9–21% Cr and 18% Cr + 2.8% Mo Stainless Steel Reinforcing Materials in Simulated Concrete Environments, *Materials and Corrosion* 64 (9), 752–763.

IPCC, Intergovernmental Panel on Climate Change (2014). *Climate Change 2014: Impacts, Adaptation, and Vulnerability. Summaries, Frequently Asked Questions, and Cross-Chapter Boxes. A Contribution of Working Group II to the Fifth Assessment Report of the Intergovernmental Panel on Climate Change*, Geneva, Switzerland: World Meteorological Organization, 190 pp.

Jayapalan, A.R., Jue, M.L., and Kurtis, K.E. (2014), Nanoparticles and Apparent Activation Energy of Portland Cement, *Journal of the American Ceramic Society* 97 (5), 1534–1542.

Jenkins, J.F. (1987). "Validation of Nitronic 33 in Reinforced and Prestressed Concrete," Final Report, No. TN-1764, Naval Civil Engineering Laboratory, 63 pp.

Johannesson, B., and Utgenannt, P. (2001), Microstructural Changes Caused by Carbonation of Cement Mortar, *Cement and Concrete Research* 31 (6), 925–931.

Jones, D.A. (1996). *Principles and Prevention of Corrosion, Second Edition*, Upper Saddle River, NJ: Prentice Hall.

Jones, S., Martys, N., Lu, Y., and Bentz, D. (2015), Simulation Studies of Methods to Delay Corrosion and Increase Service Life for Cracked Concrete Exposed to Chlorides, *Cement and Concrete Composites* 58, 59–69.

Kahn, L.F., Dill, J.C, and Reutlinger, C.G. (2002), Transfer and Development Length of 15-mm Strand in High Performance Concrete Girders, *Journal of Structural Engineering* 128 (7), 913–921.

Kaar, P.H., LaFraugh, R.W., and Mass, M.A. (1963), Influence of Concrete Strength on Transfer Length, *PCI Journal* 8 (5), 47–67.

Karl, T.R., Melillo, J.M., and Peterson, T.C. (Eds.) (2009). *Global Climate Change Impacts in the United States*, New York, NY: Cambridge University Press.

Kehl, R.J., and Carrasquillo, R.L. (1998). "Investigation of the Use of Match Cure Technology in the Precast Concrete Industry," Report, No. FHWA /TX-01/1714-2, Center for Transportation Research, The University of Texas at Austin, Austin, TX, 107 pp.

Kelham, S. (1996), The Effect of Cement Composition and Fineness on Expansion Associated with Delayed Ettringite Formation, *Cement and Concrete Composites* 18 (3), 171–179.

Kelham, S. (1997), "Effects of Cement Composition and Hydration Temperature on Volume Stability of Mortar," in: Proceeding of the 10th International Congress on the Chemistry of Cement, vol. 4, Amarkai AB and Congrex, Gothenburg, Sweden, 8 pp, 4iv060.

Kessler, R.J., Powers, R.G., Vivas, E., Paredes, M.A., and Virmani, Y.P. (2008), "Surface Resistivity as an Indicator of Concrete Chloride Penetration Resistance," in: Proceedings of the International Concrete Bridge Conference, St. Louis, MO, USA, 4–7 May, 2008.

Kheder, G.F., and Assi, D.K. (2010), Limiting Total Internal Sulphates in 15-75 MPa Concrete in Accordance to Its Mix Proportions, *Materials and Structures* 43 (1–2), 273–281.

Klieger, P. (1958), Effect of Mixing and Curing Temperature on Concrete Strength, *ACI Journal Proceedings* 54 (6), 1063–1081.

Koch, G.H., Brongers, M.P.H., Thompson, N.G., Virmani, Y.P., and Payer, J.H. (2002). "Corrosion Cost and Preventive Strategies in the United States," Report No. FHWA-RD-01-156, Federal Highway Administration.

Kurtis, K.E., and Mehta, K. (1997), A Critical Review of Deterioration of Concrete Due to Corrosion of Reinforcing Steel, *ACI Special Publication 170*, 535–554.

Kurtis, K.E., Kahn, L.F., and Nadelman, E. (2013). "Viability of Concrete Performance-Based Specification for Georgia DOT Projects," Final Report, No. FHWA-GA-14-1208, Georgia Institute of Technology, Atlanta, GA, 107 pp.

Lane, S.N. (1998). "A New Development Length Equation for Pretensioned Strands in Bridge Beams and Piles," Final Report, No. FHWA-RD-98-116, Federal Highway Administration, 131 pp.

Larive C. (1997). Apports Combinés de L'expérimentation et de la Modélisation à la Compréhension de L'alcali-Réaction et de ses Effets Mécaniques. Doctoral Thesis, Ecole Nationale des Ponts et Chaussées, 335 pp (in French).

Lawrence, C.D. (2004), "The Constitution and Specification of Portland Cements," in: P.C. Hewlett (Ed.), Lea's Chemistry of Cement and Concrete, Fourth Edition, 131-193, Elsevier, Butterworth-Heinemann.

Lo, K.H., Shek, C.H., and Lai, J.K.L. (2009), Recent Developments in Stainless Steels, *Materials Science and Engineering: R: Reports* 65 (4), 39–104.

Makarious, A.S., Bashter, I. I., Abdo, A.E.S., Azim, M.S.A., and Kansouh, W.A. (1996), On the Utilization of Heavy Concrete for Radiation Shielding, *Annals of Nuclear Energy* 23 (3), 195–206.

Martin, L.D., and Scott, N.L. (1976), Development of Prestressing Strand in Pretensioned Members, *ACI Journal* 73 (8), 453–456.

Mehta, P.K. (1980), Durability of Concrete in Marine Environment – A Review, *ACI Special Publication 65*, 1–20.

Mehta, P.K. (1991). *Concrete in the Marine Environment*, New York, NY, USA: Elsevier Science Publishers Ltd.

Mehta, P.K., and Monteiro, P.J.M. (2006). *Concrete: Microstructure, Properties, and Materials, 3rd Edition*, New York, NY, USA: McGraw-Hill.

Menendez, E., Matschei, T., and Glasser, F.P. (2013), "Sulfate Attack of Concrete", in: M. Alexander, A. Bertron, N. De Belie (Eds.), Performance of Cement-Based Materials in Aggressive Aqueous Environments, State-of-the-Art Report, RILEM TC 211-PAE, Springer.

Meyer, K.F. (2002). Transfer and Development Length of 0.6-inch Diameter Prestressing Strand in High Strength Lightweight Concrete. Doctoral Thesis, Georgia Institute of Technology, 643 pp.

Milad, M., Zreiba, V., Elhalouani, F., and Baradai, C. (2008), The Effect of Cold Work on Structure and Properties of AISI 304 Stainless Steel, *Journal of Materials Processing Technology* 203 (1-3), 80–85.

Mindess, S., Young, J.F., and Darwin, D. (2003). *Concrete, Second Edition*, Upper Saddle River, NJ: Prentice Hall.

Mitchell, D., Cook, W.D., Khan, A.A., and Tham, T. (1993), Influence of High Strength Concrete on Transfer and Development Length of Pretensioning Strand, *PCI Journal* 38 (3), 52-66.

Monteny, J., Vincke, E., Beeldens, A., De Belie, N., Taerwe, L., Van Gemert, D., and Verstraete, W. (2000), Chemical, Microbiological, and In Situ Test Methods for Biogenic Sulfuric Acid Corrosion of Concrete, *Cement and Concrete Research* 30 (4), 623–634.

Moser, R.D. (2011). High-Strength Stainless Steels for Corrosion Mitigation in Prestressed Concrete: Development and Evaluation. Doctoral Thesis, Georgia Institute of Technology, 329 pp.

Moser, R.D., Holland, B., Kahn, L.F., Singh, P.M., and Kurtis, K.E. (2011). "Durability of Precast Prestressed Concrete Piles in Marine Environment: Reinforcement Corrosion and Mitigation – Part 1," Georgia Institute of Technology, Atlanta, GA, 243 pp.

Moser, R.D., Singh, P.M., Kahn, L.F., and Kurtis, K.E. (2011), Chloride-Induced Corrosion of Prestressing Steels Considering Crevice Effects and Surface Imperfections, *Corrosion* 67 (6), 065001-1–065001-14.

Moser, R.D., Singh, P., Kahn, L.F., and Kurtis, K.E. (2012). "Durability of Precast Prestressed Concrete Piles in Marine Environment, Part 2 Volume 2: Stainless Steel Prestressing Strand and Wire," Final Report, No. FHWA-GA-12-1026, Georgia Institute of Technology, Atlanta, GA, 342 pp.

Mota, B., Matschei, T., and Scrivener, K.L. (2015), The Influence of Sodium Salts and Gypsum on Alite Hydration, *Cement and Concrete Research* 75, 53–65.

Myers, J.J., and Carrasquillo, R.L. (1998). "The Production and Quality Control of High Performance Concrete in Texas Bridge Structures," Report, No. FHWA /TX-05/9-580/589-1, Center for Transportation Research, The University of Texas at Austin, Austin, TX, 563 pp.

National Oceanic and Atmospheric Administration (NOAA), US Department of Comerce, May 24th, 2015 (website update date: March 14th, 2013), from http://stateofthecoast.noaa.gov/population/welcome.html.

Nawy, E.G. (2009). *Prestressed Concrete: A Fundamental Approach, 5th Edition*, Upper Saddle River, NJ, USA: Princeton-Hall.

Neville, A.M. (1995). *Properties of Concrete, Fourth Edition*, Essex, England: Pearson Education Limited.

Neville, A.M. (2004), The Confused World of Sulfate Attack on Concrete, *Cement and Concrete Research* 34 (8), 1275–1296.

Nguyen, T.Q., Petković, J., Dangla, P., and Baroghel-Bouny, V. (2008), Modelling of Coupled Ion and Moisture Transport in Porous Building Materials, *Construction and Building Materials* 22 (11), 2185–2195.

Nicholls, R.J, Wong, P.P., Burkett, V.R., Codignotto, J.O., Hay, J.E., McLean, R.F., Ragoonaden, S., and Woodroffe, C.D. (2007), "Coastal Systems and Low-Lying Areas," in: M.L. Parry, O.F. Canziani, J.P. Palutikof, P.J. van der Linden and C.E. Hanson (Eds.), Climate Change 2007: Impacts, Adaptation and Vulnerability. Contribution of Working Group II to the Fourth Assessment Report of the

Intergovernmental Panel on Climate Change, Cambridge, UK: Cambridge University Press, pp. 315–356.

Nordstrom, D.K., and Southam, G. (1997), "Geomicrobiology of Sulfide Mineral Oxidation," in: J.F. Banfield, K.H. Nealson (Eds.), Geomicrobiology: Interactions Between Microbes and Minerals, Vol. 35, Reviews in Mineralogy, Washington, DC: Mineralogical Society of America, pp 361–390.

Nordstrom, D.K. (2011), "Sulfide Mineral Oxidation," in: V. Reitner, J. Thiel (Eds.), Encyclopedia of Geobiology, Heidelberg, Germany: Springer, pp. 856.

Normad, R. (1986), "Review of the Performance of Concrete Coastal Structures in the Gulf Area," in: Proceeding of International Conference on Concrete in the Marine Environment, London, England: Concrete Society, pp 101–103.

Novokshchenov, V. (1994), Brittle Fractures of Prestressed Bridge Steel Exposed to Chloride-Bearing Environments Caused by Corrosion-Generated Hydrogen, *Corrosion* 50 (6), 477–485.

Nurnberger, U. (2002), Corrosion Induced Failure Mechanisms of Prestressing Steel, *Materials and Corrosion* 53 (8), 591–601.

Obserholster, R.E. (1986), "Pore Structure, Permeability and Diffusivity of Hardened Cement Paste and Concrete in Relation to Durability: Status and Prospects," in: Proceedings of the 8th International Congress on the Chemistry of Cement, Rio de Janeiro, Brazil, p. 323–335.

Oh, B.H., and Kim, E.S. (2000), Realistic Evaluation of Transfer Lengths in Pretensioned, Prestressed Concrete Members, *ACI Materials Journal* 97 (6), 821–830.

Oh, B.H., Kim, E.S., and Choi, Y.C. (2006), Theoretical Analysis of Transfer Lengths in Pretensioned Prestressed Concrete Members, *Journal of Engineering Mechanics* 132 (10), 1057–1066.

Østmoen, T., Liestøl, G., Grefstad, K.A., Sand, B.T., and Farstad, T. (1993). "Chloride Durability of Coastal Concrete Bridges," Report, Norwegian Public Roads Administration, Oslo, Norway (in Norwegian).

Ouyang, C., Nanni, A., and Chang, W.F. (1988), Internal and External Sources of Sulfate Ions in Portland Cement Mortar: Two Types of Chemical Attack, *Cement and Concrete Research* 18 (5), 699–709.

Papadakis, V.G, Vayenas, C.G., and Fardis, M.N. (1991), Experimental Investigation and Mathematical Modeling of the Concrete Carbonation Problem, *Chemical Engineering Science* 46 (5-6), 1333–1338.

Pavoine, A., Brunetaud, X., and Divet, L. (2012), The Impact of Cement Parameters on Delayed Ettringite Formation, *Cement and Concrete Composites* 34 (4), 521–528.

Petrov, N., and Tagnit-Hamou, A. (2004), Is Microcracking Really a Precursor to Delayed Ettringite Formation and Consequent Expansion?, *ACI Materials Journal* 101 (6), 442–447.

Popovics, J.S., Zemajtis, J., and Shkolnik, I. (2008), A Study of Static and Dynamic Modulus of Elasticity of Concrete, ACI-CRC Final Report.

Quennoz, A., and Scrivener, K.L. (2013), Interactions Between Alite and C_3A-Gypsum Hydrations in Model Cements, *Cement and Concrete Research* 44, 46–54.

Ramberg, W., and Osgood W.R. (1941), Determination of Stress–Strain Curves by Three Parameters, *NACA Technical Note 503*.

Ramirez, J.A., and Russell, B.W. (2008). "Transfer, Development, and Splice Length for Strand/Reinforcement in High-Strength Concrete," NCHRP Report No. 603, National Cooperative Highway Research Program, Transportation Research Board, National Research Council, 131 pp.

Ramlochan, T., Thomas, M.D.A., Hooton, R.D. (2004), The Effect of Pozzolans and Slag on the Expansion of Mortars Cured at Elevated Temperature: Part II: Microstructural and Microchemical Investigations, *Cement and Concrete Research* 34 (8), 1341–1356.

Rasheeduzzafar, Dakhil, F.H., Bader, M.A., and Khan, M.M. (1992), Performance of Corrosion-Resisting Steels in Chloride-Bearing Concrete, *ACI Materials Journal* 89 (5), 439–448.

Rasmussen, K.J.R (2003), Full-Range Stress–Strain Curves for Stainless Steel Alloys, *Journal of Constructional Steel Research* 59 (1), 47–61.

Recio, F.J., Wu, Y., Alonso, M.C., and Nurnberger, U. (2013), Hydrogen Embrittlement Risk in Cold-Drawn Stainless Steels, *Materials Science and Engineering: A* 564, 57–64.

Reutlinger, C.G. (1999). Direct Pull-Out Capacity and Transfer Length of 0.6-inch Diameter Prestressing Strand in High-Performance Concrete. Master's Thesis, Georgia Institute of Technology, 371 pp.

Rickard, D., and Luther, G.W. (2007), Chemistry of Iron Sulfides, *Chemical Reviews* 107 (2), 514–562.

Rodrigues, A., Duchesne, J., Fournier, B., Durand, B., Rivard, P., and Shehata, M. (2012), Mineralogical and Chemical Assessment of Concrete Damaged by the Oxidation of Sulfide-Bearing Aggregates: Importance of Thaumasite Formation on Reaction Mechanisms, *Cement and Concrete Research* 42 (10), 1336–1347.

Rosenberg, A., Hansson, C.M., and Andrade, C. (1989), Mechanisms of Corrosion of Steel in Concrete, *Materials Science of Concrete* 1, 285–314.

Russell, B.W. (1992). Design Guidelines for Transfer, Development and Debonding of Large Diameter Seven Wire Strands in Pretensioned Concrete Girders. Doctoral Thesis, The University of Texas at Austin.

Russell, B.W., and Burns, N.H. (1993). "Design Guidelines for Transfer, Development and Debonding of Large Diameter Seven Wire Strands in Pretensioned Concrete Girders," Research Report, No. 1210-5F, Center for Transportation Research, The University of Texas at Austin, Austin, TX, 471 pp.

Sakr, K., and El-Hakim, E. (2005), Effect of High Temperature or Fire on Heavy Weight Concrete Properties, *Cement and Concrete Research* 35 (3), 590–596.

Saleem, M., Shameem, M., Hussain, S.E., and Maslehuddin, M. (1996), Effect of Moisture, Chloride and Sulphate Contamination on the Electrical Resistivity Portland Cement Concrete, *Construction and Building Materials* 10 (3), 209–214.

Santhanam, M., Cohen, M.D., and Olek, J. (2001), Sulfate Attack Research – Whiter Now?, *Cement and Concrete Research* 31 (6), 845–851.

Scherer, G.W. (2004a), "Factors Affecting Crystallization Pressure," in K.L. Scrivener and J. Scrivener (Eds.), Internal Sulfate Attack: Proceedings of RILEM Workshop on Delayed Ettringite Formation, RILEM Paris.

Scherer, G.W. (2004b), Stress from Crystallization of Salt, *Cement and Concrete Research* 34 (9), 1613–1624.

Schindler, A.K., and Folliard, K.J. (2005), Heat of Hydration Models for Cementitious Materials, *ACI Materials Journal* 102 (1), 24–33.

Schmidt, T., Leemann, A., Gallucci, E., and Scrivener, K.L. (2011), Physical and Microstructural Aspects of Iron Sulfide Degradation in Concrete, *Cement and Concrete Research* 41 (3), 263–269.

Schmitt, R.J., and Mullen, C.X. (1969), Influence of Chromium on the Atmospheric-Corrosion Behavior of Steel, in: *Stainless Steel for Architectural Use, ASTM STP 454,* American Society for Testing and Materials, 124–136.

Schmuki, P. (2002), From Bacon to Barriers: A Review on the Passivity of Metals and Alloys, *Journal of Solid State Electrochemistry* 6 (3), 145–164.

Schuetz, D.P. (2013). Investigation of High Strength Stainless Steel Prestressing Strands. Master's Thesis, Georgia Institute of Technology, 173 pp.

Scrivener, K.L., and Skalny, J.P. (2005), Conclusions of the International RILEM TC 186-ISA Workshop on Internal Sulfate Attack and Delayed Ettringite Formation (4-6 September 2002, Villars, Switzerland), *Materials and Structures* 38 (6), 659–663.

Scrivener, K.L., and Nonat, A. (2011), Hydration of Cementitious Materials, Present and Future, *Cement and Concrete Research* 41 (7), 651–665.

Scrivener, K.L., Juilland, P., and Monteiro, P.J.M. (2015), Advances in Understanding Hydration of Portland Cement, *Cement and Concrete Research* 78, Part A, 38–56.

Sengul, O., and Gjørv, O.E. (2008), Electrical Resistivity Measurements for Quality Control During Concrete Construction, *ACI Materials Journal* 105 (6), 541–547.

Sersale, R., Cioffi, R., Frigione, G., and Zenone, F. (1991), Relationship Between Gypsum Content, Porosity and Strength in Cement. I. Effect of SO_3 on the Physical Microstructure of Portland Cement Mortars, *Cement and Concrete Research* 21 (1), 120–126.

Shirahama, S., Fang, S., Kobayashi, T., and Miyagawa, T. (1999), Basic Properties of Duplex Stainless Prestressing Steel and Flexural Behaviors of Prestressed Concrete Beams Using the Tendon, *Journal of the Society of Material Science Japan* 48 (10), 1199–1206.

Skalny, J., Marchand, J., and Odler, I. (2002). *Sulfate Attack on Concrete*, London and New York: Spon Press, Taylor & Francis Group.

Small, C., and Nicholls, R.J. (2003), A Global Analysis of Human Settlement in Coastal Zones, *Journal of Coastal Research* 19 (3), 584–599.

Small, C. (2011), "The Human Habitat", in: R.P. Cincotta and L.J. Gorenflo (Eds.), Human Population: Its Influences on Biological Diversities, Berlin, Heidelberg, Germany: Springer-Verlag.

Soroka, I., and Abayneh, M. (1986), Effect of Gypsum on Properties and Internal Structure of PC Paste, *Cement and Concrete Research* 16 (4), 495–504.

Tadros, M.K., Al-Omaishi, N., Seguirant, S.J., and Gallt, J.G. (2003). "Prestress Losses in Pretensioned High-Strength Concrete Bridge Girders," NCHRP Report No. 496, National Cooperative Highway Research Program, Transportation Research Board, National Research Council, 73 pp.

Tagnit-Hamou, A., Saric-Coric, M., and Rivard, P. (2005), Internal Deterioration of Concrete by the Oxidation of Pyrrhotitic Aggregates, *Cement and Concrete Research* 35 (1), 99–107.

Tanesi, J., and Ardani, A. (2012). "Surface Resistivity Test Evaluation as an Indicator of the Chloride Permeability of Concrete," FHWA Publication No. FHWA-HRT-13-024, Federal Highway Administration, 6 pp.

Taylor, H.F.W. (1997), *Cement Chemistry, Second Edition*, London: Thomas Telford.

Taylor, H.F.W., Famy, C., and Scrivener, K.L. (2001), Delayed Ettringite Formation, *Cement and Concrete Research* 31 (5), 683–693.

Thomas, M.D.A., Folliard, K., Drimalas, T., and Ramlochan, T. (2008), Diagnosing Delayed Ettringite Formation in Concrete Structures, *Cement and Concrete Research* 38 (6), 841–847.

Thomas, M.D.A., and Ramlochan, T. (2004), Field Cases of Delayed Ettringite, in: K. Scrivener, J. Skalny (Eds.), Proceedings of an International RILEM Workshop on Internal Sulfate Attack and Delayed Ettringite Formation, RILEM Publications SARL, 85–97.

Toribio, J., and Ovejero, E. (2005), Failure Analysis of Cold Dawn Prestressing Steel Wires Subjected to Stress Corrosion Cracking, *Engineering Failure Analysis* 12 (5), 654–661.

Tosun, K., and Baradan, B. (2010), Effect of Ettringite Morphology on DEF-related Expansion, *Cement and Concrete Composites* 32 (4), 271–280.

Tovar-Rodríguez, G., Barra, M., Pialarissi, S., Aponte, D., and Vázquez E. (2013), Expansion of Mortars with Gypsum Contaminated Fine Recycled Aggregates, *Construction and Building Materials* 38, 1211–1220.

Tsuneyuki, S., Aoki, H., Tsukada, M., and Matsui, Y. (1990), Molecular-Dynamics Study of the α to β Structural Phase Transition of Quartz, *Physical Review Letters* 64 (7), 776–779.

Tuuti, K. (1982). "Corrosion of Steel in Concrete," Research Report, Swedish Cement and Concrete Institute, Royal Institute of Technology, Stockholm, Sweden, 472 pp.

U.S. Geological Survey, USGS (2015), "Sand and Gravel (Construction)", in: USGS Mineral Commodity Summaries, U.S. Geological Survey, U.S. Department of the Interior.

van Aardt, J.H.P., and Visser, S. (1977a), Formation of Hydrogarnets: Calcium Hydroxide Attack on Clays and Feldspars, *Cement and Concrete Research* 7 (1), 39–44.

van Aardt, J.H.P., and Visser, S. (1977b), Calcium Hydroxide Attack on Feldspars and Clays: Possible Relevance to Cement-Aggregate Reactions, *Cement and Concrete Research* 7 (6), 643–648.

Wallinder, I.O., Lu, J., Bertling, S., and Leygraf, C. (2002), Release Rates of Chromium and Nickel from 304 and 316 Stainless Steel During Urban Atmospheric Exposure—A Combined Field and Laboratory Study, *Corrosion Science* 44 (10), 2303–2319.

Weyers, R.E., Sprinkel, M.M., and Brown, M.C. (2006). "Summary Report on the Performance of Epoxy-Coated Reinforcing Steel in Virginia," Final Report No.

FHWA/VTRC 06-R29, Federal Highway Administration and Virginia Department of Transportation, 37 pp.

Wight, J.K., and MacGregor, J.G. (2011). *Reinforced Concrete: Mechanics and Design (6th Ed.)*, Upper Saddle River, NJ: Prentice Hall.

Wille, K., and Naaman, A.E. (2013), Effect of Ultra-High-Performance Concrete on Pullout Behavior of High-Strength Brass-Coated Straight Steel Fibers, *ACI Materials Journal* 110 (4), 451–462.

Wu, Y., and Nurnberger, U. (2009), Corrosion-Technical Properties of High-Strength Stainless Steels for the Application in Prestressed Concrete Structures, *Materials and Corrosion* 60 (10), 771–780.

Yujuang, W., Min, D., and Mingshu, T. (2008), Alkali Release from Aggregate and the Effect on AAR Expansion, *Materials and Structures* 41 (1), 159–171.

Yunovich, M., Thompson, N.G., Balvanyos, T., and Lave, L. (2002). "Corrosion Cost and Preventive Strategies in the United States - Appendix D: Highway Bridges," Report No. FHWA-RD-01-156, Federal Highway Administration.

Zhang, X.G. (2011), Galvanic Corrosion, in: R.W. Revie (Ed.), Uhlig's Corrosion Handbook, Third Edition, John Wiley & Sons, Inc., 123–143.

Zhang, Z., Olek, J., and Diamond, S. (2002a), Studies on Delayed Ettringite Formation in Early-Age, Heat-Cured Mortars: I. Expansion Measurements, Changes in Dynamic Modulus of Elasticity, and Weight Gains, *Cement and Concrete Research* 32 (11), 1729–1736.

Zhang, Z., Olek, J., and Diamond, S. (2002b), Studies on Delayed Ettringite Formation in Early-Age, Heat-Cured Mortars: II. Characteristics of Cement that May Be Susceptible to DEF, *Cement and Concrete Research* 32 (11), 1737–1742.

Zia, P., and Mostafa, T. (1977), Development Length of Prestressing Strands, *PCI Journal* 22 (5), 54-65.